frontiers | Research Topics

Natural and artificial radionuclides as tracers of ocean processes

Edited by
Jixin Qiao, Núria Casacuberta and Paul Mcginnity

Published in
Frontiers in Marine Science

ISSN 1664-8714
ISBN 978-2-83252-177-9
DOI 10.3389/978-2-83252-177-9

About Frontiers

Frontiers is more than just an open access publisher of scholarly articles: it is a pioneering approach to the world of academia, radically improving the way scholarly research is managed. The grand vision of Frontiers is a world where all people have an equal opportunity to seek, share and generate knowledge. Frontiers provides immediate and permanent online open access to all its publications, but this alone is not enough to realize our grand goals.

Frontiers journal series

The Frontiers journal series is a multi-tier and interdisciplinary set of open-access, online journals, promising a paradigm shift from the current review, selection and dissemination processes in academic publishing. All Frontiers journals are driven by researchers for researchers; therefore, they constitute a service to the scholarly community. At the same time, the *Frontiers journal series* operates on a revolutionary invention, the tiered publishing system, initially addressing specific communities of scholars, and gradually climbing up to broader public understanding, thus serving the interests of the lay society, too.

Dedication to quality

Each Frontiers article is a landmark of the highest quality, thanks to genuinely collaborative interactions between authors and review editors, who include some of the world's best academicians. Research must be certified by peers before entering a stream of knowledge that may eventually reach the public - and shape society; therefore, Frontiers only applies the most rigorous and unbiased reviews. Frontiers revolutionizes research publishing by freely delivering the most outstanding research, evaluated with no bias from both the academic and social point of view. By applying the most advanced information technologies, Frontiers is catapulting scholarly publishing into a new generation.

What are Frontiers Research Topics?

Frontiers Research Topics are very popular trademarks of the *Frontiers journals series*: they are collections of at least ten articles, all centered on a particular subject. With their unique mix of varied contributions from Original Research to Review Articles, Frontiers Research Topics unify the most influential researchers, the latest key findings and historical advances in a hot research area.

Find out more on how to host your own Frontiers Research Topic or contribute to one as an author by contacting the Frontiers editorial office: frontiersin.org/about/contact

Natural and artificial radionuclides as tracers of ocean processes

Topic editors

Jixin Qiao — Technical University of Denmark, Denmark

Núria Casacuberta — ETH Zürich, Switzerland

Paul Mcginnity — IAEA International Atomic Energy Agency, Monaco

Citation

Qiao, J., Casacuberta, N., Mcginnity, P., eds. (2023). *Natural and artificial radionuclides as tracers of ocean processes*. Lausanne: Frontiers Media SA.

doi: 10.3389/978-2-83252-177-9

Table of contents

05 Editorial: Natural and artificial radionuclides as tracers of ocean processes
Jixin Qiao, Núria Casacuberta and Paul MC. Ginnity

08 Transport and Fate of ^{137}Cs Released From Multiple Sources in the North Atlantic and Arctic Oceans
Vladimir Maderich, Kyeong Ok Kim, Roman Bezhenar, Kyung Tae Jung, Vazira Martazinova and Igor Brovchenko

23 Lagrangian Observation of ^{234}Th and Its Application in Constraining the Sinking of Particulate Organic Carbon on the Slope of the Northeastern South China Sea
Weifeng Yang, Xiufeng Zhao, Min Chen, Yusheng Qiu and Minfang Zheng

33 Developing Accelerator Mass Spectrometry Capabilities for Anthropogenic Radionuclide Analysis to Extend the Set of Oceanographic Tracers
Karin Hain, Martin Martschini, Fadime Gülce, Maki Honda, Johannes Lachner, Michael Kern, Johanna Pitters, Francesca Quinto, Aya Sakaguchi, Peter Steier, Andreas Wiederin, Alexander Wieser, Akihiko Yokoyama and Robin Golser

50 Using Radiocarbon Measurements of Dissolved Inorganic Carbon to Determine a Revised Residence Time for Deep Baffin Bay
Sara Zeidan, Jennifer Walker, Brent G. T. Else, Lisa A. Miller, Kumiko Azetsu-Scott and Brett D. Walker

64 Rapidly Increasing Artificial Iodine Highlights Pathways of Iceland-Scotland Overflow Water and Labrador Sea Water
Maxi Castrillejo, Núria Casacuberta, Christof Vockenhuber and Pascale Lherminier

76 Sources and Cycling of Particulate Organic Matter in Baffin Bay: A Multi-Isotope δ^{13}C, δ^{15}N, and Δ^{14}C Approach
Aislinn Fox and Brett D. Walker

90 Vertical Profiles of ^{226}Ra and ^{228}Ra Activity Concentrations in the Western Subarctic Gyre of the Pacific Ocean
Hirofumi Tazoe, Hajime Obata, Takuya Hara, Mutsuo Inoue, Takahiro Tanaka and Jun Nishioka

99 Fractionation of ^{226}Ra and Ba in the Upper North Pacific Ocean
Pieter van Beek, Roger François, Makio Honda, Matthew A. Charette, Jean-Louis Reyss, Raja Ganeshram, Christophe Monnin and Susumu Honjo

114 Interannual Variations of D$^{14}C_{TOC}$ and Elemental Contents in the Laminated Sediments of the Santa Barbara Basin During the Past 200 Years
Hong-Chun Li, Yiwei Chang, William M. Berelson, Meixun Zhao, Satabdi Misra and Tzu-Tsen Shen

134 Water mass composition in Fram Strait determined from the combination of ^{129}I and ^{236}U: Changes between 2016, 2018, and 2019
A.-M. Wefing, N. Casacuberta, M. Christl and P. A. Dodd

150 Tracing the depth-dependent changes in organic carbon and nutrient fluxes using high-resolution ^{228}Ra profiles in the upper East Sea (Japan Sea)
Hyung-Mi Cho, Yongjin Han, Young-Il Kim, Cheolmin Baek and Guebuem Kim

frontiers | Frontiers in Marine Science

TYPE Editorial
PUBLISHED 31 March 2023
DOI 10.3389/fmars.2023.1170408

OPEN ACCESS

EDITED AND REVIEWED BY
Olivier Bousquet,
UMR8105 Laboratoire de l'Atmosphère et des Cyclones (LACY), France

*CORRESPONDENCE
Jixin Qiao
jiqi@dtu.dk

SPECIALTY SECTION
This article was submitted to Ocean Observation, a section of the journal Frontiers in Marine Science

RECEIVED 20 February 2023
ACCEPTED 23 March 2023
PUBLISHED 31 March 2023

CITATION
Qiao J, Casacuberta N and Ginnity PMC (2023) Editorial: Natural and artificial radionuclides as tracers of ocean processes.
Front. Mar. Sci. 10:1170408.
doi: 10.3389/fmars.2023.1170408

Editorial: Natural and artificial radionuclides as tracers of ocean processes

Jixin Qiao[1]*, Núria Casacuberta[2] and Paul MC. Ginnity[3]

[1]Department of Environmental and Resource Engineering, Technical University of Denmark (DTU), Roskilde, Denmark, [2]Department of Environmental Systems Science, ETH Zurich, Zurich, Switzerland, [3]Department of Nuclear Sciences and Applications, International Atomic Energy Agency (IAEA), Monaco, Monaco

KEYWORDS

ocean processes, ocean dynamics, natural and anthropogenic radioisotopes, radioactive sources, radiotracer applications, data portals

Editorial on the Research Topic
Natural and artificial radionuclides as tracers of ocean processes

Introduction

The global oceans are a repository of radionuclides, both naturally occurring and anthropogenic, the latter originating predominantly from fallout from past atmospheric nuclear weapons tests, discharges from nuclear reprocessing plants and releases following accidents at nuclear facilities. The sources and physical and geochemical properties (e.g., radioactive half-life, solubility, particle reactivity and bioavailability) of these radionuclides vary broadly, giving rise to their use as radiotracers and providing a rich collection of tools for improving our understanding of ocean dynamics and processes. This Research Topic demonstrates how physical oceanographers and marine biogeochemists are currently moving beyond the state-of-the-art in the application of these radiotracers for increasing our knowledge of water circulation, particle cycling and fluxes, sedimentation processes, paleoceanography and more.

Even so, more comprehensive use of radionuclides as tracers in ocean science can be hindered by various factors, including instrumental limitations, complex and laborious analytical procedures, sparse observation data and methodological uncertainty. Looking forward, we also consider below ways in which these are already being overcome.

Tracing water mass movement

Conservative radionuclides with known historical inputs in seawater can be used to track the movement of water masses, both at surface and abyssal layers, thus unraveling pathways, mixing regimes, transit times and ventilation rates. Point-source discharges of radionuclides from nuclear facilities, e.g., ^{129}I and ^{236}U and other radionuclides from the two European reprocessing plants (La Hague and Sellafield), provide a valuable means for tracking Atlantic water transport pathways (Castrillejo et al.), and for finger-printing water mass compositions and determining circulation timescales (Wefing et al.) in the North Atlantic and Arctic Ocean. Anthropogenic radionuclides (e.g., ^{137}Cs) distributed at global or regional scales are useful tracers for validating and refining ocean-earth system models (Maderich et al.), thus

facilitating improved projections of future changes in ocean circulation and the fate of contaminants in the marine environment under a changing climate. In addition, radioisotopic signatures can be exploited for estimating deep-water residence times, revealing mechanisms leading to deep-water formation [e.g., $\Delta^{14}C$ in dissolved organic carbon (Zeidan et al.)], and for deriving vertical mixing patterns in the water columns and providing holistic insights into geochemical cycles of carbon and nutrients in the ocean [e.g., ^{226}Ra-^{228}Ra (Tazoe et al.; Cho et al)].

Tracing particle dynamics

Combinations of radionuclides with different half-lives and geochemical properties can be used to estimate the rates of particulate organic carbon (POC) export to the deep ocean. The naturally occurring ^{234}Th-^{238}U radionuclide pair has been widely used to quantify the sinking flux of POC. The effects of horizontal advection and vertical diffusion (Yang et al.) can be taken into account for improved evaluation of uncertainties in the POC flux estimation using ^{234}Th-model. Coupling of signals from both radioisotopes and stable isotopes enhances the tracer approach in biogeochemical studies for understanding changes in ecosystems, e.g., by using a $\delta^{13}C$-$\delta^{15}N$-$\Delta^{14}C$ multi-isotope approach for discerning the sources and cycling of particulate organic matter (POM) in the deep ocean basin (Fox and Walker), and by studying the fractionation of stable Ba and radioactive ^{226}Ra for verifying uncertainty in the use of ^{226}Ra for marine carbonates dating (Beek et al.).

Constructing sediment chronology

Construction of sediment chronologies has been widely carried out based on dating methodologies using other naturally occurring radionuclides, e.g., ^{210}Pb and ^{14}C (Li et al.), which facilitate insights into paleoclimate records and understanding of past climatic and oceanographic variabilities. For probing more recent changes, anthropogenic radionuclides, especially those resulting from global fallout from atmospheric nuclear weapon tests (e.g., ^{14}C, ^{137}Cs, $^{239,240}Pu$, ^{241}Am), provide additional benchmarks to the sediment age-depth models.

The way forward

Advancements in analytical techniques have paved the way for the application of novel radiotracers. Continuing enhancement of techniques such as Accelerator Mass Spectrometry (AMS) is key for the future development of new tracers in the oceans. In the last decade, this has led to the emergence of long-lived radionuclides such as ^{236}U and ^{233}U as novel ocean tracers. Applied both individually and in combination with other AMS-measured radionuclides such as ^{129}I and ^{14}C, these have been proven invaluable for understanding ocean physical processes (Wefing et al.). Other recent developments in measurement techniques, such as Ion-Laser Interaction Mass Spectrometry (ILIAMS) (Hain et al.), enable the determination of radionuclide concentrations in seawater samples at ultra-low levels and have facilitated the development of novel radiotracers (e.g., ^{135}Cs).

There are many other radiotracer applications which are not covered in depth by this Research Topic but which also have the potential to revolutionize the field of tracer oceanography. New measurement techniques such as Atom Trap Trace Analysis, (a laser-based atom counting method that can reach atomic ratios as low as 10^{-16}) are emerging as powerful alternatives to the decay counting techniques that will complement the ones mentioned above and expand the suit of radionuclides (e.g., ^{81}Kr, ^{85}Kr and ^{39}Ar) available to understand oceanic processes and timescales.

Sparse observation data coverage is a major obstacle hindering broader and more comprehensive research of ocean processes utilizing radiotracers. Marine sampling campaigns and sophisticated laboratory analyses are both expensive and time-consuming. A means of mitigating this is for researchers to share their measurement results openly and accessibly, thus enabling re-use of existing data for a range of activities, such as comparison with new observations, background research for new projects, and conducting reanalysis to address new research questions.

The Marine Radioactivity Information System (MARIS), managed and developed by the IAEA Marine Environment Laboratory in Monaco, is a data portal that provides open access to a broad range of radionuclides measurements in coastal and open ocean seawater, marine sediment and biota. Currently, more than 800,000 measurements are available, sourced mainly from scientific articles and national and regional databases, covering all areas of the global oceans and from 1957 up to the present day. MARIS is currently being developed to offer improved means of identifying and accessing data, higher quality and richer metadata and support to data management principles such as FAIR and GEO. The IAEA welcomes all submissions of relevant datasets and suggestions for further enhancement.

In summary, to continue to broaden the use of radionuclides in oceanographic research, we foresee the need for further development of novel and emerging radiotracers for oceanographic studies, itself directly related to further advances in cutting-edge measuring techniques, and of open-source data platforms.

Author contributions

All authors listed have made a substantial, direct, and intellectual contribution to the work and approved it for publication.

Acknowledgments

We thank all the authors, reviewers and editors for their contribution to this Research Topic.

Conflict of interest

The authors declare that the research was conducted in the absence of any commercial or financial relationships that could be construed as a potential conflict of interest.

Publisher's note

frontiers in Marine Science

ORIGINAL RESEARCH
published: 23 December 2021
doi: 10.3389/fmars.2021.806450

Transport and Fate of ^{137}Cs Released From Multiple Sources in the North Atlantic and Arctic Oceans

Vladimir Maderich[1], Kyeong Ok Kim[2], Roman Bezhenar[1], Kyung Tae Jung[3], Vazira Martazinova[4] and Igor Brovchenko[1]*

[1] Institute of Mathematical Machine and System Problems, Kyiv, Ukraine, [2] Korea Institute of Ocean Science and Technology, Busan, South Korea, [3] Oceanic Consulting and Trading, Seoul, South Korea, [4] Ukrainian Hydrometeorological Institute, Kyiv, Ukraine

The North Atlantic and Arctic oceans, along with the North Pacific, are the main reservoirs of anthropogenic radionuclides introduced in the past 75 years. The POSEIDON-R compartment model was applied to the North Atlantic and Arctic oceans to reconstruct ^{137}Cs contamination in 1945–2020 due to multiple sources: global fallout, exchange flows with other oceans, point-source inputs in the ocean from reprocessing plants and other nuclear facilities, the impact of the Chernobyl accident and secondary contamination resulting from river runoff and redissolution from bottom sediments. The model simulated the marine environment as a system of 3D compartments comprising the water column, bottom sediment, and biota. The dynamic model described the transfer of ^{137}Cs through the pelagic and benthic food chains. The simulation results were validated using the marine database MARIS. The calculated concentrations of ^{137}Cs in the seaweed and non-piscivorous and piscivorous pelagic fish mostly followed the concentration of ^{137}Cs in water. The concentration in coastal predator fish lagged behind the concentration in water as a result of a diet that includes both pelagic and benthic organisms. The impact of each considered source on the total concentration of ^{137}Cs in non-piscivorous fish in the regions of interest was analyzed. Whereas the contribution from global fallout dominated in 1960–1970, in 1970–1990, the contribution of ^{137}Cs released from reprocessing plants exceeded the contributions from other sources in almost all considered regions. Secondary contamination due to river runoff was less than 4% of ocean influx. The maximum total inventory of ^{137}Cs in the Arctic Ocean (31,122 TBq) was reached in 1988, whereas the corresponding inventory in the bottom sediment was approximately 6% of the total. The general agreement between simulated and observed ^{137}Cs concentrations in water and bottom sediment was confirmed by the estimates of geometric mean and geometric standard deviation, which varied from 0.89 to 1.29 and from 1.22 to 1.87, respectively. The approach used is useful to synthesize measurement and simulation data in areas with observational gaps. For this purpose, 13 representative regions in the North Atlantic and Arctic oceans were selected for monitoring by using the "etalon" method for classification.

Keywords: North Atlantic, Arctic Ocean, Nordic Seas, ^{137}Cs, compartment model, dynamic food web model, classification

OPEN ACCESS

Edited by:
Jixin Qiao,
Technical University of Denmark, Denmark

Reviewed by:
Neven Cukrov,
Ruđer Bošković Institute, Croatia
Luca Giorgio Bellucci,
National Research Council (CNR), Italy

****Correspondence:***
Vladimir Maderich
vladmad@gmail.com

Specialty section:
This article was submitted to Ocean Observation, a section of the journal Frontiers in Marine Science

Received: *31 October 2021*
Accepted: *08 December 2021*
Published: *23 December 2021*

Citation:
Maderich V, Kim KO, Bezhenar R, Jung KT, Martazinova V and Brovchenko I (2021) Transport and Fate of ^{137}Cs Released From Multiple Sources in the North Atlantic and Arctic Oceans. Front. Mar. Sci. 8:806450. doi: 10.3389/fmars.2021.806450

INTRODUCTION

The North Atlantic and Arctic oceans along with the North Pacific are the main reservoirs of anthropogenic radionuclides introduced in the past 75 years from different sources (Nyffeler et al., 1996; Kershaw, 2011; Zaborska and Carroll, 2011). Both oceans are connected through the Nordic seas (Greenland, Iceland, and Norwegian seas). Therefore, they should be considered as one system. Global fallout from atmospheric nuclear weapon tests dominated in the sixties, and the main contributors were ^{137}Cs and ^{90}Sr. Regional contamination of the sea also occurred as a result of nuclear weapon tests in the atmosphere over Novaya Zemlya and as a result of underwater explosions in Chernaya Bay on the southern island of the Novaya Zemlya Archipelago. Point-source inputs in the ocean from reprocessing plants Sellafield (United Kingdom) and Cap de La Hague (France) were also significant. Several nuclear facilities located in the basins of Siberian rivers contaminated the Arctic Ocean. Two global-scale accidents [Chernobyl and Fukushima Daiichi nuclear power plants (NPPs)] and several local accidents (e.g., Thule accident) resulted in contamination of areas in both the North Atlantic and Arctic oceans. Potential point

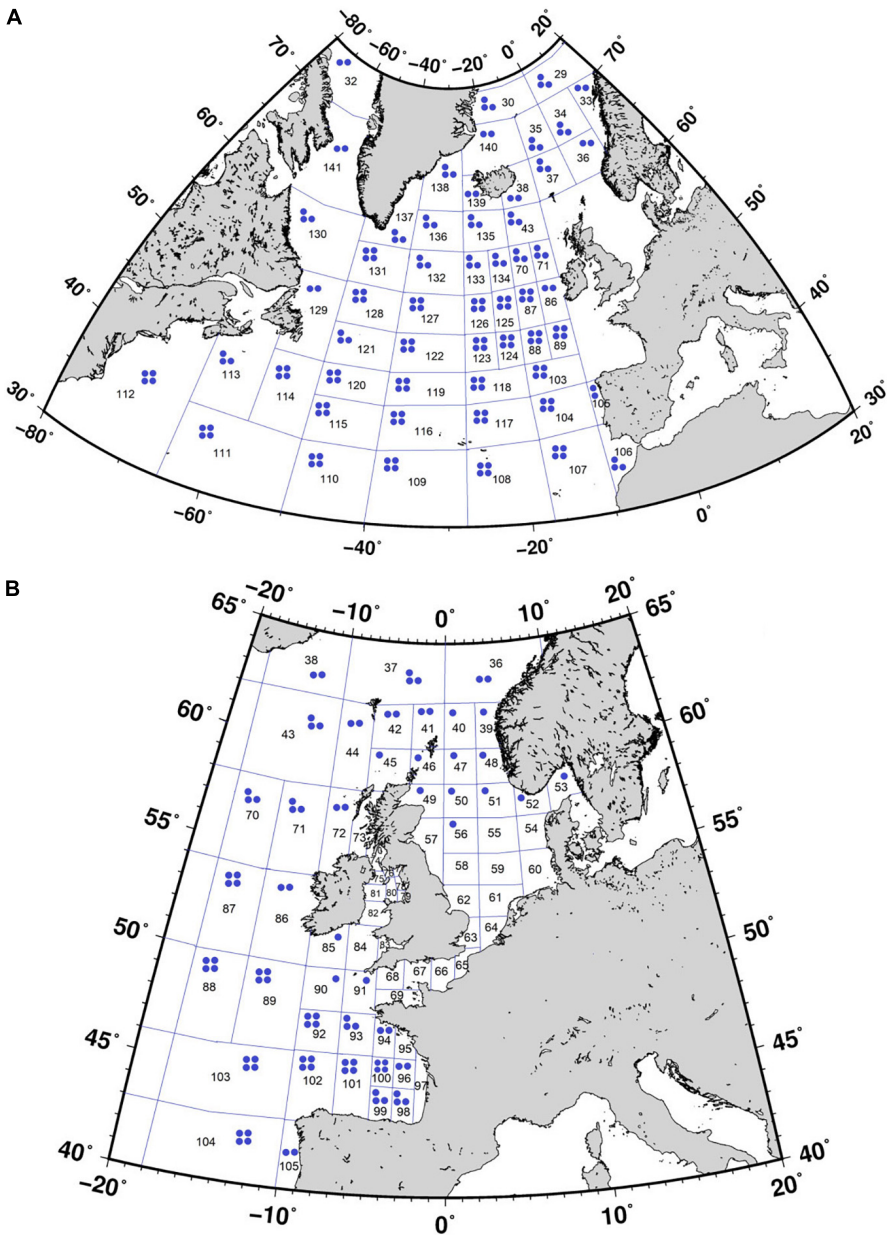

FIGURE 1 | Box system for the North Atlantic **(A)** and the North Sea, Irish Sea, and Biscay Bay **(B)**. Box numbers are shown. Each box includes a surface layer in the water column. Blue dots denote the number of layers under the surface layer.

sources of radioactivity include dumped liquid and solid nuclear wastes and sunken submarines. The released radionuclides were inhomogeneously distributed in the ocean where they were transported by currents and migrated in the bottom sediments and through the food web. Marine and river bottom sediments and river flood plains were secondary sources of contamination.

The ^{137}Cs distributions in the North Atlantic and Arctic oceans have been monitored since the sixties and have reported in several surveys (IAEA, 1995, 2005; AMAP, 1998, 2004, 2010, 2016; OSPAR, 2021). Data were collected in the frame of the ongoing LAMER (2017–2021) project and the IAEA MARIS database (MARIS, 2021). However, the monitoring data are distributed very heterogeneously in time and space. Therefore, modeling is necessary to reconstruct the distribution of radioactivity and to estimate doses for population and biota in areas with sparse measurements. Several studies have been devoted to the modeling of the intake and redistribution of cesium during the entire nuclear era in water, sediments, and biota in the marginal seas of the Atlantic Ocean, such as the Mediterranean Sea, North Sea, and Baltic Sea (e.g., CEC, 1990; EC, 2002; Maderich et al., 2018a,b; Bezhenar et al., 2019), as well as in the Arctic Ocean (Iosjpe et al., 2002; Johannessen et al., 2010). However, these studies did not consider in detail the North Atlantic and Arctic oceans as a system or the contribution from different sources to local concentrations of ^{137}Cs.

In this study, our objective was to assess long-term changes in ^{137}Cs distribution in the marine environment of the North Atlantic-Arctic Ocean system in the 1945–2020 period. The POSEIDON-R compartment model (Lepicard et al., 2004; Maderich et al., 2018b) was applied to estimate the time-varying contribution from different sources to the distribution of ^{137}Cs in water, sediments, and biota and to select representative areas for monitoring purposes. This paper is organized as follows. The compartment model and the dynamic food web model are

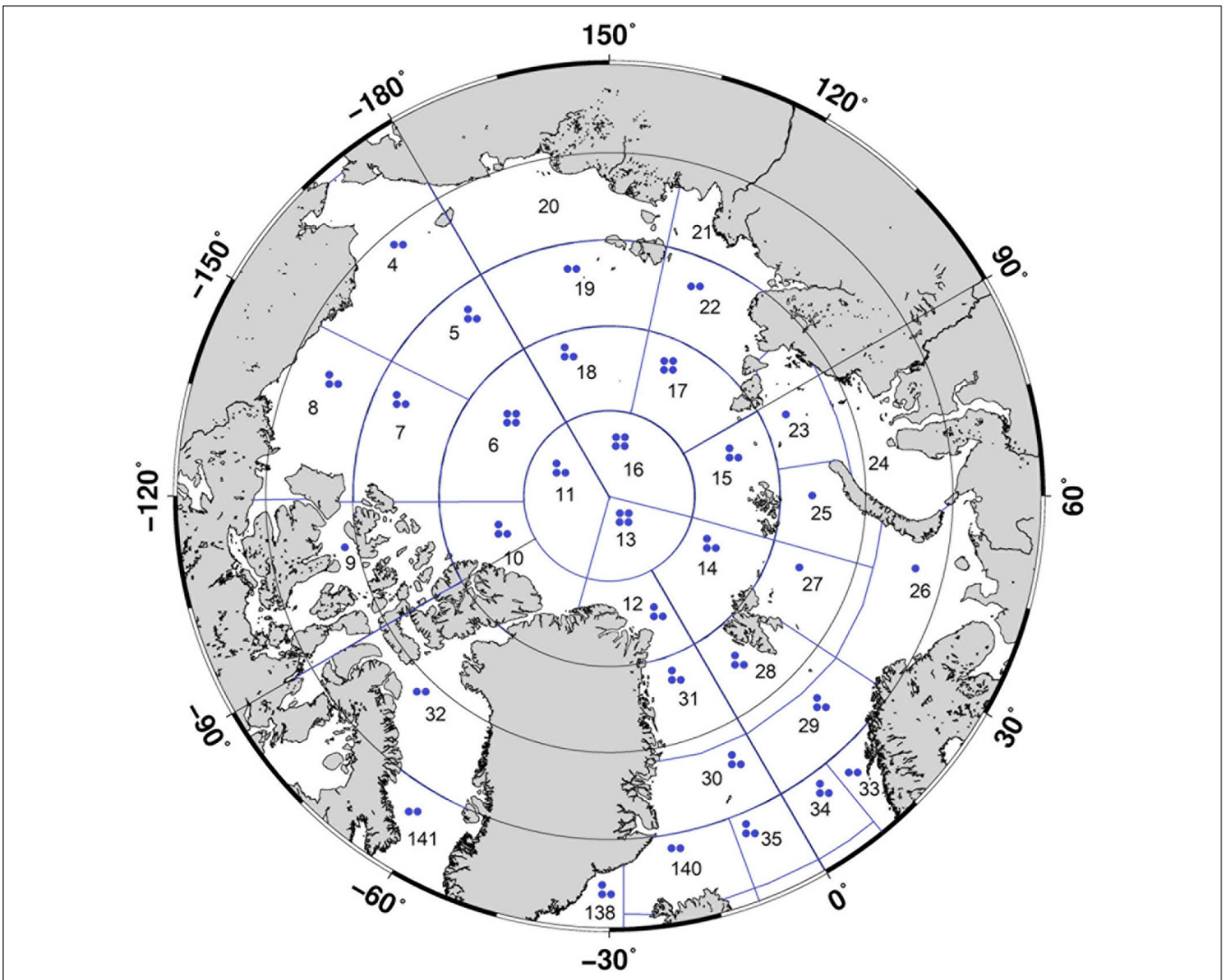

FIGURE 2 | Box system for the Arctic Ocean. Box numbers are shown. Each box includes a surface layer in the water column. Blue dots denote the number of layers under the surface layer.

briefly described in Section "MATERIALS AND METHODS," as well as the model setup to the area of interest. The modeling results for the water, sediments, and biota are presented in Section "RESULTS." Our findings are summarized in the Conclusions.

MATERIALS AND METHODS

Compartment Model POSEIDON-R

The compartment model was chosen in this study because it is well suited for long-term and large-scale assessments of radionuclide dispersion and transfer in biota (Periáñez et al., 2019). The marine environment is considered a system of 3D compartments (boxes) in the POSEIDON-R compartment model (Lepicard et al., 2004; Bezhenar et al., 2016; Maderich et al., 2018b). The compartment system includes the water column, bottom sediment, and biota compartments (**Supplementary Figure 1**). The water column compartment is vertically subdivided into layers and contains suspended matter that continuously settles down. Radionuclides in the water column are assumed to be partitioned into dissolved and particulate fractions by the distribution coefficient K_d. The radionuclide concentration in each water compartment is found as a solution of a set of differential equations, in which temporal variations in the concentration depend on the exchange of radionuclides between adjacent compartments, the exchange between radionuclides in solute, suspended sediments, and bottom sediments, and the radioactivity sources and decay.

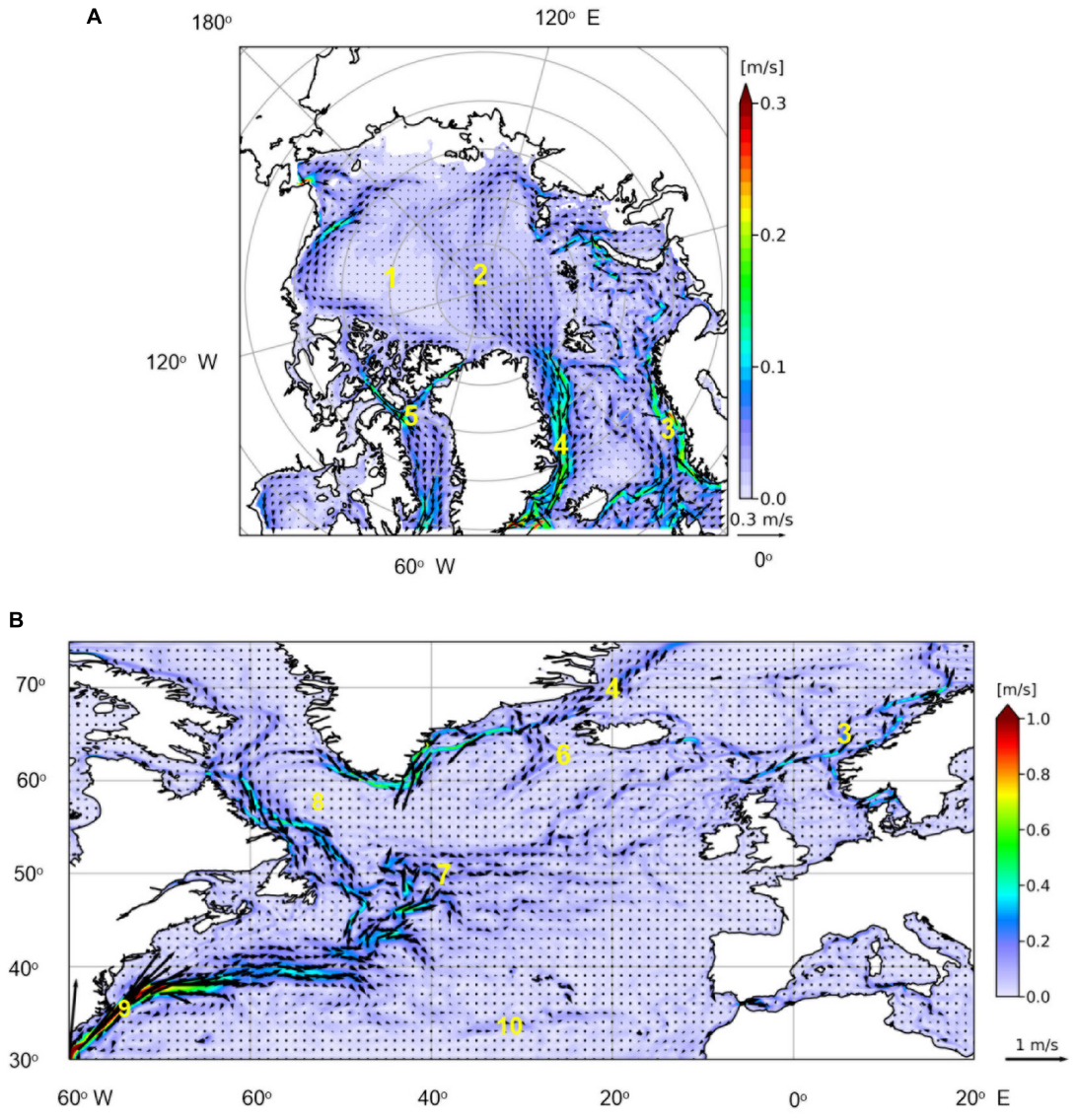

FIGURE 3 | Time-average surface currents calculated from CMEMS (2021) ocean reanalysis data in the Arctic **(A)** and North Atlantic **(B)** oceans. Main currents: 1—Beaufort Gyre, 2—Transpolar Drift, 3—Atlantic/Norwegian Current, 4—East Greenland Current, 5—Irminger Current, 6—North Atlantic Current, 7—Subpolar gyre, 8—Subtropical gyre, and 9—Gulfstream.

Exchanges between the water column compartments include radionuclide fluxes due to advection, sediment settling, and turbulent diffusion. The bottom sediment in each compartment consists of three layers. The transfer of radioactivity between the upper sediment layer and the water column is governed by resuspension, diffusion, and bioturbation processes. Only diffusion is active between the upper and middle sediment layers. Downward burial processes occur in all three sediment layers. Maderich et al. (2018b) described the POSEIDON-R compartment model in detail. The POSEIDON-R model can handle different types of radioactive releases, such as atmospheric fallout, river runoff of land-deposited radionuclides, point sources associated with both routine direct releases and accidental releases from nuclear facilities located on the coast or inland in rivers (Lepicard et al., 2004).

The uptake of radionuclides by marine organisms is dynamically modeled in the POSEIDON-R compartment model. All organisms take in radionuclides both *via* the food web and directly from the water. Pelagic and benthic food chains are described in the model (Bezhenar et al., 2016). All marine organisms are grouped into classes according to trophic level and type of species (**Supplementary Figure 1B**). In turn, radionuclides are grouped into four classes according to the type of fish tissue where they preferentially accumulate (e.g., ^{137}Cs tends to accumulate in muscle). These simplifications allow for a limited number of standard input parameters. The pelagic food chain includes primary producers (phytoplankton) and consumers [zooplankton, non-piscivorous (forage) fish, and piscivorous fish]. In the benthic food chain, radionuclides are transferred from algae and organic components of contaminated bottom sediments to deposit-feeding invertebrates, demersal fish, and benthic predators. It is assumed that radioactivity is assimilated by benthic organisms only from the organic component of the bottom deposits, which is in mutual equilibrium with an inorganic component. Crustaceans (detritus feeders), mollusks (filter feeders), and coastal predators, which feed throughout the water column in shallow coastal waters, are also considered in the model. Details of the transfer of radiocesium through the marine food web are presented by Bezhenar et al. (2016) and Maderich et al. (2018b).

Model Setup

A box system for the North Atlantic and Arctic Ocean (**Figures 1**, **2**) was built by using bathymetry data from the Copernicus Marine Environment Monitoring Service (CMEMS, 2021). The water column in each box was divided vertically into up to five layers: 0–50 (surface layer), 50–250, 250–1,000, 1,000–2,500 m, and from 2,500 m to the bottom; the number of layers in each box depends on the total water depth in that box. These boxes include three layers of bottom sediment. The total number of boxes covering the North Atlantic-Arctic Ocean is 159, of which 16 boxes correspond to the main rivers in the region (**Supplementary Table 1**). Each box in **Figures 1**, **2** has a surface layer in the water column. Blue dots denote the number of layers under the surface layer. Advective and diffusional water transport between boxes was calculated by averaging three-dimensional currents in the available CMEMS (2021) reanalysis data over 10 years (2008–2017).

The time-average surface currents calculated from reanalysis in the North Atlantic and Arctic oceans are shown in **Figure 3**. The main currents include the Gulfstream, North Atlantic Current, Atlantic/Norwegian Current, Beaufort Gyre, Transpolar Drift, and East Greenland Current. They transport contamination from sources. Subsurface currents complete the circulation. The compartment structure was chosen to describe fluxes by these main currents in the North Atlantic-Arctic Ocean system and to take into account all important coastal sources of radioactivity entering the ocean from coastal facilities and rivers. The model includes exchange flows of a radionuclide with the Mediterranean Sea obtained from the regional compartment model of the Mediterranean Sea (Bezhenar et al., 2019) and contamination fluxes through Danish straits from the regional compartment model of the Baltic Sea (Maderich et al., 2018a). Fluxes through the Bering Strait and the southern boundary of the North Atlantic were based on corresponding observed concentrations of the radionuclide. In **Figure 2B**, the box system

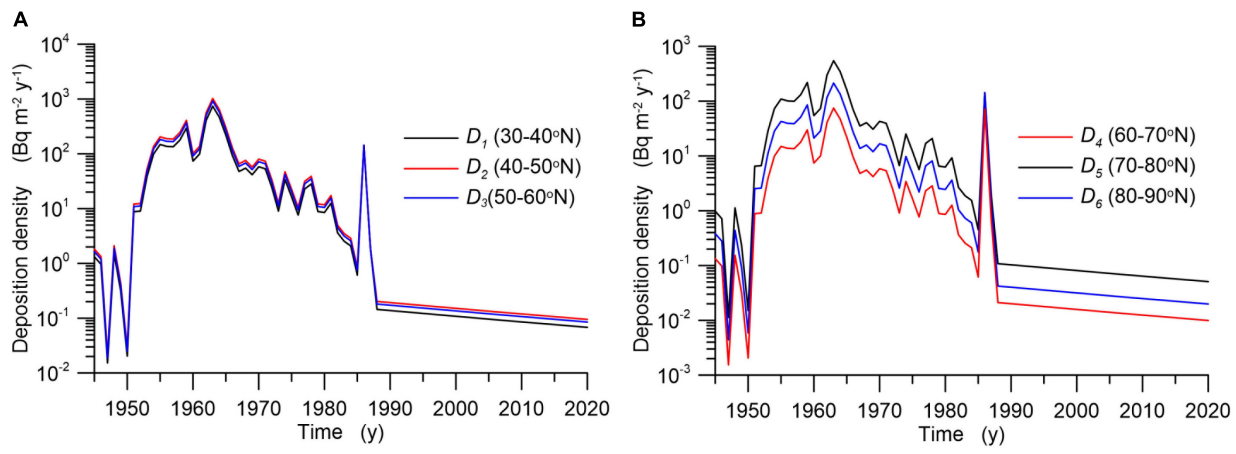

FIGURE 4 | Global deposition densities D_i (Bq m^{-2}) for the i-th latitude belts. i = 1,..,3 **(A)**, i = 4,...,6 **(B)**.

for the North and Irish seas is shown. This box system is based on the North Sea model (Maderich et al., 2018b), and it describes in detail areas around reprocessing plants (Sellafield and Cap de la Hague).

Global Deposition of ^{137}Cs Due to Nuclear Weapon Tests

Atmospheric nuclear tests in the 1950s–1960s contaminated oceans and land globally. In this study, the annual deposition of ^{137}Cs in each box due to global fallout was calculated using data (UNSCEAR, 2000) on deposition density, which depends on latitude (**Figure 4**), and box surface area. These data are available for the 1950–1987 period. For the 1988–2020 period, we made the conservative assumption that the deposition flux was equal to the average value in 1982–1987 corrected for radioactive decay. Note that the values obtained in this extrapolation are very low in comparison with historical values in previous decades; therefore, they did not affect the concentration of radionuclides in the marine environment. In the Arctic, regional fallout occurred as a result of atmospheric tests on Novaya Zemlya (Miroshnikov et al., 2017). However, there are no data on the deposition distribution. Note that the effect of underwater nuclear weapon tests conducted in the 1950s in Chernaya Bay was local (Smith et al., 2000), and this source was also not taken into account.

Source of ^{137}Cs Due to Nuclear Accidents

Two major accidents (Chernobyl and Fukushima-Daiichi) affected the contamination of the oceans. Deposition as a result of the Chernobyl accident was an important factor in northwestern Europe. Following Mitchell and Steele (1988), the apparent deposition density onto the northern area of the North Sea was 3,400 Bq m^{-2} in 1986, whereas it was 1,500 Bq m^{-2} onto the central area and 320 Bq m^{-2} onto the southern area. These values were distributed between compartments covering the North Sea accordingly. In addition, deposition due to the Chernobyl accident was included as an additional component of global deposition in 1986 (**Figure 4**). It was estimated based on measurements conducted far from the Chernobyl NPP, e.g., in Tsukuba (Japan), the deposition density of ^{137}Cs in 1986 was measured to be equal to 135 Bq m^{-2} (Aoyama, 2018). The measurements (Smith et al., 2015) suggest that the Fukushima-derived radionuclides were not deposited within the Arctic Ocean in 2011.

An increase in the ^{137}Cs concentration in the Bering Sea in 2017 (Kumamoto et al., 2017) was caused by large-scale ocean circulation resulting in an increase in transport through the Bering Strait into the Arctic Ocean [see Subsection Releases From Reprocessing Plants, Sellafield (United Kingdom) and Cap de la Hague (France)].

Releases From Reprocessing Plants, Sellafield (United Kingdom) and Cap de la Hague (France)

In the 1951–2020 period, an amount of 41.4 PBq of ^{137}Cs was released from the Sellafield reprocessing plant located in the Irish Sea, and 1.04 PBq of ^{137}Cs was released from the Cap de La Hague reprocessing plant. In **Figure 5A**, the annual values of these releases for both reprocessing plants are shown (OSPAR, 2021).

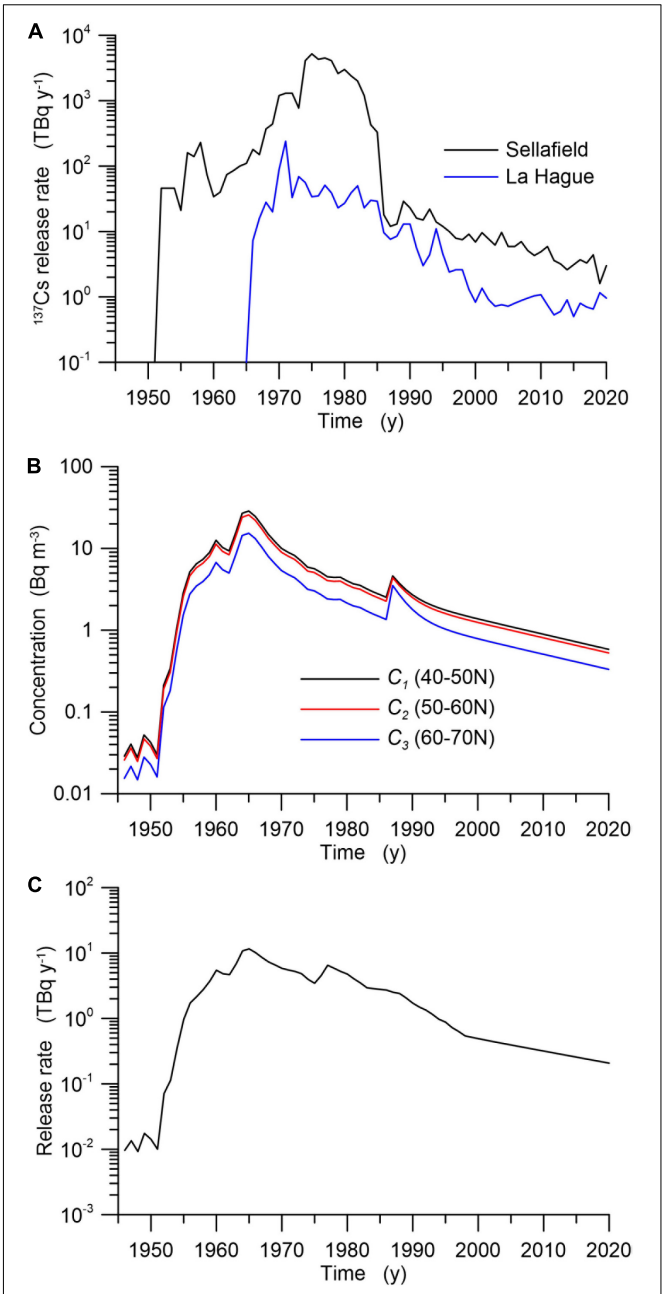

FIGURE 5 | Release rate of ^{137}Cs from the reprocessing plants (Bq y^{-1}) **(A)**; ^{137}Cs in the river mouth for different latitude belts **(B)**; and the influx of ^{137}Cs to the Kara Sea from the Yenisei River **(C)**.

The Mayak Production Association (Mayak PA) is located within the Ob′ River drainage basin. Direct discharges of radionuclides from the Mayak PA were made between 1949 and 1956 to the Techa River system, which is part of the Ob′ drainage basin. The estimated amount of released ^{137}Cs varied from 1.9 to 13 PBq (Semenkov and Miroshnikov, 2015). There were no direct measurements of the concentration in water in the estuary of the

Ob′ River during this period; however, some estimates show that less than 1% could have reached the mouth of the Ob′ River due to the long distance to the location of release (more than 2,000 km) and significant sedimentation on the entire path (Semenkov and Miroshnikov, 2015). The measurements of deposited ^{137}Cs and ^{239,240}Pu in the Ob River delta suggested that both were delivered from atmospheric fallout (Sayles et al., 1997). Therefore, we assumed no input ^{137}Cs from the Mayak PA to the Kara Sea. The inflow of ^{137}Cs in the Kara Sea from another nuclear facility in the Ob′ River basin (Siberian Chemical Combine) was also negligible (Semenkov and Miroshnikov, 2015).

The Krasnoyarsk Mining and Chemical Industrial Combine (KMCIC) is located on the Yenisei River at a distance of approximately 2,500 km upstream from the Kara Sea. The influx of ^{137}Cs with Yenisei River waters in the Kara Sea (**Figure 5C**) was estimated as the sum of the model-predicted distribution from the KMCIC source from Johannessen et al. (2010) and the generic river runoff model (Smith et al., 2004). The estimated input of ^{137}Cs into the Kara Sea as a result of KMCIC routine release was approximately 74 TBq, which was in the range of estimated 30–100 TBq by Vakulovsky et al. (1995).

Discharges of ^{137}Cs With River Waters

The influx of ^{137}Cs into the sea with river waters due to flushing of deposited radionuclide in the river basin was estimated by using a generic river runoff model (Smith et al., 2004) for the total period of calculations. In this study, we consider 16 main rivers with climatic yearly average runoff (**Supplementary Table 1**). The calculated generic model concentration of ^{137}Cs in the river water (**Figure 5B**) was multiplied by river water flux to estimate the influx of ^{137}Cs. The influx of ^{137}Cs in the Kara Sea from both river runoff and discharge from KMCIC is given in **Figure 5C**.

Fluxes of ^{137}Cs at the Open Boundaries

Four boundaries are considered in the model: Bering Strait, Central Atlantic, Gibraltar, and Danish straits. For this purpose, the source of ^{137}Cs was prescribed for the Bering Sea box to obtain the concentration, which would be in agreement (**Supplementary Figure 2C**) with corresponding measurements (MARIS, 2021). Note that the increase in ^{137}Cs concentration after 2010 was caused by contamination due to the Fukushima NPP accident (Kumamoto et al., 2017). Similarly, the fluxes of activity were prescribed for boxes on the open boundary with the Central Atlantic, where an agreement obtained in the model concentrations with measurements (MARIS, 2021) was also achieved (**Supplementary Figure 2A**). The concentration in the Gibraltar Strait (**Supplementary Figure 2B**) calculated using simulation output from the Mediterranean Sea modeling (Bezhenar et al., 2019) was in agreement with measurements (MARIS, 2021). The results of modeling for ^{137}Cs transport in the Baltic Sea (Bezhenar et al., 2016) were used to obtain the flux of activity from the Baltic Sea to the North Sea through the Danish straits (**Supplementary Figure 2D**).

RESULTS

Concentration of ^{137}Cs in the Water

In **Figure 6**, the calculated model concentrations of ^{137}Cs in the water layers in the different boxes are compared with the corresponding measurements (MARIS, 2021). The temporal changes in concentration across the Nordic seas (Norwegian, Greenland, and Iceland seas) are shown in **Figures 6A–C**. Released from the Sellafield reprocessing plant, ^{137}Cs is transported by the Norwegian current to the northeast (see **Figure 3B**). Part of the contaminated water turns to the North

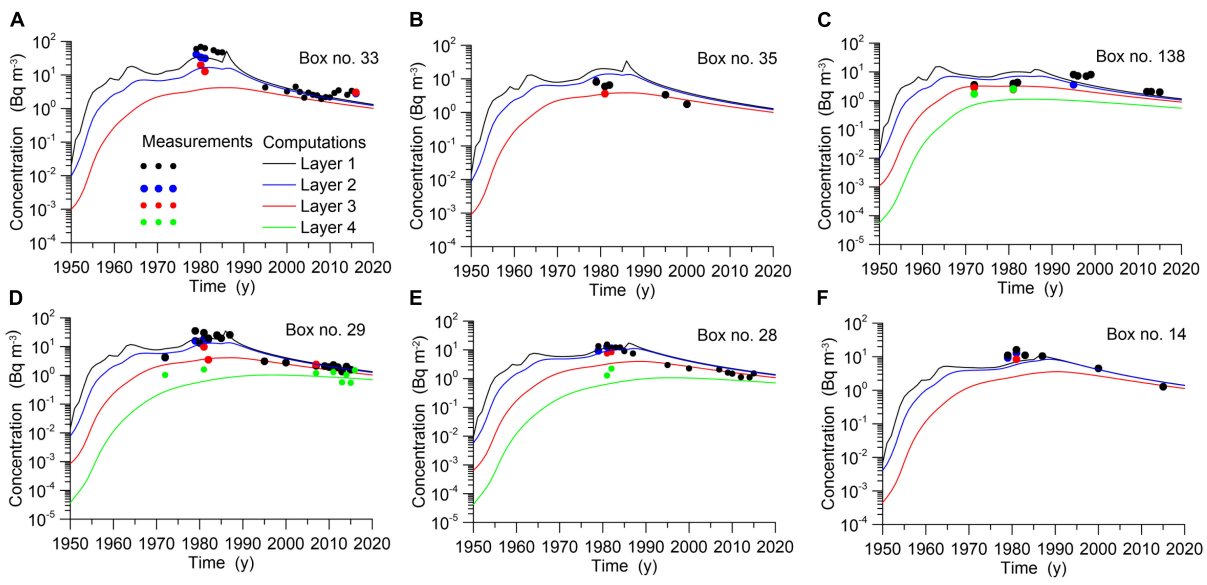

FIGURE 6 | The comparison of simulated temporal changes of ^{137}Cs in the water with measured (MARIS, 2021) concentration in Box no. 33 **(A)**, 35 **(B)**, 138 **(C)**, 29 **(D)**, 28 **(E)**, and 14 **(F)**.

Sea, whereas another part is transported by the Norwegian Current along the Norway coast (**Figure 6A**, Box no. 33). The Sellafield signal is also visible in Box nos. 35 and 138 placed in the center of the ocean and in the Denmark Strait, where contamination is transported by the East Greenland Current. The meridional distribution of ^{137}Cs is shown in **Figures 6D–F**. As seen in these figures, ^{137}Cs of Sellafield origin is transported to Spitsbergen by the West Spitsbergen Current (Box no. 33, 29, and 28), but this signal in Box 14 is weak, suggesting that radioactivity is transported by Transpolar Drift from the central Arctic. The agreement of model predictions with observations is quite good.

Concentration of ^{137}Cs in the Sediments

The temporal changes in 137Cs concentration in the bottom sediments differ for different regions of the North Atlantic and Arctic oceans. In **Figures 7A–C**, the computed concentrations in the surface layer of bottom sediment were compared with measurements (MARIS, 2021). Box no. 14 (**Figure 7A**) is located in the central Arctic. As seen in the figure, here, concentration monotonously increases in the total 1950–2020 period, which indicates a gradual influx of activity due to transport by Transpolar Drift. At the same time, the maximum in **Figure 7B** (Box no. 27) indicates the inflow of contaminated waters from Sellafield along the Norwegian coast. Following the decrease in the source intensity, the ^{137}Cs concentration decreased after 1980. In the Kara Sea (**Figure 7C**, Box no. 24), the concentration changes slightly due to gradual inflow of radioactivity: initially due to global fallout, then from river inflow, and later from the inflow of water from reprocessing plants.

Concentration of ^{137}Cs in the Barents Sea

The Barents Sea, represented by three boxes (nos. 25, 26, and 27), is a case of particular interest due to the location of the sea and the presence of multiple sources of pollution. The Barents Sea is a shallow marginal shelf sea of the Arctic Ocean located between the continent and the Spitsbergen, Franz Josef, and Novaya Zemlya archipelagos. Atlantic water inflows from the south, whereas Polar water enters the sea from the north. Multiple sources of pollution include global fallout, river influx, the inflow of water from reprocessing plants, and exchange with the Kara Sea. Therefore, the Barents Sea has been intensively monitored in the past 40 years (Zaborska et al., 2010; Gwynn et al., 2012; Leppanen et al., 2013). The temporal changes in ^{137}Cs concentration in the water, bottom sediments, and biota in Box no. 26 are given in **Figure 8**. As seen in **Figure 8**, the first maximum ^{137}Cs concentration in water caused by global fallout was observed in 1963, whereas the second maximum ^{137}Cs concentration in water in 1980–1985 was due to the influx of contaminated water from Sellafield. The last maximum in 1986–1987 was associated with Chernobyl atmospheric deposition and the subsequent inflow of Chernobyl contamination from the North Atlantic by currents. Then, the concentration in water gradually decreased. The maximum ^{137}Cs concentration in the upper layer of bottom sediments was delayed by 10 years (**Figure 8B**). Subsequently, the ^{137}Cs concentration

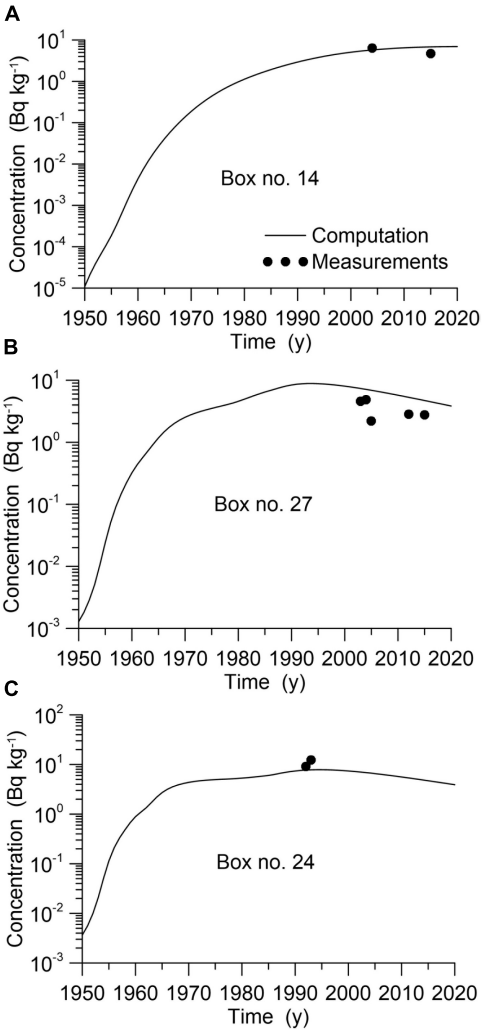

FIGURE 7 | The comparison of simulated temporal changes of ^{137}Cs in the bottom sediment with measured (MARIS, 2021) concentration in Box no. 14 **(A)**, 27 **(B)**, and 24 **(C)**.

decreased following a decrease in the intensity of the source. The concentrations of ^{137}Cs in the seaweed (**Figure 8C**) and the non-piscivorous and piscivorous pelagic fishes (**Figures 8D,E**) mostly following the concentration of ^{137}Cs dissolved in the water. At the same time, the concentration in coastal predators (represented by cod, *Gadus morhua*) lagged behind the concentration in water (**Figure 8F**). This is explained by the diet of coastal predators, which includes both pelagic and benthic organisms feeding on organic matter in the bottom sediments (Bezhenar et al., 2016).

Contribution From Different Sources to the Concentration of ^{137}Cs in Non-piscivorous Fish

Compartment modeling allows us to easily estimate the contribution from each of the sources to the pollution of the marine environment. The non-piscivorous fish were selected as

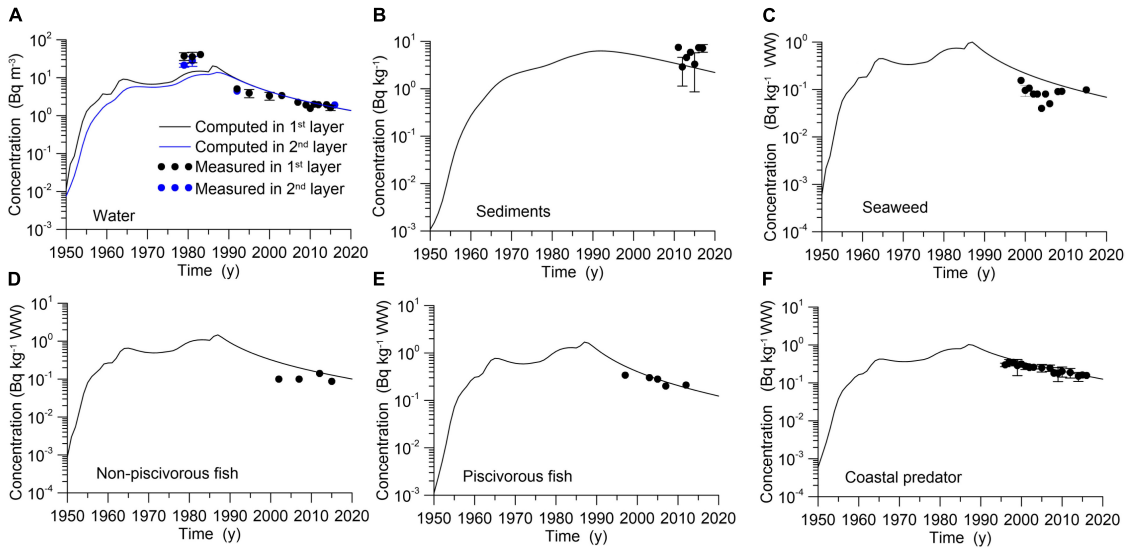

FIGURE 8 | The comparison of simulated temporal changes of ^{137}Cs with measured (MARIS, 2021) concentration in the Barents Sea (Box no. 26) in the water **(A)**, bottom sediments **(B)**, seaweed (*Fucus vesiculosus*) **(C)**, non-piscivorous fish (*Clupea harengus*) **(D)**, piscivorous fish (*Pollachius virens*) **(E)**, benthic predator (*Reinhardtius hippoglossoides*) **(F)**, and coastal predator (*Gadus morhua*) **(G)**.

the object of comparison for the contribution from different sources to the concentration of ^{137}Cs in the organism. **Figure 9** shows the contribution from (i) global deposition due to weapon testing and the Chernobyl accident (see **Figure 4**), (ii) Sellafield reprocessing plant release (**Figure 5A**), (iii) Cap La Hague reprocessing plant release (**Figure 5A**), (iv) inflow from the Yenisey River caused by release from KMCIC, (v) influx from the Baltic Sea (**Supplementary Figure 2D**), and (vi) Chernobyl accident deposition on the North Sea. As seen in **Figure 9A**, in the Irish Sea, almost all contamination in 1970–1985 was caused by routine discharge from the Sellafield plant; even in the 1990–2020 period, this contribution exceeded 90%. The contaminated water flowed from the Irish Sea to the North Atlantic and then to the North Sea, where part of the flow turned to the south (**Figure 3**), whereas the rest of the contaminated water was transported by the Norwegian Current into the Arctic Ocean. Therefore, the input from the Sellafield plant dominated (80–90%) in the North Sea (**Figures 9B,C**) in the 1975–1985 period and in the Norwegian Sea (**Figure 9D**) in the 1980–1985 period. Then, the contribution from reprocessing plants decreased, and similarly to 1950–1970, the contribution from global deposition dominated after 2000–2010. The Baltic Sea outflux contribution was relatively small in the central parts of the North Sea. The contribution from the La Hague plant dominated over the Sellafield contribution only in the southern North Sea in 1970–1975. The regional deposition on the North Sea due to the Chernobyl accident was comparable with the Sellafield contribution in the northern North Sea (**Figure 9B**) in 1986–1987 and reached 40% of the total content of ^{137}Cs, whereas global deposition was only 10% in that period. The fluxes of water from the La Hague plant and Baltic Sea were less important (maximum contributions reached 18 and 4%, respectively). As discussed in the previous section, three sources were most important in the Barents Sea (**Figure 8E**): global deposition in the 1950–1970 period and after 2010, Sellafield release (approximately 80% in 1980–1985), and Chernobyl deposition in the North Sea, whose contribution reached approximately 30% in 1988. Note that in Box no. 33, the direction of exchange between the water column and bottom deposit changed sign in 2000, indicating that sediments in the Norwegian Sea became a secondary source of contamination for the Barents Sea (see also Matishov et al., 2011). The contribution from KMCIC to contamination in the Kara Sea (**Figure 9F**) was insignificant (6%) in comparison with the input of global deposition and inflow contaminated water of Sellafield and Chernobyl origin from the Barents Sea. Note that the maximal contribution from Sellafield was reached in 1985, whereas the corresponding maximum for Chernobyl contamination was reached in 1995. The contribution from Sellafield was approximately 1.5 times less than global deposition along the Arctic coast of Canada and Baffin Bay after 1995 (**Figures 9G,H**), although these two sources dominated all others. At the same time, the corresponding maximum contribution from the Sellafield plant near Newfoundland (**Figure 9I**) was reached in 1985, indicating a shorter trajectory of water masses than in the Arctic Ocean.

Statistical Evaluation of the Model Predictions

The geometric means (GM) and the geometric standard deviation (GSD) were calculated for simulated-to-observed ratios of ^{137}Cs concentration values in the water, sediment, and marine biota. The data for different marine organisms from MARIS (2021) were used: macroalgae (*Fucus vesiculosus*), non-piscivorous fish (herring, *Clupea harengus*), piscivorous fish (coalfish, *Pollachius virens*), benthic predatory fish (halibut, *Reinhardtius*

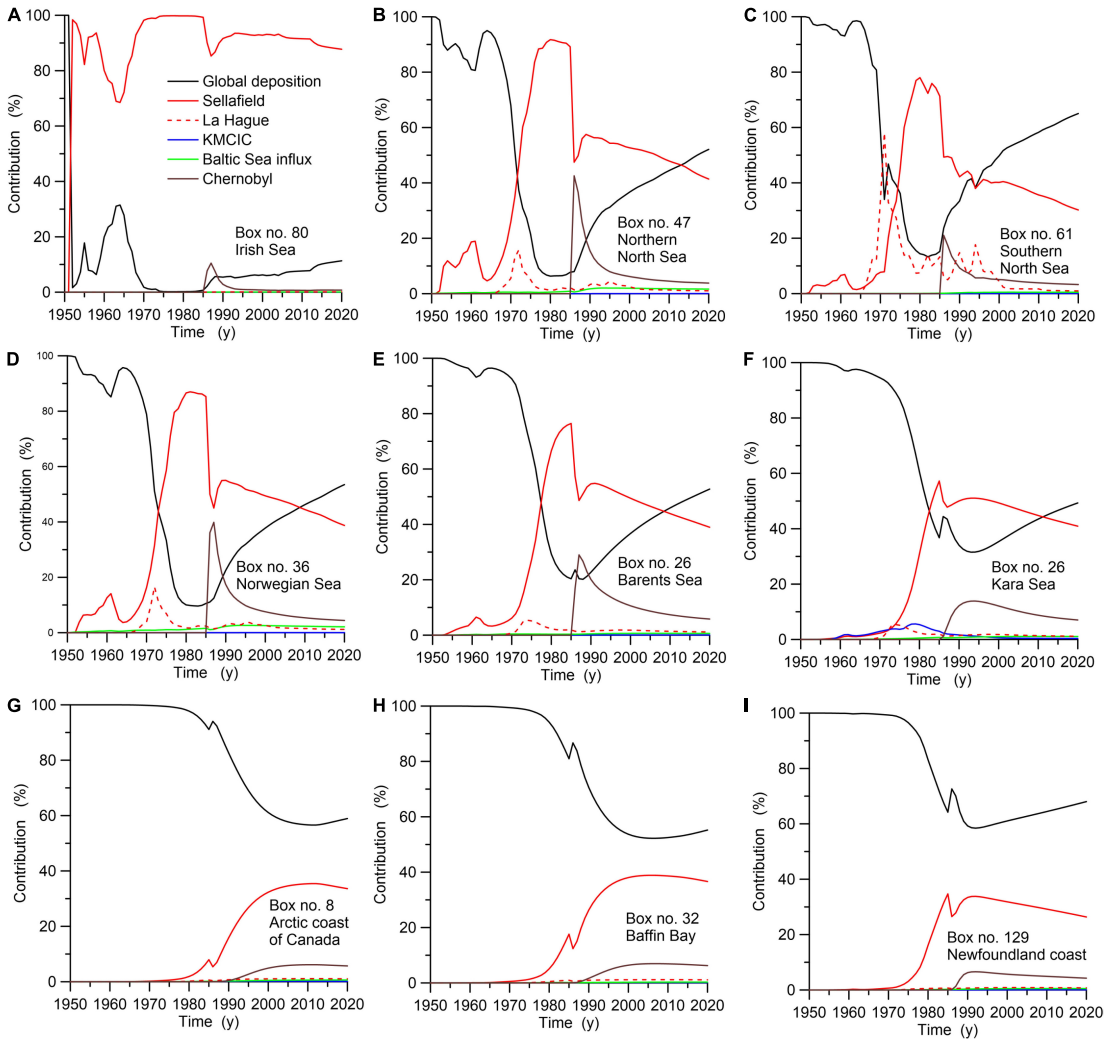

FIGURE 9 | Contribution from different sources to the concentration of ^{137}Cs in non-piscivorous fish in the Irish Sea **(A)**, northern North Sea **(B)**, southern North Sea **(C)**, Norwegian Sea **(D)**, Barents Sea **(E)**, Kara Sea **(F)**, Arctic coast of Canada **(G)**, Baffin Bay **(H)**, and Newfoundland coast **(I)**.

hippoglossoides), and coastal predatory fish (cod, *Gadus morhua*). The general agreement between simulated and observed ^{137}Cs concentrations in water and bottom sediment in the North Atlantic and Arctic oceans was confirmed by the GM and GSD values, which varied from 0.89 to 1.28 and from 1.48 to 1.87, respectively (**Table 1**). The model accurately predicted the ^{137}Cs concentrations in the different biota species in the North Atlantic and Arctic Ocean, where GM and GSD values varied in a range from 1.01 to 1.29 and from 1.22 to 1.48, respectively. The exceptions were estimates of GM and GSD for macroalgae and non-piscivorous fish in the Arctic Ocean, for which simulated concentrations overestimated measurements by almost two times.

Budget of ^{137}Cs in the Arctic Ocean

The Arctic Ocean is surrounded by Eurasia, North America, and Greenland and connected with the Pacific Ocean by the narrow and shallow Bering Strait and with the North Atlantic through the Canadian Archipelago and wide deep openings between Scandinavia and Greenland. Therefore, the Arctic Ocean

TABLE 1 | Geometric mean simulated-to-observed ratios (GM), geometric standard deviations (GSD), and the number of measurements (*N*) of each model variable for the Mediterranean and Black seas.

Model variable	North Atlantic			Arctic Ocean		
	GM	GSD	*N*	GM	GSD	*N*
Water	1.24	1.87	494	1.11	1.48	103
Sediment	1.28	1.51	36	0.89	1.69	28
Macroalgae	1.29	1.30	20	1.92	1.51	12
Non-piscivorous fish	1.19	1.22	35	1.87	1.43	7
Piscivorous fish	1.19	1.38	21	1.08	1.19	26
Demersal fish	1.27	1.44	64	–	–	–
Benthic predator fish	1.01	1.41	6	1.02	1.48	12
Coastal predator fish	1.15	1.30	71	1.20	1.29	36

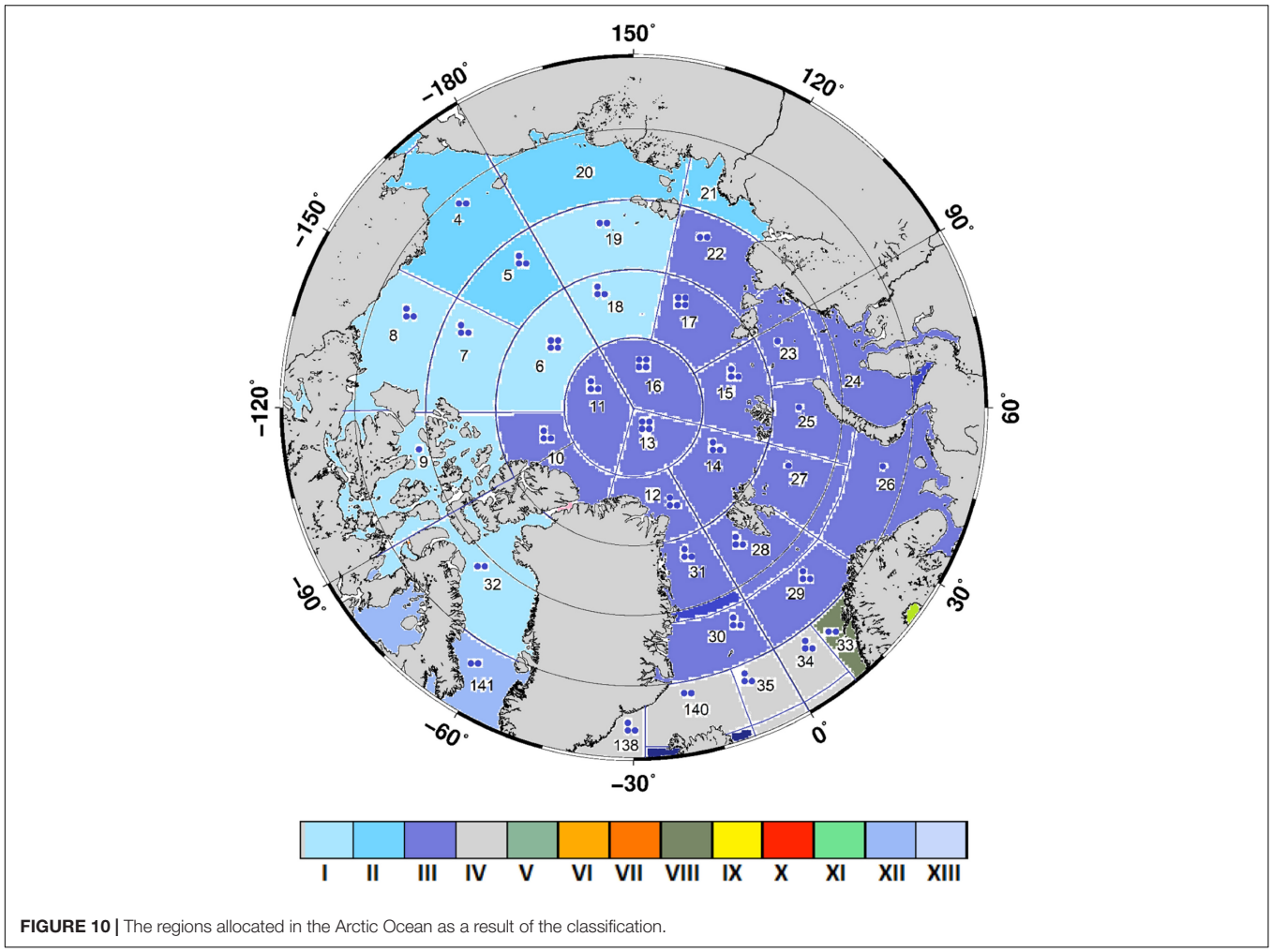

FIGURE 10 | The regions allocated in the Arctic Ocean as a result of the classification.

is often called the Arctic Mediterranean (Østerhus et al., 2019). The long-term variations in the Arctic Ocean inventory of ^{137}Cs in water and the bottom sediments (see **Supplementary Figure 3**) depend on exchange flows with other oceanic basins as well as distributed and point sources. The maximum total inventory (sum of the inventory in the water and sediment) in the Arctic Ocean (31,122 TBq) was reached in 1988 as a result of nuclear weapon tests, releases from nuclear facilities, and the Chernobyl accident. The corresponding inventory in the bottom sediments was approximately 6% of the maximum in the water. The maximum in the bottom sediments (2,306 TBq) was reached in 2004. The estimates from the simulation and decay corrected to 1960, 1980, 2000, and 2020 sources and sinks of ^{137}Cs in the Arctic Ocean are given in **Table 2**. As seen in the table, global fallout dominated in the sixties, whereas influx by currents from the North Atlantic of water contaminated due to global fallout, release from reprocessing plants, and instantaneous input after the Chernobyl accident increased with time. The influx from the Pacific Ocean was comparable to the influx from the North Atlantic in the sixties, whereas in 2020, it was only a few percent of the North Atlantic transport. Secondary contamination due to river runoff was less than 4% of ocean influx. The gradual purification of water occurred due to the removal of water into the North Atlantic, deposition of ^{137}Cs at the bottom, and decay.

Classification of ^{137}Cs Levels in the North Atlantic and Arctic Ocean

The data from monitoring the radioactivity concentration in the World Ocean collected within the framework of several projects

TABLE 2 | Estimated inventories from simulations and decay corrected to 1960, 1980, 2000, and 2020 sources and sinks (TBq) of ^{137}Cs in the Arctic Ocean (Boxes 4 to 32).

Source of marine contamination	1,960	1,980	2,000	2,020
Global fallout	3,044	6,913	5,521	3,493
Influx from Atlantic Ocean (in Box 29)	1,097	16,810	29,439	34,410
Outflux to Atlantic Ocean (from Box 30)	−87	−1,731	−7,426	−16,582
Outflux to Atlantic Ocean (from Box 32)	−190	−2,470	−5,463	−8,790
Influx from Pacific Ocean (in Box 4)	775	3,200	2,527	1,941
River runoff	54	255	218	157
MCC	2	44	42	27
Inventory in sediment	105	1,151	2,282	2,115
Inventory in water	4,590	21,870	22,576	12,541
Total inventory	4,695	23,021	24,858	14,656

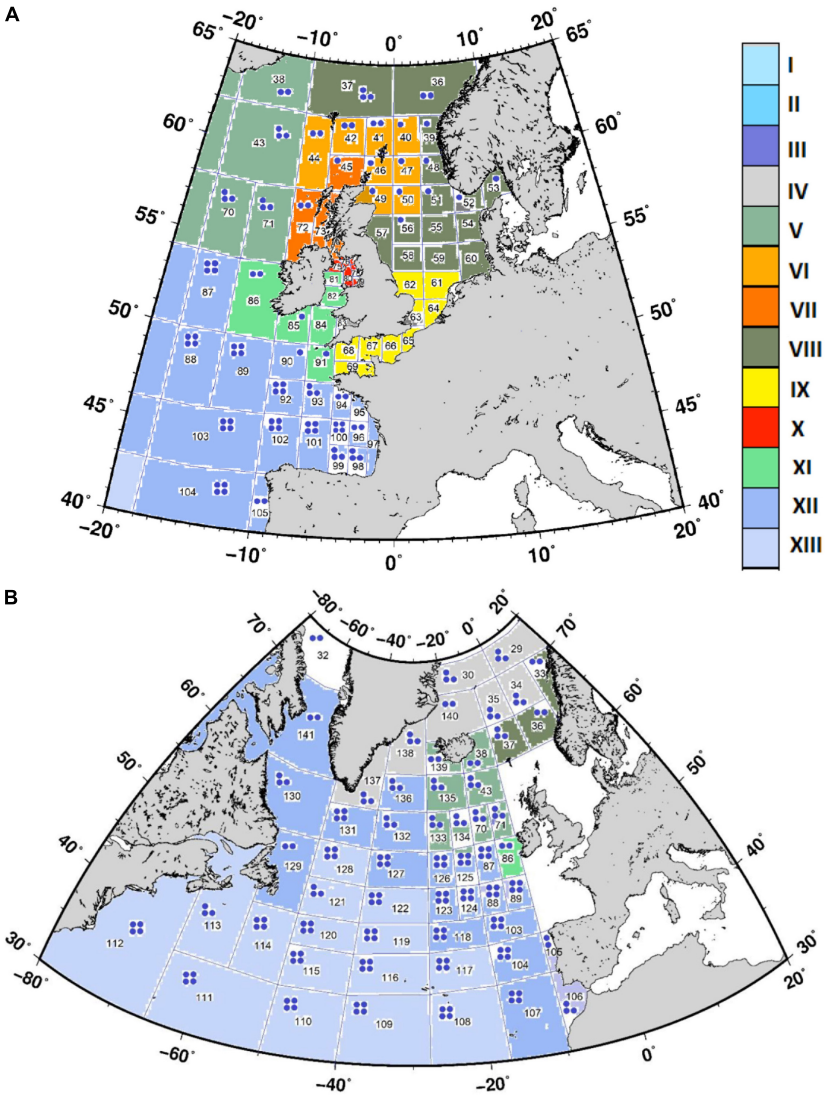

FIGURE 11 | The regions allocated in the North Sea area **(A)** and the North Atlantic **(B)** as a result of the classification.

of IAEA (1995, 2005) were grouped in large compartments to present their distribution in time and corresponding trends. These compartments were allocated on the empirical basis of knowledge of main currents in the seas and the location of sources. However, as previously noted (IAEA, 2005), "It is difficult to give meaningful average concentrations for these radionuclides in marginal seas such as the North Sea, the Baltic Sea, the Black Sea and especially, the Irish Sea." Therefore, a more detailed division of marine basins based on an objective method is necessary. The purpose of the classification of time series of radionuclide concentrations in the set of boxes is to select groups of boxes with similar temporal distributions of concentrations. The selection method is based on the "etalon" approach (Martazinova, 2005). The description of the method in detail was given by Maderich et al. (2020). This method makes it possible to identify areas of contamination with a similar distribution over time. For each area, the etalon distribution, i.e., temporal distribution that was representative of allocated areas, was determined.

The classification results are shown in **Figures 10–11**, where 13 regions with similar ^{137}Cs concentration time distributions were distinguished. Corresponding etalon distributions are shown in **Supplementary Figure 4**. The distribution of regions is due to the pattern of currents and the distribution of pollution sources. Region I (Central Arctic) in **Figure 10** is located in the Canadian Basin, and the Canadian Archipelago is separated from the western Arctic (Region III) by the Alpha/Mendeleev Ridge. An anticyclonic Beaufort Gyre governs circulation in Region I, whereas water is transported from the Central Arctic to the western Arctic by Transpolar Drift (see **Figure 3A**). As seen in etalon Box no. 18 (**Supplementary Figure 4**), the dominant factor for Region I is global deposition. Region II (eastern Arctic)

is under the influence of water inflowing from the Bering Sea (**Supplementary Figure 2C**). This leads to a doubling of the ^{137}Cs concentration compared with region I. Region III (Western Arctic) covers almost half of the Arctic Basin. Water inflows from the North Atlantic form the Atlantic/Norwegian Current (**Figure 3A**), and outflows from the East Greenland Current (**Figure 3A**). According to **Figures 9E,F**, in this region in 1950–1970, global deposition dominated, whereas in 1980–1990, the main source was contamination from Sellafield. This is confirmed by the temporal distribution of ^{137}Cs in etalon Box no. 25, where the importance of Chernobyl contamination inflow from the North Sea is also shown. Region IV (Nordic seas) covers three seas: the Norwegian, Iceland, and Greenland seas with complicated multidirectional flows. As seen in **Supplementary Figure 4**, the effects of the inflow of contaminated water from Sellafield and the contamination of Chernobyl origin from the North Sea is doubled in etalon Box no. 35 compared with Region III.

Region V (East Atlantic) is located between Iceland and Ireland, where the North Atlantic Current splits into Atlantic/Norwegian currents and the Irminger Current, as shown in **Figure 3B**. The three main sources (global deposition, release from Sellafield, and ^{137}Cs outflow of Chernobyl origin from the North Sea) were comparable in different periods, as shown in **Supplementary Figure 4** (etalon Box no. 43). Flows in Region VI (Faroe-Shetland Channel), indicated in **Figure 11**, transported essentially diluted ^{137}Cs from Sellafield. Part of the flow turns into the North Sea. The etalon Box no. 44 in **Supplementary Figure 4** shows only one maximum concentration. Only one maximum existed in Region VII (Malin Sea), which was contaminated by Sellafield plant release in 1970–1990. The main sources of contaminated water in the northern North Sea (Region VIII) were global deposition, release from the Cap de La Hague and Sellafield plants, and regional Chernobyl deposition, as shown in **Supplementary Figure 4** (etalon Box no. 55). Region IX is located in the southern North Sea and English Channel. The effects of global deposition and release from the Cap de La Hague and Sellafield plants were comparable, as seen in **Supplementary Figure 4** (etalon Box no. 66). In the Irish Sea (Region X), the Sellafield release dominated, as shown in **Supplementary Figure 4** (etalon Box no. 76). Region XI is located in the southern Irish Sea and Celtic Sea. Here, both global deposition and outflow of contaminated water from Sellafield were important, as shown in **Supplementary Figure 4** (etalon Box no. 85). Region XII is the area covering a wide strip of water formed by the spreading of the waters of the North Atlantic Current and entraining in the Subpolar and Subtropical gyres (see **Figure 3B**). Region XIII covers the Subtropical Gyre where global deposition dominated, as seen in **Supplementary Figure 4** (etalon Box no. 125).

CONCLUSION

The POSEIDON-R compartment model was applied to the North Atlantic and Arctic oceans to reconstruct ^{137}Cs contamination in 1945–2020 due to multiple sources: global fallout from atmospheric nuclear weapon tests, exchange flows with other oceans, point-source inputs in the ocean from reprocessing plants and other nuclear facilities, the impact of the Chernobyl accident and secondary contamination resulting from river runoff. The simulation results were validated using the marine database MARIS (2021). The POSEIDON-R model simulated the marine environment as a system of 3D compartments comprising the water column, bottom sediment, and biota. The dynamic model described the transfer of ^{137}Cs through the pelagic and benthic food chains. The total number of boxes covering the North Atlantic/Arctic oceans was 159, with a multilayer layer water column structure and three layers of bottom sediment. Advective and diffusional water transport between boxes was calculated by averaging three-dimensional currents from the CMEMS (2021) reanalysis over 10 years (2008–2017).

The contribution from different sources varied over time and depended on the ocean region. Model results were used for the analysis of the impact of each considered source on the total concentration of ^{137}Cs in non-piscivorous fish in the regions of interest. Whereas the contribution from global fallout dominated in 1960–1970, in 1970–1990, the contribution of ^{137}Cs released from reprocessing plants exceeded the contributions from other sources in almost all considered regions. Secondary contamination due to river runoff was less than 4% of ocean influx for the Arctic Ocean, where several large rivers flow. The maximum total inventory in the Arctic Ocean (31,122 TBq) was reached in 1988, whereas the corresponding inventory in the bottom sediment was approximately 6% of the total. The gradual purification of water in the Arctic Ocean occurred due to the removal of water into the North Atlantic, deposition of ^{137}Cs at the bottom, and decay.

Particular attention has been given to the Barents Sea due to the impact of various contamination sources and the importance of fisheries. The first maximum ^{137}Cs concentration in water caused by global fallout was observed in 1963, whereas the second maximum ^{137}Cs concentration in water in 1980–1985 was due to the influx of contaminated water from the Sellafield reprocessing plant. The last maximum in 1986–1987 was associated with Chernobyl deposition and subsequent inflow of Chernobyl contamination from the North Atlantic by currents. The concentration in coastal predators (represented by cod, *Gadus morhua*) lagged behind the concentration in water as a result of their diet that includes both pelagic and benthic organisms feeding on organic matter in the bottom sediments.

The general agreement between simulated and observed ^{137}Cs concentrations in water and bottom sediment in the North Atlantic and Arctic oceans was confirmed by the estimates of GM and GSD values, which varied from 0.89 to 1.29 and from 1.22 to 1.87, respectively. This confirmed that the approach used is useful in synthesizing measurement and simulation data. A useful application of the modeling for monitoring purposes was the selection of 13 representative regions in the North Atlantic and Arctic oceans using the "etalon" method for classification.

The considered model can be a tool for estimating contamination and corresponding dose estimates in the event of potential accidents related to sunken submarines and dumped radioactive material. An important model application

is predicting contamination due to climate warming when radionuclides buried in glaciers leak into the sea as a result of glacial melting (Miroshnikov et al., 2017; Zaborska, 2017; Matishov et al., 2018). In addition, significant changes in the circulation and corresponding transport of radionuclides in the North Atlantic and Arctic oceans should be expected (Johannessen et al., 2010) due to climate warming.

DATA AVAILABILITY STATEMENT

Publicly available datasets were analyzed in this study. This data can be found here: https://maris.iaea.org/home.

AUTHOR CONTRIBUTIONS

VlM designed the study and wrote the manuscript with support from all authors. RB contributed to the method development, simulation, and interpretation of the results. KK contributed to the simulation data analysis. KJ contributed to the data collection and manuscript editing. VaM wrote the code and carried out classification. IB contributed to the processing of circulation data and interpretation of the results. All authors contributed to the article and approved the submitted version.

FUNDING

This study was partially supported by the National Research Foundation of Ukraine project no. 2020.02/0048 (VlM), Grant for the Group of Young Scientists from the National Academy of Sciences of Ukraine (RB), KIOST major project PE99912 (KK), IAEA CRP K41017 (VlM), and HORIZON-2020 Grant no. 101003590 (IB).

SUPPLEMENTARY MATERIAL

The Supplementary Material for this article can be found online at: https://www.frontiersin.org/articles/10.3389/fmars.2021.806450/full#supplementary-material

REFERENCES

AMAP (1998). *AMAP Assessment Report: Arctic Pollution Issues*. Oslo: Arctic Monitoring and Assessment Programme (AMAP).

AMAP (2004). *AMAP Assessment 2002. Radioactivity in the Arctic*. Oslo: Arctic Monitoring and Assessment Programme (AMAP).

AMAP (2010). *AMAP Assessment 2009: Radioactivity in the Arctic*. Oslo: Arctic Monitoring and Assessment Programme (AMAP).

AMAP (2016). *AMAP Assessment 2015: Radioactivity in the Arctic*. Oslo: Arctic Monitoring and Assessment Programme (AMAP), vii+89.

Aoyama, M. (2018). Long-range transport of radiocaesium derived from global fallout and the Fukushima accident in the Pacific Ocean since 1953 through 2017—Part I: source term and surface transport. *J. Radioanal. Nucl. Chem.* 318, 1519–1542. doi: 10.1007/s10967-018-6244-z

Bezhenar, R., Jung, K. T., Maderich, V., Willemsen, S., de With, G., and Qiao, F. (2016). Transfer of radiocesium from contaminated bottom sediments to marine organisms through benthic food chain in post-Fukushima and post-Chernobyl periods. *Biogeosciences* 13, 3021–3034.

Bezhenar, R., Maderich, V., Schirone, A., Conte, F., and Martazinova, V. (2019). Transport and fate of ^{137}Cs in the Mediterranean and Black Seas system during 1945-2020 period: a modelling study. *J. Environ. Radioact.* 20:106023. doi: 10.1016/j.jenvrad.2019.106023

CEC (1990). *The Radiation Exposure of the Population of the European Community from Radioactivity in North European Marine Waters. Project 'Marina', RP 47, EUR-12483.* Luxembourg: Commission of the European Communities, 572.

CMEMS (2021). *Copernicus Marine Environment Monitoring Service*. Available online at: http://marine.copernicus.eu/ (accessed September 26, 2021).

EC (2002). *MARINA II – Update of the MARINA Project on the Radiological Exposure of the European Community from Radioactivity in North European Marine Waters. Radiation Protection 132,* Vol. II. Luxembourg: European Commission, 365.

Gwynn, J. P., Heldal, H. E., Gafvert, T., Blinova, O., Eriksson, M., Svaeren, I., et al. (2012). Radiological status of the marine environment in the Barents Sea. *J. Environ. Radioact.* 113, 155–162. doi: 10.1016/j.jenvrad.2012.06.003

IAEA (1995). *Sources of Radioactivity in the Marine Environment and Their Relative Contribution to Overall Dose Assessment From Marine Radioactivity (MARDOS), IAEA-TECDOC-838*. Vienna: IAEA, 54.

IAEA (2005). *Worldwide Marine Radioactivity Studies (WOMARS)*. Radionuclide Levels in Oceans and Seas, IAEA-TECDOC-1429. Vienna: IAEA, 187.

Iosjpe, M., Brown, J., and Strand, P. (2002). Modified approach for box modelling of radiological consequences from releases into marine environment. *J. Environ. Radioact.* 60, 91–103. doi: 10.1016/s0265-931x(01)00098-4

Johannessen, O. M., Volkov, V. A., Pettersson, L. M., Maderich, V. S., Zheleznyak, M. J., et al. (2010). *Radioactivity and Pollution in the Nordic Seas and Arctic Region. Observations, Modelling and Simulations. Springer Praxis Books Book Series (PRAXIS)*. Berlin: Springer, 408.

Kershaw. (2011). "Atlantic ocean," in *Radionuclides in Environment. Encyclopedia of Inorganic and Bioinorganic Chemistry*, ed. D. Atwood (Hoboken, NJ: John Wiley & Sons), 361–373.

Kumamoto, Y., Aoyama, M., Hamajima, Y., Nishino, S., Murata, A., and Kikuchi, T. (2017). Radiocesium in the western subarctic area of the North Pacific ocean, Bering Sea, and Arctic ocean in 2015 and 2017. *Polar Sci.* 21, 228–232. doi: 10.1016/j.apradiso.2017.02.036

Lepicard, S., Heling, R., and Maderich, V. (2004). POSEIDON/RODOS model for radiological assessment of marine environment after accidental releases: application to coastal areas of the Baltic, Black and North seas. *J. Environ. Radioact.* 72, 153–161. doi: 10.1016/S0265-931X(03)00197-8

Leppanen, A.-P., Kasatkina, N., Vaaramaa, K., Matishov, G. G., and Solatie, D. (2013). Selected anthropogenic and natural radioisotopes in the Barents Sea and off the western coast of Svalbard. *J. Environ. Radioact.* 126, 196–208. doi: 10.1016/j.jenvrad.2013.08.007

Maderich, V., Bezhenar, R., Brovchenko, I., and Martazinova, V. (2020). "Classification of radioactivity levels in the regions of the World ocean using compartment modelling," in *Mathematical Modeling and Simulation of Systems. MODS 2019. Advances in Intelligent Systems and Computing*, Vol. 1019, eds A. Palagin, A. Anisimov, A. Morozov, and S. Shkarlet (Cham: Springer), doi: 10.1007/978-3-030-25741-5_2

Maderich, V., Bezhenar, R., Tateda, Y., Aoyama, M., and Tsumune, D. (2018a). Similarities and differences of ^{137}Cs distributions in the marine environments of the Baltic and Black seas and off the Fukushima Dai-ichi nuclear power plant in model assessments. *Mar. Pollut. Bull.* 135, 895–906. doi: 10.1016/j.marpolbul.2018.08.026

Maderich, V., Bezhenar, R., Tateda, Y., Aoyama, M., Tsumune, D., Jung, K. T., et al. (2018b). The POSEIDON-R compartment model for the prediction of transport and fate of radionuclides in the marine environment. *MethodsX* 5, 1251–1266. doi: 10.1016/j.mex.2018.10.002

MARIS (2021). *Radioactivity and Stable Isotope Data in the Marine Environment*. Available online at: http://maris.iaea.org (accessed October 5, 2021).

Martazinova, V. (2005). The classification of synoptic patterns by method of analogs. *J. Environ. Eng.* 7, 61–65.

Matishov, G. G., Ilyin, G. V., Usyagina, I. S., Valuyskaya, D. A., and Deryabin, A. A. (2018). Results of marine radioecological study of fjords of western Spitsbergen. *Dokl. Earth Sci.* 480, 679–684.

Matishov, G. G., Matishov, D. G., Usyagina, I. S., Kasatkina, N. E., and Pavel'skaya, E. V. (2011). Assessment of ^{137}Cs and ^{90}Sr fluxes in the Barents Sea. *Doklady Earth Sci.* 439(Pt 2), 1190–1195.

Miroshnikov, A. Y., Laverov, N. P., Chernov, R. A., Kudikov, A. V., Ysacheva, A. A., Semenkov, I. N., et al. (2017). Radioecological investigations on the Northern Novaya Zemlya archipelago. *Oceanology* 57, 204–214.

Mitchell, N. T., and Steele, A. K. (1988). The marine impact of caesium-134 and -137 from the Chernobyl reactor accident. *J. Environ. Radioact.* 6, 163–175.

Nyffeler, F., Cigna, A. A., Dahlgaard, H., and Livingston, H. D. (1996). "Radionuclides in the Atlantic ocean: a survey," in *Radionuclides in the Oceans, Inputs and Inventories*, eds P. Guegueniat and P. Germain (Paris: Les Editions de Physique), 1–28.

OSPAR (2021). *Discharges From Nuclear Installations*. Available online at: https://www.ospar.org/work-areas/rsc/nuclear-discharges (accessed October 5, 2021).

Østerhus, S., Woodgate, R., Valdimarsson, H., Turrell, B., de Steur, L., Quadfasel, D., et al. (2019). Arctic Mediterranean exchanges: a consistent volume budget and trends in transports from two decades of observations. *Ocean Sci.* 15, 379–399. doi: 10.5194/os-15-379-2019

Periáñez, R., Bezhenar, R., Brovchenko, I., Duffa, C., Iosjpe, M., Jung, K. T., et al. (2019). Marine radionuclide transport modelling: recent developments, problems and challenges. *Environ. Model. Softw.* 122:104523. doi: 10.1016/j.envsoft.2019.104523

Sayles, F. L., Livingston, H. D., and Panteleyev, G. P. (1997). The history and source of particulate 137Cs and 239,240Pu deposition in sediments of the Ob River Delta, Siberia. *Sci. Total Environ.* 202, 25–41. doi: 10.1016/s0048-9697(97)00102-2

Semenkov, I., and Miroshnikov, A. (2015). Sources of cesium-137 pollution of bottom sediments in the Kara Sea continental catchment, Russia. *Int. J. Res. Environ. Sci.* 1, 19–29.

Smith, J. N., Brown, R. M., Williams, W. J., Robert, M., Nelson, R., and Moran, S. B. (2015). Arrival of the Fukushima radioactivity plume in North American continental waters. *Proc. Natl. Acad. Sci. U.S.A.* 112, 1310–1315. doi: 10.1073/pnas.1412814112

Smith, J. N., Ellis, K. M., Polyak, L., Ivanov, G., Forman, S. L., and Moran, S. B. (2000). ^{239,240}Pu transport into the Arctic ocean from underwater nuclear tests in Chernaya Bay, Novaya Zemlya. *Cont. Shelf Res.* 20, 255–279.

Smith, J. T., Wright, S. M., Cross, M. A., Monte, L., Kudelsky, A. V., Saxen, R., et al. (2004). Global analysis of the riverine transport of ^{90}Sr and ^{137}Cs. *Environ. Sci. Technol.* 38, 850–857. doi: 10.1016/j.scitotenv.2014.06.136

UNSCEAR (2000). *Exposures of the Public From Man-Made Sources of Radiation. In: Sources and Effects of Ionizing Radiation*. New York, NY: United Nations.

Vakulovsky, S. M., Kryshev, I. I., Nikitin, A. I., Savitsky, Y. V., Malyshev, S. V., and Tertyshnik, E. G. (1995). Radioactive contamination of the Yenisei River. *J. Environ. Radioact.* 29, 225–236.

Zaborska, A. (2017). Sources of ^{137}Cs to an arctic fjord (Hornsund, Svalbard). *J. Environ. Radioact.* 180, 19–26. doi: 10.1016/j.jenvrad.2017.09.021

Zaborska, A., and Carroll, J. (2011). "Arctic ocean," in *Radionuclides in environment. Encyclopedia of Inorganic and Bioinorganic Chemistry*, ed. D. Atwood (Hoboken, NJ: John Wiley & Sons), 389–399.

Zaborska, A., Mietelski, J. W., Carroll, J., Papucci, C., and Pempkowiak, J. (2010). Sources and distribution of ^{137}Cs, ^{238}Pu and ^{239,240}Pu radionuclides in the north-western Barents Sea. *J. Environ. Radioact.* 101, 323–331.

Conflict of Interest: KJ was employed by the company Oceanic Consulting and Trading.

The remaining authors declare that the research was conducted in the absence of any commercial or financial relationships that could be construed as a potential conflict of interest.

Publisher's Note: All claims expressed in this article are solely those of the authors and do not necessarily represent those of their affiliated organizations, or those of the publisher, the editors and the reviewers. Any product that may be evaluated in this article, or claim that may be made by its manufacturer, is not guaranteed or endorsed by the publisher.

frontiers in Marine Science

ORIGINAL RESEARCH
published: 18 February 2022
doi: 10.3389/fmars.2022.831937

Lagrangian Observation of ^{234}Th and Its Application in Constraining the Sinking of Particulate Organic Carbon on the Slope of the Northeastern South China Sea

Weifeng Yang[1,2], Xiufeng Zhao[1,2], Min Chen[2], Yusheng Qiu[2] and Minfang Zheng[2]*

[1] State Key Laboratory of Marine Environmental Science, Xiamen, China, [2] College of Ocean and Earth Sciences, Xiamen University, Xiamen, China

The ^{234}Th–^{238}U disequilibrium has been widely used to quantify the sinking flux of particulate organic carbon (POC) out of the upper ocean. However, the influence of the advection on the quantification is poorly understood due to the lack of *in situ* measured physical parameters. Here, a Lagrangian observation was deployed for 39 h to track the variability of ^{234}Th along with the current on the slope of the northeastern South China Sea (SCS). Contrasting to the general ocean interior, ^{234}Th showed deficits relative to ^{238}U in the mesopelagic waters, indicating an enhanced removal of ^{234}Th. Concurrently, elevated total particulate matter (TPM) and POC contents were observed in the mesopelagic waters, supporting the driving force of the cross-shelf dispersion of re-suspended shelf/slope sediments for the ^{234}Th removal. The widely used ^{234}Th-model (ignoring physical processes) produced a much lower sinking flux of POC than the sediment trap-derived POC flux during the same observation, indicating an unneglectable influence of advection and diffusion. By considering the main horizontal advection and vertical diffusion, the ^{234}Th–^{238}U method gave rise to comparable results to sediment trap. ^{234}Th-derived POC fluxes showed an increased pattern from 300 to 1,000 m, consistent with the more abundant POC where. These results indicated that advection represents an unneglectable process during the quantification of the sinking flux of ^{234}Th over the slope of the SCS.

Keywords: thorium-234, mesopelagic water, export flux, resuspension, South China Sea

OPEN ACCESS

Edited by:
Jixin Qiao,
Technical University of Denmark, Denmark

Reviewed by:
Chin-Chang Hung,
National Sun Yat-sen University, Taiwan
Hideki Fukuda,
The University of Tokyo, Japan

****Correspondence:***
Weifeng Yang
wyang@xmu.edu.cn

Specialty section:
This article was submitted to Marine Biogeochemistry, a section of the journal Frontiers in Marine Science

Received: *09 December 2021*
Accepted: *27 January 2022*
Published: *18 February 2022*

Citation:
Yang W, Zhao X, Chen M, Qiu Y and Zheng M (2022) Lagrangian Observation of ^{234}Th and Its Application in Constraining the Sinking of Particulate Organic Carbon on the Slope of the Northeastern South China Sea. Front. Mar. Sci. 9:831937. doi: 10.3389/fmars.2022.831937

INTRODUCTION

Particulate organic carbon (POC) settling largely dominates the ability of the oceans to sequestrate carbon dioxide. Various types of sediment traps have been used to directly determine the flux of POC (Li et al., 2018; Shih et al., 2020). Due to the requirements of long collection time (≥24 h), professional technique, and manpower for deployment and recovery of sediment traps, the radioactive method of ^{234}Th–^{238}U has later been developed and widely used in past decades (Buesseler et al., 2020). ^{234}Th ($T_{1/2}$ = 24.1 days), naturally generated from its parent of ^{238}U, is a typical particle-reactive radionuclide in seawater (Black et al., 2018). Owing to its sinking with particles, ^{234}Th is usually deficient to ^{238}U in the upper

ocean (Roca-Martí et al., 2017; Umhau et al., 2019). This deficit has thus been used to quantify the sinking flux of particulate components (especially POC) out of the euphotic zone (Buesseler et al., 2009; Maiti et al., 2016). In general, the mass balance model of ^{234}Th is applied to constrain its sinking flux. Owing to the difficulty in obtaining *in situ* physical parameters (e.g., current velocity, diffusion coefficient, etc.) and collecting up-downstream gradient of ^{234}Th, the widely adopted model usually neglects advection and diffusion processes (Coppola et al., 2002; Yang et al., 2016, 2021a). A few studies indicate that physical processes can largely affect the ^{234}Th and POC fluxes in some oceanic settings, e.g., upwelling in the Equatorial Pacific (Bacon et al., 1996) and anticyclonic eddies (Zhou et al., 2013). In marginal seas and shallow waters with dynamic currents and tides, advection, and diffusion are expected to have a larger influence on the sinking flux of ^{234}Th (Zhao et al., 2019). In addition, steady-state is often assumed to quantify the flux of ^{234}Th due to the lack of time-series observation. However, non-steady-state, to a varying degree, influences the flux calculation (Martin et al., 2011; Resplandy et al., 2012). Besides, the ratio of POC to particulate ^{234}Th used to convert ^{234}Th flux to POC flux is another factor influencing the ^{234}Th–^{238}U method. It is generally expected that POC/^{234}Th on large particles (>50 μm) represent sinking particles. However, results from sediment traps reveal that ^{234}Th is mainly carried by small sinking particles (∼70–80% of the total) in the northern South China Sea (SCS), representing the majority sinking of ^{234}Th (Hung et al., 2012). Less than 50 μm particles account for most of the bulk POC in the northeastern SCS (Hung and Gong, 2010). The largest fractions of both ^{234}Th and POC in medium-sized (10–15 μm) particles are also observed in the northwestern Pacific Ocean (Hung et al., 2010). Hence, the influence of physical processes, temporal variability, and particle size on the ^{234}Th–^{238}U method needs extensive investigations to improve the application of ^{234}Th–^{238}U.

Usually, coastal and marginal seas show complicated hydrological conditions and significant spatiotemporal variability in the abundance of both ^{234}Th and POC (Feng et al., 2021a,b), which challenges the widely used advection-excluded ^{234}Th model (Zhao et al., 2019). Based on model-simulated physical parameters, i.e., advective velocity and diffusion coefficients, a few studies indicate that ignoring advection and diffusion would lead to a large deviation of ^{234}Th fluxes in some marginal seas, e.g., the basin of the SCS (Cai et al., 2008; Zhou et al., 2013). However, another study reports that including model-simulated physical parameters in ^{234}Th-model produces unreasonable results in the northern shelf/slope of the SCS due to the poorly constrained parameters (Cai et al., 2015). Thus, we hypothesize that dynamic hydrological fields result in the complex influence of physical processes on the quantification of ^{234}Th flux and ^{234}Th-derived POC flux in the shelf/slope areas. Thus, it is necessary to conduct *in situ* Lagrangian observation to obtain parameters and examine the influence of physical processes on the application of the ^{234}Th/^{238}U method especially in oceanic settings with strong physical dynamics.

In this study, the northeastern SCS was selected to investigate the influence of horizontal advection on the estimation of ^{234}Th flux (**Figure 1**). Over the past decade, increasing studies report the widely observed cross-shelf dispersion of particulate matter (Shih et al., 2019; Shen et al., 2020; Yang et al., 2021b; Ge et al., 2022) driven by the dynamic physical processes (Li et al., 2018; Jia et al., 2019). Thus, the northeastern SCS could be an ideal site for attesting to the influence of physical processes on the application of the ^{234}Th/^{238}U method. Here, we conducted a Lagrangian observation of ^{234}Th on the northeastern slope of the SCS. The measured horizontal advection velocity and ^{234}Th in both upstream and downstream waters enable us to evaluate the influence of physical processes on the application of ^{234}Th in the SCS.

MATERIALS AND METHODS

Study Site

The study site is located in the northeastern SCS over the slope with water depths of hundreds of meters to more than a thousand meters (**Figure 1**). Recent researches have observed ubiquitous nepheloid layers (NLs) either in the mesopelagic water or in the bottom water of the northern SCS (Ma et al., 2017; Shih et al., 2019). A preliminary study indicates that internal solitary waves drive the resuspension of sediments on the slope (Jia et al., 2019). With the influence of currents, re-suspended particles disperse over a large scope as supported by the elevated particle fluxes in deeper sediment traps in the basin of the SCS (Schroeder et al., 2015; Hong et al., 2021). This dispersion of the shelf/slope sediments, mainly driven by advection, results in enhanced scavenging of particle-reactive nuclides (e.g., ^{210}Po) in the mesopelagic water of the SCS (**Figure 3**; Ma et al., 2017) and thus the sinking flux of POC (Yang et al., 2021b).

Sampling

The buoy, assembled a sediment trap array with three traps at 50, 100, and 200 m, was deployed from August 9 to 11, 2016 in the northeastern SCS (**Figure 1**). A Lagrangian observation was conducted, starting at station T1 and ending at station T2 with a duration of 39 h. Seawater was collected at both T1 and T2 from surface to 1,000 m (**Table 1**) using Niskin bottles attached to a conductivity, temperature, and depth (CTD)-rosette system aboard the *R/V Yanpin 2*. In brief, 8 L of seawater at each specific depth were collected and filtered through a pre-combusted (450°C for 4 h) and weighted quartz fiber (QMA) filter (Whatman^{TM}, Maidstone, United Kingdom). The total particulate matter (TPM) retained on the filter was de-salted using Milli-Q water for the measurements of particulate ^{234}Th (^{234}Th$_P$), POC, and TPM. Additionally, 4 L of the filtrate was collected for the analysis of dissolved ^{234}Th (^{234}Th$_D$). The euphotic zone of 0–150 m was determined by using a photosynthetically available radiation (PAR) scalar quantum irradiance sensor, defined as the depth of 0.1% of the surface light intensity.

^{234}Th and Total Particulate Matter Analyses

The particulate samples were dried at 60°C after collection and weighted to determine the difference between pure QMA filter

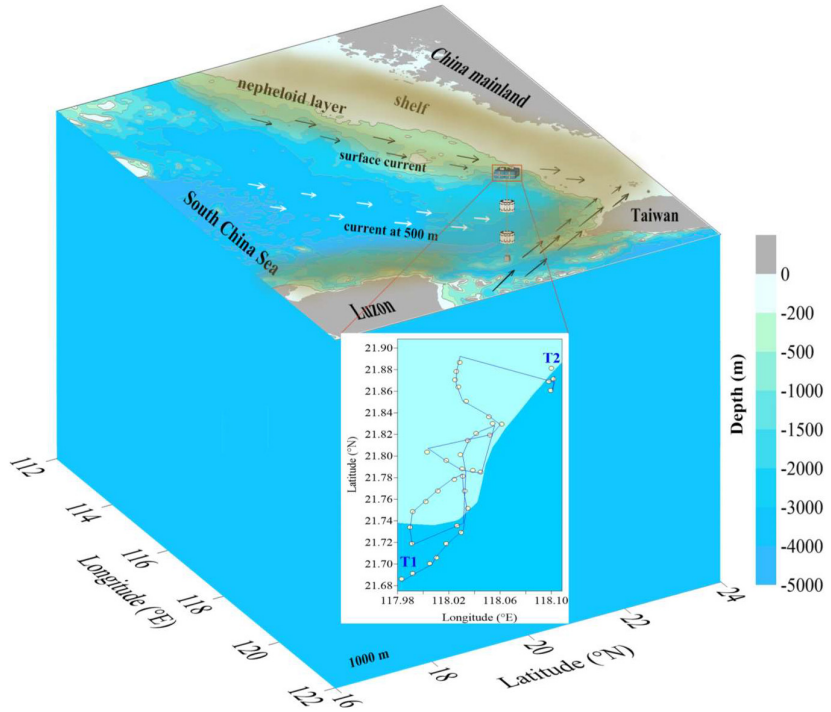

FIGURE 1 | Sampling stations in the northeastern South China Sea and the trajectory of the Lagrangian observation. The intervals between adjacent points denote the trajectory within an hour. The conceptual schematic of the nepheloid layer over the shelf/slope region highlights its ubiquity.

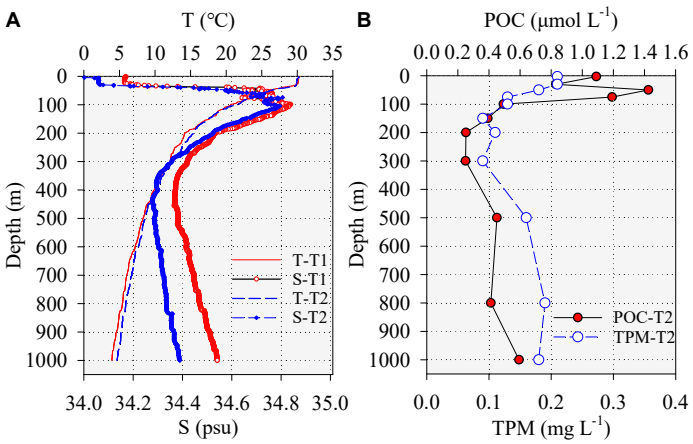

FIGURE 2 | Profiles of temperature, salinity at stations T1 and T2 **(A)**, and particulate organic carbon (POC) and total particulate matter (TPM) at T2 **(B)**.

and TPM-contained filter, i.e., the content of TPM. The activity of ^{234}Th$_P$ was counted using a gas-flow proportional low-level beta counter (RISØ GM-25-5A) as reported in our recent studies (Feng et al., 2021a,b) until the counting error was less than ±7%. A total of 150 days later, a second counting was conducted to assay the contribution of other beta emitters. ^{234}Th$_D$ in the filtrate was concentrated using the small volume MnO_2 co-precipitation method (Benitez-Nelson et al., 2001). In brief, the pH value of filtrate was adjusted to 9.0 using ammonium hydroxide, then $KMnO_4$ and $MnCl_2$ solution were added to form MnO_2 particles. After stirring and sanding for over 6 h to adsorb ^{234}Th onto MnO_2 particles, MnO_2 precipitate was separated from the solution via filtration using a QMA filter. The average recovery was 94.7 ± 2.3%, showing a stable yield. Then, the sample was dried at 60°C, the activity of ^{234}Th$_D$ was counted using the same beta counter like ^{234}Th$_P$ but with < 5% counting error. The concentrations of both ^{234}Th$_D$ and ^{234}Th$_P$ were calculated based on the two measurements and corrected for recovery, blank counts, and sampling time. The activity concentrations of the total ^{238}U were calculated using the newly updated ^{238}U-salinity

relationship (Owens et al., 2011). The presented uncertainties of ^{234}Th were propagated from the counting errors. The total ^{234}Th (^{234}Th$_T$) and ^{234}Th/^{238}U ratio uncertainties were propagated from ^{234}Th$_D$ and ^{234}Th$_P$.

Particulate Organic Carbon Analysis

The Lagrangian observation was designed to constrain the *in situ* current velocity (horizontal advection) and the gradient of ^{234}Th activity between T1 and T2. On the northern SCS shelf with prominent cross-shelf transport of re-suspended sediments, this strategy could help us constrain the influence of advection on the flux estimation of ^{234}Th and ^{234}Th-derived POC flux at station T2. Hence, POC samples collected at station T2 were determined. After the measurements of ^{234}Th$_P$, particulate-containing QMA filters were fumigated using concentrated HCl for no less than 48 h to remove inorganic carbon. Then, samples were dried at 60°C. POC content was measured using an elemental analyzer (Perkin Elmer CHN, Waltham, United States). The standard material used was IAEA-C8.

Particulate Organic Carbon Flux Calculation

The fluxes of TPM and POC was calculated from the ^{234}Th fluxes (Buesseler et al., 1992), i.e.,

$$F_{\text{TPM or POC}} = F_{\text{Th}} \times \frac{C_{\text{TPM}} \text{ or } C_{POC}}{\text{Th}_P} \quad (1)$$

where F_{TPM} and F_{POC} represent the flux of TPM (in g m^{-2} day^{-1}) and POC (in mmol-C m^{-2} day^{-1}), respectively. C_{TPM} and C_{POC} are the concentrations of TPM and POC. Th$_P$ denotes the activity concentration of ^{234}Th$_P$.

RESULTS

Overall, the buoy floated northeast-ward along the surface current over the slope (**Figure 1**) with an average velocity of 19.5 cm s^{-1}, which is close to the mean of 15 cm s^{-1} obtained from the model simulation for the upper 200 m in the study area (Gan et al., 2006). At stations T1 and T2 sampled, it is clear that the difference in salinity was discernible though temperature showed little difference (**Figure 2A**), corresponding to water mixing during the transport of seawater from T1 to T2. The tracking of the movement of the buoy enables us to obtain the real viability of parameters along the trajectory of the buoy.

The concentrations of TPM varied from 0.09 to 0.21 mg L^{-1} with an average of 0.15 ± 0.04 mg L^{-1} (**Figure 2B**). POC concentrations showed a range of 0.25–1.42 μmol L^{-1}, averaging 0.67 μmol L^{-1}. POC exhibited the highest values between 50 and 75 m (**Figure 2B**), corresponding to the widely observed depth of chlorophyll-a maximum in the SCS (Cai et al., 2015; Yang et al., 2021b). Notably, below the euphotic base (i.e., 150 m), both TPM and POC showed a downward increasing pattern (**Figure 2B**), increasing from 0.11 to 0.19 mg L^{-1} and 0.25 to 0.59 μmol L^{-1}, respectively. This phenomenon was also reported at a station near T1 during the same cruise (Yang et al., 2021b), pointing to the cross-shelf transport of re-suspended sediments.

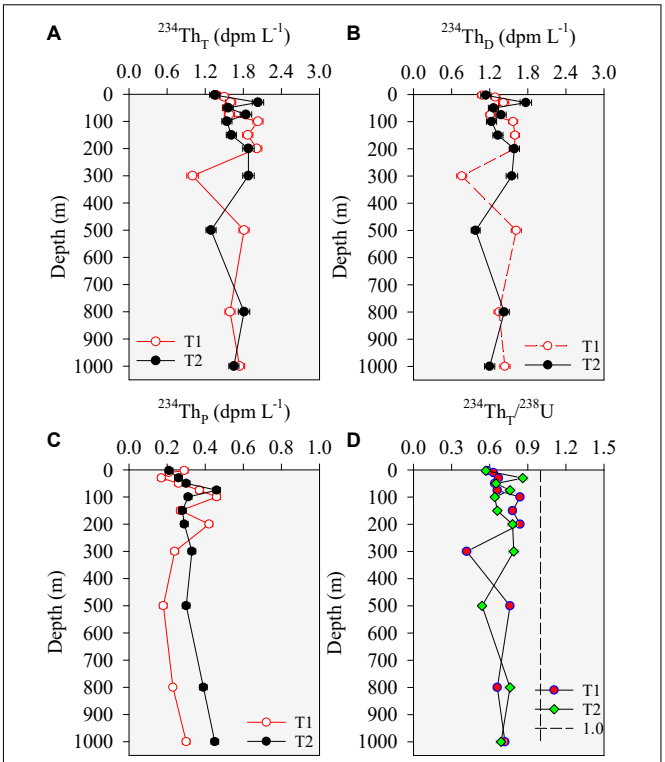

FIGURE 3 | Profiles of activity concentrations of total ^{234}Th **(A)**, dissolved ^{234}Th **(B)**, and particulate ^{234}Th **(C)**, and the activity ratios of total ^{234}Th to ^{238}U **(D)** at stations T1 and T2.

The activity concentrations of ^{234}Th$_T$ varied from 1.00 to 2.03 (avg.: 1.64 dpm L^{-1}) and 1.29–2.03 dpm L^{-1} (avg.: 1.68 dpm L^{-1}) at stations T1 and T2, respectively (**Table 1** and **Figure 3A**). On average, ^{234}Th$_D$ accounted for 67 and 63% of ^{234}Th$_T$ at T1 and T2 (**Figures 3B,C**), coinciding with the major dissolved form of ^{234}Th in the open SCS (Zhou et al., 2013; Hong et al., 2021) and contrasting with the major particulate form in the coastal SCS (Feng et al., 2021a). The activity ratios of ^{234}Th$_T$ to ^{238}U (i.e., ^{234}Th/^{238}U) ranged from 0.42 to 0.84 at T1 and 0.54 to 0.86 at T2, averaging 0.67 and 0.70, respectively. Unlike the equilibrium between ^{234}Th and ^{238}U widely observed in mesopelagic waters, ^{234}Th/^{238}U showed deficits of ^{234}Th relative to ^{238}U at both T1 and T2 (**Figure 3D**), which was similar to the deficient ^{210}Po relative to ^{210}Pb observed near T1 during the same cruise (Yang et al., 2021b).

DISCUSSION

Influence of Cross-Shelf Process on ^{234}Th Profiles

^{234}Th$_T$ was lower than ^{238}U with the ^{234}Th/^{238}U ratios of 0.58–0.84 at T1 and 0.57–0.86 at T2 between surface and 150 m (**Table 1**), indicating an efficient removal of ^{234}Th from the euphotic zone (**Figure 3**). This observation is a typical scenario in the study area as was reported in all seasons (Cai et al., 2015).

TABLE 1 | Temperature, salinity, the content of total particulate matter (TPM), the concentration of particulate organic carbon (POC), activity concentrations of dissolved ^{234}Th ($^{234}Th_D$), particulate ^{234}Th ($^{234}Th_P$), total ^{234}Th ($^{234}Th_T$), and ^{238}U, and the activity ratios of $^{234}Th_T$ to ^{238}U during the Lagrangian observation from station T1 to station T2.

Stn.	Depth	T	S	$^{234}Th_D$	$^{234}Th_P$	$^{234}Th_T$	^{238}U	$^{234}Th_T/^{238}U$
	(m)	(°C)	(psu)	(dpm L^{-1})				
T1	3	30.25	34.17	1.08 ± 0.07	0.29 ± 0.02	1.37 ± 0.07	2.37	0.58 ± 0.03
	10	30.11	34.17	1.29 ± 0.07	0.21 ± 0.01	1.50 ± 0.07	2.37	0.63 ± 0.03
	30	29.76	34.21	1.42 ± 0.08	0.17 ± 0.02	1.60 ± 0.08	2.37	0.67 ± 0.03
	50	25.95	34.67	1.27 ± 0.07	0.26 ± 0.02	1.54 ± 0.07	2.41	0.64 ± 0.03
	75	23.98	34.66	1.21 ± 0.07	0.37 ± 0.02	1.58 ± 0.08	2.41	0.66 ± 0.03
	100	20.64	34.84	1.57 ± 0.07	0.46 ± 0.02	2.03 ± 0.08	2.42	0.84 ± 0.03
	150	17.59	34.72	1.60 ± 0.07	0.27 ± 0.02	1.87 ± 0.08	2.41	0.78 ± 0.03
	200	14.21	34.53	1.59 ± 0.08	0.42 ± 0.02	2.01 ± 0.08	2.40	0.84 ± 0.03
	300	12.11	34.42	0.76 ± 0.08	0.24 ± 0.02	1.00 ± 0.09	2.39	0.42 ± 0.04
	500	8.31	34.38	1.62 ± 0.08	0.18 ± 0.02	1.81 ± 0.08	2.39	0.76 ± 0.03
	800	5.40	34.47	1.35 ± 0.08	0.23 ± 0.01	1.59 ± 0.08	2.39	0.66 ± 0.03
	1,000	3.94	34.54	1.44 ± 0.08	0.30 ± 0.02	1.74 ± 0.08	2.40	0.72 ± 0.03
T2	3	30.21	34.16	1.14 ± 0.08	0.21 ± 0.02	1.35 ± 0.08	2.37	0.57 ± 0.03
	30	29.88	34.21	1.77 ± 0.09	0.26 ± 0.02	2.03 ± 0.09	2.37	0.86 ± 0.04
	50	26.14	34.58	1.26 ± 0.08	0.30 ± 0.02	1.56 ± 0.08	2.40	0.65 ± 0.03
	75	23.81	34.78	1.38 ± 0.08	0.46 ± 0.02	1.84 ± 0.09	2.42	0.76 ± 0.04
	100	21.50	34.81	1.23 ± 0.08	0.31 ± 0.02	1.54 ± 0.08	2.42	0.64 ± 0.03
	150	17.40	34.75	1.33 ± 0.08	0.28 ± 0.02	1.61 ± 0.08	2.42	0.66 ± 0.03
	200	15.37	34.58	1.59 ± 0.08	0.29 ± 0.02	1.88 ± 0.09	2.40	0.78 ± 0.04
	300	12.48	34.41	1.55 ± 0.09	0.33 ± 0.02	1.88 ± 0.09	2.39	0.79 ± 0.04
	500	8.61	34.29	0.98 ± 0.07	0.30 ± 0.02	1.29 ± 0.08	2.38	0.54 ± 0.03
	800	5.88	34.36	1.43 ± 0.08	0.39 ± 0.02	1.81 ± 0.09	2.39	0.76 ± 0.04
	1,000	4.65	34.38	1.20 ± 0.08	0.45 ± 0.02	1.65 ± 0.08	2.39	0.69 ± 0.04

Below the euphotic zone (200–1,000 m), the $^{234}Th_T$ deficits were also observed at both T1 and T2 with the $^{234}Th/^{238}U$ ratios of 0.42–0.84. Although ^{234}Th activity in the mesopelagic water of the SCS has not been reported, it is generally expected that ^{234}Th should reach equilibrium with ^{238}U due to the sparse TPM and long residence time of ^{234}Th. In fact, equilibrium states have been observed in most mesopelagic waters in the open oceans, e.g., the southeastern tropical Pacific (Black et al., 2018), the Atlantic Ocean (Owens and Buesseler, 2015), the Indian Ocean (Anand et al., 2018), and the Atlantic sector of the Southern Ocean (Roca-Martí et al., 2017). Considering the strong particle reactivity of ^{234}Th, the deficits of ^{234}Th were attributed to its enhanced removal along with TPM sinking in the mesopelagic waters at stations T1 and T2 (**Figure 3**). On the one hand, the elevated TPM and POC concentrations (**Figure 2**) provided direct evidence for the abundant particulate matter in mesopelagic water. Another particle-reactive radionuclide ^{210}Po also showed enhanced removal together with increased TPM in the mesopelagic water during the same cruise (Yang et al., 2021b). Shelf/slope sediment resuspension and successive dispersion are thought to be the provenance of the elevated TPM in the mesopelagic water of the northern SCS (Shih et al., 2019; Yang et al., 2021b), mechanistically driven by the internal solitary waves (Jia et al., 2019). On the other hand, abundant TPM usually leads to the deficits of ^{234}Th not only in the widely investigated euphotic zone but also in the less-studied ocean interior. For instance, evident ^{234}Th deficits have been observed in deep water near the active hydrothermal vents (Yang et al., 2016, 2021a) and the hydrothermal plume (Owens and Buesseler, 2015). Thus, the deficits of ^{234}Th, together with the elevated TPM and POC contents in the mesopelagic water over the SCS slope, indicated that re-suspended sediments disperse over a large scope, supporting the influence of current advection on the spatial pattern of ^{234}Th in the study area.

The trajectory of the buoy revealed that seawater flows northeastward over the slope of the SCS (**Figure 1**). Station T1 was located upstream of the current, and T2 the downstream. Thus, the difference in ^{234}Th activities between T1 and T2 reflected the variability of ^{234}Th along the current, representing the real variation of ^{234}Th with time induced by its decay, generation from ^{238}U, and water exchange mainly horizontal advection as illustrated by the buoy movement. By taking advantage of the Lagrangian observation, these results enable us to evaluate the real advection flux of ^{234}Th and its influence on the sinking flux of ^{234}Th for the first time on the dynamic slope of the SCS.

Influence of Advection and Diffusion on the Sinking Flux of ^{234}Th

Ignoring the physical processes, the change of the amount of $^{234}Th_T$ with time can be expressed by:

$$\frac{dI_{ThT}}{dt} = \lambda_{Th}\,(I_U - I_{ThT}) - F_{Th} \quad (2)$$

where I_{ThT} and I_U are the inventories of the total ^{234}Th and ^{238}U from surface to the export depth (in dpm m^{-2}), which are calculated through the trapezoidal integration method. λ_{Th} is the decay constant of ^{234}Th (0.02876 day^{-1}). F_{Th} is the sinking flux of ^{234}Th in dpm m^{-2} day^{-1}. A sediment trap, deployed near station T2 on August 6, 2016, reports that the POC flux at 150 m was 8.4 ± 0.9 mmol-C m^{-2} day^{-1} (Li et al., 2018). The other array of sediment traps assembled to the buoy (from August 9 to 11, 2016) show the POC fluxes of 9.0 ± 0.6 mmol-C m^{-2} day^{-1} at 100 m and 9.3 ± 1.0 mmol-C m^{-2} day^{-1} at 200 m, respectively (Qiu, 2018). These consistent results indicated that particle sinking exhibited little variability during our sampling, lending support to the steady-state assumption. In addition, our sampling only covered 1.6 day, which could not enable the non-steady-state model to work well (Savoye et al., 2006). Thus, the steady-state is the best option in our study. At a steady-state, the sinking fluxes of ^{234}Th estimated from Eq. (2) varied from 3,176 to 21,197 dpm m^{-2} day^{-1} [i.e., $\lambda_{Th}(I_U - I_{ThT})$ in **Table 2**]. The sinking flux of POC, estimated from Eq. (1), was 3.6 ± 0.3 mmol-C m^{-2} day^{-1} at 200 m, significantly lower than 9.3 ± 1.0 mmol-C m^{-2} day^{-1} determined by the sediment trap attached to the buoy (Qiu, 2018). Such an inconsistency indicated that physical processes, e.g., advection and diffusion, could be non-negligible during calculating the sinking flux of ^{234}Th. Thus, the variability in total ^{234}Th should be better expressed as:

$$\frac{dI_{ThT}}{dt} = \lambda_{Th}(I_U - I_{ThT}) + u\frac{\partial I_{ThT}}{\partial x} + k_z\frac{\partial A_{ThT}}{\partial z} - F_{Th} \quad (3)$$

where u and k_z denote the horizontal advection velocity of the total ^{234}Th in cm s^{-1} and vertical diffusive coefficient in cm^2 s^{-1}. $\partial I_{ThT}/\partial x$ and $\partial A_{ThT}/\partial z$ represent the gradient of inventory and activity of the total ^{234}Th, respectively. To resolve Eq. (3), we need to assume (1) that the change rate of the inventory was uniform during the buoy transport; and (2) that the net changes of ^{234}Th inventory were caused by the sinking of transported particles on the slope. For assumption (1), the consistent POC fluxes from two sediment traps (i.e., Li et al., 2018; Qiu, 2018) seemed to favor the little variability in the sinking flux of particles during our sampling. However, water mixing appeared to influence the second assumption. As shown in **Figure 2**, both temperature and salinity revealed the mixing of the traced water body with surrounding water masses during its transport from T1 to T2. The mixing processes of various waters, probably carrying different ^{234}Th contents, could affect the estimate of ^{234}Th flux by changing the activity of ^{234}Th. The influence was evaluated through the variations of both ^{234}Th and ^{238}U between T1 and T2 by taking ^{234}Th decay into account. Results indicated that the mixing process accounted for <4% of the total ^{234}Th fluxes (ignoring physical processes from Eq. 2) estimated in the upper 200 m. Below 200 m, mixing resulted in a large influence with an average of 18%. Although this influence seemed to be acceptable for the assumption (2), Eq. (3) is still not resolved due to the lack of advection velocity and spatial gradients of ^{234}Th inventory.

The Lagrangian observation provided *in situ* velocity of current (i.e., 19.5 cm s^{-1}). However, this velocity is different from u in the second term on the right side of Eq. (3) in that particles have different transport speeds though basin-wide observations of sediment trap indicate that the transport of re-suspended sediment from the shelves is driven by lateral advection in the SCS (Schroeder et al., 2015). As an alternative strategy, we evaluated the influence of physical processes by comparing the flux of ^{234}Th at 200 m (ignoring physical processes) with that calculated through trap-derived POC at 200 m (i.e., trap-POC flux divided by the C_{POC}/Th_P ratio in Eq. 1). The sinking flux of ^{234}Th estimated from trap-POC flux was 10,775 ± 611 dpm m^{-2} day^{-1}, which was much higher than 4,136 ± 148 dpm m^{-2} day^{-1} obtained by Eq. (2). In other words, physical processes resulted in 6,639 ± 629 dpm m^{-2} day^{-1} flux of ^{234}Th. Although *in situ* observed velocity and the gradients of ^{234}Th could not be directly applied to calculate the advection term in Eq. (3), they may, to a first-order approximation, be used to highlight the difference between the actual physical influence and our observations. The transport speed of particles is usually smaller than the current. If the observed velocity was used as an upper limit of the particle transport, and the derivative (i.e., the second term on the right side of Eq. 3) was substituted for the finite difference [i.e., $u(I_{ThT,T1} - I_{ThT,T2})/\Delta x$, commonly estimated from the linear interpolation, Resplandy et al., 2012], the upper limit of advection influence was estimated to be 4,733 ± 1,831 dpm m^{-2} day^{-1} at 200 m. The vertical gradients of the total ^{234}Th (i.e., $\partial A_{ThT}/\partial z$) were estimated through the fitting curves obtained from its vertical distribution (**Figure 3A**), i.e., $A_{ThT} = 1.90e^{-0.0154z}$ ($r^2 = 0.82$) for 100–300 m. In the upper SCS, the diffusive coefficient ranges from 10^{-4} to 10^{-5} m^2 s^{-1} even though it could reach 10^{-3} m^2 s^{-1} in the mid-deep water (Wang et al., 2019). To evaluate the largest influence of the diffusion

TABLE 2 | Fluxes of $^{234}Th_T$ and the fluxes of particulate organic carbon (POC) calculated from $^{234}Th_T$ fluxes below the euphotic zone (150 m).

Depth	$\lambda_{Th}(I_U - I_{ThT})$	$u(I_{ThT,T1} - I_{ThT,T2})/\Delta x$	$k_z(\partial A_{ThT}/\partial z)$	$^{234}Th_T$ flux	POC/$^{234}Th_P$	POC flux	TPM flux
(m)	(dpm m^{-2} day^{-1})				(μmol dpm^{-1})	(mmol-C m^{-2} day^{-1})	(g m^{-2} day^{-1})
150	3,176 ± 120	2,103 ± 1,478	251 ± 39	5,529 ± 1,484	1.41	7.8 ± 2.2	1.79 ± 0.11
200	4,136 ± 148	4,733 ± 1,831	116 ± 39	8,986 ± 1,837	0.86	7.8 ± 1.6	3.46 ± 0.20
300	5,628 ± 231	−2,636 ± 1,487	25 ± 38	3,016 ± 1,505	0.75	2.3 ± 1.1	0.84 ± 0.05
500	10,240 ± 407	−7,500 ± 2,703	120 ± 6	2,860 ± 2,734	1.48	4.2 ± 4.1	1.48 ± 0.09
800	17,422 ± 642	−1,526 ± 4,280	58 ± 6	15,954 ± 4,328	1.07	17.0 ± 4.7	7.70 ± 0.37
1,000	21,197 ± 730	−3,358 ± 4,834	36 ± 6	17,874 ± 4,889	1.32	23.7 ± 6.5	7.27 ± 0.30

TPM, total particulate matter.

term, we conservatively adopted 10^{-3} m^2 s^{-1}. At 200 m, the estimated diffusion contribution to the sinking flux of ^{234}Th was 116 ± 39 dpm m^{-2} day^{-1}. Taken together, physical processes maximally accounted for 4,850 ± 1,831 dpm m^{-2} day^{-1}, lower than the actual physical effect of 6,639 ± 629 dpm m^{-2} day^{-1}. Since velocity was overestimated, the estimated lower flux indicated that there existed an addition of ^{234}Th from mixing or other processes during transport from T1 to T2, which led lower gradient and thus lower advection flux. It should be noted that although the product of the velocity of the buoy and the gradient of ^{234}Th accounted for the majority (73%) of the physical-contributed flux, it did not mean that Lagrangian observation provided actual physical parameters. Thus, Eq. (3) could not be completely resolved. Considering the fact that using these not-rigorous assumptions can present better results than those estimated by ignoring physical processes (**Figure 4A**), the observed data were used to constrain the fluxes of ^{234}Th and POC at other depths (**Table 2**). The results were compared with those obtained in the study area to further assay the rationality.

According to the model simulation (Gan et al., 2006), the current in the upper 200 m of the study area is somewhat different from that at 500 m. Simulated advection velocity of 10 cm s^{-1} below 200 m was adopted in calculating the advection flux of ^{234}Th. For diffusion, ^{234}Th$_T$ followed $A_{ThT} = 1.90e^{-0.0154z}$ ($r^2 = 0.71$) between 500 and 1,000 m. The estimated flux for each process were presented in **Table 2**.

Export Fluxes of Total Particulate Matter and Particulate Organic Carbon Estimated From the Sinking Fluxes of ^{234}Th

The ^{234}Th-derived sinking fluxes of TPM varied from 0.88 to 7.70 g m^{-2} day^{-1}, averaging 3.76 g m^{-2} day^{-1} at station T2 (**Table 2**). Over the western slope of the SCS, the ^{210}Po-derived sinking fluxes of TPM out of 1,000 m varied from 0.4 to 10.2 g m^{-2} day^{-1} with an average of 4.4 g m^{-2} day^{-1} (Ma et al., 2017). Our result of 7.27g m^{-2} day^{-1} at 1,000 m fell within this range. The minimum occurred at 300 m, corresponding to the low TPM contents (**Figures 2**, **4B**). With the increasing of TPM content to the mesopelagic bottom (i.e., 1,000 m), TPM also showed elevated sinking fluxes, indicating the cross-shelf dispersion of re-suspended sediments.

At the base of the euphotic zone (150 m), the sinking flux of POC (collected from August 9 to 11, 2016) was 7.8 mmol-C m^{-2} day^{-1} (**Table 2**), very coincident with 8.4 ± 0.9 mmol-C m^{-2} day^{-1} derived from a sediment trap near T2 (collected on August 6, 2016, Li et al., 2018), and falling in the range of sediment trap-derived scope of 2.8–9.0 mmol-C m^{-2} day^{-1} (Hung and Gong, 2010; Shih et al., 2019, 2020), satellite-derived 5.0–13.6 mmol-C m^{-2} day^{-1} (Chow et al., 2021), and ^{234}Th-derived scope of 4.6–11.8 mmol-C m^{-2} day^{-1} (Cai et al., 2015) in the northeastern SCS. In general, sediment trap directly collects particles, which largely represent the total effect of all processes including biogenic, physical, and chemical ones (Hung et al., 2016; Shih et al., 2019), though it is sometimes influenced by trapping efficiency (Coppola et al., 2002). The comparability between our results and published datasets also indicated that the considering physical processes produced better fluxes of particles than those ignoring physical processes. Owing to the requirements for technical expertise and high cost, the sediment traps are usually deployed with low spatial resolution. In contrast, the ^{234}Th method can provide POC flux data with high-resolution (Cai et al., 2008), but it suffers from poorly-constrained physical processes (Zhou et al., 2013). Biogeochemical models can decipher regional to global characteristics of POC flux, however, they often deviate from *in situ* measurements within small scope (Shih et al., 2021). Thus, accurate and high-resolution carbon export could be obtained in field studies by taking multiple methods' merits (Baker et al., 2020).

Conventionally, large particles (>53 μm) are assumed to be the representative of sinking particles for determining POC/^{234}Th ratios. However, some studies suggest that small particles (<50 μm) contribute the majority sinking of POC and ^{234}Th. For example, 1–10 and 10–50 μm fractions account

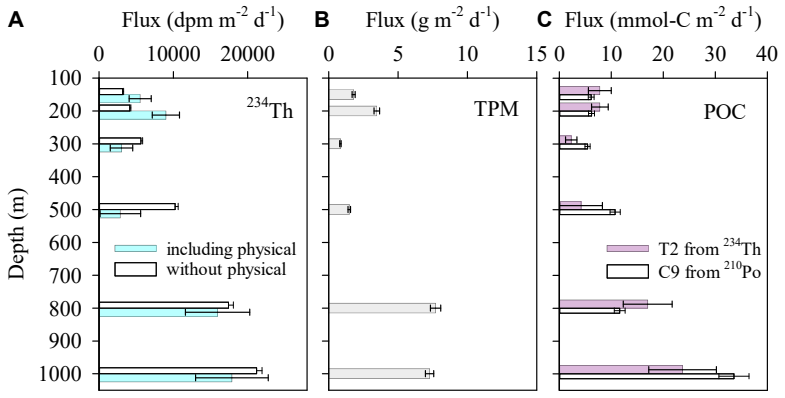

FIGURE 4 | Fluxes of ^{234}Th and particles on the northeastern shelf of the South China Sea (SCS), including **(A)** ^{234}Th fluxes ignoring physical processes and considering advection and diffusion, **(B)** ^{234}Th-derived TPM fluxes including physical processes, and **(C)** POC fluxes estimated from the ^{234}Th–^{238}U method (this study) and the ^{210}Po–^{210}Pb method (Yang et al., 2021b).

for 26–35 and 25–29% of the total POC based on the drifting sediment traps in the northern SCS (Hung and Gong, 2010). ^{234}Th carried by <50 μm particles contributes ∼70–80% of the total ^{234}Th in the northwestern Pacific Ocean (Hung et al., 2010, 2012). These results thus lend support to the conclusion that particles collected in our study represent the majority of sinking particles in the northern SCS. In addition, the POC/^{234}Th ratios varied from 0.75 to 1.48 μmol dpm^{-1} (**Table 2**), which are comparable to 0.8–1.3 μmol dpm^{-1} obtained on 1–50 μm particles from sediment traps in the northern SCS (Hung and Gong, 2010), also supporting this conclusion. Notably, the POC flux out of the euphotic zone was much higher than those observed in the northern basin (Zhou et al., 2013) and the southern basin of the SCS (mostly <5.0 mmol-C m^{-2} day^{-1}) (Cai et al., 2008; Yang et al., 2015), partly ascribed to the internal wave-induced input of nutrient-replete waters to the euphotic zone and successive phytoplankton flourish and POC settling (Li et al., 2018).

Compared with the flux at 150 m, POC showed comparable and significantly lower fluxes at 200 and 300 m, respectively (**Table 2**). In general, POC decreases with depth below the euphotic zone due to remineralization (Yang et al., 2009). Based on the ^{234}Th fluxes and POC/^{234}Th ratios (**Table 2**), it is clear that POC/^{234}Th ratios largely result in the flux descending with depth. Below 300 m, evident increases in POC flux occurred, from 4.2 to 23.7 mmol-C m^{-2} day^{-1} (**Figure 4C**). Obviously, there are additional sources of POC besides its settling from local upper water. The vertical profile of TPM (**Figure 2**) illustrates additional contributions. Internal waves can lead to the resuspension of shelf/slope sediments in the northern SCS (Jia et al., 2019). Just before our sampling, strong internal waves were observed in the study area (Li et al., 2018). Probably, internal wave-induced resuspension of organic matter resulted in the elevated POC fluxes via cross-shelf dispersion. Similar scenarios were also observed at a station near T1 during the same cruise (Yang et al., 2021b) and in another study conducted in the same area (Shih et al., 2019). The scanning electron microscope images of the sinking particles below 150 m indicate a higher proportion of lithogenic material (Shih et al., 2019), lending support to its sediment origin.

A recent study reveals that a large amount of POC is required to support the consumption of deep microbes in the SCS interior (Shen et al., 2020). Our results provide direct evidence for the cross-transport of POC. Using the lowest value at 300 m as a reference, shelf/slope sediments contributed 1.7–21.3 mmol-C m^{-2} day^{-1} to the mesopelagic waters of the SCS. At a station close to T1 during the same cruise, the sinking fluxes of POC were estimated to vary from 5.4 to 33.6 mmol-C m^{-2} day^{-1} based on the ^{210}Po–^{210}Pb method (Yang et al., 2021b). Considering the uncertainties, the ^{210}Po-derived fluxes by neglecting the horizontal advection and diffusion, were consistent with our ^{234}Th-derived results (**Figure 4**), indicating less influence of advection on the ^{210}Po–^{210}Pb method.

CONCLUSION

A Lagrangian observation of ^{234}Th was conducted over the slope of the northeastern SCS. Enhanced removal of ^{234}Th was observed in the mesopelagic waters compared with general mesopelagic oceans, pointing to the active particle dynamics below the euphotic zone of the SCS. Concurrently elevated TPM and POC concentrations with depth in the mesopelagic water revealed that re-suspended sediments from the shelf/slope dominated the removal of ^{234}Th. Combining the sediment trap results, the influence of physical processes on the sinking flux estimates of ^{234}Th was evaluated, revealing unneglectable effects of horizontal advection and vertical diffusion. Although considering the physical processes seemed to produce better sinking fluxes of ^{234}Th and POC, well-constraining the advection effect is still challenging due to the difficulty in obtaining the actual transport velocity of particles and spatial gradients.

DATA AVAILABILITY STATEMENT

The original contributions presented in the study are included in the article/supplementary material, further inquiries can be directed to the corresponding author.

AUTHOR CONTRIBUTIONS

XZ, YQ, and MZ collected and analyzed the samples. WY conceived and wrote the manuscript. MC edited the manuscript. All authors approved the submitted version.

FUNDING

This study was financially supported by the National Natural Science Foundation of China (Grant Nos. 42076030 and 41476061 to WY). Data and samples were collected onboard of *R/V* "*Yanping 2*" implementing the open research cruise NORC2016-04 supported by NSFC Shiptime Sharing Project (Grant No. 41549904).

ACKNOWLEDGMENTS

We thank the reviewers and editors for their constructive suggestions. We also thank YQ for his technical assistance during field observation and crew members of the *R/V Yanping 2* for their help during sample collection.

REFERENCES

Anand, S. S., Rengarajan, R., and Sarma, V. V. S. S. (2018). ^{234}Th-based carbon export flux along the Indian GEOTRACES LI02 section in the Arabian Sea and the Indian Ocean. *Glob. Biogeochem. Cy.* 32, 417–436. doi: 10.1002/2017GB005847

Bacon, M. P., Cochran, J. K., Hirschberg, D., Hammar, T. R., and Fleer, A. P. (1996). Export flux of carbon at the equator during the EqPac time-series cruises estimated from ^{234}Th measurements. *Deep Sea Res. II* 43, 1133–1153. doi: 10.1016/0967-0645(96)00016-1

Baker, C. A., Estapa, M. L., Iversen, M., Lampitt, R., and Buesseler, K. O. (2020). Are all sediment traps created equal? An intercomparison study of carbon export methodologies at the PAP-SO site. *Progr. Oceanogr.* 184:102317. doi: 10.1016/j.pocean.2020.102317

Benitez-Nelson, C. R., Buesseler, K. O., Rutgers van der Loeff, M. M., Andrews, J., Ball, L., Crossin, G., et al. (2001). Testing a new small-volume technique for determining ^{234}Th in seawater. *J. Radioanal. Nucl. Chem.* 248, 795–799. doi: 10.1023/A:1010621618652

Black, E. E., Buesseler, K. O., Pike, S. M., and Lam, P. J. (2018). ^{234}Th as a tracer of particulate export and remineralization in the southeastern tropical Pacific. *Mar. Chem.* 201, 35–50. doi: 10.1016/j.marchem.2017.06.009

Buesseler, K. O., Bacon, M. P., Cochran, J. K., and Livingston, H. D. (1992). Carbon and nitrogen export during the JGOFS North Atlantic bloom experiment estimated from ^{234}Th:^{238}U disequilibria. *Deep-Sea Res. I* 39, 1115–1137. doi: 10.1016/0198-0149(92)90060-7

Buesseler, K. O., Benitez-Nelson, C. R., Roca-Martí, M., Wyatt, A. M., Resplandy, L., Clevenger, S. J., et al. (2020). High-resolution spatial and temporal measurements of particulate organic carbon flux using ^{234}Th in the northeast Pacific Ocean during the export processes in the ocean from RemoTe Sensing field campaign. *Elem. Sci. Anth.* 8:1. doi: 10.1525/elementa.030

Buesseler, K. O., Pike, S., Maiti, K., Lamborg, C. H., Siegel, D. A., and Trull, T. W. (2009). ^{234}Th as a tracer of spatial, temporal and vertical variability in particle flux in the North Pacific. *Deep Sea Res. I* 56, 1143–1167. doi: 10.1016/j.dsr.2009.04.001

Cai, P., Chen, W., Dai, M., Wan, Z., Wang, D., Li, Q., et al. (2008). A high-resolution study of particle export in the southern South China Sea based on ^{234}Th:^{238}U disequilibrium. *J. Geophys. Res.* 113:C04019. doi: 10.1029/2007JC004268

Cai, P., Zhao, D., Wang, L., Huang, B., and Dai, M. (2015). Role of particle stock and phytoplankton community structure in regulating particulate organic carbon export in a large marginal sea. *J. Geophys. Res. Oceans* 120, 2063–2095. doi: 10.1002/2014JC010432

Chow, C. H., Shih, Y.-Y., Chien, Y.-T., Chen, J. Y., Fan, N., Wu, W.-C., et al. (2021). The wind effect on biogeochemistry in eddy cores in the northern South China Sea. *Front. Mar. Sci.* 8:717576. doi: 10.3389/fmars.2021.717576

Coppola, L., Roy-Barman, M., Wassmann, P., Mulsow, S., and Jeandel, C. (2002). Calibration of sediment traps and particulate organic carbon export using ^{234}Th in the Barents Sea. *Mar. Chem.* 80, 11–26. doi: 10.1016/S0304-4203(02)00071-3

Feng, N., Yang, W., Zhao, X., Chen, M., Qiu, Y., and Zheng, M. (2021a). Seasonal export of ^{234}Th and POC in Daya Bay, northern South China Sea. *Cont. Shelf Res.* 216:104359. doi: 10.1016/j.csr.2021.104359

Feng, N., Yang, W., Zhao, X., Chen, M., Qiu, Y., and Zheng, M. (2021b). Semi-enclosed bays server as hotspots for black carbon burial: a case study in Jiaozhou Bay, western Yellow Sea. *Sci. Total Environ.* 797:149100. doi: 10.1016/j.scitotenv.2021.149100

Gan, J., Li, H., Curchitser, E. N., and Haidvogel, D. B. (2006). Modeling South China Sea circulation: response to seasonal forcing regimes. *J. Geophys. Res.* 111:C06034. doi: 10.1029/2005JC003298

Ge, Z., Li, Q. P., Yang, W., Liu, X., and Wu, Z. (2022). Transparent exopolymer particle dynamics along a shelf-to-sea gradient and impacts on the regional carbon cycle. *Sci. Total Environ.* 808:152117. doi: 10.1016/j.scitotenv.2021.152117

Hong, Q., Peng, S., Zhao, D., and Cai, P. (2021). Cross-shelf export of particulate organic carbon in the northern South China Sea: insights from a ^{234}Th mass balance. *Progr. Oceanogr.* 193:102532. doi: 10.1016/j.pocean.2021.102532

Hung, C.-C., Chen, Y.-F., Hsu, S.-C., Wang, K., Chen, J., and Burdige, D. J. (2016). Using rare earth elements to constrain particulate organic carbon flux in the East China Sea. *Sci. Rep.* 6:33880. doi: 10.1038/srep33880

Hung, C.-C., and Gong, G.-C. (2010). POC/^{234}Th ratios in particles collected in sediment traps in the northern South China Sea. *Estuar. Coast. Shelf Sci.* 88, 303–310. doi: 10.1016/j.ecss.2010.04.008

Hung, C.-C., Gong, G.-C., and Santschi, H. (2012). ^{234}Th in different size classes of sediment trap collected particles from the Northwestern Pacific Ocean. *Geochim. Cosmochim. Acta* 91, 60–74. doi: 10.1016/j.gca.2012.05.017

Hung, C.-C., Xu, C., Santschi, P. H., Zhang, S.-J., Schwehr, K. A., Quigg, A., et al. (2010). Comparative evaluation of sediment trap and ^{234}Th-derived POC fluxes from the upper oligotrophic waters of the Gulf of Mexico and the subtropical northwestern Pacific Ocean. *Mar. Chem.* 121, 132–144. doi: 10.1016/j.marchem.2010.03.011

Jia, Y., Tian, Z., Shi, X., Liu, J. P., Chen, J., and Liu, X. (2019). Deep-sea sediment resuspension by internal solitary waves in the Northern South China Sea. *Sci. Rep.* 9:12137. doi: 10.1038/s41598-019-47886-y

Li, D., Chou, W.-C., Shih, Y.-Y., Chen, G.-Y., Chang, Y., Chow, C. H., et al. (2018). Elevated particulate organic carbon export flux induced by internal waves in the oligotrophic northern South China Sea. *Sci. Rep.* 8:2042. doi: 10.1038/s41598-018-20184-9

Ma, H., Yang, W., Zhang, L., Zhang, R., Chen, M., Qiu, Y., et al. (2017). Utilizing ^{210}Po deficit to constrain particle dynamics in mesopelagic water, western South China Sea. *Geochem. Geophys. Geosyst.* 18, 1594–1607. doi: 10.1002/2017GC006899

Maiti, K., Bosu, S., Dsa, E. J., Adhikari, P. L., Sutor, M., and Longnecker, K. (2016). Export fluxes in northern Gulf of Mexico–comparative evaluation of direct, indirect and satellite-based estimates. *Mar. Chem.* 184, 60–77. doi: 10.1016/j.marchem.2016.06.001

Martin, P., Lampitt, R. S., Perry, J. J., Sanders, R., Lee, C., and D'Asaro, E. (2011). Export and mesopelagic particle flux during a North Atlantic spring diatom bloom. *Deep Sea Res. I* 58, 338–349. doi: 10.1016/j.dsr.2011.01.006

Owens, S. A., and Buesseler, K. O. (2015). ^{234}Th as a tracer of particle dynamics and upper ocean export in the Atlantic Ocean. *Deep Sea Res. II* 116, 42–59. doi: 10.1016/j.dsr2.2014.11.010

Owens, S. A., Buesseler, K. O., and Sims, K. W. W. (2011). Re-evaluating the ^{238}U salinity relationship in seawater: implications for the ^{238}U-^{234}Th disequilibrium method. *Mar. Chem.* 127, 31–39. doi: 10.1016/j.marchem.2011.07.005

Qiu, Y. (2018). *Regulatory Mechanism of Plankton Community Structure on Particulate Organic Carbon Export in Different Ecosystems of Subtropical Marginal Seas.* Ph.D. Dissertation. Xiamen: Xiamen University, 42–65.

Resplandy, L., Martin, A. P., Le Moigne, F., Martin, P., Aquilina, A., Mémery, L., et al. (2012). How does dynamical variability impact ^{234}Th-derived estimates of organic export? *Deep Sea Res. I* 68, 24–45. doi: 10.1016/j.dsr2012.05.015

Roca-Martí, M., Puigcorbé, V., Iversen, M. H., Rutgers van der Leoff, M., Klaas, C., Cheah, W., et al. (2017). High particulate organic carbon export during the decline of a vast diatom bloom in the Atlantic sector of the Southern Ocean. *Deep Sea Res. II* 138, 102–115. doi: 10.1016/j.dsr2.2015.12.007

Savoye, N., Benitez-Nelson, C., Burd, A. B., Cochran, J. K., Charette, M., Buesseler, K. O., et al. (2006). ^{234}Th sorption and export models in the water column: a review. *Mar. Chem.* 100, 234–249. doi: 10.1016/j.marchem.2005.10.014

Schroeder, A., Wiesner, M. G., and Liu, Z. (2015). Fluxes of clay minerals in the South China Sea. *Earth Planet. Sci. Lett.* 430, 30–42. doi: 10.1016/j.epsl.2015.08.001

Shen, J., Jiao, N., Dai, M., Wang, H., Qiu, G., Chen, J., et al. (2020). Laterally transported particles from margins serve as a major carbon and energy source for dark ocean ecosystems. *Geophys. Res. Lett.* 47:e2020GL088971. doi: 10.1029/2020GL088971

Shih, Y.-Y., Hung, C.-C., Tuo, S.-H., Shao, H.-J., Chow, C. H., Muller, F. L. L., et al. (2020). The impact of eddies on nutrient supply, diatom biomass and carbon export in the northern South China Sea. *Front. Earth Sci.* 8:537332. doi: 10.3389/feart.2020.537332

Shih, Y.-Y., Lin, H.-H., Li, D., Hsieh, H.-H., Hung, C.-C., and Chen, C.-T. A. (2019). Elevated carbon flux in deep waters of the South China Sea. *Sci. Rep.* 9:1496. doi: 10.1038/s41598-018-37726-w

Shih, Y.-Y., Shiah, F.-K., Lai, C.-C., Chou, W.-C., Tai, J.-H., Wu, Y.-S., et al. (2021). Comparison of primary production using in situ and satellite-derived values at the SEATS station in the South China Sea. *Front. Mar. Sci.* 8:747763. doi: 10.3389/fmars.2021.747763

Umhau, B. P., Benitez-Nelson, C. R., Close, H. G., Hannides, C. S., Motta, L., Popp, B. N., et al. (2019). Seasonal and spatial changes in carbon and nitrogen fluxes estimated using ^{234}Th:^{238}U disequilibria in the North Pacific tropical and subtropical gyre. *Mar. Chem.* 217:103705. doi: 10.1016/j.marchem.2019.103705

Wang, D., Wang, Q., Cai, S., Shang, X., Peng, S., Shu, Q., et al. (2019). Advances in research of the mid-deep South China Sea circulation. *Sci. China Earth Sci.* 62, 1992–2004. doi: 10.1007/s11430-019-9546-3

Yang, W., Chen, M., Zheng, M., He, Z., Zhang, X., Qiu, Y., et al. (2015). Influence of a decaying cyclonic eddy on biogenic silica and particulate organic carbon in the tropical South China Sea based on ^{234}Th-^{238}U disequilibrium. *PLoS One* 10:e0136948. doi: 10.1371/journal.pone.0136948

Yang, W., Huang, Y., Chen, M., Qiu, Y., Peng, A., and Zhang, L. (2009). Export and remineralization of POM in the Southern Ocean and the South China Sea estimated from ^{210}Po/^{210}Pb disequilibria. *Chin. Sci. Bull.* 54, 2118–2123. doi: 10.1007/s11434-009-0043-4

Yang, W., Zhang, X., Chen, M., Fang, Z., and Qiu, Y. (2021a). Utilizing ^{234}Th/^{238}U disequilibrium to constrain particle dynamics in hydrothermal plumes in the Southwest Indian Ocean. *Acta Oceanol. Sin.* 40, 16–25. doi: 10.1007/s13131-021-1786-2

Yang, W., Zhao, X., Guo, L., Huang, B., Chen, M., Fang, Z., et al. (2021b). Utilization of soot and ^{210}Po-^{210}Pb disequilibria to constrain POC fluxes in the northeastern South China Sea. *Front. Mar. Sci.* 8:694428. doi: 10.3389/fmars.2021.694428

Yang, W., Zhang, X., Chen, M., and Qiu, Y. (2016). Unusually low ^{234}Th in a hydrothermal effluent plume over the Southwest Indian Ridge. *Geochem. Geophys. Geosyst.* 17, 3815–3824. doi: 10.1002/2016GC006580

Zhao, X., Yang, W., Ma, H., Li, J., Chen, M., Fang, Z., et al. (2019). Seasonal variations in the abundance and sinking flux of biogenic silica in Daya Bay, northern South China Sea. *Oceanologia* 61, 239–251. doi: 10.1016/j.oceano.2018

Zhou, K., Dai, M., Kao, S.-J., Wang, L., Xiu, P., Chai, F., et al. (2013). Apparent enhancement of ^{234}Th-based particle export associated with anticyclonic eddies. *Earth Planet. Sci. Lett.* 381, 198–209. doi: 10.1016/j.epsl.2013.07.039

Conflict of Interest: The authors declare that the research was conducted in the absence of any commercial or financial relationships that could be construed as a potential conflict of interest.

Publisher's Note: All claims expressed in this article are solely those of the authors and do not necessarily represent those of their affiliated organizations, or those of the publisher, the editors and the reviewers. Any product that may be evaluated in this article, or claim that may be made by its manufacturer, is not guaranteed or endorsed by the publisher.

frontiers in Marine Science

ORIGINAL RESEARCH
published: 14 March 2022
doi: 10.3389/fmars.2022.837515

Developing Accelerator Mass Spectrometry Capabilities for Anthropogenic Radionuclide Analysis to Extend the Set of Oceanographic Tracers

Karin Hain[1], Martin Martschini[1], Fadime Gülce[1], Maki Honda[1,2], Johannes Lachner[1,3], Michael Kern[1], Johanna Pitters[1], Francesca Quinto[4], Aya Sakaguchi[5], Peter Steier[1], Andreas Wiederin[1], Alexander Wieser[1], Akihiko Yokoyama[6] and Robin Golser[1]*

[1] Isotope Physics, Faculty of Physics, University of Vienna, Vienna, Austria, [2] Nuclear Safety Research Center, Japan Atomic Energy Agency, Tokai, Japan, [3] Helmholtz-Zentrum Dresden-Rossendorf, Dresden, Germany, [4] Institute for Nuclear Waste Disposal, Karlsruhe Institute of Technology, Eggenstein-Leopoldshafen, Germany, [5] Center for Research in Isotopes and Environmental Dynamics, University of Tsukuba, Tsukuba, Japan, [6] Institute of Science and Engineering, Kanazawa University, Kanazawa, Japan

OPEN ACCESS

Edited by:
Núria Casacuberta, ETH Zürich, Switzerland

Reviewed by:
Hans-Arno Synal, ETH Zürich, Switzerland
Qiaohui Fan, Northwest Institute of Eco-Environment and Resources (CAS), China

***Correspondence:**
Karin Hain
karin.hain@univie.ac.at

Specialty section:
This article was submitted to Ocean Observation, a section of the journal Frontiers in Marine Science

Received: *16 December 2021*
Accepted: *10 February 2022*
Published: *14 March 2022*

Citation:
Hain K, Martschini M, Gülce F, Honda M, Lachner J, Kern M, Pitters J, Quinto F, Sakaguchi A, Steier P, Wiederin A, Wieser A, Yokoyama A and Golser R (2022) Developing Accelerator Mass Spectrometry Capabilities for Anthropogenic Radionuclide Analysis to Extend the Set of Oceanographic Tracers. Front. Mar. Sci. 9:837515. doi: 10.3389/fmars.2022.837515

Recent major advances in Accelerator Mass Spectrometry (AMS) at the Vienna Environmental Research Accelerator (VERA) regarding detection efficiency and isobar suppression have opened possibilities for the analysis of additional long-lived radionuclides at ultra-low environmental concentrations. These radionuclides, including ^{233}U, ^{135}Cs, ^{99}Tc, and ^{90}Sr, will become important for oceanographic tracer application due to their generally conservative behavior in ocean water. In particular, the isotope ratios ^{233}U/^{236}U and ^{137}Cs/^{135}Cs have proven to be powerful fingerprints for emission source identification as they are not affected by elemental fractionation. Improved detection efficiencies allowed us to analyze all major long-lived actinides, i.e., ^{236}U, ^{237}Np, ^{239,240}Pu, ^{241}Am as well as the very rare ^{233}U, in the same 10 L water samples of a depth profile from the northwest Pacific Ocean. For this purpose, a simplified and very flexible chemical purification procedure based on extraction chromatography (a single UTEVA® column) was implemented which can be extended by a DGA® column for Am purification. The procedure was validated with the reference materials IAEA-381/385. With the additional increase in ionization efficiency expected for the extraction of actinides as fluoride molecules from the AMS ion source, a further reduction of chemical processing may become possible. This method was successfully applied to an exemplary set of air filter samples. In order to determine the quantitative ^{237}Np concentration reliably, a ^{236}Np spike material is being developed in collaboration with the University of Tsukuba, Japan. Ion-Laser Interaction Mass Spectrometry (ILIAMS), a novel technique for the efficient suppression of stable isobaric background, has been developed at VERA and provides unprecedented detection sensitivity for the fission fragments ^{135}Cs, ^{99}Tc, and ^{90}Sr. The corresponding setup is fully operational now and the isobar suppression factors of $>10^5$ achieved, in principle, allow for the detection of

the mentioned radionuclides in the environment. Especially for ^{90}Sr analysis, this new approach has already been validated for selected reference materials (e.g., IAEA-A-12) and is ready for application in oceanographic studies. We estimate that a sample volume of only (1–3) L ocean water is sufficient for ^{90}Sr as well as for ^{135}Cs analysis, respectively.

Keywords: Accelerator Mass Spectrometry, laser-photodetachment, isotopic signatures, Pacific Ocean, neptunium spike, Ion-Laser Interaction, actinides, fission products

INTRODUCTION

The application of long-lived anthropogenic radionuclides in oceanography requires ultra-sensitive detection methods to analyze trace concentrations at environmental levels while reducing the overall sample size. Smaller samples allow for the collection of a larger number of samples per cruise so that the resolution of the distribution of the radionuclides can be significantly improved. Such more detailed data is urgently needed to obtain a more accurate understanding of the complex system of ocean circulation. The interpretation of the measured data of a single nuclide tracer is often limited by mixing, dilution and sedimentation or scavenging processes. Analyzing as many nuclides as possible, which show different chemical migration behavior, from the same sample helps to disentangle the different environmental processes. For instance, it was shown that ^{236}U, which is conservatively transported in the open oceans, is partly co-precipitated in coastal areas with high organic particle concentration by comparison with ^{237}Np (López-Lora et al., 2020). In contrast, isotopic ratios, e.g., the plutonium (Pu) ratios ^{240,241}Pu/^{239}Pu [e.g., in Kelley et al. (1999), Zheng et al. (2012, 2013)], are very robust against chemical fractionation and hence, allow unambiguous identification of the emission source. The isotopic ratios of the two conservatively behaving elements uranium (U) and cesium (Cs), i.e., ^{233}U/^{236}U (Hain et al., 2020) and ^{137}Cs/^{135}Cs (Russell et al., 2015) have been introduced as two very promising oceanographic tracers because of their abilities for emission source assessment. The group of actinides is considered as especially interesting for oceanographic applications, as the individual elements show very different migration behavior depending on the ambient redox conditions. U and Np isotopes in general behave conservatively in ocean water and therefore are considered useful tracers for ocean dynamics (Dunk et al., 2002; Lindahl et al., 2005). On the other hand, Pu and Am are much more particle-reactive so that they are quickly removed from the water column by sedimentary mineral and organic particles (Lehto and Hou, 2011) and hence, they can serve as tracers for sedimentation processes (Tims et al., 2004). All the respective long-lived isotopes, i.e., ^{233,236}U, ^{239,240}Pu, ^{241}Am, and ^{237}Np, are available for routine analysis at the Vienna Environmental Research Accelerator (VERA) (Steier et al., 2019). However, quantification of the ^{237}Np concentration still suffers from the lack of sufficiently pure spike material. Until such spike material is available, environmental ^{237}Np concentrations are determined by using a non-isotopic internal ^{242}Pu spike and an external ^{237}Np/^{242}Pu standard for normalization (Qiao et al., 2010; López-Lora et al., 2019), with the drawback of possible elemental fractionation during sample preparation and measurement. There is a multitude of chemical separation procedures for actinides available (e.g., López-Lora et al., 2019) but to our knowledge none of them allows the efficient extraction of the major long-lived nuclides including ^{241}Am from the same small volume ocean sample (10 L).

As these long-lived actinides can be measured essentially background-free by Accelerator Mass Spectrometry (AMS), the minimum sample size is basically defined by the detection efficiency and the chemical yield of sample preparation. At the Vienna Environmental Research Accelerator (VERA) laboratory we have successfully increased the efficiency of the spectrometer by around one order of magnitude through several improvements of the setup and the measurement procedure (Steier et al., 2019). The AMS methodological development at VERA for actinide detection recently focused on the possibility to increase the negative ionization yield of U by adding the fluorine donator PbF_2 to the sample matrix for the cesium sputter source. Fluoride compounds of U (e.g., UF_5^-) are then extracted from the ion source instead of the previously used oxide compounds (e.g., UO^-) (Zhao et al., 2010; Cornett et al., 2015; Kazi et al., 2015). While, e.g., Hotchkis et al. (2019) report similarly high ionization efficiencies for UO^- of several percent from their ion source, this is not observed by a number of other AMS laboratories including VERA. Our previous survey on U extraction confirmed an increase of the ionization yield using fluorides by at least a factor 5 for U standard materials (Kern et al., 2022). In addition, fluoride targets have been found to produce very strong UF_5^- currents within the first half hour of sputtering which then rapidly drop to zero output. Optimization of the ion source operation is still on-going to ensure more stable measurement conditions. Consequently, the applicability of this method to environmental samples regarding accuracy and precision had to be demonstrated.

Beyond that, the novel technique of Ion-Laser Interaction Mass Spectrometry (ILIAMS) (Martschini et al., 2019b) makes new radionuclides accessible at ultra-trace concentrations. First results presented here and in Martschini et al. (2021) show that this technique will allow for AMS-measurements of the fission products ^{99}Tc, ^{135}Cs, and ^{90}Sr at environmental levels. Since these isotopes were previously inaccessible with other techniques in the general environment (^{135}Cs), required huge instrumental effort in AMS (^{99}Tc) or relied on slow and cumbersome sample preparation for radiometric detection (^{90}Sr), ILIAMS is expected to facilitate much more widespread analysis of these tracers. The fission product technetium-99 (^{99}Tc, $T_{1/2} = 2.1 \times 10^5$ yr) is usually present as the highly soluble TcO_4^+ -ion in oxic waters, which is transported conservatively with the water masses in the open oceans similar to cesium (Cs). ^{99}Tc was therefore proposed

as oceanographic tracer for the North Atlantic Ocean early on (Aarkrog et al., 1987), where elevated concentrations due to emissions of the Sellafield reprocessing plant can be analyzed by less sensitive techniques, e.g., ICP-MS. Radiostrontium in the ocean is another viable conservative tracer that is generally even better stabilized than Cs as it is less adsorbed to particles (Povinec et al., 2012). However, its behavior in surface ocean water with possible removal by celeslite particle formation is still not fully understood and source terms in coastal areas are less straightforward to assess as fluvial input to the ocean from land deposition of strontium (Sr) plays a much stronger role than for Cs (Povinec et al., 2012). Being a chemical homolog of calcium, Sr is readily incorporated into the carbonate skeleton of corals which are considered a powerful archive for past climatic conditions. ^{90}Sr archived in these time-resolved reservoirs can be used to estimate water transit times from the source of emission to the location of the collected coral core and as a proxy for past ocean chemistry (e.g., Toggweiler and Trumbore, 1985; Purdy et al., 1989). ^{135}Cs, with a not well-known half-life between 1.3 and 3 Myrs (Singh et al., 2008; MacDonald et al., 2016), is a pure beta-emitter and therefore hardly detectable via radiometric methods. The low abundance of ^{135}Cs with its high isobaric background of ^{135}Ba makes it difficult to detect, also for mass spectrometric approaches. Due to this difficulty, most studies presenting ^{135}Cs/^{137}Cs ratios were performed on water with ^{135,137}Cs/^{133}Cs ratios of 10^{-8} or higher, i.e., close to sources of contamination (Zhu et al., 2020a). Two recent studies show first results on ^{135}Cs concentration in general seawater from the west coast of Greenland. There, 40–50 L of ocean water were used for the successful detection with ICP-MS/MS (Zhu et al., 2021) and 200 mL with TIMS (Zhu et al., 2020b) characterized by a detection limit of ^{135}Cs/^{133}Cs $\sim 4 \times 10^{-10}$. The residence time of Cs is comparable to that of U and amounts to 330 kyr for Cs (Broecker and Peng, 1982), so ^{135}Cs can also be considered a conservative tracer which might have entered the marine environment due to the Fukushima accident (Zheng et al., 2014), representing a point source for radionuclide tracing.

This contribution at the one hand aims at giving an overview about the present status of method development at VERA toward quantitative analysis of the listed fission products in different compartments of the environment using ILIAMS. On the other hand, the new sample preparation and measurement procedure for routine analysis of actinides in ocean water samples will be discussed based on results for a water column from the Northwest Pacific Ocean. Furthermore, the reliability of the fluoride extraction method has been verified for ^{236}U/^{238}U results in air filters. Last but not least, we report on the current status of Np spike development at VERA within a joint project with the University of Tsukuba. This manuscript is intended to give potential users insight into the sample amount and preparation techniques required for the analysis of the respective mentioned isotopes with AMS at VERA. The presented procedures, especially those focusing on actinide detection, can be adopted by similar AMS facilities. This also holds for the suggested fission fragment tracers provided that suitable isobar suppression systems are implemented.

MATERIALS AND METHODS

Radionuclide Spikes

As ^{242}Pu isotope standard, an aliquot of the certified spike solution IRMM-085 (Institute for Reference Materials and Measurements, Belgium) and as ^{243}Am isotope standard, an aliquot of the Alpha Standard Solution (Eckert & Ziegler Nuclitec GmbH, Catalog No.: 7243, Source No.: 1637-61) were used.

A ^{95m}Tc spike, which serves as a chemical yield monitor for ^{99}Tc extraction, was produced by proton irradiation of molybdenum (Mo) foils at the Maier-Leibnitz Laboratory in Munich and at the University of Cologne according to Wacker et al. (2004). The irradiated Mo foil was dissolved in aqueous H_2O_2 (30%, 35 mL) overnight, then purified using TEVA resin (Gülce, F. et al., in preparation) and the final ^{95m}Tc concentration was characterized by gamma-spectrometry.

Samples

The developed procedures for actinide extraction were verified using certified reference material available from the International Atomic Energy Agency (IAEA), i.e., Irish Sea water (IAEA-381) and sediment (IAEA-385). Literature values for ^{233,236}U are not certified, neither for water nor for sediment, as well as for ^{237}Np in sediment, but information values (Povinec et al., 2002; Pham et al., 2008; Hain et al., 2020) or individual studies (Lee et al., 2008; Goldstein et al., 2021) are available for comparison. The new procedures were applied to ocean water samples collected at a station in the northwest Pacific Ocean (BD04, 37°49 N, 143°53 E, maximum depth 600 m) collected during the cruise KH-12-4 (GP02) of the ship R/V Hakuho Maru as part of the GEOTRACES program on August 24/25, 2012. The original 20 L samples were split so that 10 L were used for actinide analysis while the second half was kept to determine the ^{99}Tc concentration. Three samples from this water column had been analyzed before and additional details on the sampling procedure can be found in the corresponding publication (Hain et al., 2017). These samples had been also analyzed at VERA but applying a different actinide separation chemistry. Selected air filters collected in Austria (Meteorological Station Hohe Warte, Vienna, Austria) during the most active phase of atmospheric nuclear weapons testing, i.e., 1962–1965, were analyzed regarding their ^{233,236}U concentrations. To assess the accuracy of chemical ^{90}Sr extraction and subsequent AMS-measurement for various sample matrices, we applied our method to the certified IAEA reference material IAEA-A-12 (beef bone) with a recommended ^{90}Sr content of 54.8 Bq/kg for a reference date of 15.12.1981 and to the IAEA Proficiency Test sample IAEA-TEL-2015-03_05 (Syrian soil) with a target value for the ^{90}Sr content of (36.2 ± 2.7) Bq/kg on 01.01.2015. An overview of the analyzed sample materials and radionuclides is presented in **Table 1**.

Chemical Treatment for Environmental Materials

Chemical Extraction of Actinides (U, Pu, Np, and Am)

The overall sample preparation procedure which is now routinely applied for the extraction of actinides from large volume ocean

TABLE 1 | Summary of sample materials and radionuclides investigated within the scope of the present work.

Sample material	Material name	Description	Analyzed nuclides
Seawater	IAEA-381	IAEA reference material Irish Sea water	^{233,236}U, ^{239,240}Pu, ^{241}Am, ^{237}Np
	Pacific Ocean	GEOTRACES cruise KH-12-4	^{233,236}U, ^{239,240}Pu, ^{241}Am, ^{237}Np, ^{99}Tc
Marine sediment	IAEA-385	IAEA reference material Irish Sea sediment	^{233,236}U, ^{239,240}Pu, ^{237}Np
Soil	IAEA-Tel-2015-03_05	IAEA proficiency test sample Syrian soil	^{90}Sr
Beef bone	IAEA-A-12	IAEA reference material	^{90}Sr
Aerosols	Air filter	Air Filter samples from Vienna (1962–1965)	^{233,236}U

water samples (e.g., those from BD04) at VERA, is depicted in **Figure 1**. After adding the required isotopic spike solutions, i.e., 2×10^8 atoms each of ^{242}Pu for ^{239,240}Pu and ^{243}Am for ^{241}Am analysis, the volume is first reduced to half by evaporation. Actinides are then pre-concentrated from the remaining 5 L by a $Fe(OH)_3$ co-precipitation which also removes the major salt load when the pH is carefully adjusted to 8.5. The column load solution for the UTEVA® resin is obtained by first taking up the sample in 3M HNO_3-0.5M $Al(NO_3)_3$. The oxidation state of Pu and Np is then adjusted to +IV using a combination of sulfamic and ascorbic acid as well as $NaNO_2$ according to Maxwell et al. (2010). Am, usually present in oxidation state +III in most chemical conditions, passes through the UTEVA (Eichrom Technologies) along with most other metal ions from the initial environmental matrix and the large surplus of iron used for the co-precipitation. Am is strongly adsorbed onto the DGA® resin (Eichrom Technologies) which is used to purify the Am fraction as especially Fe(III+) ions pass through the resin (Pourmand and Dauphas, 2010). After the separation of the UTEVA® and the DGA® cartridge, which are set up in tandem for loading of the sample solution and rinsing, Pu and Np are eluted from UTEVA® into the same fraction by complexation with oxalic acid, U is removed from UTEVA® by 0.02M HCl and Am is eluted from the DGA® cartridge with 0.25M HCl. The presented procedure is highly flexible and can be extended by an initial leaching step using aqua regia also for solid samples as applied to rubble or using 8M HNO_3 for (sea and lake) sediment samples.

The subsequent preparation of the AMS targets depends on whether actinides are to be analyzed in oxide form or the new approach of extracting actinides in fluoride form from the ion source is applied. In the routine procedure for oxide preparation, actinides are co-precipitated with 2 mg of Fe^{3+}. Oxalates in the Pu/Np fraction need to be decomposed in a microwave oven beforehand, where the solution is slowly heated to 200°C and left at this temperature for 8 min. After centrifugation, the precipitate is washed three times and then dried at 80°C for at least 4 h. Finally, the dry Fe pellet is calcined at 800°C for 4 h in a quartz crucible and pressed into an Al sample holder. The target preparation procedure for fluoride extraction is under development, but has been already used for a comprehensive set of samples with added actinide spikes for the experiments described in section "Status of the Isotopic Spike for Quantitative ^{237}Np Analysis." Regarding environmental samples, the procedure has only been successfully applied to the U fraction so far, e.g., for the air filter samples [(Kern et al., 2022); this work]. In short, the fractions are eluted into Teflon tubes and about 200 μg of Fe is added. After evaporating the solution to dryness, one drop of acetone is added and the produced iron pellet is transferred to a quartz crucible using a pipette. The Fe is then calcined as described before and the small amount of Fe_2O_3 thus produced is carefully mixed with a large surplus of PbF_2 (mass ratio ∼1:9) which is directly pressed into a Cu sample holder. Al sample holders cannot be used in this case, as PbF_2 seems to react with Al under ion source conditions.

Extraction of Fission Products (Tc, Cs, and Sr)

^{99}*Tc*

Several procedures for chemical Tc purification adjusted to Mass Spectrometry or even AMS have been reported (summarized in Shi et al. (2012)), most of which are based on TEVA® resin (Eichrom Technologies Inc.). However, the chemical Ru suppression obtained with a single TEVA column turned out to be insufficient to allow the analysis of ^{99}Tc in certain environmental samples, e.g., peat bog samples. For this reason, a pre-treatment procedure based on LLX using 5% TIOA + Xylene for the pre-concentration of ^{99}Tc from large volume ocean water samples with high salt load was developed which also achieved a very good Ru suppression (2×10^3) and very stable ^{99}Tc recoveries (including purification with TEVA) of (89 ± 5%) (Gülce, F., in preparation). AMS targets are then prepared by adding 2 mg of Nb (in-house solution) to the Tc fraction which is then evaporated to dryness. We have performed experiments regarding the optimum temperature of the final calcination step, i.e., at 450 and 300°C, as there were indications for Tc losses at the higher temperature (^{99}Tc Detection With Accelerator Mass Spectrometry). When using ^{95m}Tc as chemical yield monitor analyzed by gamma spectrometry to correct the final AMS result, losses of Tc during the preparation of the solid sputter matrix for AMS measurements are difficult to quantify as the geometry of the sample solution and the dry solid material required for AMS cannot be directly compared. Therefore, it is of importance that the recovery of these final preparation steps is stable and close to 100%. To ensure the same geometry for gamma spectrometry we compared the ^{95m}Tc count rates of samples after slow evaporation to dryness and after calcination, obtaining in this way the recovery of the calcination step.

^{135}*Cs*

Cs extraction and purification is based on the procedure described in Zok et al. (2021). A Cs extraction with Ammonium phosphomolybdate hydrate (AMP, Alfa Aesar) is followed by an anion exchange column [Dowex 1-X8 (100-200 mesh), Alfa

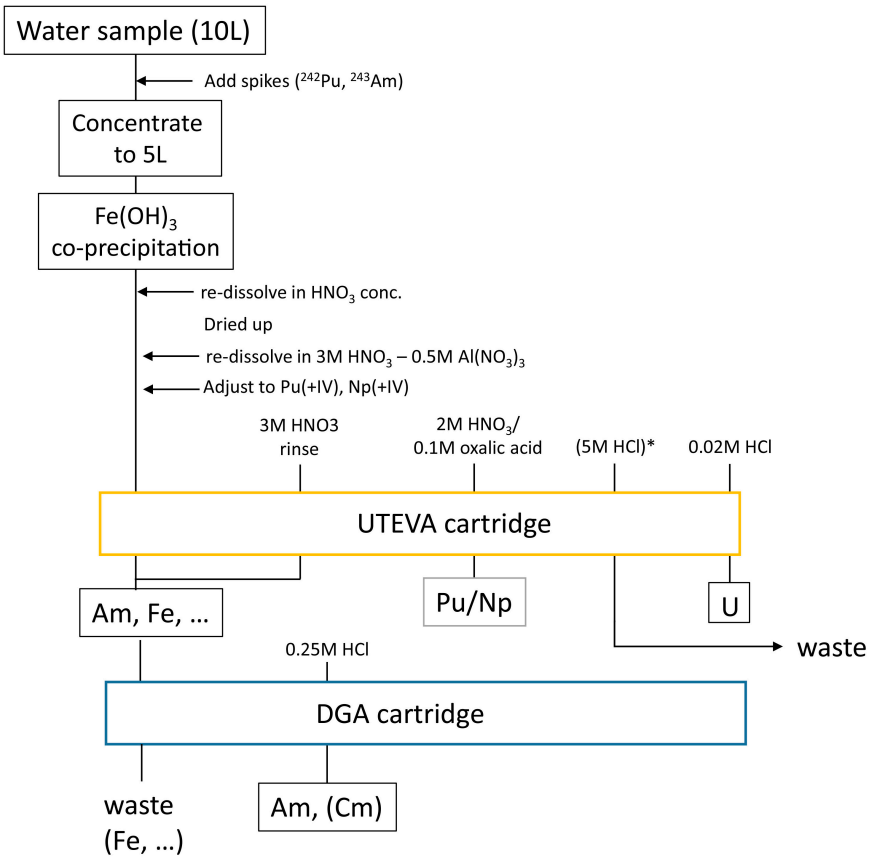

FIGURE 1 | Flow chart of applied separation chemistry to extract and purify Pu/Np, U, and Am from large volume ocean water samples using extraction chromatography. * marks a rinsing step to remove Th in the final U fraction which is only required when ^{233}U is to be analyzed.

Aesar] and a cation exchange column [AG 50W-X8 (100-200 mesh), Bio-Rad Laboratories, Inc.]. The overall process has a high yield of ca. 80%. The procedure might be simplified for ILIAMS assisted AMS measurements, which seem robust against content of other elements in the target including the presence of the Ba isobars. For the AMS target, the final purified Cs fraction in solution is mixed with a Cs carrier (Cs_2SO_4) and PbF_2 needed for the extraction of CsF_2^- from the ion source. These components are mixed in Milli-Q water and dried at 70°C for several hours. Finally the dried powder is pressed into copper target holders for the AMS measurement. Until now, this procedure to produce AMS targets was only applied to organic samples.

^{90}Sr

The chemical sample preparation procedure for AMS of ^{90}Sr has so far only been developed and tested for soil and bone samples. First, 1 mg of Sr carrier is added to the remaining ashed samples after a small part of the sample was taken to determine the amount of natural stable Sr by ICP-MS. The part with carrier added either undergoes microwave digestion or acid leaching with HNO_3. For Sr-separation from the solution, we use Sr-resin cartridges (Eichrom Industries Inc.). Finally, SrF_2 is precipitated from concentrated eluate by addition of 1 mL of HF. For soil samples, the typical sample size is 1–5 g and a recovery between 70 and 96% was achieved for different materials including soil or beef bone (M. Honda, in preparation). In principle, the same purification method can also be applied to marine samples like ocean water or corals after a pre-treatment step, i.e., either pre-concentration from liquid samples or acid decomposition of coral samples.

Accelerator Mass Spectrometry Measurement Procedures

Accelerator Mass Spectrometry of the Actinides

A detailed description of the routine analysis of actinides at VERA, in particular of the anthropogenic U isotopes, ^{236}U and ^{233}U, has been reported previously (Steier et al., 2019; Hain et al., 2020). While this is based on the extraction of the actinides as single negatively charged oxide molecules from the ion source, the procedure for fluoride extraction is identical in most parts. In short, the actinides extracted from the respective sputter matrix are injected into the accelerator after a first mass separation stage. The ions are stripped to positive charge states in a helium gas cell in the high-voltage terminal of the accelerator. Using a relatively high helium pressure in the terminal stripper to ensure the suppression of molecular background such as $(^{235}UH)^{3+}$, a stripping yield of around 21% is achieved for the

selected charge state 3+ (U^{3+}) (Steier et al., 2019). After passing additional filtering components including a second 90° magnet, a Wien filter, an electrostatic analyzer and a third 90° magnet, the remaining ions were identified in a Bragg type ionization chamber. The overall detection efficiency of the system for U atoms in the sputter target was 5×10^{-4} (Steier et al., 2019) assuming complete consumption of the sputter material. Usually, the majority of the measurement time is dedicated to the less abundant ^{233}U and the whole material is not used up.

While the count rates of the rare U isotopes are normalized to the macroscopic $^{238}U^{3+}$ ion current measurement to account for variations in detection efficiency and losses during chemical sample preparation, all the other actinides of interest are measured relative to the count rate of the respective internal isotopic spike. This presents a difficulty in the case of ^{237}Np where the count rate has to be normalized to the non-isotopic ^{242}Pu spike until now since no isotopic spike is currently available (Status of the Isotopic Spike for Quantitative ^{237}Np Analysis). In that case, variations in the detection efficiency, in particular due to element specific changes of the ionization yield, have to be corrected by measuring an external ^{237}Np/^{242}Pu standard in addition. This sample is prepared from spike solutions with a defined ^{237}Np/^{242}Pu ratio by quantitative co-precipitation or just drying up the solution. In previous studies, it has been observed that in the Cs negative ion source of AMS the production of PuO^- is usually enhanced compared to NpO^- (Fifield, 2008; Quinto et al., 2015, 2017). Both the different ionization yield of Np and Pu and their possibly different chemical yield during chemical preparation of the sample may contribute to the higher relative output. Furthermore, a variability of such an enhancement factor has been suggested, in particular in a set of 5 groundwater samples (with an average enhancement factor of Pu/Np = 1.1 ± 0.1) (Quinto et al., 2017) and in a seawater sample as well as in a sample composed purely by reagents (enhancement factor of Pu/Np = 1.2 ± 0.5 and 1.2 ± 0.7, respectively) (Quinto et al., 2015). Such phenomenon requires further investigation in order to be fully understood.

Accelerator Mass Spectrometry With Stable Isobaric Background

Conventionally, AMS suppresses stable isobaric background (e.g., ^{99}Ru in the case of ^{99}Tc, ^{135}Ba in the case of ^{135}Cs) in the final detection setup by methods adopted from nuclear physics based on element specific energy loss in matter or the different deflection in a gas-filled magnet. Since the isobaric interference of the isotopes of interest usually stems from a neighboring element, this becomes increasingly difficult for heavier nuclides, where the relative difference in the nuclear charge decreases. While ^{10}Be-^{10}B separation nowadays is accomplished at compact 300 kV tandem accelerators, even the largest AMS facilities with terminal voltages >10 MV struggle to achieve the required isobar separation on the order of 10^6 or above for isobaric systems at ∼90 amu (Koll et al., 2019; Pavetich et al., 2019) and fail to do so at higher masses, e.g., in the actinide mass region. To overcome this limitation and make nuclides like the long-lived fission products accessible at medium-sized AMS-facilities with terminal voltages of 3 MV and below, an alternative approach using element-selective neutralization of anions via laser photodetachment was developed at VERA. The corresponding Ion-Laser Interaction Mass Spectrometry (ILIAMS) setup was successfully linked to the existing AMS setup at the VERA laboratory 5 years ago (Martschini et al., 2019b). In order to facilitate the necessary ion-laser interaction times, the ion beam is decelerated to an energy at eV levels inside a radiofrequency quadrupole ion guide filled with buffer gas and overlapped with a collinear laser therein. A recent review of this method and its achievements is given by Martschini et al. (2021). For "standard" AMS isobaric systems like ^{36}Cl-^{36}S and ^{26}AlO-^{26}MgO, the ILIAMS-technique provides unprecedented isobar suppression of 10^{11}-10^{12} (Lachner et al., 2019, 2021).

Application of ILIAMS to the fission products ^{90}Sr, ^{99}Tc, and ^{135,137}Cs has required a substantial development effort, which is certainly not yet finished. The prerequisite of this technique is the identification of a suitable molecular system in which the isotope of interest has a higher detachment energy than its isobaric interference. In this case, a laser characterized by a photon energy intermediate between the detachment energies of the molecular system of the isotope of interest and that of its isobar can be applied to neutralize or decompose the isobaric molecule while leaving the anionic molecule of the isotope of interest unaffected. Unfortunately, detachment energies of many molecules of elements in the fission product or actinide region are unknown and need to be determined experimentally. For the three isotopes discussed here, fluoride molecules have proven to be well suited while formerly used oxides did not match the criteria. Hence, an adaptation of sample chemistry and subsequent studies of the influence of ion source settings and composition of the matrix on the negative ion formation probability became necessary.

Apart from the additional filter step of ILIAMS, the measurement principle is very similar to the conventional actinide AMS. The trace isotope and a reference isotope (typically a stable isotope of the same element if available) are extracted as negative ions and sequentially injected through ILIAMS into the accelerator, where the ions are stripped to the 3+ or 4+ charge state using He gas. On the high energy side, abundant isotopes are measured in Faraday cups as ion currents and compared to the single particle detector count rates of the trace isotopes to deduce raw isotopic ratios, which are then normalized with the help of reference materials with known isotopic ratios. For new nuclides, suitable AMS reference materials are typically not available and have to be produced, e.g., by a dilution series of certified materials.

Accelerator Mass Spectrometry of ^{99}Tc is complicated further by the lack of a stable Tc isotope for instrumental setup and quantification of results. Due to its similar mass, Nb has proven well-suited for beam tuning at high-energy AMS setups (Koll et al., 2019) extracted as NbO^- as well as at VERA, using both NbO^- and $NbF_5{}^-$ beams. For oxide extraction, NbO^- was also satisfactorily used for normalization of the ^{99}Tc results which was associated with an uncertainty of around 30% (Koll et al., 2019). However, this bears similar problems as discussed above for the non-isotopic Np/Pu normalization and requires thorough assessment at VERA.

RESULTS AND DISCUSSION

Multi-Actinide Results From the Pacific Ocean

For the validation of the analytical method, the literature values for the concentrations of ^{239,240}Pu, ^{237}Np, and ^{241}Am and the U isotope ratios of the analyzed reference materials are compared to our experimental values in **Table 2**. Samples were prepared by the procedure described in section "Chemical Extraction of Actinides (U, Pu, Np, and Am)" and actinides were measured in oxide form. No reference values for the ^{233}U/^{238}U and ^{233}U/^{236}U values are available until now. Apart from the ^{237}Np concentration all isotope concentrations and ratios are well reproduced within at least 2 σ uncertainty corresponding to an average accuracy of 0.2 σ for ^{239}Pu, 0.7 σ for ^{240}Pu, and 1.1 σ for ^{241}Am concentrations. The accuracy is given in terms of the literature value's uncertainty. In comparison to the value published by Eigl et al. (2013) also using the VERA setup but a different sample preparation method, our present result shows an accuracy of 2.5 σ. However, both ratios obtained with VERA are significantly lower than the information value (5 σ accuracy). Possible reasons related to the high isotope ratio of the IAEA-381 material have already been discussed in Eigl et al. (2013). It demonstrates the need for an AMS ocean water reference material in the range of ^{236}U/^{238}U = 10^{-8}. Accordingly, a very good accuracy of 0.15 σ was achieved for IAEA-385. While the IAEA-381 sample shows a deviation of 22% for the ^{237}Np concentration which has been observed as typical precision for ^{237}Np measurements when using a non-isotopic spike for normalization (Qiao et al., 2013; Quinto et al., 2015, 2017), the experimental value for IAEA-385 is 3 orders of magnitude lower than the published values. This is essentially equivalent to a complete loss of ^{237}Np during sample preparation, which, however, is not reflected by the Pu spike, in this way leading to a wrong final result for the ^{237}Np concentration in the initial sample. The inaccuracy of this result underlines the danger of using a Pu nuclide such as ^{242}Pu as non-isotopic spike for ^{237}Np determination in case the chemical yield of Np and Pu are unexpectedly different.

The measurement results on the ^{239,240}Pu and ^{241}Am concentration (blank corrected) as well as the ^{236}U/^{238}U obtained for the water column at BD04 are plotted in **Figures 2A–C**. The calculated radionuclide ratios ^{240}Pu/^{239}Pu, ^{233}U/^{236}U, and ^{237}Np/^{239}Pu, which can serve as a fingerprint to distinguish different emission sources, are shown in **Figures 2D–F**. The values and further details on the measurement are listed in **Supplementary Tables 1, 2**. Regarding the shortcomings of normalizing ^{237}Np count rates without isotopic spike, only the overall count rates including the process blank are compared without further interpretation of the absolute concentration, which therefore are not plotted in **Figure 2**. The new data for ^{239,240}Pu obtained with the present procedure were combined with the data from the previous study (Hain et al., 2017) to show the complete depth profile. Selected AMS targets such as the U fraction of BD04-20m or the Pu fraction of BD04-200m were re-measured in a different measurement to verify the reproducibility of the investigated isotopic ratios and showed good agreement within 1 σ uncertainty. The concentrations of the two particle-reactive elements Pu and Am are increasing from the water surface to the maximum depth, while the increase by a factor of 24 from 5.4×10^3 atoms/kg to 1.3×10^5 atoms/kg is stronger for ^{241}Am than for ^{239}Pu (around factor 5). The ^{241}Am count rate in the two surface water sample (0 and 20 m) are close to their corresponding blanks, i.e., BLKII and BLKI, respectively, (see **Supplementary Table 2**) leading to considerable uncertainties of the final ^{241}Am concentrations in the two samples after blank correction. This means that the limiting factor for the multi-actinide measurements is not constituted by the AMS detection efficiency including chemical sample preparation, but by the background of the procedure blanks. It is important to note that previous studies usually used sample volumes of >50 L for multi-isotope analysis (Lee et al., 2003b; Povinec et al., 2003; Rozmaric et al., 2022). For the ^{236}U/^{238}U and ^{233}U/^{238}U ratios the respective blank levels are negligible compared to the uncertainty of the measurement result. A clear signal above the blank count rates was also observed for ^{237}Np count rates, which shows the general feasibility of ^{237}Np detection at VERA.

The ^{236}U/^{238}U ratios around 1×10^{-9} in the topmost 600 m of the water column agree well with previously published data for the NW Pacific Ocean (Eigl et al., 2017). Also the presented surface $^{239+240}$Pu concentrations of 2 mBq/m^3 fit into the rather large range of $^{239+240}$Pu concentrations reported before (Lee et al., 2003a; Hirose, 2009; Lindahl et al., 2010). The comparably low maximum concentrations of 15 mBq/m^3 at 500 m depth (Hain et al., 2017) support the observation that the subsurface Pu maximum decreases in amplitude over the years due to sedimentation processes (Livingston et al., 2001). Our maximum ^{241}Am concentration at 600 m corresponding to 6.6 mBq/m^3 is also slightly below the concentration range of 7−22 mBq/m^3 published for this depth in one of the very few studies on ^{241}Am distributions in Pacific Ocean water (Povinec et al., 2003). In general, the observed depth profiles are compatible with the expected behavior of the different nuclides in the open ocean. The environmental behavior of actinides essentially depends on their oxidation state, i.e., the reduced species with oxidation state +3 and +4 are more particle-reactive than those with oxidation state +5 and +6 which quickly hydrolyze forming ionic bonds. The latter is the case for U^{6+} and Np^{5+}, present in natural waters as the dissolved uranyl ion UO_2^{2+} and neptunyl ion NpO_2^+ (Lehto and Hou, 2011) respectively, so that especially Np is conservatively transported with the water masses. In the open sea, the mobility of U is further increased as it mainly exists as carbonate complex with the long residence time of 0.5×10^6 yrs (Dunk et al., 2002). Consequently, conservative radionuclides stay at the water surface if they entered by surface deposition as observed for ^{233,236}U/^{238}U in the presented depth profiles. Contrarily, Am present in oxidation state +3 and Pu, mainly existing in valence state +3 or +4 are considered as particle-reactive and are quickly removed from the water column by sedimentary mineral or organic particles (Lehto and Hou, 2011). Hence, the corresponding concentrations are lowest at the water surface and the stronger increase observed for ^{241}Am proves the higher particle-reactivity compared to ^{239,240}Pu at the given particle concentration in the water column. A detailed discussion

TABLE 2 | Comparison of results obtained by the VERA routine analysis of long-lived actinides in reference materials with literature values.

Isotope concentration, ratio	IAEA-381		IAEA-385	
	This work	Literature value	This work	Literature value
c(^{239}Pu) [at/g]	$(9.2 \pm 2.2) \times 10^6$	$(8.89 \pm 1.10) \times 10^6$ (Povinec et al., 2002)	$(2.00 \pm 0.18) \times 10^9$	$(1.96 \pm 0.31) \times 10^9$ (Pham et al., 2008)
c(^{240}Pu) [at/g]	$(2.16 \pm 0.53) \times 10^6$	$(1.97 \pm 0.21) \times 10^6$ (Povinec et al., 2002)	$(3.62 \pm 0.34) \times 10^8$	$(3.43 \pm 0.42) \times 10^8$ (Pham et al., 2008)
c(^{237}Np) [at/g]	$(6.6 \pm 0.3) \times 10^8$	$(8.49 \pm 0.49) \times 10^8$ (Povinec et al., 2002)	$(2.5 \pm 0.5) \times 10^6$	$(1.8 \pm 0.2) \times 10^9$ $(2.12 \pm 0.02) \times 10^9$ (Goldstein et al., 2021)
c(^{241}Am) [at/g]	$(4.8 \pm 0.3) \times 10^5$	$(4.07 \pm 0.66) \times 10^{5*}$ (Povinec et al., 2002)	n.m.	
^{236}U/^{238}U	$(1.99 \pm 0.03) \times 10^{-6}$ (Hain et al., 2020)	$(2.47 \pm 0.09) \times 10^{-6}$ (Povinec et al., 2002) $(2.04 \pm 0.02) \times 10^{-6**}$ (Eigl et al., 2013)	$(2.58 \pm 0.10) \times 10^{-8}$	$(2.69 \pm 0.71) \times 10^{-8}$ (Yang et al., 2016a)
^{233}U/^{238}U	$(2.15 \pm 0.27) \times 10^{-9}$ (Hain et al., 2020)	n.a.	$(7.5 \pm 2.5) \times 10^{-11}$	n.a.
^{233}U/^{236}U	(0.11 ± 0.01)% (Hain et al., 2020)	n.a.	(0.3 ± 0.1) %	n.a.

**Corrected for build-up from ^{241}Pu decay since reference date 7 September 1993. **Information value, calculated from mass ratio. n.m., not measured; n.a., not available/published. Uncertainties are stated as ±1 σ.*

of the distributions and the inventory does not appear prudent based on the limited data set from one sampling location only. As is typical for the Pacific Ocean, the ^{240}Pu/^{239}Pu atom ratios (**Figure 2D**) are elevated compared to the literature value for global fallout on the Northern Hemisphere of 0.180 ± 0.014 (Kelley et al., 1999) marked by the vertical blue line. This result suggests the presence of tropospheric close-in fallout from the Pacific Proving Grounds. The novel data on the ^{233}U/^{236}U depth profile in an ocean water column presented in **Figure 2E** presents a weighted mean of $(1.04 \pm 0.18) \times 10^{-2}$ which is slightly lower (more than 1 σ) than the value for global nuclear weapons $(1.40 \pm 0.15) \times 10^{-2}$ fallout published only recently in Hain et al. (2020) for the first time. As discussed in this initial publication on anthropogenic ^{233}U and recently supported by data from Baltic Sea sediments (Lin et al., 2021), tropospheric fallout from smaller ^{233}U fuelled fission devices might have led to a locally more varying ^{233}U distribution. Being located west of the relevant Nevada test site, the Pacific Ocean might have received relatively small input from these smaller weapons but large amounts of ^{236}U have been released at the Pacific Proving Grounds, which could be a possible explanation for the lower ^{233}U/^{236}U ratios in the presented water column. The uncorrected 237/239 count rate ratios are in reasonable agreement with the previously published value for nuclear weapons fallout of 0.48 ± 0.07 at northern latitudes (Kelley et al., 1999). Whereas the deviation from the literature value at 100 m is not significant due to the large uncertainties of the uncorrected experimental value, the measured ratios at greater depths, i.e., 400 and 600 m are clearly lower. This could be expected because of the strong chemical fractionation between the conservatively behaving Np, which has been found to stay at the surface (López-Lora et al., 2020), and the particle-reactive Pu with a subsurface maximum at around 1000 m depth (Livingston et al., 2001) in the water column. The indicated literature value is independent from chemical fractionation as the total fallout inventory of the two nuclides was compared in the corresponding study (Kelley et al., 1999).

Validation of Uranium-Fluoride Extraction for Environmental Samples

Selected sample aliquots obtained by leaching of air filter ashes were used for the comparison of oxide and fluoride target preparation and extraction in the AMS ion source. The collection of the air filters, the chemical U purification and the results of the complete data set analyzed in oxide form will be published elsewhere (Wallner G. et al., submitted to J. Environ. Radioact.). It has to be noted, that nine times more solution was used for fluoride target preparation than for the oxides measurements, because the aim was to also analyze the much rarer ^{233}U. This led to significantly better counting statistics of ^{236}U, not attributable to fluoride extraction alone.

As shown in **Figure 3**, the ^{236}U/^{238}U ratios measured in oxide form can be very well reproduced by fluoride (UF_5^-) extraction for all samples as well as the in-house standard material Vienna-US-8 (^{236}U/^{238}U = 1.01 × 10^{-8}) within 1σ uncertainty. The uncertainties plotted in this graph and listed in **Supplementary Table 3** along with all the detailed information on both measurements also include systematic variations which usually dominate the overall uncertainty of AMS results. The final results for both methods show similar uncertainties therefore indicating that fluoride extraction did not induce a higher variability between the individual measurements. Also the ^{236}U blank level for both methods is comparable, but the considerably higher ^{238}U currents from the blanks need to be further investigated. A systematic input of ^{238}U from the new reagents involved seems most probable. Recent measurements exclude the Cu sample holder as a significant source of ^{238}U so that only PbF_2

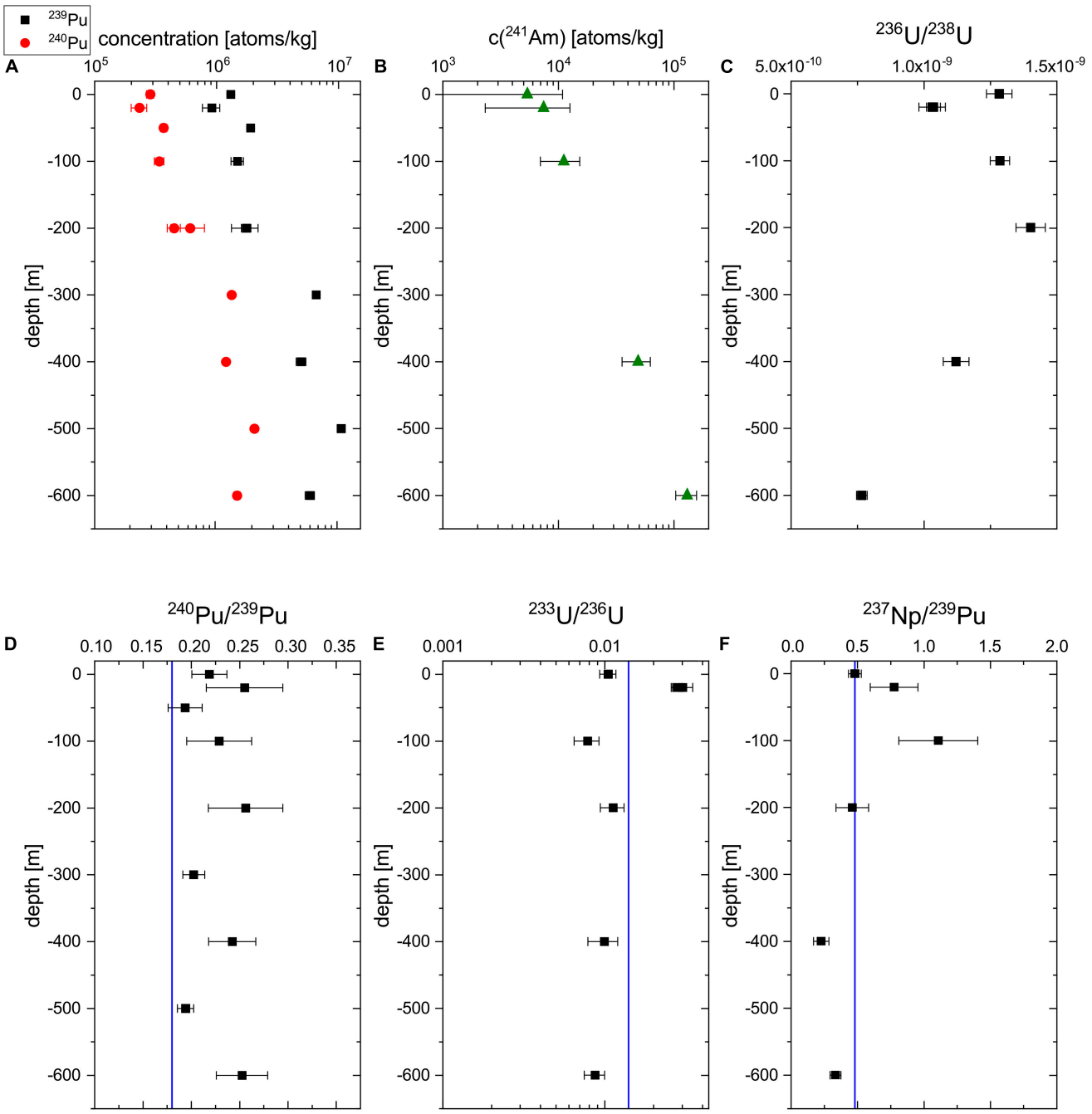

FIGURE 2 | Depth profiles of the ^{239}Pu (black) and ^{240}Pu (red) concentration **(A)**, the ^{241}Am (green) concentration **(B)**, the ^{236}U/^{238}U atom ratio **(C)**, the ^{240}Pu/^{239}Pu atom ratio **(D)**, the ^{233}U/^{236}U atom ratio **(E)**, and the ^{237}Np/^{239}Pu count rate ratio **(F)** at the sampling station BD04. The vertical blue line indicates the literature value for global fallout of the respective radionuclide ratio (Kelley et al., 1999; Hain et al., 2020). For the Pu depth profiles, the new data has been combined with the data from a previous study (Hain et al., 2017).

is left as a potential source. A direct comparison of the detection efficiency via the count rates and ion currents of the present experiment is not straightforward, as samples were split into two aliquots before chemical purification and might have suffered from different U losses during column separation. However, the consistently elevated ^{236}U count rates and ^{238}U ion currents (factor 1.7) taking into account that the initial Vienna-US-8 material was considerably diluted with PbF_2 in a mass ratio 1:9 for fluoride extraction, point to an enhanced detection efficiency. A further increase in detection efficiency is in sight as first fluoride measurements of the mass-239/mass-238 ratio for the in-house standard material Vienna-KkU (Steier et al., 2008) lower

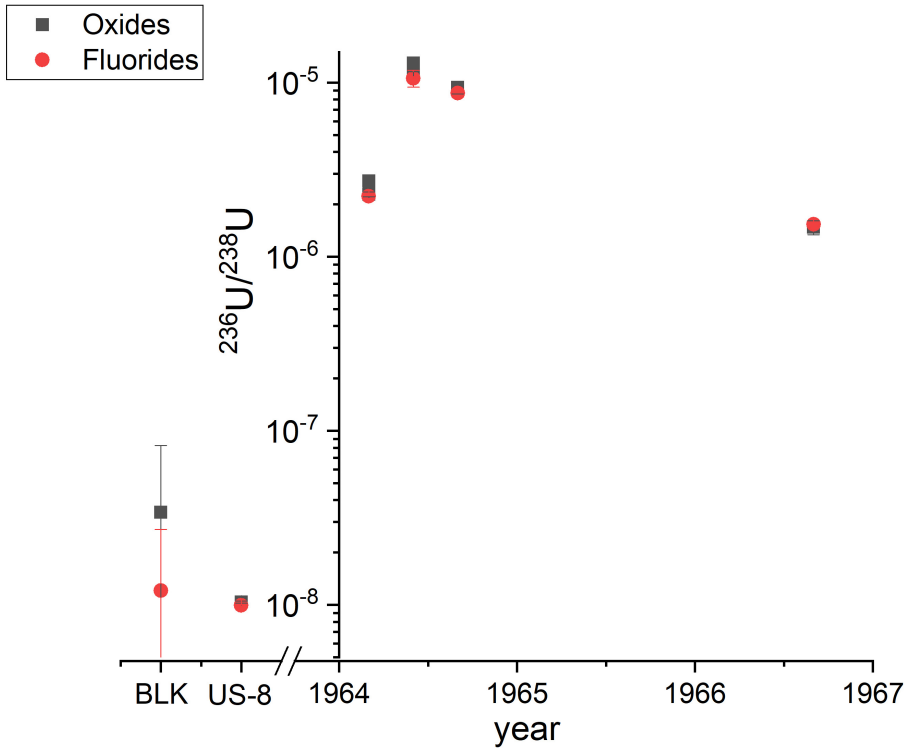

FIGURE 3 | Comparison of the $^{236}U/^{238}U$ results for air filters, either obtained by UO^- (black squares) or UF_5^- (red dots) extraction. "BLK" denotes the corresponding process blank and "US-8" is a VERA in-house standard for ^{236}U (see main text).

presence of UH^{3+} molecules. In the experiment described in Steier et al. (2019) for oxide extraction, the stripper gas pressure was decreased from 1 Pa to 0.4 Pa for which the maximum transmission of 24% for charge state 3+ has been observed. Thereby, the $m239^{3+}/^{238}U$ ratio increased from about 10^{-14} to 5×10^{-11}. In the present experiments with fluoride extraction, we reached a 50 times lower $m239^{3+}/^{238}U$ ratio at the lower stripper gas pressure of 0.4 Pa which indicates a lower formation of hydro-fluoride compounds.

Status of the Isotopic Spike for Quantitative ^{237}Np Analysis

Even though ^{237}Np is well detectable above blank level at VERA as shown in section "Multi-Actinide Results From the Pacific Ocean," and tailing from ^{238}U does not interfere in the AMS measurement ($m237/m238 < 1.8 \times 10^{-13}$ measured on Vienna-KkU), a reliable quantitative analysis of ^{237}Np concentrations requires a isotopic spike material which is sufficiently pure regarding ^{237}Np (Jerome et al., 2014) or other by-products of the irradiation such as ^{236}Pu (Efurd et al., 1991). The most promising spike candidate currently under development in a joint project with the University of Tsukuba (Japan) is ^{236}Np produced via the bombardment of ^{232}Th with ^{7}Li in the 30–40 MeV range at the RIKEN Nishina Center. AMS measurements at VERA have confirmed the production of mass m236 above background and m237/m236 ratios down to $(7.62 \pm 0.08) \times 10^{-2}$ for this material were measured. Whereas mass m237 is exclusively ^{237}Np, on mass m236 there is potential isobaric interference. For the prospective spike material, the main isobar of concern is ^{236}U co-produced either via neutron capture on ^{235}U or the decay of the excited state ^{236m}Np. Also ^{236}Pu is built-up by the decay of ^{236m}Np but usually can be easily suppressed by chemical purification. In order to be able to confirm the production of ^{236}Np, a method to identify the isobaric composition of this irradiated material had to be developed.

As pointed out before, the admixture of PbF_2^- results in *in situ* fluoridization of the actinides (An) during the sputter process in the AMS ion source. We have systematically investigated the formation ratios of the AnF_5^-, AnF_4O^-, $AnF_3\ O_2^-$, AnF_3O^- $AnF_2O_2^-$, and AnF_4^- molecular anions of the actinides U, Np, Pu, and Am. This effort has resulted in a novel isobar analysis technique based on the element specific AnF_4^-/AnF_5^- ratios that is capable of characterizing the elemental composition of the produced mass 236 in the prospective spike material (Zhao and Francisco, 2022; Wiederin, A. et al., in preparation). The observed NpF_4^-/NpF_5^- ratio in a sample with known isotopic composition was found to be a factor 10 different from the PuF_4^-/PuF_5^- and the UF_4^-/UF_5^-, respectively. First measurements based on this method of the irradiated material for Np spike production show a $m236F_4^-/m236F_5^-$ ratio which is compatible with that of the reference NpF_4^-/NpF_5^- ratio within 1 σ.

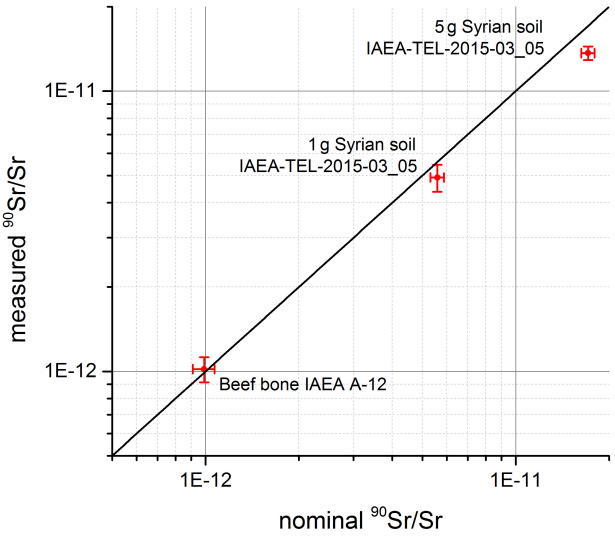

FIGURE 4 | Comparison of nominal and measured ^{90}Sr/Sr ratios for environmental IAEA-reference materials.

^{90}Sr Analysis in Reference Materials Using Ion-Laser Interaction Mass Spectrometry

The combination of SrF_3^- extraction from the ion source and ILIAMS-suppression of ZrF_3^- provides an isobaric suppression of ^{90}Zr of $>10^{10}$, which is sufficient to achieve a blank value of ^{90}Sr/Sr $\sim 5 \times 10^{-15}$ on all environmental soil and bone samples tested so far (Martschini et al., 2021). Based on the addition of 1 mg of stable Sr carrier for normalization and a total detection efficiency of 4×10^{-4}, this is equivalent to a detection limit of <0.1 mBq, i.e., 10^5 atoms of ^{90}Sr per sample. To our knowledge, this makes AMS with ILIAMS the most sensitive detection method for ^{90}Sr so far as other techniques or setups achieve at most detection limits of 3 mBq (Bu et al., 2016).

Currently, we are in the process of assessing the accuracy of this method for different environmental materials. These tests are conducted with various IAEA reference materials such as IAEA-A-12 (beef bone) and IAEA-TEL-2015-03_05 (Syrian soil) and measured against an in-house AMS-reference materials prepared from a dilution series of an LSC-reference solution. Preliminary results from this study are shown in **Figure 4**. While the value of the measured ^{90}Sr/Sr isotopic ration in the beef bone sample agrees perfectly well with its nominal value, the value measured in both soil samples is measured slightly too low compared to its nominal value. Whether the reason for this is due to some ^{90}Sr loss in chemical sample preparation, some deviations in ICP-MS determination of intrinsic stable Sr in the soil sample required to calculate back to the^{90}Sr/Sr in the environmental sample or due to issues with our in-house-reference materials is currently under investigation.

Based on the above detection limits, one can estimate the sample size of ocean water required for future analysis of ^{90}Sr. Radiostrontium levels in surface water of the general ocean, e.g., the Pacific Ocean, are reported to be around 1 Bq/m^3 at the beginning of the century with effective half residence times of 14–15 years (Povinec et al., 2012). Assuming reasonable ^{90}Sr recovery in chemical sample preparation, this means that 1–3 L of ocean water should be sufficient to stay well above background for the next decades. As the Sr-content of 1 g of aragonitic coral skeleton is almost equivalent to the Sr-content of 1 L of ocean water at the time of coral growth (Purdy et al., 1989), a few g of coral are sufficient for similar analysis.

^{135}Cs Analysis With Ion-Laser Interaction Mass Spectrometry

Using ILIAMS, the AMS system at VERA is very robust against the presence of the Ba isobars and other interferences, e.g., including the presence of Rb in the sample, which was reported to lead to molecular interferences for TIMS measurements (Zhu et al., 2020b). Additionally, because of the many energy and momentum filters, the AMS setup is not limited regarding the abundance sensitivity for the ^{135}Cs/^{133}Cs ratio by tailing effects of strong ^{133}Cs signals. Therefore, we see a potential for the application of the ILIAMS assisted AMS measurements when oceanic data far from anthropogenic sources and close to natural ^{135}Cs/^{133}Cs levels are needed. Based on the performance parameters regarding ^{135}Ba suppression and detection efficiency (Martschini et al., 2021; Wieser, A. et al. in preparation), we can now estimate the amount of ocean water sample required for the analysis of ^{135}Cs with ILIAMS.

Similar to other fissiogenic radionuclides such as ^{129}I (Fabryka-Martin, 1988), the main source of natural ^{135}Cs is from spontaneous fission of ^{238}U with a cumulative yield $Y_{sf}(^{135}Cs) = 0.052$. For the ^{135}Cs estimation in the ocean we assume a continuous input of both U and Cs to the ocean via rivers. In addition, we assume that at their origin on the continent, ^{238}U and ^{135}Cs are in secular equilibrium, which is reached after approximately ten half-lives of ^{135}Cs. Depending on the half-life of ^{135}Cs used in this context, this will result in an atomic input ratio of $(^{135}Cs/^{238}U)_{cont} = (0.8–1.5) \times 10^{-11}$. The radioactive lifetimes of ^{238}U and ^{135}Cs are much longer than their residence times in ocean water and both elements are removed from the water column before any significant build-up or decay can occur. Taking into account the difference in residence time τ_{res} for Cs and U we estimate a ^{135}Cs concentration $c\left(^{135}Cs\right)$ in the ocean water of,

$$c\left(^{135}Cs\right) = \frac{\tau_{res}\left(^{135}Cs\right)}{\tau_{res}\left(^{238}U\right)} \cdot \left(\frac{^{135}Cs}{^{238}U}\right)_{cont} \cdot c\left(^{238}U\right)$$
$$= (4.0 - 7.5) \cdot 10^4 \text{ at/L}$$

Using an average ^{133}Cs concentration of 1.3×10^{15} atoms/L (0.3 ppb) one can expect a natural ^{135}Cs/^{133}Cs background ratio in ocean water of $(3–6) \times 10^{-11}$. Due to the lower concentration of Cs relative to U in ocean water compared to the general crust, this value is higher than the expected ^{135}Cs/^{133}Cs ratio in the crust of $\sim 8 \times 10^{-12}$ (Lachner et al., 2015). The expected ^{135}Cs/^{133}Cs background ratio in ocean water is still

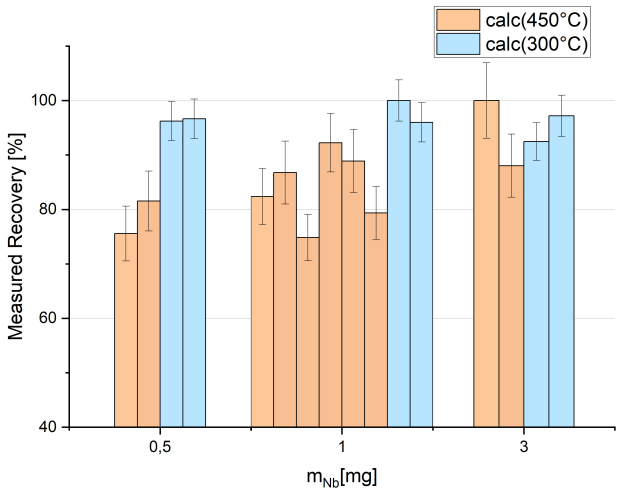

FIGURE 5 | ^{95m}Tc recovery after calcination at 450 and 300°C in comparison measured by gamma counting. ^{95m}Tc was embedded in different amounts of Niobium (Nb) and prepared in individual crucibles.

below the presently reported sensitivities for TIMS and ICP-MS/MS in ocean water samples, but can be reached using the high abundance sensitivity of $^{135}Cs/^{133}Cs < 10^{-11}$ and barium suppression of six orders of magnitude available with the ILIAMS assisted AMS facility VERA. With our present detection efficiency we expect that a sample of 1 L of ocean water is sufficient for an AMS measurement at VERA down to natural levels.

^{99}Tc Detection With Accelerator Mass Spectrometry

Figure 5 shows the results for the Tc recovery prepared with different amounts of Nb and calcined at the two different temperatures 450°C (orange) and 300°C (blue) for 1 h, respectively. The uncertainties are determined by the counting statistics of gamma spectrometry. While at 450°C variable losses of up to 25% were observed, the recovery is more stable at 300°C, independently of the amount of Nb used for the preparation of the target matrix. In the latter scenario, recoveries exceeded 90% for all samples. First test measurements with AMS did not indicate negative effects of the lower temperatures on the ion source output and the background for ^{99}Tc.

The ^{99}Tc concentrations in the water column at BD04 and a second sampling station around 1,500 km to the Northeast of BD04 were analyzed with the high-energy AMS setup at the Maier-Leibnitz Laboratory (MLL) in Munich which featured a 14 MV tandem accelerator and the Gas-filled analyzing magnet system "GAMS" (Koll et al., 2019; Quinto et al., 2019). The results obtained for BD04 of around 10^7 atoms/L, and below 5×10^6 atoms/L at greater distance to Japan (Hain, K., et al., in preparation) are in good agreement with previous studies with published values of 5×10^6 atoms/L for the transect Japan-Australia (Momoshima et al., 2005) and 7×10^7 atoms/L at the Fukuoka coast (Momoshima et al., 1995). For the GAMS setup an overall Ru suppression factor between 3×10^4 and 3×10^5 has been estimated in a previous study using samples with well-known Ru concentration (Quinto et al., 2019).

In comparison, first experiments with ILIAMS showed that TcF_5^- has to be used instead of TcO^- for laser suppression of the isobar Ru (Martschini et al., 2021). Since Ru is among the stable elements with the lowest natural abundance with typical concentrations of 1 ppt in water and 10–100 ppt in sediment (Bekov et al., 1984), a 10 L ocean water sample or a 100 g sediment sample will both contain roughly 6×10^{13} atoms of Ru. In order to assess any difference in ion formation probabilities of TcF_5^- and RuF_5^- as well as laser suppression factors, we prepared two batches of samples from a clean Nb-solution, one spiked with a similar amount of Ru (7×10^{13} atoms), the other spiked with 1×10^{10} atoms of ^{99}Tc. The count rates in the detector from procedure blanks prepared from the unspiked Nb-solution were below 0.01 cps for mass 99 amu, i.e., $^{99}Tc^{3+}$ and $^{99}Ru^{3+}$, respectively. Without laser suppression, the Ru-spiked samples showed $^{99}Ru^{3+}$ count rates of 10–30 cps. Despite much lower atom concentrations, the Tc-spiked samples also yielded 8–10 cps of $^{99}Tc^{3+}$ in the detector. Taking into account the natural abundance of ^{99}Ru of 12.76% and assuming similar transmission through the system, this yields a Ru suppression vs. Tc of 250–900 by extraction of pentafluoride anions from the ion source. In combination with the Ru-suppression factor of ILIAMS of 10^5, the direct Ru-induced background signal of an environmental sample without separation chemistry would be equivalent to at most 3×10^5 atoms ^{99}Tc in the sample. This is an excellent abundance sensitivity given that the sample preparation method gives us a substantial safety buffer by providing additional $>10^3$ isobar suppression [Extraction of Fission Products (Tc, Cs, and Sr)].

CONCLUSION AND OUTLOOK

Multi-Actinide Analysis at the Vienna Environmental Research Accelerator

A highly flexible chemical separation procedure has been developed which allows for analysis of the complete nuclide vector of ^{233,236}U, ^{239,240}Pu, ^{241}Am, and ^{237}Np from a single ocean water sample at ultra-low levels (below 10^{-3} ppq for ^{241}Am). In that way, the direct comparison of actinides with different migration behavior is possible to account for scavenging processes of radionuclides for the interpretation of the water mass transport. The new data on $^{233}U/^{236}U$ ratios in the Pacific Ocean support our previous finding that this ratio is around 10^{-2} in the general environment if no releases from nuclear power and reprocessing plants are present. Being located at a distance of 250 km north-east of the Fukushima Daiichi Nuclear Power Plant, where water masses are transported southward by the Oyashio Current, a contribution from the reactor accident at the sampling station seems rather unlikely. To be able to interpret such small deviations from the published $^{233}U/^{236}U$ ratio for nuclear weapons fallout correctly, a thorough study of the global ^{233}U distribution and its inventory as well as the characterization of the weapons fallout source term is required.

The present work shows that analysis of $^{233}U/^{236}U$ in ocean water remains challenging due to the very low abundance of $^{233}U/^{238}U$ in the lower 10^{-11} range in regions not directly affected by nuclear emissions. The $^{233}U/^{238}U$ ratio will decrease even further for larger depths (>600 m) as only little anthropogenic U is transported downward in the water column. Especially ^{233}U analysis would benefit from an enhanced detection efficiency using UF_5^- extraction which is currently investigated at VERA. The results for environmental samples obtained from oxide extraction are well reproduced in fluoride measurements with a similar precision and an at least equally high efficiency. At the same time, the final steps for target preparation are considerably simplified as the co-precipitation and washing steps are omitted. For this reason, fluoride extraction can be considered advantageous for U analysis in large batches of environmental samples already at the present time, even for AMS facilities reaching already up to few percent ionization efficiencies for actinide-oxide extraction (Hotchkis et al., 2019). In addition, the reduced background on mass 236 and mass 239 caused by uranium-hydride molecules which have been found to survive the stripping process at lower stripper gas pressure (Lachner et al., 2013) can be perceived as clear advantage for any AMS facility. As the UF_5^- formation mainly depends on the presence of sufficient PbF_2, it is also highly flexible regarding the target matrix and was successfully applied to environmental U fractions previously prepared as NdF_3 precipitate for alpha spectrometry (unpublished). Next, experiments will compare aliquots obtained after chemical separation to assess the difference in detection efficiency more reliably and the procedure will be expanded to other actinides. With a further increase in detection efficiency, a full implementation of a multi-actinide approach where all the mentioned actinides are extracted from the same sputter target as already demonstrated for low-matrix and small volume samples (Quinto et al., 2015, 2017) is within reach.

Normalization of ^{237}Np results to a non-isotopic spike using our rather simple chemical separation method did provide satisfactory results for water samples only. Provided that the ILIAMS method in combination with fluoride extraction for actinides facilitates suppression of isobars of ^{236}Np as suggested by the observed fluoride formation patterns, the use of the ^{236}Np isotopic spike will allow much more widespread and accurate ^{237}Np analysis. Even AMS facilities without photodetachment capabilities will profit from this material as soon as potential isobaric contaminations and the $^{236}Np/^{237}Np$ ratio have been carefully quantified by VERA so that ^{237}Np results for environmental samples can be corrected accordingly. Environmental samples are usually spiked with 1×10^8 atoms at VERA to ensure good counting statistics on the reference mass. This amount can be minimized to 1×10^7 if the chemical recovery of sample preparation is sufficiently high. However, with the best $^{236}Np/^{237}Np$ ratio achieved at present, this spike material would still add around 7.6×10^5 atoms of ^{237}Np to the environmental sample which is in the order of magnitude of ^{237}Np per kg water to be expected in the uppermost 1,000 m of water from the Pacific Ocean. Consequently, at least 10 L of water samples would be required to obtain reliable data on the ^{237}Np concentrations with sufficiently low uncertainties to allow interpretation in the context of water mass transport. ^{237}Np measurements are less challenging in the North Atlantic and Arctic Ocean where elevated ^{237}Np concentrations have been detected due to releases from the Sellafield reprocessing plant (López-Lora et al., 2021).

Fission Products With Stable Isobaric Background

Analysis of ^{90}Sr in environmental samples using ILIAMS is ready for applications in bone and soil samples. It provides 30 times more abundance sensitivity compared to other techniques and omits the time-consuming sample preparation for radiometric techniques. The development of ^{135}Cs and ^{137}Cs measurements using ILIAMS are promising and the measurement of those isotopes in general ocean water is within reach. The robustness of AMS against interference from other elements and the strong suppression of the isobars may be an advantage over other MS techniques. In the near future, we plan to test our approach on coral samples and on ocean water reference materials such as IAEA-443, which will require adaptations to our sample chemistry procedure. It has to be noted that presently, there are no certified reference materials for the $^{135}Cs/^{133}Cs$ nor for the $^{135}Cs/^{137}Cs$ isotopic ratio available. However, the $^{135}Cs/^{137}Cs$ was already measured in various IAEA and NIST reference materials by various groups (Snow et al., 2015; Snow and Snyder, 2016; Bu et al., 2018, 2019; Zhu et al., 2020b) and their consensus values now are commonly used for method development and validation. An important validation step in the development of ^{135}Cs measurement is to reproduce the given values for the ^{137}Cs concentration. In this context, marine water materials certified for their ^{137}Cs content, e.g., IAEA 381 and 443 (Irish Sea Water), would be of specific interest, but are presently not on stock at IAEA. Irish sea sediment (IAEA-385; reference date for decay correction: 2019-01-01) with a certified ^{137}Cs activity of (19.8 ± 0.6) Bq/kg and a weighted mean of reported $^{135}Cs/^{137}Cs$ ratios of (1.15 ± 0.11) (Yang et al., 2016b; Zheng et al., 2016; Zhu et al., 2020a) thus presently seems to be the most suitable natural reference material for the advancement of Cs isotope measurements in the marine environment. In literature, we hardly find studies on ^{137}Cs in coral cores, which reflects the inefficient incorporation of Cs in the coral skeleton. Previous data from coral material originating from a test site found detectable amounts of ^{137}Cs in g-sized samples only during the peak activities of nuclear bomb testing (Noshkin et al., 1975). The detection of the $^{135}Cs/^{137}Cs$ ratio in coral samples not closely affected by anthropogenic sources is therefore expected to be a major challenge to be addressed with ILIAMS.

First experiments at VERA demonstrate that the abundance sensitivity achieved for ^{99}Tc detection with the ILIAMS method is at least comparable to the former high-energy AMS setup GAMS at the MLL which already allowed the analysis of ^{99}Tc concentrations in 10 L samples from the Pacific Ocean. Ongoing research focuses on finding a suitable normalization of the ^{99}Tc count rate to obtain an absolute ^{99}Tc concentration. Best precision will be achieved by using an isotopic spike analogous to the discussion of ^{237}Np analysis as no elemental fractionation

processes have to be taken into account. The potential candidate ^{97}Tc ($T_{1/2}$ = 1.6 × 10^6 yrs) has the disadvantage that it's detection by mass spectrometry requires the suppression of the stable isobar ^{97}Mo which is not only omnipresent in nature but especially in the ion source being a constituent of stainless steel. Consequently, an AMS measurement of ^{99}Tc using a ^{97}Tc spike has to ensure a highly efficient isobar suppression to higher and to lower atomic charge within the same measurement. Finding a combination of laser wavelength and molecular system with suitable electron affinities to fulfill this requirement is extremely challenging (Martschini et al., 2021). Also the alternative approach of using a spike of the mono-isotopic element Rh for normalization in combination with ^{95m}Tc as chemical yield monitor as proposed by Wacker et al. (2004) is currently being pursued. This normalization method has to be adjusted to fluoride extraction in order to allow its combination with ILIAMS and it has to be ensured that changes in the ion source output of RhF_5^- scale with TcF_5^-. Finally, also the normalization on the NbF_5^- current is being investigated in more detail. It has to be noted that the latter two normalization methods require the measurement of an external standard sample with well-known ^{99}Tc/^{103}Rh and ^{99}Tc/^{93}Nb ratio, respectively.

In addition, the complementary method of high-energy AMS is developed further in collaboration with our colleagues at the Heavy Ion Accelerator Facility (HIAF) of the Australian National University (ANU) to allow for environmental ^{99}Tc detection in parallel to the ILIAMS approach. Since the closure of the MLL in Munich by the end of 2019, the HIAF facility houses the only remaining AMS setup with a 14 UD tandem accelerator reaching sufficiently high beam energies for the application of conventional isobar suppression and / or separation techniques. In contrast to the GAMS setup, AMS of ^{99}Tc at HIAF uses an 8-anode ionization chamber for isobar identification (Martschini et al., 2019a). In principle, procedures for normalization used for measurements with the GAMS measurements can be adjusted to the HIAF setup.

DATA AVAILABILITY STATEMENT

The datasets presented in this study can be found in online repositories. The names of the repository/repositories and accession number(s) can be found below: https://lehre4.rad.univie.ac.at/share/WWW_Exchange/public/Hain2021_frontiers_in_%20marine_sciences/.

AUTHOR CONTRIBUTIONS

KH: conceptualization, methodology, investigation and supervision for actinides, ^{99}Tc, and Np spike, and writing – original draft. MM: conceptualization, methodology, investigation and supervision for ^{90}Sr, ^{99}Tc, and Np spike, and writing – original draft. FG: investigation on ^{99}Tc sample preparation. MH: methodology, investigation and analysis for ^{90}Sr samples, and writing – review. JL: conceptualization, methodology, investigation and supervision for ^{135}Cs, and writing – original draft. MK: methodology, investigation, and fluoride extraction of actinides. JP: investigation and data evaluation for ^{99}Tc. FQ: methodology, sample preparation actinides and ^{99}Tc, and writing – review and editing. AS: conceptualization, methodology, and investigation chemical purification of ^{236}Np. PS: AMS methodology for actinides, data interpretation, and writing – review and editing. AnW: conceptualization, methodology, investigation on Np spike characterization, and writing – original draft on Np spike and review. AlW: investigation and writing on ^{135}Cs. AY: methodology and investigation ^{236}Np production. RG: resources and ILIAMS methodology. All authors contributed to the article and approved the submitted version.

FUNDING

This project receives funding from the European Union's Horizon 2020 Research and Innovation Program under grant agreement No. 824096 (Radiate). This work was partly funded by a bilateral project between the Austrian Science Fund (FWF): I 4803-N and Japan Society for the Promotion of Science (JSPS): JPJSBP120202001 as well as by the Austrian Science Fund (FWF): P 31614-N28 and Austrian Science Fund (FWF): P 22164-N20. The authors acknowledge financial support of the ILIAMS activities and the heavy isotope detection setup at VERA by the University of Vienna "Investitionsprojekte" program. This work was also partly supported by the JSPS Overseas Research Fellowships (No 201860538) and AS received funding from MEXT KAKENHI Grant Numbers 17H01874 and 21H03609 for parts of this work.

ACKNOWLEDGMENTS

KH is very grateful to M. Yamada (Marine Ecology Research Institute, Japan) for providing the Pacific Ocean water samples. We thank T. Gamo from The University of Tokyo and the captain, officers, and crew of the R/V Hakuho Maru for their collaboration in the sampling during the KH-12-4 cruise. We acknowledge the support of M. Schiffer (University of Cologne) for the ^{95m}Tc production and S. Lehr (University of Vienna) for the preparation of the corresponding spike solution. We also thank G. Wallner (University of Vienna) for providing aliquots of the unique air filter samples for the fluoride-oxide comparison and a ^{90}Sr-LSC-solution. Support by M. Kocadag and F. Mozina during the ^{90}Sr sample preparation was highly appreciated. In addition, we thank Dorian Zok (Leibniz University Hannover, Germany) for providing comparison samples.

SUPPLEMENTARY MATERIAL

The Supplementary Material for this article can be found online at: https://www.frontiersin.org/articles/10.3389/fmars.2022.837515/full#supplementary-material

REFERENCES

Aarkrog, A., Boelskifte, S., Dahlgaard, H., Duniec, S., Hallstadius, L., Holm, E., et al. (1987). Technetium-99 and cesium-134 as long distance tracers in Arctic waters. *Estuar. Coast. Shelf Sci.* 24, 637–647. doi: 10.1016/0272-7714(87)90103-X

Bekov, G. I., Letokhov, V. S., Radaev, V. N., Baturin, G. N., Egorov, A. S., Kursky, A. N., et al. (1984). Ruthenium in the ocean. *Nature* 312, 748–750. doi: 10.1038/312748a0

Broecker, W. S., and Peng, T. H. (1982). *Tracers In The Sea*. New York, NY: Eldigio PressEldigio Press.

Bu, W., Ni, Y., Steinhauser, G., Zheng, W., Zheng, J., and Furuta, N. (2018). The role of mass spectrometry in radioactive contamination assessment after the Fukushima nuclear accident. *J. Anal. At. Spectrom.* 33, 519–546. doi: 10.1039/c7ja00401j

Bu, W., Tang, L., Liu, X., Wang, Z., Fukuda, M., Zheng, J., et al. (2019). Ultra-trace determination of the $^{135}Cs/^{137}Cs$ isotopic ratio by thermal ionization mass spectrometry with application to Fukushima marine sediment samples. *J. Anal. At. Spectrom.* 34, 301–309. doi: 10.1039/C8JA00380G

Bu, W., Zheng, J., Liu, X., Long, K., Hu, S., and Uchida, S. (2016). Mass spectrometry for the determination of fission products ^{135}Cs, ^{137}Cs and 90Sr: a review of methodology and applications. *Spectrochim. Acta Part B* 119, 65–75. doi: 10.1016/j.sab.2016.03.008

Cornett, R. J., Kazi, Z. H., Zhao, X.-L., Chartrand, M. G., Charles, R. J., and Kieser, W. E. (2015). Actinide measurements by AMS using fluoride matrices. *Nucl. Instrum. Meth. in Phys. Res. B* 361, 317–321. doi: 10.1016/j.nimb.2015.02.039

Dunk, R., Mills, R., and Jenkins, W. (2002). A reevaluation of the oceanic uranium budget for the Holocene. *Chem. Geol.* 190, 45–67. doi: 10.1016/S0009-2541(02)00110-9

Efurd, D. W., Roensch, F. R., Drake, J., and Perrin, R. E. (1991). Production, Separation, and Purification of ^{236}Np and ^{236}Pu. *Radiochim. Acta* 54, 159–162. doi: 10.1524/ract.1991.54.4.159

Eigl, R., Srncik, M., Steier, P., and Wallner, G. (2013). $^{236}U/^{238}U$ and $^{240}Pu/^{239}Pu$ isotopic ratios in small (2 L) sea and river water samples. *J. Environ. Radioact.* 116, 54–58. doi: 10.1016/j.jenvrad.2012.09.013

Eigl, R., Steier, P., Sakata, K., and Sakaguchi, A. (2017). Vertical distribution of ^{236}U in the North Pacific Ocean. *J. Environ. Radioact.* 169-170, 70–78. doi: 10.1016/j.jenvrad.2016.12.010

Fabryka-Martin, J. T. (1988). *Production Of Radionuclides In The Earth And Their Hydrogeologic Significance, With Emphasis On Chlorine-36 And Iodine-129.* Ph.D. thesis. Tucson, AZ: University of Arizona.

Fifield, L. K. (2008). Accelerator mass spectrometry of the actinides. *Quat. Geochronol.* 3, 276–290. doi: 10.1016/j.quageo.2007.10.003

Goldstein, S. J., Price, A. A., Hinrichs, K. A., Lamont, S. P., Nunn, A. J., Amato, R. S., et al. (2021). High-precision measurement of U-Pu-Np-Am concentrations and isotope ratios in environmental reference materials by mass spectrometry. *J. Environ. Radioact.* 237:106689. doi: 10.1016/j.jenvrad.2021.106689

Hain, K., Faestermann, T., Fimiani, L., Golser, R., Gómez-Guzmán, J. M., Korschinek, G., et al. (2017). Plutonium isotopes ($^{239-241}Pu$) dissolved in pacific ocean waters detected by accelerator mass spectrometry: no effects of the fukushima accident observed. *Environ. Sci. Technol.* 51, 2031–2037. doi: 10.1021/acs.est.6b05605

Hain, K., Steier, P., Froehlich, M. B., Golser, R., Hou, X., Lachner, J., et al. (2020). $^{233}U/^{236}U$ signature allows to distinguish environmental emissions of civil nuclear industry from weapons fallout. *Nat. Commun.* 11:1275. doi: 10.1038/s41467-020-15008-2

Hirose, K. (2009). Plutonium in the ocean environment: its distributions and behavior. *J. Nucl. Radiochem. Sci.* 10, 1_R7–1_R16. doi: 10.14494/jnrs.10.1_R7

Hotchkis, M., Child, D. P., Froehlich, M. B., Wallner, A., Wilcken, K., and Williams, M. (2019). Actinides AMS on the VEGA accelerator. *Nucl. Instrum. Meth. in Phys. Res. B.* 438, 70–76. doi: 10.1016/j.nimb.2018.07.029

Jerome, S. M., Ivanov, P., Larijani, C., Parker, D. J., and Regan, P. H. (2014). The production of neptunium-236g. *J. Environ. Radioact.* 138, 315–322. doi: 10.1016/j.jenvrad.2014.02.029

Kazi, Z. H., Cornett, R. J., Zhao, X., and Kieser, W. E. (2015). Comparison of the measurement of Pu and Am isotopes by AMS using fluoride and oxide anion beams. *J. Anal. At. Spectrom.* 30, 2235–2240. doi: 10.1039/C5JA00195A

Kelley, J. M., Bond, L. A., and Beasley, T. M. (1999). Global distribution of Pu isotopes and ^{237}Np. *Sci. Total Environ.* 237-238, 483–500. doi: 10.1016/S0048-9697(99)00160-6

Kern, M., Hain, K., Prášek, T., Steier, P., Wiederin, A. and Golser, R. (2022). R-003 Increasing the negative ionization yield for the efficient detection of ^{233}U and ^{236}U by AMS (Version 2). *Zenodo*. doi: 10.5281/zenodo.6256795

Koll, D., Busser, C., Faestermann, T., Gómez-Guzmán, J. M., Hain, K., Kinast, A., et al. (2019). Recent developments for AMS at the Munich tandem accelerator. *Nucl. Instrum. Meth. in Phys. Res. B* 438, 180–183. doi: 10.1016/j.nimb.2018.05.002

Lachner, J., Christl, M., Vockenhuber, C., and Synal, H.-A. (2013). Detection of UH3+ and ThH3+ molecules and ^{236}U background studies with low-energy AMS. *Nucl. Instrum. Meth. in Phys. Res. B* 294, 364–368. doi: 10.1016/j.nimb.2012.02.010

Lachner, J., Kasberger, M., Martschini, M., Priller, A., Steier, P., and Golser, R. (2015). Developments towards detection of ^{135}Cs at VERA. *Nucl. Instrum. Meth. in Phys. Res. B* 361, 440–444. doi: 10.1016/j.nimb.2015.01.032

Lachner, J., Marek, C., Martschini, M., Priller, A., Steier, P., and Golser, R. (2019). ^{36}Cl in a new light: AMS measurements assisted by ion-laser interaction. *Nucl. Instrum. Meth. in Phys. Res. B* 456, 163–168. doi: 10.1016/j.nimb.2019.05.061

Lachner, J., Martschini, M., Kalb, A., Kern, M., Marchhart, O., Plasser, F., et al. (2021). Highly sensitive ^{26}Al measurements by Ion-Laser-InterAction Mass Spectrometry. *Int. J. Mass Spectrom.* 465:116576. doi: 10.1016/j.ijms.2021.116576

Lee, S. H., Povinec, P. P., Wyse, E., and Hotchkis, M. A. C. (2008). Ultra-low-level determination of ^{236}U in IAEA marine reference materials by ICPMS and AMS. *Appl. Radiat. Isot.* 66, 823–828. doi: 10.1016/j.apradiso.2008.02.020

Lee, S.-H., La Rosa, J. J., Levy-Palomo, I., Oregioni, B., Pham, M. K., Povinec, P. P., et al. (2003b). Recent inputs and budgets of ^{90}Sr, ^{137}Cs, $^{239,240}Pu$ and ^{241}Am in the northwest Mediterranean Sea. *Deep-Sea Res. II* 50, 2817–2834. doi: 10.1016/S0967-0645(03)00144-9

Lee, S.-H., Gastaud, J., Povinec, P. P., Hong, G.-H., Kim, S.-H., Chung, C.-S., et al. (2003a). Distribution of plutonium and americium in the marginal seas of the northwest Pacific Ocean. *Deep-Sea Res. II: Top. Stud. Oceanogr.* 50, 2727–2750. doi: 10.1016/S0967-0645(03)00150-4

Lehto, J., and Hou, X. (2011). *Chemistry And Analysis Of Radionuclides*. Weinheim: Laboratory techniques and methodology Wiley-VCH-Verl.

Lin, M., Qiao, J., Hou, X., Dellwig, O., Steier, P., Hain, K., et al. (2021). 70-Year Anthropogenic Uranium Imprints of Nuclear Activities in Baltic Sea Sediments. *Environ. Sci. Technol.* 55, 8918–8927. doi: 10.1021/acs.est.1c02136

Lindahl, P., Lee, S.-H., Worsfold, P., and Keith-Roach, M. (2010). Plutonium isotopes as tracers for ocean processes: a review. *Mar. Environ. Res.* 69, 73–84. doi: 10.1016/j.marenvres.2009.08.002

Lindahl, P., Roos, P., Holm, E., and Dahlgaard, H. (2005). Studies of Np and Pu in the marine environment of Swedish-Danish waters and the North Atlantic Ocean. *J. Environ. Radioact.* 82, 285–301. doi: 10.1016/j.jenvrad.2005.01.011

Livingston, H. D., Povinec, P. P., Ito, T., and Togawa, O. (2001). "Plutonium in the environment," in *Proceedings of the Second International Symposium*. (Amsterdam: Elsevier), 267–292.

López-Lora, M., Chamizo, E., Levy, I., Christl, M., Casacuberta, N., and Kenna, T. C. (2021). ^{236}U, ^{237}Np and $^{239,240}Pu$ as complementary fingerprints of radioactiveeffluents in the western Mediterranean Sea and in the Canada Basin (Arctic Ocean). *Sci. Total Environ.* 765:142741. doi: 10.1016/j.scitotenv.2020.142741

López-Lora, M., Chamizo, E., Rožmarić, M., and Louw, D. C. (2020). Presence of ^{236}U and ^{237}Np in a marine ecosystem: the northern Benguela Upwelling System, a case study. *Sci. Total Environ.* 708:135222. doi: 10.1016/j.scitotenv.2019.135222

López-Lora, M., Levy, I., and Chamizo, E. (2019). Simple and fast method for the analysis of ^{236}U, ^{237}Np, ^{239}Pu and ^{240}Pu from seawater samples by accelerator mass spectrometry. *Talanta* 200, 22–30. doi: 10.1016/j.talanta.2019.03.036

MacDonald, C. M., Cornett, R. J., Charles, C. R. J., Zhao, X. L., and Kieser, W. E. (2016). Measurement of the ^{135}Cs half-life with accelerator mass spectrometry and inductively coupled plasma mass spectrometry. *Phys. Rev. C* 93:014310. doi: 10.1103/PhysRevC.93.014310

Martschini, M., Hanstorp, D., Lachner, J., Marek, C., Priller, A., Steier, P., et al. (2019b). The ILIAMS project – An RFQ ion beam cooler for selective laser

photodetachment at VERA. *Nucl. Instrum. Meth. in Phys. Res. B* 456, 213–217. doi: 10.1016/j.nimb.2019.04.039

Martschini, M., Fifield, L. K., Froehlich, M. B., Leckenby, G., Pavetich, S., Tims, S. G., et al. (2019a). New and upgraded ionization chambers for AMS at the Australian National University. *Nucl. Instrum. Meth. in Phys. Res. B* 438, 141–147. doi: 10.1016/j.nimb.2018.05.039

Martschini, M., Lachner, J., Hain, K., Kern, M., Marchhart, O., Pitters, J., et al. (2021). 5 years of ion-laser iinteraction mass spectrometry—status and prospects of isobar suppression in AMS by lasers. *Radiocarbon* 1–14. doi: 10.1017/RDC.2021.73

Maxwell, S. L., Culligan, B. K., Jones, V. D., Nichols, S. T., Bernard, M. A., and Noyes, G. W. (2010). Determination of ^{237}Np and Pu isotopes in large soil samples by inductively coupled plasma mass spectrometry. *Anal. Chim. Acta* 682, 130–136. doi: 10.1016/j.aca.2010.10.001

Momoshima, N., Sayad, M., and Takashima, Y. (1995). Determination of 99Tc in coastal seawater collected in Fukuoka. *Japan. J. Radioanal. Nucl. Chem.* 197, 245–251. doi: 10.1007/bf02036003

Momoshima, N., Sayad, M., Yamada, M., Takamura, M., and Kawamura, H. (2005). Global fallout levels of ^{99}Tc and activity ratio of ^{99}Tc/^{137}Cs in the Pacific Ocean. *J. Radioanal. Nucl. Chem.* 266, 455–460. doi: 10.1007/s10967-005-0931-2

Noshkin, V. E., Wong, K. M., Eagle, R. J., and Gatrousis, C. (1975). Transuranics and other radionuclides in Bikini Lagoon: concentration data retrieved from aged coral sections. *Limnol. Oceanogr.* 20, 729–742. doi: 10.4319/lo.1975.20.5.0729

Pavetich, S., Carey, A., Fifield, L. K., Froehlich, M. B., Halfon, S., Kinast, A., et al. (2019). ^{93}Zr developments at the heavy ion accelerator Facility at ANU. *Nucl. Instrum. Meth. in Phys. Res. B* 438, 77–83. doi: 10.1016/j.nimb.2018.07.019

Pham, M. K., Sanchez-Cabeza, J. A., Povinec, P. P., Andor, K., Arnold, D., Benmansour, M., et al. (2008). A new certified reference material for radionuclides in irish sea sediment (IAEA-385). *Appl. Radiat. Isot.* 66, 1711–1717. doi: 10.1016/j.apradiso.2007.10.020

Pourmand, A., and Dauphas, N. (2010). Distribution coefficients of 60 elements on TODGA resin: application to Ca, Lu, Hf, U and Th isotope geochemistry. *Talanta* 81, 741–753. doi: 10.1016/j.talanta.2010.01.008

Povinec, P. P., Badie, C., and Baeza, A. (2002). Certified reference material for radionuclides in seawater IAEA-381 (Irish Sea Water). *J. Radioanal. Nucl. Chem.* 251, 369–374. doi: 10.1023/a:1014861620713

Povinec, P. P., Hirose, K., and Aoyama, M. (2012). Radiostrontium in the western North Pacific: characteristics, behavior, and the Fukushima impact. *Environ. Sci. Technol.* 46, 10356–10363. doi: 10.1021/es301997c

Povinec, P. P., Livingston, H. D., Shima, S., Aoyama, M., Gastaud, J., Goroncy, I., et al. (2003). IAEA'97 expedition to the NW Pacific Ocean—results of oceanographic and radionuclide investigations of the water column. *Deep Sea Res. II* 50, 2607–2637. doi: 10.1016/S0967-0645(03)00138-3

Purdy, C. B., Druffel, E. R., and Hugh, D. L. (1989). Anomalous levels of ^{90}Sr and ^{239,240}Pu in Florida corals: Evidence of coastal processes. *Geochim. Cosmochim. Acta* 53, 1401–1410. doi: 10.1016/0016-7037(89)90072-0

Qiao, J., Hou, X., Roos, P., and Miró, M. (2010). Rapid and simultaneous determination of neptunium and plutonium isotopes in environmental samples by extraction chromatography using sequential injection analysis and ICP-MS. *J. Anal. At. Spectrom.* 25:1769. doi: 10.1039/c003222k

Qiao, J., Hou, X., Roos, P., Lachner, J., Christl, M., and Xu, Y. (2013). Sequential injection approach for simultaneous determination of ultratrace plutonium and neptunium in urine with accelerator mass spectrometry. *Anal. Chem.* 85, 8826–8833. doi: 10.1021/ac4020319

Quinto, F., Blechschmidt, I., Garcia Perez, C., Geckeis, H., Geyer, F., Golser, R., et al. (2017). Multiactinide analysis with accelerator mass spectrometry for ultratrace determination in small samples: application to an in situ radionuclide tracer test within the colloid formation and migration experiment at the grimsel test site (Switzerland). *Anal. Chem.* 89, 7182–7189. doi: 10.1021/acs.analchem.7b01359

Quinto, F., Busser, C., Faestermann, T., Hain, K., Koll, D., Korschinek, G., et al. (2019). Ultratrace determination of ^{99}Tc in small natural water samples by accelerator mass spectrometry with the gas-filled analyzing magnet system. *Anal. Chem.* 91, 4585–4591. doi: 10.1021/acs.analchem.8b05765

Quinto, F., Golser, R., Lagos, M., Plaschke, M., Schäfer, T., Steier, P., et al. (2015). Accelerator mass spectrometry of actinides in ground- and seawater: an innovative method allowing for the simultaneous analysis of U, NP, PU, AM, and CM isotopes below ppq levels. *Anal. Chem.* 87, 5766–5773. doi: 10.1021/acs.analchem.5b00980

Rozmaric, M., Chamizo, E., Louw, D. C., López-Lora, M., Blinova, O., Levy, I., et al. (2022). Fate of anthropogenic radionuclides (^{90}Sr, ^{137}Cs, ^{238}Pu, ^{239}Pu, ^{240}Pu, ^{241}Am) in seawater in the northern Benguela upwelling system off Namibia. *Chemosphere* 286, 131514. doi: 10.1016/j.chemosphere.2021.131514

Russell, B. C., Croudace, I. W., and Warwick, P. E. (2015). Determination of ^{135}Cs and ^{137}Cs in environmental samples: a review. *Anal. Chim. Acta* 890, 7–20. doi: 10.1016/j.aca.2015.06.037

Shi, K., Hou, X., Roos, P., and Wu, W. (2012). Determination of technetium-99 in environmental samples: a review. *Anal. Chim. Acta* 709, 1–20. doi: 10.1016/j.aca.2011.10.020

Singh, B., Rodionov, A. A., and Khazov, Y. L. (2008). Nuclear data sheets for A = 135. *Nuclear Data Sheets* 109, 517–698. doi: 10.1016/j.nds.2008.02.001

Snow, M. S., and Snyder, D. C. (2016). ^{135}Cs/^{137}Cs isotopic composition of environmental samples across Europe: environmental transport and source term emission applications. *J. Environ. Radioact.* 151, 258–263. doi: 10.1016/j.jenvrad.2015.10.025

Snow, M. S., Snyder, D. C., Mann, N. R., and White, B. M. (2015). Method for ultra-trace cesium isotope ratio measurements from environmental samples using thermal ionization mass spectrometry. *Int. J. Mass Spectrom.* 38, 17–24. doi: 10.1016/j.ijms.2015.03.006

Steier, P., Bichler, M., Keith Fifield, L., Golser, R., Kutschera, W., Priller, A., et al. (2008). Natural and anthropogenic ^{236}U in environmental samples. *Nucl. Instrum. Meth. in Phys. Res. B* 266, 2246–2250. doi: 10.1016/j.nimb.2008.03.002

Steier, P., Hain, K., Klötzli, U., Lachner, J., Priller, A., Winkler, S., et al. (2019). The actinide beamline at VERA. *Nucl. Instrum. Meth. in Phys. Res. B* 458, 82–89. doi: 10.1016/j.nimb.2019.07.031

Tims, S., Hancock, G., Wacker, L., and Fifield, L. (2004). Measurements of Pu and Ra isotopes in soils and sediments by AMS. *Nucl. Instrum. Meth. in Phys. Res. B* 223-224, 796–801. doi: 10.1016/j.nimb.2004.04.147

Toggweiler, J. R., and Trumbore, S. (1985). Bomb-test ^{90}Sr in Pacific and Indian Ocean surface water as recorded by banded corals. *Earth Planet. Sci. Lett.* 74, 306–314. doi: 10.1016/S0012-821X(85)80002-9

Wacker, L., Fifield, L., and Tims, S. (2004). Developments in AMS of ^{99}Tc. *Nucl. Instrum. Meth. in Phys. Res. B* 223-224, 185–189. doi: 10.1016/j.nimb.2004.04.038

Yang, G., Tazoe, H., and Yamada, M. (2016b). Rapid determination of ^{135}Cs and precise ^{135}Cs/^{137}Cs atomic ratio in environmental samples by single-column chromatography coupled to triple-quadrupole inductively coupled plasma-mass spectrometry. *Anal. Chim. Acta* 908, 177–184. doi: 10.1016/j.aca.2015.12.041

Yang, G., Tazoe, H., and Yamada, M. (2016a). Determination of ^{236}U in environmental samples by single extraction chromatography coupled to triple-quadrupole inductively coupled plasma-mass spectrometry. *Anal. Chim. Acta* 944, 44–50. doi: 10.1016/j.aca.2016.09.033

Zhao, X.-L., and Francisco, B. (2022). Matrix-assisted production of actinide molecular anions for AMS. *Nucl. Instrum. Meth. in Phys. Res. B* 510, 10–19. doi: 10.1016/j.nimb.2021.10.013

Zhao, X.-L., Litherland, A. E., Eliades, J., Kieser, W. E., and Liu, Q. (2010). Studies of anions from sputtering I: survey of. *Nucl. Instrum. Meth. in Phys. Res. B* 268, 807–811. doi: 10.1016/j.nimb.2009.10.036

Zheng, J., Cao, L., Tagami, K., and Uchida, S. (2016). Triple-quadrupole inductively coupled plasma-mass spectrometry with a high-efficiency sample introduction system for ultratrace determination of ^{135}Cs and ^{137}Cs in environmental samples at femtogram levels. *Anal. Chem.* 88, 8772–8779. doi: 10.1021/acs.analchem.6b02150

Zheng, J., Tagami, K., and Uchida, S. (2013). Release of plutonium isotopes into the environment from the fukushima daiichi nuclear power plant accident: what is known and what needs to be known. *Environ. Sci. Technol.* 47, 9584–9595. doi: 10.1021/es402212v

Zheng, J., Tagami, K., Bu, W., Uchida, S., Watanabe, Y., Kubota, Y., et al. (2014). ^{135}Cs/^{137}Cs isotopic ratio as a new tracer of radiocesium released from the Fukushima nuclear accident. *Environ. Sci. Technol.* 48, 5433–5438. doi: 10.1021/es500403h

Zheng, J., Tagami, K., Watanabe, Y., Uchida, S., Aono, T., Ishii, N., et al. (2012). Isotopic evidence of plutonium release into the environment from the Fukushima DNPP accident. *Sci. Rep.* 2:304. doi: 10.1038/srep00304

Zhu, L., Hou, X., and Qiao, J. (2020a). Determination of ultralow Level ^{135}Cs and ^{135}Cs/^{137}Cs ratio in environmental samples by chemical separation and triple quadrupole ICP-MS. *Anal. Chem.* 92, 7884–7892. doi: 10.1021/acs.analchem.0c01153

Zhu, L., Hou, X., and Qiao, J. (2021). Determination of low-level ^{135}Cs and ^{135}Cs/^{137}Cs atomic ratios in large volume of seawater by chemical separation coupled with triple-quadrupole inductively coupled plasma mass spectrometry measurement for its oceanographic applications. *Talanta* 226:122121. doi: 10.1016/j.talanta.2021.122121

Zhu, L., Xu, C., Hou, X., Qiao, J., Zhao, Y., and Liu, G. (2020b). Determination of ultratrace level ^{135}Cs and ^{135}Cs/^{137}Cs ratio in small volume seawater by chemical separation and thermal ionization mass spectrometry. *Anal. Chem.* 92, 6709–6718. doi: 10.1021/acs.analchem.0c00688

Zok, D., Blenke, T., Reinhard, S., Sprott, S., Kegler, F., Syrbe, L., et al. (2021). Determination of characteristic vs anomalous ^{135}Cs/^{137}Cs isotopic ratios in radioactively contaminated environmental samples. *Environ. Sci. Technol.* 55, 4984–4991. doi: 10.1021/acs.est.1c00180

Conflict of Interest: The authors declare that the research was conducted in the absence of any commercial or financial relationships that could be construed as a potential conflict of interest.

Publisher's Note: All claims expressed in this article are solely those of the authors and do not necessarily represent those of their affiliated organizations, or those of the publisher, the editors and the reviewers. Any product that may be evaluated in this article, or claim that may be made by its manufacturer, is not guaranteed or endorsed by the publisher.

frontiers | Frontiers in Marine Science

ORIGINAL RESEARCH
published: 27 April 2022
doi: 10.3389/fmars.2022.845536

Using Radiocarbon Measurements of Dissolved Inorganic Carbon to Determine a Revised Residence Time for Deep Baffin Bay

*Sara Zeidan[1], Jennifer Walker[1], Brent G. T. Else[2], Lisa A. Miller[3], Kumiko Azetsu-Scott[4] and Brett D. Walker[1]**

[1] Department of Earth and Environmental Science, University of Ottawa, Ottawa, ON, Canada, [2] Department of Geography, University of Calgary, Calgary, AB, Canada, [3] Institute of Ocean Sciences, Fisheries and Oceans Canada, Sidney, BC, Canada, [4] Bedford Institute of Oceanography, Department of Fisheries and Oceans Canada, Dartmouth, NS, Canada

OPEN ACCESS

Edited by:
Núria Casacuberta, ETH Zürich, Switzerland

Reviewed by:
Ann P. McNichol, Woods Hole Oceanographic Institution, United States
Terry Whitledge, Retired, Fairbanks, AK, United States

***Correspondence:**
Brett D. Walker
brett.walker@uottawa.ca

Specialty section:
This article was submitted to Marine Biogeochemistry, a section of the journal Frontiers in Marine Science

Received: *29 December 2021*
Accepted: *22 March 2022*
Published: *27 April 2022*

Citation:
Zeidan S, Walker J, Else BGT, Miller LA, Azetsu-Scott K and Walker BD (2022) Using Radiocarbon Measurements of Dissolved Inorganic Carbon to Determine a Revised Residence Time for Deep Baffin Bay. Front. Mar. Sci. 9:845536. doi: 10.3389/fmars.2022.845536

The Canadian Arctic is warming at three times the rate of the rest of the planet and the effects of climate change on the Arctic marine carbon cycle remains unconstrained. Baffin Bay is a semi-enclosed, Arctic basin that connects the Arctic Ocean to the north to the Labrador Sea to the south. While the physical oceanography of surface Baffin Bay is well characterized, less is known about deep water formation mechanisms within the Basin. Only a few residence-time estimates for Baffin Bay Deep Water (BBDW) exist and range from 20 to 1450 years. Better residence time estimates are needed to understand the oceanographic significance of Baffin Bay. Here we report stable carbon ($\delta^{13}C$) and radiocarbon ($\Delta^{14}C$) values of dissolved inorganic carbon (DIC) collected aboard the CCGS *Amundsen* in 2019. DIC $\delta^{13}C$ and $\Delta^{14}C$ values between ranged between -0.7‰ to +1.9‰ and -90.0‰ to +29.8‰, respectively. Surface DIC $\delta^{13}C$ values were between +0.7‰ to +1.9‰, while deep (>100m) values were 0.0 to -0.7‰. Surface DIC $\Delta^{14}C$ values ranged between -5.4‰ to +22.9‰, while deep DIC (>1400m) DIC $\Delta^{14}C$ averaged -82.2 ± 8.5‰ (n = 9). To constrain natural DIC $\Delta^{14}C$ values, we quantified the amount of atmospheric "bomb" ^{14}C in DIC ($\Delta^{14}C_{bomb}$; using the potential alkalinity method; P_{alk}) and anthropogenic DIC (DIC_{anth}; using the ΔC^* method). Both proxies indicate an absence of $\Delta^{14}C_{bomb}$ and DIC_{anth} below 1000m. Using two previously proposed deep water formation mechanisms and our corrected DIC $\Delta^{14}C_{natural}$ values, we estimated a ^{14}C-based residence time of 360-690 years for BBDW. Based on these residence times, we infer carbon is likely stored for centuries in deep Baffin Bay.

Keywords: dissolved inorganic carbon, DIC, 13C, 14C, anthropogenic, bomb, residence time, Baffin Bay

INTRODUCTION

Approximately half of the carbon dioxide (CO_2) emitted into the atmosphere from fossil fuels has been absorbed by the oceans. It has been suggested the oceans comprise the only true sink of atmospheric CO_2 over the past 200 years, storing carbon in the deep ocean on timescales of ~1000 years (Sabine et al., 2004). Most of this oceanic carbon is stored as dissolved inorganic carbon (DIC; ~38,000 GtC), the largest marine carbon reservoir (Heinze, 2014). The Arctic Ocean is an important region for the marine carbon cycle (Hamilton and Wu, 2013) and is warming at three times the rate of the rest of the planet (Arctic Monitoring and Assessment Programme Arctic Climate Change Update, 2021). The effect of climate change on the marine carbon cycle in the Arctic remains unconstrained.

Many Arctic regions act as sinks of anthropogenic carbon below the mixed layer, through the export of particulate organic carbon (POC) and downwelling of surface DIC. Previous studies have used DIC concentrations in Arctic gateways coupled with mass transport models to establish an Arctic Ocean DIC budget (e.g., MacGilchrist et al., 2014; Olsen et al., 2015). The Arctic Ocean absorbs roughly 225 ± 49 Tg C yr^{-1} *via* air-sea gas exchange during the summer months (MacGilchrist et al., 2014). These studies suggest the Arctic Ocean is a carbon sink for most of the year. Open water biological activity and air-sea gas exchange account for most CO_2 uptake. The sink is assumed to be minimal during the winter due to sea ice cover (Shadwick et al., 2011). While DIC and total alkalinity measurements have played a critical role in our understanding of Arctic carbon cycling and ocean acidification, these studies require repetition of high spatial resolution field measurements to estimate carbon fluxes. Most Arctic sampling campaigns are limited to the summer/fall, limiting air-sea gas exchange estimates (Bates and Mathis, 2009).

Marine DIC radiocarbon ($\Delta^{14}C$) and stable carbon ($\delta^{13}C$) measurements are powerful tracers of water mass sources, ages, and advection. Additionally, the decrease in atmospheric $\delta^{13}CO_2$ (i.e., the Suess effect) has been used as key evidence for anthropogenic carbon sequestration in the form of marine DIC (Körtzinger et al., 2003). DIC $\delta^{13}C$ values serve as valuable endmembers for understanding DIC cycling in dynamic Arctic Ocean environments. For example, surface DIC $\delta^{13}C$ values in the Arctic Ocean range between -0.6 and +2.2‰, with deep DIC $\delta^{13}C$ ranging from -1.0 to +2.0‰, in both the Canadian and Eurasian Basins (Griffith et al., 2012; Bauch et al., 2015). DIC $\delta^{13}C$ values in the Beaufort Sea, which feeds Pacific water to the Canadian Arctic Archipelago (CAA), range between -0.5 to +2.2‰ (Mol, 2017). The North Atlantic Ocean, which receives Arctic water through Davis and Fram Strait, consists of DIC $\delta^{13}C$ between -0.1 to +1.9‰ (Humphreys et al., 2016).

Radiocarbon is naturally produced in the stratosphere through the capture of slow cosmic ray neutrons by atmospheric ^{14}N nuclei (Trumbore et al., 2016). In addition, the infiltration of atmospheric "bomb" CO_2 into the global oceans since the 1960s has made ^{14}C a useful physical oceanographic tracer. Northern hemisphere atmospheric $\Delta^{14}C$ values reached +1000‰ with surface marine DIC $\Delta^{14}C$ peaking at roughly +200‰ a decade later. Atmospheric CO_2 $\Delta^{14}C$ values have declined to 0‰ today, due to dilution of this signal *via* increased fossil fuel output and the incorporation of atmospheric CO_2 into the oceans and terrestrial biosphere (Guilderson et al., 2000; Brown and Reimer, 2004). Similarly, the influx of fossil ($\Delta^{14}C$ = -1000‰) CO_2 into the marine DIC reservoir (i.e., the Suess Effect) has proven a useful tool for quantifying anthropogenic impacts on the ocean (Chen and Millero, 1979). However, to date, only a handful of Arctic DIC $\Delta^{14}C$ measurements have been published. DIC $\Delta^{14}C$ values of -60‰ were found in the deep Eurasian Basin, and values as low as -105‰ to -112‰ in the deep Canada Basin (Östlund et al., 1987). Surface DIC $\Delta^{14}C$ values range between -35‰ to +19‰ in the Beaufort Sea, and a value of +52‰ was measured at a single station in the Amundsen Basin (Druffel et al., 2017). Deep DIC $\Delta^{14}C$ values in the Beaufort Sea were as low as -111‰ (Griffith et al., 2012).

In this study, we present the first DIC $\Delta^{14}C$ and new $\delta^{13}C$ data for Baffin Bay. We use $\Delta^{14}C$ and $\delta^{13}C$ values of DIC to trace water mass characteristics, DIC sources, the penetration of bomb vs. anthropogenic (fossil) $\Delta^{14}C$ and to estimate the first ^{14}C-based residence time of deep Baffin Bay.

METHODS

Sample Collection

DIC samples for isotopic analysis were collected from 11 stations throughout Baffin Bay in July 2019 aboard the icebreaker CCGS *Amundsen* (**Figures 1A–C**). Water samples were collected throughout the water column for each station using a rosette equipped with the SBE 911plus conductivity, temperature, depth probe (CTD) and 24 × 12L Niskin bottles. Prior to DIC $\Delta^{14}C$ and $\delta^{13}C$ sample collection, 250 mL Pyrex bottles (Corning #1395-250), caps and 45 mm clear pouring rings were cleaned by soaking in 10% HCl for 1 hour, rinsed with copious amounts of 18.2 MΩ Milli-Q water (TOC <4ppb) and dried overnight. The bottles were then baked at 540°C for 2 hours. Samples for DIC and Total Alkalinity (A_T) concentrations were collected into 250 mL borosilicate glass bottles, overflowed three times, poisoned with 100µL of saturated $HgCl_2$, sealed with Apezion M grease on ground glass stoppers and secured with electrical tape. Samples for DIC $\Delta^{14}C$ followed a similar process but were re-opened briefly after collection in the wet lab, poisoned, re-capped and stored in the dark at room temperature. Nutrient samples were collected in 20 mL polyethylene flasks and measured immediately at sea.

DIC, Total Alkalinity, Salinity, and Nutrient Analysis

DIC concentrations were analyzed by coulometry (Johnson et al., 1993) and A_T by open cell potentiometric titration after (Dickson et al., 2007). DIC and A_T samples were analyzed within 15 months of collection at both the Bedford Institute of Oceanography (BIO; stations 193, 196, and 224) and the Institute of Ocean Sciences (IOS; stations BB15, BB18, 227, 224, BB2, 204, 210 108, and 323). Analytical precision was determined by repeated analysis of a bulk seawater sample. For samples analyzed at Bedford Institute of

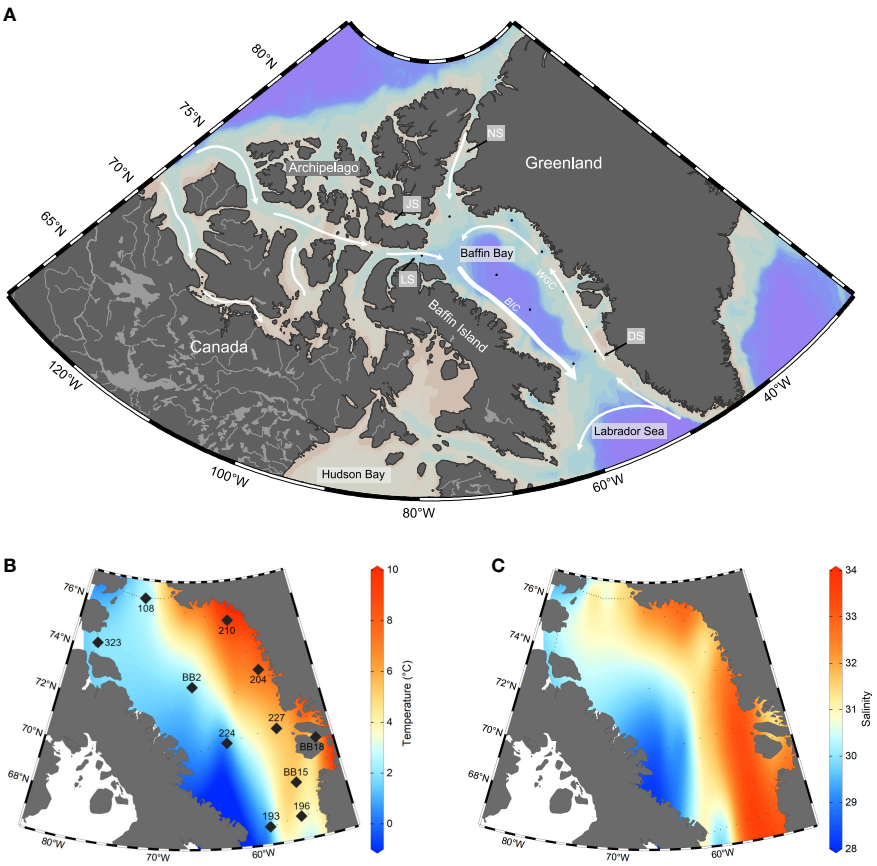

FIGURE 1 | Area and station maps with temperature and salinity in Baffin Bay. **(A)** broader area map indicates major currents (white arrows) land masses and Baffin Bay gateways (grey boxes). Gateways include Davis Strait (DS; 640m), Nares Strait (NS; 250m), Jones Sound (JS; 120m), and Lancaster Sound (LS; 300-800m). **(B)** Data from all stations visited in the 2019 research cruise were used to create the interpolated surface distributions of sea surface temperature (°C). Stations sampled for DIC are indicated by large black diamonds and labeled. **(C)** Data from all stations visited in the 2019 research cruise were used to create the interpolated surface distributions of salinity from 2-3 metres depth are reported in Practical Salinity Units (PSU). Plots b and c are Ocean Data View interpolations resulting from all CTD casts on the cruise (small black dots; n=52 stations) and are used to indicate the presence of the Baffin Island Current (BIC) and Western Greenland Currents (WGC) during the time of sampling.

Oceanography, precision for DIC and A_T was ±0.03%. ± 0.05%, respectively. Results for DIC and A_T at IOS were calibrated against certified reference material (CRM) supplied provided by Dr. Andrew Dickson (Scripps Oceanographic Institution, San Diego, USA), and the analytical precision, based on the average difference between replicates, was ±1.1 μmol kg^{-1} for DIC and ±2.0 μmol kg^{-1} for A_T. An inter-lab comparison of DIC and A_T concentrations yielded errors of ±7.76 μmol kg^{-1} and ±14.27 μmol kg^{-1} (n = 24), respectively. Bottle salinity data were collected from the rosette system and analyzed onboard using an AUTOSAL 8400B salinometer and reported in the Practical Salinity Scale units (PSU). Nutrient concentrations were measured by colorimetry following Aminot and Kérouel (2007) at Université Laval with an analytical precision of ±1 μmol kg^{-1}.

Stable Isotope (δ^{13}C) Analysis

For each sample, 1 mL of seawater was transferred into a pre-cleaned 12 mL Exetainer vials, which had been flushed with UHP He gas within a glove bag to remove of any atmospheric CO_2. 100 μL of 85% H_3PO_4 was then added to each sample, which was shaken and left to equilibrate for at least 12 hours at room temperature. This allowed the DIC to equilibrate with CO_2 in the headspace of the vials (Olack et al., 2018). Isotopic standards were prepared using external calcite and limestone standards (IAEA NBS-18, δ^{13}C = -5.01‰; IAEA NBS-19, δ^{13}C = +1.95). Internal bicarbonate standards for calibration correction were also used (VL-1 δ^{13}C = -3.21‰; VL-2 δ^{13}C = -15.80‰; VL-3 δ^{13}C = -13.89‰ from Ján Veizer Stable Isotope Laboratory; OXG δ^{13}C = -7.5‰ from Oxford University). DIC δ^{13}C values were measured using a Thermo-Finnigan Gas Bench coupled to a Thermo-Finnigan Delta V-Plus Continuous Flow Isotope-Ratio Mass Spectrometer (IRMS) at the University of Ottawa, Ján Veizer Stable Isotope Laboratory. Results are reported in standard per mil (‰) notation and relative to Vienna Pee Dee Belemnite (V-PDB) for δ^{13}C. Average external precision based on sample replicates (n = 100) was ±0.1‰.

Natural Abundance Radiocarbon ($\Delta^{14}C$) Analysis

Seawater DIC was extracted using the headspace CO_2 method for $\Delta^{14}C$ following Gao and co-workers (2014). Approximately 40 mL of seawater was transferred to pre-cleaned and pre-weighed 60 mL vials (Fisher Scientific #5719398) by decanting in a glove bag flushed multiple times with ultra-high purity (UHP) N_2 gas. Vials were filled with ~40mL sample, were then sealed with Viton and silicone septa, secured with caps, and re-weighed to calculate seawater volume. Each vial was then injected with 0.5 mL of 85% H_3PO_4 (Fisher Scientific #A260500) using a 5mL gas-tight glass syringe (Hamilton #81520) and a 23-gauge side-port needle (Fisher Scientific #14815488). Acidified samples were gently shaken and heated in a block at 75°C for 2 hours.

Isotopic standards were prepared using in-house carbonate standards (Fm = 0.9444 ± 0.0018; Coral STD, UC Irvine), IAEA-C2 travertine (Fm = 0.4114 ± 0.0003), and ^{14}C-free $NaHCO_3$ (Fm = 0, uOttawa). Standards were weighed and transferred in a glove bag into pre-cleaned 60 mL I-Chem vials, along with 40 mL of stripped standard water (100 mL of Milli-Q water stripped with UHP N_2 gas for 15 minutes) and sealed. Standards were then acidified with 0.5 mL of 85% H_3PO_4 and heated at 75°C for 2 hours.

Combusted OX-1 (Fm = 1.0398), OX-2 (Fm = 1.3407) standards and in-house Glycine (Fm = 0) were used as modern normalization standards and dead process blank standards during AMS sample analysis. These standards were weighed into pre-baked (540°C/2 hrs) 6 mm quartz tubes with ~150 mg of CuO, sealed under vacuum and combusted (850°C/3 hrs). Combusted standards were then expanded into a vacuum line to cryogenically purify the resultant CO_2 that was then graphitized using the sealed-tube Zn method (Xu et al., 2007).

DIC samples and standard headspace was extracted using a pre-flushed 60 mL BD Luer-Lock syringe equipped with a BD 2.5 cm needle and inserted into the vacuum line system through a septum. The CO_2 was then cryogenically purified with liquid nitrogen and quantified manometrically. Purified CO_2 was graphitized using the sealed-tube Zn method (Xu et al., 2007), pressed into targets at uOttawa and analyzed for $\Delta^{14}C$ at the Keck Carbon Cycle AMS facility at the University of California Irvine. DIC radiocarbon data is reported as Fraction Modern (Fm), $\Delta^{14}C$ and apparent ^{14}C age following the conventions set forth by (Stuiver and Polach, 1977) and corrected for year of sample collection and for modern vs. dead C blanks associated with sample preparation and extraction.

Estimation of Anthropogenic (DIC_{anth}) and "Bomb" DIC ^{14}C

Our measured DIC $\Delta^{14}C$ values include contributions of both atmospheric "bomb" ^{14}C (from 1950s above-ground thermonuclear weapons testing) and fossil (anthropogenic) CO_2 that are incorporated into the DIC reservoir through air-sea gas exchange. This DIC mixture is expressed in Equation 1.

$$DIC_{measured}\Delta^{14}C_{measured} = DIC_{natural}\Delta^{14}C_{natural} + DIC_{bomb}\Delta^{14}C_{bomb} + DIC_{anth}\Delta^{14}C_{anth} \quad (1)$$

We use two methods to correct DIC $\Delta^{14}C_{measured}$ values to $\Delta^{14}C_{natural}$ values which can then be used to estimate a ^{14}C-residence time for BBDW. The potential alkalinity method (P_{alk}) proposed by Rubin and Key (2002) was used to separate the amount of $\Delta^{14}C_{bomb}$ from $\Delta^{14}C_{natural}$. P_{alk} is first calculated using measured total alkalinity (A_T), then corrected for biological activity using nitrate concentrations and normalized to salinity (Equation 2). $\Delta^{14}C_{bomb\ corr}$ was then calculated based on the regression statistics between global $\Delta^{14}C$ versus potential alkalinity measurements (Equation 3) corrected for a global surface potential alkalinity value of 2320, known as P_{alk0}. $\Delta^{14}C_{bomb}$ was determined by calculating the difference between $\Delta^{14}C_{measured}$ and $\Delta^{14}C_{bomb\ corr}$ for each sample.

$$P_{alk} = (A_T + \text{Nitrate}) \times 35/\text{Salinity} \quad (2)$$

$$\Delta^{14}C_{bomb\ \ corr} = -59.0 - 0.962(P_{alk} - 2320) \quad (3)$$

The amount of anthropogenic carbon present in DIC (DIC_{anth}) was calculated by using the quasi-conservative tracer (ΔC^*) method following Lee et al. (2003). ΔC^* is calculated using measured DIC ($DIC_{measured}$) and alkalinity concentrations (A_T) in Equation 4 and is reported in μmol kg^{-1}. $O_{2\ measured}$ and $O_{2\ eq}$ represent measured oxygen concentrations and oxygen saturation levels at a given temperature and salinity, respectively. Preformed alkalinity concentrations (A_T^0) are determined using Equation 5. Here, NO represents the relationship between oxygen and nitrate concentrations (Equation 6) and $R_{C:O}$ and $R_{N:O}$ represent the stoichiometric ratios which relate inorganic carbon (C), nitrate (N), and dissolved oxygen (O). $R_{C:O}$ and $R_{N:O}$ are based on the Redfield Ratio proposed by (Anderson and Sarmiento, 1994). DIC_{eq} is the DIC in equilibrium with pre-industrial atmospheric CO_2 levels with a fugacity of 280 μatm (Equation 7).

$$\Delta C^* = DIC_{measured} + R_{C:O}(O_{2\,eq} - O_{2\,measured}) - 0.5\left[(A_{T\,measured} - A_T^0) - R_{N:O}(O_{2\,eq} - O_{2\,measured})\right] - DIC_{eq}(fCO_2 = 280\mu atm, A_T^0, \theta, S) \quad (4)$$

$$A_T^0(\mu\text{mol kg}^{-1}) = 335.7 + 55.80 \times S + 0.08924 \times NO \quad (5)$$

$$NO = O_2 - R_{O:N} \times N \quad (6)$$

$$DIC_{eq} = 2077 - 8.517(\theta - 9) + 3.523(S - 35) + 0.6399(A_T^0 - 2320) \quad (7)$$

Final DIC_{anth} concentrations are calculated using Equation 8, with ΔDIC_{diseq} values from Lee et al. (2003) based on seawater potential density. In our study, DIC_{anth} values <5 μmol kg^{-1} were assumed to contain zero DIC_{anth} (see **Supplementary Table 2**).

$$DIC_{anth} = \Delta C^* - \Delta DIC_{diseq} \quad (8)$$

In comparing North Atlantic vs. Baffin Bay DIC_{anth} and $\Delta^{14}C_{bomb}$ depth profiles, we find that the P_{alk} proxy grossly overestimated $\Delta^{14}C_{bomb}$ values for depths shallower than 400m. We found estimated DIC_{anth} values *via* the ΔC^* proxy gave realistic values, albeit lower than in the North Atlantic. Both proxies were parameterized for the subtropical North Atlantic and have recognized limitations at high latitudes (Rubin and Key, 2002; Lee et al., 2003).

To correct our $\Delta^{14}C_{measured}$ for DIC_{anth} and DIC_{bomb} $\Delta^{14}C$ contributions, a two-endmember mixing model was used to determine the $\Delta^{14}C$ per mil equivalence of DIC_{anth}, that accounts for DIC_{anth}, $DIC_{measured}$, and a $\Delta^{14}C_{anth}$ value of -1000‰. For stations above 500m, only the per mil equivalence DIC_{anth} was subtracted from $\Delta^{14}C_{measured}$. For stations below 500m, both $\Delta^{14}C_{bomb}$ and the per mil equivalence of DIC_{anth} were subtracted from $\Delta^{14}C_{measured}$, to determine $\Delta^{14}C_{natural}$. DIC $\Delta^{14}C_{natural}$ values were converted to a fraction modern (Fm) value and then to an apparent ^{14}C-age based on a half-life of 5730 years. To calculate a residence time of the region, we used DIC $\Delta^{14}C$ and other relevant measurements from the A16N line in the North Atlantic in 2013 (https://cchdo.ucsd.edu/cruise/33RO20130803). DIC_{anth} and $\Delta^{14}C_{bomb}$ corrections made to $\Delta^{14}C_{natural}$ values and a corrected apparent ^{14}C-age.

RESULTS

DIC $\delta^{13}C$ Values

DIC $\delta^{13}C$ values ranged from -0.7‰ to +1.9‰ across Baffin Bay (**Figure 2A**). Enriched DIC $\delta^{13}C$ values were observed at surface depths (+0.7‰ to +1.9‰) and depleted DIC $\delta^{13}C$ were observed at depths greater than 100m (-0.0‰ to -0.7‰). Surface DIC $\delta^{13}C$ values (less than 20m) were enriched along the coast of Greenland and in the Northern gateways (stations BB18, 227, 210, 108 and 323; $\delta^{13}C$ = +1.3 ± 0.4‰, *n* = 12), while more depleted values were found along Davis Strait and central Baffin Bay (stations 193, 196, BB2, and 224; $\delta^{13}C$ = +0.9 ± 0.3‰, *n* = 8). Mid-depth (200 – 700m) DIC $\delta^{13}C$ ranged from -0.4‰ to +0.2‰, with slightly depleted values found at stations BB18 and 227 ($\delta^{13}C$ = -0.30 ± 0.07‰; *n* = 4). Below 750m in Baffin Bay, DIC $\delta^{13}C$ values had a narrow range (-0.28 ± 0.16‰; *n* = 19). Deep water (>1200m) at Station 224 was more depleted (-0.51 ± 0.11‰; *n* = 4) than DIC $\delta^{13}C$ values at station BB2 (-0.27 ± 0.07‰; *n* = 4).

DIC $\Delta^{14}C$ Values

Our measured Baffin Bay DIC $\Delta^{14}C$ values had a ~120‰ range (from –90.0‰ to +29.8‰; **Figure 2B**). Surface (less than 20m) DIC $\Delta^{14}C$ values ranged between -5.4‰ to +22.9‰. Positive surface DIC $\Delta^{14}C$ were found along coastal Greenland (stations 196, BB15, BB18, 227 204, and 210; $\Delta^{14}C$ = +17.6 ± 2.5‰, *n* = 12). In contrast, more negative DIC $\Delta^{14}C$ surface values were found in the Northern gateways (stations 108 and 323; $\Delta^{14}C$ = -1.7 ± 3.3‰, *n* = 3). Surface DIC $\Delta^{14}C$ values at central stations (193, BB2, 224) fell between these two end members ($\Delta^{14}C$ = +8.5 ± 3.7‰; *n* = 6). Mid-depth waters (200 – 700m) had DIC $\Delta^{14}C$ between -1.11‰ and +29.8‰, with positive $\Delta^{14}C$ values found in Northern Baffin Bay (stations BB2, 108, and 323; $\Delta^{14}C$ = +23.8 ± 3.9‰, *n* = 7). Below 750m, DIC $\Delta^{14}C$ values gradually decreased from +7.7‰ to –90.0‰, with the deepest water (1400 – 2400m) having the most negative $\Delta^{14}C$ values (-82.2 ± 8.5‰; *n* = 9).

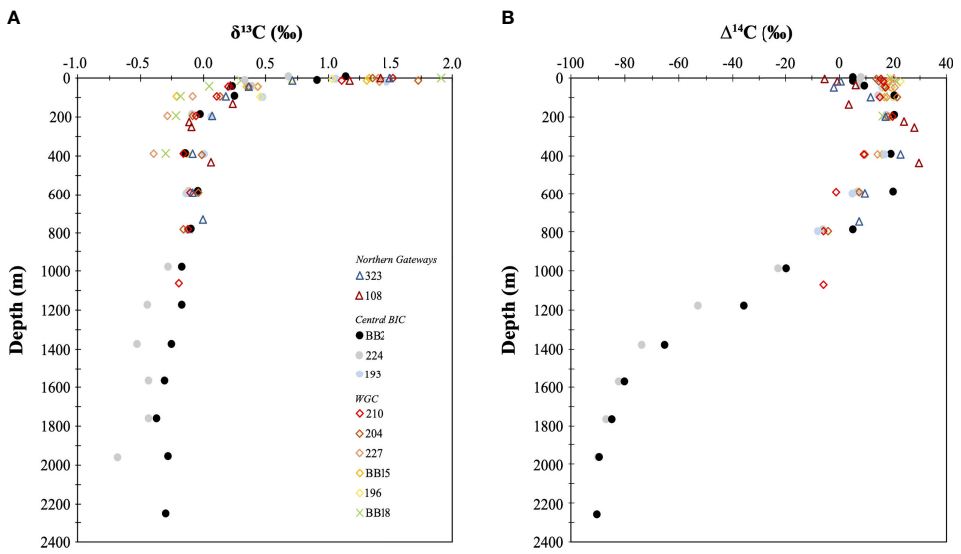

FIGURE 2 | Depth profiles of DIC $\delta^{13}C$ and $\Delta^{14}C$ values in Baffin Bay. **(A)** measured DIC $\delta^{13}C$ values, ± 0.1‰ (See *Stable Isotope ($\delta^{13}C$) Analysis*). Different sampled stations (**Figure 1**) indicated by legend, which cover the extent of the Baffin Island Current (BIC) in central Baffin Bay (circles), the Western Greenland Current (WGC) along the coast of Greenland, (diamonds). and the Northern gateways of Nares Strait and Lancaster Sound (triangles). **(B)** DIC $\Delta^{14}C$ signatures, with errors ranging between ±1.2 to 2.0‰ (See "*Natural Abundance Radiocarbon ($\Delta^{14}C$) Analysis*" and "*Estimation of Anthropogenic (DIC_{anth}) and "Bomb" DIC ^{14}C*").

DISCUSSION

Baffin Bay – Hydrographic Setting

Wide ranges in Baffin Bay surface water salinity and temperature were observed (**Figures 1B, C**; **Figures 3A, B**). Surface water (above 50m) on the western side of Baffin Bay was cooler and fresher, while surface water on the eastern side was warmer and more saline (Fox and Walker (2022), accepted). We note that the Ocean Data View interpolation of n=52 stations from Baffin Bay in **Figure 1** are meant for visualizing these differences and do not reflect the true spatial structure of temperature or salinity. These surface water summer conditions are influenced by surface processes such as solar insulation, wind-driven mixing, and ice melt (Fissel et al., 1982). Surface water variance is also influenced by the current systems within Baffin Bay. Baffin Bay is a marginal sea ice zone experiencing full sea-ice coverage from December to April. Due to the relatively warm West Greenland Current, ice cover decreases earlier along the Greenland coast than on the western side of Baffin Bay . By late summer, Baffin Bay is typically clear of extensive sea-ice, although icebergs are common, especially in proximity to fjords. Sources of freshwater in Baffin Bay include local precipitation, river runoff, sea ice, ice bergs and glacial meltwater, and the Arctic Ocean outflow. It is estimated Baffin Bay has a total river inflow of ~100 km^3 y^{-1} (Shiklomanov et al., 2020). Work by Azetsu-Scott et al. (2012) suggests that glacial melt on the Greenland Shelf comprises ~6% total freshwater and that Arctic outflow water from the CAA and Northern Gateways dominates freshwater flux in Baffin Bay (~60% in Western Davis Strait). The Arctic outflow water from the CAA includes Pacific (31.5 < S < 33), sea ice meltwater and meteoric (Mackenzie R. and CAA tributaries) water endmembers. A small portion of meteoric water enters Baffin Bay *via* Nares Strait from Russian rivers (Mungall et al., 2017; Burgers et al., 2017).

Baffin Bay water masses are indicated on **Figure 3B**. Two main surface currents dominate Baffin Bay: the Baffin Island Current (BIC) and the West Greenland Current (WGC). The BIC is a southerly flowing current containing Arctic Water (AW) to depths of 300m and has water temperatures <-1.6°C and salinities <33.8 (Münchow et al., 2015). AW enters Baffin Bay *via* the Northern Gateways (Nares Strait and Lancaster Sound) and is modified through glacial and sea ice discharge (Curry et al., 2011). In this study, AW was observed at both central stations (BB2, 224) between 100-300m. Western Greenland Shelf Water (WGSW) was evident along the coast of Greenland and was both warm (7°C) and saline (34.1), with a density anomaly ($\sigma_\theta = \rho_\theta - 1000$, where ρ is density and θ indicates potential temperature) ranging between 25.5 and 27.3 kg m^{-3}. WGSW is composed of waters from the East Greenland Current (EGC), which originate from AW exiting through Fram Strait and later enter Baffin Bay *via* the WGC (Cuny et al., 2002). As the WGSW progresses northward along the WGC extension, it becomes fresher and cooler, due to mixing with glacial meltwater (Münchow et al., 2015).

At depth, several water masses are present in Baffin Bay. West Greenland Irminger Water (WGIW) is defined by salinities >34.1, potential temperatures >2°C, and a density anomaly range of 27.3 to 28 kg m^{-3} (Curry et al., 2011). WGIW originates from warm, saline water found in the Irminger Sea. Transitional Water (TrW) found below 250m, is modified AW that has mixed with WGIW (Curry et al., 2011). The TrW typically has temperatures >2°C, salinities <33.7, and σ_θ of 25.5 – 27.3kg m^{-3} (Curry et al., 2011). Baffin Bay Deep Water (BBDW) has a temperature and salinity of 0°C and ~34.5, respectively, and is found between 1200 and

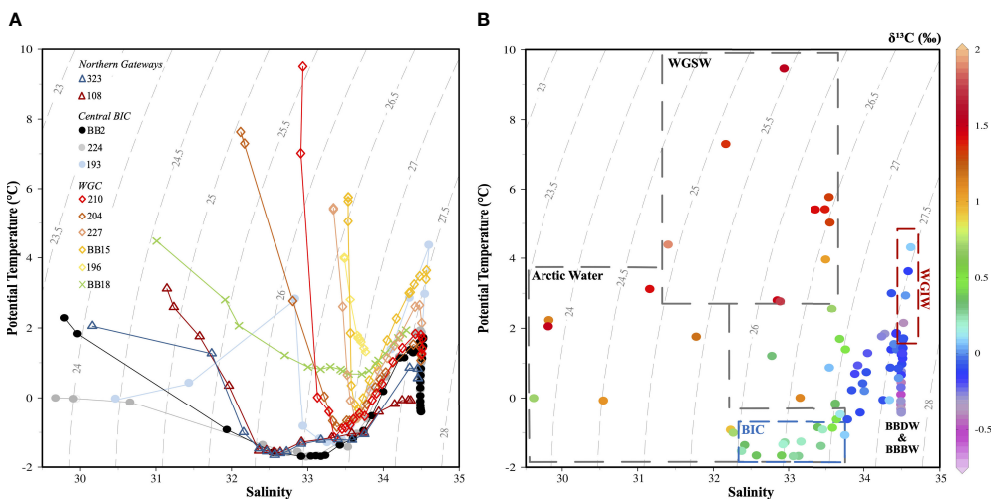

FIGURE 3 | Potential temperature-salinity diagram with DIC δ^{13}C values throughout Baffin Bay. **(A)** Bottle salinity and potential temperature values plotted for each collected station. Different sampled stations (**Figure 1**) indicated by legend; Baffin Island Current (circles), Western Greenland Current (diamonds), Northern gateways (triangles). Dashed grey lines represent potential density anomaly contours. **(B)** Potential temperature versus salinity with DIC δ^{13}C (color bar). Dashed boxes indicate designated currents and water masses; Arctic Water (AW), western Greenland shelf water (WGSW), Baffin Island current (BIC), West Greenland Irminger water (WGIW), and Baffin Bay deep and bottom water (BBDW; BBBW). Note: fewer data points on plot b are since not all Niskin bottle depths were sampled for DIC δ^{13}C.

1800m (Curry et al., 2011). Baffin Bay Bottom Water (BBBW) has a temperature and salinity of -0.4°C and ~34.5, respectively. BBBW is more difficult to distinguish using temperature, salinity, and water mass density alone (Lehmann et al., 2019).

DIC δ^{13}C as a Surface Water Mass Tracer

Surface DIC δ^{13}C values can provide useful constraints on DIC source contributions. In Baffin Bay there are several possible DIC sources in the BIC and WGC, including: Pacific, North Atlantic, Arctic water, regional sea ice melt and glacial melt water. The many surface DIC sources in Baffin Bay results in a diversity of isotopic endmember values that could also contribute to deep-water DIC δ^{13}C values. Understanding the processes shaping surface DIC δ^{13}C distributions are therefore important to understanding the DIC cycle within Baffin Bay. Here we discuss surface and intermediate water DIC δ^{13}C values as water mass tracers.

Our observed depth trends in DIC δ^{13}C values are broadly consistent with the open ocean. Surface DIC δ^{13}C values are enriched, whereas deep DIC δ^{13}C values are depleted (**Figures 2A**, **3B**). These trends in DIC δ^{13}C are attributed to air-sea gas exchange with some isotopic fractionation of CO_2 across the air-liquid boundary and to a much lesser extent the fractionation of organic carbon through photosynthesis (Zhang et al., 1995). Depleted DIC δ^{13}C values at depth can be attributed to the preferential oxidation of ^{13}C-depleted sinking particulate and dissolved organic matter (POM; DOM) *via* heterotrophic respiration. Older aged water masses typically contain depleted DIC δ^{13}C values, since there is more time for remineralization (Kroopnick, 1985; Emerson and Hedges, 2008).

Surface (above 20m) DIC δ^{13}C is variable in Baffin Bay. The warm WGSW along the coast of Greenland contains enriched DIC δ^{13}C values (>+1.03‰). These values are consistent with previously reported DIC δ^{13}C from the North Atlantic along the southern tip of Greenland (+1.09 to +1.90‰; Humphreys et al., 2016). Within WGSW, we observe an increase in surface DIC δ^{13}C values from station 196 to 210 (+1.03 to +1.90‰, respectively). One possible explanation for this trend is high nutrient loading from melting Greenland glaciers, leading to enhanced primary production and enriched DIC δ^{13}C values as the WGC flows north. For example, station BB18, located in the Viagat Fjord behind Disko Island, had the highest surface DIC δ^{13}C (+1.90‰). This station also had high POM and chlorophyll-*a* concentrations due to an abundance of diatoms (Fox and Walker (2022), accepted; Lovejoy pers. comm.). This marginal sea ice region and the inflow of saline Atlantic water have been previously shown to promote primary production (Krawczyk et al., 2021).

Northern Gateway stations (108 and 323) had enriched surface DIC δ^{13}C values (+0.71 to +1.42‰). Surface water in Smith Sound (Station 108) is a mixture of both the inflow of AW from Nares Strait and WGSW (Hamilton and Wu, 2013). Thus, Station 108 does not represent a pure AW endmember. Surface water in Lancaster Sound (Station 323) contains Pacific Water entering Baffin Bay *via* the CAA. Enriched surface DIC δ^{13}C values in Lancaster Sound may be indicative of this Pacific influence, which has been observed to have DIC δ^{13}C values up to +2.20% in the Amundsen Gulf (Mol, 2017). Lancaster Sound is also a region of seasonal sea ice cover, high nutrient, primary production, and diatom species richness (Krawczyk et al., 2021). These factors contribute to the enriched surface DIC δ^{13}C values at Station 323. Variability in surface DIC δ^{13}C in Baffin Bay can also be attributed to sea-ice and glacial melt, as evident in large ranges in observed surface salinity as shown in **Figure 3A**.

Central Baffin Bay stations BB2 and 224 had more depleted surface DIC δ^{13}C values (+1.06 to +1.50‰) than Eastern Baffin Bay stations along coastal Greenland (**Figure 3**). These lower DIC δ^{13}C values coincide with AW within the BIC. The Arctic Ocean is covered in sea ice for most of the year, inhibiting air-sea gas exchange and increasing the time in which heterotrophic respiration can result in depleted DIC δ^{13}C values (Morée et al., 2018). DIC δ^{13}C values within the BIC (20 – 200m; +0.07 to +0.37‰) are significantly higher than that of WGIW (-0.39 to +0.07‰), reflecting more recent air-sea gas exchange in the BIC vs. older, intermediate water (Münchow et al., 2015).

Overall, the trends we observe in DIC δ^{13}C values in temperature-salinity space (**Figure 3B**) suggest that DIC δ^{13}C can be used as an effective tool for distinguishing carbon sources within water masses. A simple least squares regression of DIC δ^{13}C (y) and potential density (x) resulted in statistically significant correlations at all stations in Baffin Bay; in particular for coastal Greenland (R^2 = 0.78-0.98) and Northern Gateways stations (R^2 = 0.85-0.96; see **Table S3** and **Figures S1** and **S3**). Surface DIC δ^{13}C variability is strongly affected by sea-ice melt (more positive DIC δ^{13}C) and the inflow of saline Atlantic water (more negative δ^{13}C). This is especially true for several coastal Greenland stations adjacent to large fjord regions (Stations BB18, 227, 210; **Figure S4** and **Table S5**). In contrast, deep DIC δ^{13}C variability is driven by slow heterotrophic respiration at depth. This is indicated by depleted DIC δ^{13}C values >1000m (σ_θ = ~27.7 kg/m^3) at stations 224 and BB2 (-0.27 to -0.68‰ at 1000 to 2000m and -0.16 to -0.36‰ at 1200 to 2300m, respectively).

DIC Δ^{14}C Distributions in Baffin Bay

We observe a wide range in DIC Δ^{14}C values within Baffin Bay (-90.0‰ to +29.8‰; **Figure 2B**). DIC Δ^{14}C values can reflect water mass aging *via* radioactive decay, varying degrees of recent air-sea gas exchange or allochthonous DIC Δ^{14}C sources. For example, the advection of waters with different ^{14}C reservoir ages (i.e., surface DIC Δ^{14}C vs. atmospheric Δ^{14}C offsets). With deep-water formation, modern surface DIC Δ^{14}C can also contribute to observed deep ocean DIC Δ^{14}C values (e.g., in the North Atlantic Ocean; Broecker et al., 1960).

Surface (<20m) DIC Δ^{14}C ranged between -5.4‰ to +22.9‰. Surface DIC Δ^{14}C values at Greenland stations (196, BB15, 227, 204, 210) had the most positive DIC Δ^{14}C values (+14.3‰ to +22.9‰). These values represent positive DIC Δ^{14}C endmembers from the North Atlantic at depths <150m (+30.2‰ to +62.3‰; Bullister and Barigner, 2020), indicating the WGSW has a large impact on DIC Δ^{14}C values in Eastern Baffin Bay. Previous studies have noted summer upwelling of warmer, saline WGSW along Greenland (Melling et al., 2010) which would clearly contribute DIC with positive Δ^{14}C values.

Surface water (above 20m) at the Northern gateway stations (108, 323) had far lower DIC $\Delta^{14}C$ values (-5.4‰ to +0.9‰). These stations contain Arctic and CAA contributions to the Smith and Lancaster Sounds, respectively. Surface DIC $\Delta^{14}C$ values in the Amundsen Gulf and Beaufort Sea range between -35‰ to +19‰, whereas a value of +52‰ was measured in the Eurasian Basin (Druffel et al., 2017). Thus, the lower DIC $\Delta^{14}C$ values we observe in Lancaster Sound (station 323) are consistent with advection of Pacific water with low DIC $\Delta^{14}C$ to Baffin Bay from the CAA. Pacific water nutrient contributions to Baffin Bay were recently reported (Lehmann et al., 2019), again suggesting this is a plausible explanation for our low Station 323 DIC $\Delta^{14}C$ values. The low DIC $\Delta^{14}C$ values we observe for Smith Sound (Station 108) are likely impacted by both AW entering from the Lincoln Sea and WGC water. While no DIC $\Delta^{14}C$ data exist for the Lincoln Sea, this station experiences extended periods of sea ice cover – inhibiting air-sea gas exchange and likely resulting in lower surface DIC $\Delta^{14}C$ values.

Surface DIC $\Delta^{14}C$ values in central Baffin Bay are modern (BB2, 224; +5.8‰ to +15.7‰) and possibly comprise a mixture of low AW DIC $\Delta^{14}C$ with positive DIC $\Delta^{14}C$ from WGSW and the influence of seasonal sea ice cover. At these stations, large DIC $\Delta^{14}C$ gradients (-90.0 to +20.6‰) were present in deep (>500m) water of similar densities (σ_θ = 27.56 to 27.72 kg m^{-3}). Below 1200m, DIC $\Delta^{14}C$ values gradually decrease from -35.4‰ to -90.0‰ (or 225 to 675 ^{14}C-years) towards the bottom (σ_θ = 27.70 ± 0.02 kg m^{-3}, BBDW). Unlike DIC $\delta^{13}C$, no significant relationships were found between potential density and DIC $\Delta^{14}C$ (**Table S4**; **Figure S2**). This is because similar, modern DIC $\Delta^{14}C$ values were measured across large surface salinity (and density) gradients. Conversely, at Stations BB2, 224, large gradients in DIC $\Delta^{14}C$ values were present in mid-depth (500-1200 m) waters of relatively invariant σ_θ (e.g., 27.7 kg m^{-3}; **Figures 2B**; **S2F, G**).

While the distributions of DIC $\Delta^{14}C$ appear consistent with the physical oceanography of Baffin Bay, measured DIC $\Delta^{14}C$ values can also include atmospheric "bomb" carbon ($\Delta^{14}C$ = -1000‰; Mahadevan, 2001; Sweeney et al., 2007) or anthropogenic fossil fuel carbon (DIC$_{anth}$; Carter et al., 2019). The contribution of DIC$_{anth}$ and $\Delta^{14}C_{bomb}$ are ever present in the modern global surface ocean, but their relative contributions and depth of infiltration in the water column vary widely. Since our goal is to derive a ^{14}C-based residence age of Baffin Bay, we next quantify these contributions to deep Baffin Bay water.

Estimation of DIC $\Delta^{14}C_{bomb}$ Contributions

Our estimates of $\Delta^{14}C_{bomb}$ using the P_{alk} method (see *Estimation of Anthropogenic (DIC$_{anth}$) and "Bomb" DIC ^{14}C*) for Station BB2 are shown in **Figure 4**. Both DIC $\Delta^{14}C_{bomb}$ and $\Delta^{14}C_{bomb\ corr}$ values are highly unconstrained above 400m, with very negative $\Delta^{14}C_{bomb\ corr}$ values and very positive $\Delta^{14}C_{bomb}$ values beyond what would be reasonably expected for seawater DIC $\Delta^{14}C$ in 2019. This is a known limitation of the P_{alk} proxy which was parameterized for the subtropical and tropical Atlantic (<60°N/S) with salinities averaging 36.31 ± 0.35, and surface alkalinity averaging 2377 ± 22 μmol kg^{-1} (Jiang et al., 2014). In comparison, surface Baffin Bay salinity and total alkalinity values average 32.2 ± 1.2 and 2194 ± 59 μmol kg^{-1}, respectively. Lower surface salinity and alkalinity values, combined with seasonal sea ice cover in Baffin Bay, limits the application of the P_{alk} method in the Arctic. The overestimation of bomb $\Delta^{14}C$ above 400m in Baffin Bay is particularly telling. At their peak, global surface DIC $\Delta^{14}C$ values reached +200‰ in the late 1960s (Rodgers et al., 2000). We note that Rubin and Key (2002) recognized the P_{alk} proxy predicts lower than expected $\Delta^{14}C_{bomb\ corr}$ values north of 58°N and suggested a more reliable calibration value (P_{alk0}) of 2330 μmol kg^{-1} for high latitudes. However, we find surface $\Delta^{14}C_{bomb\ corr}$ values to remain unconstrained even using this P_{alk0} value and that more work is needed to refine the P_{alk} proxy in the Arctic.

Despite the unconstrained surface estimates of $\Delta^{14}C_{bomb}$ and $\Delta^{14}C_{bomb\ corr}$, these parameters provide realistic values at depth (**Figure 4**). The confluence of the corrected and measured values suggests the P_{alk} proxy can accurately predict $\Delta^{14}C_{bomb\ corr}$ at depth, and an absence of $\Delta^{14}C_{bomb}$ in BBDW and BBBW. We believe the reliability of the P_{alk} proxy below 400m can be attributed to the similar salinity, nitrate, and alkalinity values in North Atlantic Deep Water (NADW) and deep Baffin Bay. For example, NADW below 1200m in the tropics (35°N to Equator) has average salinity and alkalinity values of 35.4 ± 1.1 and 2371 ± 37 μmol kg^{-1}, respectively (Takahashi et al., 1981). Average salinity and total alkalinity values below 1000m in BBDW are 34.39 ± 0.01 and 2290 ± 13 μmol kg^{-1}, respectively. While these deep ocean values are not identical, it appears that they fall within a range for which the P_{alk} proxy was developed (i.e., closer to deep sub-tropical Atlantic values). Because deep water alkalinity is globally less variable than surface waters, it is also possible the P_{alk} method is simply more robust in deep waters than in surface waters. Ultimately, since we can find no evidence of $\Delta^{14}C_{bomb}$ below 1400m, there is no need to correct our deepest measured DIC $\Delta^{14}C$ values for $\Delta^{14}C_{bomb}$ when determining a ^{14}C-based residence time.

Anthropogenic DIC Contributions

Calculated DIC$_{anth}$ concentrations suggest an influx of DIC$_{anth}$ *via* Davis Strait (**Figure 5**). At Station 193, DIC$_{anth}$ = 25 - 40 μmol kg^{-1} between 100 and 400 m and at Station 196, DIC$_{anth}$ = 20 - 33 μmol kg^{-1} at 0-100m (**Figures 5A, B**; **Table S2**). DIC$_{anth}$ enters Davis Strait *via* the WGC and advects north within WGSW into central Baffin Bay. Davis Strait DIC$_{anth}$ concentrations are only slightly lower than those previously reported for the North Atlantic (Lee et al., 2003). Thus, we conclude the North Atlantic supplies significant DIC$_{anth}$ to Baffin Bay. DIC$_{anth}$ contributions were lower at our Northern Gateway stations 108 and 323 (9.4 to 41.5 μmol kg^{-1}), and no DIC$_{anth}$ was found below 100m at these stations. Between 150-300m the southward BIC also contains little DIC$_{anth}$. We note that the Ocean Data View interpolation in **Figure 5** is from a limited number of stations, and thus meant for illustrative purposes only. The Ocean Data View distributions does not necessarily reflect the fine-scale spatial structure of DIC$_{anth}$ in Baffin Bay.

Although we are the first to apply the ΔC^* proxy to Baffin Bay, Earth System models estimate low DIC$_{anth}$ inventories in the Arctic due to seasonal sea ice and limited air-sea gas exchange (Tjiputra et al., 2010). Lee and co-workers (2003) also found low DIC$_{anth}$ inventories in surface waters at higher Atlantic Ocean

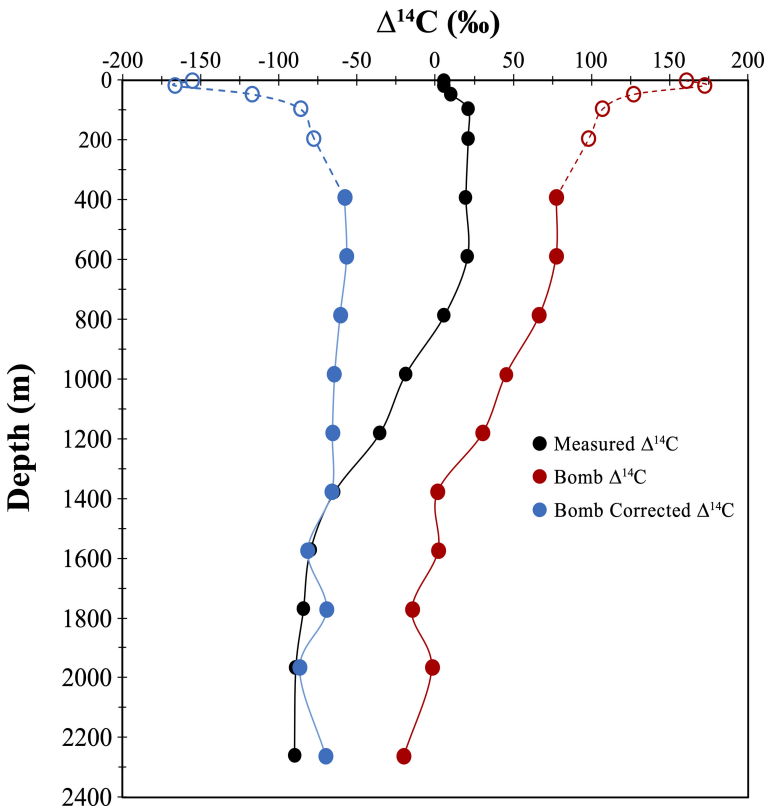

FIGURE 4 | Calculated bomb $\Delta^{14}C$ and natural $\Delta^{14}C$ values for Baffin Bay deep water. Measured DIC $\Delta^{14}C$ values for deepest station collected in Baffin Bay, BB2 (**Figure 1**). Calculated $\Delta^{14}C_{bomb}$ and $\Delta^{14}C_{bomb\ corr}$ values derived using the Potential Alkalinity (P_{alk}) method (Rubin and Key, 2002) method (*see Estimation of Anthropogenic (DIC_{anth}) and "Bomb" DIC ^{14}C*). Dashed lines and open circle indicate overestimated bomb and underestimated natural $\Delta^{14}C$ values above 400m.

latitudes (~65°N). Low DIC_{anth} at higher latitudes may also be attributed to mixing of intermediate waters with deeper "DIC_{anth} free" water. Short residence times (~2 years) of surface water within Baffin Bay may also limit the region's surface DIC_{anth} inventories (Rudels, 1986; Poisson and Chen, 1987; Hoppema et al., 2001). Large volumes of water are annually exported south through Davis Strait (2.3 ± 0.7 Sv; Curry et al., 2011) perhaps also precluding the BIC from containing significant DIC_{anth} (**Figure 5**).

Above 50m, DIC_{anth} is variable in Baffin Bay. High DIC_{anth} is found in surface water along the coast of Greenland (29-46 µmol kg^{-1}) although surface DIC_{anth} was not found in the Vaigat Fjord (Station BB18) and on the west side of Davis Strait (193). Such wide-ranging DIC_{anth} in surface waters directly in contact with the atmosphere demonstrates limitations in the ΔC^* proxy at low temperatures and salinities. Like the P_{alk} method, the ΔC^* proxy was also developed for the mid-latitude open ocean. As a result, many of our surface DIC_{anth} values had high errors and/or negative values. The ΔC^* proxy however appears to provide more reasonable estimates of anthropogenic carbon in surface water than the P_{alk} method does for $\Delta^{14}C_{bomb}$. With the limitation of the P_{alk} method throughout Baffin Bay surface water, we assume the absence of $\Delta^{14}C_{bomb}$ when DIC_{anth} is undetectable. As mentioned in *section 2.5*, DIC_{anth} values <5 µmol kg^{-1} (including negative values) were considered free of DIC_{anth} (0 µmol kg^{-1}). Despite these DIC_{anth} proxy limitations, we do not observe the presence of DIC_{anth} in Baffin Bay below 800m. We believe this to be reasonable given the absence of $\Delta^{14}C_{bomb}$ in BBDW. Thus, our deep water measured DIC $\Delta^{14}C$ values do not require further correction for the addition of fossil C.

Estimating a ^{14}C-Based Residence Age for Deep Baffin Bay

The formation of BBDW and BBBW is a topic of ongoing debate. Two main formation mechanisms have been proposed: mixing of cold, saline, brine-enriched surface shelf water with either Arctic Intermediate Water in Nares Strait and Smith Sound (Bailey, 1956; Collin, 1965; Bourke et al., 1989; Bourke and Paquette, 1991) or with Labrador Sea intermediate water entering *via* Davis Strait (Tang et al., 2004). Some research has argued that the depth of convective mixing from freezing would be too shallow (<100m) to produce the bottom water in Northern Baffin Bay (Muench, 1970), but this would not necessarily preclude downslope transport of dense water from northern shelves (Tang et al., 2004).

To constrain a ^{14}C-residence age for deep Baffin Bay, it is important to consider each of these formation mechanisms. The addition of winter brine to AW at intermediate depths in Smith Sound has been previously supported by temperature, salinity

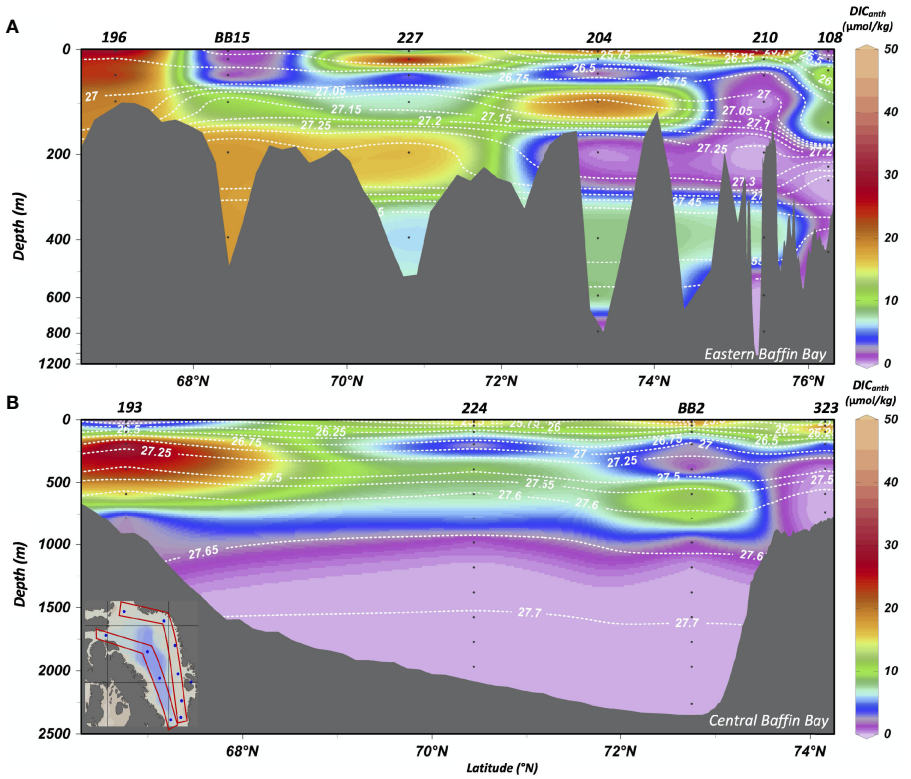

FIGURE 5 | Calculated DIC_{anth} concentrations found throughout central and Eastern Baffin Bay. Distributions of DIC_{anth} concentrations plotted from two transects along **(A)** the west coast of Greenland and **(B)** central Baffin Bay, as indicated by the inset on b). DIC_{anth} concentrations calculated based on methods by Lee et al. (2003). DIC_{anth} values <5µmol kg^{-1} are assumed to contain zero DIC_{anth} (See *Estimation of Anthropogenic (DIC_{anth}) and "Bomb" DIC ^{14}C*). Sample depths and locations are indicated by black dots, with station names labelled at the top of the plots. Dashed white contours are density anomaly (σ_θ in kg m^{-3}) isopycnals. We note that Ocean Data View interpolations of DIC_{anth} (from n=11 stations) are meant for interpretation and do not reflect an accurate spatial distribution of DIC_{anth}.

and $\delta^{18}O$ isotopic data (Bailey, 1956; Tan and Strain, 1980). Nares Strait is a relatively shallow region (~200m in Kane Basin). The potential density anomaly at 225m in Station 108 was 27.27 kg m^{-3}, which would not be dense enough to contribute directly to BBDW (σ_θ = 27.72 kg/m^3). However, Bourke et al. (1989) suggested that mixing brine-enriched winter waters produced in the North Water Polynya in Smith Sound, with Arctic Intermediate Water could produce deep water densities. If we use measured DIC $\Delta^{14}C$ values from 200-300 m at Station 108 (where C_{ath} was not detected and presumably little additional bomb $\Delta^{14}C$ is present; **Table S2**) as a deep-water source endmember ($\Delta^{14}C$ = +26.3‰; *n* = 2), then the ^{14}C residence time of BBDW (σ_θ > 27.7 kg/m^3, $\Delta^{14}C$ = -90.7‰) would be roughly approximate to its apparent ^{14}C age (690 ± 35 years).

The second plausible source of BBDW is water entering Davis Strait from the Labrador Sea over a 640m depth sill. Sverdrup et al. (1942) suggested the cooling of Labrador Sea deep water with winter surface water brine as a formation mechanism. The WGC is cooler and fresher than the EGC (3.0°C < θ < 5.5°C and 34.4 < S < 35.0) or the Irminger Current (3.5°C < θ < 5.5°C, S ~ 35.0; Lobb, 2004). In the northern Labrador Sea, the Irminger Current lies below the WGC (Rykova et al., 2009). As it flows northward, the upper portion of the Irminger Current mixes with the cooler and fresher WGC (Cuny et al., 2002). Inflow of WGIW *via* Davis Strait is seasonal and extends to depth of up to 1000m during the fall (Curry et al., 2014).

We use North Atlantic DIC $\Delta^{14}C$ values (A16N GO-SHIP, Station 4; Bullister and Barigner, 2020) from the Davis Strait sill depth (640m) with a density anomaly (σ_θ = 27.53 to 27.67 kg m^{-3}) as a second source endmember from which to estimate a ^{14}C residence time for Baffin Bay. We applied both the P_{alk} and ΔC^* proxies to correct for $\Delta^{14}C_{bomb}$ and DIC_{anth} from measured North Atlantic DIC $\Delta^{14}C$ to determine a $\Delta^{14}C_{natural}$ depth profile (**Figure 6**). Both proxies provided robust estimates of $\Delta^{14}C_{bomb}$ and DIC_{anth} for the North Atlantic station, consistent with previously published values (Rubin and Key, 2002; Lee et al., 2003). This North Atlantic BBDW source end-member was determined to have a ^{14}C-age of 330 ± 35 years. Subtracting this age from the apparent ^{14}C age of BBDW (690 ± 35 years) results in an estimated ^{14}C residence time of 360 ± 35 years. Since both bomb $\Delta^{14}C$ and DIC_{anth} are present in the North Atlantic, this BBDW formation mechanism requires extremely slow deep water formation rates.

Our two estimated ^{14}C residence times (360-690 years) for deep Baffin Bay provide new constraints on the ventilation age of this ocean basin. Our residence times fall between those previously

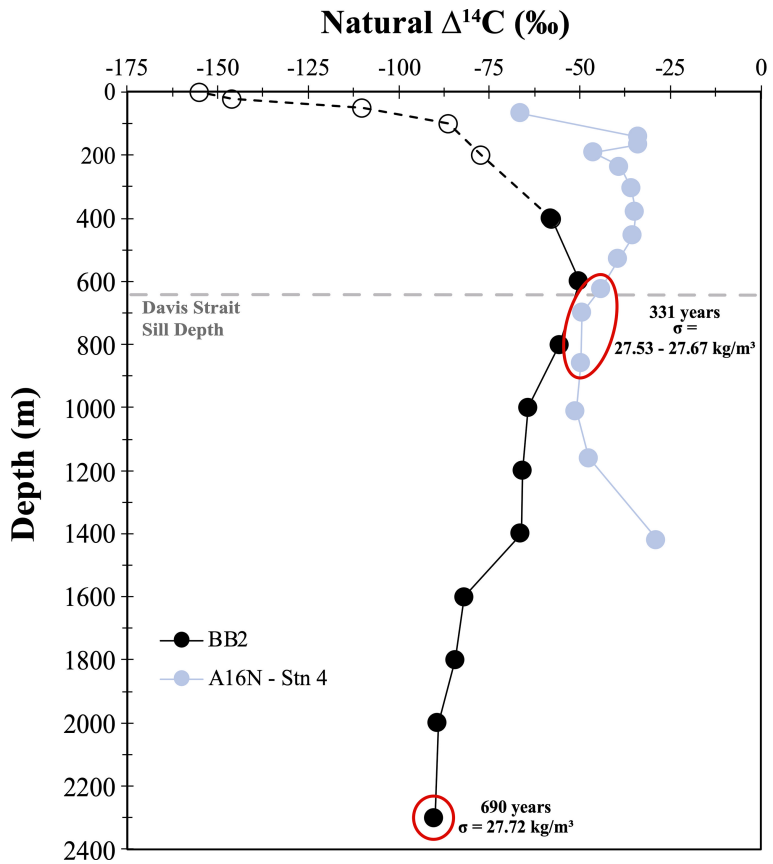

FIGURE 6 | DIC $\Delta^{14}C_{natural}$ depth profiles, corrected for both $\Delta^{14}C_{bomb}$ and DIC_{anth} contributions for Station BB2 and A16N. DIC $\Delta^{14}C_{natural}$ values from A16N (Station 4; 62.75°N, -20.00°W just south of Iceland) were corrected for DIC_{anth} and $\Delta^{14}C_{bomb}$. Apparent ^{14}C-ages are calculated based on $\Delta^{14}C_{natural}$ values (*see Natural Abundance Radiocarbon ($\Delta^{14}C$) Analysis*) for depths with potential densities close to BBBW values (θ_σ = 27.7 kg m^{-3}). Dashed horizontal grey line indicates depth of the Davis Strait sill, at 640m. Dashed line with open circles for BB2 profile indicate unconstrained $\Delta^{14}C_{natural}$ values based on limitation of the P_{alk} proxy. Red circles indicate depths at which apparent ^{14}C-ages were calculated.

estimated for BBDW of 20 to 1,450 years (Sadler, 1976; Top et al., 1980; Wallace, 1985). Both deep water formation mechanisms require cooling and brine rejection during sea ice formation that would increase the local DIC concentration of underlying waters (Rysgaard et al., 2007; Moreau et al., 2016; König et al., 2018). This increase in DIC would also selectively preconcentrate DIC with modern $\Delta^{14}C$ (atmospheric), $\Delta^{14}C_{bomb}$, and fossil (C_{anth}) $\Delta^{14}C$ values. Since we do not detect these $\Delta^{14}C$ endmembers in BBDW, significant dilution must occur during such a deep-water formation mechanism (e.g., "shaving" of the deep-water plume; Bourke et al., 1989). This would also suggest that our estimated ^{14}C residence times are *minimum* age estimates. Nevertheless, with a minimum residence time of 360 ± 35years, BBDW has the potential to store carbon on centennial timescales.

SUMMARY AND IMPLICATIONS

Seawater DIC $\delta^{13}C$ and $\Delta^{14}C$ values place new constraints on the sources and cycling of carbon in the Arctic. Baffin Bay is a dynamic region, with Arctic, Pacific, and Atlantic carbon source endmembers, as well as glacial inputs along the coast of Greenland. $\Delta^{14}C_{bomb}$ and DIC_{anth} estimates through the ΔC^* and P_{alk} proxies are limited in their scope of application in the Arctic but highlight important DIC source constraints to Baffin Bay water masses. We observe DIC_{anth}-replete water entering from the North Atlantic Ocean, DIC_{anth}-free AW in Northern Baffin Bay, and no DIC_{anth} or bomb $\Delta^{14}C$ in BBDW. Using two possible deep water formation mechanisms for BBDW, we determine a Baffin Bay ^{14}C residence time of 360-690 years, suggesting deep Baffin Bay stores carbon for several centuries.

Baffin Bay exports cold, dense water to the Labrador Sea which is critical for North Atlantic Deep Water (NADW) formation (Goosse et al., 1997). Global climate change has resulted in warming and freshening of Arctic surface water exported through Baffin Bay and increased stratification in the North Atlantic Ocean. This stratification is now reducing NADW formation (Caesar et al., 2021). We now observe warming temperatures in the Arctic Ocean acting to reduce sea ice extent but also CO_2 uptake (MacGilchrist et al., 2014). With a residence time of 360-690 years, Baffin Bay may

partially moderate Arctic climate change through storage of deep carbon on centennial timescales.

DATA AVAILABILITY STATEMENT

The original contributions presented in the study are included in the article/**Supplementary Material**. Further inquiries can be directed to the corresponding author.

AUTHOR CONTRIBUTIONS

BW conceived the hypothesis and the objectives of this investigation. SZ and BW drafted the manuscript with input from JW, BE, LM, and KA-S. SZ, BW, and JW performed radiocarbon and stable isotopic analysis of DIC samples. LM and KA-S contributed total alkalinity and DIC concentration data. All authors read, edited, and approved the final manuscript.

FUNDING

This work was supported by the Natural Sciences and Engineering Research Council (NSERC) of Canada through a Discovery Grant, Accelerator and Launch Supplements (RGPIN-2020-06501, RGPAS-2020-00071, DGECR-2020-00256; to BW), a Discovery Grant (RGPIN-2015-04780 to BE), the Canada Research Chairs program (BW), the NSERC Alexander Graham Bell Canadian Graduate Scholarship (SZ), the Ontario Graduate Scholarship (SZ), and Fisheries and Oceans Canada. This work is a contribution to ArcticNet, a Network of Centres of Excellence Canada.

ACKNOWLEDGMENTS

We gratefully acknowledge Chief Scientist Alexandre Forest, Anissa Merzouk and the staff of Amundsen Science and the crew of the CCGS *Amundsen* for the opportunity to participate in the 2019 research cruise. We also would like to thank Dr. Cara Manning for her help in coordinating the sampling and logistics of the Biogeochemistry groups aboard the CCGS *Amundsen*. Tonya Burgers (University of Manitoba) and Shawn Marriott (University of Calgary) collected DIC and A_T samples. Danielle Caleb and Marty Davelaar (Institute of Ocean Sciences) performed DIC and A_T analyses. We thank Drs. Xiaomei Xu and John Southon of the UC Irvine Keck Carbon Cycle AMS lab for their expertise and help with ^{14}C analysis, Paul Middlestead, and the staff of the Ján Veizer Stable Isotope Laboratory at the University of Ottawa for aiding in δ^{13}C analysis, Jonathan Gagnon, and Jean-Éric Tremblay (Université Laval) for nutrient measurements and Aislinn Fox for ODV analysis and providing site map figures. Finally, we acknowledge the reviewers, whose constructive comments greatly improved the paper.

SUPPLEMENTARY MATERIAL

The Supplementary Material for this article can be found online at: https://www.frontiersin.org/articles/10.3389/fmars.2022.845536/full#supplementary-material

REFERENCES

Aminot, A., and Kérouel, R. (2007). Dosage Automatique Des Nutriments Dans Les Eaux Marines: Méthodes En Flux Continu, Edited by: IFREMER. *Méthodes. d'analyse. en milieu. marin.* 188. 0–188

Anderson, L. A., and Sarmiento, J. L. (1994). Redfield Ratios of Remineralization Determined by Nutrient Data Analysis. *Global Biogeochem. Cycles.* 8 (1), 65–80. doi: 10.1029/93gb03318

Arctic Monitoring and Assessment Programme Arctic Climate Change Update (2021) *Key Trends and Impacts - Summary for Policy-Makers. Arctic Council Secretariat, Summary Report*. Available at: https://oaarchive.arctic-council.org/handle/11374/2621 (Accessed September 15, 2021).

Azetsu-Scott, K., Petrie, B., Yeats, P., and Lee, C. (2012). Composition and Fluxes of Freshwater Through Davis Strait Using Multiple Chemical Tracers. *J. Geophys. Res. Oceans.* 117, C12011. doi: 10.1029/2012JC008172

Bailey, W. B. (1956). On the Origin of Deep Baffin Bay Water. *J. Fisheries. Board. Canada.* 13 (3), 303–308. doi: 10.1139/f56-020

Bates, N. R., and Mathis, J. T. (2009). The Arctic Ocean Marine Carbon Cycle: Evaluation of Air-Sea CO2 Exchanges, Ocean Acidification Impacts and Potential Feedbacks. *Biogeosciences* 6 (11), 2433–2459. doi: 10.5194/bg-6-2433-2009

Bauch, D., Polyak, L., and Ortiz, J. D. (2015). A Baseline for the Vertical Distribution of the Stable Carbon Isotopes of Dissolved Inorganic Carbon (δ13cdic) in the Arctic Ocean. *Arktos* 1 (1), 15. doi: 10.1007/s41063-015-0001-0

Bourke, R. H., Addison, V. G., and Paquette, R. G. (1989). Oceanography of Nares Strait and Northern Baffin Bay in 1986 With Emphasis on Deep and Bottom Water Formation. *J. Geophys. Res.* 94 (C6), 8289. doi: 10.1029/jc094ic06p08289

Bourke, R. H., and Paquette, R. G. (1991). Formation of Baffin Bay Bottom and Deep Waters. *Elsevier. Oceanogr. Ser.* 57, 135–155. doi: 10.1016/s0422-9894(08)70065-5

Broecker, W. S., Gerard, R., Ewing, M., and Heezen, B. C. (1960). Natural Radiocarbon in the Atlantic Ocean. *J. Geophys. Res.* 65 (9), 2903–2931. doi: 10.1029/jz065i009p02903

Brown, T. A., and Reimer, R. W. (2004). Discussion: Reporting and Calibration of Post-Bomb 14c Data. *Radiocarbon* 46 (3), 1299–1304. doi: 10.1017/s0033822200033154

Bullister, J., and Barigner, M. (2020) *Bottle Data From Cruise 33RO20130803, Exchange Version* (CCHDO). Available at: https://cchdo.ucsd.edu/cruise/33RO20130803 (Accessed September 15, 2021).

Burgers, T. M., Miller, L. A., Thomas, H., Else, B. G. T., Gosselin, M., and Papakyriakou, T. (2017). Surface Water pco_2 Variations and Sea-Air CO_2 Fluxes During Summer in the Eastern Canadian Arctic. *J. Geophys. Res. Oceans.* 122, 9663–9678. doi: 10.1002/2017JC013250

Caesar, L., McCarthy, G. D., Thornalley, D. J. R., Cahill, N., and Rahmstorf, S. (2021). Current Atlantic Meridional Overturning Circulation Weakest in Last Millennium. *Nat. Geosci.* 14, 118–120. doi: 10.1038/s41561-021-00699-z

Carter, B. R., Feely, R. A., Wanninkhof, R., Kouketsu, S., Sonnerup, R. E., Pardo, P. C., et al. (2019). Pacific Anthropogenic Carbon Between 1991 and 2017. *Global Biogeochem. Cycles.* 33 (5), 597–617. doi: 10.1029/2018gb006154

Chen, G. T., and Millero, F. J. (1979). Gradual Increase of Oceanic CO2. *Nature* 277 (5693), 205–206. doi: 10.1038/277205a0

Collin, A. E. (1965). Oceanographic Observations in Nares Strait, Northern Baffin Bay 1963 and 1964. Bedford Institute of Oceanography Fourth Annual Report, Dartmouth, NS. *Bio Rep.* 65-5, 9. Available at: https://publications.gc.ca/collections/collection_2015/mpo-dfo/Fs97-16-5-5-eng.pdf

Cuny, J., Rhines, P. B., Niiler, P. P., and Bacon, S. (2002). Labrador Sea Boundary Currents and the Fate of the Irminger Sea Water. *J. Phys. Oceanogr.* 32 (2), 627–647. doi: 10.1175/1520-0485(2002)032<0627:lsbcat>2.0.co;2

Curry, B., Lee, C. M., and Petrie, B. (2011). Volume, Freshwater, and Heat Fluxes Through Davis Strait 2004–05. *J. Phys. Oceanogr.* 41 (3), 429–436. doi: 10.1175/2010jpo4536.1

Curry, B., Lee, C. M., Petrie, B., Moritz, R. E., and Kwok, R. (2014). Multiyear Volume, Liquid Freshwater, and Sea Ice Transports Through Davis Strait 2004–10. *J. Phys. Oceanogr.* 44 (4), 1244–1266. doi: 10.1175/jpo-d-13-0177.1

Dickson, A. G., Sabine, C. L., and Christian, J. R. (2007). *Guide to Best Practices for Ocean CO2 Measurement. (PICES Special Publication 3; IOCCP Report 8)* (Sidney, British Columbia: North Pacific Marine Science Organization), 191. doi: 10.25607/OBP-1342

Druffel, E. R. M., Griffin, S., Glynn, C. S., Benner, R., and Walker, B. D. (2017). Radiocarbon in Dissolved Organic and Inorganic Carbon of the Arctic Ocean. *Geophys. Res. Lett.* 44 (5), 2369–2376. doi: 10.1002/2016gl072138

Emerson, S., and Hedges, J. (2008). Chemical Oceanography and the Marine Carbon Cycle. Cambridge: Cambridge University Press. doi: 10.1017/CBO9780511793202

Fissel, D. B., Lemon, D. D., and Birch, J. R. (1982). Major Features of the Summer Near-Surface Circulation of Western Baffin Bay 1978 and 1979. *ARCTIC* 35 (1), 180–200. doi: 10.14430/arctic2318

Fox, A., and Walker, B. D. (2022). Sources and Cycling of Particulate Organic Matter in Baffin Bay: a multi-isotope $\delta^{13}C$, $\delta^{15}N$, and $\Delta^{14}C$ approach. *Front. Mar. Sci.* 35 (1), 180–200. doi: 10.14430/arctic2318 Cambridge

Gao, P., Xu, X., Zhou, L., Pack, M. A., Griffin, S., Santos, G. M., et al. (2014). Rapid Sample Preparation of Dissolved Inorganic Carbon in Natural Waters Using a Headspace-Extraction Approach for Radiocarbon Analysis by Accelerator Mass Spectrometry. *Limnol. Oceanogr: Methods* 12 (4), 174–190. doi: 10.4319/lom.2014.12.174

Goosse, H., Fichefet, T., and Campin, J. M. (1997). The Effects of the Water Flow Through the Canadian Archipelago in a Global Ice-Ocean Model. *Geophys. Res. Lett.* 24 (12), 1507–1510. doi: 10.1029/97gl01352

Griffith, D. R., McNichol, A. P., Xu, L., McLaughlin, F. A., Macdonald, R. W., Brown, K. A., et al. (2012). Carbon Dynamics in the Western Arctic Ocean: Insights From Full-Depth Carbon Isotope Profiles of DIC, DOC, and POC. *Biogeosciences* 9 (3), 1217–1224. doi: 10.5194/bg-9-1217-2012

Guilderson, T. P., Caldeira, K., and Duffy, P. B. (2000). Radiocarbon as a Diagnostic Tracer in Ocean and Carbon Cycle Modeling. *Global Biogeochem. Cycles.* 14 (3), 887–902. doi: 10.1029/1999gb001192

Hamilton, J., and Wu, Y. (2013). Synopsis and Trends in the Physical Environment of Baffin Bay and Davis Strait. *Ocean. Ecosystem. Sci. Division. Maritimes. Region*. Dartmouth, Nova Scotia: Fisheries. Oceans. Canada. Available at: publications.gc.ca/pub?id=9.504781&sl=0

Heinze, C. (2014). The Role of the Ocean Carbon Cycle in Climate Change. *Eur. Rev.* 22 (1), 97–105. doi: 10.1017/s1062798713000665

Hoppema, M., Roether, W., Bellerby, R. G. J., and de Baar, H. J. W. (2001). Direct Measurements Reveal Insignificant Storage of Anthropogenic CO2 in the Abyssal Weddell Sea. *Geophys. Res. Lett.* 28 (9), 1747–1750. doi: 10.1029/2000gl012443

Humphreys, M. P., Greatrix, F. M., Tynan, E., Achterberg, E. P., Griffiths, A. M., Fry, C. H., et al. (2016). Stable Carbon Isotopes of Dissolved Inorganic Carbon for a Zonal Transect Across the Subpolar North Atlantic Ocean in Summer 2014. *Earth Syst. Sci. Data* 8 (1), 221–233. doi: 10.5194/essd-8-221-2016

Jiang, Z. P., Tyrrell, T., Hydes, D. J., Dai, M., and Hartman, S. E. (2014). Variability of Alkalinity and the Alkalinity-Salinity Relationship in the Tropical and Subtropical Surface Ocean. *Global Biogeochem. Cycles.* 28 (7), 729–742. doi: 10.1002/2013gb004678

Johnson, K. M., Wills, K. D., Butler, D. B., Johnson, W. K., and Wong, C. S. (1993). Coulometric Total Carbon Dioxide Analysis for Marine Studies: Maximizing the Performance of an Automated Gas Extraction System and Coulometric Detector. *Mar. Chem.* 44 (2-4), 167–187. doi: 10.1016/0304-4203(93)90201-x

König, D., Miller, L. A., Simpson, K. G., and Vagle, S. (2018). Carbon Dynamics During the Formation of Sea Ice at Different Growth Rates. *Front. Earth Sci.* 6. doi: 10.3389/feart.2018.00234

Körtzinger, A., Quay, P. D., and Sonnerup, R. E. (2003). Relationship Between Anthropogenic CO_2 and the ^{13}C Suess Effect in the North Atlantic Ocean. *Global Biogeochem. Cycles.* 17 (1), 5–1. doi: 10.1029/2001GB001427

Krawczyk, D. W., Kryk, A., Juggins, S., Burmeister, A., Pearce, C., Seidenkrantz, M. S., et al. (2021). Spatio-Temporal Changes in Ocean Conditions and Primary Production in Baffin Bay and the Labrador Sea. *Palaeogeograph. Palaeoclimatolog. Palaeoecol.* 563, 110175. doi: 10.1016/j.palaeo.2020.110175

Kroopnick, P. M. (1985). The Distribution of 13C of ΣCO2 in the World Oceans. Deep Sea Research Part A. *Oceanogr. Res. Papers.* 32 (1), 57–84. doi: 10.1016/0198-0149(85)90017-2

Lee, K., Choi, S. D., Park, G. H., Wanninkhof, R., Peng, T. H., Key, R. M., et al. (2003). An Updated Anthropogenic CO2 Inventory in the Atlantic Ocean. *Global Biogeochem. Cycles.* 17 (4), 1116, 1–17. doi: 10.1029/2003gb002067

Lehmann, N., Kienast, M., Granger, J., Bourbonnais, A., Altabet, M. A., and Tremblay, J. E. (2019). Remote Western Arctic Nutrients Fuel Remineralization in Deep Baffin Bay. *Global Biogeochem. Cycles.* 33 (6), 649–667. doi: 10.1029/2018gb006134

Lobb, J. (2004). On Arctic and Atlantic Halocline Interactions in Baffin Bay. [Ph.D. Thesis] (Victoria, Canada: University of Victoria).

MacGilchrist, G. A., Naviera, A. C., Garabato, N., Tsubouchi, T., Bacon, S., Torres-Valdés, S., et al. (2014). The Arctic Ocean Carbon Sink. *Deep. Sea. Res. Part I: Oceanogr. Res. Papers.* 86, 39–55. doi: 10.1016/j.dsr.2014.01.002

Mahadevan, A. (2001). An Analysis of Bomb Radiocarbon Trends in the Pacific. *Mar. Chem.* 73 (3–4), 273–290. doi: 10.1016/s0304-4203(00)00113-4

Melling, H., Gratton, Y., and Ingram, G. (2010). Ocean Circulation Within the North Water Polynya of Baffin Bay. *Atmosphere-Ocean* 39 (3), 301–325. doi: 10.1080/07055900.2001.9649683

Mol, J. (2017). *The Exchange of Inorganic Carbon on the Canadian Beaufort Shelf. [MSc Thesis]* (Halifax, Canada: Dalhousie University). Available at: http://hdl.handle.net/10222/72992.

Moreau, S., Vancoppenolle, M., Bopp, L., Aumont, O., Madec, G., Delille, B., et al. (2016). Assessment of the Sea-Ice Carbon Pump: Insights From a Three-Dimensional Ocean-Sea-Ice Biogeochemical Model (NEMO-LIM-PISCES) Assessment of the Sea-Ice Carbon Pump. *Elementa.: Sci. Anthropocene.* 4, 122. doi: 10.12952/journal.elementa.000122

Morée, A. L., Schwinger, J., and Heinze, C. (2018). Southern Ocean Controls of the Vertical Marine $\delta^{13}C$ Gradient – A Modelling Study. *Biogeosciences* 15, 7205–23. doi: 10.5194/bg-15-7205-2018

Muench, R. D. (1970). *The Physical Oceanography of the Northern Baffin Bay Region. [Ph.D. Thesis]* (Seattle, USA: University of Washington).

Münchow, A., Falkner, K. K., and Melling, H. (2015). Baffin Island and West Greenland Current Systems in Northern Baffin Bay. *Prog. Oceanogr.* 132, 305–317. doi: 10.1016/j.pocean.2014.04.001

Mungall, E. L., Abbatt, J. P. D., Wentzell, J. J. B., Lee, A. K. Y., Thomas, J. L., Blais, M., et al. (2017). Microlayer Source of Oxygenated Volatile Organic Compounds in the Summertime Marine Arctic Boundary Layer. *Proc. Natl. Acad. Sci.* 114, 6203–6208. doi: 10.1073/pnas.1620571114

Olack, G. A., Colman, A. S., Pfister, C. A., and Wootton, J. T. (2018). Seawater DIC Analysis: The Effects of Blanks and Long-Term Storage on Measurements of Concentration and Stable Isotope Composition: The Analysis of Seawater Carbon. *Limnol. Oceanogr.: Methods* 16 (3), 160–179. doi: 10.1002/lom3.10235

Olsen, A., Anderson, L. G., and Heinze, C. (2015). "Arctic Carbon Cycle: Patterns, Impacts and Possible Changes," in *The New Arctic*. Eds. B. Evengård, J. Nymand Larsen and O. Paasche (Cham: Springer). doi: 10.1007/978-3-319-17602-4_8

Östlund, H. G., Possnert, G., and Swift, J. H. (1987). Ventilation Rate of the Deep Arctic Ocean From Carbon 14 Data. *J. Geophys. Res.: Oceans.* 92 (C4), 3769–3777. doi: 10.1029/jc092ic04p03769

Poisson, A., and Chen, C. T. A. (1987). Why is There Little Anthropogenic CO2 in the Antarctic Bottom Water? Deep Sea Research Part A. *Oceanograph. Res. Papers.* 34 (7), 1255–1275. doi: 10.1016/0198-0149(87)90075-6

Rodgers, K. B., Schrag, D. P., Cane, M. A., and Naik, N. H. (2000). The Bomb 14C Transient in the Pacific Ocean. *J. Geophys. Res.: Oceans.* 105 (C4), 8489–8512. doi: 10.1029/1999jc900228

Rubin, S. I., and Key, R. M. (2002). Separating Natural and Bomb-Produced Radiocarbon in the Ocean: The Potential Alkalinity Method. *Global Biogeochem. Cycles* 16 (4), 110552-1-52–19. doi: 10.1029/2001gb001432

Rudels, B. (1986). The Outflow of Polar Water Through the Arctic Archipelago and the Oceanographic Conditions in Baffin Bay. *Polar. Res.* 4 (2), 161–180. doi: 10.3402/polar.v4i2.6929

Rykova, T., Straneo, F., Lilly, J. M., and Yashayaev, I. (2009). Irminger Current Anticyclones in the Labrador Sea Observed in the Hydrographic Record 1990–2004. *J. Mar. Res.* 67 (3), 361–384. doi: 10.1357/002224009789954739

Rysgaard, S., Glud, R. N., Sejr, M. K., Bendtsen, J., and Christensen, P. B. (2007). Inorganic Carbon Transport During Sea Ice Growth and Decay: A Carbon Pump in Polar Seas. *J. Geophys. Res.: Oceans.* 1978–2012), 112. doi: 10.1029/2006jc003572

Sabine, C. L., Feely, R. A., Gruber, N., Key, R. M., Lee, K., Bullister, J. L., et al. (2004). The Oceanic Sink for Anthropogenic CO2. *Science* 305 (5682), 367–371. doi: 10.1126/science.1097403

Sadler, H. E. (1976). Water, Heat, and Salt Transports Through Nares Strait, Ellesmere Island. *J. Fisheries Board. Canada* 33 (10), 2286–2295. doi: 10.1139/f76-275

Shadwick, E. H., Thomas, H., Chierici, M., Else, B., Fransson, A., Michel, C., et al. (2011). Seasonal Variability of the Inorganic Carbon System in the Amundsen Gulf Region of the Southeastern Beaufort Sea. *Limnol. Oceanogr.* 56 (1), 303–322. doi: 10.4319/lo.2011.56.1.0303

Shiklomanov, A., Déry, S., Tretiakov, M., Yang, D., Magritsky, D., Georgiadi, A., et al. (2020). "River Freshwater Flux to the Arctic Ocean" in D. Yang and D.L. Kane . Eds *Arctic Hydrology, Permafrost and Ecosystems* (Springer, Cham). p. 703–738. doi: 10.1007/978-3-030-50930-9_24

Stuiver, M., and Polach, H. A. (1977). Discussion Reporting of 14C Data. *Radiocarbon* 19, 3, 355–363. doi: 10.1017/s0033822200003672

Sverdrup, H. V., Johnson, M. W., and Fleming, R. H. (1942). *The Ocean, Their Physics, Chemistry and General Biology* (Englewood Cliffs, NJ, USA: Prentice-Hall), p. 1087. doi: 10.2307/520072

Sweeney, C., Gloor, E., Jacobson, A. R., Key, R. M., McKinley, G., Sarmiento, J. L., et al. (2007). Constraining Global Air-Sea Gas Exchange for CO2 With Recent Bomb 14C Measurements. *Global Biogeochem. Cycles.* 21 (2), 1–10. doi: 10.1029/2006gb002784

Takahashi, T., Broecker, W. S., and Bainbridge, A. E. (1981). "Carbon Cycle Modelling" in *The Alkalinity and Total Carbon Dioxide Concentration in the World Oceans*. 16 (3078), p. 271–86B Bolin. Scientific Committee on Problems of the Environment (SCOPE of the International Council of Scientific Unions (ICSU) in Collaboration with the United Nations Environment Programme

Tang, C. C. L., Ross, C. K., Yao, T., Petrie, B., DeTracey, B. M., and Dunlap, E. (2004). The Circulation, Water Masses and Sea Ice of Baffin Bay. *Prog. Oceanogr.* 63 (4), 183–228. doi: 10.1016/j.pocean.2004.09.005

Tan, F. C., and Strain, P. M. (1980). The Distribution of Sea Ice Meltwater in the Eastern Canadian Arctic. *J. Geophys. Res.: Oceans.* 85 (C4), 1925–1932. doi: 10.1029/jc085ic04p01925

Tjiputra, J. F., Assmann, K., and Heinze, C. (2010). Anthropogenic Carbon Dynamics in the Changing Ocean. *Ocean. Sci.* 6 (3), 605–614. doi: 10.5194/os-6-605-2010

Top, Z., Clarke, W. B., Eismont, W. C., and Jones, E. P. (1980). Radiogenic Helium in Baffin Bay Bottom Water. *J. Mar. Res.* 38 (3), 435–452. doi: 10.4095/119621

Trumbore, S.E., Sierra, C.A., and Hicks Pries, C.E. (2016). "*Radiocarbon Nomenclature, Theory, Models, and Interpretation: Measuring Age, Determining Cycling Rates, and Tracing Source Pools*. Eds " in E. Schuur, E. Druffel and S. Trumbore, Radiocarbon and Climate Change (Springer, Cham). doi: 10.1007/978-3-319-25643-6_3

Wallace, D. W. R. (1985). *A Study of the Ventilation of Arctic Water Using Chlorofluoromethanes as Tracers. [Ph.D. Thesis]*. Ed. N. S. Halifax (Canada: Dalhousie University).

Xu, X., Trumbore, S. E., Zheng, S., Southon, J. R., McDuffee, K. E., Luttgen, M., et al. (2007). Modifying a Sealed Tube Zinc Reduction Method for Preparation of AMS Graphite Targets: Reducing Background and Attaining High Precision. *Nucl. Instruments. Methods Phys. Res. Sec. B: Beam. Interact. Material. Atoms.* 259 (1), 320–329. doi: 10.1016/j.nimb.2007.01.175

Zhang, J., Quay, P. D., and Wilbur, D. O. (1995). Carbon Isotope Fractionation During Gas-Water Exchange and Dissolution of CO2. *Geochimica. Cosmochimica. Acta* 59 (1), 107–114. doi: 10.1016/0016-7037(95)91550-d

Conflict of Interest: The authors declare that the research was conducted in the absence of any commercial or financial relationships that could be construed as a potential conflict of interest.

frontiers | Frontiers in Marine Science

ORIGINAL RESEARCH
published: 06 May 2022
doi: 10.3389/fmars.2022.897729

Rapidly Increasing Artificial Iodine Highlights Pathways of Iceland-Scotland Overflow Water and Labrador Sea Water

Maxi Castrillejo[1,2]*, *Núria Casacuberta*[1,3,4], *Christof Vockenhuber*[1] *and Pascale Lherminier*[5]

[1] Laboratory of Ion Beam Physics, ETH Zurich, Zurich, Switzerland, [2] Department of Physics, Imperial College London, London, United Kingdom, [3] Institute of Biogeochemistry and Pollutant Dynamics, Environmental Physics, ETH Zurich, Zurich, Switzerland, [4] Department of Environmental Systems Science, ETH Zurich, Zurich, Switzerland, [5] Ifremer, Univ. Brest, CNRS, IRD, Laboratoire d' Océanographie Physique et Spatiale, IUEM, Plouzané, France

OPEN ACCESS

Edited by:
Jixin Qiao,
Technical University of Denmark, Denmark

Reviewed by:
Luyuan Zhang,
Institute of Earth Environment (CAS), China
Ala Aldahan,
United Arab Emirates University, United Arab Emirates

***Correspondence:**
Maxi Castrillejo
m.castrillejo-iridoy@imperial.ac.uk

Specialty section:
This article was submitted to Ocean Observation, a section of the journal Frontiers in Marine Science

Received: 16 March 2022
Accepted: 07 April 2022
Published: 06 May 2022

Citation:
Castrillejo M, Casacuberta N, Vockenhuber C and Lherminier P (2022) Rapidly Increasing Artificial Iodine Highlights Pathways of Iceland-Scotland Overflow Water and Labrador Sea Water. Front. Mar. Sci. 9:897729. doi: 10.3389/fmars.2022.897729

Iceland-Scotland Overflow Water (ISOW) and Labrador Seawater (LSW) are major water masses of the lower Atlantic Meridional Overturning Circulation (AMOC). Therefore, the investigation of their transport pathways is important to understand the structure of the AMOC and how climate properties are exported from the North Atlantic to lower latitudes. There is growing evidence from Lagrangian model simulations and observations that ISOW and LSW detach from boundary currents and spread off-boundary, into the basin interior in the Atlantic Ocean. Nuclear fuel reprocessing facilities of Sellafield and La Hague have been releasing artificial iodine (^{129}I) into the northeastern Atlantic since the 1960ies. As a result, ^{129}I is supplied from north of the Greenland-Scotland passages into the subpolar region labelling waters of the southward flowing lower AMOC. To explore the potential of ^{129}I as tracer of boundary and interior ISOW and LSW transport pathways, we analyzed the tracer concentrations in seawater collected during four oceanographic cruises in the subpolar and subtropical North Atlantic regions between 2017 and 2019. The new tracer observations showed that deep tracer maxima highlighted the spreading of ISOW along the flanks of Reykjanes Ridge, across fracture zones and into the eastern subpolar North Atlantic supporting recent Lagrangian studies. Further, we found that ^{129}I is intruding the Atlantic Ocean at unprecedented rate and labelling much larger extensions and water masses than in the recent past. This has enabled the use of ^{129}I for other purposes aside from tracing ISOW. For example, increasing tracer levels allowed us to differentiate between newly formed ^{129}I-rich LSW and older vintages poorer in ^{129}I content. Further, ^{129}I concentration maxima at intermediate depths could be used to track the spreading of LSW beyond the subpolar region and far into subtropical seas near Bermuda. Considering that ^{129}I releases from Sellafield and La Hague have increased or levelled off during the last decades, it is very likely that the tracer invasion will continue providing new tracing opportunities for ^{129}I in the near future.

Keywords: artificial radionuclides, ^{129}I, ISOW, LSW, AMOC, iodine, ocean circulation

INTRODUCTION

The water circulation in the subpolar North Atlantic (SPNA) plays a key role on the conduit of greenhouse gases and other climate properties from the sea surface down to the ocean interior (e.g., Perez et al., 2018). Climate signals are then exported southward through the lower limb of the Atlantic Meridional Overturning Circulation (AMOC). This limb is mainly composed by the Labrador Sea Water (LSW) and the two dense overflows supplied from the Nordic Seas, namely, the Denmark Strait Overflow Water (DSOW) and the Iceland-Scotland Overflow Water (ISOW). The circulation of DSOW is being investigated in the Labrador Sea and further south off the north American shore using time series observations of artificial iodine (^{129}I) that started in the early 1990's (Smith et al., 2005; Orre et al., 2010; Smith et al., 2016). The focus of this study is on exploring the potential of ^{129}I to trace the complex pathways of ISOW and LSW in the SPNA and further south into the subtropical North Atlantic Ocean.

Among the two water masses, ISOW is the less well understood due to its complex transport pathways, temporal variability and strong mixing with contiguous water bodies. The historical ISOW circulation scheme describes a single boundary transport (magenta solid lines in **Figure 1**). In that depiction, ISOW spills from the Nordic Seas into the SPNA through the sills between Iceland and Scotland (Hansen and Østerhus, 2007; Beaird et al., 2013), and follows a westward journey along the perimeter of the Iceland Basin passing primarily through the Charlie – Gibbs Fracture Zone into the Irminger Sea (Saunders, 1994; Bower and Furey, 2017). Then ISOW turns northward as part of the boundary current in the western flank of Reykjanes Ridge and eventually joins the southward flowing Deep Western Boundary Current in the east Greenland Slope (Dickson and Brown, 1994; Schott et al., 1999). However, there is growing evidence from numerical simulations and field observations (e.g., Zou et al., 2020) to portray a more complex circulation scheme in which ISOW travels, more often than previously thought, off boundary currents (magenta dotted lines in **Figure 1**). For example, a number of Lagrangian floats deployed at the Reykjanes Ridge and programmed to drift at ISOW levels showed trajectories that detach from the boundary current to travel westward into the Irminger Sea, southward along the flanks of the Mid Atlantic Ridge, or eastward to the afar West European Basin (Bower et al., 2002; Lankhorst and Zenk, 2006; Xu et al., 2010; Zou et al., 2017; Racapé et al., 2019; Zou et al., 2020).

Along the journey in the SPNA, ISOW mixes with other water masses, especially with central waters carried by the North Atlantic Current and LSW (Yashayaev et al., 2007; Beaird et al., 2013; Devana et al., 2021). LSW forms by winter convection in the Labrador Sea and Irminger Sea and constitutes the major intermediate water mass spreading across the North Atlantic (Clarke and Gascard, 1983; Yashayaev et al., 2007; Piron et al., 2017). The transport pathways of LSW are better known, yet similar to ISOW, drifting buoy observations indicate strong recirculation of this water mass eastward into interior basins (e.g., Bower et al., 2009). The number of floats might still be insufficient, especially for ISOW, but the emerging views are already compelling for the export of climate anomalies and suggest that further investigation is needed to provide a better understanding of the structure of the AMOC (Bower et al., 2019).

Radionuclide transient tracers are valuable tools to complement the information obtained from floats and other physical observations. Hydrographic tracer distributions integrate past circulation as if floats were released in great number. A strong tracer candidate for the investigation of the overflows and LSW is ^{129}I, which is released by the nuclear fuel reprocessing industry into the surface seawater in the North Sea region and eventually transported into the SPNA (Yiou et al., 1994; Edmonds et al., 2001; Alfimov et al., 2004; Smith et al., 2005; Smith et al., 2011; Alfimov et al., 2013; Gómez-Guzmán et al., 2013; He et al., 2013a; He et al., 2013b; Smith et al., 2016; Casacuberta et al., 2018; Castrillejo et al., 2018; Vivo-Vilches et al., 2018; Wefing et al., 2018). This tracer has already been successfully employed to identify and follow DSOW between the Irminger Sea and Bermuda based on its increasing concentrations that can be measured with high sensitivity, i.e., million atoms per liter of seawater (Smith et al., 2005; Smith et al., 2016). However, measurements of ^{129}I conducted prior to Castrillejo et al. (2018) and this study indicated that tracer levels in ISOW and LSW were not large enough to allow the clear differentiation of these water masses in the North Atlantic (Santschi et al., 1996; Edmonds et al., 2001). On the other hand, numerical modelling (Orre et al., 2010) projects a rise in ^{129}I concentrations at depths typically occupied by ISOW in the eastern SPNA in response to increased radionuclide discharge rates in recent decades. A glimpse of such tracer increase in ISOW was captured for the first time in 2014 in the Iceland Basin (Castrillejo et al., 2018). Additionally, the ^{129}I time series conducted in the AR7W line show increasing tracer concentrations in LSW between 1993 and present (Smith et al., 2005; Orre et al., 2010; Smith et al., 2016). These results imply that if ^{129}I was to continue increasing, the tracer could potentially reveal ISOW and LSW transport pathways in parts of the North Atlantic where their identification can be challenging if using properties such as salinity and temperature alone.

The aim of this work is to further explore the potential of ^{129}I to trace ISOW and LSW transport pathways in the near future. To that end, we measured ^{129}I from over 200 seawater samples collected across the subpolar and subtropical North Atlantic between 2017 and 2019. The new ^{129}I dataset captured deep tracer maxima associated with density, salinity and potential temperatures expected for ISOW. Using ^{129}I depth profiles we were able to provide an independent validation of ISOW pathways being redrawn by Lagrangian studies. Specifically, we observed ISOW spreading along the boundary current in the eastern flank of the Reykjanes Ridge, over the ridge through the Bight Fracture Zone and off the boundary current following interior routes into the Iceland Basin and the West European Basin. The comparison of the new ^{129}I dataset to earlier distributions shows that tracer concentrations increased

notably in recent years, allowing for the first time the straightforward tracking of ISOW by using this tracer. Further, we found that ^{129}I increased at an unprecedented rate after 2014 intruding other water masses in the SPNA. For example, ^{129}I allows distinguishing between different vintages of LSW in the SPNA and following the southward export of LSW through interior pathways into the subtropical region.

SOURCES OF ^{129}I

The presence of ^{129}I in the North Atlantic is dominated by authorized, marine liquid discharges occurring since the 1960ies until present from the nuclear fuel reprocessing plants of La Hague into the English Channel and Sellafield into the Irish Sea (**Figure 1**). The ^{129}I discharges have been documented over the past decades in reports of the European OSPAR commission, the Environmental Agency of the UK, or by companies running the nuclear installations (e.g., OSPAR, 2015; UK Environmental Agency, 2015). The two facilities alone have discharged more than 6000 kg of ^{129}I to regional waters (He et al., 2013a), which is well above the ~90 kg globally dispersed in the 1950ies/60ies as fallout through atmospheric nuclear weapon tests (Wagner et al., 1996; Raisbeck and Yiou, 1999; Hou, 2004). The combined marine discharge rate of the two reprocessing plants increased gradually from < 1 kg/yr to about 100 kg/yr in the first 20 years, then escalated through the 1990s to peak at > 350 kg/yr in the early 2000s and remained above 200 kg/yr in the most recent part (**Figure 1**). The long residence time of iodine in the ocean water column [over 300,000 yr (Broecker and Peng, 1982; Wong, 1991)] and the limited interaction with organic particles in the photic layer (Schink et al., 1995) suggest that iodine behaves almost conservatively in the ocean. This conservative behavior is confirmed by the long-distance transport of marine ^{129}I discharges (e.g. Santschi et al., 1996; Smith et al., 2016) through the North Sea, the Nordic Seas, the Arctic Ocean and as far as the subtropical North Atlantic (see the routes schematically depicted in **Figure 1**). Consequently, the ^{129}I content in waters circulating between the point of discharge and the Arctic Ocean can be 6 to 12 orders of magnitude above the natural levels (< 0.1 $\times 10^7$ at/kg; atoms per kilogram of seawater) (Snyder et al., 2010) or weapon tests fallout levels (<< 10 $\times 10^7$ at/kg) (Edmonds et al., 2001). Further transport and mixing of waters from the Arctic, North Sea and northeast Atlantic leads to the entrainment of ^{129}I in different water masses and streams within the Nordic Seas. The overall result is a supply of *northern waters* with ^{129}I in the range of $\times 10^8$ - $\times 10^{10}$ at/kg *via* the Greenland – Scotland passages into the SPNA. These northern waters mix with northward flowing *southern waters* originating from lower latitudes (e.g., tropical and South Atlantic). The lower latitude waters may present small impacts of reprocessing marine discharges due to shallow water recirculation in the North Atlantic (He et al., 2013b), but they are generally affected by weapon tests alone and thus carry 10 to 10,000 times less ^{129}I than the northern waters (Castrillejo et al., 2018).

METHODS

Sample Collection

Sea water samples were collected strategically to investigate the pathways of the southward lower AMOC in the subpolar and subtropical North Atlantic Ocean between 2017 and 2019. Colored dots in **Figure 1** show the locations visited during the four cruises: i) the Iceland Basin and the West European Basin on board the Dutch *R/V Pelagia* during the PE424 (PE) cruise in July-August 2017; ii) between Lisbon, Portugal, and Cape

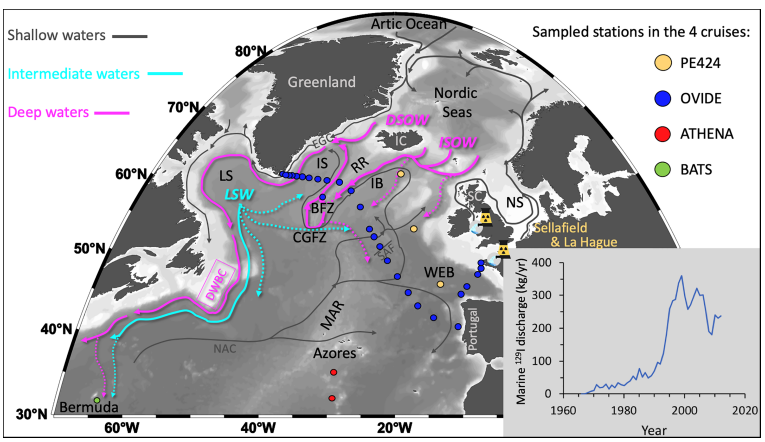

FIGURE 1 | Sampling sites during the four cruises (PE424, OVIDE, ATHENA and BATS), the combined ^{129}I marine discharge from the nuclear reprocessing plants of Sellafield and La Hague since the 1960s until the recent past (e.g. OSPAR, 2015; UK Environmental Agency, 2015), and the schematic circulation adapted from Daniault et al. (2016) to highlight boundary (solid lines) and interior (dotted lines) pathways of ISOW, LSW and DSOW. Acronyms in figure: Bight Fracture Zone, (BFZ); Charlie – Gibbs Fracture Zone, (CGFZ); Denmark Strait Overflow Water, (DSOW); Deep Western Boundary Current, (DWBC); East Greenland Current, (EGC); Iceland Basin, (IB); Iceland, (IC); Iceland Scotland Overflow Water, (ISOW); Irminger Sea, (IS); Labrador Sea, (LS); Labrador Sea Water, (LSW); Mid Atlantic Ridge, (MAR); North Atlantic Current, (NAC); North Sea, (NS); Reykjanes Ridge, (RR); Sub-Arctic Front, (SAF); Scotland, (SC); and West European Basin, (WEB).

Farewell, Greenland, on board the French *R/V Thalassa* during OVIDE (OV) cruise in June-July 2018; iii) south of the Azores Archipelago in the tropical North Atlantic during ATHENA (ATH) cruise on board the German *R/V Meteor* in October 2018; and iv) the Bermuda Atlantic Time Series (BATS) station on board the North American *R/V Atlantic Explorer* in June 2019.

In all cruises surface seawater was collected using a surface pump and the water column was sampled using rosettes equipped with Niskin bottles and CTD oxygen-conductivity-temperature-pressure sensors. The seawater was transferred to 500 mL dark plastic bottles after rinsing them 3 times with seawater. Samples were either processed onboard or at land-based laboratories at ETH-Zurich.

Radiochemistry and AMS Measurement of Iodine Isotopes

Iodine was extracted from about 400 mL of seawater at ETH-Zurich following the methods described in Castrillejo et al. (2018). Each sample was spiked with about 1.5 mg of Woodward stable iodine carrier (^{127}I). All iodine in seawater was oxidized to iodate upon addition of 2% $Ca(ClO)_2$ and then reduced to iodide by adding $Na_2S_2O_5$ and 1M of $NH_3O{\bullet}HCl$ solution. Columns filled with DOWEX® 1X8 ion exchange resin were conditioned with deionized water and diluted 0.5 M KNO_3 solution. The loading of the sample in the column was followed by the elution of all the iodine by adding 2.25 M KNO_3 solution and precipitation as AgI using $AgNO_3$. The precipitate was mixed with about 4 mg of Ag and pressed into cathodes for Accelerator Mass Spectrometry (AMS). Replicates of a seawater sample (n=11) were conducted to check internal consistency. Blanks (n=48) were prepared using deionized water and treated following the same procedure as for the seawater samples.

The calculation of ^{129}I concentrations was done based on the measured ^{129}I/^{127}I ratio and the well-known amounts of ^{127}I carrier spiked to each sample. The ^{129}I/^{127}I atom ratios were measured using the compact 0.5 MV Tandy AMS system at ETH-Zurich (Vockenhuber et al., 2015). The ^{129}I/^{127}I ratios were normalized with the ETH-Zurich in-house standard D22 with nominal ^{129}I/^{127}I of $(50.35 \pm 0.16) \times 10^{-12}$ (Christl et al., 2013) and secondary standards with ratios of 5×10^{-12} that are linked to D22. Blanks presented (2-8) $\times 10^5$ atoms/kg of ^{129}I, corresponding to 1-5% of the total ^{129}I measured in seawater samples.

RESULTS

^{129}I Concentrations in the SPNA Between 2017 and 2019

All measured ^{129}I concentrations are reported in **Table S1** along with temperature, salinity and dissolved oxygen data. In the SPNA we sampled 17 depth profiles which are represented in **Figure 2**. And, collected additionally 10 surface and 6 near bottom samples which are not shown in **Figure 2**.

The ^{129}I concentrations in all seawater samples ranged between $(0.05 \pm 0.05) \times 10^7$ at/kg and $(275 \pm 4) \times 10^7$ at/kg. The lowest ^{129}I concentrations represent natural waters without anthropogenic influence or that contain a small amount of nuclear weapon test fallout. On the other end, the highest ^{129}I concentrations indicate a strong influence of marine discharges from Sellafield and La Hague. **Figure 2** displays a map of ^{129}I depth profiles along the OVIDE line (**Figure 2A**) which are arranged in three panels from low- (**Figure 2B**), mid- (**Figure 2C**), to high- (**Figure 2D**) tracer concentrations. The ^{129}I concentrations generally increased from east to west. We found the lowest values at depths greater than 3000 m in the West European Basin (OV7-33, **Figure 2B**). The Iceland Basin (OV43-104, **Figure 2C**) represented a region of transition where we began to observe higher ^{129}I concentrations in the intermediate range of (10 - 40) $\times 10^7$ at/kg. The bottom layer of the Irminger Sea and the east Greenland shelf (OV76-93, **Figure 2D**) presented the highest ^{129}I concentrations in the order of $\times 10^8$ - $\times 10^9$ at/kg. The ^{129}I concentrations from PE stations were similar to those found in the Iceland Basin and the West European Basin during OVIDE (**Figure 2C**).

All acronyms used hereinafter to denote water masses, currents and geographic locations are listed in **Table 1** and explained in the figure captions.

Relationship Between ^{129}I and Water Masses in the SPNA

To discuss the transport pathways of ISOW and LSW on basis of ^{129}I concentrations it is first necessary to understand how tracer

TABLE 1 | Acronyms used to denote water masses, currents and geographic locations.

BATS	Bermuda Atlantic Time Series	MC	Maury Channel
BFZ	Bight Fracture Zone	NAC	North Atlantic Current
CGFZ	Charlie – Gibbs Fracture Zone	NADW	North Atlantic Deep Water
DSOW	Denmark Strait Overflow Water	NEADW	North East Atlantic Deep Water
DWBC	Deep Western Boundary Current	NS	North Sea
EGC	East Greenland Current	PIW	Polar Intermediate Waters
ENACW	Eastern North Atlantic Central Water	RP	Rockall Plateau
IB	Iceland Basin	RT	Rockall Through
IC	Iceland	RR	Reykjanes Ridge
ISOW	Iceland Scotland Overflow Water	SAF	Sub-Arctic Front
IS	Irminger Sea	SC	Scotland
LS	Labrador Sea	SPMW	Subpolar Mode Waters
LSW	Labrador Sea Water	WEB	West European Basin
MAR	Mid Atlantic Ridge		

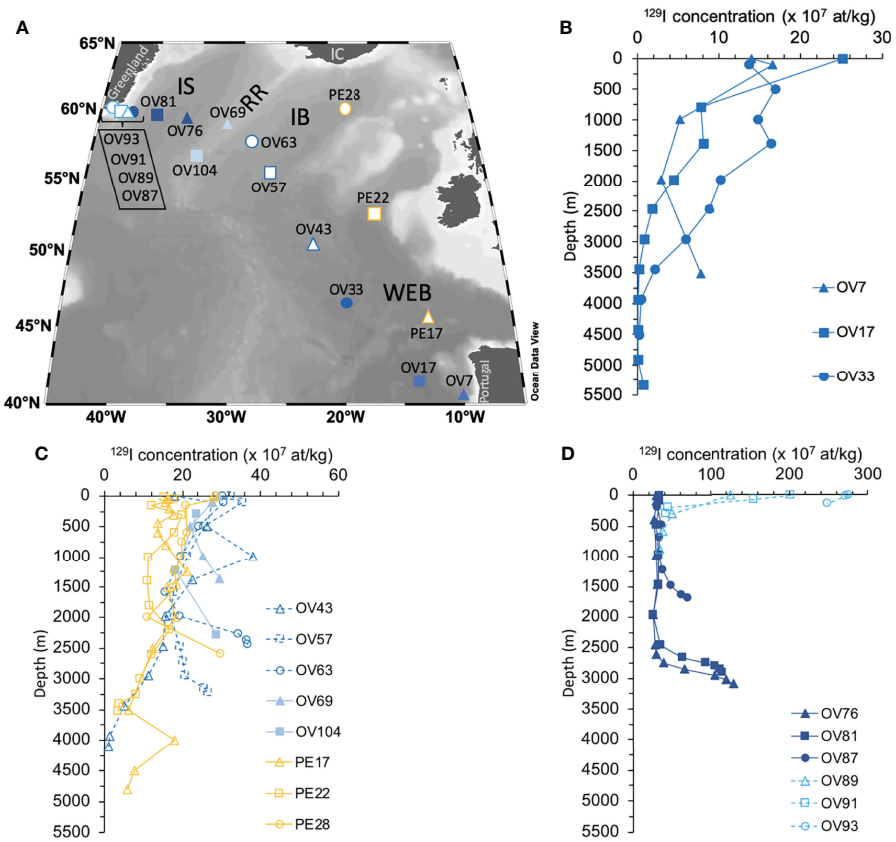

FIGURE 2 | **(A)** Map of ^{129}I depth profiles displayed from **(B)** low-, **(C)** mid-, to **(D)** high- concentrations. The legends include all stations sampled during the PE424 cruise in 2017 (PE) and the OVIDE cruise in 2018 (OV). Acronyms in figure: Iceland Basin, (IB); Iceland, (IC); Irminger Sea, (IS); Reykjanes Ridge, (RR); and West European Basin, (WEB).

concentrations relate to the water mass structure. Here we focus on OVIDE data because the location of the section is representative for ^{129}I concentrations and water masses that reign in the SPNA (OVIDE+PE), and that are to large extent, present in lower latitudes of the Atlantic Ocean (BATS+ATH). Firstly, we plot the radionuclide concentrations from the OVIDE line versus potential temperature (θ) and salinity (S) in θ - S diagrams (**Figure 3A**). The water mass endmembers (diamond symbols in **Figure 3A**) are chosen based on the most recent water mass classification for the OVIDE line (García-Ibáñez et al., 2018). Secondly, we represent the zonal distribution of ^{129}I with the overlaid water mass structure (**Figure 3B**). The water mass structure was inferred from the θ - S diagrams (**Figure 3A**) and zonal distributions of S, θ and O_2 (**Figure S1**).

The θ - S diagrams (**Figure 3A**) show the purest ISOW east of the Reykjanes Ridge characterized by salinity above 34.95, potential temperature of 2-3°C and density in the range of 27.85 – 27.90 kg/m^3. In the SPNA, ISOW entrains and mixes mainly with LSW (McCartney and Talley, 1982; Yashayaev et al., 2007) to form the upper North East Atlantic Deep Water ($NEADW_U$). The lower branch ($NEADW_L$) has less ISOW and a larger contribution of Lower Deep Water from Antarctica (van Aken, 2000a). The lower and upper branches of NEADW fall roughly in a similar density range as for ISOW but are comparably fresher and colder. West of Reykjanes Ridge ISOW further mixes with underlying DSOW and overlying LSW. Compared to ISOW, DSOW presents a lower salinity (~ 34.90) and potential temperature (< 2°C), and a density greater than 27.90 kg/m^3. The LSW present in the Irminger Sea is fresher (S < 34.90), warmer (θ ~ 3°C) and lighter (27.75 kg/m^3) than the two overflows. This LSW probably includes waters formed during strong winter convection events in 2013-2014 that have been further renewed with LSW produced during 2015-2017 in the Labrador Sea and the Irminger Sea (Yashayaev and Loder, 2016; Piron et al., 2017). For simplicity we will differentiate between this LSW (LSW_{new}) and use the term LSW_{old} for the LSW that left the convection regions and has travelled further (south)east in the SPNA suffering significant entrainment and mixing during its downstream journey. Other water masses in the SPNA include: the southward flowing Subpolar Mode Waters (SPMWs, other than LSW) that result from cooling and freshening of Eastern North Atlantic Central Water (ENACW) through convection events in the SPNA; Polar Intermediate Water (PIW), the freshest and coldest water originating from

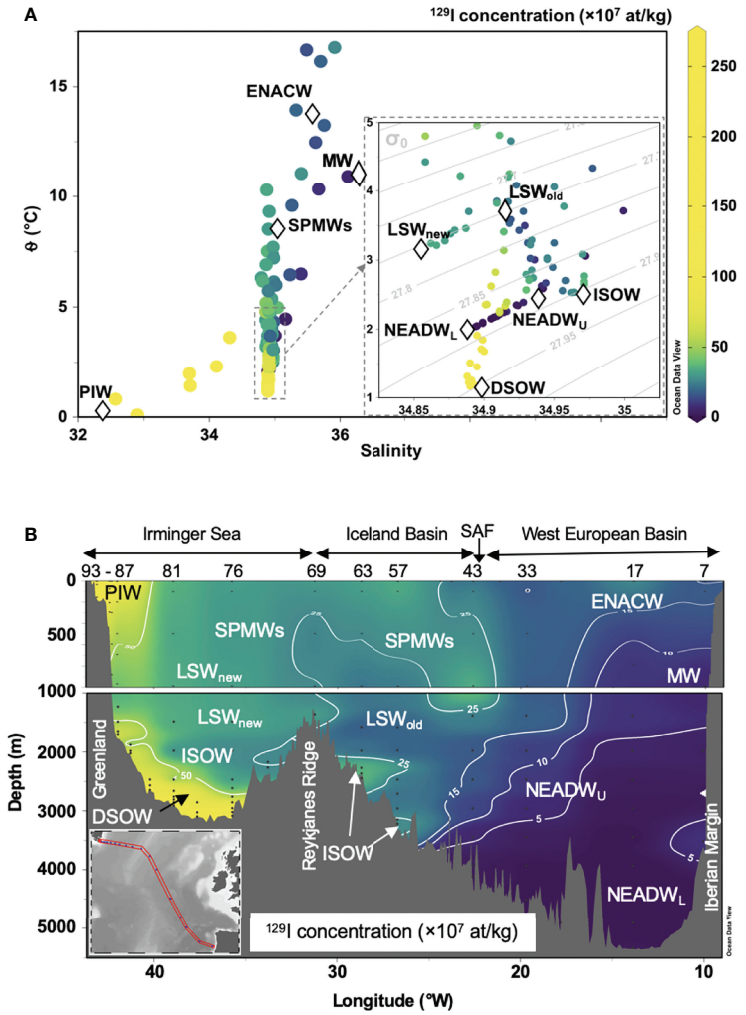

FIGURE 3 | Relationship of ^{129}I with water masses in the SPNA. **(A)** Potential temperature (θ) – salinity diagrams. The color bar indicates the ^{129}I concentrations. **(B)** Zonal section of ^{129}I concentrations. The color coding is the same as for **(A)**. The acronyms of the water masses shown in **(A)** are also represented in **(B)**. Data correspond to the OVIDE cruise in 2018. Acronyms in figure: Denmark Strait Overflow Water, (DSOW); East North Atlantic Central Water, (ENACW); Iceland Scotland Overflow Water, (ISOW); Labrador Sea Water, (LSW); Mediterranean Water, (MW); North East Atlantic Deep Water, (NEADW, lower and upper); Polar Intermediate Water, (PIW); Sub-Arctic Front, (SAF); Subpolar Mode Water, (SPMW).

the Arctic Ocean; and the Mediterranean Water (MW) characterized by the highest salinity along the OVIDE line.

The vertical distribution of ^{129}I along the OVIDE section (**Figure 3B**) allows the straightforward distinction between northern and southern origin water masses. Waters of northern origin generally presented ^{129}I concentrations above 20 ×10^7 at/kg and occupied the region west of 22.5°W which is geographically delimited by the position of the Sub-Arctic Front. In this group we observe ISOW with ^{129}I concentrations in the (25-40) ×10^7 at/kg range, PIW along the east Greenland shelf carrying the highest ^{129}I concentrations (> 100 ×10^7 at/kg), the core of DSOW filling the bottom of the Irminger Sea with ^{129}I concentrations slightly above 100 ×10^7 at/kg, and LSW and SPMWs with concentrations in the range of (15 – 40) ×10^7 at/kg. LSW$_{new}$ filling the Irminger Sea water column carries more ^{129}I than the older LSW that is present east of Reykjanes Ridge. Southern waters dominated the region east of the Sub-Arctic Front and carried little ^{129}I (< 15 ×10^7 at/kg) in comparison to northern waters. Because of this reason, the identification of ISOW and LSW was easily accomplished by searching for ^{129}I spikes at deep and intermediate depths (e.g., eastern flank of Reykjanes Ridge in **Figure 3B**), even when these water masses were difficult to distinguish by using S, θ and O_2 alone (**Figure S1**).

DISCUSSION

Observed ISOW Pathways in 2017-2018

Here we provide an independent means of validating transport pathways of ISOW. Our approach is based on the identification of

deep, high ^{129}I concentrations (> 15 $\times10^7$ at/kg) captured at the layer with 27.85 – 27.90 kg/m^3 potential density, S >34.95 and θ of 2-3°C. We focus on cases where there is a large ^{129}I concentration gradient between ISOW and surrounding water masses. These conditions are met in the Reykjanes Ridge, Iceland Basin and the West European Basin, but not in the Irminger Sea because there the ^{129}I concentrations of ISOW are surpassed by higher tracer amounts carried by the underlying DSOW.

We found seven ^{129}I depth profiles from OVIDE and PE424 cruises that captured the mentioned deep tracer spike in 2017/2018 (yellow and blue data in Figs. 4A-4C). Station positions are shown in **Figure 4D**. The largest ^{129}I spike, of (36.8 ± 0.8) $\times10^7$ at/kg, was measured at 2440 m depth in station OV63 located in the eastern flank of Reykjanes Ridge (**Figure 4A**). The result is consistent with a substantial amount of ISOW following the counterclockwise boundary current in the Iceland Basin towards the ridge (e.g., Daniault et al., 2016). The crossing of ISOW from the Iceland Basin into the Irminger Sea occurs primarily *via* fracture zones (Petit et al., 2018). Traditionally it was thought that the principal origin of ISOW found in the boundary current along the western flank of the Reykjanes Ridge (Daniault et al., 2016) was the Charlie Gibbs Fracture Zone. However, there is growing evidence from modelled and observed float trajectories that Bight Fracture Zone is a very important pathway of ISOW into the western flank of the ridge (Bower et al., 2002; Xu et al., 2010; Zou et al., 2017; Zou et al., 2020). For example, some floats deployed at ISOW densities in the Bight Fracture Zone (Bower et al., 2002; Lankhorst and Zenk, 2006; Zou et al., 2017) have described northward flows connecting with the boundary current while the majority of RAFOS and Deep Argo floats released at the Charlie Gibbs Fracture Zone followed west-northwest interior pathways or took a southward direction along the Mid Atlantic Ridge (Racapé et al., 2019; Zou et al., 2020). To check whether there was ISOW at the Bight Fracture Zone during OVIDE 2018 we collected a near-bottom seawater sample at 2280 m depth in station OV104 (**Figure 4A**). The unequivocal ^{129}I spike [(28.8 ± 0.4) $\times10^7$ at/kg] was observed again indicating the presence of ISOW that was warmer and lighter than the one found in the eastern flank of Reykjanes Ridge (**Table S1**).

In the eastern North Atlantic, ^{129}I observations suggest that several veins of ISOW spread following interior routes. The ^{129}I peak of about (26 – 30) $\times10^7$ at/kg was easily identified in near bottom waters collected at stations PE28 and OV57 (**Figure 4B**)

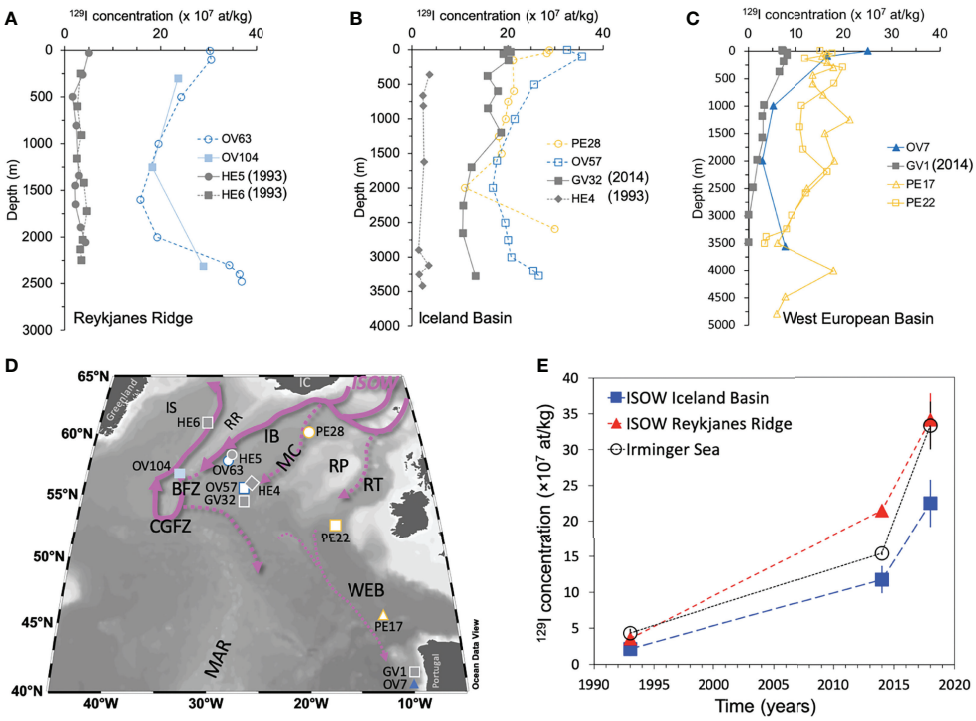

FIGURE 4 | ^{129}I in the Northeastern Atlantic Ocean. Depth profiles of ^{129}I obtained during OVIDE cruise in 2018 (OV, blue) and the PE424 cruise in 2017 (PE, yellow) at **(A)** Reykjanes Ridge, **(B)** the Iceland Basin, and **(C)** the West European Basin, are represented and compared to nearby depth profiles available in the literature (grey profiles): HE sites measured in 1993 by Edmonds et al. (2001) and GV sites from the GEOVIDE cruise in 2014 (Castrillejo et al., 2018) revisited during OVIDE in 2018. **(D)** Map showing the stations (*) and boundary (solid lines) and interior pathways of ISOW (dotted lines). *Stations GV1 and GV32 were at the same location as OV7 and OV57 respectively. **(E)** Temporal evolution of mean ^{129}I concentrations in ISOW at the Reykjanes Ridge, Iceland Basin and the Irminger Sea. Data used for **(E)** are summarized in **Table S2**. Acronyms in figure: Bight Fracture Zone, (BFZ); Charlie – Gibbs Fracture Zone, (CGFZ); Iceland Basin, (IB); Iceland, (IC); Iceland Scotland Overflow Water, (ISOW); Irminger Sea, (IS); Maury Channel, (MC); Mid Atlantic Ridge, (MAR); Reykjanes Ridge, (RR); Rockall Plateau, (RP); Rockall Through, (RT); and West European Basin, (WEB).

pointing to ISOW passages near Maury Channel in the eastern Iceland Basin (**Figure 4D**). This result agrees with modelled and deployed float trajectories (Xu et al., 2010; Zou et al., 2017; Zou et al., 2020) as well as with hydrographic surveys (Daniault et al., 2016), although the limited sampling resolution in this study does not allow confirming if ISOW captured at PE28 and OV57 corresponds to a southward branch detached from the boundary current (as in Zou et al., 2017) or to water that recirculated eastward from the Mid Atlantic Ridge. In comparison to the Iceland Basin, in the West European Basin deep tracer maxima were more diluted due to greater mixing of ISOW with southern components of NEADW (**Figure 4C**). Yet, one could still use ^{129}I to distinguish ISOW contributions to NEADW even when the two water masses display similar salinities and potential temperatures (García-Ibáñez et al., 2018). For example, PE22 captures a small peak of ^{129}I ((16.6 ± 0.2) $\times10^7$ at/kg) at 2200 m depth in the intersect between Rockall Through and the West European Basin consistent with a small southward flow of ISOW (Sherwin et al., 2008; Chang et al., 2009; Zou et al., 2017). And further south and below 3000 m depth, station PE17 and OV7 presented tracer peaks of (17.9 ± 0.2) $\times10^7$ at/kg and (7.8 ± 0.2) $\times10^7$ at/kg, respectively. These tracer maxima can only be explained by the lateral advection of dense overflows like ISOW into the West European Basin in the absence of other sources of ^{129}I at low latitudes (van Aken, 2000a; Fleischmann et al., 2001; Zou et al., 2017; Xu et al., 2018), but their travel path is still unrevealed.

Temporal Evolution of ^{129}I in ISOW

In the 1990s sufficient ^{129}I was found only in DSOW while the tracer content was close to the natural background in other waters of the North Atlantic Ocean (Santschi et al., 1996; Edmonds et al., 2001; Smith et al., 2005). Thus, when did ^{129}I begin to reveal ISOW pathways? To answer this question, we compare the ^{129}I depth profiles from 2017-2018 to previous observations (grey profiles) in the SPNA (**Figure 4**). Edmonds et al. (2001) reported the first ^{129}I depth profiles (stations labelled as 'HE' in **Figure 4D**) in the eastern (HE5) and western (HE6) flanks of the Reykjanes Ridge and southwest of the Rockall Plateau in the Iceland Basin (HE4) for samples collected in 1993. Their ^{129}I profiles (**Figures 4A, B**) showed very low tracer concentrations throughout the water column. On the contrary, the overflow water begun to carry sufficient ^{129}I in the Iceland Basin (station GV32) in 2014 (Castrillejo et al., 2018). And it was not until 2018 that a strong tracer signal unraveled the passage of ISOW in the Iceland Basin (OV 57) and other parts of the SPNA.

To provide a more comprehensive view on the temporal evolution of ^{129}I in ISOW, we calculated the mean tracer concentrations using all available measurements in the overflow found east of Greenland and west of the West European Basin. We exclude the West European Basin from the calculations because tracer data are insufficient to infer any temporal trend in that region. West of the West European Basin, ^{129}I observations are also limited (**Table S2**), yet **Figure 4E** convincingly shows a clear increase in tracer values between 1993 and 2018. Whether tracer concentrations increased linearly or stepwise cannot be inferred based on the limited tracer measurements. But it is clear that during the 25-year time period the ^{129}I concentration in ISOW was multiplied 10 times on average, from lower than 5 $\times10^7$ at/kg in the 1990s to higher than 30 $\times10^7$ at/kg in the 2010s. Half of the ^{129}I increase occurred between 1993 and 2014 while tracer levels doubled in the short time span between 2014 and 2018. Will ^{129}I continue labelling ISOW? The answer is: very likely yes. It is reasonable to think that in comparison to present, future ISOW will carry similar quantities of ^{129}I, or more, because of two reasons: firstly, the repeated ^{129}I measurements in DSOW show that its tracer content is still rising (see **Figure 3** in Smith et al., 2016); secondly, the marine radionuclide discharge from the reprocessing facilities in Europe has either increased or levelled off during the last decades (see *Sources of ^{129}I*). The expected implications are that ^{129}I will stand out in ISOW and that the tracer has potential to shed light on time scales of ISOW circulation between the source and the SPNA and further downstream provided there is a continuation of ^{129}I observations to extend the so far limited time series displayed in **Figure 4E**.

Spreading of ^{129}I in LSW

To investigate whether ^{129}I was increasing rapidly in other water masses of the SPNA we compared the vertical distribution of ^{129}I along the OVIDE line between 2014 and 2018 (**Figure 5A**). The colored dots and contour lines (in spite of the excessive interpolation) show that ^{129}I concentrations in the region occupied by northern waters were in all cases higher (i.e., positive values) in 2018 than in 2014, while southern waters showed small differences in the tracer field (< 5 $\times10^7$ at/kg). The influence of increased ^{129}I releases from the European reprocessing plants (see *Sources of ^{129}I*) is most notorious in the area delimited by difference contour lines of (5-10) $\times10^7$ at/kg. Apart from the overflows and shallow waters, the area comprised by these contour lines is mainly filled by LSW. In **Figure 3** we showed that it is possible to distinguish young LSW vintages in the Irminger Sea by their higher ^{129}I concentrations from the tracer poorer and older LSW that spread (south)eastward passing the Reykjanes Ridge. This is consistent with the formation process of LSW that incorporates ^{129}I-rich Arctic-origin fresh water during convective events in the Labrador Sea (van Aken, 2000b). Following that reasoning, we suggest that the spreading of LSW plays an important role in setting intermediate and deep ^{129}I values of the SPNA (**Figure 5A**). For example, ^{129}I concentrations increased more than 10 $\times10^7$ at/kg at depths occupied by LSW_{new} in the Irminger Sea. And the eastward tracer increases delimited by the 5 $\times10^7$ at/kg contour line possibly indicates the transport of older and tracer-poorer LSW.

To further explore if ^{129}I could unveil off-boundary pathways of LSW beyond the SPNA (turquoise dotted lines in **Figure 5B**) we visited three sites in the western and eastern subtropical North Atlantic Ocean (Figs. 5C and 5D). In the subtropical region, consistently with the literature, we preferred to call $NADW_U$ and $NEADW_U$ the water-masses derived from LSW far from its formation region, and $NADW_L$ for DSOW. To the best of our knowledge, the tracer observations presented here for BATS (**Figure 5C**) constitute the first full-depth profile of ^{129}I in the low latitude North Atlantic aside from the two full depth profiles measured off the North American Slope in 1993/1994 (Santschi et al., 1996). In their ^{129}I dataset, a near bottom tracer peak could be

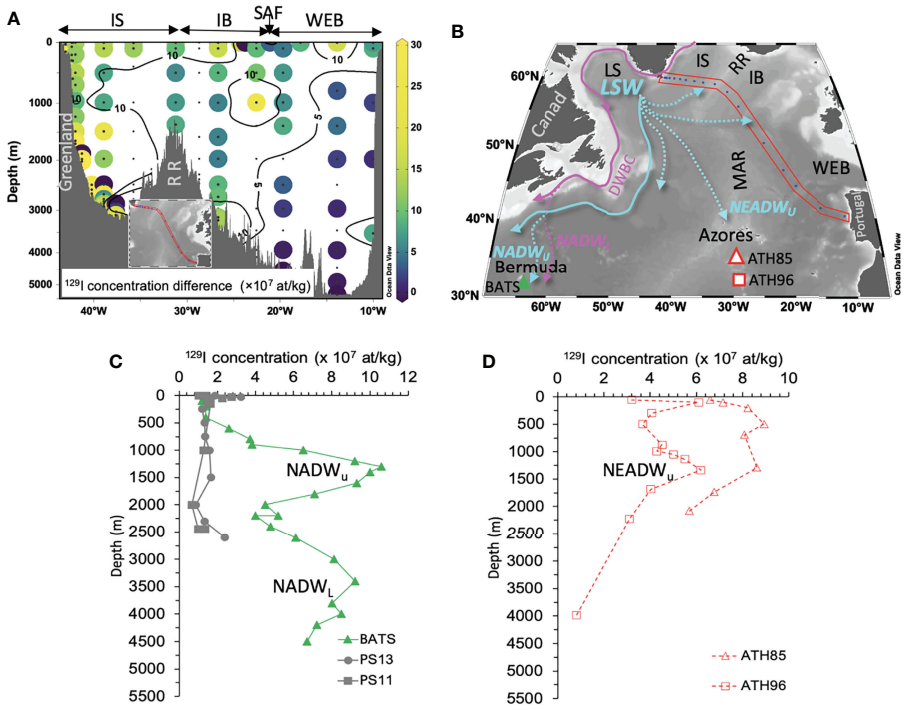

FIGURE 5 | **(A)** Temporal change of ^{129}I concentrations along the OVIDE line between 2014 (Castrillejo et al., 2018) and 2018 (this study) estimated as the subtraction of 2014 tracer values from 2018 observations overlapping at similar locations. **(B)** Map with the section plotted in **(A)** and the location of ^{129}I depth profiles at **(C)** BATS and **(D)** ATHENA stations in the subtropical North Atlantic. Plot **(C)** includes the two ^{129}I depth profiles sampled in 1993-1994 near the northeastern American slope at stations 13 (PS13, 36.3981°N, 74.2358°E) and 11 (PS11, 36.5081°N, 74.0908°E) reported by Peter H. Santschi et al. (1996). Acronyms in figure: Deep Western Boundary Current, (DWBC); Iceland Basin, (IB); Irminger Sea, (IS); Labrador Sea, (LS); Labrador Sea Water, (LSW); Mid Atlantic Ridge, (MAR); North Atlantic Deep Water, (NADW); North East Atlantic Deep Water, (NEADW); Reykjanes Ridge, (RR); Sub-Arctic Front, (SAF); and West European Basin, (WEB).

observed associated to the transport of $NADW_L$ *via* the Deep Western Boundary Current (**Figure 5C**). More recently another study by Smith et al. (2016) focused on the off-boundary transport of the same lower branch in our study area east of Bermuda (magenta dotted lines in **Figure 5B**). But they did not report ^{129}I values for shallower depths occupied by $NADW_U$. In our BATS profile (**Figure 5C**) we observed a very clear peak of ^{129}I centered at about 1500 m depth coinciding with potential densities (σ_θ ~27.75 kg/m^3, see **Table S1**) and a local salinity minimum (S~35) that characterize the LSW in the North Atlantic (McCartney and Talley, 1982). This tracer peak at 1500 m depth therefore shows that ^{129}I data allow the straightforward identification of $NADW_U$ taking off-boundary pathways near Bermuda (turquoise dotted lines in **Figure 5B**). We also sampled two partial depth profiles south of the Azores Archipelago during ATHENA (**Figure 5D**). This far east ^{129}I concentrations were lower than at BATS. The depths occupied by the $NEADW_U$ only showed slightly more elevated ^{129}I concentrations at station ATH95 and a little further south at ATH96 the ~1500 m depth tracer peak could not be recognized. We learnt from other transient tracer observations, i. e. chlorofluorocarbons (CFCs), that highest fractions of LSW in the subtropical region are found in the DWBC and that the presence of young vintages is very limited east of the Mid Atlantic Ridge (e. g. Rhein et al., 2015). The three ^{129}I depth profiles in **Figures 5C, D** show an eastward decrease in tracer concentrations that generally agrees with the spreading of LSW (or $NEADW_U$) inferred from CFC tracer fields. Yet, more ^{129}I data are certainly needed to alleviate the sampling gap between the western and eastern subtropical North Atlantic and to confirm the relationship between the tracer distribution and the spreading of intermediate waters in the subtropical gyre.

The new ^{129}I observations presented here show that deep ventilation in the subpolar region plays an important role on the sequestration of the tracer from shallow to deeper water layers supporting the modelling work of Orre et al. (2010) and Snyder, Aldahan and Possnert et al. (2010). While ^{129}I has been used to infer mixing and transport timescales of DSOW in the SPNA (Smith et al., 2005) and down to Bermuda (Santschi et al., 1996; Smith et al., 2016), no published work has used ^{129}I for investigating LSW or ISOW advection yet. This work clearly demonstrates that ^{129}I is now being supplied at unprecedented rate (**Figure 5A**) through the Greenland-Scotland passages making more northern water masses traceable in the North Atlantic and that measurable tracer peaks extend at least as far as 30°N (**Figures 4**, **5C**). The tracer intrusion in the North Atlantic shows that LSW and the overflows commonly take off-boundary pathways in agreement with drifting float (Bower et al., 2009; Bower et al., 2019) and CFC observations (Rhein et al., 2015). The clarity of ^{129}I peaks captured at the stations sampled afar

from the boundary regions (**Figures 4**, **5C**) indicates that recirculation through interior pathways must be important for the southward lower limb of the AMOC. Deflections of LSW and ISOW off the boundary currents appear to be related to latitudinal and meridional displacements of the North Atlantic Current (Bower et al., 2009; Bower and Furey, 2017; Xu et al., 2018) and its deep-reaching eddies and meanders (e.g., Zou et al., 2020). The partition between northern and southern waters also depends on the positioning of the North Atlantic Current, with southern (northern) waters with low (high) ^{129}I concentrations generally occupying the regions east (west) of the main North Atlantic Current front. In this regard, a higher density sampling of ^{129}I across North Atlantic Current boundaries in the subtropical and subpolar North Atlantic may be of interest to further investigate the driving forces of LSW and ISOW pathways. We think that the findings presented here are encouraging for the radionuclide tracer community. And thus, we call for a larger effort to build continued ^{129}I time series which can help us better understand the structure and spreading rates of the AMOC.

DATA AVAILABILITY STATEMENT

The original contributions presented in the study are included in the article/**Supplementary Material**. Further inquiries can be directed to the corresponding author. The iodine-129 data from the OVIDE 2018 cruise are available at SEANOE (Lherminier et al., 2022).

AUTHOR CONTRIBUTIONS

MC collected the samples during OVIDE 2018 cruise and processed all seawater samples, he led the interpretation of data and the drafting of the manuscript. MC also raised part of the funds. NC managed the seawater sampling of PE424, BATS and ATHENA cruises, raised part of the funds for research and conducted the AMS measurements of iodine isotopes together with CV. PL led the OVIDE 2018 cruise facilitating the collection of samples and assessed the physical oceanographic aspects discussed in this work. All authors contributed to the article and approved the submitted version.

FUNDING

The research of MC was partly funded by the ETH Career Seed Grant (SEED-06 19-2) and the Swiss National Science Foundation Postdoc Mobility Program (P400P2_199289). NC's funding came from the European Research Council (ERC Consolidator GAP-101001451) and the Swiss National Science Foundation (AMBIZIONE PZ00P2_154805 and PRIMA PR00P2_193091). The participation in the OVIDE 2018 Cruise onboard *R/V Thalassa* (https://doi.org/10.17600/18000510) was supported by PL and funds from the Laboratory of Ion Beam Physics. Support to process samples from PE424 cruise onboard *R/V* Pelagia and to participate on BATS monitoring onboard R/V Atlantic Explorer came from Swiss National Science Foundation Ambizione grant of NC. Funding for ATHENA Cruise (M151) onboard *R/V Meteor* came from Deutsche Forschungsgemeinschaft. The analysis of long-lived isotopes of iodine was possible thanks to internal funds of the Laboratory of Ion Beam Physics at ETH-Zurich and its consortium partners EAWAG, EMPA, and PSI. Open access funding provided by ETH Zürich.

ACKNOWLEDGMENTS

Captains, crew and scientific staff of the four cruises are thanked for their dedication in collecting the samples used in this study. Thanks go to A. M. Wefing for her assistance in sample collection and comments on the manuscript and to A. Schlatter and K. Kündig for help in the laboratory. Norbert Frank is thanked for inviting us to participate in cruise ATHENA (M151). Acknowledgements go to Loes Gerringa and Rob Middag (NIOZ) who collected samples during the PE424 cruise. Rod Johnson (BIOS) and Anita Schlatter (EAWAG) collected the ^{129}I profile during one of their monitoring cruises at BATS station. The analysis of waters masses would not have been possible without the hydrographic data that was kindly produced by different groups from many nationalities, thus, a big thank you to all. The constructive comments from the two reviewers are greatly appreciated.

SUPPLEMENTARY MATERIAL

The Supplementary Material for this article can be found online at: https://www.frontiersin.org/articles/10.3389/fmars.2022.897729/full#supplementary-material

REFERENCES

Alfimov, V., Aldahan, A., and Possnert, G. (2004). Tracing Water Masses With ^{129}I in the Western Nordic Seas in Early Spring 2002. *Geophys. Res. Lett.* 31 (19), 10–13. doi: 10.1029/2004GL020863

Alfimov, V., Aldahan, A., and Possnert, G. (2013). "Water Masses and ^{129}I Distribution in the Nordic Seas" in *Nuclear Instruments and Methods in Physics Research, Section B: Beam Interactions with Materials and Atoms*. Elsevier. pp. 542–546. doi: 10.1016/j.nimb.2012.07.042

Beaird, N. L., Rhines, P. B., and Eriksen, C. C. (2013). Overflow Waters at the Iceland–Faroe Ridge Observed in Multiyear Seaglider Surveys. *J. Phys. Oceanogr.* 43 (11), 2334–2351. doi: 10.1175/JPO-D-13-029.1

Bower, A., and Furey, H. (2017). Iceland-Scotland Overflow Water Transport Variability Through the Charlie-Gibbs Fracture Zone and the Impact of the North Atlantic Current. *J. Geophys. Res.: Oceans* 122 (9), 6989–7012. doi: 10.1002/2017JC012698

Bower, A. S., le Cann, B., Rossby, T., Zenk, W., Gould, J., Speer, K., et al. (2002). Directly Measured Mid-Depth Circulation in the Northeastern North Atlantic Ocean. *Nature* 419 (6907), 603–607. doi: 10.1038/nature01078

Bower, A., Lozier, S., Biastoch, A., Drouin, K., Foukal, N., Furey, H., et al. (2019). Lagrangian Views of the Pathways of the Atlantic Meridional Overturning Circulation. *J. Geophys. Res.: Oceans* 124 (8), 5313–5335. doi: 10.1029/2019JC015014

Bower, A. S., Lozier, M. S., Gary, S. F., and Böning, C. W. (2009). Interior Pathways of the North Atlantic Meridional Overturning Circulation. *Nature* 459 (7244), 243–247. doi: 10.1038/nature07979

Broecker, W. S., and Peng, T. H. (1982). *Tracers in the Sea* (Palisades, New York: Eldigio Press).

Casacuberta, N., Christl, M., Vockenhuber, C., Wefing, A. M., Wacker, L., Masqué, P., et al. (2018). Tracing the Three Atlantic Branches Entering the Arctic Ocean With ^{129}I and ^{236}U. *J. Geophys. Res.: Oceans* 123 (9), 6909–6921. doi: 10.1029/2018JC014168

Castrillejo, M., Casacuberta, N., Christl, M., Vockenhuber, C., Synal, H.-A., García-Ibáñez, M. I., et al. (2018). Tracing Water Masses With 129I and ^{236}U in the Subpolar North Atlantic Along the GEOTRACES GA01 Section. *Biogeosciences* 15, 5545–5564. doi: 10.5194/bg-2018-228

Chang, Y. S., Garraffo, Z. D., Peters, H., and Özgökmen, T. M. (2009). Pathways of Nordic Overflows From Climate Model Scale and Eddy Resolving Simulations. *Ocean Model.* 29 (1), 66–84. doi: 10.1016/j.ocemod.2009.03.003

Christl, M., Vockenhuber, C., Kubik, P. W., Wacker, L., Lachner, J., Alfimov, V., et al. (2013). The ETH Zurich AMS Facilities: Performance Parameters and Reference Materials. *Nucl. Instruments Methods Phys. Res. Section B.: Beam Interact. Mater. Atoms* 294, 29–38. doi: 10.1016/j.nimb.2012.03.004

Clarke, R. A., and Gascard, J.-C. (1983). The Formation of Labrador Sea Water. Part I: Large-Scale Processes. *J. Phys. Oceanogr.* 13 (10), 1764–1778. doi: 10.1175/1520-0485(1983)013<1764:TFOLSW>2.0.CO;2

Daniault, N., Mercier, H., Lherminier, P., Sarafanov, A., Falina, A., Zunino, P., et al. (2016). The Northern North Atlantic Ocean Mean Circulation in the Early 21st Century. *Prog. Oceanogr.* 146, 142–158. doi: 10.1016/j.pocean.2016.06.007

Devana, M. S., Johns, W. E., Houk, A., and Zou, S. (2021). Rapid Freshening of Iceland Scotland Overflow Water Driven by Entrainment of a Major Upper Ocean Salinity Anomaly. *Geophys. Res. Lett.* 48, (22). doi: 10.1029/2021GL094396

Dickson, R. R., and Brown, J. (1994). The Production of North Atlantic Deep Water: Sources, Rates, and Pathways. *J. Geophys. Res.* 99 (C6), 12319. doi: 10.1029/94JC00530

Edmonds, H. N., Zhou, Z. Q., Raisbeck, G. M., Yiou, F., Kilius, L., and Edmond, J. M. (2001). Distribution and Behavior of Anthropogenic ^{129}I in Water Masses Ventilating the North Atlantic Ocean. *J. Geophys. Res.: Oceans* 106 (C4), 6881–6894. doi: 10.1029/1999jc000282

Fleischmann, U., Hildebrandt, H., Putzka, A., and Bayer, R. (2001). Transport of Newly Ventilated Deep Water From the Iceland Basin to the Westeuropean Basin. *Deep-Sea Res. I* 48. doi: 10.1016/S0967-0637(00)00107-2

García-Ibáñez, M. I., Pérez, F. F., Lherminier, P., Zunino, P., Mercier, H., and Tréguer, P. (2018). Water Mass Distributions and Transports for the 2014 GEOVIDE Cruise in the North Atlantic. *Biogeosciences* 15 (7), 2075–2090. doi: 10.5194/bg-15-2075-2018

Gómez-Guzmán, J. M., Villa, M., le Moigne, F., López-Gutiérrez, J. M., and García-León, M. (2013). AMS Measurements of ^{129}I in Seawater Around Iceland and the Irminger Sea. *Nucl. Instruments Methods Phys. Res. Section B.: Beam Interact. Mater. Atoms* 294, 547–551. doi: 10.1016/j.nimb.2012.07.045

Hansen, B., and Østerhus, S. (2007). Faroe Bank Channel Overflow 1995–2005. *Prog. Oceanogr.* 75 (4), 817–856. doi: 10.1016/j.pocean.2007.09.004

He, P., Aldahan, A., Possnert, G., and Hou, X. L. (2013a). "A Summary of Global ^{129}I in Marine Waters" in *Nuclear Instruments and Methods in Physics Research, Section B: Beam Interactions with Materials and Atoms*. Berlin, Germany: Springer Nature 537–541. doi: 10.1016/j.nimb.2012.08.036

He, P., Hou, X., Aldahan, A., Possnert, G., and Yi, P. (2013b). Iodine Isotopes Species Fingerprinting Environmental Conditions in Surface Water Along the Northeastern Atlantic Ocean. *Sci. Rep.* 3, 1–8. doi: 10.1038/srep02685

Hou, X. (2004). Application of 129 I as an Environmental Tracer. *J. Radioanal. Nucl. Chem.* 262 (1), 67–75.

Lankhorst, M., and Zenk, W. (2006). *Lagrangian Observations of the Middepth and Deep Velocity Fields of the Northeastern Atlantic Ocean*. American Meteorological Society. doi: 10.1175/JPO2869.1

Lherminier, P., Perez Fiz, F., Branellec, P., Mercier, H., Velo, A., Messias, M. -J., et al. (2022). GO-SHIP A25 - OVIDE 2018 Cruise Data. *SEANOE*. doi: 10.17882/87394

McCartney, M. S., and Talley, L. D. (1982). The Subpolar Mode Water of the North Atlantic Ocean. *J. Phys. Oceanogr.* 12 (11), 1169–1188. doi: 10.1175/1520-0485(1982)012<1169:TSMWOT>2.0.CO;2

Orre, S., Smith, J. N., Alfimov, V., and Bentsen, M. (2010). Simulating Transport of ^{129}I and Idealized Tracers in the Northern North Atlantic Ocean. *Environ. Fluid Mech.* 10 (1), 213–233. doi: 10.1007/s10652-009-9138-3

OSPAR (2015). *OSPAR Data & Information Management System. 2015* (United Kingdom: OSPAR Liquid Discharges from Nuclear Installations- 2015). Available at: https://odims.ospar.org/en/search/?datastream=liquid_discharges.

Perez, F. F., Fontela, M., García-Ibáñez, M. I., Mercier, H., Velo, A., Lherminier, P., et al. (2018). Meridional Overturning Circulation Conveys Fast Acidification to the Deep Atlantic Ocean. *Nature* 554 (7693), 515–518. doi: 10.1038/nature25493

Petit, T., Mercier, H., and Thierry, V. (2018). First Direct Estimates of Volume and Water Mass Transports Across the Reykjanes Ridge. *J. Geophys. Res.: Oceans* 123 (9), 6703–6719. doi: 10.1029/2018JC013999

Piron, A., Thierry, V., Mercier, H., and Caniaux, G. (2017). Gyre-Scale Deep Convection in the Subpolar North Atlantic Ocean During Winter 2014–2015. *Geophys. Res. Lett.* 44 (3), 1439–1447. doi: 10.1002/2016GL071895

Racapé, V., Thierry, V., Mercier, H., and Cabanes, C. (2019). ISOW Spreading and Mixing as Revealed by Deep-Argo Floats Launched in the Charlie-Gibbs Fracture Zone. *J. Geophys. Res.: Oceans* 124 (10), 6787–6808. doi: 10.1029/2019JC015040

Raisbeck, G. M., and Yiou, F. (1999). ^{129}I in the Oceans: Origins and Applications. *Sci. Total Environ.* 237–238, 31–41. doi: 10.1016/S0048-9697(99)00122-9

Rhein, M., Kieke, D., and Steinfeldt, R. (2015). Advection of North Atlantic Deep Water From the Labrador Sea to the Southern Hemisphere. *J. Geophys. Res. C.: Oceans* 120 (4), 2471–2487. doi: 10.1002/2014JC010605

Santschi, P. H., Schink, D. R., Corapcioglu, O., Oktay-Marshall, S., Fehn, U., and Sharma, P. (1996). Evidence for Elevated Levels of Iodine-129 in the Deep Western Boundary Current in the Middle Atlantic Bight. *Deep Sea Res. Part I Oceanogr. Res. Pap.* 43, 2 59–265. doi: 10.1016/0967-0637(96)00005-2

Saunders, P. M. (1994). The Flux of Overflow Water Through the Charlie-Gibbs Fracture Zone. *J. Geophys. Res.* 99 (C6), 12343. doi: 10.1029/94JC00527

Schink, D. R., Santschi, P. H., Corapcioglu, O., and Fehn, U. (1995). Prospects for Iodine-129 Dating of Marine Organic Matter Using AMS. *Nucl. Instruments Methods Phys. Res. B.* 99, 524–527. doi: 10.1016/0168-583X(94)00695-4

Schott, F., Stramma, L., and Fischer, J. (1999). Interaction of the North Atlantic Current With the Deep Charlie Gibbs Fracture Zone Throughflow. *Geophys. Res. Lett.* 26 (3), 369–372. doi: 10.1029/1998GL900223

Sherwin, T. J., Griffiths, C. R., Inall, M. E., and Turrell, W. R. (2008). Quantifying the Overflow Across the Wyville Thomson Ridge Into the Rockall Trough. *Deep Sea Res. Part I.: Oceanogr. Res. Papers* 55 (4), 396–404. doi: 10.1016/j.dsr.2007.12.006

Smith, J. N., Jones, E. P., Moran, S. B., Smethie, J. M., and Kfieser, W. E. (2005). Iodine 129/CFC 11 Transit Times for Denmark Strait Overflow Water in the Labrador and Irminger Seas. *J. Geophys. Res. C.: Oceans* 110 (5), 1–16. doi: 10.1029/2004JC002516

Smith, J. N., McLaughlin, F. A., Smethie, W. M., Moran, S. B., and Lepore, K. (2011). Iodine-129, 137Cs, and CFC-11 Tracer Transit Time Distributions in the Arctic Ocean. *J. Geophys. Res.: Oceans* 116 (4), 1–19. doi: 10.1029/2010JC006471

Smith, J. N. Jr, Smethie, W. M., Yashayev, I., Curry, R., and Azetsu-Scott, K. (2016). Time Series Measurements of Transient Tracers and Tracer-Derived Transport in the Deep Western Boundary Current Between the Labrador Sea and the Subtropical Atlantic Ocean at Line W. *J. Geophys. Res.: Oceans*, 121, 1–14. doi: 10.1002/2015JC011486.Received

Snyder, G., Aldahan, A., and Possnert, G. (2010). Global Distribution and Long-Term Fate of Anthropogenic ^{129}I in Marine and Surface Water Reservoirs. *Geochem. Geophysics Geosystems* 11 (4), 1–19. doi: 10.1029/2009GC002910

UK Environmental Agency (2015). *Radioactivity in Food and the Environment (RIFE) Reports. 2015* (United Kingdom: RIFE -2015). Available at: https://www.gov.uk/government/publications/radioactivity-in-food-and-the-environment-rife-reports.

van Aken, H. M. (2000a). The Hydrography of the Mid-Latitude Northeast Atlantic Ocean I: The Deep Water Masses. *Deep-Sea Res. I* 47, 757–788. doi: 10.1016/S0967-0637(99)00092-8

van Aken, H. M. (2000b). The Hydrography of the Mid-Latitude Northeast Atlantic Ocean II: The Intermediate Water Masses. *Deep Sea Res. Part I.:*

Oceanographic Res. Papers 47 (5), 789–824. doi: 10.1016/S0967-0637(99)00112-0

Vivo-Vilches, C., López-Gutiérrez, J. M., Periáñez, R., Marcinko, C., le Moigne, F., McGinnity, P., et al. (2018). Recent Evolution Of ^{129}I Levels in the Nordic Seas and the North Atlantic Ocean. *Sci. Total Environ.* 621, 376–386. doi: 10.1016/j.scitotenv.2017.11.268

Vockenhuber, C., Casacuberta, N., Christl, M., and Synal, H. A. (2015). Accelerator Mass Spectrometry of ^{129}I Towards its Lower Limits. *Nucl. Instruments Methods Phys. Res. Section B.: Beam Interact. Mater. Atoms* 361, 445–449. doi: 10.1016/j.nimb.2015.01.061

Wagner, M. J. M., Dittrich-Hannen, B., Synal, H.-A., Suter, M., and Schotterer, U. (1996). Increase of ^{129}I in the Environment. *Nucl. Instruments Methods Phys. Res. Section B.: Beam Interact. Mater. Atoms* 113 (1–4), 490–494. doi: 10.1016/0168-583X(95)01348-2

Wefing, A.-M., Christl, M., Vockenhuber, C., van der Loeff, M.R., and Casacuberta, N. (2018). Tracing Atlantic Waters Using ^{129}I and ^{236}U in the Fram Strait in 2016. *J. Geophys. Res.: Oceans*. 124, 882–896. doi: 10.1029/2018JC014399

Wong, G. T. F. (1991). The Marine Geochemistry of Iodine. *Rev. Aquat. Sci.* 4, 45–73.

Xu, X., Bower, A., Furey, H., and Chassignet, E. P. (2018). Variability of the Iceland-Scotland Overflow Water Transport Through the Charlie-Gibbs Fracture Zone: Results From an Eddying Simulation and Observations. *J. Geophys Res.: Oceans* 123 (8), 5808–5823. doi: 10.1029/2018JC013895

Xu, X., Schmitz, W. J., Hurlburt, H. E., Hogan, P. J., and Chassignet, E. P. (2010). Transport of Nordic Seas Overflow Water Into and Within the Irminger Sea: An Eddy-Resolving Simulation and Observations. *J. Geophys Res.: Oceans* 115, (12). doi: 10.1029/2010JC006351

Yashayaev, I., Bersch, M., and van Aken, H. M. (2007). Spreading of the Labrador Sea Water to the Irminger and Iceland Basins. *Geophys Res. Lett.* 34 (10), L10602. doi: 10.1029/2006GL028999

Yashayaev, I., and Loder, J. W. (2016). Recurrent Replenishment of Labrador Sea Water and Associated Decadal-Scale Variability. *J. Geophys Res.: Oceans* 121 (11), 8095–8114. doi: 10.1002/2016JC012046

Yiou, F., Raisbeck, G. M., Zhou, Z. Q., and Kilius, L. R. (1994). ^{129}I From Nuclear Fuel Reprocessing; Potential as an Oceanographic Tracer. *Nucl. Inst. Methods Phys. Res. B.* 92 (1–4), 436–439. doi: 10.1016/0168-583X(94)96050-X

Zou, S., Bower, A., Furey, H., Susan Lozier, M., and Xu, X. (2020). Redrawing the Iceland–Scotland Overflow Water Pathways in the North Atlantic. *Nat. Commun.* 11 (1), 1–8. doi: 10.1038/s41467-020-15513-4

Zou, S., Lozier, S., Zenk, W., Bower, A., and Johns, W. (2017). Observed and Modeled Pathways of the Iceland Scotland Overflow Water in the Eastern North Atlantic. *Prog. Oceanography* 159, 211–222. doi: 10.1016/j.pocean.2017.10.003

Conflict of Interest: The authors declare that the research was conducted in the absence of any commercial or financial relationships that could be construed as a potential conflict of interest.

Publisher's Note: All claims expressed in this article are solely those of the authors and do not necessarily represent those of their affiliated organizations, or those of the publisher, the editors and the reviewers. Any product that may be evaluated in this article, or claim that may be made by its manufacturer, is not guaranteed or endorsed by the publisher.

frontiers | Frontiers in Marine Science

ORIGINAL RESEARCH
published: 23 May 2022
doi: 10.3389/fmars.2022.846025

Sources and Cycling of Particulate Organic Matter in Baffin Bay: A Multi-Isotope $\delta^{13}C$, $\delta^{15}N$, and $\Delta^{14}C$ Approach

*Aislinn Fox and Brett D. Walker**

Department of Earth and Environmental Science, University of Ottawa, Ottawa, ON, Canada

The Canadian Arctic is warming three times faster than the rest of the planet. The impact of climate change on the Arctic carbon cycle, and in particular for Baffin Bay, remains poorly constrained. Sinking particulate organic matter (POM_{sink}) is a key component of the biological carbon pump and provides a direct linkage between surface productivity and the preservation of carbon in marine sediments. While POM_{sink} provides a rapid POM shunt to the deep ocean (days) the majority of marine POM is suspended (POM_{susp}) persists for years in the water column. Stable carbon ($\delta^{13}C$), nitrogen ($\delta^{15}N$) and radiocarbon ($\Delta^{14}C$) measurements are powerful tools for evaluating sources and cycling of POM. In this study, we measure depth-integrated (0-400m) POM_{susp} stable carbon ($\delta^{13}C$), nitrogen ($\delta^{15}N$) and radiocarbon ($\Delta^{14}C$) values at 11 stations in Baffin Bay. We use POM $C:N_a$ ratios to evaluate its diagenetic state. POM_{susp} $\delta^{13}C$ and $\delta^{15}N$ values ranged from –21.6‰ to –29.5‰, and +3.84‰ to +7.21‰, respectively. POM_{susp} $\Delta^{14}C$ values ranged from –41.8‰ to +76.8‰. Together, our results suggest Baffin Bay POM_{susp} has multiple carbon and nitrogen sources. POM_{susp} $\delta^{13}C$ and $\Delta^{14}C$ are strongly correlated to surface salinity, indicating surface water has a strong influence on POM_{susp} isotopic composition and ^{14}C-age. POM_{susp} from coastal Greenland stations have similar $\Delta^{14}C$ values to surface dissolved inorganic carbon (DIC) and POM concentrations, consistent with primary production as the predominant POM_{susp} source in Eastern Baffin Bay. Positive POM_{susp} $\Delta^{14}C$ values in central Baffin Bay suggest an accumulation of atmospheric "bomb" ^{14}C in the sub-polar gyre. POM_{susp} exiting Davis Strait *via* the Baffin Island Current was determined to have a significant degraded, resuspended sediment component. Finally, POM_{susp} $\delta^{15}N$ values highlight two distinct N sources in Baffin Bay: Pacific and Arctic nutrients at Northern gateway stations vs. the influx of Atlantic nutrients *via* Davis Strait along coastal Greenland. Overall, these first Baffin Bay POM_{susp} $\Delta^{14}C$ values provide useful baseline data for rapidly changing Arctic ecosystem.

Keywords: particulate organic matter, radiocarbon, ^{13}C, ^{15}N, ^{14}C, Baffin Bay, Arctic, C:N

OPEN ACCESS

Edited by:
Jixin Qiao,
Technical University of Denmark, Denmark

Reviewed by:
Guodong Jia,
Tongji University, China
Frank Dehairs,
Vrije University Brussel, Belgium

***Correspondence:**
Brett D. Walker
brett.walker@uottawa.ca

Specialty section:
This article was submitted to Marine Biogeochemistry, a section of the journal Frontiers in Marine Science

Received: *30 December 2021*
Accepted: *01 April 2022*
Published: *23 May 2022*

Citation:
Fox A and Walker BD (2022) Sources and Cycling of Particulate Organic Matter in Baffin Bay: A Multi-Isotope $\delta^{13}C$, $\delta^{15}N$, and $\Delta^{14}C$ Approach. Front. Mar. Sci. 9:846025. doi: 10.3389/fmars.2022.846025

INTRODUCTION

Particulate organic matter (POM) is one of the most important and biologically active reservoirs of carbon and nitrogen in the oceans. Whereas the POM pool (30 ± 5 GtC, ~2.3 GtN) is smaller than that of dissolved organic matter (~662 GtC, 32-77GtN) and dissolved inorganic carbon (DIC; 38,000 GtC), marine POM cycles rapidly (Hansell et al., 2009; Sarmiento, 2013; Walker et al., 2016; Beaupré, 2019). POM is operationally defined as all organic matter retained by a 0.1μm filter. However, studies typically employ 2.0μm quartz or 0.7μm glass fiber filters as they can be combusted prior to collection. POM therefore includes all living marine organisms larger than a bacterial cell, but approximately 90% of POM is non-living detritus (Cauwet, 1981; Volkman and Tanoue, 2002). POM is produced by primary producers *via* photosynthetic carbon fixation in the euphotic zone. The re-packaging of phytoplankton through zooplankton heterotrophy results in rapid export of sinking POM (POM_{sink}) to the seafloor. Commonly known as the "biological carbon pump" (BCP), POM_{sink} is exported to the sediments at rates of 2.8-5.7 GtC yr^{-1} (Buesseler et al., 2020). However, only a small portion of POM_{sink} reaches the sediment as most is remineralized to CO_2 or transformed to dissolved organic matter (DOM) *via* heterotrophic microbes prior to burial (Smith et al., 1992; Denman et al., 2007). Approximately ~90% of recently deposited POM in sediments is remineralized at the sediment/water interface. Nevertheless, POM burial at rates of 0.2 to 0.4 GtC yr^{-1} allows for the long-term sequestration of atmospheric CO_2 (Passow and Carlson, 2012; Middelburg, 2019). The efficiency of the BCP varies with the availability of light, nutrients, sea surface temperature (SST), resident phytoplankton and zooplankton communities and polar sea-ice conditions (Honjo et al., 2010). Most BCP studies have focused on POM_{sink} as the main carbon burial vector. However, recent work suggests small phytoplankton cells found in the suspended POM pool (POM_{susp}) are important contributors to the BCP (Richardson and Jackson, 2007; Close et al., 2013).

Stable carbon ($\delta^{13}C$) and nitrogen ($\delta^{15}N$) isotope measurements are useful tools for understanding organic matter sources and cycling. Whereas historical POM cycling studies relied on time-intensive and laborious deployment of sediment traps and mooring time-series, isotopic measurements provide detailed evidence for physical/biological processes and controlling POM cycling rates without the inherent need for long-term deployments and repeat study. It should be noted that long-term deployments provide information about temporal evolution, while CTD cast sampling reflects a short temporal window "snap shot" of POM cycling. POM $\delta^{13}C$ and $\delta^{15}N$ inform us of organic matter sources (e.g., terrestrial vs. marine) as well as biological processes (autotrophy vs. heterotrophy), with isotopic ratios being controlled by mass-dependent fractionation *via* carbon and nitrogen fixation pathways, trophic level enrichment, and nutrient sources (Descolas-Gros and Fontugne, 1990; Rau et al., 1992; Williams et al., 1992; Sigman and Casciotti, 2001; Fawcett et al., 2011). Marine phytoplankton $\delta^{13}C$ and $\delta^{15}N$ show a wide range of values (from −35‰ to −15‰ and −1‰ to +10‰, respectively). POM $\delta^{13}C$ values in temperate waters typically range between −18‰ and −22‰, but more negative values are observed in polar regions as a result of temperature-dependent fractionation (Rau et al., 1982; Goericke and Fry, 1994).

In Baffin Bay, possible POM_{susp} $\delta^{13}C$ sources include: i) slow-growing marine phytoplankton in colder, fresher waters (−27 to −30‰; Brown et al., 2014), ii) fast-growing phytoplankton in warmer, fresher waters affected by glacial meltwater (−21.8 to −24‰; Limoges et al., 2020) iii) canonical marine plankton values for this region (−24 to −26‰; Goericke and Fry, 1994), iv) sea-ice algae (−20 to −17‰; Tamelander et al., 2006; Roy et al., 2015; De La Vega et al., 2019), v) glacial run-off POM (−28.5‰; Holding et al., 2017) and vi) terrestrial plants (mosses, lichen, grasses; −28 to −20‰; Lee et al., 2009). POM_{susp} $\delta^{15}N$ values are typically associated with nutrient sources (nitrate) fueling primary production, or the predominant mode of autotrophic or heterotrophic metabolism. For example, nitrate $\delta^{15}N$ ($\delta^{15}NO_3$) in the surface ocean has a large range (+2 to +20‰; Rafter et al., 2019), and is largely determined by nutrient availability and biological processes fractionating the surface nitrate pool (e.g., assimilation vs. denitrification and remineralization). Probable $\delta^{15}NO_3$ signatures that can be incorporated into surface POM $\delta^{15}N$ in Baffin Bay include nitrate from: the Atlantic Ocean (+4 to +6‰; Sherwood et al., 2021), the Pacific Ocean *via* the CAA (+7 to +8‰; Brown et al., 2015; Granger et al., 2018), and the Arctic Ocean (+5 to +7‰; Fripiat et al., 2018; Rafter et al., 2019).

Radiocarbon ($\Delta^{14}C$) measurements serve as both a carbon source indicator (e.g. fossil vs. modern vs. atmospheric "bomb" carbon) and as a geochronometer (*via* radioactive decay). In addition to naturally produced ^{14}C in the atmopshere, above-ground thermonuclear weapons testing in 1960s resulted in an atmospheric "bomb peak" that has allowed $\Delta^{14}C$ to be used as a modern tracer of atmospheric carbon on short timescales. Previous studies have used POM $\Delta^{14}C$ and stable isotope measurements of POM to evaluate POM cycling rates, and relative contributions of allochthonous vs. autochthonous detrital materials in a variety of systems. A study of size-fractionated POM_{susp} $\Delta^{14}C$ from the California Current upwelling system showed that while most POM_{susp} is comprised of recently fixed photosynthetic material, the presence of negative POM_{susp} $\Delta^{14}C$ values suggested contributions of pre-aged, re-suspended sediments to POM_{susp} in coastal systems (Walker et al., 2014). Hwang and co-workers (2010) used POM_{sink} $\Delta^{14}C$ and %Al values to estimate the global contribution of pre-aged, continental margin material to open ocean POM.

POM is also a complex geochemical mixture. Compound class separations of total lipid extracts (TLE), acid soluble (AS) and acid-insoluble (AI) fractions suggest POM comprises materials with heterogeneous ^{14}C-ages and chemical composition. Here TLE- and AI-POM are "pre-aged" and molecularly uncharacterized material, whereas AS-POM appears to be rich in biomolecules and has a $\Delta^{14}C$ signature similar to surface DIC throughout the water column (Hwang and Druffel, 2003;

Hwang and Druffel, 2006; Roland et al., 2008). Previous work has also demonstrated a clear compositional and ^{14}C-age difference between large vs. small POM size fractions. Whereas POM_{sink} and large POM size-fractions (dominated by large autotrophs) are biochemically "fresh" and have younger ^{14}C-ages, most evidence suggests $POM_{susp,}$ and small POM size-fractions (dominated by re-suspended sediments and microbial cells) are "degraded" and have older ^{14}C-ages (Walker et al., 2014; Benner and Amon, 2015; Walker et al., 2016). Whereas POM_{susp} can appear ^{14}C-modern and chemically "fresh" if derived from recent plankton blooms (e.g., Walker et al., 2014), coastal POM_{susp} is also considered a source of ^{14}C-depleted OM to the open ocean (Bauer and Druffel, 1998; Hwang et al., 2006; Roland et al., 2008).

Declining sea-ice cover and a prolonged "open water" season may cause considerable increases in primary production across the Arctic, with consequences for POM cycling (Arrigo and Dijken, 2015). Previous POM studies in Baffin Bay have focused on deployment of sediment traps to estimate export production and POM flux in the high-productivity North Water Polynya. These studies suggest high rates of POM export in Norther Baffin bay (5.9 g C m^{-2} yr^{-1}) and seasonal variance in POM export. Most POM export occurs in the Spring and some retention of POM in the upper water column (100m) has been observed in late summer (Caron et al., 2004; Lalande et al., 2009). However, these flux estimates do not provide us with an understanding of the biological lability or geochemical impact of POM exported to deep Baffin Bay. There is a paucity of Arctic POM isotopic data and, to the best of our knowledge, no POM Δ^{14}C data exist for Baffin Bay. Here we use the first POM_{susp} Δ^{14}C values with contemporaneous $C:N_a$, δ^{13}C and δ^{15}N values to evaluate POM sources and cycling in Baffin Bay.

METHODS

Baffin Bay Hydrographic Setting

Here we briefly describe the surface currents present in Baffin Bay and origin of surface waters sampled during the study (**Figure 1**). Baffin Bay is a large marginal sea lying between Kalaaliit Nunaat (Greenland) and Qikiqtaaluk (Baffin Island), connected by straits to the Arctic Ocean and the Atlantic Ocean. Baffin Bay is characterized by dynamic surface currents environment, with a stark contrast in oceanographic conditions (e.g., SST, salinity, fluorescence, and nutrients) in Western vs. Eastern Baffin Bay (**Figures 2A, B**; **S1–4**). The Baffin Island Current (BIC) flows southward along the Baffin Island shelf and slope before exiting Davis Strait into the Labrador Sea. The BIC is composed of cool, fresh Arctic Water (AW) from recent sea-ice melt from the Arctic Ocean and Canadian Arctic Archipelago (CAA) which enters Baffin Bay *via* several northern gateways (NG) – Nares Strait, Jones Strait, and Lancaster Sound. In Eastern Baffin Bay, relatively warm and salty waters enter from the North Atlantic, forming the West Greenland Current (WGC), and flow north along the Greenland shelf. The WGC is a continuation of the East Greenland Current (EGC), composed of Arctic waters flowing southwards along the eastern coast of Greenland, with contributions from the warm and saline Irminger Current in the North Atlantic (Hamilton and Wu, 2013). As the WGC progresses northward, it becomes fresher and cooler, due to mixing with glacial meltwater and mixing with central Baffin Bay water (Münchow et al., 2015). The WGC terminates near Smith Sound (75°N-77°N), before joining Arctic Water outflows from the CAA to form the BIC (Melling et al., 2001; Tang et al., 2004). Together, the northwards-flowing WGC and southwards-flowing BIC form a cyclonic circulation pattern and sub-polar gyre in Baffin Bay. The eastern side of Baffin Bay also receives more meteoric

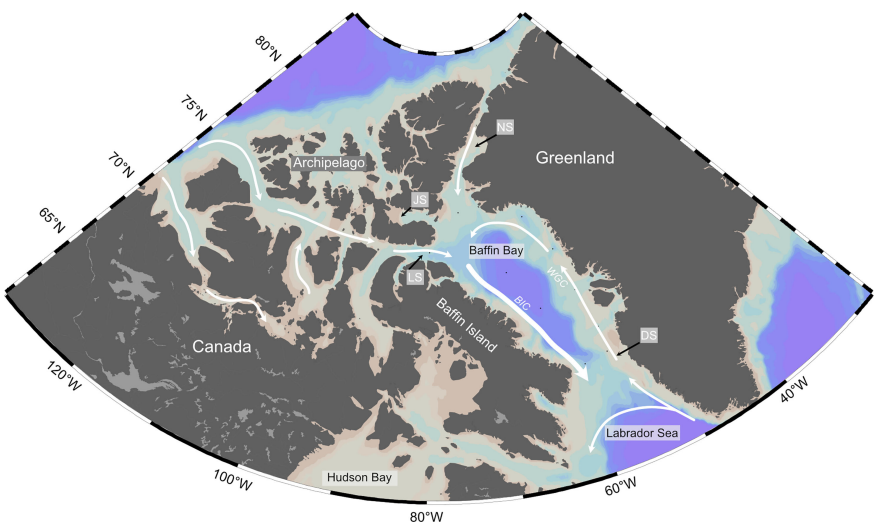

FIGURE 1 | Area Map of Canadian Arctic. White arrows indicate simplified surface currents and directions. The Western Greenland Current (WGC) and Baffin Island Currents (BIC) are specifically indicated. Locations of Baffin Bay gateways – Davis Strait (DS), Lancaster Sound (LS), Jones Sound (JS), and Nares Strait (NS) – are indicated with black arrows. Small black dots in Baffin Bay represent POM sampling locations from the 2019 research cruise.

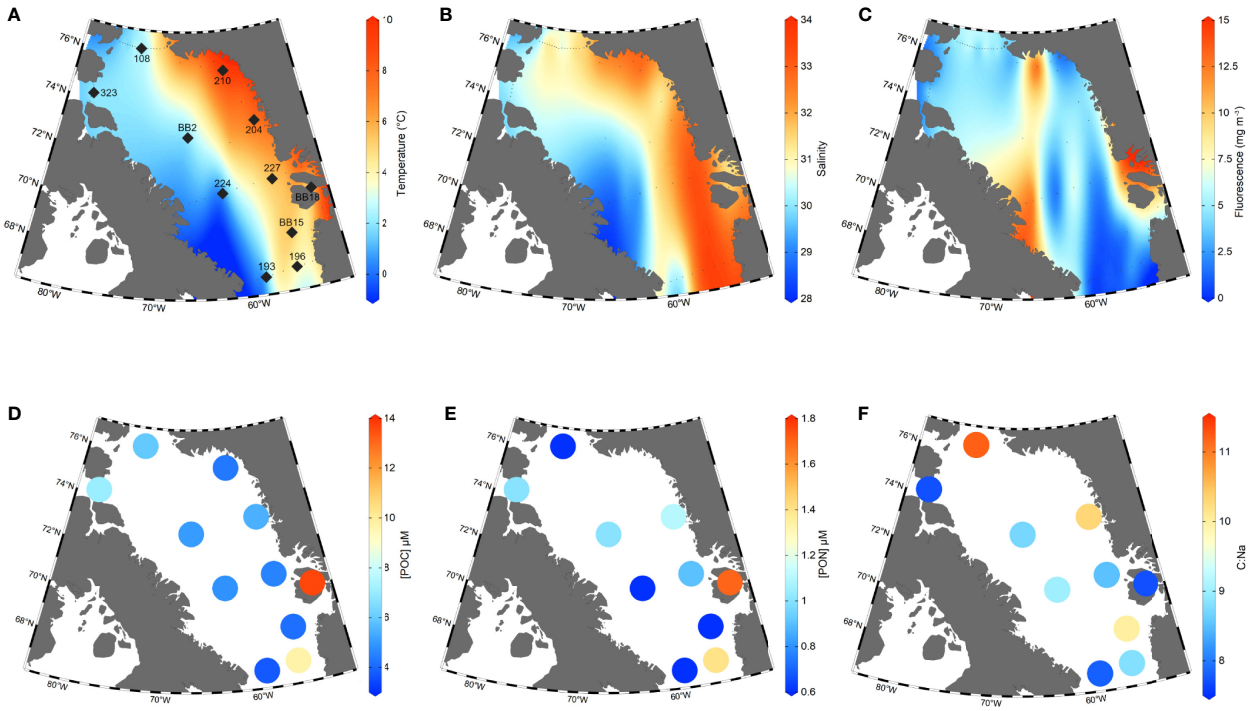

FIGURE 2 | Station map together with sea surface temperature, salinity, fluorescence, [POC], [PON], and C:N. Plots **(A–C)**: Data from all stations visited in the 2019 research cruise were used to create the interpolated surface distributions of sea surface temperature (**A**; SST), salinity **(B)** and fluorescence at the deep chlorophyll maximum **(C)**. Here, SSTs are CTD temperatures from 2-3 metres depth (°C), sea surface salinities are CTD data from 2-3 metres depth and reported in Practical Salinity Units (PSU), and fluorescence values are for the deep chlorophyll-*a* maximum depth (30-40m). Stations from which POM samples were collected are indicated by large black diamonds on Plot **(A)** All other cruise stations in which CTD data was collected (such as temperature, salinity, and fluorescence) are indicated by small black dots. Plots **(D–F)** show [POC], [PON] concentrations in µmol L^{-1} and C:N_a ratios from each station.

freshwater input from melting of the Greenland ice sheet (Hamilton and Wu, 2013). This difference in East vs. West surface water properties results in differences in phytoplankton communities, sea ice conditions and rates of primary production in the region. For example, the timing and intensity of phytoplankton blooms is different on the Eastern vs. Western side of Baffin Bay and can clearly be seen in fluorescence values of the deep chlorophyll-*a* maximum (DCM; **Figure 2C**). The depth of the DCM in our sample stations ranged from 13 to 44 metres, with an average of depth of 32 ± 10 metres (n=11; **Figure S3**). Annual POM flux is generally higher on the eastern side of northern Baffin Bay relative to the western side (Lalande et al., 2009). It is important to note that Baffin Bay is a marginal sea ice zone. The region experiences full sea-ice coverage from December to April. Due to the relatively warm West Greenland Current, ice cover decreases earlier along the Greenland coast than on the western side of Baffin Bay (Tang et al., 2004). By late summer, Baffin Bay is typically clear of extensive sea-ice, although icebergs are common, especially in proximity to fjords.

Sampling Collection and Preparation

POM_{susp} samples were collected from 11 stations in July 2019 aboard the CCGS *Amundsen* (**Figure 2A**). A main goal of this broader study was to sample depth profiles for isotopic characterization of dissolved organic carbon. Due to a restricted water budget, low expected POM concentrations, collected POM_{susp} samples comprise depth integrated filtrations of seawater from 0 to 400m depth, filtered directly from 12L Niskin bottles. POM_{susp} was filtered either by gravity and/or by a peristaltic pump using acid cleaned (10% HCl) silicone tubing onto pre-combusted (540°C/2h) 70mm quartz fiber filters (Whatman QMA; 2.0µm) held in a custom stainless-steel manifold. Samples comprise seawater POM from 15 to 20 discrete Niskin bottles, depending on the depth of the station. Between 60 ± 10 mL and 1.50 ± 0.12 L of seawater from each Niskin was passed through the filter. Larger seawater volumes (>1 liter) were sampled at depths of 0m, 20m, 50m, 100m, 200m, 300m, and 400m. Between 4.9 ± 0.2 L and 12.2 ± 0.3 L were passed through filters in total, with most stations having ~7.1 liters in total. After sample collection, POM_{susp} QMA filters were placed in pre-combusted (540°C/2h) aluminum foil envelopes, frozen immediately and stored at -20°C until sample processing at the University of Ottawa. Measurements of SST, salinity, and fluorescence were taken *via* the CTD rosette instrument package equipped with 24, 12L Niskin bottles including a Seabird SBE911plus CTD profiler and ECO-Fl Chlorophyll-*a* fluorometer for 53 stations in Baffin Bay (**Figures 2A–C**).

In the lab, filters were oven dried overnight (50°C/8h) and vapor-phase acidified at ambient pressure in a clean glass desiccator bell with 5 mL of 12N HCl for 4 hours to remove particulate inorganic carbon (PIC). To avoid the use of hydrocarbon-containing grease, the desiccator bell was sealed with ~1mL 85% phosphoric acid placed on its stoneground glass joint. POM filters were subsampled by cutting approximately one-third of the filter. A time of 4 hours was used instead of common 12h or "overnight" acidification methods based on lab tests showing complete removal of 10 mg of $NaHCO_3$ on filters under similar conditions in less than 2 hours (S. Beaupré and B. Walker, unpublished data). Our filters contain far less than 10 mg of total mass, and substantially less inorganic carbon. After acidification, sample filters were again oven dried (50°C overnight) to remove HCl and H_2O vapor and stored in a low humidity, desiccator cabinet until further processing for isotopic analysis.

POM_{susp} Concentrations, Stable Isotope and $\Delta^{14}C$ Analysis

All filters were sub-sampled prior to elemental and isotopic analysis. For POM_{susp} $\Delta^{14}C$ analysis we evenly cut 1/3 of the 70mm filter for all stations except for station BB2 where 1/4 filter was used due to repeated analysis attempts. Filter subsamples were rolled and placed into pre-combusted (540°C/2h) 9mm quartz tubes with ~100mg CuO wire, evacuated to 10^{-7} torr on a vacuum line and flame sealed. Sealed 9mm tubes with filters were then combusted at 850°C for 3h and the resultant CO_2 cryogenically purified and manometrically quantified on a vacuum line system at the University of Ottawa. A small split of isotopically equilibrated CO_2 gas was subsampled on the vacuum line and sealed in 3mm Pyrex tubes for $\delta^{13}C$ measurement *via* Gas Bench isotope ratio mass spectrometry (GB-IRMS). The primary fraction of CO_2 gas graphitized using the sealed tube zinc method for both large (>100μgC) and ultra-small (<100μgC) samples (Xu et al., 2007; Walker and Xu, 2019). After graphitization samples were pressed into aluminum cathodes at the University of Ottawa and analyzed for $\Delta^{14}C$ *via* accelerator mass spectrometry (AMS) at the W.M. Keck-Carbon Cycle AMS facility at the University of California, Irvine. Small 3mm Pyrex tube gas splits were also measured for $\delta^{13}C$ *via* GB-IRMS at UC Irvine. Station 210 was not determined due to repeated failures to graphitize for $\Delta^{14}C$ leaving no material for further analysis. These failed attempts are difficult to explain as the sample combustion did not yield high quantities of non-condensable gas but could perhaps be due to high concentrations of sulfur in the POM sample inhibiting the graphitization reaction. POM $\Delta^{14}C$ data are reported following the conventions put forth by Stuiver and Polach (1977). POM GB-IRMS $\delta^{13}C$ results are reported in standard per mille (‰) notation and relative to Vienna Pee Dee Belemnite (V-PDB) and have measurement errors of ±0.1-0.2‰. Due to the presence of extraneous carbon on QMA filters, both $\Delta^{14}C$ and $\delta^{13}C$ data were subsequently blank corrected and errors propagated (*see section 2.4*).

Finally, between 1/4 to 1/6 of the remaining filter material was subsampled for elemental analysis (EA) IRMS at the stable isotope facility at University of California, Santa Cruz. EA-IRMS was used for the determination of POM_{susp} carbon and nitrogen (POC_{susp}, PON_{susp}) concentrations, atomic C:N ratio ($C:N_a$), $\delta^{13}C$ and $\delta^{15}N$ values. POM $C:N_a$ was calculated by dividing the wt. %C by wt. %N of combusted material and multiplying by the ratio of molar masses of nitrogen (14.00 g mol^{-1}) to carbon (12.01 g mol^{-1}). Replicate analysis of POM_{susp} $\delta^{13}C$ *via* EA-IRMS at UC Santa Cruz resulted in similar data, with most sample $\delta^{13}C$ values falling within 0.5‰ of those measured by GB-IRMS. The average measured $\delta^{13}C$ offset between UCI and UC Santa Cruz were 0.05 ± 0.82‰ (n=10). Since POM $\delta^{13}C$ values between labs were statistically indistinguishable, we only use those generated by GB-IRMS at UCI herein. EA-IRMS $\delta^{15}N$ values (±0.2-0.4‰; **Table 1**) are referenced relative to air and reported in standard per mille (‰) notation. EA-IRMS isotopic values were corrected using internal acetanilide and Princeton University gelatin working standards.

Finally, POM carbon and nitrogen (POC, PON; μmol L^{-1}) concentrations were determined by EA-IRMS or manometric vacuum line purification (for POC) steps mentioned above and using known filtered seawater volumes. The mass POC or PON measured was multiplied by the corresponding filter sub-fraction used to estimate the total mass of carbon or nitrogen on each 70mm filter. POM concentration errors were propagated using known errors in %C, %N *via* EA-IRMS analysis and assuming a 10% error in total volume filtered.

Isotopic ($\Delta^{14}C$ and $\delta^{13}C$) Blank Correction and Error Propagation

All POM filters contain extraneous carbon contributions associated with filter handling, sampling, and processing. To quantify a procedural blank for POM filters, we ran a blank pre-combusted 70mm QMA filter through our processing methods (including long term storage after baking). Combustion of this procedural blank yielded 61.2 ± 2 μgC. Since only 1/3 filter was subsampled for $\Delta^{14}C$ analysis, an extraneous POC blank of 20.4 ± 2 μgC was assigned to all stations except for Station BB2 (1/4 filter, 15.3 μgC). This blank corresponds to approximately 10 to 16% of the total filter carbon. Blanks of this size are not unheard of due to the increased handling of POM samples (McNichol and Aluwihare, 2007). Since no nitrogen was detected on blank filters, measured POM $\delta^{15}N$ values were not blank corrected.

Measured POM_{susp} $\Delta^{14}C$ and $\delta^{13}C$ values were blank corrected *via* isotopic mass balance (Equations 1 and 2). In all isotopic mass balances, errors were propagated following established methods (Taylor, 1997).

$$(1)\,[POM]_{meas} \times \Delta^{14}C_{meas} = [POM]_{sample} \times \Delta^{14}C_{sample} + [POM]_{blank} \times \Delta^{14}C_{blank}$$

$$(2)\,[POM]_{meas} \times \delta^{13}C_{meas} = [POM]_{sample} \times \delta^{13}C_{sample} + [POM]_{blank} \times \delta^{13}C_{blank}$$

The filter procedural blank (61.2 ± 2 μgC) had a measured $\Delta^{14}C$ value of −801.7 ± 3.5‰. While no procedural blank was established for $\delta^{13}C$, we assumed that the only reasonable source of dead C to the filters could possibly be residual hydrocarbon

TABLE 1 | Summary of measured Baffin Bay hydrographic and POM data.

Station	Region/ Current	Lat. (°N)	Long. (°W)	Depth (m)	Temp. (°C)	Salinity	[POC]† (μM)	±	[PON] (μM)	±	FL (mg m^{-3})	C:N_a	$\delta^{13}C$ (‰)	±	$\delta^{15}N$ (‰)	±	$\Delta^{14}C$ (‰)	±
196	WGC	66.987	-56.061	132	3.98	33.50	9.7	0.5	1.4	0.1	2.56	8.8	-26.0	0.2	4.2	0.3	26.1	10.0
BB15	WGC	68.451	-55.900	494	5.76	33.54	4.1	0.2	0.6	0.1	0.66	10.0	-26.1	0.2	3.8	0.4	8.5	21.4
BB18	WGC	70.091	-52.743	500	4.39	31.40	13.6	0.7	1.7	0.1	11.75	7.7	-21.6	0.1	3.9	0.2	12.2	4.8
227	WGC	70.797	-56.988	538	5.41	33.49	4.5	0.2	0.9	0.1	3.23	8.5	-26.6	0.2	4.3	0.4	15.1	15.0
204	WGC	73.270	-58.000	961	7.30	32.17	5.4	0.3	1.1	0.1	2.68	10.3	-27.8	0.2	5.1	0.3	54.4	13.5
210§	WGC	75.420	-61.561	1173	9.34	32.90	4.3	0.2	N.D.		2.32	N.D.	-26.5	0.2	N.D.		N.D.	
108	NG	76.259	-74.602	445	3.12	31.16	5.9	0.3	0.6	0.1	3.05	11.2	-24.0	0.1	7.2	0.4	2.9	6.5
323	NG	74.159	-80.470	445	2.06	30.14	7.0	0.4	1.0	0.1	4.91	7.7	-25.1	0.2	6.6	0.3	-11.8	9.2
BB2	BIC	72.750	-67.000	2368	2.19	29.81	5.0	0.3	1.0	0.1	5.64	8.7	-29.5	0.2	5.7	0.2	51.6	18.9
224	BIC	70.300	-63.000	2101	0.00	29.68	4.8	0.3	0.6	0.1	1.14	9.0	-28.2	0.2	4.9	0.4	76.8	15.4
193	BIC	66.770	-59.339	959	-0.07	30.54	3.7	0.2	0.6	0.1	0.59	7.8	-28.0	0.2	5.0	0.3	-41.8	9.7

Sea surface temperature (SST), salinity and chlorophyll-a fluorescence (FL) values were generated from the CTD instrument suite (see methods section 2.2). †POM concentrations were determined using total filter mass carbon and nitrogen divided by the estimated volume filtered. POM concentration errors were propagated using known mass and volume uncertainties. POM $\delta^{13}C$ values were determined by closed tube combustion, manometric purification and GB-IRMS at UC Irvine. POM $\delta^{15}N$ and atomic C:N values were determined by EA-IRMS at UC Santa Cruz. $\Delta^{14}C$ values were determined by accelerator mass spectrometry at UC Irvine. High $\pm\Delta^{14}C$ errors were blank corrected and propagated. Lower $\Delta^{14}C$ precision reported here is due to analysis of filter sub-fractions containing little carbon mass (<300 μgC). §$\delta^{15}N$ and $\Delta^{14}C$ values were not determined (N.D.) for Station 210 due to a lack of sample material after repeated attempts at graphitization for $\Delta^{14}C$ analysis.

lubricant present on the Al foil during manufacturing (e.g., combusted to CO_2 that was subsequently absorbed by the QMA filter in its sealed Al foil envelope). Thus, we used $\Delta^{14}C$ and $\delta^{13}C$ blank values of −801.7 ± 3.5‰ and −28.0 ± 1.0‰, respectively in our isotopic mass balances (Cherrier et al., 2014; Walker et al., 2017). Since many of our measured POM $\delta^{13}C$ values were isotopically light (−25 to −29‰), this blank correction resulted in only small corrections to our measured POM $\delta^{13}C$ values (<0.3‰).

RESULTS

POM Concentrations, C:N_a Ratios, and Fluorescence

A summary of all POM concentrations, C:N_a ratios and deep chlorophyll-*a* maximum (DCM) fluorescence values are provided in **Table 1**. For simplicity, we hereafter refer to POM_{susp} as 'POM', unless making a distinction between POM_{sink} and POM_{susp}. We observe large ranges in POC and PON concentrations across Baffin Bay (**Figures 2D, E**). POC concentrations ranged from 4.1 ± 0.2 μM C L^{-1} at station BB15 to 13.6 ± 0.7 μM C L^{-1} at BB18, with an average value of 6.2 ± 3.0 μM C L^{-1} (*n*=11). PON concentrations averaged 1.0 ± 0.4 μM N L^{-1} (*n*=11) and had a smaller range – from 0.6 ± 0.1 μM N L^{-1} at stations BB15, 108, 224 and 193 to 1.7 ± 0.1 μM N L^{-1} at stations BB18. Excluding station BB18, which had the highest POC and PON concentrations, Eastern Baffin Bay had generally higher POC and PON values (5.6 ± 2.3 μM C L^{-1} and 1.0 ± 0.3 μM N L^{-1}, *n*=5) than Western Baffin Bay (4.5 ± 0.7 μM C L^{-1} and 0.7 ± 0.2 μM N L^{-1}, *n*=3), however these differences are not significant to the 95% confidence interval (2σ). Northern station (108, 323) POC concentrations (6.5 ± 0.8 μM C L^{-1}, *n*=2) were significantly higher than Western Baffin Bay.

POM C:N_a ratios ranged from 7.7 to 11.2, with an average value of 9.0 ± 1.2 (*n*=10) (**Figure 2F**). We observed qualitatively higher C:N_a ratios in Northern (9.5 ± 2.3, *n*=2) and Eastern (9.1 ± 1.1, *n*=5) Baffin Bay vs. Western Baffin Bay (8.5 ± 0.6, *n*=3). However, unlike regional POC concentrations, there was no statistically significant difference between POM C:N_a when averaging Baffin Bay regions. Smith Sound (108) had the highest C:N_a value (11.2). Stations with the lowest C:N_a ratios (BB18, 323 and 193) had values approximating Redfield (7.7-7.8).

The DCM, as determined by a water column fluorescence maximum, was present at depths of 20-40m throughout Baffin Bay at the time of sampling. The distribution of DCM fluorescence values reveals clear differences in phytoplankton abundance across Baffin Bay. In general, Western Baffin Bay has higher fluorescence values than Eastern Baffin Bay and some elevated fluorescence values can be seen at the Northern Gateways (**Figure 2C**). We observe the highest fluorescence values (10-15 mg m^{-3}) at coastal Greenland stations adjacent to glacial fjords (**Figure 2C**). At sampled POM stations, fluorescence values at the DCM ranged from 0.59 mg m^{-3} (193) to 11.75 mg m^{-3} (BB18) with an average of 3.8 ± 3.2 mg m^{-3} (*n*=11; **Table 1**). Fluorescence was high at Northern gateway stations (108, 323; 3.05 and 4.91 mg m^{-3}, respectively) and along Baffin Island at 70°N, with fluorescence decreasing into the centre of Baffin Bay from 5.64 mg m^{-3} at station BB2 to 1.14 at station 224. While fluorescence had a high range in Baffin Bay, averages of our individual stations by region (East, West and Northern) did not suggest significant regional differences – at least for the POM stations we sampled.

POM_{susp} $\delta^{13}C$, $\delta^{15}N$ and $\Delta^{14}C$ Values

POM $\delta^{13}C$ and $\delta^{15}N$ values comprise a total range of 7.8‰ and 3.4‰, respectively (**Table 1**). POM $\delta^{13}C$ ranged from −21.6‰ at station BB18 to −29.5‰ at BB2, with an average value of −26.3 ± 2.1‰ (*n* = 11). Negative POM $\delta^{13}C$ values were observed in Central-West Baffin Bay (−29.6 ± 0.8‰, *n* = 3). Excluding the significantly less negative POM $\delta^{13}C$ value from BB18, higher POM $\delta^{13}C$ values (−26.2 ± 0.3‰, *n* = 3) were present in Southeastern Baffin Bay (196, BB15, 227). POM $\delta^{15}N$ ranged from +3.8‰ at BB15 to +7.2‰ at 108, with an average value of

+5.1 ± 1.1‰ (n = 10). The highest POM $\delta^{15}N$ values were observed in the Northern gateways (108 and 323; $\delta^{15}N$ = +6.9 ± 0.3‰, n = 2). The elevation of these Northern POM $\delta^{15}N$ values was statistically significant (at ±2σ) from Eastern (+4.3 ± 0.5‰, n =5) and Western Baffin Bay (+5.2 ± 0.4‰, n = 3) regions. The lowest values were observed in the Southeastern region of Baffin Bay (196, BB15, BB18, 227, $\delta^{15}N$ = +4.1 ± 0.2‰, n = 4).

Blank-corrected POM $\Delta^{14}C$ values span a ~119‰ range, with an average POM $\Delta^{14}C$ value of +19.4 ± 34.6‰ (n = 10; **Table 1**). While 224 had the highest POM $\Delta^{14}C$ value (+76.8 ± 15.4‰), BB2 and 204 also had very positive POM $\Delta^{14}C$ values (+51.6 ± 18.9‰ and +54.4 ± 13.5‰, respectively). Stations 193 and 323 were the only stations with negative POM $\Delta^{14}C$ values (−41.8 ± 9.7‰ and −11.8 ± 9.2‰, respectively). The remaining stations (196, BB15, BB18, 227, 108; n = 5) fall in a relatively narrow $\Delta^{14}C$ range between +2.9 ± 6.5‰ (108) and +26.1 ± 10.0‰ (196).

DISCUSSION

POM Concentrations, C:N_a Ratios and Diagenetic State

POC and PON concentrations were high throughout Baffin Bay (**Table 1**), consistent with previous studies showing high POM concentrations and rates of primary production in Baffin Bay (Lalande et al., 2009; Ardyna et al., 2011). POC and PON concentrations were not significantly correlated to SST or salinity (R^2 <0.0003), suggesting a biological control on the elemental composition of Baffin Bay POM. This is different from many studies showing water mass advection and upwelling as strong predictors of POM stoichiometry (e.g., Hill and Wheeler, 2002; Walker and McCarthy, 2012). Along the WGC extension, POC and PON increase from station BB15 (4.1 μM C L^{-1}; 0.6 μM N L^{-1}) to stations 227 and 204 (4.5 and 5.4 μM C L^{-1}; 0.9 and 1.1 μM N L^{-1}), respectively (**Figures 2D, E**). Low [POM] along the Davis Strait and Southwest Greenland shelf could be the result of nutrient limitation, as phytoplankton blooms in regions occur earlier in the year due to ice break-up (Tang et al. 2004). It is also conceivable that aged N. Atlantic waters flowing into Baffin Bay in Eastern Davis Strait are iron-limited relative to Northern Stations with high glacial influx. Increased [POC] and [PON] along the WGC extension may result from elevated micronutrient delivery from the Greenland ice sheet. For example, we observe the highest fluorescence (11.75 mg m^{-3}) and POM concentrations (13.6 μM C L^{-1}, 1.7 μM N L^{-1}) at Station BB18 in the Vaigat Fjord. These high values are indicative of a local phytoplankton bloom at the time of sampling, stimulated by summer glacial discharge (Arrigo, et al., 2017). Northern gateway stations (108, 323) show further increases in POC concentration (5.9-7.0 μM C L^{-1}) and fluorescence values (**Figures 2C, D**; **Table 1**).

POM concentrations decrease south of central Baffin Bay within the BIC – from BB2 (5.0 μM C L^{-1}; 1.0 μM N L^{-1}) to 224 (4.8 μM C L^{-1}; 0.6 μM N L^{-1}) and 193 (3.7 μM C L^{-1}; 0.6 μM N L^{-1}), respectively (**Figure 2D**). This decrease in [POM] is also reflected in decreasing DCM fluorescence values (**Table 1**). Whereas Stations 224 and BB2 (Western Baffin Bay) had nearly identical POM concentrations, these stations had quite different DCM fluorescence values – suggesting differences in autotrophic POM abundance at the time of sampling. Higher BB2 fluorescence values may indicate higher primary production fueled by Pacific nutrients from Lancaster Sound (Lehmann et al., 2019). Station 224 is located "downstream" in the BIC extension, possibly indicating lower POM concentrations resulting from POM_{susp} degradation within the BIC.

POM C:N_a ratios are valuable indicators of POM diagenetic state (e.g., Cowie and Hedges, 1994) and provide useful information regarding autochthonous vs. allochthonous POM contributions and POM chemical "freshness". The stoichiometric model of Redfield describes the elemental composition of marine organic matter and can be used generally to link the production of new POM to nutrients. The ratio of carbon to nitrogen in POM produced by marine phytoplankton generally follows the Redfield ratio of 106:16:1 (C:N:P; Redfield, 1958), or ~7.7 as C:N_a. Deviation from standard Redfield stoichiometry can be used as an indicator of nutrient limitation, or the relative diagenetic state (i.e., chemical "freshness") of POM. The relationship between organic matter C:N_a ratio and degradation state have described previously for dissolved organic matter (DOM), suspended vs. sinking POM, and marine sediments (Cowie and Hedges, 1994; Loh and Bauer, 2000; Hopkinson and Vallino, 2005; Walker and McCarthy, 2012; Walker et al., 2014; Walker et al., 2016). Here, POM with low C:N_a ratios (especially those approximating Redfield) represents recently produced and chemically "fresh" material. In contrast, POM with high C:N_a, typically represents older, "degraded" POM contributions either from allochthonous sources or *in situ* degradation of fresh material (e.g., heterotrophic re-working of a senescent phytoplankton bloom). In this way, C:N_a ratios are a useful tool for evaluating the relative diagenetic state of marine POM.

In Baffin Bay, all POM C:N_a (7.7 to 11.2) had canonical "marine" values, equal to or higher than regular Redfield ratios (**Figure 2F**). The mean value of C:N_a in this study (9.0 ± 1.2) closely resembles POM C:N_a (8.9) previously reported for the Eastern Greenland shelf, in which high C:N_a was attributed to nitrate limitation, and the dominance of carbon-rich diatoms (Daly, et al., 1999). Our POM C:N_a values together with observed seawater salinities, precludes significant terrestrial (C:N_a ~40) POM contributions. High POM C:N_a values (10.0-11.2) at stations 108, 204, and BB15 potentially indicate higher contributions of degraded POM. Previously work has shown POM C:N_a ratios in the North Water polynya (i.e., near Station 108) found C:N_a increases in early spring and summer with concomitant increases in irradiance and decreases in nitrate (Mei, et al., 2005). Prolonged periods of high irradiance can lead to elevated POM C:N_a under nitrogen limitation, as phytoplankton synthesize N-poor photoprotective pigments (Levasseur and Therriault, 1987; Dubinsky and Berman-Frank, 2001). We observed Redfield POM C:N_a values (7.7) at three stations BB18, 323, and 193. These stations comprise a wide spatial range and are found in distinct marine ecosystems in Baffin Bay. As previously mentioned, station BB18 is in the glacial meltwater-dominated Vaigat Fjord, whereas stations 323 is in one of Baffin Bay's Northern gateways. Surprisingly, Station

193, the southernmost extent of the BIC, had very low [POM] concentrations. Thus, while low C:N_a values are often associated with abundant "fresh" POM produced under nutrient-replete conditions, this is not always the case. One explanation of these data could be a non-traditional allochthonous POM_{susp} source. For example, POM_{sink} contributions at Station 193 could explain low C:N_a and low POC concentrations. Alternatively, re-suspension and lateral advection of recently exported ("fresh") POM from sediments could also explain this low C:N_a ratio. Such re-suspended sedimentary organic carbon (SOC) contributions to POM_{susp} have been observed previously in the coastal ocean (e.g., Walker et al., 2014).

Sources of Particulate Organic Carbon and Nitrogen in Baffin Bay

Our measured POM $\delta^{13}C$ values (−21.6‰ to −29.5‰) are consistent with previous work from Baffin Bay showing the prevalence of both fast-growing plankton in glacial meltwater, in addition slow-growing phytoplankton from high latitudes with negative $\delta^{13}C$ values (Goericke and Fry, 1994). Similarly, the large range in POM $\delta^{15}N$ values (~3.4‰) can likely be attributed to disparate nitrate sources in Baffin Bay (Lehmann et al., 2019). For example, the advection of surface water masses (e.g. Atlantic, Arctic, Pacific/CAA) in Baffin Bay deliver allochthonous nutrients and POM_{susp} to the region. While annual freshwater contributions to Baffin Bay are estimated to be 100 km^3 y^{-1} (Shiklomanov et al., 2021), the salinity at our stations was never below 29.6, and outside of station BB18, was always associated with the BIC (e.g., dominated by Arctic outflow water; Azetsu-Scott et al., 2012). This, combined with low POM C:N_a found at all stations, precludes significant contributions of terrestrial POM affecting our $\delta^{13}C$ values.

We observe several trends in POM $\delta^{13}C$ and $\delta^{15}N$ values in relation to surface water salinity (**Figures 3A, B**). Our WGC stations 196, BB15, 227, 204, and 210 have similar salinity (>32.17), $\delta^{13}C$ and $\delta^{15}N$ values (**Figures 3A, B**). WGC POM $\delta^{13}C$ values are generally consistent with canonical POM $\delta^{13}C$ values for high-latitude phytoplankton ($\delta^{13}C$ = −24 to −26‰; De La Vega et al., 2019). For example, excluding the most negative WGC POM $\delta^{13}C$ value (204; −27.8‰), the average WGC POM $\delta^{13}C$ value is −26.3 ± 0.3‰ (n = 4). These stations similarly cluster together in $\delta^{13}C$-$\delta^{15}N$ space, with an average $\delta^{15}N$ = 4.1 ± 0.3‰ (n = 3; **Figure 3B**). Thus, we conclude that for most WGC stations, POM $\delta^{13}C$ and $\delta^{15}N$ values can be attributed to the prevalence of high-latitude phytoplankton utilizing the inflow of WGC and Irminger Current water as their main $\delta^{15}NO_3$ source (+4-6‰; Sherwood et al., 2021). Station 204 has negative POM $\delta^{13}C$ (−27.8‰) and positive $\delta^{13}N$(+5.1‰) values, but falls on a continuum between Atlantic WGC water to Central Baffin Bay isotopic endmembers (**Figure 3B**). We believe these isotopic trends between the WGC and Central Baffin Bay are due to both mixing and recycling of PON and/or NO_3^- contributing the $\delta^{15}N$ enrichment of POM.

BIC Stations (BB2, 224, and 193) have low SST (0-2°C) and salinity (S<30.54), negative POM $\delta^{13}C$ (−28.6 ± 0.81‰, n = 3) and intermediate $\delta^{15}N$ (+5.2 ± 0.4‰, n = 3) values (**Table 1**; **Figures 3A, B**). Negative BIC POM $\delta^{13}C$ values are consistent with slow-growing, cold-water phytoplankton as a major POM source. Station BB2 has the highest $\delta^{15}N$ (+5.7‰) outside of the Northern gateway stations and is influenced by the Northern BIC. Similarly, high POM $\delta^{15}N$ values for Stations 224 and 193 in the BIC are likely influenced by the Pacific $\delta^{15}NO_3$ propagating south from Lancaster Sound. This interpretation would be consistent with recent work showing the Pacific $\delta^{15}NO_3$ signature is not only entrained into the BIC, but subsequently carried into the Labrador Current (Sherwood et al., 2021).

POM at the Northern gateways (323, 108) had the highest $\delta^{15}N$ values of +6.6‰ and +7.2‰ and, excluding station BB18, the highest $\delta^{13}C$ values of −25.1‰ and −24.0‰ (**Figures 3A, B**). Both stations likely contain moderate contributions of sea-ice algae POM. Station 323 in Lancaster Sound is a gateway for entering Pacific water that is a precursor to the BIC (S = 30.14; Münchow et al., 2015). Station 323 had more positive $\delta^{13}C$ (−25.1‰) than other BIC stations (BB2, 224, 193; −28.6 ± 0.81‰) that can likely be attributed to seasonal variability and/or local sea-ice algae POM contributions. These results are consistent with previous Station 323 POM $\delta^{13}C$ values of −24.2‰ reported in October 2011 that were also attributed to sea-ice algae (Roy, et al., 2015). Station 108 in the Smith Sound (S = 31.16) comprises several water mass contributions, including the WGC, Arctic water from Nares Strait and glacial meltwater from coastal Greenland. Previous POM $\delta^{13}C$ values from the North Water polynya (near Station 108) were −22.3‰ and −27.6‰ for samples collected in April 1998 and October 2011, respectively (Hobson et al., 2002; Roy et al., 2015). Thus, Northern Baffin Bay POM likely contains more sea-ice algae POM in spring following ice break-up, and fewer contributions of positive $\delta^{13}C$ sea-ice algae in the fall (−20 to −18‰; Hobson et al., 2002; De La Vega et al., 2019). The high POM $\delta^{15}N$ values we observe from 323 and 108 are clearly influenced by the influx of high $\delta^{15}N$ Pacific nutrients (NO_3^-) entering Baffin Bay *via* the CAA as has been previously observed for Lancaster Sound (e.g. Lehmann et al., 2019). Together our POM $\delta^{13}C$ and $\delta^{15}N$ values from station 323 and 108 suggest Pacific nutrients, a polar marine plankton and sea-ice algae as the dominant POM carbon and nitrogen sources in Northern Baffin Bay.

Station BB18 is a clear outlier in the sample set and had the highest $\delta^{13}C$ value (−21.6‰) and one of the lowest $\delta^{15}N$ values (+3.9‰; **Figures 3A, B**). Station BB18 is located within the Vaigat fjord and had the lowest salinity of all coastal Greenland stations (S=31.40) and highest POM concentrations. The stable isotopic signature of BB18 POM can be attributed to high phytoplankton growth in the stratified fjord waters at the time of sampling (**Figure S1–4**). BB18 POM $\delta^{15}N$ is similar to Atlantic $\delta^{15}NO_3$, indicating an influx of Atlantic nitrate and high glacial meltwater delivery of iron can fuel high rates of primary production, as has been observed previously (Bhatia, et al., 2013; Meire, et al., 2017).

Disparate POM $\Delta^{14}C$ Sources and Cycling Rates

To further elucidate POM sources and cycling in Baffin Bay, here we discuss POM radiocarbon ($\Delta^{14}C$) values. Due to the short residence time of sinking and suspended POM in the water

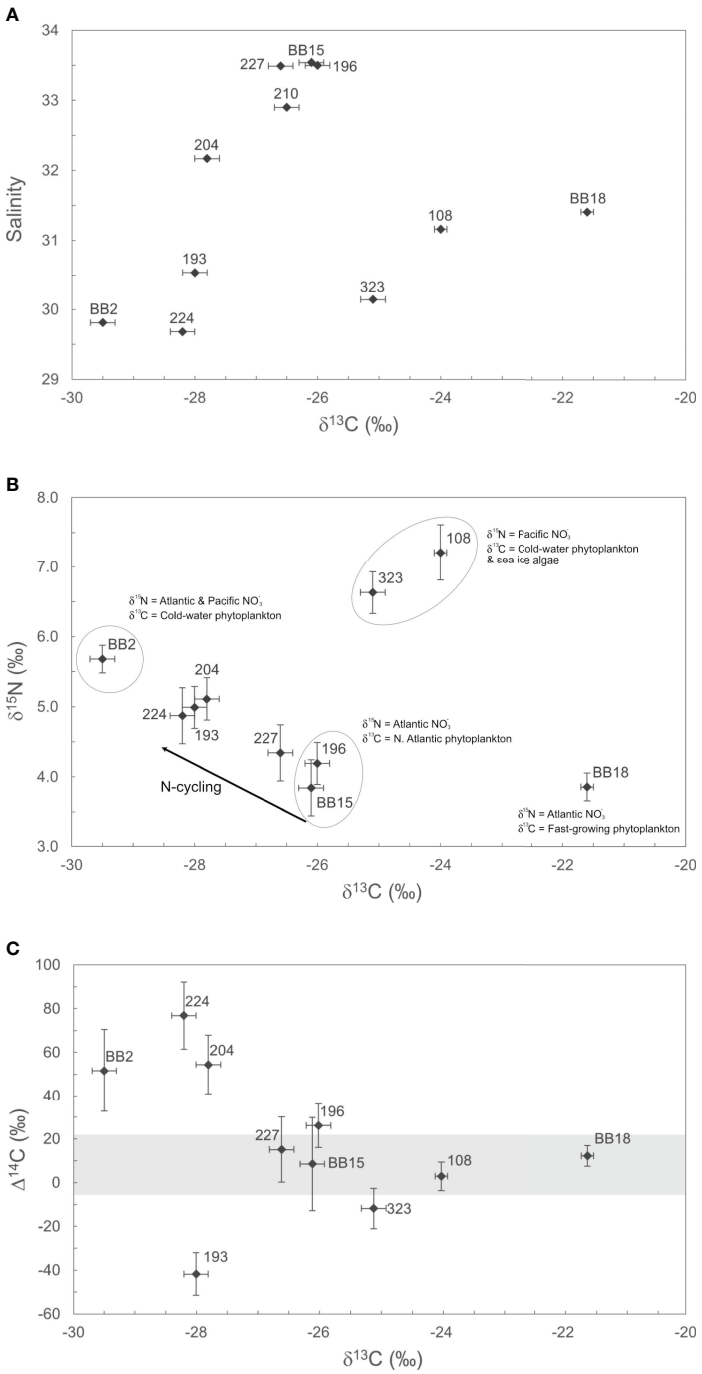

FIGURE 3 | Isotopic ($\delta^{13}C$, $\delta^{15}N$, $\Delta^{14}C$) composition of POM in Baffin Bay. **(A)** The relationship between POM $\delta^{13}C$ values (‰) and Salinity (PSU) is shown. Salinity is used here to highlight differences in POM sources *via* water mass origin. **(B)** The stable isotopic ($\delta^{13}C$, $\delta^{15}N$) composition of POM is shown, with observed isotopic endmembers. **(C)** the distribution of POM $\Delta^{14}C$ and $\delta^{13}C$ values is shown. The horizontal grey bar represents the full range in measured DIC $\Delta^{14}C$ values for Baffin Bay (Zeidan et al., 2022). For all plots, isotope valued errors (± 1σ) are listed in **Table 1**.

column (days to years), POM $\Delta^{14}C$ values are largely determined by carbon *sources* as opposed to *ages via* radioactive decay. Possible POM $\Delta^{14}C$ sources in Baffin Bay are: i) modern surface and pre-aged, upwelled DIC used in primary production, ii) modern or pre-aged allochthonous POM contributions advected from other regions, iii) modern or "bomb" terrestrial POM, iv) pre-aged glacial meltwater, v) re-mobilization of ancient permafrost and vi) pre-aged re-

suspended SOC. Marine POM with $\Delta^{14}C$ values similar to that of surface DIC $\Delta^{14}C$ indicates a prevalence of *in situ* primary production as a major POM source (e.g., POM with a higher proportion of phytoplankton-derived, autochthonous POM) and POM $\Delta^{14}C$ values that fall outside the range of DIC $\Delta^{14}C$ could indicate allochthonous POM contributions with pre-aged (negative $\Delta^{14}C$) or "bomb" (positive $\Delta^{14}C$) signatures.

The ~119‰ range in POM $\Delta^{14}C$ values we observe throughout Baffin Bay is both striking and somewhat unexpected given the overall "freshness" of POM samples (i.e., generally low C:N_a ratios, high POM concentrations) and their stable isotopic composition largely indicating planktonic carbon and local nutrient sources (**Figures 2**, **3**). This range in surface POM $\Delta^{14}C$ values is also especially high for a single oceanographic region. For example, the range in POM $\Delta^{14}C$ values we observe exceeds the range previously reported from an intense California upwelling system (~101‰; Walker et al., 2014). Whereas most POM $\Delta^{14}C$ samples fall within the range of measured surface DIC $\Delta^{14}C$ values, four of our POM $\Delta^{14}C$ values fall outside this range – indicating allochthonous POM contributions (**Figure 3C**).

Three stations (BB2, 224, 204) had higher $\Delta^{14}C$ values (> ± 2σ) than surface DIC $\Delta^{14}C$ (**Figure 3C**). Stations BB2 and 224 are in the central gyre, with $\Delta^{14}C$ of +51.6±18.9‰ and +76.8 ±15.4‰, respectively. Station 204, near coastal Greenland, had $\Delta^{14}C$ of +54.5±13.5‰. Measured surface DIC $\Delta^{14}C$ values for BB2, 224, and 204, are +5.6‰, +14.1‰, and +14.2‰, respectively (errors ±1.5‰; Zeidan et al., 2022). This large disparity between DIC $\Delta^{14}C$ and POC $\Delta^{14}C$ indicates the clear presence of allochthonous POM with an atmospheric "bomb" $\Delta^{14}C$ signature within central Baffin Bay. These positive POM $\Delta^{14}C$ values likely arise from POM contributions that were synthesized during periods of high atmospheric ^{14}C. This would require POM in central Baffin Bay to be decades old. Atmospheric $\Delta^{14}CO_2$ was last at +80‰ approximately 16 years before our sampling (e.g., between 2001-2003; Levin et al., 2010) and marine DIC reached this value in the 1970's (Druffel, 1996). Thus, our results suggest that a portion of the POM_{susp} pool may be retained in the central gyre of Baffin Bay and possibly recycled in the surface for several decades. Additional sources of bomb $\Delta^{14}C$ could be advected POM from the North Atlantic (+100 to +140‰ in 1992; Druffel et al., 1992), or *via* the CAA (Beaufort Sea DIC $\Delta^{14}C$ = +82‰ in 2012; Druffel et al., 2017). However, neither our Northern nor Southern gateway stations (323, 108, 193, 196) contained highly positive POM or DIC $\Delta^{14}C$ values. In addition, POM $\delta^{13}C$ values from these three stations (−28.5 ± 0.9‰) are consistent with slow-growing, cold-water phytoplankton from higher latitudes (Holding et al., 2017). Thus, it is more likely that these cold-water phytoplankton, along with some pre-existing bomb ^{14}C persisting in the central gyre, are responsible for our observed POM $\Delta^{14}C$ and $\delta^{13}C$ values in central Baffin Bay. Lastly, station 204 on the north-central Greenland shelf, more closely resembles BIC stations isotopically ($\Delta^{14}C$, $\delta^{13}C$, $\delta^{15}N$), suggesting a similar POM source to central Baffin Bay at the time of sampling. Surface admixture of WGC waters with surface water from the gyre as evidenced from its lower salinity value (32.17) relative to other WGC stations (>32.9) is a distinct probability.

We observe a highly negative POM $\Delta^{14}C$ value at station 193 (−41.8±9.7‰). This POM $\Delta^{14}C$ value is significantly different from surface *in situ* DIC $\Delta^{14}C$ (+15.6‰; Zeidan et al., 2022). As mentioned above, this sample had the low POM concentrations and C:N_a. We believe contributions of resuspended SOC to Station 193 POM the be the most reasonable explanation of these data. SOC contributions to POM are now widely recognized as a common pathway through which ^{14}C-depleted carbon can be transported laterally from the coastal ocean and incorporated into the POM pool (Rau et al., 1986; Druffel et al., 1992; Druffel et al., 1996; Druffel et al., 1998; Hwang et al., 2005; Hwang et al., 2010; Walker et al., 2014). SOC $\delta^{13}C$ values for the Arctic average −22‰ to −26‰, with end-member values being −27 to −28‰ (Drenzek et al., 2007; Magen et al., 2010; Roy et al., 2015). Thus, the Station 193 $\delta^{13}C$ value of −28.0‰ is plausible. Additionally, C:N (wt/wt) ratios of sediments from the Bering and south Chukchi seas showed open shelf sediments generally had C:N less than 7 (Naidu, et al., 1993). The C:N ratio for station 193 when calculated by weight is 6.7. From these multiple lines of evidence, we hypothesize POM at station 193 contains resuspended SOC contributions, albeit perhaps recently exported, "fresh" SOC with a low C:N_a. Future work on the shelf/slope of Davis Strait could target re-suspended sediment POM contributions through the use of %Al or sedimentary biomarker measurements.

While the deviation of POM $\Delta^{14}C$ from *in situ* DIC $\Delta^{14}C$ values reveal an interesting diversity of Baffin Bay POM sources and cycling, most of our POM $\Delta^{14}C$ fall within the range of measured surface DIC $\Delta^{14}C$ (**Figure 3C**). All these samples are from WGC (196, BB15, 227, BB18), or the Northern gateway (108, 323) stations. Here, POM $\Delta^{14}C$ values are statistically indistinguishable from *in situ* DIC $\Delta^{14}C$ (± 2σ). The similarity of POM and DIC $\Delta^{14}C$ values at these locations has important implications for carbon cycling within Baffin Bay. For example, these data suggest that most of the *de novo* POM synthesis in Baffin Bay occurs along coastal Greenland fueled by Atlantic macronutrients (nitrate) and glacial micronutrients (iron). This primary production largely governs export production within Baffin Bay. With future climate change scenarios indicating warming of Baffin Bay and enhanced Greenland ice sheet melting, favoring large centric diatoms, and extended ice-free conditions (Krawczyk et al., 2021), it stands to reason that these regions of Baffin Bay will continue to support most POM export and burial in Baffin Bay.

SUMMARY AND IMPLICATIONS

As a detrital organic matter reservoir, POM_{susp} represents a complex geochemical mixture of non-living materials. The chemical composition of POM does not always match that of resident plankton communities and can be strongly influenced by pre-aged, allochthonous POM contributions. The bulk elemental and isotopic composition of POM presented in this

study provides us with a new understanding of the sources, diagenetic state, and the geochemical impact of POM in Baffin Bay. These first POM $\Delta^{14}C$ data, together with $\delta^{13}C$ and $\delta^{15}N$ suggest a diversity of POM carbon and nitrogen sources in Baffin Bay. Overall, POM isotopic $\delta^{13}C$, $\delta^{15}N$, and $\Delta^{14}C$ signatures are controlled by surface water mass circulation, local algal communities and nutrient sources, and to a lesser extent, contributions from allochthonous POM sources. Primary production fueled by Atlantic nitrate is a major source of new POM in Eastern Baffin Bay. In particular, the coastal fjords along Greenland are unique, high-productivity environments decoupled from the broader surface circulation-driven POM trends. The Northern gateways, through which Arctic and Pacific waters flow into Baffin Bay, also show considerable POM contributions from *in situ* production from both high latitude phytoplankton and sea-ice algae utilizing Pacific nitrate. Stations in central Baffin Bay are strongly influenced by the cold and fresh BIC, with POM contributions mainly from slow-growing cold water phytoplankton again fueled by Pacific nitrate entering Baffin Bay *via* the CAA.

Measured POM $\Delta^{14}C$ values add to this emerging picture of POM cycling in several ways. First, POM $\Delta^{14}C$ within the WGC and Northern gateways matches that of *in situ* DIC $\Delta^{14}C$, suggesting that primary production results in ^{14}C-modern POM in these regions. In this way, these regions serve as the primary drivers POM export and carbon cycling in Baffin Bay. Second, POM with highly positive $\Delta^{14}C$ values is found in the central gyre – indicating the presence of bomb ^{14}C. POM synthesized in the western Canadian Arctic (i.e., Beaufort Sea) and advected through the CAA represents a possible source of positive POM $\Delta^{14}C$ to Baffin Bay. Other possibilities could include recycling of bomb ^{14}C within the central Baffin Bay POM_{susp} reservoir or influx of terrestrial POM. However, stable isotopic ($\delta^{13}C$, $\delta^{15}N$) signatures and $C{:}N_a$ ratios do not support the latter. The former scenario would necessitate the decadal persistence of a recalcitrant POM_{susp} fraction in the gyre. None of these scenarios have simple explanations and further work is required to confirm the persistence of bomb ^{14}C in central Baffin Bay. Finally, POM exiting Baffin Bay *via* the western Davis Strait has highly negative $\Delta^{14}C$ values. Together with [POC], [PON] and $C{:}N_a$ data, we believe resuspended sediments were a major contributor to this POM sample. Such contributions are supported by previous geochemical and global ^{14}C studies of the POM pool. The export of POM with negative $\Delta^{14}C$ values has important implications for the geochemical impact of the BIC on the Labrador Sea. If entrained in North Atlantic Deep Water during its formation, this could represent a previously unrecognized source of ^{14}C-depleted POM to the deep ocean.

POM isotopic ($\Delta^{14}C$, $\delta^{13}C$, $\delta^{15}N$) data remain sparse for this region, yet provide invaluable baseline data for evaluating carbon and nitrogen cycling in a rapidly changing Arctic region. Future work focused on increasing the spatial resolution of POM $\Delta^{14}C$ observations, together with compound-class or compound specific isotopic analysis, would improve our understanding of the cycling of fresh vs. recalcitrant POM components in Baffin Bay. These measurements have proven useful in parsing out individual allochthonous POM components, such as contributions from resuspended sediment (e.g., Roland et al., 2008).

DATA AVAILABILITY STATEMENT

The original contributions presented in the study are included in the article/**Supplementary Material**. Further inquiries can be directed to the corresponding author.

AUTHOR CONTRIBUTIONS

BW conceived the hypothesis and the objectives of this investigation. BW collected the POM samples at sea. AF processed the samples in the lab for isotopic analysis with BW. AF wrote the manuscript with input from BW. All authors contributed to the article and approved the submitted version.

FUNDING

Funding for this project was provided by the Natural Sciences and Engineering Research Council (NSERC) of Canada through a Discovery Grant, Accelerator and Launch Supplements (RGPIN-2020-06501, RGPAS-2020-00071, DGECR-2020-00256; to BW). A portion of this work was supported through the Canada Research Chairs program (to BW).

ACKNOWLEDGMENTS

We would like to thank Chief Scientist Alexandre Forest, Anissa Merzouk and the staff of Amundsen Science and the crew of the CCGS *Amundsen* for the opportunity to participate in the 2019 research cruise and for providing CTD data. We thank Drs. Cara Manning and Brent Else for their help in coordinating the sampling and logistics of the Biogeochemistry groups aboard the CCGS *Amundsen*. We thank Drs. Xiaomei Xu and John Southon of the UC Irvine Keck Carbon Cycle AMS lab for their expertise and help with ^{14}C analysis of our graphite targets and GB-IRMS $\delta^{13}C$ measurements. We thank Colin Carney at UC Santa Cruz for additional POM stable isotope ($\delta^{13}C$, $\delta^{15}N$) measurements.

SUPPLEMENTARY MATERIAL

The Supplementary Material for this article can be found online at: https://www.frontiersin.org/articles/10.3389/fmars.2022.846025/full#supplementary-material

REFERENCES

Ardyna, M., Gosselin, M., Michel, C., Poulin, M., and Tremblay, J.-E. (2011). Environmental Forcing of Phytoplankton Community Structure and Function in the Canadian High Arctic: Contrasting Oligotrophic and Eutrophic Regions. *Mar. Ecol. Prog. Ser.* 442, 37–57. doi: 10.3354/meps09378

Arrigo, K., and Dijken, G. (2015). Continued Increases in Arctic Ocean Primary Production. *Prog. Oceanogr.* 136, 60–70. doi: 10.1016/j.pocean.2015.05.002

Arrigo, K., Dijken, G., Castelao, R., Luo, H., Rennermalm, Å, Tedesco, M., et al. (2017). Melting Glaciers Stimulate Large Summer Phytoplankton Blooms in Southwest Greenland Waters. *Geophys. Res. Lett.* 44 (12), 6278–6285. doi: 10.1002/2017GL073583

Azetsu-Scott, K., Petrie, B., Yeats, P., and Lee, C. (2012). Composition and Fluxes of Freshwater Through Davis Strait Using Multiple Chemical Tracers. *Geophys. Res. Ocean.* 117, C12011. doi: 10.1029/2012JC008172

Bauer, K., and Druffel, E. (1998). Ocean Margins as a Significant Source of Organic Matter to the Deep Open Ocean. *Nature* 392, 482–485. doi: 10.1038/33122

Beaupré, S. (2019). "Radiocarbon-Based Insights Into the Biogeochemical Cycles of Marine Dissolved and Particulate Organic Carbon," in *Encyclopedia of Ocean Sciences*. Eds. K. Cochran, H. Bokuniewicz and P. Yager (London: Academic Press), 245–252. doi: 10.1016/B978-0-12-409548-9.09522-1

Benner, R., and Amon, R. M. W. (2015). The Size-Reactivity Continuum of Major Bioelements in the Ocean. *Ann. Rev. Mar. Sci.* 7, 185–205.

Bhatia, M., Das, S., Xu, L., Charette, M., Wadham, J., and Kujawinski, E. (2013). Organic Carbon Export From the Greenland Ice Sheet. *Geochim. Cosmochim. Acta* 109, 329–344. doi: 10.1016/j.gca.2013.02.006

Bhatia, M., Kujawinski, E., Das, S., Breier, C., Henderson, P., and Charette, M. (2013). Greenland Meltwater as a Significant and Potentially Bioavailable Source of Iron to the Ocean. *Nat. Geosci.* 6, 274–278. doi: 10.1038/ngeo1746

Brown, Z., Casciotti, K., Pickart, R., Swift, J., and Arrigo, K. (2015). Aspects of the Marine Nitrogen Cycle of the Chukchi Sea Shelf and Canada Basin. *Deep. Sea. Res. Part II Top. Stud. Oceanogr.* 118, Part A, 73–87. doi: 10.1016/j.dsr2.2015.02.009

Brown, K., McLaughlin, F., Tortell, P., Varela, D., Yamamoto-Kawai, M., Hunt, B., et al. (2014). Determination of Particulate Organic Carbon Sources to the Surface Mixed Layer of the Canada Basin, Arctic Ocean. *J. Geophys. Res. Ocean.* 119 (2), 1084–1102. doi: 10.1002/2013JC009197

Buesseler, K., Boyd, P., Black, E., and Siegel, D. (2020). Metrics That Matter for Assessing the Ocean Biological Carbon Pump. *Proc. Natl. Acad. Sci. U. S. A.* 117 (18), 9679–9687. doi: 10.1073/pnas.1918114117

Caron, G., Michel, C., and Gosselin, M. (2004). Seasonal Contributions of Phytoplankton and Fecal Pellets to the Organic Carbon Sinking Flux in the North Water (Northern Baffin Bay). *Mar. Ecol. Prog. Ser.* 283, 1–13. doi: 10.3354/meps283001

Cauwet, G. (1981). Chapter 4 Non-Living Particulate Matter. *Elsevier. Oceanogr. Ser.* 31, 71–89. doi: 10.1016/S0422-9894(08)70326-X

Cherrier, J., Sarkodee-Adoo, J., Guilderson, T., and Chanton, J. (2014). Fossil Carbon in Particulate Organic Matter in the Gulf of Mexico Following the Deepwater Horizon Event. *Environ. Sci. Technol. Lett.* 1 (1), 108–112. doi: 10.1021/ez400149c

Close, H., Shah, S., Ingalls, A., Diefendorf, A., Brodie, E., Hansman, R., et al. (2013). Export of Submicron Particulate Organic Matter to Mesopelagic Depth in an Oligotrophic Gyre. *Proc. Natl. Acad. Sci. U. S. A.* 110 (31), 12565–12570. doi: 10.1073/pnas.1217514110

Cowie, G., and Hedges, J. (1994). Biochemical Indicators of Diagenetic Alteration in Natural Organic Matter Mixtures. *Nature* 369, 304–307. doi: 10.1038/369304a0

Daly, K., Wallace, D., Smith, W., Skoog, A., Lara, R., Gosselin, M., et al. (1999). Non-Redfield Carbon and Nitrogen Cycling in the Arctic' Effects of Ecosystem Structure and Dynamics. *J. Geophys. Res.* 104, 3185–3199. doi: 10.1029/1998JC900071

De La Vega, C., Jeffreys, R., Tuerena, R., Ganeshram, R., and Mahaffey, C. (2019). Temporal and Spatial Trends in Marine Carbon Isotopes in the Arctic Ocean and Implications for Food Web Studies. *Glob. Change Biol.* 25, 4116–4130. doi: 10.1111/gcb.14832

Denman, K., Brasseur, G., Chidthaisong, A., Ciais, P., Cox, P., Dickinson, R., et al. (2007). "Couplings Between Changes in the Climate System and Biogeochemistry," in *Climate Change 2007: The Physical Science Basis. Contribution of Working Group I to the Fourth Assessment Report of the Intergovernmental Panel on Climate Change*. Eds. S. Solomon, D. Qin, M. Manning, Z. Chen, M. Marquis, K. Averyt and H. Miller (Cambridge, UKNew York, USA: Cambridge University Press), 499–587.

Descolas-Gros, C., and Fontugne, M. (1990). Stable Carbon Isotope Fractionation by Marine Phytoplankton During Photosynthesis. *Plant Cell Environ.* 13, 207–218. doi: 10.1111/j.1365-3040.1990.tb01305.x

Drenzek, N., Montlucon, D., Yunker, M., Macdonald, R., and Eglinton, T. (2007). Constraints on the Origin of Sedimentary Organic Carbon in the Beaufort Sea From Coupled Molecular 13C and 14C Measurements. *Mar. Chem.* 103, 146–162. doi: 10.1016/j.marchem.2006.06.017

Druffel, E. (1996). Post-Bomb Radiocarbon Records of Surface Corals from the Tropical Atlantic Ocean. *Radiocarbon* 38 (3), 563–572. doi: 10.1017/S0033822200030095

Druffel, E., Bauer, J., Williams, P., Griffin, S., and Wolgast, D. (1996). Seasonal Variability of Particulate Organic Radiocarbon in the Northeast Pacific Ocean. *J. Geophys. Res. Ocean.* 101 (C9), 20543–20552. doi: 10.1029/96JC01850

Druffel, E., Griffin, S., Bauer, J., Wolgast, D., and Wang, X.-C. (1998). Distribution of Particulate Organic Carbon and Radiocarbon in the Water Column From the Upper Slope to the Abyssal NE Pacific Ocean. *Deep. Sea. Res. Part II Top. Stud. Oceanogr.* 45 (4-5), 667–, 687. doi: 10.1016/S0967-0645(98)00002-2

Druffel, E., Griffin, S., Glynn, C., Benner, R., and Walker, B. (2017). Radiocarbon in Dissolved Organic and Inorganic Carbon of the Arctic Ocean. *Geophys. Res. Lett.* 44 (5), 2369–2376. doi: 10.1002/2016GL072138

Druffel, E., Williams, P., Bauer, J., and Ertel, J. (1992). Cycling of Dissolved and Particulate Organic Matter in the Open Ocean. *J. Geophys. Res. Ocean.* 97 (C10), 15639–15659. doi: 10.1029/92JC01511

Dubinsky, Z., and Berman-Frank, I (2001). Ncoupling Primary Production From Population Growth in Photosynthesizing Organisms in Aquatic Ecosystems. *Aquat. Sci.* 63 (4), 17. doi: 10.1007/PL00001343

Fawcett, S., Lomas, M., Casey, J., Ward, B., and Sigman, D. (2011). Assimilation of Upwelled Nitrate by Small Eukaryotes in the Sargasso Sea. *Nat. Geosci.* 4, 717–722. doi: 10.1038/ngeo1265

Fripiat, F., Declerq, M., Sapart, C., Anderson, L., Bruechert, V., Deman, F., et al. (2018). Influence of the Bordering Shelves on Nutrient Distribution in the Arctic Halocline Inferred From Water Column Nitrate Isotopes. *Limno. Oceanogr.* 63 (5), 2154–2170. doi: 10.1002/lno.10930

Goericke, R., and Fry, B. (1994). Variations of Marine Plankton δ13c With Latitude, Temperature, and Dissolved CO2 in the World Ocean. *Glob. Biogeochem. Cycle.* 8, 85–90. doi: 10.1029/93GB03272

Granger, J., Sigman, D. M., Gagnon, J., Tremblay, J., and Mucci, E. (2018). On the Properties of the Arctic Halocline and Deep Water Masses of the Canada Basin From Nitrate Isotope Ratios. *J. Geophys. Res. Oceans* 123(8), 5443–58. doi: 10.1029/2018JC014110

Hansell, D. A., Carlson, C. A., Repeta, D. J., and Schlitzer, (2009). Dissolved Organic Matter In The Ocean: A Controversy Stimulates New Insights. *Oceanography* 22(4), 202–11. doi: 10.5670/Oceanog.2009.109

Hamilton, J., and Wu, Y. (2013). Synopsis and Trends in the Physical Environment of Baffin. *Can. Tech. Rep. Hydrogr. Ocean. Sci.* 282, 39

Hill, J., and Wheeler, P. (2002). Organic Carbon and Nitrogen in the Northern California Current System: Comparison of Offshore, River Plume, and Coastally Upwelled Waters. *Prog. Oceanogr.* 53 (2-4), 369–387. doi: 10.1016/S0079-6611(02)00037-X

Hobson, K., Fisk, A., Karnovsky, N., Holst, M., Gagnon, J., and Fortier, M. (2002). A Stable Isotope (δ13c, δ15n) Model for the North Water Food Web: Implications for Evaluating Trophodynamics and the Flow of Energy and Contaminants. *Deep. Sea. Res. Part II Top. Stud. Oceanogr.* 42, 5131–5150. doi: 10.1016/S0967-0645(02)00182-0

Holding, J., Carlos, D., Delgado-Huertas, A., Soetaert, K., Vonk, K., Agusti, S., et al. (2017). Autochthonous and Allochthonous Contributions of Organic Carbon to Microbial Food Webs in Svalbard Fjords. *Limnol. Oceanogr.* 62 (3), 1307–1323. doi: 10.1002/lno.10526

Honjo, S., Krishfield, R., Eglinton, T., Manganini, S., Kemp, J., Doherty, K., et al. (2010). Biological Pump Processes in the Cryopelagic and Hemipelagic Arctic Ocean: Canada Basin and Chukchi Rise. *Prog. Oceanogr.* 85 (3-4), 137–170. doi: 10.1016/j.pocean.2010.02.009

Hopkinson, C., and Vallino, J. (2005). Efficient Export of Carbon to the Deep Ocean Through Dissolved Organic Matter. *Nature* 433, 142–145. doi: 10.1038/nature03191

Hwang, J., and Druffel, E. (2003). Lipid-Like Material as the Source of the Uncharacterized Organic Carbon in the Ocean? *Science* 299 (5608), 881–884. doi: 10.1126/science.1078508

Hwang, J., Druffel, E., and Eglinton, T. (2010). Widespread Influence of Resuspended Sediments on Oceanic Particulate Organic Carbon: Insights From Radiocarbon and Aluminum Contents in Sinking Particles. *Glob. Biogeochem. Cycle.* 24, GB4016. doi: 10.1029/2010GB003802

Hwang, J., Druffel, E., and Komada, T. (2005). Transport of Organic Carbon From the California Coast to the Slope Region: A Study of Δ14C and δ13c Signatures of Organic Compound Classes. *Global Biogeochem. Cycles.* 19 (2), GB2018. doi: 10.1029/2004GB002422

Hwang, J., and Druffel, E. R. M. (2006). Carbon Isotope Ratios of Organic Compound Fractions in Oceanic Suspended Particles. *Geophys. Res. Lett.* 33, L23610. doi: 10.1029/2006GL027928

Hwang, J., Druffel, E. R. M., and Bauer, J. (2006). Incorporation of Aged Dissolved Organic Carbon (DOC) By Oceanic Particulate Organic Carbon (POC): An Experimental Approach Using Natural Carbon Isotopes? *Marine Chemistry* 98, 315–322.

Krawczyk, D., Kryk, A., Juggins, S., Burmeister, A., Pearce, C., Seidenkrantz, M.-S., et al. (2021). Spatio-Temporal Changes in Ocean Conditions and Primary Production in Baffin Bay and the Labrador Sea. *Palaeogeogr. Palaeoclimatol. Palaeoecol.* 563, 110175. doi: 10.1016/j.palaeo.2020.110175

Lalande, C., Forest, A., Barber, D., Gratton, Y., and Fortier, L. (2009). Variability in the Annual Cycle of Vertical Particulate Organic Carbon Export on Arctic Shelves: Contrasting the Laptev Sea, Northern Baffin Bay and the Beaufort Sea. *Cont. Shelf. Res.* 29 (17), 2157–2165. doi: 10.1016/j.csr.2009.08.009

Lee, Y., Lim, H., and Yoon, H. (2009). Carbon and Nitrogen Isotope Composition of Vegetation on King George Island, Maritime Antarctic. *Polar. Biol.* 32, 1607–1615. doi: 10.1007/s00300-009-0659-5

Lehmann, N., Kienast, M., Granger, J., Bourbonnais, A., Altabet, M., and Tremblay, J.-E. (2019). Remote Western Arctic Nutrients Fuel Remineralization in Deep Baffin Bay. *Glob. Biogeochem. Cycle.*, 33 (6) 649–667. doi: 10.1029/2018GB006134

Levasseur, M. E., and Therriault, J. C. (1987). Phytoplankton Biomass and Nutrient Dynamics in a Tidally Induced Upwelling: The Role of NO3:Si (OH)4 Ratio. *Mar. Ecol. Prog. Ser.*, 39, 87–97. doi: 10.3354/meps039087

Levin, I., Naegler, T., Kromer, B., Diehl, M., Francey, R., Gomez-Pelaez, A., et al. (2010). Observations and Modelling of the Global Distribution and Long-Term Trend of Atmospheric 14CO2. *Tellus. B Chem. Phys. Meteorol.* 62 (1), 26–46. doi: 10.1111/j.1600-0889.2009.00446.x

Limoges, A., Weckström, K., Ribeiro, S., Georgiadis, E., Hansen, K., Martinez, P., et al. (2020). Learning From the Past: Impact of the Arctic Oscillation on Sea Ice and Marine Productivity Off Northwest Greenland Over the Last 9,000 Years. *Glob. Chang. Biol.* 26 (12), 6767–6786. doi: 10.1111/gcb.15334

Loh, A. N., and Bauer, J. (2000). Distribution, Partitioning and Fluxes of Dissolved and Particulate Organic C, N and P in the Eastern North Pacific and Southern Oceans. *Deep. Sea. Res. Part I Oceanogr. Res. Pap.* 47 (12), 2287–2316. doi: 10.1016/S0967-0637(00)00027-3

Magen, C., Chaillou, G., Crowe, S., Mucci, A., Sundby, B., Gao, A., et al. (2010). Origin and Fate of Particulate Organic Matter in the Southern Beaufort Sea – Amundsen Gulf Region, Canadian Arctic. *Estuar. Coast. Shelf. Sci.* 86 (1), 31–41. doi: 10.1016/j.ecss.2009.09.009

McNichol, A., and Aluwihare, L. (2007). The Power of Radiocarbon in Biogeochemical Studies of the MarineCarbon Cycle: Insights From Studies of Dissolved and Particulate Organic Carbon (DOC and POC). *Chem. Rev.* 107 (2), 443–466. doi: 10.1021/cr050374g

Mei, Z.-P., Legendre, L., Tremblay, J.-É., Miller, L., Gratton, Y., Lovejoy, C., et al. (2005). Carbon to Nitrogen (C:N) Stoichiometry of the Spring–Summer Phytoplankton Bloom in the North Water Polynya (NOW). *Deep. Sea. Res. Part I Oceanogr. Res. Pap.* 52 (12), 2301–2314. doi: 10.1016/j.dsr.2005.07.001

Meire, L., Mortensen, J., Meire, P., Juul-Pedersen, T., Sejr, M., Rysgaard, S., et al. (2017). Marine-Terminating Glaciers Sustain High Productivity in Greenland Fjords. *Glob. Chang. Biol.* 23 (12), 5344–5357. doi: 10.1111/gcb.13801

Melling, G., Gratton, Y., and Ingram, G. (2001). Ocean Circulation Within the North Water Polynya of Baffin Bay. *Atmosphere-Ocean* 39, 301–325. doi: 10.1080/07055900.2001.9649683

Middelburg, J. (2019). "Carbon Processing at the Seafloor," in *Marine Carbon Biogeochemistry* (Cham: Springer). doi: 10.1007/978-3-030-10822-9_4

Münchow, A., Falker, K., and Melling, H. (2015). Baffin Island and West Greenland Current Systems in Northern Baffin Bay. *Prog. Oceanogr.* 132, 305–317. doi: 10.1016/j.pocean.2014.04.001

Naidu, A., Scalan, R., Feder, H., Goering, J., Hameedi, M., Parker, P., et al. (1993). Stable Organic Carbon Isotopes in Sediments of the North Bering-South Chukchi Seas, Alaskan-Soviet Arctic Shelf. *Cont. Shelf. Res.* 13 (5-6), 669–691. doi: 10.1016/0278-4343(93)90099-J

Passow, U., and Carlson, C. (2012). The Biological Pump in a High CO2 World. *Mar. Ecol. Prog. Ser.* 470, 249–271. doi: 10.3354/meps09985

Rafter, P., Bagnell, A., Marconi, D., and DeVries, T. (2019). Global Trends in Marine Nitrate N Isotopes From Observations and a Neural Network-Based Climatology. *Biogeosciences* 16, 2617–2633. doi: 10.5194/bg-16-2617-2019

Rau, G., Karl, D., and Carney, R. (1986). Does Inorganic Carbon Assimilation Cause 14C Depletion in Deep-Sea Organisms? *Deep. Sea. Res. Part I Oceanogr. Res. Pap.* 33(3), 349–357. doi: 10.1016/0198-0149(86)90096-8

Rau, G., Sweeney, R., and Kaplan, I. (1982). Plankton 13C:12C Ratio Changes With Latitude: Differences Between Northern and Southern Oceans☆. *Deep. Sea. Res. Part I Oceanogr. Res. Pap.*, 29 (8), 1035–1039. doi: 10.1016/0198-0149(82)90026-7

Rau, G., Takahashi, T., Des Marais, D., Repeta, D., and Martin, J. (1992). The Relationship Between δ13c of Organic Matter and [CO2 (Aq)] in Ocean Surface Water: Data From a JGOFS Site in the Northeast Atlantic Ocean and a Model. *Geochim. Cosmochim. Acta* 56, 1413–1419. doi: 10.1016/0016-7037(92)90073-R

Redfield, A. (1958). The Biological Control of Chemical Factors in the Environment. *Am. Sci.* 46 (3), 230A–221.

Richardson, T., and Jackson, G. (2007). Small Phytoplankton and Carbon Export From the Surface Ocean. *Science* 315 (5813), 838–840. doi: 10.1126/science.1133471

Roland, L., McCarthy, M., and Guilderson, T. (2008). Sources of Molecularly Uncharacterized Organic Carbon in Sinking Particles From Three Ocean Basins: A Coupled Δ14C and δ13c Approach. *Mar. Chem.* 111 (3-4), 199–213. doi: 10.1016/j.marchem.2008.05.010

Roy, V., Iken, K., Gosselin, M., Tremblay, J.-E., Belanger, S., and Archambault, P. (2015). Benthic Faunal Assimilation Pathways and Depth-Related Changes in Food-Web Structure Across the Canadian Arctic. *Deep. Sea. Res. Part I Oceanogr. Res. Pap.* 102, 55–71. doi: 10.1016/j.dsr.2015.04.009

Sarmiento, J. (2013). *Ocean Biogeochemical Dynamics* (Princeton: Princeton University Press). doi: 10.1515/9781400849079

Sherwood, O., Davin, S., Lehmann, N., Buchwald, C., Edinger, E., Lehmann, M., et al. (2021). Stable Isotope Ratios in Seawater Nitrate Reflect the Influence of Pacific Water Along the Northwest Atlantic Margin. *Biogeosciences* 18 (15), 4491–4510. doi: 10.5194/bg-18-4491-2021

Shiklomanov, A., Déry, S., Tretiakov, M., Yang, D., Magritsky, D., Georgiadi, A., et al. (2021). "River Freshwater Flux to the Arctic," in *Arctic Hydrology, Permafrost and Ecosystems*. Eds. D. Yang and D. L. Kane (Cham: Springer), 703–738. doi: 10.1007/978-3-030-50930-9_24

Sigman, D., and Casciotti, K. (2001). "Nitrogen Isotopes in the Ocean," in *Encyclopedia of Ocean Sciences*. Ed. J. Steele (Oxford: Academic Press), 1884–1894. doi: 10.1006/rwos.2001.0172

Smith, D., Simon, M., Alldredge, A., and Azam, F. (1992). Intense Hydrolytic Enzyme Activity on Marine Aggregates and Implications for Rapid Particle Dissolution. *Nature* 359, 139–142. doi: 10.1038/359139a0

Stuiver, M., and Polach, H. A. (1977). Discussion; Reporting of C-14 Data. *Radiocarbon* 19, 355–363. doi: 10.1017/S0033822200003672

Tamelander, T., Renaud, P., Hop, H., Carroll, M., Ambrose, W., and Hobson, K. (2006). Trophic Relationships and Pelagic–Benthic Coupling During Summer in the Barents Sea Marginal Ice Zone, Revealed by Stable Carbon and Nitrogen Isotope Measurements. *Mar. Ecol. Prog. Ser.* 310, 33–46. doi: 10.3354/meps310033

Tang, C., Ross, C., Yao, T., Petrie, B., DeTracey, B., and Dunlap, E. (2004). The Circulation, Water Masses and Sea-Ice of Baffin Bay. *Prog. Oceanogr.* 63 (4), 183–228. doi: 10.1016/j.pocean.2004.09.005

Taylor, J. (1997). *An Introduction to Error Analysis: The Study of Uncertainties in Physical Measurements (2nd Edition Ed.)* (Saussalito, CA: University Science Books).

Volkman, J., and Tanoue, E. (2002). Chemical and Biological Studies of Particulate Organic Matter in the Ocean. *J. Oceanogr.* 58, 265–279. doi: 10.1023/A:1015809708632

Walker, B., Beaupre, S., Guilderson, T., McCarthy, M., and Druffel, E. (2016). Pacific Carbon Cycling Constrained by Organic Matter Size, Age and Composition Relationships. *Nat. Geosci.* 9, 888–891. doi: 10.1038/ngeo2830

Walker, B., Druffel, E., Kolasinki, J., Roberts, B., Xu, X., and Rosenheim, B. (2017). Stable and Radiocarbon Isotopic Composition of Dissolved Organic Matter in the Gulf of Mexico. *Geophys. Res. Lett.* 44, 8424–8434. doi: 10.1002/2017GL074155

Walker, B., Guilderson, T., Okimura, K., Peacock, M., and McCarthy, M. (2014). Radiocarbon Signatures and Size–Age–Composition Relationships of Major Organic Matter Pools Within a Unique California Upwelling System. *Geochim. Cosmochim. Acta* 126, 1–17. doi: 10.1016/j.gca.2013.10.039

Walker, B., and McCarthy, M. (2012). Elemental and Isotopic Characterization of Dissolved and Particulate Organic Matter in a Unique California Upwelling System: Importance of Size and Composition in the Export of Labile Material. *Limnol. Oceanogr.* 57 (6), 1757–1774. doi: 10.4319/lo.2012.57.6.1757

Walker, B., and Xu, X. (2019). An Improved Method for the Sealed-Tube Zinc Graphitization of Microgram Carbon Samples and 14C AMS Measurement. *Nucl. Instrum. Methods Phys. Res. B* 438, 58–65. doi: 10.1016/j.nimb.2018.08.004

Williams, P., Robertson, K., Soutar, A., Griffin, S., and Druffel, E. (1992). Isotopic Signatures (14C, 13C, 15N) as Tracers of Sources and Cycling of Soluble and Particulate Organic Matter in the Santa Monica Basin, California. *Prog. Oceanog.* 30, 253–290. doi: 10.1016/0079-6611(92)90015-R

Xu, X., Trumbore, S., Zheng, S., Southon, J., McDuffee, K., Luttgen, M., et al. (2007). Modifying a Sealed Tube Zinc Reduction Method for Preparation of AMS Graphite Targets: Reducing Background and Attaining High Precision. *Nucl. Instrum. Methods Phys. Res. B* 259 (1), 320–329. doi: 10.1016/j.nimb.2007.01.175

Zeidan, S., Walker, J., Else, B. G. T., Miller, L. A., Azetsu-Scott, K., and Walker, B. D. (2022). Using Radiocarbon Measurements of Dissolved Inorganic Carbon to Determine a Revised Residence Time for Deep Baffin Bay? *Front. Mar. Sci.* 9, 845536. doi: 10.3389/fmars.2022.845536

Conflict of Interest: The authors declare that the research was conducted in the absence of any commercial or financial relationships that could be construed as a potential conflict of interest.

frontiers | Frontiers in Marine Science

ORIGINAL RESEARCH
published: 31 May 2022
doi: 10.3389/fmars.2022.824862

Vertical Profiles of ^{226}Ra and ^{228}Ra Activity Concentrations in the Western Subarctic Gyre of the Pacific Ocean

Hirofumi Tazoe[1], Hajime Obata[2], Takuya Hara[2], Mutsuo Inoue[3], Takahiro Tanaka[4] and Jun Nishioka[5]*

[1] Institute of Radiation Emergency Medicine, Hirosaki University, Hirosaki, Japan, [2] Atmosphere and Ocean Research Institute, The University of Tokyo, Kashiwa, Japan, [3] Low Level Radioactivity Laboratory, Institute of Nature and Environmental Technology, Kanazawa University, Nomi, Japan, [4] Fisheries Resources Institute, Japan Fisheries Research and Education Agency, Shiogama, Japan, [5] Institute of Low Temperature Science, Hokkaido University, Sapporo, Japan

The vertical activity concentration distributions of the radium isotopes, ^{226}Ra and ^{228}Ra, which are useful as radiotracers, were obtained for the first time in the western Subarctic Pacific Gyre (WSAG). It was possible to detect short-lived ^{228}Ra present from the surface to 400 m depth by analyzing large seawater samples. Low ^{228}Ra and high ^{226}Ra activity concentrations in the surface layer in the WSAG were strongly influenced by upwelled deeper water with nutrients. The activity concentration distribution of ^{226}Ra especially was in good agreement with the silicate concentration distribution, which was consistent with previous reported findings. These distributions were uniform from the surface to 100 m of the dichothermal layer due to vertical mixing in winter. ^{228}Ra activity concentration decreased with water depth below the pycnocline and reached the undetectable level at 600 m which was within the oxygen minimum layer. Estimations of vertical fluxes of ^{228}Ra and nitrate according to ^{228}Ra decay indicated that the vertical transport by eddy diffusion was a minor process for the ^{228}Ra and nitrate fluxes, and lateral transport mainly affected ^{228}Ra in the intermediate warm water, that is, the mesothermal layer below the main pycnocline. Vertical mixing or submarine underground water and lateral transport to the WSAG could yield this ^{228}Ra in the intermediate depth.

Keywords: radium-228, radium-226, Subarctic Gyre of the Pacific Ocean, vertical flux, lateral transport

OPEN ACCESS

Edited by:
Paul Mcginnity, IAEA International Atomic Energy Agency, Monaco

Reviewed by:
Su Mei Liu, Ocean University of China, China
Wei-Jen Huang, National Sun Yat-sen University, Taiwan

****Correspondence:***
Hirofumi Tazoe
tazoe@hirosaki-u.ac.jp

Specialty section:
This article was submitted to Ocean Observation, a section of the journal Frontiers in Marine Science

Received: *29 November 2021*
Accepted: *29 April 2022*
Published: *31 May 2022*

Citation:
Tazoe H, Obata H, Hara T, Inoue M, Tanaka T and Nishioka J (2022) Vertical Profiles of ^{226}Ra and ^{228}Ra Activity Concentrations in the Western Subarctic Gyre of the Pacific Ocean. Front. Mar. Sci. 9:824862. doi: 10.3389/fmars.2022.824862

INTRODUCTION

Radium-228 (^{228}Ra, half-life, 5.75 yr) is a naturally occurring radionuclide produced by the decay of ^{232}Th, which is abundant in sediments and soils, and it is provided from rivers and sediments to seawater of the continental shelf (Moore, 1969; Nozaki et al., 1998). The activity concentration of ^{228}Ra in surface seawater decreases as it is transported from the coast to the open ocean because of radioactive decay and eddy diffusion (Moore, 1972; Ku et al., 1995; Nozaki and Yamamoto, 2001). From a vertical profile of ^{228}Ra, Moore (1972) estimated the rates of mixing across the thermocline, which brings nutrients from deeper layers to the euphotic zone. Coupled vertical profiles of ^{228}Ra

and nutrients should provide an estimate of vertical flux of nutrients in the upper ocean. ^{228}Ra has also been used as a tracer in studies on seawater mixing in coastal areas and above seafloors (Moore et al., 1986; Rutgers van der Loeff et al., 1995; Rutgers van der Loeff et al., 2003; Kadko and Muench, 2005; Nakano-Ohta and Sato, 2006; Kawakami and Kusakabe, 2008; Inoue et al., 2012; Inoue et al., 2016; Inoue et al., 2020), studies on the transport of particulate matter in the water column (Legeleux and Reyss, 1996; van Beek et al., 2007), and studies on the vertical flux of nutrients in the upper oceans (Ku et al., 1995; Nozaki and Yamamoto, 2001; Cai et al., 2002).

Ra-226 (half-life, 1600 yr) is also a naturally occurring radionuclide and it is produced from ^{230}Th enriched in bottom sediments. The ^{226}Ra activity concentration gradient from the coast to the ocean is lower than that of ^{228}Ra due to the longer half-life of ^{226}Ra. Recently, ^{226}Ra and ^{228}Ra along with the short-lived Ra isotopes ^{233}Ra and ^{234}Ra have been used for estimation of flux of submarine groundwater discharge (Kwon et al., 2014; Le Gland et al., 2017; Cho et al., 2018). Together with the distributions of nutrients and dissolved oxygen, these tracers have provided unique means to estimate the rates of metabolism in biogeochemical cycling.

The western subarctic Pacific Gyre (WSAG) is well known as a high nutrient, low chlorophyll area (HNLC), in which nutrients remain undepleted in surface waters throughout the year. In this area, phytoplankton growth is limited by iron (Fe) availability (Tsuda et al., 2003; Boyd et al., 2004), and the area has been reported to have the largest biological CO_2 drawdown among all the world's oceans (Takahashi et al., 2002). The high productivity of the region's ecosystem and fisheries (Sakurai, 2007) must be sustained by supplies of both Fe and nutrients entering the euphotic zone. The sub-surface pycnocline divides nutrient-poor surface mixed layers and nutrient-rich lower layers in the open ocean (Longhurst, 2007). The water exchange between these layers is regulated by the vertical eddy diffusivity that causes upward nutrient transport. Recent work (Nishioka et al., 2020) based on the combination of a comprehensive Fe observation dataset and vertical eddy diffusivity obtained by physical observations has implied that the formation of a high nutrient intermediate water pool, which is strongly influenced by lateral water transport from marginal seas (the Bering and Okhotsk Seas) and the existence of a nutrient return path from the intermediate water at potential density (σ_θ) of 26.8-27.2 to the surface due to strong mixing around the Kuril and Aleutian Island chains are important for understanding how HNLC water is formed in the North Pacific. The horizontal distribution indicated by isopycnal analysis clearly presented evidence that the high, dissolved Fe source in the intermediate waters in the western subarctic Pacific is the marginal seas (Nishioka et al., 2020). Dissolved Fe concentration in the North Pacific Intermediate Water (NPIW) is high across a wide area in the western subarctic Pacific, particularly along the northern part of the WSAG including the areas southeast of the Kamchatka Peninsula, the western Bering Sea basin, and around the eastern Aleutian Islands. These findings suggest that clarifying the formation and pathways of NPIW is essential for a better understanding of the mechanisms of biological production in the WSAG.

Around the WSAG, the shelf sediments in marginal seas, such as the East China Sea, Sea of Japan and Okhotsk Sea are known to play an important role in supplying Ra isotopes as well as nutrients (Kawakami and Kusakabe, 2008; Inoue et al., 2016). Then, Ra isotopes are supplied from the marginal seas, and they are laterally transported toward it. This signature and temporal change by radioactive decay can be used as a chronological tracer during advective transportation. The ^{226}Ra and ^{228}Ra activity concentrations in the Okhotsk Sea and around the Kuril Islands reported in the literature (Kawakami and Kusakabe, 2008; Inoue et al., 2016) were relatively high, indicating the possible influence of the continent and the continental shelf. However, ^{228}Ra data were too limited to debate the contribution of lateral transportation from the margin. Especially, information on ^{228}Ra activity concentrations in subsurface waters is not available in the WSAG, although such information could be key to resolving geochemical cycles for the lithogenic elements. In this study, we determined vertical profiles at Station K2 in the WSAG for concentrations of the natural radionuclides, ^{226}Ra and ^{228}Ra.

EXPERIMENTAL

Seawater samples were collected using acid-cleaned 12 L NISKIN-X samplers with external springs mounted on a CTD-CMS at Station K2 (47°00'N, 165°00'E; **Figure 1A**) during a research cruise of the TS Oshoro-Maru from 19 May to 15 July 2016. Samples of 200 L were collected for ^{226}Ra and ^{228}Ra analyses at 10, 49, 99, 199, 397, and 594 m depths on 25-28 June.

The detailed procedures for ^{226}Ra and ^{228}Ra analyses can be found elsewhere (Nakano et al., 2008). In brief, a seawater sample was acidified by adding 1.8 L of 61% HNO_3. Then, 0.48 g of a minimally Ra-contaminated Ba carrier solution with Fe carrier (3 g of Fe) was added. After stirring for 15 min, 600 mL of 5% Na_2SO_4 solution was also added. 1.5 L of aqueous ammonium was gradually added to get a pH from 6 to 8. Ra isotopes were precipitated together with $BaSO_4$ and $Fe(OH)_3$ precipitates. The solution was allowed to stand for 24 h so that all particles sank to the bottom of the container. The precipitates were siphoned from the container and the supernatant was discarded by decantation. The yield of Ra isotopes was 82-96%, determined by gravimetric $BaSO_4$ yield.

Low-background gamma-spectrometry was performed on $BaSO_4$ fractions using Ge-detectors at the Ogoya Underground Laboratory, Japan (Hamajima and Komura, 2004). ^{226}Ra (^{214}Pb; 295 and 352 keV) activity concentrations were calibrated using a mock-up sample prepared from a $BaSO_4$-$Fe(OH)_3$ mixture, a uranium standard issued from the New Brunswick Laboratory, USA (NBL-42-1) and KCl, while ^{228}Ra (^{228}Ac; 338 and 911 keV) activity concentrations were based on a detection efficiency curve obtained from the mock-up sample. For each seawater sample, counting was typically performed over 3-7 d for ^{226}Ra and ^{228}Ra. Under the present analytical conditions, the lowest amounts of

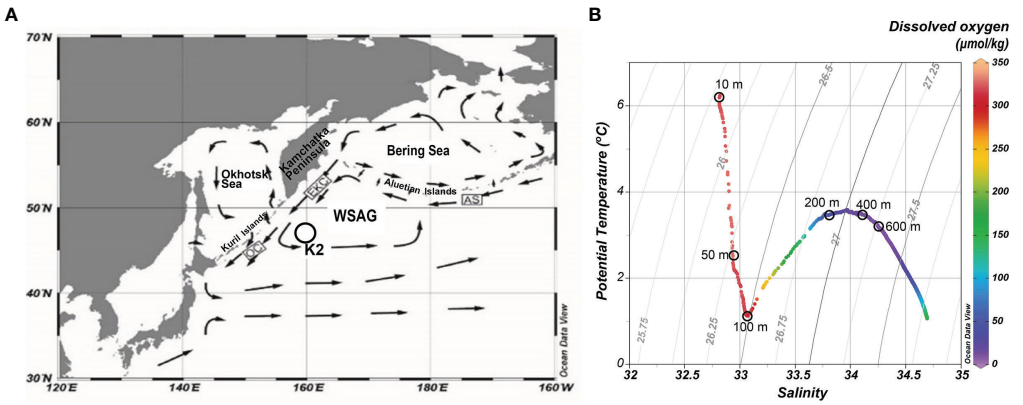

FIGURE 1 | **(A)** Location of Station K2 in the western Subarctic Gyre (WSAG). The surface current system in the western North Pacific, the Bering Sea and the Okhotsk Sea is also displayed and it includes the East Kamchatka Current (EKC), Oyashio Current (OC), Alaskan Stream (AS). **(B)** Potential temperature-salinity diagram for K2 with oxygen concentration. Open circles shows sampling depths for Ra samples.

^{228}Ra that can be determined in the seawater sample were ~4 mBq for 2-3 counting days, which yields a minimum detectable activity concentration of ~0.02 Bq m^{-3} for ^{228}Ra using a 200 L seawater sample (Nakano et al., 2008). The concentrations of all radionuclides measured were decay-corrected based on the sampling date (Hamajima and Komura, 2004).

Nutrient (nitrate-plus-nitrite, phosphate, and silicate) concentrations were also analyzed in seawater samples collected from Station K2. Nutrient concentrations were measured using a BRAN-LUEBBE autoanalyzer (TRACCS 800) and a BL-Tec autoanalyzer (QuAAtro) (Gordon et al., 1992). Most of the nutrient measurements in this study were quality controlled using KANSO reference materials (KANSO Company).

Salinity and temperature were measured using a CTD sensor, and dissolved oxygen concentrations were measured using an oxygen sensor. The dissolved oxygen concentrations were also measured on board the ship by the Winkler titration method, and the dissolved oxygen concentrations obtained by the sensor (SBE 43 Dissolved Oxygen Sensor, Sea-Bird Scientific) were calibrated using those determined by the Winkler method (Carpenter, 1965). The eddy diffusivity K_z value was measured using a free-fall vertical microstructure profiler (VMP500 Rockland Scientific International Co.).

RESULTS AND DISCUSSION

Hydrography

The elevated temperatures above the 50 m depth enhanced seasonal stratification in summer in the WSAG (**Figure 2A**). A subsurface temperature minimum (1.14°C) existed around the 100 m depth for which potential density was around 26.5 (**Figure 1B**); this was consistent with previous studies (e.g. Ueno and Yasuda, 2000). The mixed layer reaches more deeply in winter and it is overlaid by warmer and fresher water in summer (Yasuda, 1997). Low temperature water (<1.5°C) at σ_θ=26.5 was distributed along the East Kamchatka Current (EKC) from the western Bering Sea. Depths at σ_θ=26.5 in the western Bering Sea and near the Bering Strait (around 50 - 70 m) were shallower than those in the WSAG. The vertical distribution of dissolved oxygen concentrations (**Figure 2D**) was almost constant from the surface to the depth of the temperature minimum. Macronutrients were at relatively high concentrations. The concentrations of silicate and nitrate were 1.4 μmol kg^{-1}, 18 μmol kg^{-1}, respectively, in surface water (**Figures 2E, F**). From these values, we thought it was likely that biological activity was controlled by another parameter, such as iron, in this HNLC area as has been reported in the literature (Nishioka et al., 2013; Nishioka et al., 2020).

The halocline increasing in salinity from 33.1 to 33.7 (**Figure 2B**) yielded the elevation of potential density, pycnocline (σ_θ=26.5 – 26.8, **Figure 2C**) between 110 m and 160 m depth. In addition, this yielded a rapid increase of macronutrients by limitation of the vertical transportation. Potential temperature increased with depth and an intermediate maximum potential temperature of 3.57°C was observed at 250 m depth (σ_θ=26.99), which generated a temperature inversion structure. The shallower temperature minimum layer and deeper temperature maximum layer called dichothermal and mesothermal waters, respectively, exist in the WSAG (Ueno and Yasuda, 2000; Ueno and Yasuda, 2005). All macronutrients rapidly increased with the decrease in dissolved oxygen concentration. Ueno and Yasuda (2000; 2005)also reported the dissolved oxygen concentration minimum was at 600 m. The present measurements showed the oxygen minimum layer (15.8-20.8 μmol kg^{-1}, σ_θ=27.1-27.5 at 350–1000 m depth) was deeper than the temperature maximum.

Low-oxygen and high-silicate and high-nitrate water exist in the WSAG and Bering Gyre at the potential densities of 26.9 and 27.15, corresponding to 199 m and 397 m depths at Station K2, respectively (**Figure S1**). At shallower depths than σ_θ=26.9, dissolved oxygen-rich water was observed along the EKC. Low dissolved oxygen water (<60 μmol/kg) at the potential density of

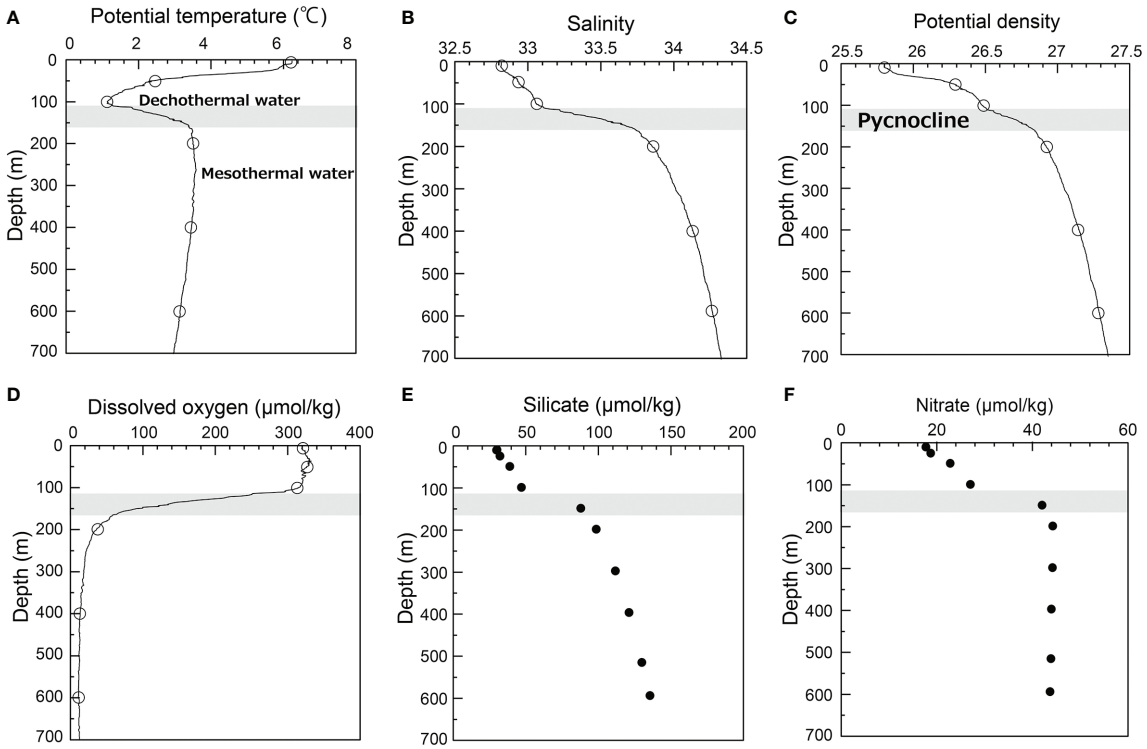

FIGURE 2 | Vertical profiles at Station K2 in the WSAG for: **(A)** potential temperature, **(B)** salinity and **(C)** potential density. Vertical profiles of concentrations at K2 for **(D)** dissolved oxygen and nutrients, **(E)** silicate and **(F)** nitrate. The gray band indicates the pycnocline overlying the mesothermal layer.

27.15, derived from the western Bering Sea, is found in the WSAG. Contrastingly, west of 155°E in the Oyashio Region and the Okhotsk Sea, high-dissolved oxygen water (>100 μmol/kg) is found. The Okhotsk Sea Intermediate Water (OSIW), characterized by relatively high-dissolved oxygen and dissolved Fe-rich water, flows out to the Pacific through the Kuril Straits, which has a strong influence on the extension region through the Oyashio Current. It propagates along the 26.8 σ_θ isopycnal surface to the western North Pacific (mainly west of 155°E). The hydrography at Station K2 we observed in this study indicated that the influence from the OSIW was minor. Station K2 was located at the rim of the anti-clockwise gyre system (**Figure 1A**). The relatively lower salinity water signature (>33.8) at the potential density of 26.9 σ_θ can be traced back to the EKC along the Kamchatka Peninsula and the western Bering Gyre.

Surface Ra Isotopes

Radium-226 activity concentrations were almost constant across the seasonal thermocline but slightly decreased with depth from the surface to 99 m, ranging from 1.9 to 2.2 Bq m^{-3} (**Table 1**; **Figure 3A**), which corresponded to the depth above the pycnocline. Previous studies have reported surface distributions of

TABLE 1 | Activity concentrations of ^{226}Ra and ^{228}Ra and their ratios at station K2 in the western subarctic pacific gyre.

Depth (m)	Potential Temperature (°C)	Potential density (kg m-3)	Salinity (psu)	Dissolved oxygen (μmol/kg)	Nitrate (μmol/kg)	Silicate (μmol/kg)	Phosphate (μmol/kg)	^{226}Ra(Bq m^{-3})	^{228}Ra (Bq m^{-3})	^{228}Ra/^{226}Ra
10.2	6.092	25.821	32.824	328.8	17.7	29.9	1.47	2.24 ± 0.02	0.099 ± 0.017	0.044 ± 0.008
49.1	2.235	26.315	32.954	330.3	22.8	39.0	1.83	2.11 ± 0.03	0.099 ± 0.019	0.047 ± 0.009
99.3	1.390	26.483	33.117	295.5	27.1	47.0	2.10	1.94 ± 0.02	0.081 ± 0.017	0.042 ± 0.009
198.5	3.520	26.939	33.875	34.4	44.3	98.6	3.17	3.20 ± 0.04	0.067 ± 0.020	0.021 ± 0.006
396.5	3.437	27.161	34.141	17.8	44.0	121.2	3.18	3.20 ± 0.03	0.040 ± 0.011	0.012 ± 0.003
594.0	3.123	27.302	34.281	15.8	43.7	135.7	3.17	4.24 ± 0.03	< 0.02	< 0.005

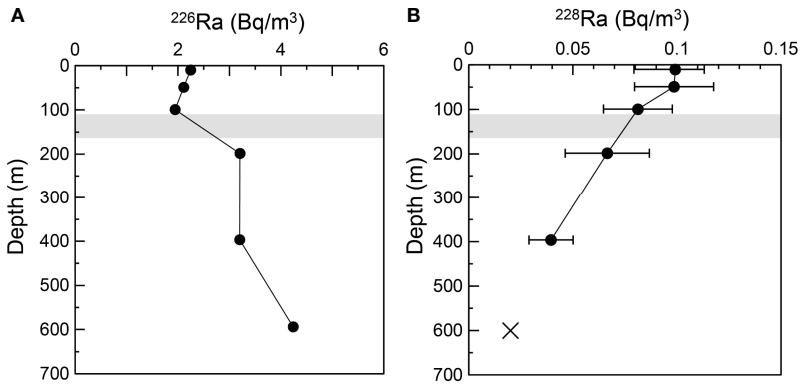

FIGURE 3 | Vertical profiles at Station K2 in the WSAG for **(A)** ^{226}Ra and **(B)** ^{228}Ra activity concentrations. The letter x indicates the minimum detectable ^{228}Ra activity concentration (0.02 Bq m^{-3}) in this study.

^{226}Ra activity concentrations in the western North Pacific involving the Kuroshio Extension area and the Okhotsk Sea (Nozaki et al., 1990; Kawakami and Kusakabe, 2008; Inoue et al., 2016; **Figure S1**), excluding the area in this study. Surface ^{226}Ra activity concentration range was reported to be from 1.4 Bq m^{-3} to 2.3 Bq m^{-3} in the WSAG, and the present study was consistent with that. The presently obtained high ^{226}Ra activity concentrations were comparable to those reported in the Bering Sea (1.3-2.5 Bq m^{-3}; Nozaki et al., 1990; Li et al., 2017; Inoue et al., 2020). Low ^{226}Ra activity concentrations (0.6-1.2 Bq m^{-3}) have been observed in a coastal area along the Kamchatka Peninsula, which reflected freshwater input from the land (Inoue et al., 2016). On the other hand, ^{226}Ra activity concentrations in the Kuroshio Current (1.0-1.4 Bq m^{-3}) and Kuroshio Extension (1.1-1.5 Bq m^{-3}) areas (Yamada and Nozaki, 1986; Nozaki et al., 1990; Kawakami and Kusakabe, 2008) were found to be lower than those of the subarctic region. ^{226}Ra activity concentrations in the Alaskan Gyre (1.4-1.9 Bq m^{-3}, Nozaki et al., 1990) were also lower than those of the WSAG and the Bering Sea.

The ^{226}Ra distribution trend resembled those of silicate and nitrate, which indicated ^{226}Ra was supplied from subsurface water by vertical transport processes. A high ^{226}Ra activity concentration (2.3 Bq m^{-3}) in the surface was also observed in the Okhotsk Sea and Oyashio Current area (Inoue et al., 2016). Broecker et al. (1976) and Nozaki et al. (1990) showed ^{226}Ra in surface waters linearly correlated with dissolved silicate. Both these groups also reported that like silicate, surface ^{226}Ra was derived from the deeper layer. Nozaki et al. (1990) noted that ^{226}Ra in surface waters linearly correlated with dissolved silicate concentration with a best fit line of [^{226}Ra (Bq m^{-3})] = 1.3 + 0.021 [SiO_2 (μmol kg^{-1})] for the North Pacific. Our ^{226}Ra activity concentration at 10 m agreed with the calculated ^{226}Ra activity concentration based on the silicate concentration. In addition, deeper water to 600 m also followed this best fit relationship, which indicated that both ^{226}Ra and silicate were supplied from subsurface and deeper water in the WSAG. The dataset of ^{226}Ra and silicate concentrations in the Okhotsk Sea is limited in the Kuril Basin (Inoue et al., 2016), but there is a difference between ^{226}Ra and silicate concentrations in the Okhotsk Sea as can be seen in **Figure S2**. High ^{226}Ra activity concentration in the Kuril basin in the Okhotsk Sea was reported with lower concentrations of macronutrients than those in the WSAG, which reflected ^{226}Ra released from the shelf sediments in the Okhotsk Sea (Kawakami and Kusakabe, 2008).

We found ^{228}Ra activity concentrations in the mixed layer were 0.099 ± 0.017 Bq m^{-3} at 10 m depth and 0.099 ± 0.019 Bq m^{-3} at 49 m depth (**Figure 3B**). ^{228}Ra activity concentration (0.081 ± 0.017) at 99 m above the pycnocline was slightly lower than that of the upper layer. Nozaki et al. (1990) suggested that the effect of radioactive decay of ^{228}Ra in the surface layer was much smaller than the effect of lateral transportation and mixing due to the rapid surface velocity. The surface distribution in the North Pacific seemingly reflected spatial variabilities of the ^{228}Ra source (**Figure S1**). Low ^{228}Ra activity concentrations were reported in the WSAG (0.1 Bq m^{-3}; this study and Inoue et al., 2016) and the Bering Sea Gyre (0.04 - 0.09 Bq m^{-3}; Nozaki et al., 1990; Li et al., 2017; Inoue et al., 2020). Hydrographic data (**Figure 1**) indicated that the Okhotsk Sea water did not influence our observation at Station K2 in the WSAG and EKC dominated the surface layer. There are high ^{228}Ra source regions in the Okhotsk Sea (0.49 – 0.98 Bq m^{-3}; Kawakami and Kusakabe, 2008; Inoue et al., 2016), Sea of Japan (1.5-2.2 Bq m^{-3}; Inoue et al., 2012) and shelf and shelf slope in the Bering Sea (0.3-0.9 Bq m^{-3}, Li et al., 2017; Inoue et al., 2020). ^{228}Ra is supplied from sediments in the continental shelf, which differs from ^{226}Ra supplied from sub-surface and deep water in the WSAG. Contrary to ^{226}Ra, ^{228}Ra, a short half-life radionuclide, is depleted in the deeper layers by radioactive decay. ^{228}Ra activity concentration in the Sea of Japan is higher than those in the Kuril Basin in the Okhotsk Sea. Surface water from the Sea of Japan passes through the Tsugaru Strait and has an impact on surface ^{228}Ra in the Kuroshio-Oyashio Transition Zone (0.25 to 1.51 Bq m^{-3}). Therefore, the relative contribution of ^{228}Ra from the margins is larger than that of ^{226}Ra in the WSAG.

Vertical Profiles of Ra Isotopes

The dataset of ^{226}Ra and ^{228}Ra vertical profiles we obtained in this study is the first reported for the WSAG. ^{226}Ra activity concentrations in the dichothermal water at 100 m below the seasonal thermocline were consistent with those in surface water (**Figure 3A**). Below the pycnocline, ^{226}Ra activity concentrations between 110 and 160 m increased with depth. ^{226}Ra activity concentrations were constant (3.2 Bq m^{-3}) at 199 m and 397 m depths, then increased to 4.2 Bq m^{-3} at 594 m. We observed that ^{226}Ra in deeper waters from 199 m to 594 m also followed the linear relationship with silicate concentrations as seen in the surface layer. This feature was consistent with our understanding that ^{226}Ra was vertically supplied from a deeper layer in a high latitude area, such as the WSAG.

Radium-228 activity concentrations gradually decreased with depth from 0.08 Bq m^{-3} at 10 m to 0.04 ± 0.01 Bq m^{-3} at 399 m. ^{228}Ra activity concentrations was less than the detectable level (<0.02 Bq m^{-3}) at 594 m depth. The vertical distribution of ^{228}Ra activity concentrations was in contrast to that of ^{226}Ra activity concentrations due to radioactive decay in the deeper layer. In addition, ^{228}Ra activity concentrations below the pycnocline were much lower compared with ^{228}Ra activity concentrations obtained in marginal seas such as the southwest Okhotsk Sea (0.3-0.4 Bq m^{-3}; Inoue et al., 2012) and the Sea of Japan (0.1-0.2 Bq m^{-3}; Okubo, 1980). We concluded that both Ra isotopes and their activity ratios are good tracers to identify the source of intermediate water in the WSAG. We also note that detectable ^{228}Ra exists below the pycnocline, nevertheless vertical stratification is obvious in the WSAG due to low salinity in the mixed layer. Since ^{228}Ra decreases by radioactive decay with a half-life of 5.8 yr, the ^{228}Ra activity concentration and ^{228}Ra/^{226}Ra activity ratio can be used as a transient tracer for horizontal transport when underlying waters are isolated from the surface layer and a new supply is lacking.

Our ^{228}Ra measurements were limited to water layers above 600 m and sparse due to the need for time-consuming large-volume water sampling during a short cruise. However, ultra-low background gamma-ray detection is possible for a low minimum detectable activity. To calculate the inventory of ^{228}Ra in the water column, we interpolated ^{228}Ra activity concentrations with depth between the surface to 397 m. ^{228}Ra activity concentrations below 397 m depth were extrapolated using the relationship from 199 to 397 m depths. ^{228}Ra activity concentrations were assumed to decrease with depth and reach zero around 700 m depth. Calculated ^{228}Ra activity concentration at 600 m depth was 0.01 Bq m^{-3}, which was lower than the detectable ^{228}Ra activity concentration (0.02 Bq m^{-3}).

Vertical Flux Estimation of ^{228}Ra

We examined the inventory of ^{228}Ra between depth z_1 and z_2 in the water column as:

$$^{228}Ra_{inventory,\ z1-Z2} = \int_{z1}^{Z2} {}^{228}Ra(z)dz\,. \quad (1)$$

Calculated ^{228}Ra inventories are shown in **Table 2**. ^{228}Ra inventories below the depth z_1 to bottom are also shown. ^{228}Ra inventories in the mixed layer (0 to 50 m) and dichothermal layer (50 to 110 m) was 5.0 Bq m^{-2} and 5.3 Bq m^{-1}, respectively. On the other hand, ^{228}Ra inventories in the mesothermal layer underlying the pycnocline (below 160 m depth) was 19.4 Bq m^{-2}, which was comparable to the inventory in the surface layer.

Here, if we assumed the steady state, supply of ^{228}Ra ($F_{Ra\text{-}228}$) should be balanced with the reduction rate of ^{228}Ra inventory by radioactive decay as the following equation.

$$R_{Ra-228} = \lambda_{^{228}Ra} \times {}^{228}Ra_{inventory,\ \ below\ z} \quad (2)$$

Here, $^{\lambda 228}Ra$ is decay constant of ^{228}Ra (3.82 × 10^{-9} s^{-1}).

Ku et al. (1995) and Nozaki and Yamamoto (2001) reported that ^{228}Ra in the mixed layer was transported downwardly by vertical eddy diffusion (one-dimensional model) and its inventory was decreased by radioactive decay. We did not consider other possible processes, such as lateral advection, biological uptake and regeneration processes, in accordance with previous studies (Ku et al., 1995; Nozaki and Yamamoto, 2001).

In addition, ^{228}Ra below the pycnocline could be supplied only from the upper water by vertical eddy diffusion. We calculated the vertical eddy diffusive flux of ^{228}Ra ($F_{Ra\text{-}228}$) across the depth horizon z as the product of vertical eddy diffusivity K_z (m^2 s^{-1}) obtained from turbulence observation using microstructure profiler and vertical gradient of ^{228}Ra activity concentration, ($\partial\ ^{228}Ra\ /\ \partial z$) in the depth profile (**Table 3**).

$$F_{Ra-228} = -K_z \times \left(\frac{\partial\, ^{228}Ra}{\partial\, z}\right)_z \quad (3)$$

TABLE 2 | ^{228}Ra inventory reduction rate by radioactive decay.

	Depth (m)		^{228}Ra activity concentration (Bq m^{-3})	^{228}Ra inventory z_1-z_2 (Bq m^{-2})	^{228}Ra inventory below z_1 (Bq m^{-3})	Reduction rate of ^{228}Ra by radioactive decay $R_{Ra\text{-}228}$ (Bq m^{-2} d^{-1})
	z_1	z_2				
Mixed layer	0 -	50	0.099	5.0	33.4	0.0110
Dichothermal layer	50 -	110	0.099	5.3	28.5	0.0094
Pycnocline	110 -	160	0.078	3.7	23.2	0.0076
Mesothermal layer	160 -		0.072	19.4	19.4	0.0064

TABLE 3 | Comparison between ^{228}Ra diffusive flux and reduction rate by radioactive decay.

Depth(m)	K_z(m^2 s^{-1})	dRa/dz(Bq m^{-4})	^{228}Ra diffusive flux$F_{Ra\text{-}228}$(Bq m^{-2} d^{-1})	$F_{Ra\text{-}228}/R_{Ra\text{-}228}$
10	0.0159	–	–	–
25	0.0080	–	–	–
50	0.0000096	-0.000017	0.000014	0.1%
100	0.0000019	-0.00014	0.000024	0.3%
125	0.0000023	-0.00015	0.000029	0.4%
150	0.0000027	-0.00015	0.000034	0.4%
175	0.0000038	-0.00015	0.000048	0.8%
200	0.0000049	-0.00014	0.000060	0.9%
225	0.0000053	-0.00014	0.000062	1.0%
250	0.0000056	-0.00014	0.000066	1.0%

The ^{228}Ra activity concentrations were uniform in the mixed layer (0-50 m) and no vertical concentration gradient could be distinguished. On the other hand, the vertical eddy diffusive flux of ^{228}Ra entraining in the deeper layer and crossing over the pycnocline was ranged from 0.000029 Bq m^{-2} d^{-1} (125 m) to 0.000034 Bq m^{-2} d^{-1} (150 m). It was two orders of magnitude smaller (0.4%) than the reduction rate of ^{228}Ra inventory in the water column even if a large uncertainty of vertical gradients of ^{228}Ra activity concentration derived from ^{228}Ra analysis was considered. Assuming the steady state, the imbalance between the fluxes strongly suggested that ^{228}Ra below the mixed layer was supplied by lateral advection.

According to Ku et al. (1995), nitrate flux between 100 m and 200 m was estimated as 3-10 mmol m^{-2} d^{-1} by using vertical profiles of ^{228}Ra and nitrate, and the ^{228}Ra-based diffusive nitrate flux in this study was in the same range. Previously, Nozaki and Yamamoto (2001) also calculated nitrate fluxes in the eastern Indian Ocean, and pointed out the lateral transport of ^{228}Ra might elevate activity concentrations of ^{228}Ra in intermediate water, resulting in overestimation of the fluxes. Here, we considered this was the case in the WSAG. The nitrate flux range based on the ^{228}Ra profile was two to four orders of magnitude greater than the reported values in the subarctic Pacific (0.03-0.7 mmol m^{-2} d^{-1}; Nishioka et al., 2020). This discrepancy implied ^{228}Ra below the pycnocline in the WSAG was supplied from lateral advection. Nishioka et al. (2020) reported that the nitrate fluxes were largest in the Kuril Straits (~100 mmol m^{-2} d^{-1}) and second largest along the Aleutian Islands (~10 mmol m^{-2} d^{-1}), which was caused only by enhanced turbulent diapycnal mixing near the marginal area (Itoh et al., 2010; Itoh et al., 2011; Yagi and Yasuda, 2012). It is important to study the ^{228}Ra source and its supply process to mesothermal water in the intermediate depth for better understanding of biogeochemical cycles of nutrients in the WSAG. Low-oxygen and high-silicate and high-nitrate water are found in the WSAG and Bering Gyre at the isopycnal surfaces of 26.9 and 27.15, corresponding to 199 m and 397 m depths at Station K2, respectively (**Figure S2**). We could trace the relatively lower salinity water signature (>33.8) at σ_θ = 26.9 back to the EKC along the Kamchatka Peninsula and the western Bering Gyre.

Higher ^{228}Ra/^{226}Ra ratios were reported near the Kamchatka Peninsula in the WSAG and in the Bering Gyre. The highest ratio (0.15) was reported for the continental shelf area in the Bering Sea (Li et al., 2017; Inoue et al., 2020). Assuming simple mixing between surface water in the continental shelf in the Bering Sea (^{228}Ra/^{226}Ra =0.15, salinity = 32.8; Inoue et al., 2020) and

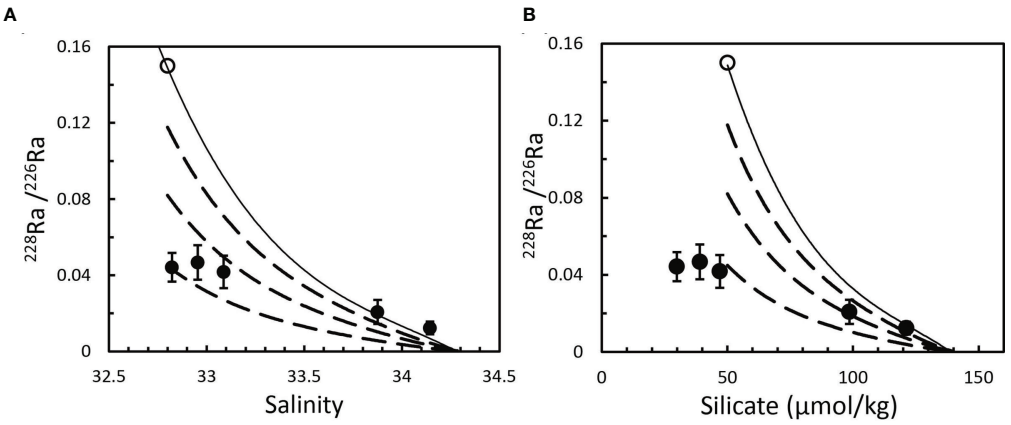

FIGURE 4 | Relationships of ^{228}Ra/^{226}Ra activity ratio with **(A)** salinity and **(B)** silicate concentration. Open circles indicate previously observed data in the continental shelf in the Bering Sea (Inoue et al., 2020). The solid lines are the mixing curves between the oxygen minimum layer and surface water in the continental shelf in the Bering Sea. The dashed lines are considered to represent ^{228}Ra depletion by radioactive decay at elapsed times of 2, 5, and 10 yr before mixing.

intermediate water at the oxygen minimum layer ($^{228}Ra/^{226}Ra$ =0, salinity = 34.3) without radioactive decay, the calculated $^{228}Ra/^{226}Ra$ in the mesothermal layer exceeded the observed values (**Figure 4**). If the surface water in the continental shelf was penetrated within 2 years for salinity and 7 years for silicate, the calculated ratios were close to the observed values. To investigate the lateral transport process of Ra isotopes in the WSAG, we need more information on the possible ^{228}Ra sources near the Kamchatka Peninsula and the Bering Gyre.

CONCLUSION

The vertical distributions of the Ra isotopes, ^{226}Ra and ^{228}Ra, were determined for the first time from large-volume seawater sampling done at Station K2 in the western Subarctic Pacific Gyre (WSAG).

1. The ^{228}Ra activity concentrations in the surface layer were controlled by the mixture of the low-^{228}Ra activity concentration EKC water and the high-^{228}Ra activity concentration surface water in the Okhotsk Sea, and the ^{228}Ra activity concentrations were highly correlated with salinity in the WSAG.
2. The vertical distributions of ^{226}Ra and ^{228}Ra activity concentrations were uniform from the surface to the dichothermal layer of 100 m depth due to vertical mixing in winter.
3. ^{228}Ra activity concentrations decreased with water depth below the main pycnocline. The vertical transport by eddy diffusion was concluded to be a minor process for the ^{228}Ra flux, and the horizontal transport possibly supplied ^{228}Ra in the intermediate mesothermal water (200-400 m depths) in the open ocean in the WSAG.
4. Observed ^{228}Ra activity concentrations in the mesothermal layer implied that water with a relatively high $^{228}Ra/^{226}Ra$ activity ratio, which can be found in the EKC, was supplied to the interior of the WSAG and laterally advected.

DATA AVAILABILITY STATEMENT

The original contributions presented in the study are included in the article/**Supplementary Material**. Further inquiries can be directed to the corresponding author.

AUTHOR CONTRIBUTIONS

HT and HO wrote the first draft of the manuscript. TH, JN, and MI performed the experiments and statistical analysis. HT, HO, and TT contributed to the conception and design of the study. All authors contributed to manuscript revision, read, and approved the submitted version.

FUNDING

This work was supported by the Grant-in-Aid for Scientific Research on Innovative Areas, the Ocean Mixing Processes: OMIX Project (Grants JP15H05820, JP15H05817, and 17H00775) the Grant-in-Aid for Scientific Research (S) (21H05056) and the cooperative research program of Institute of Nature and Environmental Technology, Kanazawa University (18025).

ACKNOWLEDGMENTS

We thank the captain, crew, and scientists on board the research vessel TS Oshoro-Maru for their help with observations and sample collection.

SUPPLEMENTARY MATERIAL

The Supplementary Material for this article can be found online at: https://www.frontiersin.org/articles/10.3389/fmars.2022.824862/full#supplementary-material

REFERENCES

Boyd, P. W., Law, C. S., Wong, C. S., Nojiri, Y., Tsuda, A., Levasseur, M., et al. (2004). The Decline and Fate of an Iron-Induced Subarctic Phytoplankton Bloom. *Nature* 428 (6982), 549–553. doi: 10.1038/nature02437

Broecker, W. S., Doddard, J., and Sarmiento, J. (1976). The Distribution of ^{226}Ra in the Atlantic Ocean. *Ear. Planet. Sci. Lett.* 32, 220–235. doi: 10.1016/0012-821X(76)90063-7

Cai, P., Huang, Y., Chen, M., Guo, L., Li, G., and Qiu, Y. (2002). New Production Based on ^{228}Ra-Derived Nutrient Budgets and Thorium-Estimated POC Export at the Intercalibration Station in the South China Sea. *Deep-Sea. Res. Pt. I.* 49 (1), 53–66. doi: 10.1016/S0967-0637(01)00040-1

Carpenter, J. H. (1965). The Chesapeake Bay Institute Technique for the Winkler Dissolved Oxygen Method. *Limnol. Oceanogr.* 10, 141–143. doi: 10.4319/lo.1965.10.1.0141

Cho, H. M., Kim, G., Kwon, E. Y., Moosdorf, N., Garcia-Orellana, J., and Santos, I. R. (2018). Radium Tracing Nutrient Inputs Through Submarine Groundwater Discharge in the Global Ocean. *Sci. Rep.* 8 (1), 2439. doi: 10.1038/s41598-018-20806-2

Gordon, L. I., Jennings, J. C.Jr., Ross, A. A., and Krest, J. M. (1992). An Suggested Protocol for Continuous Flow Automated Analysis of Seawater Nutrients (Phosphate, Nitrate, Nitrite and Silicic Acid) in the WOCE Hydrographic Program and the Joint Global Ocean Fluxes Study, OSU Coll. Of Oc. *Descr. Chem. Oc. Grp. Tech. Rpt.* 92-1

Hamajima, Y., and Komura, K. (2004). Background Components of Ge Detectors in Ogoya Underground Laboratory. *Appl. Radiat. Isot.* 61, 179–183. doi: 10.1016/j.apradiso.2004.03.041

Inoue, M., Shirotani, Y., Nagao, S., Kofuji, H., Volkov, Y. N., and Nishioka, J. (2016). Migration of the FDNPP-Derived ^{134}Cs and ^{137}Cs Along With ^{226}Ra and ^{228}Ra Concentrations Across the Northwestern North Pacific Ocean. *J. Environ. Radioact.* 162–163, 33–38. doi: 10.1016/j.jenvrad.2016.05.011

Inoue, M., Takehara, R., Hanaki, S., Kameyama, H., Nishioka, J., and Nagao, S. (2020). Distributions of Radiocesium and Radium Isotopes in the Western Bering Sea in 2018. *Mar. Chem.* 225, 103843. doi: 10.1016/j.marchem.2020.103843

Inoue, M., Yoshida, K., Minakawa, M., Kofuji, H., Nagao, S., Hamajima, Y., et al. (2012). Spatial Variations of ^{226}Ra, ^{228}Ra, ^{137}Cs and ^{228}Th Activities in the Southwestern Okhotsk Sea. *J. Environ. Radioact.* 104, 75–80. doi: 10.1016/j.jenvrad.2011.09.007

Itoh, S., Yasuda, I., Nakatsuka, T., Nishioka, J., and Volkov, Y. N. (2010). Fine- and Microstructure Observations in the Urup Strait, Kuril Islands, During August 2006. *J. Geophys. Res.: Ocean.* 115 (C08004), 1–12. doi: 10.1029/2009JC005629

Itoh, S., Yasuda, I., Yagi, M., Osafune, S., Kaneko, H., Nishioka, J., et al. (2011). Strong Vertical Mixing in the Urup Strait, *Geophys. Res. Lett.* 38 (16). doi: 10.1029/2011GL048507

Kadko, D., and Muench, R. (2005). Evaluation of Shelf–Basin Interaction in the Western Arctic by Use of Short-Lived Radium Isotopes: The Importance of Mesoscale Processes. *Deep-Sea. Res. Pt. II.* 52 (24), 3227–3244. doi: 10.1016/j.dsr2.2005.10.008

Kawakami, H., and Kusakabe, M. (2008). Surface Water Mixing Estimated From ^{228}Ra and ^{226}Ra in the Northwestern North Pacific. *J. Environ. Radioact.* 99 (8), 1335–1340. doi: 10.1016/j.jenvrad.2008.04.011

Ku, T. L., Luo, S., Kusakabe, M., and Bishop, J. K. B. (1995). ^{228}Ra-Derived Nutrient Budgets in the Upper Equatorial Pacific and the Role of "New" Silicate in Limiting Productivity. *Deep. Sea. Res. Pt. II.* 42 (2), 479–497. doi: 10.1016/0967-0645(95)00020-Q

Kwon, E. Y., Kim, G., Primeau, F., Moore, W. S., Cho, H. M., De Vries, T., et al. (2014). Global Estimate of Submarine Groundwater Discharge Based on an Observationally Constrained Radium Isotope Model. *Geophys. Res. Lett.* 41 (23), 8438–8444. doi: 10.1002/2014gl061574

Legeleux, F., and Reyss, J. L. (1996). ^{228}Ra^{226}Ra Activity Ratio in Oceanic Settling Particles: Implications Regarding the Use of Barium as a Proxy for Paleoproductivity Reconstruction. *Deep. Sea. Res. Pt. I.: Ocean.* 43 (11), 1857–1863. doi: 10.1016/S0967-0637(96)00086-6

Le Gland, G., Mémery, L., Aumont, O., and Resplandy, L. (2017). Improving the Inverse Modeling of a Trace Isotope: How Precisely can Radium-228 Fluxes Toward the Ocean and Submarine Groundwater Discharge be Estimated? *Biogeosciences* 14 (13), 3171–3189. doi: 10.5194/bg-14-3171-2017

Li, Q., Chen, M., Jia, R., Zeng, J., Lin, H., Zhen, M., et al. (2017). Transit Time of River Water in the Bering and Chukchi Seas Estimated From δ^{18}O and Radium Isotopes. *Prog. Oceanogr.* 159, 115–129. doi: 10.1016/j.pocean.2017.08.004

Longhurst, A. (2007). *Ecological Geography of the Sea* (London: Academic Press). doi: 10.1016/B978-012455521-1/50002-4

Moore, W. S. (1969). Measurement of Ra228 and Th228 in Sea Water. *J. Geophys. Res.* 74 (2), 694–704. doi: 10.1029/JB074i002p00694

Moore, W. S. (1972). Radium-228: Application to Thermocline Mixing Studies. *Earth. Planet. Sci. Lett.* 16 (3), 421–422. doi: 10.1016/0012-821X(72)90161-6

Moore, W. S., Sarmiento, J. L., and Key, R. (1986). Tracing the Amazon Component of Surface Atlantic Water Using ^{228}Ra, Salinity and Silica. *J. Geophys. Res.: Ocean.* 91 (C2), 2574–2580. doi: 10.1029/JC091iC02p02574

Nakano, Y., Inoue, M., and Komura, K. (2008). Simple Coprecipitation Method Combined With Low-Background γ-Spectrometry: Determination of ^{7}Be, ^{137}Cs, ^{210}Pb, and Radium and Thorium Isotopes in Small-Volume Coastal Water Samples. *J. Oceanogr.* 64 (5), 713–717. doi: 10.1007/s10872-008-0060-y

Nakano-Ohta, T., and Sato, J. (2006). Determination of ^{228}Ra and ^{226}Ra in Seawater Collected on Manganese-Impregnated Acrylic Fiber. *Radioisotopes* 55 (8), 443–449. doi: 10.3769/radioisotopes.55.443

Nishioka, J., Nakatsuka, T., Watanabe, Y. W., Yasuda, I., Kuma, K., Ogawa, H., et al. (2013). Intensive Mixing Along an Island Chain Controls Oceanic Biogeochemical Cycles. *Global Biogeochem. Cy.* 27 (3), 920–929. doi: 10.1002/gbc.20088

Nishioka, J., Obata, H., Ogawa, H., Ono, K., Yamashita, Y., Lee, K., et al. (2020). Subpolar Marginal Seas Fuel the North Pacific Through the Intermediate Water at the Termination of the Global Ocean Circulation. *Proc. Natl. Acad. Sci. U.S.A.* 117 (23), 12665–12673. doi: 10.1073/pnas.2000658117

Nozaki, Y., Dobashi, F., Kato, Y., and Yamamoto, Y. (1998). Distribution of Ra Isotopes and the 210Pb and 210Po Balance in Surface Seawaters of the Mid Northern Hemisphere. *Deep. Sea. Res. Pt. I.: Ocean.* 45 (8), 1263–1284. doi: 10.1016/S0967-0637(98)00016-8

Nozaki, Y., Kasemsupaya, V., and Tsubota, H. (1990). The Distribution of ^{228}Ra and ^{226}Ra in the Surface Waters of the Northern North Pacific. *Geochem. J.* 24 (1), 1–6. doi: 10.2343/geochemj.24.1

Nozaki, Y., and Yamamoto, Y. (2001). Radium 228 Based Nitrate Fluxes in the Eastern Indian Ocean and the South China Sea and a Silicon-Induced "Alkalinity Pump" Hypothesis. *Global Biogeochem. Cy.* 15 (3), 555–567. doi: 10.1029/2000gb001309

Okubo, T. (1980). Radium-228 in the Japan Sea. *J. Oceanogr. Soc Japan.* 36 (5), 263–268. doi: 10.1007/BF02072128

Rutgers van der Loeff, M. M., Key, R. M., Scholten, J., Bauch, D., and Michel, A. (1995). ^{228}Ra as a Tracer for Shelf Water in the Arctic Ocean. *Deep-Sea. Res. Pt. II.* 42 (6), 1533–1553. doi: 10.1016/0967-0645(95)00053-4

Rutgers van der Loeff, M. M., Kühne, S., Wahsner, M., Höltzen, H., Frank, M., Ekwurzel, B., et al. (2003). ^{228}Ra and ^{226}Ra in the Kara and Laptev Seas. *Cont. Shelf Res.* 23 (1), 113–124. doi: 10.1016/S0278-4343(02)00169-3

Sakurai, Y. (2007). An Overview of the Oyashio Ecosystem. *Deep-Sea. Res. Pt. II.* 54 (23), 2526–2542. doi: 10.1016/j.dsr2.2007.02.007

Takahashi, T., Sutherland, S. C., Sweeney, C., Poisson, A., Metzl, N., Tilbrook, B., et al. (2002). Global Sea–Air CO_2 Flux Based on Climatological Surface Ocean Pco_2, and Seasonal Biological and Temperature Effects. *Deep-Sea. Res. Pt. II.* 49 (9), 1601–1622. doi: 10.1016/S0967-0645(02)00003-6

Tsuda, A., Takeda, S., Saito, H., Nishioka, J., Nojiri, Y., Kudo, I., et al. (2003). A Mesoscale Iron Enrichment in the Western Subarctic Pacific Induces a Large Centric Diatom Bloom. *Science* 300 (5621), 958–961. doi: 10.1126/science.1082000

Ueno, H., and Yasuda, I. (2000). Distribution and Formation of the Mesothermal Structure (Temperature Inversions) in the North Pacific Subarctic Region. *J. Geophys. Res.: Ocean.* 105 (C7), 16885–16897. doi: 10.1029/2000JC900020

Ueno, H., and Yasuda, I. (2005). Temperature Inversions in the Subarctic North Pacific. *J. Phys. Oceanogr.* 35 (12), 2444–2456. doi: 10.1175/jpo2829.1

van Beek, P., François, R., Conte, M., Reyss, J. L., Souhaut, M., and Charette, M. (2007). ^{228}Ra/^{226}Ra and ^{226}Ra/Ba Ratios to Track Barite Formation and Transport in the Water Column. *Geochim. Cosmochim. Acta* 71 (1), 71–86. doi: 10.1016/j.gca.2006.07.041

Yagi, M., and Yasuda, I. (2012). Deep Intense Vertical Mixing in the Bussol' Strait. *Geophys Res. Lett.* 39 (1), 1–5. doi: doi:10.1029/2011GL050349

Yamada, M., and Nozaki, Y. (1986). Radium Isotopes in Coastal and Open Ocean Surface Waters of the Western North Pacific. *Mar. Chem.* 19 (4), 379–389. doi: 10.1016/0304-4203(86)90057-5

Yasuda, I. (1997). The Origin of the North Pacific Intermediate Water. *J. Geophys. Res.: Ocean.* 102 (C1), 893–909. doi: 10.1029/96JC02938

Conflict of Interest: The authors declare that the research was conducted in the absence of any commercial or financial relationships that could be construed as a potential conflict of interest.

Publisher's Note: All claims expressed in this article are solely those of the authors and do not necessarily represent those of their affiliated organizations, or those of the publisher, the editors and the reviewers. Any product that may be evaluated in this article, or claim that may be made by its manufacturer, is not guaranteed or endorsed by the publisher.

frontiers | Frontiers in Marine Science

ORIGINAL RESEARCH
published: 15 July 2022
doi: 10.3389/fmars.2022.859117

Fractionation of ^{226}Ra and Ba in the Upper North Pacific Ocean

Pieter van Beek[1], Roger François[2], Makio Honda[3], Matthew A. Charette[4], Jean-Louis Reyss[5], Raja Ganeshram[6], Christophe Monnin[7] and Susumu Honjo[4†]*

[1] Laboratoire d'Etudes en Géophysique et Océanographie Spatiales (LEGOS), Université de Toulouse, CNES/CNRS/IRD/ Université Toulouse III Paul Sabatier, Toulouse, France, [2] Department of Earth, Ocean, and Atmospheric Sciences, University of British Columbia, Vancouver, BC, Canada, [3] Department of Environmental Geochemical Cycle Research (DEGCR), Japan Agency for Marine-Earth Science and Technology (JAMSTEC), Yokosuka, Japan, [4] Department of Marine Chemistry and Geochemistry, Woods Hole Oceanographic Institution, WoodsHole, MA, United States, [5] Laboratoire des Sciences du Climat et de l'Environnement, Gif-sur-Yvette, France, [6] School of Geosciences, Grant Institute, University of Edinburgh, Edinburgh, United Kingdom, [7] Géosciences Environnement Toulouse (CNRS/UPS/IRD/CNES), Observatoire Midi Pyrénées, Toulouse, France

Investigations conducted during the GEOSECS program concluded that radium-226 ($T_{1/2}$ = 1602 y) and barium are tightly correlated in waters above 2500 m in the Atlantic, Pacific and Antarctic Oceans, with a fairly uniform ^{226}Ra/Ba ratio of 2.3 ± 0.2 dpm µmol^{-1} (4.6 nmol ^{226}Ra/mol Ba). Here, we report new ^{226}Ra and Ba data obtained at three different stations in the Pacific Ocean: stations K1 and K3 in the North-West Pacific and station old Hale Aloha, off Hawaii Island. The relationship between ^{226}Ra and Ba found at these stations is broadly consistent with that reported during the GEOSECS program. At the three investigated stations, however, we find that the ^{226}Ra/Ba ratios are significantly lower in the upper 500 m of the water column than at greater depths, a pattern that was overlooked during the GEOSECS program, either because of the precision of the measurements or because of the relatively low sampling resolution in the upper 500 m. Although not always apparent in individual GEOSECS profiles, this trend was noted before from the non-zero intercept of the linear regression when plotting the global data set of Ba versus ^{226}Ra seawater concentration and was attributed, at least in part, to the predominance of surface input from rivers for Ba versus bottom input from sediments for ^{226}Ra. Similarly, low ^{226}Ra/Ba ratios in the upper 500 m have been reported in other oceanic basins (e.g. Atlantic Ocean). Parallel to the low ^{226}Ra/Ba ratios in seawater, higher ^{226}Ra/Ba ratios were found in suspended particles collected in the upper 500 m. This suggests that fractionation between the two elements may contribute to the lower ^{226}Ra/Ba ratios found in the upper 500 m, with ^{226}Ra being preferentially removed from surface water, possibly as a result of mass fractionation during celestite formation by acantharians and/or barite precipitation, since both chemical elements have similar ionic radius and the same configuration of valence electrons. This finding has implications for dating of marine carbonates by ^{226}Ra, which requires a constant initial ^{226}Ra/Ba ratio incorporated in the shells and for using ^{226}Ra as an abyssal circulation and mixing tracer.

Keywords: radium, barium, seawater, ratio, fractionation, dating, ocean circulation, suspended particles

OPEN ACCESS

Edited by:
Paul Mcginnity, IAEA International Atomic Energy Agency, Monaco

Reviewed by:
Zvi Steiner, Helmholtz Association of German Research Centres (HZ), Germany
Frank Dehairs, Vrije University Brussel, Belgium

****Correspondence:***
Pieter van Beek
vanbeek@legos.obs-mip.fr

[†]Deceased

Specialty section:
This article was submitted to Ocean Observation, a section of the journal Frontiers in Marine Science

Received: *20 January 2022*
Accepted: *25 May 2022*
Published: *15 July 2022*

Citation:
van Beek P, François R, Honda M, Charette MA, Reyss J-L, Ganeshram R, Monnin C and Honjo S (2022) Fractionation of ^{226}Ra and Ba in the Upper North Pacific Ocean. Front. Mar. Sci. 9:859117. doi: 10.3389/fmars.2022.859117

INTRODUCTION

Seawater radium (Ra) and barium (Ba) distributions were measured extensively in all major ocean basins during the GEOSECS program (Broecker et al., 1967; Wolgemuth and Broecker, 1970; Bacon and Edmond, 1972; Broecker et al., 1976; Chan et al., 1976; Ku and Lin, 1976; Chung and Craig, 1980; Ku et al., 1980) and more recently during the GEOTRACES program (see e.g. Le Roy et al., 2018). Because of their similar chemical properties, it was argued that Ba and ^{226}Ra would not be biologically fractionated and that ^{226}Ra/Ba ratios would only be affected by the decay of ^{226}Ra, providing an independent clock that would complement the information obtained from $^{14}C/^{12}C$ ratios to yield important constraints on the circulation and mixing of abyssal waters (e.g. Ku and Luo, 1994). The GEOSECS data showed that ^{226}Ra and Ba are linearly correlated over much of the water column in the Atlantic, Pacific and Indian Oceans (**Figure 1 of the Supplementary Material**), resulting in a fairly constant ^{226}Ra/Ba ratio of 2.3 ± 0.2 dpm μmol^{-1} or 4.6 nmol mol^{-1} (Li et al., 1973; Chan et al., 1976; Ku et al., 1980; Foster et al., 2004). Several factors, however, have complicated the use of ^{226}Ra/Ba as a large scale abyssal circulation and mixing tracer. The source of Ba, which is added mainly to the upper ocean by rivers and submarine groundwater discharge, is different from the source of ^{226}Ra, which has a significant oceanic source through diffusion from deep-sea sediments. As a result, the linear correlation between Ba and ^{226}Ra breaks down in near-bottom waters, where ^{226}Ra activities are significantly higher than predicted from the radium-barium relationship (Chung, 1974; Chan et al., 1976; Chung and Craig, 1980; Ku et al., 1980; Rhein and Schlitzer, 1988). Furthermore, the rate of ^{226}Ra diffusion from the bottom is variable and depends on particle settling flux and mineral dissolution on the seafloor, which dictate the ^{230}Th concentration of the sediment that generates ^{226}Ra by decay (Chan et al., 1976; Chung, 1976). Likewise, an inherent assumption when using ^{226}Ra/Ba as a circulation/mixing tracer is that biological recycling does not fractionate Ba and Ra, i.e. they are taken up and released in the same ratio at which they are found in seawater. This assumption, however, has never been rigorously verified (Ku and Luo, 1994).

The increasing concentration of ^{226}Ra and Ba from the surface to the deep ocean indicates that these elements are removed from surface seawater by sinking particles and released back to seawater at depth. Ku and Luo (1994) argue that most of the release happens on the seafloor rather than from sinking particles. Uptake of Ba and ^{226}Ra in the upper water column may occur through substitution for calcium in calcareous skeletons (Lea and Boyle, 1989; Lea and Boyle, 1990), adsorption onto diatom frustules or Fe hydroxides (Bishop, 1988; Ganeshram et al., 2003; Sternberg et al., 2005), substitution for Sr in celestite skeletons produced by acantharians (Bernstein et al., 1987; Bernstein et al., 1992; Jacquet et al., 2007) and barite ($BaSO_4$) precipitation (Chow and Goldberg, 1960; Dehairs et al., 1980; Bishop, 1988; Dehairs et al., 1990; Dehairs et al., 1991; Stroobants et al., 1991). Barite crystals are generally viewed as the most important Ba and Ra carriers in the water column (Dehairs et al., 1980; Dehairs et al., 1990; Moore and Dymond, 1991; Legeleux and Reyss, 1996). The observation of higher particulate Ba concentrations in the mesopelagic layer (ca. 200-600 m) thus led to conclude that barite predominantly forms in this depth interval (e.g. Dehairs et al., 1980), a pattern that was confirmed by the study of the ^{228}Ra/^{226}Ra signature of sinking particles (Legeleux and Reyss, 1996) and more recently by the analysis of barium stable isotopes (Horner et al., 2015; Hsieh and Hendersom, 2017).

Although the exact mechanism of barite formation in seawater is still not fully understood, it is generally accepted that barite precipitates in subsurface waters within supersaturated microenvironments that result from the decay of organic matter exported from the euphotic layer (Chow and Goldberg, 1960; Dehairs et al., 1980; Bishop, 1988; Stroobants et al., 1991; Legeleux and Reyss, 1996). Biogenic aggregates are thus considered as the necessary substrate for barite formation, a feature that was also confirmed by *in vitro* experiments (Ganeshram et al., 2003; Gonzales-Munoz et al., 2003; Sternberg et al., 2005). The observed relationship between particulate Ba (predominantly barite), oxygen and pCO_2 concentrations in the water column highlighted the potential role of bacteria in barite precipitation (Dehairs et al., 1990; Dehairs et al., 2008; Jacquet et al., 2011). More recently, it was shown that extracellular polymeric substances (EPS) - that are known to bind many chemical elements - could serve as nucleation sites that favor Ba accumulation, thus leading to the saturated microenvironment required for barite precipitation in undersaturated waters (Martinez-Ruiz et al., 2020). Alternatively, the high Ba concentrations found in celestite ($SrSO_4$) skeletons produced by acantharians led to the suggestion that the dissolution of these highly soluble skeletons could contribute to barite formation by releasing Ba and sulfate in the microenvironment of settling particles (Bernstein et al., 1987; Bernstein et al., 1992; Bernstein et al., 1998; Bernstein and Byrne, 2004).

Finally, in addition to being a useful tracer of ocean circulation and mixing, ^{226}Ra - with a half-life of 1602 y - has been used for dating marine samples within the Holocene epoch (eg., Schmidt and Cochran, 2010). In particular, the decay of ^{226}Ra incorporated in barite has been used to derive sedimentation rates in deep-sea sediments (Paytan et al., 1996; van Beek and Reyss, 2001; van Beek et al., 2002; van Beek et al., 2004) and to provide estimates of past sea-surface reservoir ages by comparing ages deduced from ^{226}Ra activities in barite and ^{14}C ages derived from planktic foraminifers (van Beek et al., 2002). Likewise, carbonate minerals can be dated by assuming that they acquire their initial ^{226}Ra/Ba ratio from ambient seawater (Berkman and Ku, 1998; Staubwasser et al., 2004). The accuracy of these dating methods, however, relies on knowing the initial ^{226}Ra activity (or initial ^{226}Ra/Ba ratio) incorporated in the samples and on their constancy over the dating period (i.e. the Holocene).

In this work, we report vertical profiles of ^{226}Ra, Ba and ^{226}Ra/Ba from three different locations in the Pacific Ocean (stations K1 and K3 in the North-West Pacific and old station Hale Aloha, off Hawaii) to better assess the variability of ^{226}Ra/Ba in seawater. We also document the underlying causes for the observed variations by i) conducting leaching experiments on the suspended particles that aim at characterizing the different Ba carriers in the

water column, ii) characterizing the saturation state of the water column with respect to barite and iii) studying the Ra isotopic signature (^{228}Ra/^{226}Ra) of the suspended particles to provide information on the depth of particulate Ba formation and transport in the water column.

MATERIAL AND METHODS

Study Sites

Samples were collected in the North-West Pacific in December 2002 on board RV Mirai, as part of the JPAC program (PIs: Makio Honda and Susumu Honjo) at station K1 (51°N-165°E; 5,130 m) in the Western Subarctic Gyre and at station K3 (39°N-160°E; 5,470 m) usually located north of the Kuroshio Front (**Figure 1**). We also report data on samples collected at old station Hale Aloha (22°28'N; 158°8' W) located north of Hawaii in June 2002 on board RV *Ka'imikai-o-Kanaloa* (*KoK)* and in August 2002 on board RV Wecoma (PI: Mike Bacon). This station is located south of station ALOHA that is the site of the Hawaii Ocean Time-series program (HOT, 22.75°N; 158.00°W). These sites off Hawaii are oligotrophic (low macronutrient and therefore low chlorophyll concentration; Karl and Lukas, 1996) with warm waters, whereas the waters of the Western Subarctic Gyre are cold and mesotrophic (Honda, 2003; Buesseler et al., 2008). Coccolithophorids ($CaCO_3$) are common off Hawaii (Cortes et al., 2001), whereas the waters of the Western Subarctic Gyre (e.g. stations K2 and K1; **Figure 1**) are dominated by diatoms (Honda et al., 2002; Honda et al., 2006). Station K3 also located in the northwestern North Pacific subarctic region is expected to be dominated by diatoms, based on sediment trap data from a nearby station (40°N/165°E) indicating that biogenic opal is predominant (Honda et al., 2002). The export of carbon is also higher in the Subarctic Gyre compared with the oligotrophic region off Hawaii (Buesseler et al., 2008).

The two investigated areas were studied later in the framework of the VERtical Transport In the Global Ocean, VERTIGO project, in years 2004 and 2005 (i.e., station Aloha, off Hawaii and station K2 in the Western Subarctic Gyre) (Buesseler et al., 2008). In particular, the Ba dataset (dissolved Ba and particulate Ba concentrations) obtained in the JPAC project on the entire water column can be compared to the Ba dataset collected during the VERTIGO project in the "twilight zone" (0-1000 m) (Dehairs et al., 2008). In addition, the vertical distribution of the ^{226}Ra activities reported here complement the study of Kawakami and Kusakabe (2008) who investigated the horizontal distribution of ^{226}Ra (and ^{228}Ra) in surface waters of the northwestern North Pacific Ocean. Time-series sediment trap moorings have been deployed in the northwestern North Pacific Ocean and provide information on sinking particle fluxes in the region (Honda, 2003).

The vertical profiles of potential temperature, salinity and potential density are reported in **Figure 2 of the Supplementary Material** for both stations K1 and K3. Station K3 is usually located north of the Kuroshio Front. However, Argo floats measurements conducted in the Northwest Pacific (Oka et al., 2015) indicate that the Kuroshio may sometimes extent toward station K3 (**Figure 3 of Supplementary Material**). This was the case in 2002, when station K3 was investigated in the present study, as indicated by the higher potential temperature and higher salinity in the upper 400 m at station K3 (**Figure 2 of Supplementary Material**) and by geochemical tracers (see *Ra Isotopic Ratios (^{228}Ra/^{226}Ra)*).

Sample Collection

Seawater samples were collected using 12 liter-Niskin bottles. Between 35 and 56 kg of seawater were collected at old station Hale Aloha and between 74 and 130 kg per depth were collected at stations K1 and K3 to a depth of 5200 m. Such relatively large seawater volumes were collected in order to allow the determination of ^{228}Ra - in addition to ^{226}Ra - which displays

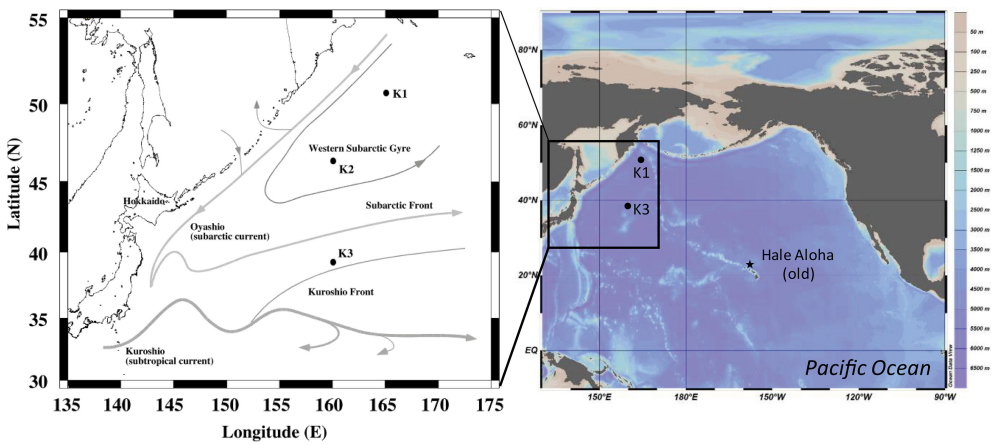

FIGURE 1 | Location of stations K1 and K3 investigated in the North-West Pacific. Station K2 investigated during the VERTIGO project is shown. Old station Hale Aloha, also investigated in this study, is located north of Hawaii Island, south of station ALOHA.

low concentrations in seawater. A separate aliquot (60 ml seawater) was collected for the determination of dissolved Ba concentrations. The large volume seawater samples (between 35 and 130 kg) were passed through a cartridge filled with acrylic fiber impregnated with MnO_2 (so called "Mn fibers"), following the technique described by Moore and Reid (1973). We used a flow-rate of 200 ml min^{-1} to ensure the quantitative separation of ^{226}Ra from seawater (Moore et al., 1985; van Beek et al., 2010).

Suspended particles were collected using McLane large volume pumps (WTS, McLane Labs, Falmouth, Ma, USA). Large volumes of seawater were filtered *in situ* through 142-mm diameter Versapor filters (acrylic copolymer on a nylon substrate; Pall Corporation), with a pore size of 0.8 µm. These large volume samples were required for gamma spectrometry and ICP-MS analyses. Additionally, seawater samples (9-11 L) were collected at station K3 using Niskin bottles and were passed through 47-mm polycarbonate filters with a pore size of 0.8 µm. To investigate the different Ba carriers within the suspended particles, the filters were sequentially leached using i, MilliQ water; ii, 10% (v/v) HNO_3; iii, 3% HCl; iv, hot 50% (v/v) HNO_3, following Ganeshram et al. (2003), slightly modified. Steps 1 to 3 were conducted on the ship immediately after collection using the clean room facility on RV Mirai. Step 4 was conducted back in the laboratory at the Woods Hole Oceanographic Institution (WHOI). Step 1 (MilliQ water) rinses dissolved Ba associated with residual seawater, weakly sorbed Ba and Ba released by cell lysis. 10% (v/v) nitric acid removes readily exchangeable and easily hydrolysable organically bound Ba. Celestite skeletons of acantharians, metal hydroxides and potentially also extracellular polymeric substances (EPS) are expected to be dissolved during steps 1 and 2. Step 3 - slightly modified from Ganeshram et al. (2003) following Weast et al. (1966), as done in van Beek and Reyss (2001) - dissolves $BaSO_4$. Finally, step 4 removes Ba associated with refractory organic matter.

Analytical Methods

For dissolved ^{226}Ra, the Mn fibers were ashed in a furnace for 16 hours at 820°C (Charette et al., 2001). The ash was then transferred into counting vials, sealed to prevent any Rn loss and analyzed for their radium activity using the low-background gamma spectrometers at the underground laboratory of Modane (Laboratoire Souterrain de Modane, LSM, French Alps) and at the underground laboratory of Ferrières (LAboratoire de mesure des FAibles RAdioactivités, LAFARA, French Pyrénées). High-efficiency, low-background, well-type germanium detectors (430 cm^3 and 950 cm^3 at LSM, Reyss et al., 1995; 280 cm^3 at LAFARA, van Beek et al., 2010; van Beek et al., 2013) were used. ^{226}Ra activities were determined using the ^{214}Pb (295 keV and 352 keV) and ^{214}Bi (609 keV) peaks. ^{228}Ra activities were determined using the 338, 911 and 969 keV peaks of ^{228}Ac. Counting times for each sample ranged from 2 to 5 days, in order to allow the detection of the low ^{228}Ra activities in addition to ^{226}Ra activities. Uncertainties for ^{226}Ra activities are errors due to counting statistics. The low counting background afforded by the counting facilities, the large sample volumes and the long counting times resulted in uncertainties for ^{226}Ra (ie. ± 1 to ± 3%) smaller than reported from most of the measurements performed during the GEOSECS program (± 3% to ± 10%).

For dissolved Ba, aliquots of seawater were analysed by isotope dilution using ^{135}Ba. The determination of dissolved Ba concentrations at old station Hale Aloha was conducted using the ICP-MS facility (Element, Finnigan) at WHOI. For samples collected in the North West Pacific (K1 and K3 stations), analyses were made using the ICP-MS facility at Scottish Universities Research and Reactor Centre, East Kilbride, Scotland (VG PlasmaQuad II). Uncertainty on the Ba concentrations is estimated at ± 2%.

For particulate ^{226}Ra and Ba, the filters were first placed in a counting tube and sealed prior to analysis to prevent any Rn loss, and counted for Ra isotopes using the low background gamma spectrometers at the underground laboratory of Modane (Laboratoire Souterrain de Modane, LSM, French Alps) using the same method as for dissolved ^{226}Ra. The Versapor filters were subsequently dissolved in a Teflon beaker with a mixture of HNO_3 (ultrapure acid), HF (ultrapure acid), and $HClO_4$ (pure acid) on a hot plate to measure Ba, ^{238}U and ^{232}Th using the ICP-MS facility at Observatoire Midi Pyrénées, Toulouse (Elan 6000 Perkin-Elmer), as described in van Beek et al. (2009). Excess Ba (Ba_{ex}), excess ^{226}Ra activities ($^{226}Ra_{ex}$) and excess ^{228}Ra activities ($^{228}Ra_{ex}$) in suspended particles were determined by subtracting the Ba, ^{226}Ra, and ^{228}Ra associated with the lithogenic component, as described in van Beek et al. (2007). The solutions obtained during sequential leaching were analyzed using the ICP-MS facility (Element, Finnigan) at WHOI.

Calculation of the Barite Saturation Index

The barite saturation index is defined as the ratio of the aqueous barium sulfate ionic product to the barite solubility product at a given temperature and pressure. For a given seawater sample, the concentrations of Na, K, Ca, Mg, Cl and SO_4 are calculated from the measured salinity and from the ionic composition of standard seawater (Millero, 2006). The measured Ba and Sr concentrations are then used along with the major element concentrations to calculate ionic activities in the Na-K-Ca-Mg-Ba-Sr-Cl-SO_4-H_2O system based on Pitzer's ion interaction model (Monnin and Galinier, 1988; Monnin, 1999), for the temperature and pressure of the sample under consideration. Sr substitution in barite has a limited influence on the barite saturation index (Monnin and Cividini, 2006).

RESULTS

Radium and Barium in Seawater

The ^{226}Ra activities and Ba concentrations determined in seawater at old station Hale Aloha, station K1, and station K3 are reported in **Tables 1-3 of the Supplementary Material**, and the vertical profiles are shown on **Figure 2**. Both increase with depth, reflecting uptake during particle formation in shallow waters and subsequent release at depth. Similar profiles were reported in the North Pacific during the GEOSECS program (Chung, 1976; Chung and Craig, 1980). The ^{226}Ra and Ba profiles

are similar at the three stations, but above 3000 m, Ba concentrations (and ^{226}Ra) are higher in the Subarctic Gyre (station K1) than at station K3 (**Figure 2**), while below 3000 m, there is a clear decrease in Ba concentrations at K1. The Ba concentrations at old station Hale Aloha are similar in June (lower sampling resolution) and August 2002 (**Table 1 of the Supplementary Material**). In the upper water column, the ^{226}Ra and Ba concentrations at station K1 are higher than those at stations located further south (K3 and old Hale Aloha), a pattern that was also observed during previous projects (Dehairs et al., 2008; Kawakami and Kusakabe, 2008). The higher concentrations in the upper waters of the northwestern North Pacific subarctic region are likely explained by the impact of the continents and continental margins in these regions (eg., Amakawa et al., 2004; Hawakami and Kusakabe, 2008; Lam and Bishop, 2008).

Barite Saturation Index

The barite saturation index was calculated at stations K1 and K3 considering either pure $BaSO_4$ or $(Ba,Sr)SO_4$ (**Figure 3**). The surface waters at K1 and K3 are undersaturated with respect to barite. Equilibrium is reached at approximately 500 m depth at station K1 and at approximately 1000 m depth at station K3. Below these depths, the waters are either in equilibrium or supersaturated with respect to barite down to approximately 3500 m at station K1 and down to approximately 5000 m at station K3. This pattern is characteristic of Pacific waters and agrees with that reported by previous studies (Monnin et al., 1999; Monnin and Cividini, 2006). This index can be used to provide information on the fate of barite within the water column (preservation *versus* dissolution), which may in turn impact the distributions of ^{226}Ra and Ba in the water column. Our data agree with those obtained at station K2 in the Western Subarctic Gyre and station Aloha off Hawaii by Dehairs et al. (2008) during the VERTIGO project.

^{226}Ra/Ba Ratio in Seawater

The Ba and ^{226}Ra concentrations are broadly consistent with the GEOSECS data set (Broecker et al., 1967; Wolgemuth and Broecker, 1970; Broecker et al., 1976; Chan et al., 1976; Chan et al., 1977; Moore et al., 1985). The ^{226}Ra/Ba ratios below 500 m agree with the GEOSECS value of 2.3 dpm μmol^{-1}. In contrast to many GEOSECS profiles, however, the data reported here display significantly lower ^{226}Ra/Ba ratios in the upper 500 m at stations K1, K3 and old station Hale Aloha (**Figure 4**). Near the seafloor, a decrease in the ^{226}Ra/Ba ratio is also observed at stations K1 and K3.

Barium and Radium in Suspended Particles

Some studies have reported Ra activities determined either in suspended particles (van Beek et al., 2007; van Beek et al., 2009;

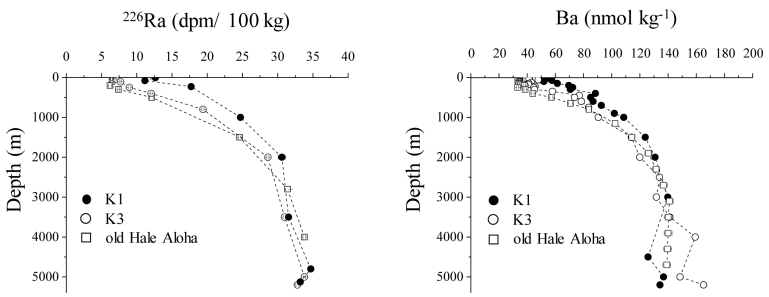

FIGURE 2 | Left panel: vertical profiles of ^{226}Ra at stations old Hale Aloha, K1 and K3 in the North Pacific. Right panel: vertical profiles of dissolved Ba at stations old Hale Aloha (August 2002 data), K1 and K3 in the North Pacific.

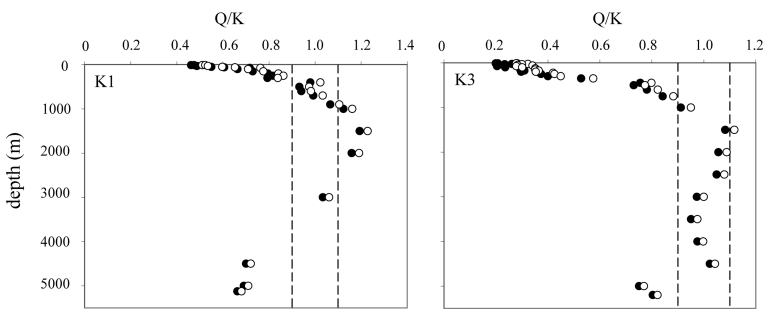

FIGURE 3 | Barite saturation index profiles at stations K1 and K3, considering either pure barite, $BaSO_4$ (black circles) or $(Ba,Sr)SO_4$ (open circles) in the calculations. Undersaturation is indicated by a saturation index lower than 1.0.

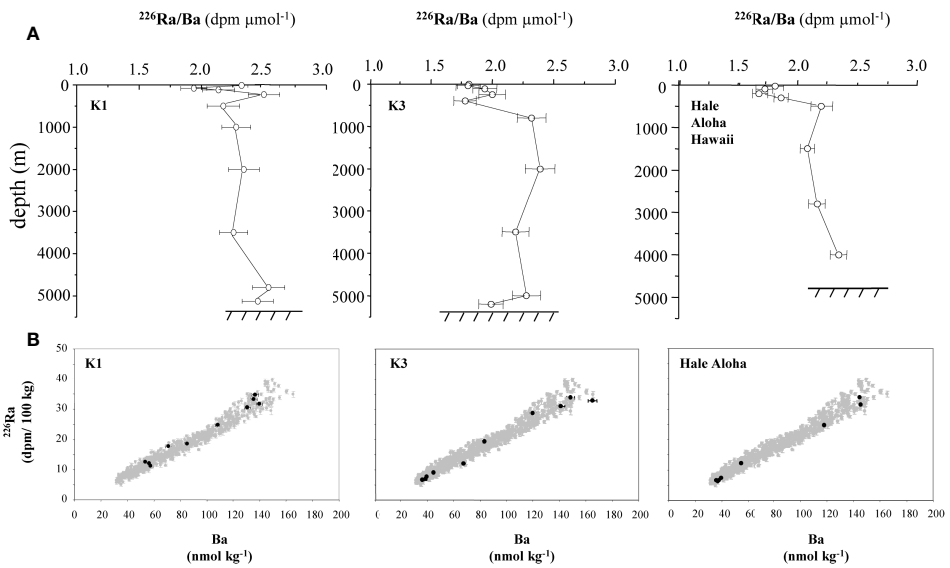

FIGURE 4 | Vertical profiles of ^{226}Ra/Ba ratios in seawater at the three investigated sites: stations K1 and K3 in the North West Pacific; old station Hale Aloha, off Hawaii **(A)**. The relationship between Ba and ^{226}Ra found at these stations (solid circles) is also compared to the Ba-^{226}Ra relationship reported from the GEOSECS program **(B)**.

Bourquin et al., 2011; van Beek et al., 2013) or in sinking particles collected with sediment traps (Moore and Dymond, 1991; Legeleux and Reyss, 1996; van Beek et al., 2007; van Beek et al., 2009) in the ocean. The vertical profiles of excess Ba concentrations (Ba_{ex}) and excess ^{226}Ra activities ($^{226}Ra_{ex}$) in suspended particles at stations K1 and K3 display maximum values between 200 and 500 m (**Figure 5**), similar to other oceanic basins (Dehairs et al., 1980; Dehairs et al., 1990; Jacquet et al., 2007; van Beek et al., 2007; Dehairs et al., 2008; Jacquet et al., 2008; van Beek et al., 2009). The Ba_{ex} and $^{226}Ra_{ex}$ vertical profiles at station K1 are remarkably similar, with both profiles displaying a double peak in the upper 400 m. For old station Hale Aloha, we report total ^{226}Ra activities that have not been corrected for lithogenic ^{226}Ra, though this correction is generally quite small (**Table 4 of the Supplementary Material**). The ^{226}Ra activities that have been determined at that station in June and August 2002 agree well with each other and display a maximum value at 250 m, a pattern that is also observed at station K1 (maximum ^{226}Ra activity at 230 m). The ^{226}Ra activities in suspended particles are lower at old station Hale Aloha than at stations K1 and K3 (**Figure 5**). The Ba_{ex} data that we report here for stations K1 and K3 agree with the values reported by Dehairs et al. (2008) at station K2 in the Western Subarctic Gyre during the VERTIGO project, with maximum values being approximately 500 pmol kg^{-1} in the upper 500 m. Dehairs et al. (2008) report Ba_{ex} concentrations that were lower at station

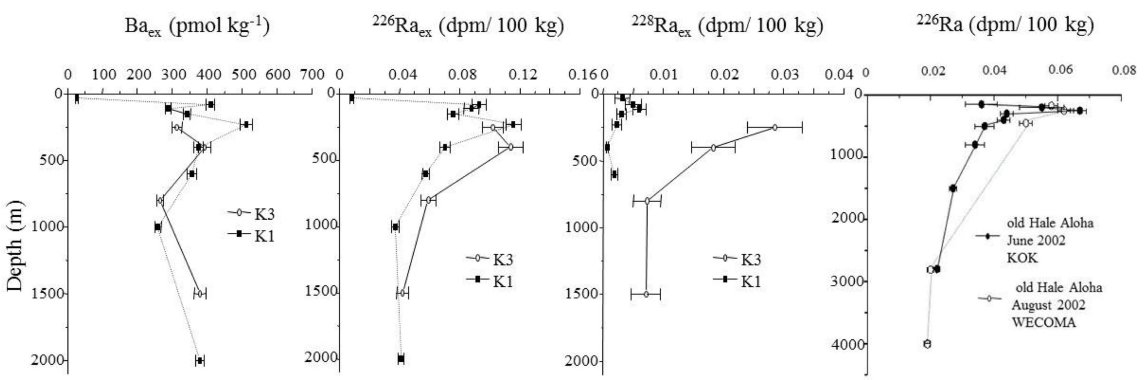

FIGURE 5 | Vertical profiles of excess Ba (Ba_{ex}) concentrations, excess ^{226}Ra ($^{226}Ra_{ex}$) activities and excess ^{228}Ra ($^{228}Ra_{ex}$) determined in suspended particles collected at stations K1 and K3. We also report the ^{226}Ra activities (not corrected for the supported ^{226}Ra) determined in the suspended particles collected at old station Hale Aloha in June and August 2002.

Aloha than at station K2, a pattern that is similar for the $^{226}Ra_{ex}$ activities reported here. We also report $^{228}Ra_{ex}$ activities determined at stations K1 and K3 (**Figure 5**). The $^{228}Ra_{ex}$ activities are higher in the upper 500 m of the water column, a pattern that was also observed in other oceanic basins (van Beek et al., 2007; van Beek et al., 2009). We will later compare the $^{228}Ra/^{226}Ra$ ratios of the suspended particles to the dissolved $^{228}Ra/^{226}Ra$ ratios (see *Ra Isotopic Ratios ($^{228}Ra/^{226}Ra$)*).

DISCUSSION

The phases that are believed to incorporate or adsorb Ba (and Ra) in the water column are i) barite, ii) celestite produced by acantharians (Dehairs et al., 1980; Bernstein et al., 1992), iii) extracellular polymeric substances (EPS; Martinez-Ruiz et al., 2020), iv) Fe hydroxides (Sternberg et al., 2005), v) diatoms or metal hydroxides attached to diatoms (Bishop, 1988; Ganeshram et al., 2003; Sternberg et al., 2005), vi) calcareous skeletons (Lea and Boyle, 1989), with barite being often cited as the main Ba (and Ra) carrier in the water column (Dehairs et al., 1980; Moore and Dymond, 1991; Legeleux and Reyss, 1996; Martinez-Ruiz et al., 2020). Since the world's oceans are mostly undersaturated with respect to barite (Church and Wolgemuth, 1972; Monnin et al., 1999; Rushdi et al., 2000; Monnin and Cividini, 2006), it was proposed that barite precipitation takes place in the upper water column within supersaturated microenvironments of decaying organic matter (Chow and Goldberg, 1960; Dehairs et al., 1980; Bishop, 1988; Dehairs et al., 1990; Dehairs et al., 1991; Dehairs et al., 1992; Ganeshram et al., 2003). In the North Pacific, the waters are undersaturated with respect to barite in the upper 500 m (K1) and 1000 m (K3) (**Figure 3**) and in the upper 1000 m at station ALOHA (Dehairs et al., 2008). The Ba_{ex} and $^{226}Ra_{ex}$ maxima observed in suspended particles in the upper 500 m are thus located within undersaturated waters, further suggesting that barite forms within microenvironments. Besides barite, acantharian celestite, EPS or Fe hydroxides may contribute significantly to Ba_{ex} and $^{226}Ra_{ex}$. Because acantharians are mostly found in the upper 150 m (Bishop et al., 1977; Bishop et al., 1978; Michaels, 1988; Bernstein et al., 1992; Michaels et al., 1995), their contribution must be restricted to shallow water.

^{226}Ra/Ba Ratio in Suspended Particles

The ^{226}Ra/Ba ratios in suspended particles are higher in the upper water column and decrease with increasing water depth (**Figure 6**). Two samples collected at station K3 in the upper 500 m display ^{226}Ra/Ba ratios that are higher than the 2.3 dpm μmol^{-1} (i.e. 3.2±0.3 dpm μmol^{-1} at 250 m and 2.9±0.3 dpm μmol^{-1} at 400 m). At station K1, two samples collected in waters above 150 m display high ratios (3.0 dpm μmol^{-1} at 30 m and 110 m), but ratios close to 2.3 dpm μmol^{-1} were also found at 80 m, 150 m and 230 m, indicating spatial heterogeneity in the composition/origin of the suspended particles.

Below 400-500 m, the ^{226}Ra/Ba ratios in suspended particles are equal to or lower than the 2.3 dpm μmol^{-1} value. Similar patterns were found in other oceanic basins (van Beek et al., 2007; van Beek et al., 2009). The higher ^{226}Ra/Ba ratios found in suspended particles compared to the ratio in seawater at the same depth indicates that fractionation between ^{226}Ra and Ba takes place during formation of suspended particles in the water column, contrary to earlier assumptions (Wolgemuth and Broecker, 1970; Ku and Luo, 1994).

Ba Carriers at Station K3

The sequential leaching method of Ganeshram et al. (2003) was applied to an entire vertical profile of suspended particles collected with Niskin bottles (station K3) in order to provide additional information on the different Ba carriers within the water column (**Table 1**). In surface waters down to 110 m, Ba is mostly found in the fractions released by the first two leaching steps (MilliQ water and 10% HNO_3), which suggests that the Ba pool in surface waters down to 110 m is relatively labile (**Figure 7**). The labile pool of Ba at these depths likely consists in i) labile organic matter, including potentially EPS, ii) acantharians that are generally concentrated in surface waters (Michaels, 1988; Michaels et al., 1995) and iii) oxy-hydroxides. This labile pool of Ba then decreases with increasing water depth

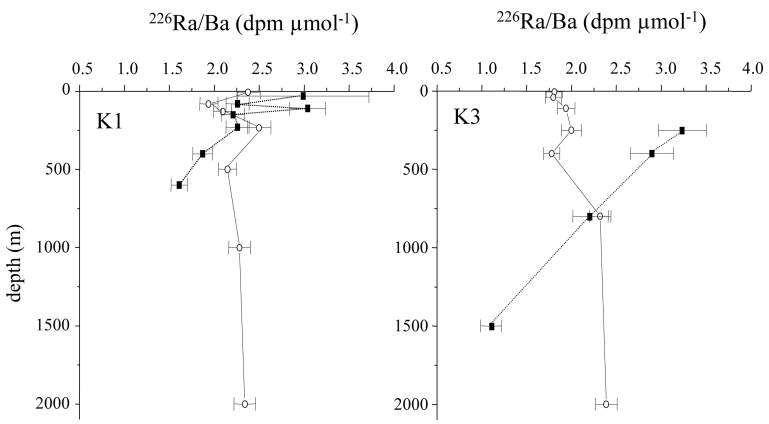

FIGURE 6 | Vertical profiles of ^{226}Ra/Ba ratios determined at stations K1 and K3 in suspended particles (black squares) and in seawater (open circles).

TABLE 1 | Ba concentrations (pmol kg^{-1}) determined in the different particulate fractions at station K3 using the sequential leaching method of Ganeshram et al. (2003), slightly modified.

Depth (m)	Ba (pmol kg $^{-1}$) ± 2%	%	Ba (pmol kg $^{-1}$) ± 2%	%	Ba (pmol kg $^{-1}$) ± 2%	%	Ba (pmol kg $^{-1}$) ± 2%	%	Sr (pmol kg $^{-1}$) ± 3%	Sr/Ba (mol/mol) ± 7%
	Fraction #1 ***Labile matter*** **(MilliQ water)**		**Fraction #2** ***Labile matter*** **(10% HNO_3)**		**Fraction #3** ***$BaSO_4$*** **(3% HCl)**		**Fraction #4** ***Refractory OM*** **(hot HNO_3)**		**Fraction #3** ***$BaSO_4$*** **(3% HCl)**	**Fraction #3** ***$BaSO_4$*** **(3% HCl)**
40	122	12.2	406	40.8	194	19.5	274	27.5	199	1.026
110	52	8.6	311	51.2	205	33.8	39	6.4	265	1.293
250	24	1.1	174	8.2	1680	79.1	245	11.5	38	0.023
400	32	4.7	144	21.2	445	65.5	58	8.5	_	_
800	29	3.6	244	30	403	49.3	136	16.7	14	0.035
2000	55	5.9	177	18.9	629	67.1	76	8.1	12	0.019
3500	29	6.4	91	23.0	236	59.6	40	10.1	20	0.085
5000	20	7.0	85	29.8	166	58.2	14	4.9	11	0.066

The Sr concentration (pmol kg^{-1}) and the Sr/Ba (mol/mol) determined in fraction #3 (assumed to be $BaSO_4$) are also reported. The relative contribution of each fraction is also reported (%).

such that below 200 m, barite appears to be the dominant Ba carrier. This pattern thus agrees with the view that the decrease in the labile pool of Ba - following the decay of organic matter or dissolution of acantharian celestite - provides Ba in the microenvironment for barite precipitation in subsurface water (Chow and Goldberg, 1960; Dehairs et al., 1980; Legeleux and Reyss, 1996; Ganeshram et al., 2003; Sternberg et al., 2005; Martinez-Ruiz et al., 2020). The Ba_{ex} concentrations (non lithogenic Ba) are often considered to reflect barite, although Ba_{ex} may also include Ba associated with the different fractions invoked above; these latter Ba carriers can be considered as relatively minor contributors below 110 m (**Table 1**). The Ba_{ex} concentrations determined in suspended particles collected using *in situ* pumps below the surface down to 2000 m (250-550 pmol kg^{-1}; **Figure 5**) are in relatively good agreement with the Ba concentrations associated with $BaSO_4$ in fraction #3 (200-630 pmol kg^{-1}; **Figure 7**) over the same depth interval, with the exception of a sharp peak at 250 m found in the sequential leaching experiment (1680 pmol kg^{-1}). This discrepancy may reflect spatial variability that leads to slightly different samples collected by the two methods (Niskin bottles versus *in situ* pumps). Note that such high particulate Ba concentrations (1680 pmol kg^{-1}) have already been reported by previous studies in other oceanic regions (Jacquet et al., 2007; van Beek et al., 2009) and correspond to a depth where the rate of barite precipitation is believed to be highest (e.g., Legeleux and Reyss, 1996). Maximal Ba_{ex} and $^{226}Ra_{ex}$ concentrations were also found at this depth (**Figure 5**). The Ba concentration associated with $BaSO_4$ remains relatively high down to 2000 m (629 pmol kg^{-1}; **Figure 7**), a pattern that may be related to the saturation state of intermediate waters with respect to barite in the North Pacific that preserves barite or limits its dissolution while settling (**Figure 3**). At 5000 m, the Ba concentration associated with $BaSO_4$ is significantly lower than in the upper 500 m (166 pmol kg^{-1}), suggesting dissolution in water undersaturated with respect to barite. The pool of Ba associated with refractory

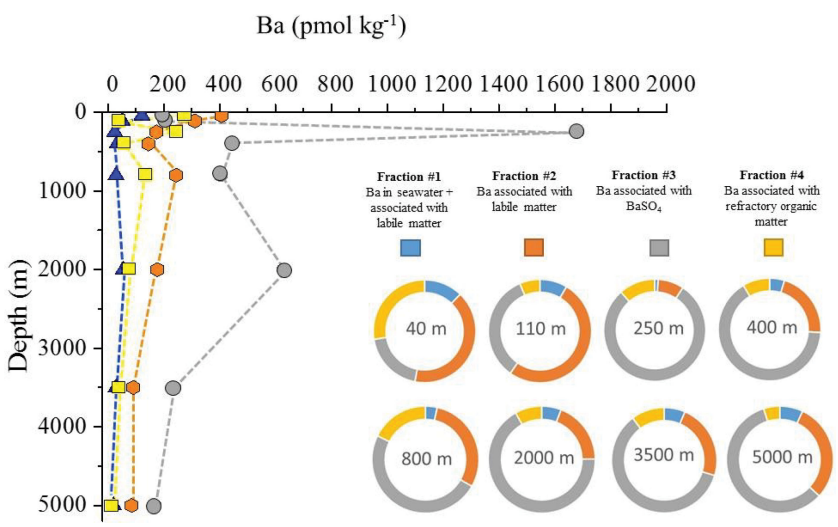

FIGURE 7 | Vertical profiles of Ba concentrations determined in the different particulate fractions collected using the sequential leaching method of Ganeshram et al. (2003) at station K3. The relative importance of the different fractions is also shown at each depth.

organic matter decreases from the surface to the bottom. While the sharp decrease in the labile Ba pool in the upper 500 m may be the main contributor to barite precipitation in the upper water column, the release of the Ba associated with refractory organic matter at depth may also contribute to barite precipitation in waters below 500 m (van Beek et al., 2007).

The Sr concentration and the Sr/Ba ratio was also investigated in fraction #3 that is associated to $BaSO_4$ (**Table 1**). High Sr concentrations and high Sr/Ba ratios (1.0-1.1 mol/mol) were found in samples collected in surface waters (40 m and 110 m). Since acantharian skeletons are expected to dissolve in the first two leaching steps, the high Sr concentrations found in fraction #3 are unlikely from acantharians, but must be included in $BaSO_4$. The high Sr content in these barite samples may indicate that barite found at these depths precipitated in microenvironments where significant dissolution of celestite took place and/or following a prior step of Sr-Ba bioaccumulation by EPS (since EPS was shown to concentrate Sr in addition to Ba; Martinez-Ruiz et al., 2020). Below 250 m, the Sr/Ba ratios are lower (0.019-0.085 mol/mol). These latter values are in good agreement with the ratios reported in barite separated from sediments collected in the Pacific Ocean (0.03-0.05 mol/mol; van Beek et al., 2003). This observation further supports the association of fraction #3 with $BaSO_4$. The different Sr/Ba ratios in $BaSO_4$ found either above or below 110 m may indicate a larger influence of the dissolution of acantharian skeletons - that releases Ba, Sr and Ra into the microenvironments - in barite formation in the upper 110 m or an evolution of the ratio following dissolution of barite during settling. Like the Sr/Ba ratio in fraction #3, the $^{226}Ra_{ex}$/Ba_{ex} ratio in suspended particles is also higher in the upper water column and decreases with increasing depth (**Figure 6**). This pattern is also observed in the Sr concentrations and Sr/Ba ratios determined in suspended particles collected with *in situ* pumps (**Table 4 of the Supplementary Material**). The latter Sr/Ba ratios being higher than the Sr/Ba ratio determined from the sequential leaching in fraction #3 may be explained by the different Sr and Ba contributors in these samples (i.e. residual seawater, carbonates, barite, celestite), which would serve to mask the Sr/Ba ratio in barite. Similar relationships were found in the upper 150 m between Ra, Sr and Ba at the OFP station in the Sargasso Sea and at the DYFAMED station in the western Mediterranean Sea: high ^{226}Ra/Ba ratios were found in both suspended and sinking particles with ratios being much higher than the ambient seawater ^{226}Ra/Ba ratios. Values up to 3.8 dpm μmol^{-1} were observed at 120 m in the Sargasso Sea (van Beek et al., 2007) and up to 8.4 dpm μmol^{-1} at 140 m in the western Mediterranean Sea (van Beek et al., 2009), at depths where acantharians are found. In these latter studies, the relationship with acantharians was further suggested by the high particulate Sr content determined in the suspended particles in the upper 150 m of the two regions (van Beek et al., 2007; van Beek et al., 2009) and by the observation of acantharian skeletons on filters collected in the western Mediterranean Sea (van Beek et al., 2009).

Ra Isotopic Ratios (^{228}Ra/^{226}Ra)

The vertical gradient of the dissolved ^{228}Ra/^{226}Ra ratio in the water column allows us to investigate the depth of particulate Ba formation in the water column (Legeleux and Reyss, 1996; van Beek et al., 2007; **Figure 8**). The much higher dissolved ^{228}Ra/^{226}Ra ratios in the upper 500 m at station K3 compared with station K1 are due to higher dissolved ^{228}Ra activities (**Figure 9**) resulting from the northward extension of the Kuroshio to station K3 in 2002 (Oka et al., 2015; **Figures 2** and **3 of Supplementary Material**). These waters acquired ^{228}Ra when interacting with the sediments of the continental shelf when they were flowing northeastward along Honshu (Kaufman et al., 1973; Kawakami and Kusakabe, 2008; Charette et al., 2013). Consequently, the $^{228}Ra_{ex}$ signature of the suspended particles is also higher at station K3 in comparison to station K1 (**Figure 5**). At station K1, the ^{228}Ra/^{226}Ra ratios in the suspended particles collected in the upper 500 m generally match the ^{228}Ra/^{226}Ra ratios in the dissolved phase (**Figure 8**): the ^{228}Ra/^{226}Ra ratios in the particulate phase in the upper 500 m follow the profile of the dissolved phase. This suggests that the particulate Ba collected at each of these depths was formed at these water depths and thus incorporated the ^{228}Ra/^{226}Ra signature of the dissolved phase. This observation agrees with previous studies conducted in other oceanic basins (van Beek et al., 2007; van Beek et al., 2009). At station K3, the ^{228}Ra/^{226}Ra ratios in the particulate phase in the upper 500 m are slightly higher than the dissolved phase, but

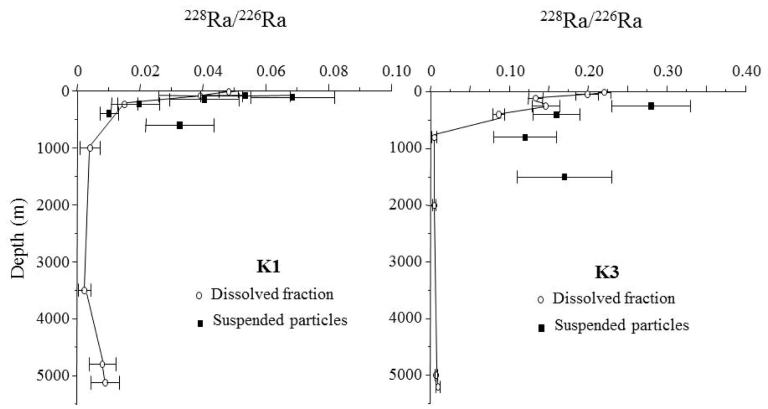

FIGURE 8 | Comparison of the ^{228}Ra/^{226}Ra ratios determined in the dissolved phases and suspended particles at stations K1 and K3.

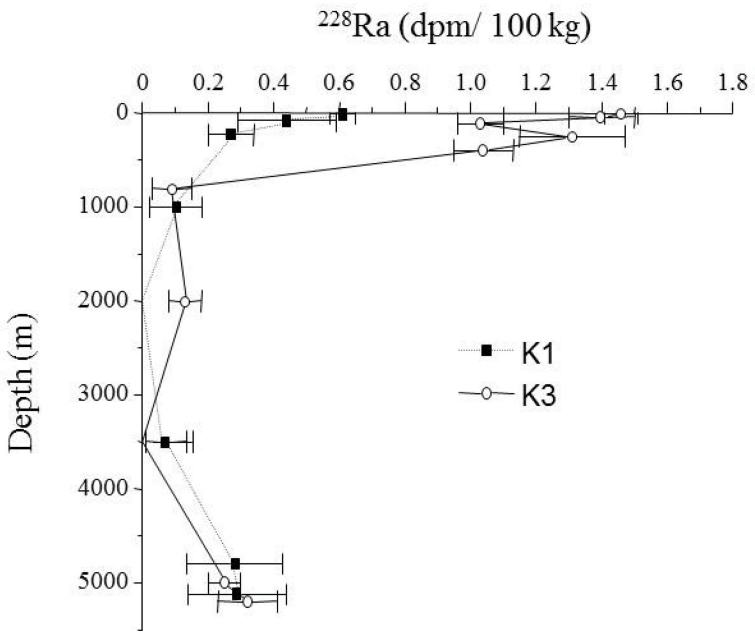

FIGURE 9 | Vertical profiles of dissolved ^{228}Ra activities determined at stations K1 and K3 in the North Pacific. The large difference in ^{228}Ra activities the upper 500 m between stations K1 and K3 is attributed to the extension of the Kurushio current that reached station K3 in year 2002 during the present study.

remain close to the seawater ratios. Like at station K1, this may suggest that the particles incorporated the ^{228}Ra/^{226}Ra signature of the dissolved phase at these depths.

Below 500 m, the ^{228}Ra/^{226}Ra ratios in the particulate phase are higher than the seawater ratios at the corresponding depth at both stations K1 and K3 suggesting that particulate Ba originates from shallower depths, where it acquired a higher ^{228}Ra/^{226}Ra ratio. At these depths, the particulate Ba is mostly associated with barite (**Figure 7**) that are found at depths where the waters are in equilibrium or supersaturated with respect to barite (**Figure 3**). This indicates that the particulate Ba at intermediate depths (500-1500 m) mostly consists of settling barite that was formed in the upper 500 m of the water column. Such high particulate ^{228}Ra/^{226}Ra ratios indicating an export of barite formed in shallower waters were previously observed in other oceanic basins but only in sinking particles collected with sediment traps (Legeleux and Reyss, 1996; van Beek et al., 2007; van Beek et al., 2009) and not in suspended particles (e.g. van Beek et al., 2007). The sharp decrease in the Ba concentration associated with barite (fraction #3) below the Ba peak at 250 m (**Figure 7**) - that indicates a maximum rate of barite formation at these depths - suggests that a large fraction of barite then dissolves in the upper 500 m of the water column (that were shown to be undersaturated with respect to barite) and are not exported to greater depth.

^{226}Ra-Ba Relationship

The general relationship between Ba and ^{226}Ra (**Figure 1 of Supplementary Material**) led Chan et al. (1976) to propose that there was a constant ratio between Ba and ^{226}Ra in the ocean above 2500 m (4.6 nmol ^{226}Ra/mol Ba, equivalent to 2.3 dpm μmol^{-1}). The data reported here indicate that ^{226}Ra/Ba ratios significantly lower than 2.3 dpm μmol^{-1} can be found in the upper 500 m of the water column. A similar trend was observed in the Sargasso Sea (Ocean Flux Program Time-Series; van Beek et al., 2007; **Figure 10**). van Beek et al. (2009) also reported low ^{226}Ra/Ba ratios (1.3-1.8 dpm μmol^{-1}) at the DYFAMED Time-Series in the Mediterranean Sea, but these low ratios were found throughout the water column (van Beek et al., 2009; **Figure 10**). Data from the Mediterranean Sea thus clearly fall below the regression obtained with the GEOSECS data (**Figure 10B**), a pattern that may - at least partly - be explained by the anti-estuarine circulation in the Mediterranean Sea that fills the entire basin with water originating from the upper water column of the Atlantic Ocean (expected to display a low ^{226}Ra/Ba ratio, following van Beek et al., 2007). The data from the Mediterranean Sea also clearly highlight the temporal variability of the ^{226}Ra/Ba ratio at the DYFAMED station.

Many of the vertical profiles obtained during GEOSECS do not show lower ^{226}Ra/Ba ratios in the upper water column. This could be attributed to the lower sampling resolution and precision of the GEOSECS Ba and ^{226}Ra measurements (Ku and Luo, 1994). We note however, that when all the ^{226}Ra/Ba profiles obtained during the GEOSECS program for each ocean basins are plotted versus depth, the lowest ^{226}Ra/Ba ratios are invariably found in the upper 500 m of the water column (left of the vertical line on **Figure 11**). Likewise, as noted before (Wolgemuth and Broecker, 1970; Chan et al., 1976; Ku and Luo, 1994), the linear regression of ^{226}Ra activity versus Ba concentration has a significant, positive intercept on the Ba

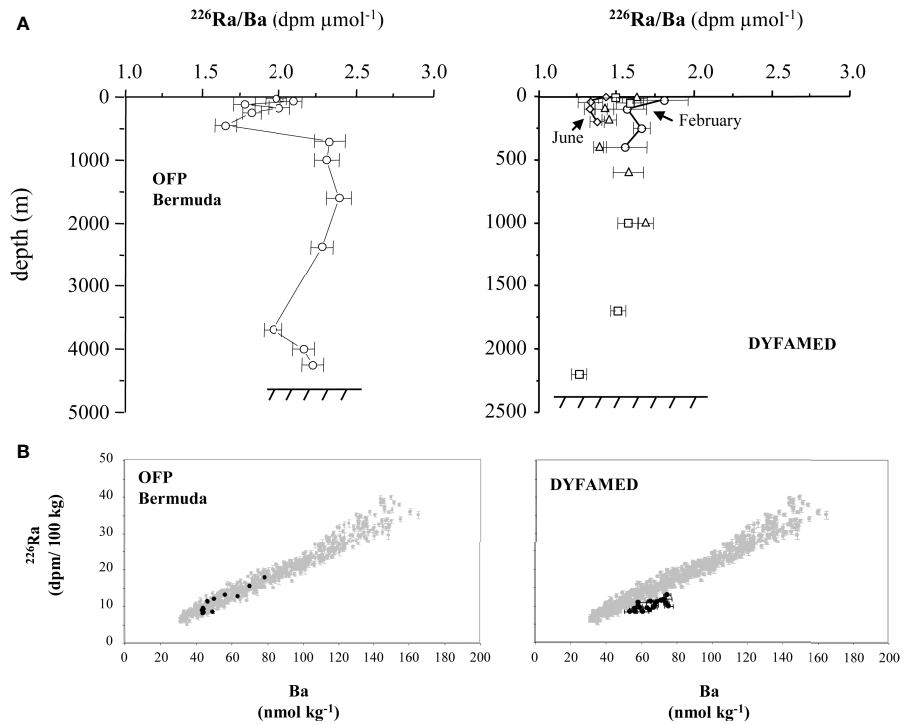

FIGURE 10 | Vertical profiles of ^{226}Ra/Ba ratios reported in seawater in other oceanic basins by previous studies: Sargasso Sea, Atlantic Ocean (van Beek et al., 2007) and Mediterranean Sea (van Beek et al., 2009) **(A)**. The relationship between Ba and ^{226}Ra found at these stations is also compared to the Ba-^{226}Ra relationship reported from the GEOSECS program **(B)**.

axis (**Figure 1 of the Supplementary Material**). The pattern reported here (i.e., low ^{226}Ra/Ba ratios in the upper 500 m) does not appear universal, however. In particular, data from Foster et al. (2004) and Staubwasser et al. (2004) indicate that surface waters in the Ross Sea have ^{226}Ra/Ba ratios similar to deep waters. This pattern is consistent with the deep convective mixing that dominates this region, which may mask fractionation observed in other regions. This is further confirmed by the lack of an intercept when regressing ^{226}Ra activity and Ba concentration measured in samples from the Southern Ocean (Li et al., 1973).

Processes Affecting the ^{226}Ra/Ba Ratios

The intercept on the regression of ^{226}Ra activity versus Ba concentration has been attributed to the differences in the source of the two elements (Wolgemuth and Broecker, 1970; Chan et al., 1976; Ku and Luo, 1994). While Ba is mainly added to the upper ocean by rivers and potentially also by SGD, ^{226}Ra is mostly added to the ocean by diffusion from deep-sea sediments. Simple two box models show that such differences in input can generate a lower ^{226}Ra/Ba in the upper water column (Chan et al., 1976). However, the difference in the ratio produced by these simple models is smaller than those observed in the measurements reported here, suggesting that other mechanisms contribute to the observed vertical changes in Ra/Ba.

Barite, celestite, EPS and hydroxides (e.g. Fe, Mn hydroxides) are known to incorporate or adsorb Ba and Ra. Barite and celestite are believed to be the main Ba carriers in the water column, and to explain the vertical profiles of particulate Ba_{ex} and $^{226}Ra_{ex}$, which have higher concentrations in the upper ca. 500 m. The two main Ba (and Ra) carriers are not found at exactly the same water depth: the presence of celestite is mostly restricted to the upper 150 m, whereas barite is usually found below that depth (maximum concentration often observed at ca. 200-250 m). The high ^{226}Ra/Ba ratios in suspended particles reported in this study were found both at shallow depths dominated by acantharians, as deduced from elevated particulate Sr concentrations (30 m and 110 m, station K1) and barite (250 m and 400 m, station K3). Because celestite is expected to be enriched in radium compared to barium (Bernstein et al., 1998), the high ^{226}Ra/Ba ratios found in suspended particles in the upper ca. 150 m may be attributed to acantharian skeletons; such a fractionation process may thus contribute to decrease the dissolved ^{226}Ra/Ba ratios in the upper water column. As deduced from the leaching experiments, barite (fraction #3) formed in the upper 110 m displays high Sr/Ba ratios, suggesting a potential link between acantharian skeletons and barite formation at these depths. The high ^{226}Ra/Ba ratios found

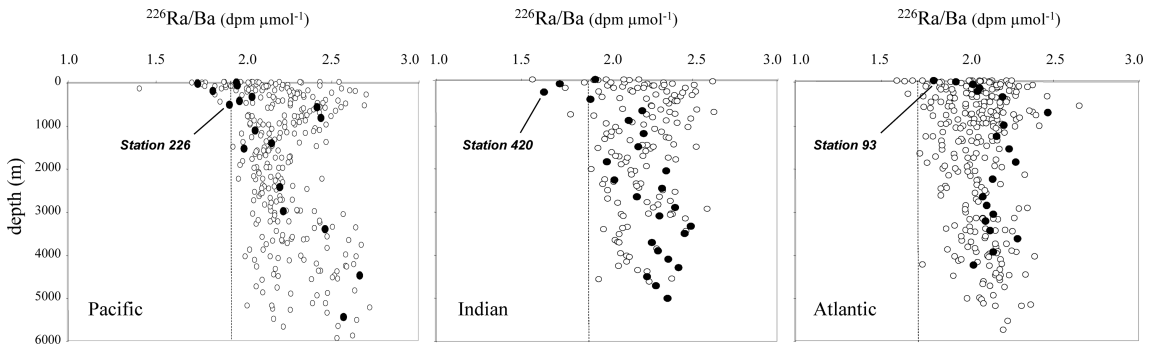

FIGURE 11 | Compilation of the vertical distributions of ^{226}Ra/Ba ratios reported in the Pacific, Indian and Atlantic Oceans during the GEOSECS program (open circles). Ratios found at station #226 (Pacific Ocean), station #420 (Indian Ocean) and station #93 (Atlantic Ocean) are underlined on the graphs (closed circles). The vertical line is placed to highlight the lower ^{226}Ra/Ba ratios found in the upper water column (left of the line) at several stations.

in the suspended particles at shallow depths may thus be related to celestite and to barite precipitating in microenvironments in which celestite - with a high ^{226}Ra/Ba ratio - rapidly dissolves (Bernstein et al., 1987; Bernstein et al., 1992). Deeper in the water column, the leaching experiments showed that the decrease in the labile pool of Ba down to ca. 250 m (e.g. decay of labile organic matter) was accompanied by increased barite formation. Fractionation between Ba and Ra may thus take place during the bioaccumulation phase of Ba-Ra prior to barite formation within the microenvironments (e.g. adsorption onto bacterial biofilms; Martinez-Ruiz et al., 2020) or during barite precipitation itself. Below 500 m, the ^{226}Ra/Ba ratios in suspended particles are lower than the ambient seawater ^{226}Ra/Ba ratios in the three studies that have investigated both particulate and dissolved Ba and Ra (van Beek et al., 2007; van Beek et al., 2009; this study). The ^{226}Ra/Ba ratios may thus be impacted during dissolution of barite that settles in undersaturated waters.

CONCLUSION

Seawater ^{226}Ra/Ba ratios close to 2.3 dpm µmol^{-1} were found below 500 m at three sites in the North Pacific Ocean, in agreement with ratios reported during the GEOSECS program. In contrast, we report significantly lower ^{226}Ra/Ba ratios in the upper 500 m of the water column. This pattern is similar to that observed in other areas of the world's ocean, such as the Sargasso Sea (van Beek et al., 2007) and the western Mediterranean Sea (van Beek et al., 2009). While this trend may partly be attributed to differences in the source of these two elements, other processes must be contributing to the contrast between the ^{226}Ra/Ba ratio of surface and deep waters. The ^{226}Ra/Ba ratio in suspended particles indicates that fractionation between Ba and ^{226}Ra takes place in the upper ca. 500 m of the water column.

Our results suggest that ^{226}Ra enrichment relative to Ba in celestite and mass fractionation during barite formation (or during a precursor stage of barite formation, i.e. when Ba and Ra accumulate within the microenvironments, involving potentially bacterial biofilms as proposed by Martinez-Ruiz et al., 2020) may lead to such fractionation between Ba and Ra in the upper 500 m. The spatial and seasonal variability of upper ocean ^{226}Ra/Ba ratios and fractionation between Ba and Ra have implications for the use of ^{226}Ra as a dating tool or as a tracer of abyssal circulation and mixing, which rely on a lack of fractionation between the two elements during biological cycling (Ku and Luo, 1994). This assumption now appears to be violated for large regions of the ocean. In addition, dating methods based on the decay of ^{226}Ra require that the initial ^{226}Ra/Ba be known and constant. For example, previous studies have assumed that the initial ratio was the mean value obtained from GEOSECS (i.e., 2.3 dpm µmol^{-1}). While this assumption may be valid for Antarctic samples (Staubwasser et al., 2004), it might not be the case for most other oceanic regions, if the sample to be dated has been formed in shallow waters.

DATA AVAILABILITY STATEMENT

The original contributions presented in the study are included in the article/**Supplementary Material**. Further inquiries can be directed to the corresponding author.

AUTHOR CONTRIBUTIONS

PB, RF, MH, and SH designed and coordinated the different studies. PB performed the sampling, analyses and provided the datasets. J-LR contributed to the analyses. CM provided the barite saturation index. PB, RF, MH, MC, RG, and CM contributed to the interpretation of data. PB wrote the first draft of the manuscript and all authors contributed to the final version of the manuscript.

ACKNOWLEDGMENTS

We are grateful to the crews and captains of RV WECOMA (USA), RV Ka'imikai-o-Kanaloa (USA) and RV Mirai (Japan). We thank Mike Bacon, chief scientists on board RV WECOMA and RV KoK. We thank Kazuhiro Hayashi and Markus Kienast for their help during sampling on board RV Mirai. We thank Larry Ball and David Schneider at the ICP/MS of WHOI, USA, and Valérie Olive at the ICP/MS of East Kilbride, Scotland, UK. We also thank Alan Fleer and Susan Brown-Léger at WHOI for their help in the lab and at sea (Hale Aloha). We thank Charlotte Riccio, Thierry Sampieri and Jean-Louis Saury at the underground laboratory of Modane (LSM). We thank Rémi Freydier and Marc Souhaut for their help at the ICP/MS at Observatoire Midi Pyrénées. We thank Steven Manganini and Jerzy Blusztajn for constructive discussions on the project. This work was supported by a Lavoisier fellowship attributed by the French Ministry of Foreign Affairs to PB in year 2002 and by the Woods Hole Oceanographic Institution (WHOI). This work was completed at the University of Edinburgh in 2003, while PB was a postdoctoral fellow there, with a Marie Curie fellowship from the European Union. The European Union is thus also thanked. MC acknowledges support from the National Science Foundation, Chemical Oceanography program. We thank the two reviewers for their constructive comments that allowed us to improve the quality of the manuscript, as well as Nuria Casacuberta and Paul MacGinnity, associate editors. This paper is dedicated to the memory of SH.

PB and Markus Kienast are sampling Niskin bottles on board RV Mirai in the NW Pacific under the supervision of Susumu Honjo (December 2002).

SUPPLEMENTARY MATERIAL

The Supplementary Material for this article can be found online at: https://www.frontiersin.org/articles/10.3389/fmars.2022.859117/full#supplementary-material

REFERENCES

Amakawa, H., Nozaki, Y., Sotto Alibo, D., Zhang, J., Fukugawa, K., and Nagai, H. (2004). Neodymium Isotopic Variations in Northwest Pacific Waters. *Geochim. Cosmochim. Acta* 68, 715–727. doi: 10.1016/S0016-7037(03)00501-5

Bacon, M. P., and Edmond, J. M. (1972). Barium at GEOSECS III in the Southwest Pacific. *Earth Planet Sci. Lett.* 16, 66–74. doi: 10.1016/0012-821X(72)90237-3

Berkman, P. A., and Ku, T.-L. (1998). ^{226}Ra/Ba Ratios for Dating Holocene Biogenic Carbonates in the Southern Ocean : Preliminary Evidence From Antarctic Coastal Mollusc Shells. *Chem. Geol.* 144, 331–334. doi: 10.1016/S0009-2541(97)00137-X

Bernstein, R. E., Betzer, P. R., Feely, R. A., Byrne, R. H., Lamb, M. F., and Michaels, A. F. (1987). Acantharian Fluxes and Strontium to Chlorinity Ratios in the North Pacific Ocean. *Science* 237, 1490–1494. doi: 10.1126/science.237.4821.1490

Bernstein, R. E., and Byrne, R. H. (2004). Acantharians and Marine Barite. *Mar. Chem.* 86, 45–50. doi: 10.1016/j.marchem.2003.12.003

Bernstein, R. E., Byrne, R. H., Betzer, P. R., and Greco, A. M. (1992). Morphologies and Transformations of Celestite in Seawater: The Role of Acantharians in Strontium and Barium Geochemistry. *Geochim. Cosmochim. Acta* 56, 3273–3279. doi: 10.1016/0016-7037(92)90304-2

Bernstein, R. E., Byrne, R. H., and Schijf, J. (1998). Acantharians: A Missing Link in the Oceanic Biogeochemistry of Barium. *Deep-Sea Res. II* 45, 491–505. doi: 10.1016/S0967-0637(97)00095-2

Bishop, J. K. B. (1988). The Barite-Opal-Organic Carbon Association in Oceanic Particulate Matter. *Nature* 332, 341–343. doi: 10.1038/332341a0

Bishop, J. K. B., Edmond, J. M., Ketten, D. R., Bacon, M. P., and Silker, W. B. (1977). The Chemistry, Biology, and Vertical Flux of Particulate Matter From the Upper 400 M of the Equatorial Atlantic Ocean. *Deep-Sea Res.* 24, 511–548. doi: 10.1016/0146-6291(77)90526-4

Bishop, J. K. B., Ketten, D. R., and Edmond, J. M. (1978). The Chemistry, Biology, and Vertical Flux of Particulate Matter From the Upper 400 M of the Cape Basin in the Southeast Atlantic Ocean. *Deep-Sea Res.* 25, 1121–1161. doi: 10.1016/0146-6291(78)90010-3

Bourquin, M., van Beek, P., Reyss, J. L., Riotte, J., and Freydier, R. (2011). Determination of ^{226}Ra Concentrations in Seawater and Suspended Particles (NW Pacific) Using MC-ICP-MS. *Mar. Chem.* 126, 132-138. doi: 10.1016/j.marchem.2011.05.001

Broecker, W. S., Goddard, J., and Sarmiento, J. L. (1976). The Distribution of ^{226}Ra in the Atlantic Ocean. *Earth Planet Sci. Lett.* 32, 220–235. doi: 10.1016/0012-821X(76)90063-7

Broecker, W. S., Li, Y. H., and Cromwell, J. (1967). Radium-226 and Radon-222: Concentration in Atlantic and Pacific Oceans. *Science* 158, 1307–1310. doi: 10.1126/science.158.3806.1307

Buesseler, K.O., Trull, T.W., Steinberg, D.K., Silver, M.W., Siegel, D.A., Saitoh, S.-I., et al. (2008). VERTIGO (VERtical Transport In the Global Ocean): A Study of Particle Sources and Flux Attenuation in the North Pacific. *Deep-Sea Res. II* 55, 1522–1539. doi: 10.1016/j.dsr2.2008.04.024

Chan, L. H., Drummond, D., Edmond, J. M., and Grant, B. (1977). On the Barium Data From the Atlantic GEOSECS Expedition. *Deep-Sea Res.* 24, 613–649. doi: 10.1016/0146-6291(77)90505-7

Chan, L. H., Edmond, J. M., Stallard, R. F., Broecker, W. S., Chung, Y. C., Weiss, R. F., et al. (1976). Radium and Barium at GEOSECS Stations in the Atlantic and Pacific. *Earth Planet Sci. Lett.* 32, 258–267. doi: 10.1016/0012-821X(76)90066-2

Charette, M. A., Breier, C. F., Henderson, P. B., Pike, S. M., Rypina, I. I., Jayne, S. R., et al. (2013). Radium-Based Estimates of Cesium Isotope Transport and Total Direct Ocean Discharges From the Fukushima Nuclear Power Plant Accident. *Biogeosciences* 10, 2159–2167. doi: 10.5194/bg-10-2159-2013

Charette, M. A., Buesseler, K. O., and Andrews, J. E. (2001). Utility of Radium Isotopes for Evaluating the Input and Transport of Groundwater-Derived Nitrogen to a Cape Cod Estuary. *Limnol. Oceanogr.* 46 (2), 465–470. doi: 10.4319/lo.2001.46.2.0465

Chow, T. J., and Goldberg, E. D. (1960). On the Marine Geochemistry of Barium. *Geochim. Cosmochim. Acta* 20, 192–198. doi: 10.1016/0016-7037(60)90073-9

Chung, Y.-C. (1974). Radium-226 and Ra-Ba Relationships in Antarctic and Pacific Waters. *Earth Planet Sci. Lett.* 23, 125–135. doi: 10.1016/0012-821X(74)90039-9

Chung, Y.-C. (1976). A Deep ^{226}Ra Maximum in the Northeast Pacific. *Earth Planet Sci. Lett.* 32, 249–257. doi: 10.1016/0012-821X(76)90065-0

Chung, Y.-C., and Craig, H. (1980). ^{226}Ra in the Pacific Ocean. *Earth Planet Sci. Lett.* 49, 267–292. doi: 10.1016/0012-821X(80)90072-2

Church, T. M., and Wolgemuth, K. (1972). Marine Barite Saturation. *Earth Planet. Sci. Lett.* 15, 35–44.

Cortes, M. Y., Bollmann, J., and Thierstein, H. R. (2001). Coccolithophore Ecology at the HOT Station ALOHA, Hawaii. *Deep-Sea Res. II* 48, 1957–1981. doi: 10.1016/S0967-0645(00)00165-X

Dehairs, F., Baeyens, W., and Goeyens, L. (1992). Accumulation of Suspended Barite at Mesopelagic Depths and Export Production in the Southern Ocean. *Science* 258, 1332–1335. doi: 10.1126/science.258.5086.1332

Dehairs, F., Chesselet, R., and Jedwab, J. (1980). Discrete Suspended Particles of Barite and the Barium Cycle in the Open Ocean. *Earth Planet Sci. Lett.* 49, 528–550. doi: 10.1016/0012-821X(80)90094-1

Dehairs, F., Goeyens, L., Stroobants, N., Bernard, P., Goyet, C., Poisson, A., et al. (1990). On Suspended Barite and the Oxygen Minimum in the Southern Ocean. *Global Biogeochem. Cycles* 4 (1), 85–102. doi: 10.1029/GB004i001p00085

Dehairs, F., Jacquet, S., Savoye, N., Van Mooy, B. A. S., Buesseler, K. O., Bishop, J. K. B., et al. (2008). Barium in Twilight Zone Suspended Matter as a Potential Proxy for Particulate Organic Carbon Remineralization: Results for the North Pacifi. *Deep Sea Res. Part II: Topical Stud. Oceanogr.* 55, 1673–1683 doi: 10.1016/j.dsr2.2008.04.020

Dehairs, F., Stroobants, N., and Goeyens, L. (1991). Suspended Barite as Tracer of Biological Activity in the Southern Ocean. *Mar. Chem.* 35, 399–410. doi: 10.1016/S0304-4203(09)90032-9

Foster, D. A., Staubwasser, M., and Henderson, G. M. (2004). ^{226}Ra and Ba Concentrations in the Ross Sea Measured With Multicollector ICP Mass Spectrometry. *Mar. Chem.* 87, 59–71. doi: 10.1016/j.marchem.2004.02.003

Ganeshram, R. S., François, R., Commeau, J., and Brown-Leger, S. L. (2003). An Experimental Investigation of Barite Formation in Seawater. *Geochim. Cosmochim. Acta* 67 (14), 2599–2605. doi: 10.1016/S0016-7037(03)00164-9

González-Muñoz, M. T., Fernández-Luque, B., Martínez-Ruiz, F., Ben Chekroun, K., Arias, J. M., Rodríguez-Gallego, M., et al. (2003). Precipitation of Barite by Myxococcus Xanthus: Possible Implications for the Biogeochemical Cycle of Barium. *Appl. Environ. Microbiol.* 69, 5722–5725. doi: 10.1128/AEM.69.9.5722-5725.2003

Honda, M. C. (2003). Biological Pump in the Northwestern North Pacific. *J. Oceanogr.* 59, 671–684. doi: 10.1023/B:JOCE.0000009596.57705.0c

Honda, M. C., Imai, K., Nojiri, Y., Hoshi, F., Sugawara, T., and Kusakabe, M. (2002). The Biological Pump in the Northwestern North Pacific Based on Fluxes and Major Component of Particulate Matter Obtained by Sediment Trap Experiments, (1997–2000). *Deep Sea Res. Part II* 49, 5595–5625. doi: 10.1016/S0967-0645(02)00201-1

Honda, M. C., Kawakami, H., Sasaoka, K., Watanabe, S., and Dickey, T. (2006). Quick Transport of Primary Produced Organic Carbon to the Ocean Interior. *Geophys. Res. Lett.* 33, 1-4. doi: 10.1029/2006GL026466

Horner, T. J., Kinsley, C. W., and Nielsen, S. G. (2015). Barium-Isotopic Fractionation in Seawater Mediated by Barite Cycling and Oceanic Circulation. *Earth Planet Sci. Lett.* 430, 511–522. doi: 10.1016/j.epsl.2015.07.027

Hsieh, Y.-T., and Henderson, G. M. (2017). Barium Stable Isotopes in the Global Ocean: Tracer of Ba Inputs and Utilization. *Earth Planet Sci. Lett.* 473, 269–278. doi: 10.1016/j.epsl.2017.06.024

Jacquet, S. H. M., Dehairs, F., Dumont, I., Becquevort, S., Cavagna, A.-J., and Cardinal, D. (2011). Twilight Zone Organic Carbon Remineralization in the Polar Front Zone and Subantarctic Zone South of Tasmania. *Deep Sea Res. Part II Top. Stud. Oceanogr.* 58, 2222–2234. doi: 10.1016/j.dsr2.2011.05.029

Jacquet, S. H. M., Dehairs, F., Savoye, N., Obernosterer, I., Christaki, U., Monnin, C., et al. (2008). Mesopelagic Organic Carbon Mineralization in the Kerguelen Plateau Region Tracked by Biogenic Particulate Ba. *Deep-Sea Res. II* 55, 868–879. doi: 10.1016/j.dsr2.2007.12.038

Jacquet, S. H. M., Henjes, J., Dehairs, F., Worobiec, A., Savoye, N., and Cardinal, D. (2007). Particulate Ba-Barite and Acantharians in the Southern Ocean During the European Iron Fertilization Experiment (EIFEX). *J. Geophys. Res.* 112, G04006. doi: 10.1029/2006JG000394

Karl, D. M., and Lukas, R. (1996). The Hawaii Ocean Time-Series (HOT) Program: Background, Rationale and Field Implementation. *Deep-Sea Res. II* 43, 129–156. doi: 10.1016/0967-0645(96)00005-7

Kaufman, A., Trier, R. M., Broecker, W. S., and Feely, H. W. (1973). Distribution of 228Ra in the World Ocean. *J. Geophys. Res.* 78 (36), 8827–8848. doi: 10.1029/JC078i036p08827

Kawakami, H., and Kusakabe, M. (2008). Surface Water Mixing Estimated From ^{228}Ra and ^{226}Ra in the Northwestern North Pacific. *J. Environ. Radioact.* 99, 1335–1340. doi: 10.1016/j.jenvrad.2008.04.011

Ku, T.-L., Huh, C.-A., and Chen, P. S. (1980). Meridional Distribution of ^{226}Ra in the Eastern Pacific Along GEOSECS Cruise Tracks. *Earth Planet Sci. Lett.* 49, 293–308. doi: 10.1016/0012-821X(80)90073-4

Ku, T.-L., and Lin, M.-C. (1976). ^{226}Ra Distribution in the Antarctic Ocean. *Earth Planet Sci. Lett.* 32, 236–248. doi: 10.1016/0012-821X(76)90064-9

Ku, T.-L., and Luo, S. (1994). New Appraisal of Radium-226 as a Large-Scale Oceanic Mixing Tracer. *J. Geophys. Res.* 99, 255–210. doi: 10.1029/94JC00089

Lam, P. J., and Bishop, J. K. B. (2008). The Continental Margin is a Key Source of Iron to the HNLC North Pacific Ocean. *Geophys. Res. Lett.* 35 (7), 1–5. doi: 10.1029/2008gl033294

Lea, D. W., and Boyle, E. A. (1989). Barium Content of Benthic Foraminifera Controlled by Bottom-Water Composition. *Nature* 338, 751–753. doi: 10.1038/338751a0

Lea, D. W., and Boyle, E. A. (1990). A 210,000-Year Record of Barium Variability in the Deep Northwest Atlantic Ocean. *Nature* 347, 269–272. doi: 10.1038/347269a0

Legeleux, F., and Reyss, J.-L. (1996). Ra-228/ Ra-226 Activity Ratio in Oceanic Settling Particles : Implications Regarding the Use of Barium as a Proxy for Paleoproductivity Reconstruction. *Deep-Sea Res. I* 43 (11-12), 1857–1863. doi: 10.1016/S0967-0637(96)00086-6

Le Roy, E., Sanial, V., Charette, M. A., van Beek, P., Lacan, F., Jacquet, S., et al. (2018). Study of the 226Ra-Ba Relationship Along the GA01-GEOTRACES Section in the North Atlantic. *Biogeosciences* 15 (9), 3027–3048. doi: 10.5194/bg-15-3027-2018

Li, Y. H., Ku, T. L., Mathieu, G. G., and Wolgemuth, K. (1973). Barium in the Antarctic Ocean and Implications Regarding the Marine Geochemistry of Ba and ^{226}Ra. *Earth Planet Sci. Lett.* 19, 352–358. doi: 10.1016/0012-821X(73)90085-X

Martinez-Ruiz, F., Paytan, A., Gonzalez-Munoz, M. T., Jroundi, F., Abad, M. M., Lam, P. J., et al. (2020). Barite Precipitation on Suspended Organic Matter in the Mesopelagic Zone. *Front. Earth Sci.* 8. doi: 10.3389/feart.2020.567714

Michaels, A. F. (1988). Vertical Distribution and Abundance of Acantharia and Their Symbionts. *Mar. Biol.* 97, 559–569. doi: 10.1007/BF00391052

Michaels, A. F., Caron, D. A., Swanberg, N. R., Howse, F. A., and Michaels, C. (1995). Planktonic Sarcodines (Acantharia, Radiolaria, Foraminifera) in Surface Waters Near Bermuda: Abundance, Biomass and Vertical Flux. *J. Plankton Res.* 17 (1), 131–163. doi: 10.1093/plankt/17.1.131

Millero, F.J. (2005). Chemical Oceanography (*3rd eds.*). *CRC Press.* doi: 10.1201/9780429258718

Monnin, C. (1999). A Thermodynamic Model for the Solubility of Barite and Celestite in Electrolyte Solutions and Seawater From 0 to 200°C and to 1kbar. *Chem. Geol.* 153, 187–209. doi: 10.1016/S0009-2541(98)00171-5

Monnin, C., and Cividini, D. (2006). The Saturation State of the World's Ocean With Respect to (Ba,Sr)SO_4 Solid Solutions. *Geochim. Cosmochim. Acta* 70, 3290–3298. doi: 10.1016/j.gca.2006.04.002

Monnin, C., and Galinier, C. (1988). The Solubility of Celestite and Barite in Electrolyte Solutions and Natural Waters at 25°C. A Thermodynamic Study. *Chem. Geol.* 71-, 283–296 doi: 10.1016/0009-2541(88)90055-1

Monnin, C., Jeandel, C., Cattaldo, T., and Dehairs, F. (1999). The Marine Barite Saturation State of the World's Oceans. *Mar. Chem.* 65, 253–261. doi: 10.1016/S0304-4203(99)00016-X

Moore, W. S., and Dymond, J. (1991). Fluxes of Ra-226 and Barium in the Pacific Ocean : The Importance of Boundary Processes. *Earth Planet Sci. Lett.* 107, 55–68. doi: 10.1016/0012-821X(91)90043-H

Moore, W. S., Key, R. M., and Sarmiento, J. L. (1985). Techniques for Precise Mapping of 226Ra and 228Ra in the Ocean. *J. Geophys. Res.* 90, 6983–6995. doi: 10.1029/JC090iC04p06983

Moore, W. S., and Reid, D. F. (1973). Extraction of Radium From Natural Waters Using Manganese-Impregnated Acrylic Fibers. *J. Geophys. Res.* 78, 8880–8886. doi: 10.1029/JC078i036p08880

Oka, E., Qiu, B., Takatani, Y., Enyo, K., Sasano, D., Kosgi, N., et al. (2015). Decadal Variability of Subtropical Mode Water Subduction and its Impact on Biogeochemistry. *J. Oceanogr.* 71, 389–400. doi: 10.1007/s10872-015-0300-x

Paytan, A., Moore, W. S., and Kastner, M. (1996). Sedimentation Rate as Determined by ^{226}Ra Activity in Marine Barite. *Geochim. Cosmochim. Acta* 60 (22), 4313–4319. doi: 10.1016/S0016-7037(96)00267-0

Qiu, B., Chen, S., Schneider, N., and Taguchi, B. (2014). A Coupled Decadal Prediction of the Dynamic State of the Kuroshio Extension System. *J. Clim.* 27, 1751–1764. doi: 10.1175/JCLI-D-13-00318.1

Reyss, J.-L., Schmidt, S., Legeleux, F., and Bonte, P. (1995). Large, Low Background Well-Type Detectors for Measurements of Environmental Radioactivity. *Nucl. Inst. Meth. A* 357, 391–397. doi: 10.1016/0168-9002(95)00021-6

Rhein, M., and Schlitzer, R. (1988). Radium-226 and Barium Sources in the Deep East Atlantic. *Deep-Sea Res.* 35 (9), 1499–1510. doi: 10.1016/0198-0149(88)90099-4

Rushdi, A., McManus, J., and Collier, R. (2000). Marine Barite and Celestite Saturation in Seawater. *Mar. Chem.* 69, 19–31. doi: 10.1016/s0304-4203(99)00089-4

Schmidt, S., and Cochran, J. K. (2010). Radium and Radium-Daughter Nuclides in Carbonates: A Brief Overview of Strategies for Determining Chronologies. *J. Environ. Radioact.* 101, 530–537. doi: 10.1016/j.jenvrad.2009.10.006

Staubwasser, M., Henderson, G. M., Berkman, P. A., and Hall, B. L. (2004). Ba, Ra, Th, and U in Marine Mollusc Shells and the Potential of 226Ra/Ba Dating of Holocene Marine Carbonate Shells. *Geochim. Cosmochim. Acta* 68 (1), 89–100. doi: 10.1016/S0016-7037(03)00279-5

Sternberg, E., Tang, D., Tung-Yuan, H., Jeandel, C., and Morel, F. (2005). Barium Uptake and Adsorption in Diatoms. *Geochim. Cosmochim. Acta* 69, 2745–2752. doi: 10.1016/j.gca.2004.11.026

Stroobants, N., Dehairs, F., Goeyens, L., Vanderheijden, N., and van Grieken, R. (1991). Barite Formation in the Southern Ocean Water Column. *Mar. Chem.* 35, 411–421. doi: 10.1016/S0304-4203(09)90033-0

van Beek, P., François, R., Conte, M., Reyss, J.-L., Souhaut, M., and Charrette, M. (2007). $^{228}Ra_{ex}/^{226}Ra_{ex}$ and $^{226}Ra_{ex}$/Ba Ratios to Track Barite Formation and Transport in the Water Column. *Geochim. Cosmochim. Acta* 71, 71–86. doi: 10.1016/j.gca.2006.07.041

van Beek, P., and Reyss, J.-L. (2001). ^{226}Ra in Marine Barite: New Constraints on Supported ^{226}Ra. *Earth Planet Sci. Lett.* 187, 147–161. doi: 10.1016/S0012-821X(01)00288-6

van Beek, P., Reyss, J.-L., Bonte, P., and Schmidt, S. (2003). Sr/Ba in barite: a proxy of barite preservation in marine sediments? *Mar. Geol.* 199, 205–220 doi: 10.1016/S0025-3227(03)00220-2

van Beek, P., Reyss, J.-L., DeMaster, D., and Paterne, M. (2004). ^{226}Ra-in Marine Barite : Relationship With Carbonate Dissolution and Sediment Focusing in the Equatorial Pacific. *Deep-Sea Res. I* 51, 235–261. doi: 10.1016/j.dsr.2003.10.007

van Beek, P., Reyss, J.-L., Gersonde, R., Paterne, M., Rutgers van der Loeff, M., and Kuhn, G. (2002). ^{226}Ra in Barite : Absolute Dating of Holocene Southern Ocean Sediments and Reconstruction of Sea-Surface Reservoir Ages. *Geology* 30 (8), 731–734 doi: 10.1130/0091-7613(2002)030<0731:RIBADO>2.0.CO;2

van Beek, P., Souhaut, M., Lansard, B., Bourquin, M., Reyss, J.-L., Jean, P., et al. (2013). LAFARA : A New Underground Laboratory in the French Pyrénées for Low-Background Gamma Spectrometry. *J. Environ. Radioact.* 116, 152–158. doi: 10.1016/j.jenvrad.2012.10.002

van Beek, P., Souhaut, M., and Reyss, J.-L. (2010). Measuring the Radium Quartet (^{226}Ra, ^{228}Ra, ^{224}Ra, ^{223}Ra) in Water Samples Using Gamma Spectrometry. *J. Environ. Radioact.* 101, 521–529. doi: 10.1016/j.jenvrad.2009.12.002

van Beek, P., Sternberg, E., Reyss, J.-L., Souhaut, M., Robin, E., and Jeandel, C. (2009). ^{228}Ra/^{226}Ra and ^{226}Ra/Ba Ratios in the Western Mediterranean Sea: Barite Formation and Transport in the Water Column. *Geochim. Cosmochim. Acta* 73, 4720–4737. doi: 10.1016/j.gca.2009.05.063

Weast, R. C., Selby, S. M., and Hodgman, C. D. (1966). *Handbook of Chemistry and Physics. 46th edition* (Cleveland: the chemical rubber co), 1713 pp.

Wolgemuth, K., and Broecker, W. S. (1970). Barium in Sea Water. *Earth Planet Sci. Lett.* 8, 372–378. doi: 10.1016/0012-821X(70)90110-X

Conflict of Interest: The authors declare that the research was conducted in the absence of any commercial or financial relationships that could be construed as a potential conflict of interest.

frontiers | Frontiers in Marine Science

ORIGINAL RESEARCH
published: 28 July 2022
doi: 10.3389/fmars.2022.823793

Interannual Variations of $D^{14}C_{TOC}$ and Elemental Contents in the Laminated Sediments of the Santa Barbara Basin During the Past 200 Years

Hong-Chun Li[1,2], Yiwei Chang[1], William M. Berelson[3], Meixun Zhao[2], Satabdi Misra[1] and Tzu-Tsen Shen[1]*

[1]Department of Geosciences, National Taiwan University, Taipei, Taiwan, [2]Frontiers Science Center for Deep Ocean Multispheres and Earth System, and Key Laboratory of Marine Chemistry Theory and Technology, Ministry of Education, Ocean University of China, Qingdao, China, [3]Department of Earth Sciences, University of Southern California, Los Angeles, CA, United States

OPEN ACCESS

Edited by:
Núria Casacuberta, ETH Zürich, Switzerland

Reviewed by:
Fasong Yuan, Cleveland State University, United States
Amzad Hussain Laskar, Physical Research Laboratory, India
Haiyan Jin, Ministry of Natural Resources, China

***Correspondence:**
Hong-Chun Li
hcli1960@ntu.edu.tw

Specialty section:
This article was submitted to Marine Biogeochemistry, a section of the journal Frontiers in Marine Science

Received: *28 November 2021*
Accepted: *15 June 2022*
Published: *28 July 2022*

Citation:
Li H-C, Chang Y, Berelson WM, Zhao M, Misra S and Shen T-T (2022) Interannual Variations of $D^{14}C_{TOC}$ and Elemental Contents in the Laminated Sediments of the Santa Barbara Basin During the Past 200 Years. Front. Mar. Sci. 9:823793. doi: 10.3389/fmars.2022.823793

A 51-cm core (SBB-8-2012) from the depo-center of Santa Barbara Basin (SBB), California has been dated by ^{210}Pb dating and varve counting, spanning a depositional history during 1815-2011 CE. A total of 89 AMS ^{14}C measurements on samples from 66 horizons, including animal cartilage, shell and total organic carbon (TOC) in the sediments show apparent ^{14}C ages between 500 and 4000 yr BP. Among these AMS dates, $D^{14}C$ values measured in 78 samples from 62 horizons vary in the range of -64.3‰ to -383.8‰. The $^{14}C_{TOC}$ ages much older than predicted from our sedimentation model are influenced by the input of terrigenous sediments, changes in ocean circulation, biological input and carbon remineralization. Three strong old $^{14}C_{TOC}$ excursions at 1964~69, 1884~87 and 1819~21 CE indicate higher old carbon input caused by some unusual events (e.g., oil spill, flood event and earthquake). On multi-decadal timescales, the $D^{14}C_{TOC}$ shifts in three zones were mainly caused by changes in fossil carbon emission from the seafloor, fraction of marine productivity to terrigenous input of organic carbon (OC) and the atmospheric nuclear bomb testing input of ^{14}C into the SBB. On interannual to decadal timescales, variations of $D^{14}C_{TOC}$ correspond to El Niño-Southern Oscillation effects. During the La Niña period, stronger upwelling and northerly California Current bring nutrient-enriched water into SBB and lead to higher productivity hence more marine OC with higher $D^{14}C_{TOC}$. In addition, reduced terrigenous input of OC with lower $D^{14}C$ under less coastal rainfall during La Niña could further elevate the $D^{14}C_{TOC}$. Lower scanning XRF (K+Ti)/2 (indicating lower terrigenous input), higher scanning XRF Sr/Ti as well as acid-leachable elements (reflecting higher biogenic components), and higher $D^{14}C_{TOC}$ occur during La Niña. During the El Niño period, the phenomena are opposite. Spectrum analyses of the Southern Oscillation Index (SOI) and the $D^{14}C_{TOC}$ as well as the comparison of SOI and SBB-8-2012 records support our scenarios.

Keywords: $^{14}C_{TOC}$ variation, elemental content, laminated sediment, Santa Barbara basin, El Niño/La Niña, iTRAX XRF scan corer, Icp-oes analysis, acid-leachable elements

1 INTRODUCTION

With anoxic conditions on the bottom of Santa Barbara Basin (SBB) offshore of California, laminated sediments have regularly been used to reconstruct high-resolution paleoclimate records (Kennett and Brassell, 1992; Schimmelmann and Lange, 1992; Kennett and Ingram, 1995; Heusser, 1998; Schimmelmann et al., 1998; Schimmelmann et al., 2003; Robert, 2004; Schimmelmann et al., 2006; Barron and Bukry, 2010; Barron et al., 2015; Sarno et al., 2020), and natural disaster signals such as earthquake and flooding events (Schimmelmann et al., 2001; Schimmelmann et al., 2013; Hendy et al., 2015; Du et al., 2018). Numerous investigations of SBB water column, sediment trap and sediment core analyses have been conducted on carbon and nitrogen cycles (e.g., Andrew and Peter, 1977; Pisias, 1978; Lynn and Simpson, 1990; Schimmelmann and Tegner, 1991; Thunell, 1998; Emmer and Thunell, 2000; Thunell, 2003; Tems et al., 2015; Davis et al., 2019; White et al., 2019), biological productivity and chemical conditions in the basin and their linkage to climate and water mixing (e.g., Browne, 1994; Gorsline, 1996; Weinheimer and Cayan, 1997; Warrick et al., 2005; Lund, 2011; Berelson et al., 2019; Napier et al., 2019).

Terrestrial organic carbon input by episodic discharge events from the mountain river systems can survive in coastal processing near Santa Barbara Channel (Kolpack and Drake, 1984; Thunell et al., 1995; Schimmelmann and Lange, 1996). The organic carbon (OC) can be rapidly transported to low-oxygen seafloor sediments in SBB where remineralization is less efficient (Sarno et al., 2020). Due to restricted circulation below the basin sills, oxygen supply to the bottom water of SBB is limited, so a suboxic environment exists at a depth below 480 m (Li et al., 2009). The anoxic condition in SBB is also attributed to the emission of methane and crude oil from oil seeps in the region contribute reduced carbon. For instance, the Coal Oil Point seep field, located at near shore of SBB, is one of the largest natural submarine hydrocarbon emission areas in the world (Allen and Mikolaj, 1970; Hornafius et al., 1999; Valentine et al., 2010) and likely contributes fossil carbon input to SBB. With those exogenous carbons (old and dead carbons), the ^{14}C reservoir age in SBB is older than that of the average world ocean and varies over time (Kennett et al., 1997). Several groups have studied the ΔR (regional differences in the radiocarbon age between sea-surface water and average world surface water, McFadgen and Manning, 1990) in SBB *via* different methods. Ingram and Southon (1996) used mollusc shell ^{14}C measurements in SBB and found the ΔR of 233±60 years for the Santa Barbara Channel region, close to the average for the coast of California. Kennett et al. (1997) used ^{14}C dates of marine shell and charcoal pairs from finely stratified archaeological deposits at Daisy Cave and Cave of the Chimneys located on San Miguel Island and concluded that the ΔR varied from -360 to 310 years during the Holocene. Hendy et al. (2013) compared 49 mixed planktonic foraminiferal carbonate and 20 terrigenous organic carbon (such as wood, leaves, seeds or charcoal) ^{14}C dates to the varve chronology in a sediment core from SBB and found that the ΔR between 80 and 350 years during the past 2000 years. Therefore, it is necessary to further understand the factors that affect the ^{14}C reservoir ages of SBB.

The ^{14}C reservoir age in SBB is related to oceanic circulation, upwelling of the Pacific deep water, El Niño–Southern Oscillation (ENSO) and Pacific Decadal Oscillation (PDO) (Kennett et al., 1997; Hendy et al., 2013; Du et al., 2018). This is because the regional rainfall of southern California, oceanic circulation and upwelling along the southern California coast are strongly influenced by summer insolation, ENSO and PDO (Kennett et al., 1997 and references therein; Lynn and Bograd, 2002; Jacox et al., 2015). During the warm phases of ENSO (El Niño state) and PDO, rainfall and river discharge increase around SBB, supplying more terrestrial sediments to the depo-center of SBB (Shipe et al., 2002; Warrick and Farnsworth, 2009; Hendy et al., 2015). During this period, the southerly flow of California Counter Current brings warm, nutrient-depleted water from the equatorial Pacific to suppress northerly flow and nutrient-rich California Current as well as upwelling, resulting in low marine productivity (Bray et al., 1999; Bograd and Lynn, 2001; Bograd et al., 2002; Venrick, 2012). On the other hand, increase (decrease) in summer insolation results in warmer air masses over western North America, enhancing (reducing) northwesterly winds and upwelling intensity along the California coast (Kennett et al., 1997). However, up to date, there is no annual to interannual variability of ^{14}C reservoir age in the SBB sediment records to provide evidence for the above scenario. We address this topic in our work here. Furthermore, Hendy et al. (2015) used a 250-yr varved core (SPR0901-04BC) from SBB to identify droughts and floods related to ENSO impact by using changes in elemental contents measured with scanning X-ray fluorescence (XRF), inductively coupled plasma atomic emission spectrometer (ICP-AES) and inductively coupled plasma mass spectrometer (ICPMS). They have found that siliciclastic sediments containing the elements Ti, Fe, K, Al, Si, and Rb have higher scanning XRF intensities during El Niño events and positive (warm) phases of PDO, and biogenic indicators such as Ca/Ti, Sr/Ti and Br/Cl have lower values during El Niño events and negative (cool) phases of the PDO (Hendy et al., 2015). Are we able to reproduce such conclusions?

This study presents results of ^{14}C measurement, scanning XRF elemental content and acid-leachable elemental concentration of the sediments in a 51-cm core from the depo-center of SBB. The core was dated by ^{210}Pb and varve counting. The refined chronology of the core indicates that the sedimentary history of the core covers 1815-2011 CE. The high-resolution (3-yr) $D^{14}C_{TOC}$ record combined with the elemental records allows us to understand sedimentary variations under influence of climatic and oceanographic changes. In this paper, we will discuss the influencing factors of the $D^{14}C_{TOC}$ (i.e., apparent ^{14}C age of total organic carbon) in SBB sediments. The outputs of our results benefit not only the understanding of the variation of the ^{14}C reservoir effect in the Santa Barbara Channel, but also the reconstruction of paleoclimate and paleo-ENSO changes.

2 MATERIALS AND METHODS

2.1 SBB-8-2012 Core and Sampling

SBB-8-2012 (34°17'N, 120°03'W) was a 51-cm long core collected by a multi-core device in the depo center of the Santa Barbara Basin at a water depth of 580 m by the research team of Prof. William Berelson at the University of Southern California (USC) in August 2012 (**Figure 1**). The core was split in half and kept in a cold room at 4°C in the Department of Earth Sciences at USC. Half of the core was transported to the Department of Geosciences at the National Taiwan University (NTU) in 2015. During the transportation, the sediments below 12.5 cm separated from the section above, perhaps caused by differential drying due to changes in grain size, density and organic content, etc. (**Figure 2A**). This shrinkage resulted in a 3-cm gap in the core. Therefore, we have to calibrate the scanned and sampling depths back to the original depths (**Figure 2B**). Owing to changes in moisture content of the core during the storage (more than 3 years) at USC and transportation from USC to NTU, the water content of the sediments was not measured.

The half core was scanned by an iTRAX core scanner at NTU. After the scan, the core was subsampled at 1-cm interval for ^{210}Pb dating, then subsampled at 2~3-mm interval (roughly 4 samples within one centimeter) with a stainless steel knife for fine resolution analyses. During the sampling, any visible shells, plant or animal remains in the sediments, were picked up individually for ^{14}C dating purposes. Only less than 1/2 of the sediments throughout the half core were taken at NTU, and the rest was sent back to USC where δ^{13}C, δ^{15}N and C/N of the organic matter were planned to be analyzed. Due to the limited amount of subsamples, we did not measure grain size, bulk density and TOC for every sample. All sediment samples were freeze-dried by a Freeze vacuum dryer (model EYELA FDU-1200), then ground and mixed well. The samples were placed in plastic bags and stored in a refrigerator at 8°C until analysis.

2.2 iTRAX XRF Core Scan

The iTRAX XRF scan was performed at NTU with an iTRAX core scanner (Li et al., 2015; Löwemark and Itrax operators, 2019). The core with smooth and flat surface was placed in the XRF scanner which contains a digital optical RBG image, a digital radiographic image, and a μ-XRF elemental profile. The scanning condition was using a Mo tube set at 30 kV and 30 mA, a sampling interval of 200 μm and an exposure time of 40 s. For duplicating checks, the core was scanned twice along two parallel tracks which are 3-mm apart. Elements including Fe, Ca, Sr, K, Ti, Mn, Rb, Zn, Ni, Cu, Si, S, Cl, V, Cr, Co, Y, Zr, Nb, Pd, Cd, In, Sn, Sb, Al, Ba and Pb were measured, but only part of the elements provided meaningful results. The criteria for selecting meaningful data are: 1. The maximum intensity of an element during the entire scan should be greater than 200 counts per second (cps); and 2. The correlation coefficient (R^2) of the element along the two duplicated tracks should be greater than 0.6. With such criteria, only Fe, Ca, Sr, K, Ti, Mn, Rb, Zn, Ni, Cu, Si, Cl, Y, Zr and Pb provide meaningful results.

2.3 ^{210}Pb Dating

^{210}Pb dating method was originally established by Goldberg (1963). ^{210}Pb profile of a sedimentary sequence can be described by the following equation:

$$^{210}Pb = {}^{210}Pb_0 * e^{-\lambda t} = {}^{210}Pb_0 * e^{-\lambda * D/SR} \quad (1)$$

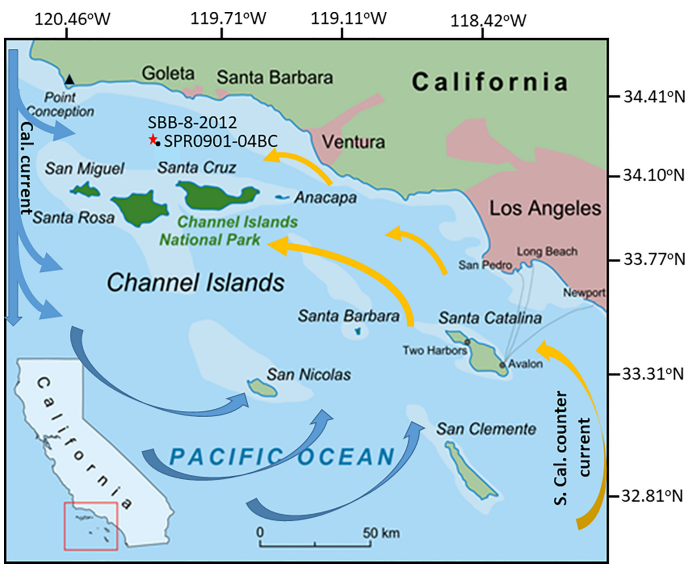

FIGURE 1 | Location map of the study area. The red star shows the location of core SBB-8-2012 site in Santa Barbara Basin and the black dot indicates core SPR0901-04BC location of Hendy et al. (2015). Blue arrows present cold and nutrient-rich current from north, whereas the orange arrows reflect warm and nutrient-depleted current from south.

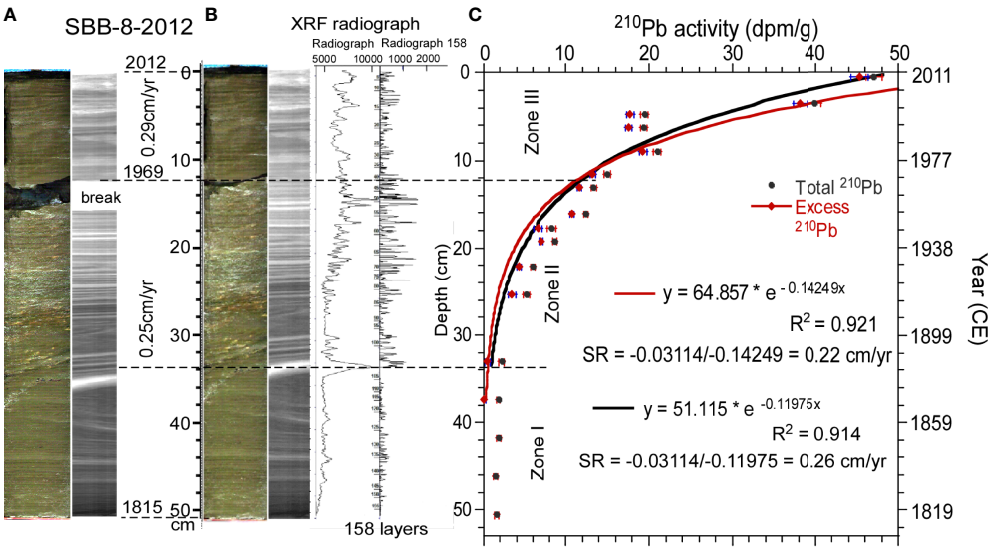

FIGURE 2 | Picture, X-ray radiograph, lamination counting and ^{210}Pb dating of Core SBB-8-2012. **(A)** Core photo during XRF scanning and sampling. The breaking gap between 12cm and 13cm was formed during the transportation from USA to Taiwan. **(B)** Core photo after adjusted the depths to remove the breaking gap. The lighter bands in the radiograph reflect the layers with less density. The brightest band at 34 cm indicates an organic rich layer in which all elemental contents by iTRAX XRF scanning are low. **(C)** ^{210}Pb profile of the core. The constructed ages are shown on the right-hand side of the plot. The red curve and black curve fittings are using different ending depths of excess ^{210}Pb, which result different sedimentation rates.

where $^{210}Pb_0$ and ^{210}Pb are the initial activity and activity at a past time (or depth), respectively. λ is the decay constant of ^{210}Pb (0.0311 yr^{-1}). D stands for depth in a sedimentary profile. SR refers to the linear sedimentation rate. Taking logarithms to Eqn. (1), we have:

$$Ln^{210}Pb = Ln^{210}Pb_0 - \lambda * D / SR \quad (2)$$

If $^{210}Pb_0$ and SR are relatively constant, the slope of Ln ^{210}Pb — D should yield a linear sedimentation rate SR. This is the fundamental concept of ^{210}Pb dating.

Since the subsample of the core was not enough for our gamma spectrometry, ^{210}Po alpha method was used for the ^{210}Pb dating (Baskaran and Iliffe, 1993; Baskaran and Krishnamurthy, 1993; Li et al., 1996; Paulsen et al., 2003; Li et al., 2011; Kuo et al., 2011; Yin et al., 2014; Zhao et al., 2015; Yin et al., 2017; Zhao et al., 2017a; Yin et al., 2019). As a daughter product of ^{210}Pb decay, ^{210}Po has a half-life of 138.38 days. Hence, within a couple of years, ^{210}Pb and ^{210}Po reach secular equilibrium. The ^{210}Po activity equals that of ^{210}Pb in the measured samples.

A total of 17 horizons from the 1-cm interval samples were selected throughout the core for ^{210}Po dating in the AMS ^{14}C dating Lab at NTU (the NTUAMS Lab) (**Table 1**). Each dry sample of 0.3~0.5 g was spiked with ^{209}Po in a Teflon beaker and dissolved by aqua regia on a hot plate at 95°C overnight. The sample solution was evaporated to dryness, then added 4N HCl to dissolve residues. The sample solution was transferred into a centrifuge tube for the removal of any detritus. After centrifuge, the supernatant was poured back into the Teflon beaker and evaporated to dryness. Ten ml 1.0 N HCl was added into the Teflon beaker to dissolve the sample. Then, transfer the sample into a 50-ml plastic centrifuge tube. Ascorbic acid powder was added to the solution until it became clear (yellow color would be disappeared) in order to remove the influence of Fe. A silver disc (0.8 cm in diameter) was placed at the bottom of the centrifuge tube. The Po in the sample was self-precipitated onto the silver disc within an 80°C water bath for 6 hours. After washing with deionized water (DIW), the silver disc was counted for ^{210}Po (5304 keV) and ^{209}Po (4884 keV) by an ORTEC alpha spectrometer at NTU. **Table 1** lists the ^{210}Po dating results.

2.4 AMS ^{14}C Dating

Accelerator mass spectrometry (AMS) ^{14}C dating was performed in the NTUAMS Lab at NTU with a 1.0 MV Tandetron Model 4110 BO AMS. About 50~100 mg of dry sediments were weighted for TOC ^{14}C dating and acid-leachable element analysis. The sample was dissolved in 15 ml 0.5N HCl for removal of carbonates. Using pH paper to check the solution, when pH<3, all inorganic carbons were dissolved by the acid leaching. Centrifuging the sample and washing the residue with DIW, and collecting the supernatant for inductively coupled plasma-optical emission spectrometer (ICP-OES) analysis. The residue was dried at 50°C. The TOC of the dried residue sample was oxidized into CO_2 under 850°C. Then, the purified CO_2 was made into graphite following the description in Yang et al. (2017) and Zhao et al. (2017b). Six samples (samples with # symbol in **Table 2**) were used a different acidification treatment for AMS ^{14}C dating. For these samples, the sample was placed in a reaction vessel on a vacuum line for CO_2 collection. The sediment sample in

TABLE 1 | ^{210}Pb dating results. The excess ^{210}Pb is determined by the ^{210}Po at each layer subtracting the mean ^{210}Po value averaged from the four ^{210}Po values in the deep part.

Sample ID	Weight (g)	Depth (cm)	^{210}Po (dpm/g)	Excess ^{210}Pb (dpm/g)
SBB-8 0-1	0.37	0.5	47.06±0.98	45.35±0.98
SBB-8 3-4	0.30	3.5	39.89±0.81	38.18±0.81
SBB-8 4-5.5	0.56	4.8	19.46±0.48	17.75±0.48
SBB-8 5.5-7	0.48	6.3	19.30±0.40	17.59±0.40
SBB-8 8-10	0.54	9.0	21.00±0.47	19.29±0.47
SBB-8 10-12	0.49	11.5	14.95±0.37	13.24±0.37
SBB-8 15.5-17	0.51	13.1	13.35±0.30	11.64±0.30
SBB-8 18-20	0.53	16.1	12.44±0.27	10.73±0.27
SBB-8 20-21	0.31	17.7	8.31±0.49	6.60±0.49
SBB-8 21-22.5	0.64	19.1	8.69±0.26	6.98±0.26
SBB-8 24-25	0.37	22.0	5.96±0.25	4.25±0.25
SBB-8 27-28	0.31	25.4	5.16±0.41	3.45±0.41
SBB-8 34-35	0.30	33.1	2.19±0.32	0.48±0.32
SBB-8 38-39	0.37	37.4	1.82±0.22	0.11±0.22
SBB-8 42-43	0.30	41.8	1.88±0.28	
SBB-8 46-47	0.35	46.1	1.50±0.23	
SBB-8 50-51	0.47	50.6	1.64±0.25	

the reaction vessel was reacted with 1 ml of 100% H_3PO_4 on the vacuum line. After the CO_2 extraction of the total inorganic carbon (TIC) in the sample was done, the collected CO_2 was made into graphite for ^{14}C dating following the description in Zhao et al. (2015). The residue in the reaction vessel was collected into a centrifuge tube and washed by DIW. After centrifuging, the residue was dried at 50°C. The TOC in the dried residue was processed for ^{14}C dating according to the above description. In so doing, we can compare the ^{14}C results of TOC and TIC from the same sediment samples. For every batch of the samples, at least three oxalic acid standards (OXII, SRM 4990C), three organic carbon backgrounds (BKG, made from anthracite), three carbonate backgrounds (NTUB, made from Upper Devonian limestone) and two known-age inter-comparison samples (IRI, distributed by the University of Glasgow) were processed in the same procedures and measured with the sample targets.

One sample is animal cartilage (looks like a fish spine). This sample was just cleaned with DIW, and placed into a 9-mm size quartz tube with pre-combusted CuO powder. The tube was sealed under a vacuum of 10^{-5} mbar, and then combusted for 6 h at 850°C in a muffle furnace. The carbon from this sample came from mainly organic components, so that we classified its ^{14}C dating as TOC ^{14}C dating. There are four TIC ^{14}C dates of sediment samples (samples with @ symbol in **Table 2**) and two ^{14}C dates of a conch shell. These samples had the same procedure for TIC ^{14}C dating as described earlier for the samples with # symbol.

The AMS measured both ^{14}C/^{12}C and ^{13}C/^{12}C ratios on all graphite targets. The AMS measurement was setup for four cycles and each cycle contained 50 blocks (30 seconds for every block). When the ^{14}C counts in a measurement cycle reached 40,000, the counting would stop. Therefore, ^{14}C counts of OXII are normally greater than 40,000, with a statistic error<0.5%. In general, the precision of the ^{14}C dating at the NTUAMS Lab is better than 3%.

The percent modern carbon (pMC) was calculated by background corrected and ^{13}C/^{12}C fractionation corrected ^{14}C/^{12}C ratios between sample and OXII following the concept and definition in Stuiver and Polach (1977); Kim et al. (2001) and Stenström et al. (2011):

$$pMC = \frac{\left(\frac{^{14}C}{^{12}C}\right)_{s,bkg,corr}}{\left(\frac{^{14}C}{^{12}C}\right)_{oxII,bkg,corr}} \times 100\% = \frac{\left(\frac{^{14}C}{^{12}C}\right)_{s-bkg} \times \left(1 - \frac{2\times(25+\delta(^{13}C)_s}{1000}\right)}{\left(\frac{^{14}C}{^{12}C}\right)_{oxII-bkg} \times \left(1 - \frac{2\times(25-18)}{1000}\right)} \times 100\% \quad (3)$$

where ^{14}C/^{12}C with subscripts of s,bkg,corr and oxII,bkg,corr represents background and δ^{13}C corrected ^{14}C/^{12}C value of sample and standard, respectively. The ^{14}C/^{12}C with subscripts of s-bkg and oxII-bkg refers to background corrected ^{14}C/^{12}C value of sample and standard, respectively. Note that δ^{13}C correction for AMS ^{14}C dating must use ^{13}C/^{12}C measurement on the AMS, but not δ^{13}C measured by an isotope ratio mass spectrometry (IRMS) because the isotopic fractionation is different for the two processes. The δ^{13}C value of OXII is -17.88‰ (round to -18‰). δ^{13}C value of a sample [$\delta(^{13}$C)s] determined by the AMS was calculated by equation (4):

$$\delta(^{13}C)_S = \left[\frac{\left(\frac{^{13}C}{^{12}C}\right)_S \times \left(1 - \frac{18}{1000}\right)}{\left(\frac{^{13}C}{^{12}C}\right)_{OXII}} - 1\right] \times 1000‰ \quad (4)$$

TABLE 2 | All AMS data uncertainties have 2σ error.

Lab code (NTUAMS-)	Sample ID	Type	Depth (cm)	pMC (%)	$D^{14}C$ (‰)	^{14}C age (year BP)	Calendar year by ^{210}Pb dating (CE)
2772-2	SBB 0-0.8	TOC	0.4	93.57±1.21	-64.3±0.8	534±104	2011
4125-2	SBB 0-1cm TIC	TIC	0.5	85.17±0.96	-148.3±1.7	1289±90	2010
3830	SBB 1.1cm	TOC	1.1	90.58±0.91	-94.2±0.9	795±81	2008
2773	SBB 2-2.2	TOC	2.1	90.74±1.14	-92.6±1.2	781±101	2005
3831	SBB 3.1cm	TOC	3.1	90.10±0.91	-99.0±1.0	838±81	2001
3603	SBB 3-4cm TIC	TIC	3.5	74.07±1.17	-259.3±4.1	2411±127	2000
3802	SBB 3-4cm TOC	TOC	3.5	88.09±0.93	-119.1±1.3	1019±85	2000
2774	SBB 4-4.2	TOC	4.1	92.60±1.18	-74.0±0.9	617±102	1998
3832	SBB 5.1cm	TOC	5.1	88.50±0.93	-115.0±1.2	982±84	1994
4192	SBB 6.1 cm	TOC	6.1	83.69±0.84	-163.1±1.6	1430±80	1991
3604	SBB 5.5-7cm TIC	TIC	6.75	82.03±0.89	-179.7±1.9	1591±87	1990
3803	SBB 5.5-7cm TOC	TOC#	6.75	88.28±0.92	-117.2±1.2	1002±83	1990
3833	SBB 7.1cm	TOC	7.1	86.76±0.90	-132.4±1.4	1141±83	1988
4194	SBB 8.1cm	TOC	8.1	86.96±0.98	-130.4±1.5	1122±90	1984
2776-1	SBB 8-8.2cm	TOC	8.1	88.98±0.58	-110.2±0.7	938±53	1984
3834	SBB 9.1cm	TOC	9.1	88.51±1.00	-114.9±1.3	981±91	1981
2777-1	SBB 10-10.2cm	TOC	10.1	91.53±0.59	-84.7±0.5	711±52	1977
2777-2	SBB 10-10.2cm	TOC	10.1	92.42±0.58	-75.8±0.5	633±51	1977
4126	SBB 10-11cm TIC	TIC	10.5	85.21±0.69	-147.9±1.2	1286±65	1974
3870	SBB 11.1cm	TOC	11.1	89.63±0.77	-103.7±0.9	879±69	1974
3871	SBB 12.1cm	TOC	12.1	88.99±0.76	-110.1±0.9	937±68	1970
2778-1	SBB 12.2-12.4cm	TOC	12.3	86.90±0.56	-131.0±0.8	1128±51	1970
2778-2	SBB 12.2-12.4cm	TOC	12.3	86.57±0.61	-134.3±0.9	1159±56	1970
2779-1	SBB 15.8-16.0cm	TOC	15.9	85.25±0.58	-147.5±1.0	1282±54	1968
4053	SBB 16.9cm	TOC	16.9	71.84±0.76	-281.6±3.0	2657±85	1964
4015	SBB 17-18cm TIC	TIC	17.5	89.53±0.74	-104.7±0.9	888±66	1962
3872	SBB 18.1cm	TOC	18.1	89.71±0.67	-102.9±0.8	872±60	1959
2781-1	SBB 19-19.2cm	TOC	19.1	87.97±0.52	-120.3±0.7	1029±47	1954
3873	SBB 20.1cm	TOC	20.1	86.28±0.67	-137.2±1.1	1185±63	1950
2782	SBB 21-21.2cm	TOC	21.1	85.28±0.51	-147.2±0.9	1279±48	1945
2783	SBB 23-23.2cm	TOC	23.1	82.11±0.51	-178.9±1.1	1583±50	1937
3874	SBB 24.1cm	TOC	24.1	85.02±0.65	-149.8±1.2	1304±62	1932
2681-1	SBB 25-25.2cm	TOC	25.1	84.39±0.73	-156.1±1.3	1363±69	1928
2681-2	SBB 25-25.2cm	TOC	25.1	84.64±0.73	-153.6±1.3	1340±69	1928
3072	SBB-25.5CM	TOC	25.5	82.15±0.65	-178.5±1.4	1580±63	1926
3073	SBB-26.5CM	TOC	26.5	81.33±0.63	-186.7±1.4	1660±62	1922
2680-1	SBB 27-27.2cm	TOC	27.1	81.26±0.71	-187.4±1.6	1667±71	1919
2680-2	SBB 27-27.2cm	TOC	27.1	80.19±0.69	-198.1±1.7	1774±69	1919
3234	SBB 28.2~28.4	TOC	28.4	77.83±0.43	-221.7±1.2	2014±45	1914
3235-1	SBB 28.6~28.8	TOC	28.7	79.79±0.37	-202.1±0.9	1814±37	1912
3235-2	SBB 28.6~28.8	TOC	28.7	80.12±0.38	-198.8±0.9	1781±38	1912
2679-1	SBB 29-29.2cm	TOC	29.1	83.47±0.74	-165.3±1.5	1452±72	1910
2679-2	SBB 29-29.2cm	TOC	29.1	83.11±0.74	-168.9±1.5	1487±71	1910
3074	SBB-29.5CM	TOC	29.5	83.15±0.71	-168.5±1.4	1482±69	1909
3236-2	SBB 30.2~30.4	TOC	30.3	80.50±0.40	-195.0±1.0	1743±40	1905
3237-2	SBB 30.6~30.8	TOC	30.7	80.58±0.47	-194.2±1.1	1734±47	1903
2678-1	SBB 31-31.2cm	TOC	31.1	83.41±0.72	-165.9±1.4	1457±69	1902
2678-2	SBB 31-31.2cm	TOC	31.1	82.24±0.79	-177.6±1.7	1570±77	1902
3238-1	SBB 31.6-31.8	TOC	31.4	79.39±0.53	-206.1±1.4	1854±54	1899
3238-2	SBB 31.6-31.8	TOC	31.4	80.79±0.52	-192.1±1.2	1713±52	1899
3239-1	SBB 32.2-32.4	TOC	32.3	75.28±0.72	-247.2±2.4	2281±77	1896
3239-2	SBB 32.2-32.4	TOC	32.3	79.48±0.52	-205.2±1.3	1845±52	1896
3240	SBB 32.6-32-8	TOC	32.4	78.24±0.57	-217.6±1.6	1972±59	1895
2677-1	SBB 33-33.2cm	TOC	33.1	80.66±0.75	-193.4±1.8	1726±75	1893
2677-2	SBB 33-33.2cm	TOC	33.1	81.31±0.73	-186.9±1.7	1662±72	1893
3241	SBB 33.8-34.0	TOC	33.9	79.23±0.56	-207.7±1.5	1871±56	1889
3605	SBB 34-35cm TIC	TIC	34.5	79.68±0.99	-203.2±2.5	1825±100	1888
3801	SBB 34-35cm TOC	TOC#	34.5	76.62±0.80	-233.8±2.4	2139±83	1888
3242-1	SBB 34.6-34.8	TOC	34.7	78.45±0.51	-215.5±1.4	1949±52	1886
3242-2	SBB 34.6-34.8	TOC	34.7	78.14±0.52	-218.6±1.5	1981±54	1886
2676-1	SBB 35-35.2cm	TOC	35.1	69.24±0.67	-307.6±3.0	2952±77	1884
2676-2	SBB 35-35.2cm	TOC	35.1	68.79±0.64	-312.1±2.9	3006±75	1884

(Continued)

TABLE 2 | Continued

Lab code (NTUAMS-)	Sample ID	Type	Depth (cm)	pMC (%)	$D^{14}C$ (‰)	^{14}C age (year BP)	Calendar year by ^{210}Pb dating (CE)
2675	SBB 35.5-37 TOC	Cartilage	36.25	93.78±0.83	-62.2±0.6	516±71	1881
3075	SBB-36.5CM	TOC	36.5	79.06±0.61	-209.4±1.6	1888±62	1878
3606	SBB 38-39cm	TIC	38.5	73.53±0.89	-264.7±3.2	2469±97	1869
3804	SBB 38-39cm TOC	TOC	38.5	75.06±0.77	-249.4±2.6	2304±83	1869
3077	SBB-38.5CM	TOC	38.5	76.04±0.62	-239.6±2.0	2201±66	1869
2674-1	SBB 38.5cm Conch	Shell	38.5	88.51±0.80	-114.9±1.0	980±73	1869
2674-2	SBB 38.5cm Conch	Shell	38.5	88.18±0.80	-118.2±1.1	1010±73	1869
3078	SBB-39.1CM	TOC	39.1	79.91±0.62	-200.9±1.6	1802±63	1867
3079	SBB-39.5CM	TOC	39.5	77.64±0.62	-223.6±1.8	2033±64	1865
3080	SBB-40.1CM	TOC	40.1	80.06±0.62	-199.4±1.5	1786±62	1862
3875	SBB 41.1cm	TOC	41.1	77.62±0.69	-223.8±2.0	2035±71	1858
3450	SBB 42.1cm	TOC	42.1	72.71±0.80	-272.9±3.0	2560±85	1854
3876	SBB 43.1cm	TOC	43.1	78.44±0.61	-215.6±1.7	1951±62	1849
4054	SBB 43.9cm	TOC	43.9	73.10±0.75	-269.0±2.8	2517±83	1846
4193	SBB 44.1cm TIC	TOC	44.1	72.56±0.64	-274.4±2.4	2577±71	1845
3557	SBB 44.1cm TOC	TOC#	44.1	70.67±0.58	-293.3±2.4	2788±65	1845
3877	SBB 45.1cm	TOC	45.1	80.25±0.70	-197.5±1.7	1768±70	1840
3452	SBB 46.1cm	TOC	46.1	75.55±0.83	-244.5±2.7	2252±75	1836
3783	SBB 46-47cm TIC	TIC	46.5	77.47±0.94	-225.3±2.7	2051±98	1834
3828	SBB 46-47cm TOC	TOC#	46.5	77.28±0.79	-227.2±2.3	2070±82	1834
3878	SBB 47.1cm	TOC	47.1	78.57±0.70	-214.3±1.9	1937±71	1832
3453	SBB 48.1cm	TOC	48.1	74.81±0.85	-251.9±2.9	2332±78	1827
4055	SBB 49.1cm	TOC	49.1	69.66±0.80	-303.4±3.5	2904±92	1823
4056	SBB 49.9cm	TOC	49.9	61.62±0.65	-383.8±4.1	3889±85	1819
3784	SBB 50-51cm TIC	TIC	50.5	77.58±1.02	-224.2±2.9	2040±105	1817
3829	SBB 50-51cm TOC	TOC#	50.5	74.18±0.78	-258.2±2.7	2400±85	1817
3454	SBB 50.9cm	TOC	50.9	73.88±0.81	-261.2±2.9	2432±81	1815

All total organic carbon (TOC) samples are treated by 0.5N HCl, except samples with # symbol. The samples with # symbol were extracted CO_2 by H_3PO_4 first, then the samples were used for TOC dating. In the NTUAMS Lab code, -1 or -2 following the code indicates that the sample has enough CO_2 to split two aliquots for making graphite target.

By Eqns. (3) and (4), pMC is obtained with background and $\delta^{13}C$ (to -25‰) corrections. $D^{14}C$ and apparent age of the sample were calculated by Eqns. (5) and (6), respectively:

$$D^{14}C = \left(\frac{pMC}{100} - 1 \right) \times 1000‰ \quad (5)$$

$$\mathrm{Age}\left(yr\,BP \right) = -8033 \times \ln\left(\frac{pMC}{100} \right) \quad (6)$$

We do not use $\Delta^{14}C$ value which represents the activity ratio of a sample (A_s) to the atmospheric CO_2 (A_{abs}) without age correction (Stenström et al., 2011), whereas A_{abs} refers to the hypothetical specific activity of atmospheric carbon of year 1950. The relationship between $\Delta^{14}C$ and $D^{14}C$ can be described by Eqn. (7):

$$\Delta^{14}C = \left(D^{14}C + 10^{-3} \right) e^{(y-1950)/8267} + 10^{-3} \quad (7)$$

where y in Eqn. (7) is the measurement year. As this study does not focus on the ^{14}C variation in the atmosphere, there is no need to use $\Delta^{14}C$. Furthermore, in order to show the age difference between ^{14}C and ^{210}Pb results, we also calculated the ^{14}C ages. As these ^{14}C dates contain old carbon influences, there is no meaning to provide the calibration dates. We will use the apparent (measured) ^{14}C dates and $D^{14}C$ values for discussion. All $D^{14}C$ values and ^{14}C dates are listed in **Table 2**.

2.5 Acid-Leachable Elemental Analysis

A total of 72 horizons from the core were subsampled for acid-leachable elemental measurement. The sample weight ranged from 48.45 mg to 325.15 mg with an average and standard deviation of 96.34±51.11 mg (n = 72), implying a very limited sample amount. These samples were leached by 15 ml 0.5N HCl. This procedure is not only for the removal of inorganic carbon during TOC ^{14}C dating, but also for the dissolution of elements that exist in authigenic (precipitated in water column) minerals such as carbonates (both inorganically precipitated in surface water and in biological shells) and oxides as well as absorbed on the particle surface. This procedure does not affect organic components and detrital phases in the sediments. The elements in the solution are considered as an active portion which reflects chemical conditions and productivity in the water column. The sample solution was measured by a PerkinElmer (PE) Optima 8000DV ICP-OES in the NTUAMS Lab. Elements of Ca, Fe, Mg, Ti, Al, Sr, Ba, Mn, Zn, Cr, Cu and Pb were selected for analysis. The concentrations of all elements measured by ICP-OES need to be calculated by the standard curves made from different concentrations of the standard solutions. The standard solutions were made from ICP multi-element standard IV (Certipur® 1.11255.0100) produced by *Marck KaGaA*, Germany. During the ICP-OES runs, the standard solutions were measured with the sample solutions multiple times. The correlation coefficient (R^2) of intensity-concentration relationship for each element is normally greater than 0.98. For the first three batches of ICP-OES

TABLE 3 | Acid-leachable (0.5 N HCl) elemental concentrations in the sediments of Core SBB-8-2012.

Depth (cm)	Age (CE)	Ca	Fe	Mg	Al	Sr	Mn
0.4	2011	31.48	13.81	11.78	2.86	267.44	131.97
1.1	2008	35.73	28.91	10.89	5.75	281.80	184.49
1.5	2007	11.61	20.49	11.91	6.44	201.76	348.50
2.1	2005	13.97	6.00	3.63	2.27	92.73	89.37
2.5	2003	27.74	15.91	9.00	6.37	164.02	177.86
3.1	2001	38.85	65.99	24.93	32.86	274.71	390.35
3.5	2000	17.84	22.94	9.24	6.95	115.28	203.96
4.1	1998	20.49	21.08	6.58	3.38	119.60	130.86
4.5	1996	32.10	27.85	9.45	5.76	201.96	200.17
5.1	1994	91.33	45.94	21.2	35.08	496.00	342.86
5.5	1993	36.52	19.37	8.93	6.63	203.82	239.92
6.1	1991	31.42	11.69	8.01	3.42	210.53	169.25
6.5	1990	39.80	19.69	9.88	7.70	213.82	223.12
7.1	1988	133.63	83.82	42.62	37.43	778.70	670.28
7.5	1986	38.04	17.93	9.95	6.70	200.02	179.61
8.1	1984	31.79	10.29	7.16	3.35	170.13	102.08
8.5	1983	42.17	21.02	10.27	8.24	231.19	234.47
9.1	1981	114.21	56.27	28.62	23.99	661.25	465.58
9.5	1979	33.06	22.61	11.37	8.83	191.30	264.72
10.1	1977	29.80	19.18	7.84	3.86	165.90	149.85
10.5	1976	36.32	22.24	9.38	5.87	200.87	197.25
11.1	1974	48.03	17.73	7.44	3.63	265.32	94.24
11.5	1972	37.94	22.09	11.14	7.52	217.73	208.84
12.1	1970	44.90	10.48	6.76	3.70	267.26	77.96
12.3	1970	31.46	8.49	6.09	3.17	184.74	122.16
12.7	1968	24.66	7.63	5.55	3.12	141.33	117.77
13.8	1964	58.53	35.49	14.56	9.33	335.37	226.32
14	1963	18.98	12.42	5.67	2.89	111.06	112.88
15.1	1959	27.32	18.52	6.50	3.68	150.79	99.09
16.2	1954	10.22	3.87	3.25	1.58	81.76	95.27
17.3	1950	33.22	15.49	8.92	5.21	185.75	158.07
18.4	1945	23.63	11.17	5.43	3.20	122.78	100.06
20.6	1937	16.72	11.27	5.87	4.50	119.15	116.60
21.7	1932	39.49	14.02	7.27	4.44	224.64	127.90
22.8	1928	20.03	12.20	6.77	3.84	119.48	162.15
23.2	1926	20.40	22.01	10.73	8.82	131.83	239.61
23.9	1924	26.96	27.42	11.34	10.38	163.00	262.51
24.3	1922	34.10	28.62	10.99	9.06	193.13	244.20
24.9	1919	24.58	18.68	8.91	7.08	161.04	194.98
25.4	1917	36.48	28.14	12.5	10.4	182.72	253.78
26	1915	12.47	17.21	7.20	6.25	75.73	160.29
26.5	1913	26.01	26.60	9.50	8.76	151.70	205.88
27.1	1910	18.74	9.59	5.10	3.50	98.95	112.93
28.2	1906	14.53	12.15	5.81	4.59	91.20	157.52
29.3	1902	15.57	12.93	5.85	4.02	101.60	166.67
30.4	1897	23.24	29.89	9.50	9.96	136.92	216.41
31.5	1893	27.38	14.64	8.08	5.67	164.89	183.51
32.6	1889	25.03	21.91	10.67	9.35	154.85	226.90
33	1887	12.23	13.58	6.49	5.70	80.10	147.45
33.7	1884	19.11	17.46	10.98	7.42	121.35	206.02
34.1	1882	16.15	18.05	9.05	7.16	105.42	202.65
34.6	1881	28.70	25.90	11.97	9.25	160.09	244.21
35.2	1878	27.27	12.05	7.73	3.97	140.41	135.50
35.9	1875	14.45	14.66	8.92	3.59	91.42	147.14
36.3	1874	12.75	14.47	9.57	3.20	84.57	116.20
37	1871	8.98	9.46	6.19	2.36	60.95	124.48
37.4	1869	21.43	14.52	8.17	4.38	112.57	136.65
38.1	1867	26.8	11.78	7.80	5.86	197.02	148.66
38.5	1865	36.82	13.01	8.88	4.60	186.75	133.95
39.2	1862	40.36	11.08	8.16	4.04	199.70	124.88
40.3	1858	45.87	9.90	7.72	3.98	233.71	99.45
41.4	1854	29.21	4.49	5.42	2.50	218.52	105.91
42.5	1849	45.20	9.61	8.33	3.74	227.23	90.73
43.3	1846	87.51	25.4	18.46	10.00	450.54	229.61

(Continued)

TABLE 3 | Continued

Depth (cm)	Age (CE)	Ca	Fe	Mg	Al	Sr	Mn
43.5	1845	28.74	5.01	6.07	2.79	192.40	115.88
44.6	1840	52.37	11.81	8.50	3.52	256.73	112.35
45.7	1836	34.70	6.55	7.62	3.07	207.10	131.39
46.8	1832	48.89	9.49	7.20	3.27	255.56	99.41
47.9	1827	48.29	5.51	6.63	2.79	292.07	120.30
49	1823	72.04	15.91	12.22	5.46	341.97	187.91
49.9	1819	46.99	13.73	8.72	5.48	285.52	185.34
51	1815	36.16	6.04	6.51	2.61	230.67	107.08

The unit for Ca, Fe, Mg and Al is g/Kg, whereas the unit for Sr and Mn is mg/Kg.

runs, 1 ml sample solution was diluted with 9 ml 0.5N HNO_3. However, some heavy metal elements such as Zn and Pb were not detectable. In the final run, 5 ml sample solution was diluted with 5 ml 0.5N HNO_3. But, the intensity of Ti, Ba, Zn, Cr, Cu and Pb were still low, and might contain some memorial effects from the 100 ppm (mg/L) standard solution during the measurement. Therefore, the measurements of those elemental concentrations may not be reliable. For Ca, Fe, Mg, Al, Sr and Mn which have high concentrations and sensitivities for the ICP-OES measurements, their results should be reliable for discussion. For these elements, the detection limit is about 1 ppb with precision normally better than 2%. **Table 3** lists the concentrations of the acid-leachable elements.

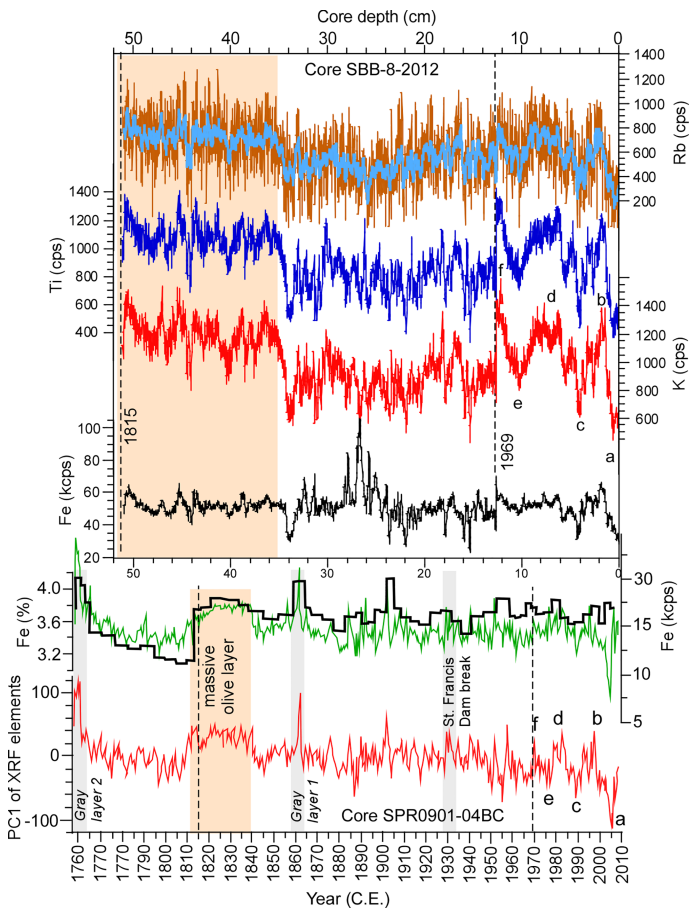

FIGURE 3 | Comparison of scanned XRF elemental contents between Core SBB-8-2012 (this study) and Core SPR0901-04BC (Hendy et al., 2015) from the Santa Barbara Basin. Curves for Fe, K and Ti are 9-point running average of the raw data (roughly monthly resolution). For Rb, the orange curve represents the raw data, and the light blue curve stands for 9-point running average of the raw data.

3 RESULTS

3.1 Sediment Features of the Core

The sediments of the core are generally fine clay in size with an average TOC of 3.82% and dry bulk density of 0.85 g/cm^3. The core sediments show clear laminations on the X-ray radiograph (**Figure 2B**) with lighter bands reflecting less dense, organic-rich layers. An outstanding light band appears at 34-35 cm depth. The sediments of the core can be classified into three zones: Zone I (35-51 cm depth), the sediments had higher density with thinner lamination. Zone II (12-34 cm depth), the sediments became less dense (increasing light intensity in the radiograph) with clear laminations. Between 26 cm and 27 cm depth, a visible brownish band existed, which was probably caused by a high concentration of Fe oxide (scanning XRF results in **Figure 3** show the evidence). In this zone, the sediments contain some white materials (light spots shown in **Figure 2B**), but they are not carbonates because acid-leachable elements especially Ca, Mg and Sr do not show high concentrations. Zone III (0-12 cm depth), the sediments in this zone have darker color and thick laminations. As we will discuss them in later sections, the criteria for dividing the core into 3 zones are based on four reasons: (1) changes in the D^{14}C trend; (2) changes in the elemental contents; (3) two outstanding depositional layers: one is at 12-13 cm and the other is at 34-35 cm; and (4) changes in the sedimentary features including color and thickness of laminations as described above.

3.2 Chronology of the Core

The radiograph generated by the iTRAX core scanner allows us to count laminations of the sediments using a computer software called ItraxPlot (https://www.raddec.com/software-itraxplot.php). The counting result indicates that the sediment core has 158 contrast (a dark and light couplet) layers (**Figure 2B**). If the laminations are annual, then the sediment core contains 158 years with a mean sedimentation rate of 0.32 cm/yr. However, the varve counting may not be accurate and its annual assumption may not be valid. Thus, we applied ^{210}Pb dating to the core.

The total ^{210}Pb activity in the core ranges from 47.06 to 1.50 dpm/g, with an exponential decay trend from the surface toward to bottom (**Figure 2C**). The ^{210}Pb activities at 4-7 cm depth are slightly low, perhaps due to lower initial ^{210}Pb activity in the input materials. The ^{210}Pb activities below 37 cm depth (ranging from 1.5 to 1.88 dpm/g) are relatively invariant, reflecting supported ^{210}Pb activity. Hence, we use the average of the four deepest ^{210}Pb activities to represent the supported ^{210}Pb which is 1.71 dpm/g. The excess ^{210}Pb value of each layer equals the total ^{210}Pb value subtracting the supported ^{210}Pb (**Table 1**). Using exponential fitting of the excess ^{210}Pb with depth, we get an equation of $y = 64.857^{*}e^{-0.14249x}$. The sedimentation rate (SR) is 0.22 cm/y. Based on this sedimentation rate, the 51-cm long core would cover about 230 years of depositional history, which is significantly longer than the varve counting result (158 years). In fact, ^{210}Pb dating has about 5% uncertainty, especially depending on the determination of the ending point of the excess ^{210}Pb. For example, if we decide the ending point of excess ^{210}Pb is at 33-cm depth instead of 37-cm, the fitting curve (black line in **Figure 2C**) provides a sedimentation rate of 0.26 cm/yr, which gives 196-year depositional history. Nevertheless, based on the ^{210}Pb dating, the sedimentation rate is around 0.22~0.26 cm/yr. In addition, since the ^{210}Pb dating assumes a constant sedimentation rate and constant initial ^{210}Pb concentration, the conditions may not be valid. Therefore, we need to further refine the chronology of the core.

Hendy et al. (2015) published elemental contents measured by both scanning XRF and ICPMS analyses of bulk elemental concentrations in the sediments of Core SPR0901-04BC (34°16.7' N, 120°02.49' W, 588 m) which had a close location to our core (**Figure 1**). This core covers a sedimentary history of 1755-2008 CE. The chronology of this core was determined by "the distinctive changes in the sedimentary fabric of SBB cores created by the strong El Niño events of 1941, 1957, 1983, and 1997", "the gray layer at 1761 AD, the turbidite at 1811 AD, and the bioturbated *Macoma* event at 1841 AD" and varve chronology (Hendy et al., 2015). Although this core did not have direct radiometric dating, the historic events and varve chronology recorded in the sediments made its chronology with an error of ±2 years around those controlling points (Hendy et al., 2015). Comparison of the scanning XRF results between Core SPR0901-04BC and Core SBB-8-2012 can help us to refine the chronology of SBB-8-2012.

In **Figure 3**, the lower panel shows the profiles of the first principal component (PC1, which explains 45.5% of the elemental variance in the core) of scanning XRF elements which include Al, Fe, K, Rb, Si and Ti) and Fe variations measured by both scanning XRF and ICP-MS during 1755-2008 CE (Hendy et al., 2015). The upper panel displays the profiles of Fe, K, Rb and Ti measured by scanning XRF in Core SBB-8-2012 with depth. First of all, scanning XRF measurement of the elements should be the total elemental content of all types including organic, authigenic and detrital phases in the materials within a few hundred micrometers (μm) (the penetration depth of the X-ray). Since scanning XRF is semi-quantitative in nature, the XRF elemental content cannot represent the total elemental concentration measured by ICP-MS in the sediment, and the latter should be the true elemental concentration. Secondly, the XRF scan has a very high-resolution (200 μm sampling interval), whereas the ICP-MS measurement has much lower resolution in general (1 cm sampling interval for the lower panel in **Figure 3**). Thirdly, once a core opened to air, oxidation of the surface sediments will allow some oxidation of reduced compounds (e.g., FeS can be oxidized to produce Fe_2O_3). Therefore, for the scanning XRF elements which can be influenced by the oxidation (e.g., Ca and Fe), discrepancies between XRF and ICP-MS trends are understandable. However, the variation trends of Fe, K, Ti, Rb and Al measured by both scanning XRF and ICP-MS in Core SPR0901-04BC agree with each other in general (Hendy et al., 2015), indicating that the XRF results of these elements reflect variations of the total elemental concentration. The variations of scanning XRF K, Rb, Ti, Mn and Si in Core SBB-8-2012 are very similar each other (Si is plotted in **Figure 5**). Aluminum content in our core is very low (the maximum intensity is less than 50 cps), so it is excluded in the discussion. Therefore, we compare Fe, K, Rb, Ti and Si contents in Core SBB-8-2012 with the PC1 and Fe in Core SPR0901-04BC.

Figure 3 shows the comparison of the two cores. Only two major similarities are certainly identified: (1) variations of K, Rb and Ti in the upper 12 cm (0-12 cm) of SBB-8-2012 are similar to the variations of PC1 during 1969-2008 in SPR0901-04BC; and (2) the high K, Rb and Ti contents below 36 cm depth in SBB-8-2012 are similar to the PC1 XRF elements in the massive olive layer during 1812-1840 in SPR0901-04BC. As we mentioned before, the sediment was broken at 12.5 cm depth during the transportation from USC to NTU, perhaps due to the sudden change in the sedimentary feature at this depth. The flood event of 1969 had been recorded in the sedimentary deposits of SBB (Schimmelmann et al., 2013). According to the report of Santa Barbara County Flood Control & Water Conservation District (https://www.countyofsb.org/uploadedFiles/pwd/Content/Water/1969FloodRpt.pdf), severe flood events occurred in 1964, 1967 and 1969, but "the 1969 12-hour rainfall equaled or exceeded the so-called 100-year storm in the upper Santa Ynez watershed". In addition, the Santa Barbara oil spill occurred in January and February 1969, which is the third-largest oil spill in the world (Foster et al., 1971). The severe oil spill in the Santa Barbara Channel could have affected sedimentation. Thus, possibly the 12.5-cm depth break may reflect the 1969 flood event and oil spill. If we use 2011 CE for the core top and 1969 CE for 12.5-cm depth, an estimated mean sedimentation rate can be calculated: 12cm/(2011-1969) = 0.29 cm/yr, which is slightly higher than the 0.22-0.26 cm/yr estimated by the ^{210}Pb dating. According to **Figure 3**, the PC1 XRF elements in SPR0901-04BC during 1770-1810 were very low. A strong drop in the PC1 XRF elements from 1815 to 1805 does not appear in the K, Rb and Ti in SBB-8-2012. If we assume the bottom of SBB-8-2012 is 1815 CE, then a mean sedimentation rate can be calculated: (51-12)/(1969-1815) = 0.25 cm/yr, which agrees with the 0.22-0.26 cm/yr estimated by the ^{210}Pb dating. We did not find gray layers identified in SPR0901-04BC. Although K, Rb and Ti contents in Core SBB-8-2012 show a peak value around 30 cm depth, this peak is not very outstanding and does not exist in Fe content. Thus, the above-mentioned age marks: (A) the 1969 flood event and oil spill at the 12-cm depth break and (B) 1815 CE at the bottom of Core SBB-8-2012 help us to further constrain the chronology. With the lamination and the ^{210}Pb dating estimations, we use a 0.29 cm/yr sedimentation rate for 0-12 cm and 0.25 cm/yr for 12-51 cm for constructing the chronology of the core. According to Inman and Jenkins (1999), the suspended sedimentary flux to SBB during the wet 25 years of 1969-1995 was five times greater than the previous 25 dry years (Schimmelmann et al., 2013). It is reasonable that the sedimentation rate in Zone III was higher. Nevertheless, based on the two sedimentation rates we calculate the chronology of the core which shows on the right-hand side of **Figure 2C**. The core contains a depositional history from 1815 CE to 2011 CE. We admit that the chronology assumes linear sedimentation rates in the segments and contains about 5% relative uncertainty. The chronology has an error of 1-2 years for the upper 12 cm deposition, and an error of 2-5 years between 12 cm and 51 cm depths.

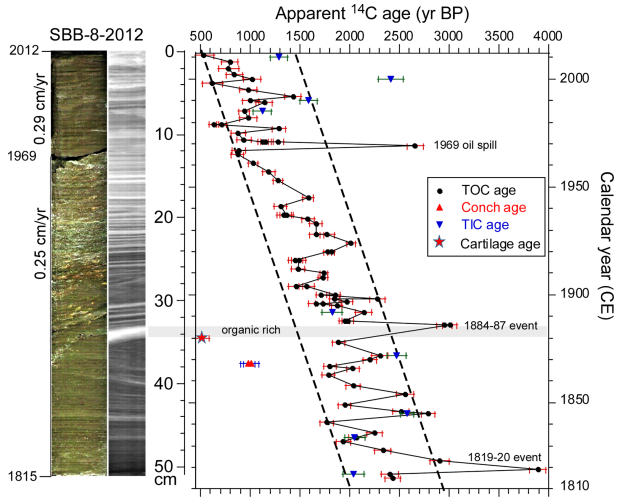

FIGURE 4 | The measured ^{14}C ages of all samples in Core SBB-8-2012. The two parallel dashed lines indicate the envelope of general variations of the measured ^{14}C ages on total organic carbon in the sediments except for three outstanding horizons.

3.3 ^{14}C Age and D$^{14}C_{TOC}$ Variation of the Core

Table 2 lists 89 AMS ^{14}C dates. Amongst these dates, 77 dates are for TOC and 12 dates are for TIC. These ^{14}C ages range from 516±71 to 3889±85 yr BP, much older than the depositional ages of 1815-2011 CE. Of the 77 TOC dates, one is animal cartilage and 13 dates are duplicated measurements on the sediments from 13 horizon samples. The duplicated measurements illustrate that the results are in good agreement within uncertainties, indicating the dating results are reliable. In the 12 TIC dates, 6 TIC dates are coupled with TOC dates from the sediments. They are generally in the same order of their coupled $^{14}C_{TOC}$ dates, reflecting approximately similar sources of TOC and TIC in the sediments. Two $^{14}C_{TIC}$ dates are from the same conch shell sample, showing agreement within uncertainties (**Table 2**). Four $^{14}C_{TIC}$ dates (marked with @ symbol in **Table 2**) are from independent layers, showing the ^{14}C ages ranging from 888±66 to 2577±71 yr BP. In this study, we will focus on the discussion of $^{14}C_{TOC}$ dates. Therefore, the $^{14}C_{TOC}$ dates from 62 horizons from the core will be used for interpretations of changes in paleoclimate and paleoceanography and the input of different sources of TOC to SBB.

Figure 4 displays the variations of apparent ^{14}C ages throughout the core. The age of the cartilage is the youngest, being 516±71 yr BP without reservoir age correction. However, the true age of this animal remain should be around 1880 CE based on the ^{210}Pb dating and varve counting. This means that if the organism formed in the water column in SBB, the basin water should have a ^{14}C reservoir age of at least 400 years which is much older than the reservoir age (233±60 years) of modern surface water in SBB (Ingram and Southon, 1996). The age of the conch shell is about 980~1010 yr BP, reflecting again the reservoir effect in the Santa Barbara Basin. These two ages imply that the reservoir age in SBB

may vary largely on annual-to-decadal time scales. It is interesting that the $^{14}C_{TOC}$ ages varied generally within the two paralleled dashed lines shown in **Figure 4** except for the three layers which have much older ages. The dashed line on the younger side covers the ages from 2000 yr BP at the bottom of the core to 500 yr BP on the core top. As the depositional age of the total core is 200 years, radioactive decay could not cause such a change. If the TOC of the samples on the younger side of the dashed line reflects primarily the organic matters mixed from terrestrial input (allogenic/allochthonous) and from endogenic input (autochthonous) through photosynthesis in the water column of SBB, then the significant age change (~1500 years) implies that either the reservoir age of the SBB water varied a lot during the past 200 years, or the ratio of allochthonous/autochthonous OC input has changed significantly and systematically. Nevertheless, the variations of the ^{14}C ages shown in **Figure 4** demonstrate that radiocarbon dating on either organic or inorganic carbon formed in the water column of SBB is problematic. Only terrestrial plant remains in the sediments appear as a valid way to provide "true" depositional ages in SBB.

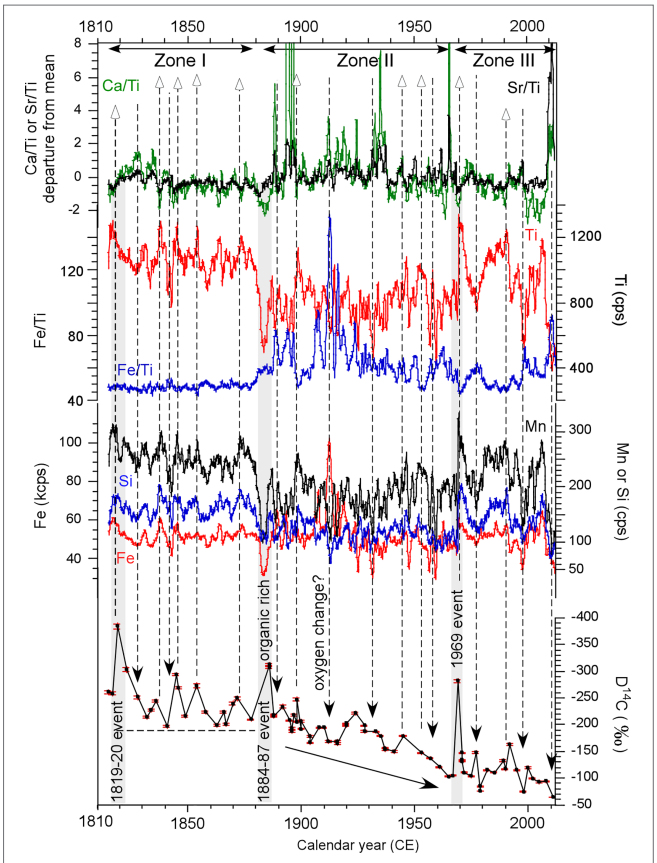

FIGURE 5 | Comparison of the variations in $D^{14}C_{TOC}$ values and the scanning XRF elemental contents in Core SBB-8-2012. In general, more depleted $D^{14}C$ value corresponds to higher siliciclastic elements (K, Ti, Si, Mn and Rb) and lower biogenic proxies (Ca/Ti, Sr/Ti and Fe/Ti); and vice versa. The dashed vertical lines with open arrow refer the periods of more depleted $D^{14}C$ value, whereas the dashed vertical lines with solid arrow show the intervals with less depleted $D^{14}C$ value.

Since the ^{14}C ages do not provide age meaning and our discussions focus on the ^{14}C variation of TOC, we use $D^{14}C_{TOC}$ values for further discussion.

3.4 Elemental Contents Measured by Scanning XRF

As the fore-mentioned scanning XRF elements represent total contents of all phases including organic, authigenic and detrital components. The elements which have meaningful results (by meeting the two criteria) show the intensity in the following order with their average intensity (cps) in the bracket: Fe (51206) > Ca (4771) > Sr (2399) > Cl (1241) > K (1015) > Ti (919) > Rb (597) > Zn (352) > Zr (235) > Mn (213) > Ni (205) > Y (192) > Cu (144) > Si (138) > S (82) > Pb (50). In this study, we only select Fe, Ca, Sr, K, Rb, Ti, Si and Mn for discussion.

The K, Ti, Rb, Si and Mn are lithophile elements that mainly come from terrestrial detrital input (Goldschmidt, 1926). However, Si and Mn can also be influenced by diagenesis and biogenic input. **Figures 3**, **5** show the variations of K, Ti, Rb, Si and Mn are positively correlated, indicating that they likely have the same sources. The correlation coefficient (R^2) between K and Ti, Si, Mn, or Rb are 0.96, 0.84, 0.91 and 0.74, respectively, implying that the scanning XRF Si and Mn were mainly from detrital input. These elements were considered as siliciclastic elements and grouped in PC1 by Hendy et al. (2015). Since Ti is commonly attributed to terrigenous inputs in pelagic sediments, we can use it to normalize for siliciclastic input. The lithophile elements (K, Ti, Si and Mn) appear different average contents: high in Zone I, low in Zone II and moderately high in Zone III. For example, the average intensities (cps) with standard deviation (numbers of data points) of K content are 1190±120 (n = 755), 867±136 (n = 1019) and 1044±208 (n = 633) in Zone I (1815-1880 CE), II (1880-1969 CE) and III (1969-2011 CE), respectively. Similarly, the average intensities of Ti content are 1071±109, 789±139 and 947±212 in Zone I, II and III, respectively. The changes in the average contents of the lithophile elements in three zones indicate that the terrestrial detrital input to the sediments was the highest in Zone I and the lowest in Zone II, which helps us in understanding of the $D^{14}C_{TOC}$ change of the core.

Although Fe, Ca and Sr are also lithophile elements, but their contents in the sediments can be influenced by the chemical and biological conditions in the water column. These elements can have significantly authigenic compositions compared with the detrital compositions. For example, Ca and Sr are easy to co-precipitate into carbonates, resulting a strong positive correlation between the two. However, the scanning XRF Ca and Sr do not have a strong correlation (R^2 = 0.4), although the variations of the two are very similar (**Figures 5**, **6**). As mentioned before, oxidation (e.g., $FeS_2 + O_2 \rightarrow Fe_2O_3 + H_2S$) of the scanned surface sediment layer when the core opened to the air for long time could affect some scanning XRF elements including Fe, Ca and Sr. Interpretations of the XRF Fe, Ca and Sr results should be caution. The Ca/Ti and Sr/Ti are considered as indicators of biogenic components to be normalized for the siliciclastic input (Hendy et al., 2015). Their variations are dominated by the variations of Ca

and Sr intensities. The higher Ca/Ti and Sr/Ti reflect a stronger productivity.

The variations of Ca/Ti and Sr/Ti shown in **Figure 5** vary generally opposite to the siliciclastic elements (K, Ti, Si and Mn), indicating a higher portion of biogenic component corresponding to the lower siliciclastic component. It is interesting to see that less depleted (or less negative) $D^{14}C$ values correspond to higher Ca/Ti and Sr/Ti values; and vice versa (**Figure 5**). This means that more OC formed in the water column and less old carbon from siliciclastic source lead to smaller ^{14}C reservoir age. In general, Ca/Ti and Sr/Ti values were high in Zone II, especially several high Ca/Ti peaks, reflecting strongly increased biogenic input into the sediments. These changes should reflect variations in the chemical and oceanographic conditions in SBB.

Although Hendy et al. (2015) considered Fe as a siliciclastic element and used Fe/Ti as a proxy of terrigenous input, Fe can be strongly affected by redox conditions in the environment. The Fe profile in **Figures 3, 5** shows that the highest content throughout the core was around 1910 CE, whereas other scanning XRF elements were low. The high Fe content in this period is also visible in the core photo, showing the brown band. In **Figure 5**, Fe/Ti shows totally different patterns with the other siliciclastic elements: low and relatively invariant values in Zone I, high and strongly fluctuated values in Zone II, and moderately high and variant values in Zone III. The Fe/Ti values in Zones II and III clearly co-vary with Ca/Ti and Sr/Ti but opposite to the siliciclastic elements, reflecting biogenic input into the sediments. This situation is quite different from the Fe variations in Core SPR0901-04BC (Hendy et al., 2015). Nevertheless, we are not able to use Fe or Fe/Ti variations as an indicator of siliciclastic input given by Hendy et al. (2015). Instead, the Fe/Ti in Zones II and III together with probably Ca/Ti and Sr/Ti reflected biogenic input into the sediments. Another reason for the Fe profiles discrepancies between our core and Core SPR0901-04BC may be attributed to the oxidation effect of Core SBB-8-2012 as it opened to the air for many years. If it is true, the scanning XRF Fe/Ti and Ca/Ti do not represent the original situation in the sediments. To avoid the oxidation effect, we use Sr/Ti only as an indicator of biogenic input.

Another important phenomenon is that all XRF elements were the lowest in the light band at 34-cm depth (around 1885 CE). This light band showed a strongly depleted $D^{14}C_{TOC}$ value (**Figure 5**) with the lowest contents of all scanning XRF elements and less density, indicating that this layer may be enriched in organic matter. Although we do not know the cause of this organic rich layer, a few historic references may provide insight on this event. According to the timeline of Santa Barbara (https://www.santabarbaraca.gov/services/community/historic/historysb/timeline.asp), crude oil was first extracted from the Santa Barbara Channel along the coast at Summerland in 1886. Another unusual observation was that a large abundant kelp forest about 300 yards off Santa Barbara coast in 1887 (Fewkes, 1889), which occurred in other places along the coast of Southern California. Schimmelmann et al. (1995) interpreted this as evidence that no severely destructive storm and wave events has occurred in Santa Barbara for a few years prior to 1887 CE. Less terrestrial detrital input due to less surface runoff and highly abundant marine productivity caused by some oceanographic condition changes agree with our results. Whether there was a significant influence from the first extraction of crude oil in the Santa Barbara Channel is unclear. Nevertheless, the scanning XRF elemental contents will help us in understanding the paleoclimate and paleoceanography change on annual-to-multidecadal scales.

In summary, the siliciclastic elements (K, Ti) reflect mainly terrigenous input from the river inflow around SBB, whereas Ca/Ti, Sr/Ti and Fe/Ti reflect chiefly biogenic input from the marine system in SBB. The two groups have generally opposite trend, and higher values of the siliciclastic elements and lower values of biogenic indicators correspond to less depleted (larger) $D^{14}C_{TOC}$ values; and vice versa. In this study, (K+Ti)/2 is used for terrigenous input, whereas Sr/Ti is used for biogenic input. The sediments of Core SBB-8-2012 showed significant changes in terms of geochemical and biological features from Zone I to Zone II after an organic-rich layer was deposited around 1885

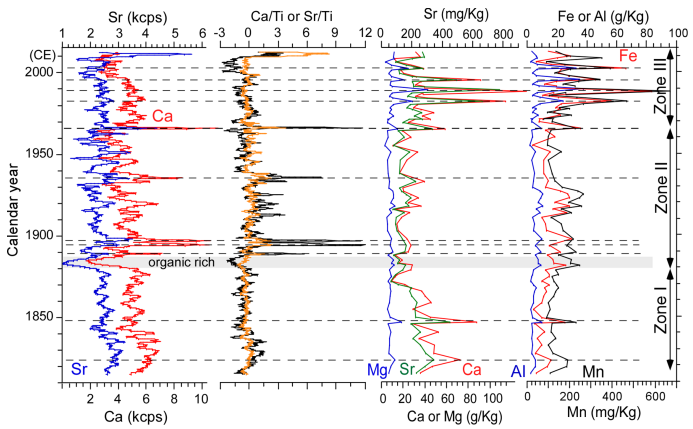

FIGURE 6 | Comparison of the variations in elemental contents measured by XRF scanning and ICP-OES methods in Core SBB-8-2012. Note that elemental concentration has different units, being g/Kg for Fe, Mg and Ca, and mg/Kg for Mn and Sr. The horizontal dashed lines show the comparisons when the acid-leachable elemental concentrations were relatively high.

CE (34-35 cm depth) with more terrigenous input in Zone I and more biogenic input in Zone II.

3.5 Acid-Leachable Elemental Concentrations Measured by ICP-OES

The ALE concentrations of Ca, Fe, Mg, Al, Sr and Mn were listed in **Table 3**. Their average concentrations (mg/Kg) with standard deviations are in the following order: Ca (34299±21926) > Fe (18655±13279) > Mg (9685±5738) > Al (6835±6753) > Sr (202±120) > Mn (180±94).

Figure 6 exhibits the ALE concentrations of Ca, Mg, Sr, Fe and Mn and comparisons with the scanning XRF results in the core. The ALE Ca and Sr have a strong correlation ($R^2 = 0.95$), indicating the same source inputs and similar chemical behavior between the two. The same feature does not occur between the scanning XRF Ca and Sr. This is because the ALE Ca and Sr come mainly from authigenic phase, whereas the scanning XRF Ca and Sr count for both authigenic and detrital phases. The correlations (R^2) between ALE Fe and ALE Mg, ALE Al or ALE Mn are 0.86, 0.85 and 0.83, respectively, showing that they come from the same sources. The ALE Fe, Mg, Al and Mn have no significant correlations with the ALE Ca ($R^2 < 0.5$) except for five high Ca points (>60 g/Kg), indicating that these five layers contain abundant elements from the authigenic input. In addition, Zone I had the lowest ALE Fe, Mg, Al and Mn, but moderately high ALE Ca and Sr. This means that the sediments in Zone I have more siliciclastic feature because detritus contain less ALE Fe, Mg, Al and Mn.

The comparisons of the scanning XRF contents and the ALE concentrations of Ca and Sr show significant discrepancies in terms on long and short time scales. The ALE concentrations of Ca and Sr were relatively low in Zone II, while the scanning XRF Ca and Sr did not show this. Secondly, several distinct ALE Ca and Sr peaks (i.e., around 1822, 1849, 1982, 1994 and 1999) were not corresponding either to scanning XRF Ca and Sr or Ca/Ti and Sr/Ti. As mentioned before, scanning XRF involves a measured element in all phases, with a matrix effect, very small scan area and semi-quantitative nature. It is understandable that the scanning XRF results may not have relationship with the ALE elements. However, the peaks of ALE elements should reflect oceanic conditions for higher productivity, while the troughs of ALE elements may correspond to low productivity periods. The variations of the ALE concentrations will shed the light on chemical and biological conditions in the water column of SBB.

4 DISCUSSIONS

4.1 Factors Influencing $D^{14}C$ Variation in Core SBB-8-2012

OC in the sediments of the SBB depo-center comes from three possible major sources: (1) biological products in the marine system of the Santa Barbara Channel (Thunell, 1998; Barron and Bukry 2010); (2) terrestrial inputs from surface runoff which comes mainly from the Ventura River, Santa Clara River and creeks in the Santa Ynez Mountain drainage basin (Kolpack and Drake, 1984; Thunell et al., 1995; Schimmelmann and Lange, 1996); and (3) fossil OC from leakages in the marine system (e.g., oil spill in surface water; gas and oil are seeping from oil seepage such as from the Coal Oil Point seep field) (Hornafius et al., 1999) and/or lateral transported sediments from other locations inside or outside of SBB (**Figure 7**).

The ^{14}C activity of the first OC source which is produced in the SBB water column is influenced by (1) the atmospheric ^{14}C variation and CO_2 exchange with the water; (2) variation of oceanic circulation in the SBB channel; and (3) fossil C emission from the seafloor. In general, the $D^{14}C$ of the atmospheric CO_2 is much greater than that of the fossil C emission which is -1000‰. The atmospheric $D^{14}C$ at 1950 CE was 0‰ and strongly increased due to nuclear tests (reached to 785‰ in North Hemisphere in 1964) (Hua et al., 2013). The nuclear bomb ^{14}C signal reached a peak during 1970~1976 in the ocean (Grottoli and Eakin, 2007). The highest $\Delta^{14}C$ value was ~140‰ in 1974 in the Atlantic coral (Druffel, 1996), and was ~190‰ in 1975 in the Pacific coral (Andrews et al., 2016), showing the bomb ^{14}C significantly affected the ^{14}C reservoir age in oceans.

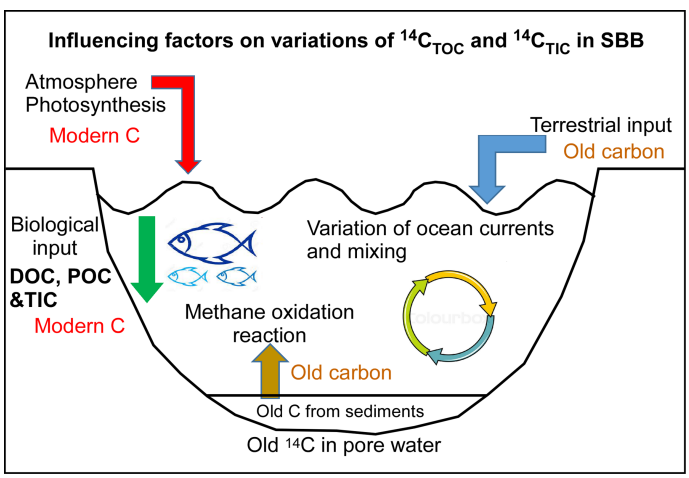

FIGURE 7 | A conceptual box model of the influencing factors on the carbon cycles in Santa Barbara Basin.

On the other hand, fossil carbon input in SBB is a well-known phenomenon. The Coal Oil Point seep field located at near shore of SBB is one of the largest natural submarine hydrocarbon emission areas in the world (Allen and Mikolaj, 1970; Valentine et al., 2010). Methane and crude oil are emitted from the seafloor (Hornafius et al., 1999). Most of the emitted hydrocarbons are consumed by methanotrophic bacteria in surface sediments or in the water column (Treude and Ziebis, 2010). The fossil carbon emission from the seafloor in SBB may vary with tidal changes and/or seismic activity (Hornafius et al., 1999; Eichhubl et al., 2000; Boles and Clark, 2001).

According to Kennett et al. (1997), the oceanic circulation in the Santa Barbara Channel influences ^{14}C activity of the marine reservoir as follows: The ^{14}C-depleted California current and associated southern California Eddy flow southward, and bring cold and low salinity water dominated in the winter-spring season (**Figure 1**). In contrast, the California counter-current flows northward and transports the relatively ^{14}C-rich, warm and saline equatorial water along the southern California coast during the summer-fall season (**Figure 1**). This annual circulation pattern and upwelling of Pacific intermediate water along the California coast can be modified by summer insolation change (Bakun, 1990; van Geen and Husby, 1996), and ENSO events (McGowan, 1984; Rassmusson, 1984; Ramage, 1986) on interannual scales.

Although many previous studies have found the anomalies of marine ^{14}C reservoir age in SBB (e.g., Ingram and Kennett, 1995; Kennett and Ingram, 1995; Kennett et al., 1997; Roark et al., 2003; Schimmelmann et al., 2006; Hendy et al., 2013; Du et al., 2018), those studies are generally for long time scales (>1000 years). Below, we will discuss the variations of $D^{14}C_{TOC}$ and their causes during 1815~2011 CE. We will focus our discussion on ENSO influences.

4.2 Causes of Strong Depleted $D^{14}C$ Excursions in Core SBB-8-2012

In **Figures 4**, **5**, the three negative $D^{14}C_{TOC}$ (old age) excursions around 1964-69, 1884-87 and 1819-20 CE could be attributed to "extra old carbon influence". The $D^{14}C_{TOC}$ values of these excursions exceeded significantly the general variation envelope (two paralleled dash lines), so that their old carbon influence should be caused by some abnormal reasons. For the youngest excursion, one reason could be the oil spill event in 1969. During a 10-day period in early 1969, about 4 million gallons of crude oil spilled into the Santa Barbara Channel after a blowout six miles offshore on a Union Oil drilling platform (Foster et al., 1971). This disaster is the third largest oil spill in the world up to date. Organisms and particles could take up the oil to deposit on the seafloor, so that the $D^{14}C_{TOC}$ of this layer could be strongly influenced by the oil. In addition, as we discussed above, flood events in 1964, 1967 and 1969 (especially the 1969 flood) could transport larger portion of old OC in terrigenous sediments in the TOC of this layer. Soil OC from terrestrial input may have ^{14}C age of several thousand years or older than the date of their erosion and deposition. Thus, strong flood events may carry those soil OC into the SBB sediments. The peaks of the lithophile elements in the same layer shown in **Figure 5** support the flood impact.

For the 1884-87 excursion, the strongly depleted $D^{14}C_{TOC}$ occurred on the layer of organic rich and minimum concentrations of all scanning XRF elements (**Figure 5**). The low scanning XRF elements reflect that the depleted $D^{14}C_{TOC}$ should not be attributed to flood events. Two possible events may explain the old carbon influence: 1. Possible sudden short leak of fossil carbon from the Coal Oil Point seep field during the first extraction in 1886; and 2. Strongly increased upwelling from the Pacific deep water entered the basin, which might bring abundant nutrients to cause a surge of biological productivity in SBB, reflected by a large abundant kelp forest along Santa Barbara coast in 1887 (Fewkes, 1889). The ^{14}C activity in the Pacific deep water should be much lower than that of surface water. The abundant OC deposited in the sediments can be preserved due to anoxic conditions on the seafloor of SBB. The above hypothesis needs more direct evidence to support it, especially the reconstruction of upwelling strength during this period. Analysis of the organic compounds in this layer would help reveal its source.

The 1819-20 excursion in the $D^{14}C_{TOC}$ may be explained by the strong input of soil OC into the SBB sediments as the scanning XRF Si, Ti and K (detrital origins) showed high contents in this layer (**Figures 5**, **9**). In addition, if the 1812 Ventura earthquake (also known as the Santa Barbara earthquake) (7.1–7.5 magnitude) caused strongly increased fossil carbon leakage from the Coal Oil Point seep field (Eichhubl et al., 2000), then the leaked fossil carbon could be consumed by methanotrophic bacteria and deposited in the sediments in this layer, given the chronology has an uncertainty of several years in this part.

4.3 The $D^{14}C_{TOC}$ Changes in Different Zones

The $D^{14}C_{TOC}$ variation shown in **Figure 5** has experienced three different features. If the $D^{14}C_{TOC}$ value at 35-35.2 cm is excluded as this sample is unlike some sediment samples (organic rich), the mean $D^{14}C_{TOC}$ values and their standard deviations for Zone I, II and III are -247.0±44.4‰ (n = 22), -181.9±34.1‰ (n = 34) and -119.7±45.2‰ (n = 21), respectively. Since the core sediments have only about 200-year history, ^{14}C decay (half-life is 5730 years) should not cause such a large difference. In Zone I (1815~1880 CE), the maxima $D^{14}C_{TOC}$ values (ca. youngest ages) are around -201.8‰ (-197.5‰ at 44.6 cm, -199.4‰ at 39.2 cm, -200.9‰ at 38.1 cm and -209.4‰ at 35.5 cm), no apparent enrichment trend (referred by a horizontal dash line in **Figure 5**). The much smaller (lower, or lighter) average $D^{14}C_{TOC}$ value and relatively constant maximum $D^{14}C_{TOC}$ value of Zone I indicate that the OC in the sediments during this period contains more old carbon influence and the carbon reservoir effect of the marine system may be larger. The scanning XRF K, Ti, Si and Mn were higher in Zone I, which provides evidence of more soil OC from terrigenous sediments (**Figure 5**). Other two contributions to the lower mean $D^{14}C_{TOC}$ value in Zone I could be: (1) higher emission flux of fossil carbon from the Coal Oil Point seep field compared to the later periods since the extraction of the fossil fuel began in 1886; and (2) lower marine productivity compared

to the later periods. The second hypothesis can be seen in low values of Ca/Ti, Sr/Ti and Fe/Ti which are indicators of biogenic components in the sediments. For the first hypothesis, more studies on the OC budget in SBB are needed.

In Zone II (1885-1969 CE), the $D^{14}C_{TOC}$ value has smaller variations and show an apparently increasing trend. The $D^{14}C_{TOC}$ enrichment trend in Zone II can be explained by two reasons: one is that the fossil carbon emission from the seafloor had been reduced since the extraction beginning in 1886; and another one is increased the biogenic carbon flux into the sediments perhaps due to an enhanced nutrient availability in SBB. As the nutrient supply increased, the primary productivity in SBB produced more OC from endogenic input in the water column. Thus, the portion of OC from terrigenous sediments became smaller. In fact, scanning XRF had relatively lower contents in Zone II, reflecting less contribution of terrigenous sediments. High Ca/Ti, Sr/Ti and Fe/Ti values in Zone II illustrate high biogenic components in the sediments.

The $D^{14}C_{TOC}$ values in Zone III (1969~2011 CE) still show a slightly enrichment trend, and the three maxima values are -75.8‰ in 1977, -74.0‰ in 1998 and -64.3‰ in 2011. Since the nuclear bomb ^{14}C signal from the atmospheric CO_2 entered into the ocean in late 1960s and reached its peak in 1975, the enrichment trend of the $D^{14}C_{TOC}$ in Zone III can be influenced by the bomb ^{14}C. However, none of the $D^{14}C_{TOC}$ values are greater than zero in the core (**Table 2**), indicating that the bomb ^{14}C signal is masked by the ^{14}C reservoir effects in SBB and older terrestrial OC input.

If we assume the cartilage sample at 36 cm depth was formed in the water column, this sample does not contain OC from terrigenous sediments, and has a $D^{14}C$ value of -62.2‰ and ^{14}C age of 516±71 yr BP (**Table 2**). The calibrated ^{14}C age without reservoir correction of this sample is 92.5% in the range of 454-660 yr BP (2σ) or 560±105 yr BP by using the calibration curve IntCal13. This age is significantly older than the ^{14}C reservoir age (233±60 yr) of modern ocean surface water in SBB (Ingram and Southon, 1996). If we use the $D^{14}C$ value of this sample as the endmember of marine biological carbon in SBB, we may estimate the OC contribution from the marine system and terrigenous input. In **Figure 5**, the heavier (higher) $D^{14}C$ values are generally corresponding to low scanning XRF K, Ti, Si and Mn (siliciclastic), and high Ca/Ti, Sr/Ti and Fe/Ti (biogenic), whereas the lighter (lower) $D^{14}C$ value are generally corresponding to high siliciclastic elements but low biogenic elements except for the organic-rich layer around 1885 CE.

4.4 ENSO Influence on the $D^{14}C$ Variation of Core SBB-8-2012

The variations of the $D^{14}C_{TOC}$ in the sediments show interannual-to-decadal cycles (**Figure 5**), reflecting the impact of climatic changes on the terrigenous input of soil TOC and on the productivity of biological marine TOC. Since the precipitation in southern California including Santa Barbara is strongly influenced by ENSO (McGowan, 1984) and oceanic circulation in Santa Barbara Channel is also related to ENSO (Rassmusson, 1984), the $D^{14}C_{TOC}$ variation may be affected by ENSO. For this purpose, we have done spectrum analysis on both the Southern Oscillation Index (SOI) and the $D^{14}C_{TOC}$ record. **Figure 8** displays the results. The monthly data of SOI from 1866 to 2021 was downloaded from https://crudata.uea.ac.uk/cru/data/soi/ (Ropelewski and Jones, 1987; Allan et al., 1991). The cycles of 3.6-yr, 5.7-yr and 6.4-yr fall into the 4-7 year band of El Niño/La Niña cycles. The $D^{14}C$ data sets have age intervals on the order of 1-8 years (**Table 2**). In order to perform the spectrum analysis, the interval should be uniform. Thus, we interpolate the data to annual resolution by using the excel program (linear interpolation), and the spectrum analysis shows that the $D^{14}C_{TOC}$ record has cycles of 4.9-yr, 5.8-yr, 7.3-yr, 8.7-yr, 9.7-yr and 13-yr (**Figure 8B**). As the resolution of $D^{14}C$ data allows the highest frequent cycle of 6-yr, the 4.9-yr cycle is not considered. The group of 5.8-yr

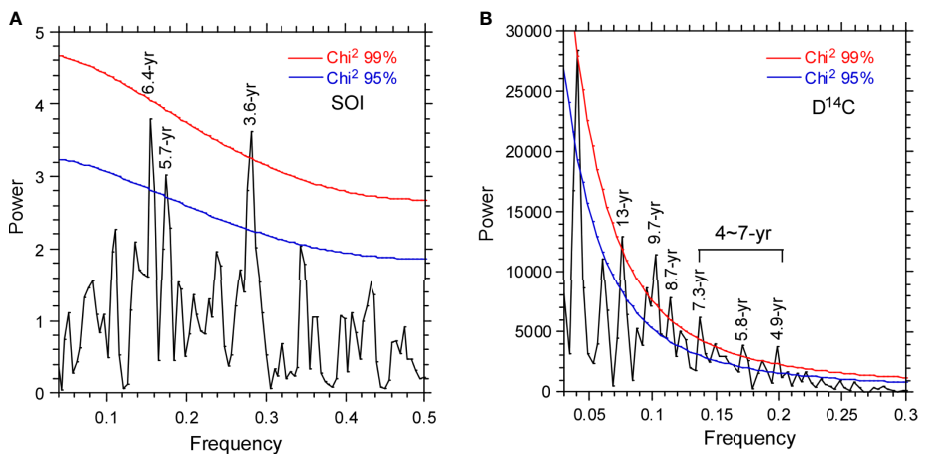

FIGURE 8 | Spectrum analysis for the SOI (data source: https://crudata.uea.ac.uk/cru/data/soi/) **(A)** and the D14CT OC **(B)**. The blue curve and red curve indicate confidence level and 95% and 99%, respectively. The numbers marked in the plots denote the possible cycles above 95% confidence level.

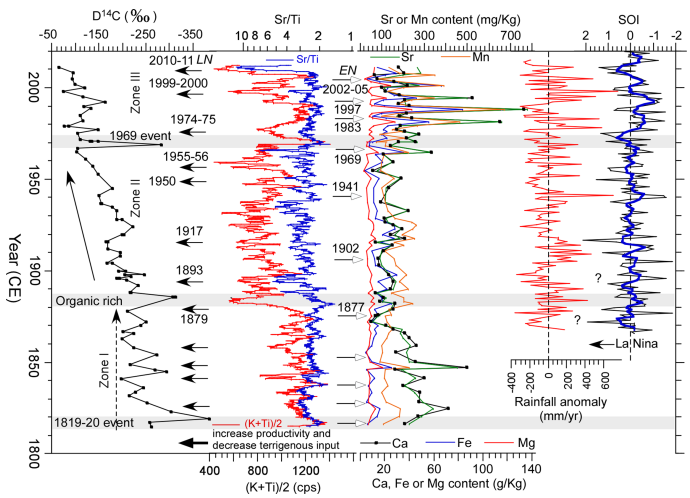

FIGURE 9 | Comparisons of the $D^{14}C$, scanning XRF elemental content, ICP-OES measured acid-leachable elemental concentration with the historical rainfall (the data was downloaded from **https://www.santabarbaraca.gov/SBdocuments/Advisory_Groups/Water_Commission** before it was removed.) and SOI records. The open head arrows refer El Niño events, and the solid head arrows reflect La Niña events. Note that the relationship between the rainfall in southern California and ENSO events is not fixed. For example, negative SOI values around late 1890s (shown by a question mark there) did not result in high rainfalls. Another question mark around 1870 shows the comparison is not valid, because low rainfall during this La Niña event would lead to high ALE contents but low scanning XRF siliciclastic elemental contents. This outliner may be caused by chronological uncertainty.

and 7.3-yr cyclicities may reflect the 4~7-year ENSO cycle, whereas the group of 8.7-yr, 9.7-yr and 13-yr cyclicities may represent double of the 4~7-year ENSO cycle.

Since the $D^{14}C_{TOC}$ record has only ~200 years, changes in summer insolation may vary small. Therefore, we focus on the influence of ENSO on the rainfall and oceanic circulation variations in SBB. During El Niño year, the marine biological productivity should decrease (Lange et al., 1987), and heavy rains are frequent along southern California. The ratio of terrigenous soil OC/biogenic OC increases with high input of siliciclastic elements and low ALE in the SBB sediments during El Niño events. In contrast, during La Niña years stronger California Current and upwelling bring abundant nutrients to elevate the marine productivity, resulting higher biological OC content in the sediments and higher $D^{14}C_{TOC}$.

In **Figure 9**, we compare the $D^{14}C_{TOC}$, scanning XRF siliciclastic elements (K+Ti)/2, proxy of biogenic components (Sr/Ti) and ALE contents (Ca, Fe, Mg, Sr and Mn) with the SOI and south coast annual precipitation records. The comparisons show that during strong El Niño years (open head arrows, e.g., 1902, 1941, 1969, 1982-83, 1997 and 2002-05) higher (K+Ti)/2, lower Sr/Ti, minima the ALE contents and decreased $D^{14}C_{TOC}$ were dominant. In contrast, low scanning XRF (K+Ti)/2, higher Sr/Ti, high ALE contents and enriched $D^{14}C_{TOC}$ were corresponding La Niña conditions (solid head arrows). It is worth to mention that our record cannot be accurate on annual scale, so that comparison with low rainfall periods is more reasonable than with individual El Niño or La Niña years. The above comparison between our record with the instrumental records (rainfall and SOI) perhaps also demonstrates that our chronology of the core is reliable as the instrumental records have precise age control.

5 CONCLUSIONS

A 51-cm long core SBB-8-2012 from SSB was dated by ^{210}Pb and varve counting. The chronology of the core was refined by comparing with a previous well-dated core from the same area, showing the depositional history of 1815-2011 CE with sedimentation rates of 0.25-0.29 cm/yr. The core has been measured for scanning XRF on an ITRAX core scanner, acid-leachable (0.5N HCl) elemental concentrations by an ICP-OES, and a total of 89 ^{14}C dates by AMS. Based on the sedimentary features and the above measured results, the core sediments can be classified into three zones: Zone I (1815-1880 CE) contains denser sediments with thinner laminations, higher scanning XRF K, Ti, Si, Mn and Rb, lower Fe/Ti, Ca/Ti and Sr/Ti, and lower $D^{14}C_{TOC}$ values. Zone II (1880-1969 CE) includes less dense sediments with thicker laminations, the lowest scanning XRF K, Ti, Si, Mn and Rb, highest Fe/Ti, Ca/Ti and Sr/Ti, and strongly enriched $D^{14}C_{TOC}$ trends. Zone III (1969-2011 CE) covers well laminated sediments with high $CaCO_3$ contents, high acid-leachable elemental concentrations, strongly fluctuated XRF elemental contents and higher $D^{14}C_{TOC}$ values.

The apparent ^{14}C ages of the 200-year sediment core vary between 500 and 4000 yr BP with $D^{14}C$ values ranging from -62.2‰ to -383.8‰, reflecting influences of terrigenous soil OC input, fossil carbon emission from the Coal Oil Point seep field and ^{14}C reservoir effect controlled by oceanic and atmospheric circulations. The three strongly negative $D^{14}C_{TOC}$ excursions around 1819-20, 1884-87 and 1964-69 CE might be respectively related to the 1812 Santa Barbara earthquake, the first oil extraction in 1886 and unusual marine biological productivity in 1887, and the 1969 oil spill as well as flood

events. The long-term mean $D^{14}C_{TOC}$ shifts in three zones were probably caused by relatively high terrigenous soil OC input and fossil carbon emission from the Coal Oil Point seep field in Zone I, reduced fossil carbon emission due to the oil extraction and enhanced biological productivity in Zone II, and nuclear bomb ^{14}C influence in Zone III. Nevertheless, the ^{14}C reservoir effect in Santa Barbara Channel has been changed significantly during the past 200 years.

The ENSO events show strong influences on the $D^{14}C_{TOC}$, detrital elemental content and acid-leachable elemental concentration in the SBB sediments. During the La Niña period, stronger upwelling and northerly California Current bring nutrient enriched water into SBB and lead to higher productivity. Combining the effect of less terrigenous soil OC input during the La Niña period, lower scanning XRF K, Ti, Si, Mn and Rb, higher acid-leachable elements and higher $D^{14}C_{TOC}$ values can be resulted in the sediments. During the El Nino period, the phenomena are opposite.

AUTHOR CONTRIBUTIONS

H-CL supervised the study, performed sampling of the core, participated lab experiment and wrote the manuscript. YC conducted the study for his MSc thesis. WB provided the core, initiated and discussed the study. MZ discussed the study and helped in revising the manuscript. SM and T-TS helped in data process. All authors contributed to the article and approved the submitted version.

DATA AVAILABILITY STATEMENT

Publicly available datasets were analyzed in this study. This data can be found here: SOI (data source: https://crudata.uea.ac.uk/cru/data/soi/).

FUNDING

This study was supported by grants from Ministry of Science and Technology of Taiwan (MOST 106-2116-M-002-012, MOST 107-2116-M-002-005, MOST 108-2116-M-002-012 and MOST 109-2116-M-002-018) to H-CL, and by the National Natural Science Foundation of China (Grant No. 41630966) to MZ.

ACKNOWLEDGMENTS

We thank Ms. Su-Chen Kang and Ms. Chun-Yen Chou at the NTUAMS Lab for their help in the AMS ^{14}C dating. The iTRAX Lab in the Department of Geosciences and the NTUAMS Lab in the Instrumentation Center at NTU are acknowledged for their contribution to this study.

SUPPLEMENTARY MATERIAL

The Supplementary Material for this article can be found online at: https://www.frontiersin.org/articles/10.3389/fmars.2022.823793/full#supplementary-material

REFERENCES

Allan, R. J., Nicholls, N., Jones, P. D. and Butterworth, I. J. (1991). A Further Extension of the Tahiti-Darwin SOI, Early SOI Results and Darwin Pressure. *J. Climate* 4, 743–749. doi: 10.1175/1520-0442(1991)004<0743:AFEOTT>2.0.CO;2

Allen, A. A. and Mikolaj, P. G. (1970). Natural Oil Seepage at Coal Oil Point, Santa Barbara, California. *Science* 170, 974–980. doi: 10.1126/science.170.3961.974

Andrew, S. and Peter, A. C. (1977). Sedimentation and Climatic Patterns in the Santa Barbara Basin During the 19th and 20th Centuries. *Geolog. Soc. America Bull.*, 88, (8). 1161–1172. doi: 10.1130/0016-7606(1977)88<1161:SACPIT>2.0.CO;2

Andrews, A. H., Asami, R., Iryu, Y., Kobayashi, D. R. and Camacho, F. (2016). Bomb-Produced Radiocarbon in the Western Tropical Pacific Ocean: Guam Coral Reveals Operation-Specific Signals From the Pacific Proving Grounds, *J. Geophys. Res. Oceans* 121, 6351–6366. doi: 10.1002/2016JC012043

Bakun, A. (1990). Global Climate Change and Intensification of Coastal Ocean Upwelling. *Science* 247, 198–201. doi: 10.1126/science.247.4939.198

Barron, J. A. and Bukry, D. (2010). Santa Barbara Basin Diatom and Silicoflagellate Response to Global Climate Anomalies During the Past 2200 Years. *Quaternary Int.*, 215, 34–44. doi: 10.1016/j.quaint.2008.08.007

Barron, J. A., Bukry, D. and Hendy, I. L. (2015). High-Resolution Paleoclimatology of the Santa Barbara Basin During the Medieval Climate Anomaly and Early Little Ice Age Based on Diatom and Silicoflagellate Assemblages in Kasten Core SPR0901-02kc. *Quat. Int.* 387, 13–22. doi: 10.1016/j.quaint.2014.04.020

Baskaran, M. and Krishnamurthy, R. V. (1993). Speleothems as Proxy for the Carbon Isotope Composition of Atmospheric CO2. *Geophys. Res. Lett.* 20 (24), 2905–2908. doi: 10.1029/93GL02690

Baskaran, M. and Iliffe, T.M. (1993). Age Determination of Recent Cave Deposits Using Excess 210Pb—a New Technique. *Geophys. Res. Lett.* 20, 603–606.

Berelson, W. M., Morine, L., Sessions, A., Rollins, N., Fleming, J. C. and Schwalbach, J. (2019). Santa Barbara Basin Flood Layers: Impact on Sediment Diagenesis. In: From the Mountains to the Abyss: The California Borderland as an Archive of Southern California Geologic Evolution. *SEPM Special Publ. No. 110* p, 233–240. doi: 10.2110/sepmsp.110.11

Bograd, S. J. and Lynn, R. J. (2001). Physical-Biological Coupling in the California Current During the 1997–99 El Niño-La Niña Cycle. *Geophys. Res. Lett.* 28 (2), 275–278. doi: 10.1029/2000GL012047

Bograd, S. J., Schwing, F. B., Castro, C. G. and Timothy, D. A. (2002). Bottom Water Renewal in the Santa Barbara Basin. *J. Geophys. Res.* 107 (C12). 3216. doi: 10.1029/2001jc001291

Boles, J. R. and Clark, J. F. (2001). Temporal Variation in Natural Methane Seep Rate Due to Tides, Coal Oil Point Area, California. *J. Geophys. Res.* 106, 27077–27086. doi: 10.1029/2000JC000774

Bray, N. A., Keyes, A. and Morawitz, W. M. (1999). The California Current System in the Southern California Bight and the Santa Barbara Channel. *J. Geophys. Res.* 104 (C4), 7695–7714. doi: 10.1029/1998jc900038

Browne, D. R. (1994). Understanding the Oceanic Circulation in and Around the Santa Barbara Channel. *Fourth California Islands Symposium: Update Status Resour.* (Santa Barbara Museum of Natural History: Santa Barbara, California), 27–, 34.

Davis, C. V., Ontiveros-Cuadras, J. F., Benitez-Nelson, C., Schmittner, A., Tappa, E. J., Osborne, E., et al. (2019). Ongoing Increase in Eastern Tropical North Pacific Denitrification as Interpreted Through the Santa Barbara Basin Sedimentary $\delta^{15}n$ Record. *Paleoceanogr. Paleoclimatol.* 34, 1554–1567. doi: 10.1029/2019PA003578

Druffel, E. M. (1996). Post-Bomb Radiocarbon Records of Surface Corals Tropical Atlantic Ocean. *Radiocarbon* 38, 563–572. doi: 10.1017/S0033822200030095

Du, X. J., Hendy, I. and Schimmelmann, A. (2018). A 9000-Year Flood History for Southern California: A Revised Stratigraphy of Varved Sediments in Santa Barbara Basin. *Mar. Geol.* 397, 29–42. doi: 10.1016/j.margeo.2017.11.014

Emmer, E. and Thunell, R. C. (2000). Nitrogen Isotope Variations in Santa Barbara Basin Sediments: Implications for Denitrification in the Eastern Tropical North Pacific During the Last 50,000 Years. *Paleoceanography* 15 (4), 377–387. doi: 10.1029/1999pa000417

Eichhubl, P., Greene, H. G., Naehr, T., Maher, N. (2000). Structural Control of Fluid Flow: Offshore Fluid Seepage in the Santa Barbara Basin, California. *Geochem. Explor.* 69–70, 545-549. doi.org/10.1016/S0375-6742(00)00107-2

Fewkes, J. W. (1889). Across the Santa Barbara Channel. *Am. Nat.* 23, 211–217 387-394. doi: 10.1086/274906

Foster, M., Charters, A. C. and Neushul, M. (1971). The Santa Barbara Oil Spill. Part 1: Initial Quantities and Distribution of Pollutant Crude Oil. *Environ. pollut.* 2 (2), 97–113. doi: 10.1016/0013-9327(71)90014-0

Goldberg, E. D. (1963). "Geochronology With 210Pb," in *Radioactive Dating* (Vienna: . International Atomic Energy Agency), 121–131.

Goldschmidt, V. M. (1926). The Laws of Crystal Chemistry. *Naturwissenschaften* 14, 477–485. doi: 10.1007/BF01507527

Gorsline, D. S. (1996). Depositional Events in Santa Monica Basin, California Borderland, Over the Past Five Centuries. *Sedimentary Geol.* 104, 73–88. doi: 10.1016/0037-0738(95)00121-2

Grottoli, A. G. and Eakin, C. M. (2007). A Review of Modern Coral δ^{18}o and Δ^{14}C Proxy Records. *Earth-Science Rev.* 81, 67–91. doi: 10.1016/j.earscirev.2006.10.001

Hendy, I. L., Dunn, L., Schimmelmann, A. and Pak, D. K. (2013). Resolving Varve and Radiocarbon Chronology Differences During the Last 2000 Years in the Santa Barbara Basin Sedimentary Record, California. *Quat. Int.* 310, 155–168. doi: 10.1016/j.quaint.2012.09.006

Hendy, I. L. and Napier, T. J. Schimmelmann, A. (2015). From Extreme Rainfall to Drought: 250 Years of Annually Resolved Sediment Deposition in Santa Barbara Basin, California. *Quaternary Int.*387, 3–12. doi: 10.1016/j.quaint.2015.01.026

Heusser, L. (1998). Direct Correlation of Millennial-Scale Changes in Western North American Vegetation and Climate With Changes in the California Current System Over the Past ~60 Kyr. *Paleoceanography* 13, 252–262. doi: 10.1029/98PA00670

Hornafius, J. S., Quigley, D. and Luyendyk, B. P. (1999). The World's Most Spectacular Marine Hydrocarbon Seeps (Coal Oil Point, Santa Barbara Channel, California): Quantification of Emissions. *J. Geophys. Res.* 104, 20703–20711. doi: 10.1029/1999JC900148

Hua, Q., Barbetti, M. and Rakowski, A. Z. (2013). Atmospheric Radiocarbon for the Period 1950-2010. *Radiocarbon* 55, 2059–2072. doi: 10.2458/azu_js_rc.v55i2.16177

Ingram, B. L. and Kennett, D. J. (1995). Radiocarbon Chronology and Planktonic–Benthic Foraminifera ^{14}C Age Differences in Santa Barbara Basin Sediments, Hole 893A. *Proc. Ocean. Drill. Program Sci. Results* 146 (Pt. 2), 19–27. doi: 10.2973/odp.proc.sr.146-2.278.1995

Ingram, B. L. and Southon, J. R. (1996). Reservoir Ages in Eastern Pacific Coastal and Estuarine Waters. *Radiocarbon* 38, 573–582. doi: 10.1017/S0033822200030101

Inman, D. L. and Jenkins, S. A. (1999). Climate Change and the Episodicity of Sediment Flux of Small California Rivers. *J. Geol.* 107, 251–270. doi: 10.1086/314346

Jacox, M. G., Fiechter, J., Moore, A. M. and Edwards, C. A. (2015). ENSO and the California Current Coastal Upwelling Response. *J. Geophys. Research: Oceans* 120, 1691–1702. doi: 10.1002/2014JC010650

Kennett, D. J. and Brassell, S. C. (1992). Molecular Records of Twentieth Century El Niño Events in Laminated Sediments From Santa Barbara Basin. *Nature* 357, 62–64. doi: 10.1038/357062a0

Kennett, J. P. and Ingram, B. L. (1995). A 20,000 Year Record of Ocean Circulation and Climate Change From the Santa Barbara Basin. *Nature* 377, 510–514. doi: 10.1038/377510a0

Kennett, D. J., Ingram, B. L., Erlandson, J. M. and Walker, P. (1997). Evidence for Temporal Fluctuations in Marine Radiocarbon Reservoir Ages in the Santa Barbara Channel, Southern California. *J. Archaeolog Sci.* 24, 1051–1059. doi: 10.1006/jasc.1996.0184

Kim, J. C., Park, J. H., Kim, I. C., Lee, C., Cheoun, M. K., Kang, J., et al. (2001). Progress at the Seoul National University AMS Facility. *J. Korean Phys. Soc.* 39 (4), 23–35. doi: 10.1017/S0033822200037966

Kolpack, R. L. and Drake, D. E. (1984). Transport of Clays in the Eastern Part of Santa-Barbara Channel, California. *Geo-Mar. Lett.* 4, 191–196. doi: 10.1007/BF02281704

Kuo, T.-S., Liu, Z.-Q., Li, H.-C., Wan, N.-J., Shen, C.-C. and Ku, T.-L. (2011). Climate and Environmental Changes During the Past Millennium in Central Western Guizhou Reflected by Stalagmite ZJD-21 Record. *J. Asian Earth Sci.* 40, 1111–1120. doi: 10.1016/j.jseaes.2011.01.001

Lange, C. B., Berger, W. H., Burke, S. K., Casey, R. E., Schimmelmann, A., Soutar, A., et al. (1987). El Niño in Santa Barbara Basin: Diatom, Radiolarian and Foraminiferan Responses to the "1983 El Niño" Event. *Mar. Geol.* 78, 153–160. doi: 10.1016/0025-3227(87)90074-0

Li, H.-C., Ku, T.-L., Chen, W.-J., Jiao, W.-Q., Zhao, S.-S., Chen, T.-M., et al. (1996). Isotope Studies of Shihua Cave, Beijing – II: Radiocarbon Dating and Age Correction of Stalagmite. *Seismol. Geol.* 18, 329–338.

Li, H.-C., Lee, Z.-H., Wan, N.-J., Shen, C.-C., Li, T.-Y., Yuan, D.-X., et al. (2011). Interpretations of ^{18}O and ^{13}C in Aragonite Stalagmites From Furong Cave, Chongqing, China: A 2000-Year Record of Monsoonal Climate, J. *Asian Earth Sci.* 40, 1121–1130. doi: 10.1016/j.jseaes.2010.06.011

Li, C., Sessions, A. L., Kinnaman, F. S. and Valentine, D. L. (2009). Hydrogen-Isotopic Variability in Lipids From Santa Barbara Basin Sediments. *Geochimica. Cosmochimica. Acta* 73 (16), 4803–4823. doi: 10.1016/j.gca.2009.05.056

Li, H.-C., Zhao, M., Tsai, C.-H., Mii, H.-S. and Wei, K.-Y. (2015). The First High-Resolution Stalagmite Record From Taiwan: Climate and Environmental Changes During the Past 1300 Years. *J. Asian Earth Sci.* 114, 574–587. doi: 10.1016/j.jseaes.2015.07.025

Löwemark, L.Itrax operators (2019). Practical Guidelines and Recent Advances in the Itrax XRF Core-Scanning Procedure. *Quaternary Int.* 514, 16–29. doi: 10.1016/j.quaint.2018.10.044

Lund, D. C. (2011). Increased Ventilation Age of the Deep Northeast Pacific Ocean During the Last Deglaciation. *Nat. Geosci.* 4, 771–774. doi: 10.1038/ngeo1272

Lynn, R. J. and Bograd, S. J. (2002). Dynamic Evolution of the 1997–1999 El Niño–La Niña Cycle in the Southern California Current System. *Prog. Oceanogr.* 54 (1-4), 59–75. doi: 10.1016/S0079-6611(02)00043-5

Lynn, R. J. and Simpson, J. J. (1990). The Flow of the Undercurrent Over the Continental Borderland Off Southern California. *J. Geophys. Res.* 95 (C8), 12,995–13,008. doi: 10.1029/JC095iC08p12995

McFadgen, B. and Manning, M. R. (1990). Calibrating New Zealand Radiocarbon Dates of Marine Shells. *Radiocarbon* 32 (2), 229–232. doi: 10.1017/S0033822200040194

McGowan, J. A. (1984). The California El Niño 1983. *Oceanus* 27 (2), 5–12.

Napier, T. J., Hendy, I. L., Fahnestock, M. F. and Bryce, J. G. (2019). Provenance of Detrital Sediments in Santa Barbara Basin, California, USA: Changes in Source Contributions Between the Last Glacial Maximum and Holocene. *GSA Bull.* 132 (1–2), 65–84. doi: 10.1130/B32035.1

Paulsen, D. E., Li, H.-C. and Ku, T.-L. (2003). Climate Variability in Central China Over the Last 1270 Years Revealed by High-Resolution Stalagmite Records. *Quat. Sci. Rev.* 22, 691–701. doi: 10.1016/S0277-3791(02)00240-8

Pisias, N. G. (1978). Paleoceanography of the Santa Barbara Basin During the Last 8000 Years. *Quaternary Res.* 10, 366–384. doi: 10.1016/0033-5894(78)90027-3

Ramage, C. S. (1986). El Niño. *Am. Scientist* 254, 77–83.

Rassmusson, E. M. (1984). El Niño: The Ocean/Atmosphere Connection. *Oceanus* 27 (2), 5–12.

Roark, E. B., Ingram, B. L., Southon, J. R. and Kennett, J. P. (2003). Holocene Foraminiferal Radiocarbon Record of Paleocirculation in the Santa Barbara Basin. *Geology* 31, 379–382. doi: 10.1130/0091-7613(2003)031<0379:HFRROP>2.0.CO;2

Robert, C. (2004). Late Quaternary Variability of Precipitation in Southern California and Climatic Implications: Clay Mineral Evidence From the Santa Barbara Basin, ODP Site 893. *Quat. Sci. Rev.* 23, 1029–1040. doi: 10.1016/j.quascirev.2003.11.005

Ropelewski, C. F. and Jones, P. D. (1987). An Extension of the Tahiti-Darwin Southern Oscillation Index. *Monthly Weather Rev.* 115, 2161–2165. doi: 10.1175/1520-0493(1987)115<2161:AEOTTS>2.0.CO;2

Sarno, C. T., Benitez-Nelson, C. R., Ziolkowski, L. A., Hendy, I. L., Davis, C. V., Tappa, E. J., et al. (2020). The Impacts of Flood, Drought, and Turbidites on Organic Carbon Burial Over the Past 2,000 Years in the Santa Barbara Basin. *California Paleoceanogr. Paleoclimatol.* 35 (7), e2020PA00384. doi: 10.1029/2020PA003849

Schimmelmann, A., Hendy, I. L., Dunn, L., Pak, D. K. and Lange, C. B. (2013). Revised ~2000-Year Chronostratigraphy of Partially Varved Marine Sediment in Santa Barbara Basin, California. *GFF* 135 (3–4), 258–264. doi: 10.1080/11035897.2013.773066

Schimmelmann, A. and Lange, C. B. (1992). Extreme Climatic Conditions Recorded in Santa Barbara Basin Laminated Sediments: The 1835-1840 Macoma Event. *Mar. Geol.* pp, 279–299. doi: 10.1016/0025-3227(92)90134-4

Schimmelmann, A. and Lange, C. B. (1996). Tales of 1001 Varves: A Review of Santa Barbara Basin Sediment Studies. *Geolog. Soc. London Special Publications* 116, 121–141. doi: 10.1144/GSL.SP.1996.116.01.12

Schimmelmann, A., Lange, C. B. and Li, H.-C. (2001). Major Flood Events of the Past 2,000 Years Recorded in Santa Barbara Basin Sediment. *Paclim. Conf. Proc.* pp, 82–103.

Schimmelmann, A., Lange, C. B. and Meggers, B. J. (2003). Palaeoclimatic and Archaeological Evidence for a 200-Yr Recurrence of Floods and Droughts Linking California, Mesoamerica and South America Over the Past 2000 Years. *Holocene.* 13 (5), 763–778. doi: 10.1191/0959683603hl661rp

Schimmelmann, A., Lange, C. B., Roark, E. B. and Ingram, B. L. (2006). Resources for Paleoceanographic and Paleoclimatic Analysis: A 6,700-Year Stratigraphy and Regional Radiocarbon Reservoir-Age (ΔR) Record Based on Varve Counting and ^{14}C-AMS Dating for the Santa Barbara Basin, Offshore California, U.S.A. *J. Sediment. Res.* 76, 74–80. doi: 10.2110/jsr.2006.04

Schimmelmann, A. and Tegner, M. J. (1991). Historical Oceanographic Events Reflected in ^{13}C/^{12}C Ratio of Total Organic Carbon in Laminated Santa Barbara Basin Sediment. *Global biogeochem. cycles* 5, 173–188. doi: 10.1029/91GB00382

Schimmelmann, A., Zhao, M., Harvey, C. C. and Lange, C. B. (1998). A Large California Flood and Correlative Global Climatic Events 400 Years Ago. *Quaternary Res.* 49 (1), 51–61. doi: 10.1006/qres.1997.1937

Schimmelmann, A., Zhao, M., Kuhn, G. G. and Tegner, M. J. (1995). "Sea Surface Temperature and Paleo-El Niño Events in Santa Barbara Basin, AD 1841-1941," in *Proceedings of the Eleventh Annual Pafic Climate (PACLIM) Workshop, April 19-22, 1994. Interagency Ecological Program. Technical Report 40*. Eds. Isaacs, C. M. and Tharp, V. L. (California Department of Water Resources), 93–105.

Shipe, R. F., Passow, U., Brzezinski, M. A., Graham, W. M., Pak, D. K., Siegel, D. A., et al. (2002). Effects of the 1997–98 El Niño on Seasonal Variations in Suspended and Sinking Particles in the Santa Barbara Basin. *Prog. Oceanogr.* 54, 105–127. doi: 10.1016/S0079-6611(02)00045-9

Stenström, K. E., Skog, G., Georgiadou, E., Genberg, J. and Johansson, A. (2011). "A Guide to Radiocarbon Units and Calculations," in *Internal Report LUNFD6(NFFR-3111)/1-17/(2011), Division of Nuclear Physics* (Sweden: Department of Physics, Lund University).

Stuiver, M. and Polach, H. A. (1977). Discussion/Reporting of ^{14}C Data. *Radiocarbon* 19, 355–363. doi: 10.1017/S0033822200003672

Tems, C. E., Berelson, W. M. and Prokopenko, M. G. (2015). Particulate δ^{15}n in Laminated Marine Sediments as a Proxy for Mixing Between the California Undercurrent and the California Current: A Proof of Concept. *Geophys. Res. Lett.* 42, 419–427. doi: 10.1002/2014GL061993

Thunell, R. C. (1998). Particle Fluxes in a Coastal Upwelling Zone: Sediment Trap Results From Santa Barbara Basin, California. *Deep-Sea Res. Part Ii-Topical Stud. Oceanogr.* 45, 1863–1884. doi: 10.1016/S0967-0645(98)80020-9

Thunell, R. C. (2003). Distinguishing Between Water Column and Sedimentary Denitrification in the Santa Barbara Basin Using the Stable Isotopes of Nitrate. *Geochem. Geophys. Geosyst.* 4 (5), 1040. doi: 10.1029/2002gc000384

Thunell, R. C., Tappa, E. and Anderson, D. M. (1995). Sediment Fluxes and Varve Formation in Santa Barbara Basin, Offshore California. *Geology* 23, 1083–1086. doi: 10.1130/0091-7613(1995)023<1083:SFAVFI>2.3.CO;2

Treude, T. and Ziebis, W. (2010). Methane Oxidation in Permeable Sediments at Hydrocarbon Seeps in the Santa Barbara Channel, California. *Biogeosciences* 7, 3095–3108. doi: 10.5194/bg-7-3095-2010

Valentine, D. L., Reddy, C. A., Farwell, C., Hill, T. M., Pizarro, O., Yoerger, D. R., et al. (2010). Asphalt Volcanoes as Potential Source of Methane to Late Pleistocene Coastal Waters, Nat. *Geosci.* 3, 345–348. doi: 10.1038/NGEO848

van Geen, A. and Husby, D. M. (1996). Cadmium in the California Current System: Tracer of Past and Present Upwelling. *J. Geophys. Res. (Oceans)* 101, 3489–3507. doi: 10.1029/95JC03302

Venrick, E. L. (2012). Phytoplankton in the California Current System Off Southern California: Changes in a Changing Environment. *Prog. Oceanogr.* 104, 46–58. doi: 10.1016/j.pocean.2012.05.005

Warrick, J. A. and Farnsworth, K. L. (2009). "Sources of Sediment to the Coastal Waters of the Southern California Bight," in *Earth Science in the Urban Ocean: The Southern California Continental Borderland, Geological Society of America Special Paper*, vol. 454 . Eds. Lee, H. J. and Normark, W. R., 39–52). doi: 10.1130/2009.2454(2.2

Warrick, J. A., Washburn, L., Brzezinski, M. A. and Siegel, D. A. (2005). Nutrient Contributions to the Santa Barbara Channel, California, From the Ephemeral Santa Clara River. *Estuarine Coast. Shelf Sci.* 62 (4), 559–574. doi: 10.1016/j.ecss.2004.09.033

Weinheimer, A. L. and Cayan, D. R. (1997). Radiolarian Assemblages From Santa Barbara Basin Sediments: Recent Interdecadal Variability. *Paleoceanography* 12, 658–670. doi: 10.1029/97PA00986

White, M. E., Rafter, P. A., Stephens, B. M., Wankel, S. D. and Aluwihare, L. I. (2019). Recent Increases in Water Column Denitrification in the Seasonally Suboxic Bottom Waters of the Santa Barbara Basin. *Geophys. Res. Lett.* 46, 6786–6795. doi: 10.1029/2019GL082075

Yang, Q. N., Zhao, H. Y., Li, H.-C., Li, H. K., Bu, Z. J., Wang, S. Z., et al. (2017). Distributions of "Bomb ^{14}C", Biogeochemistry and Elemental Concentration in Hani Mire Peat Profiles, NE China: Implications of Environmental Change. *Quat. Int.* 447, 128–143. doi: 10.1016/j.quaint.2017.06.033

Yin, J. J., Li, H.-C., Rao, Z.-G., Shen, C.-C., Mii, H.-S., Pillutla, R. K., et al. (2017). Variations of Monsoonal Rain and Vegetation During the Past Millennium in Tiangui Mountain, North China Reflected by Stalagmite δ^{18}O and δ^{13}C Records From Zhenzhu Cave. *Quaternary Int.* 447, 89–101. doi: 10.1016/j.quaint.2017.06.039

Yin, J. J., Li, H.-C., Tang, W., Wang, Z. J., Mii, H.-S. and Lin, Y. S. (2019). Rainfall Variability and Vegetation Recovery in Rocky Desertification Areas Recorded in Recently-Deposited Stalagmites From Guilin, South China. *Quaternary Int.* 528, 109–119. doi: 10.1016/j.quaint.2019.01.039

Yin, J. J., Yuan, D. X., Li, H.-C., Cheng, H., Li, T. Y., Edwards, R. L., et al. (2014). Variation in the Asian Monsoon Intensity and Dry–Wet Condition Since the Little Ice Age in Central China Revealed by an Aragonite Stalagmite. *Clim. Past* 10, 1803–1816. doi: 10.5194/cp-10-1803-2014

Zhao, M., Li, H.-C., Liu, Z.-H., Mii, H.-S., Sun, H.-S. and Shen, C.-C. (2015). Changes in Climate and Vegetation of Central Guizhou in Southwest China Since the Last Glacial Reflected by Stalagmite Records From Yelang Cave. *J. Asian Earth Sci.* 114, 549–561. doi: 10.1016/j.jseaes.2015.07.021

Zhao, M., Li, H.-C., Shen, C.-C., Kang, S.-C. and Chou, C.-Y. (2017a). δ^{18}O, δ^{13}C, Elemental Content and Depositional Features of a Stalagmite From Yelang Cave Reflecting Climate and Vegetation Changes Since Late Pleistocene in Central Guizhou, China. *Quaternary Int.* 452, 102–115. doi: 10.1016/j.quaint.2016.07.022

Zhao, M., Shen, G.-J., He, J.-N., Cao, B. and Li, H.-C. (2017b). AMS ^{14}C Dating of the Hominin Archaeological Site Chuandong Cave in Guizhou Province, Southwestern China. *Quaternary Int.* 447, 102–110. doi: 10.1016/j.quaint.2017.04.037

Conflict of Interest: The authors declare that the research was conducted in the absence of any commercial or financial relationships that could be construed as a potential conflict of interest.

frontiers | Frontiers in Marine Science

TYPE Original Research
PUBLISHED 07 September 2022
DOI 10.3389/fmars.2022.973507

OPEN ACCESS

EDITED BY
Gilles Reverdin,
Centre National de la Recherche Scientifique (CNRS), France

REVIEWED BY
Tsuneo Ono,
Japan Fisheries Research and Education Agency (FRA), Japan
Paul Myers,
University of Alberta, Canada

*CORRESPONDENCE
A.-M. Wefing
annemarie.wefing@usys.ethz.ch

SPECIALTY SECTION
This article was submitted to Ocean Observation, a section of the journal Frontiers in Marine Science

RECEIVED 20 June 2022
ACCEPTED 03 August 2022
PUBLISHED 07 September 2022

CITATION
Wefing A-M, Casacuberta N, Christl M and Dodd PA (2022) Water mass composition in Fram Strait determined from the combination of ^{129}I and ^{236}U: Changes between 2016, fmars.2022.9735072018, and 2019. *Front. Mar. Sci.* 9:973507. doi: 10.3389/fmars.2022.973507

Water mass composition in Fram Strait determined from the combination of ^{129}I and ^{236}U: Changes between 2016, 2018, and 2019

A.-M. Wefing[1]*, N. Casacuberta[1,2], M. Christl[2] and P. A. Dodd[3]

[1]Physical Oceanography, Institute of Biogeochemistry and Pollutant Dynamics, Department of Environmental Systems Science, ETH Zurich, Zurich, Switzerland, [2]Laboratory of Ion Beam Physics, Department of Physics, ETH Zurich, Zurich, Switzerland, [3]Norwegian Polar Institute, Fram Centre, Tromsø, Norway

Changes in the provenance and composition of waters exported from the Arctic Ocean have the potential to impact large-scale ocean circulation processes in the sub-polar North Atlantic. The main conveyor of waters from the Arctic Ocean to lower latitudes is the East Greenland Current (EGC), flowing southward through Fram Strait. It is therefore crucial to determine and monitor the composition of the EGC, a mixture of polar waters of different origins. Here we present a pilot study on the potential of the long-lived anthropogenic radionuclides ^{129}I and ^{236}U as tracers of the EGC water mass composition, based on a time series of ^{236}U and ^{129}I concentrations measured across Fram Strait in the years 2016, 2018, and 2019. The overall spatial distribution of ^{236}U and ^{129}I was similar among the three sampling years, but a decrease in concentration was observed in the upper water column of the EGC. The observed changes could only partly be attributed to the transient nature of the radionuclide signals, but instead pointed to changes in the EGC water mass composition. To investigate these changes, ^{236}U and ^{129}I were first combined in a mixing model featuring the endmembers expected in the upper EGC. We distinguished between Pacific Water (PAC), Atlantic Water advected from the Arctic Ocean (ATL), and Atlantic Water recirculating in Fram Strait (RAC). In ^{236}U-^{129}I tracer space, PAC and RAC showed similar tracer signatures, but were well distinguished from ATL. From 2016 to 2018/19, a decrease in the ATL fraction was evident for the upper EGC. Secondly, the respective combination of ^{236}U and ^{129}I with salinity showed differences in absolute water mass fractions, but similar temporal trends. Both suggested an increase in PAC of about 20% for the uppermost layer of the EGC (samples with potential densities below 26.5) and an increase in RAC of about 10–20 % for denser samples. ^{129}I and ^{236}U, in combination with salinity, were shown to be suitable tracers to investigate water mass composition in Fram Strait, with the advantage that they

can distinguish Atlantic Water advected from the Arctic Ocean from that recirculating in Fram Strait.

KEYWORDS

radionuclides, tracers, Fram Strait, water mass, East Greenland current

1 Introduction

Anthropogenic climate change leads to rapid transformations in the Arctic Ocean, including Atlantic Water transport of heat and anthropogenic carbon, increased sea-ice melt, as well as changes in the meteoric water budget (Muilwijk et al., 2018; Arthun et al., 2019; Forryan et al., 2019; Terhaar et al., 2020; Timmermans and Marshall, 2020; Wang et al., 2020). *Via* the Canadian Arctic Archipelago, the Barents Sea, and Fram Strait, the Arctic Ocean is connected to the North Atlantic Ocean. Changes in the properties of waters transported from the Arctic Ocean to lower latitudes will eventually affect the global ocean circulation *via* its influence on deep-water formation in the sub-polar North Atlantic, an important driver of the Atlantic Meridional Overturning Circulation (Rahmstorf et al., 2015; Holliday et al., 2020).

The up to 2600 m deep Fram Strait, located between Greenland and Svalbard (Figure 1), is the only gateway allowing for a two-way exchange of waters between the Arctic and the North Atlantic Ocean. In eastern Fram Strait, the West Spitsbergen Current (WSC) carries warm and saline Atlantic Water into the Arctic Ocean. In western Fram Strait, the East Greenland Current (EGC) transports cold and fresh Arctic-derived waters as well as sea-ice southwards to the Nordic Seas (e.g., Beszczynska-Moller et al., 2011; Havik et al., 2017). In total, about half of the Arctic Ocean freshwater (sea ice and liquid freshwater relative to a reference salinity of 34.8) is exported through Fram Strait (Serreze et al., 2006; Haine et al., 2015). Pacific Water contributes to the Arctic Ocean freshwater pool due to its lower salinity compared to Atlantic Water. Over time, significant changes in the Arctic Ocean freshwater export through Fram Strait have been observed (Dodd et al., 2012; de Steur et al., 2015; de Steur et al., 2017; de Steur et al., 2018). The most recent study on freshwater transport in the EGC based on mooring observations pointed to an "Atlantification" of the western Fram Strait (Karpouzoglou et al., 2022).

To understand causes of the observed changes, the water mass composition of the EGC needs to be resolved. To this aim, the combination of different chemical tracers has been used in the past. Salinity and stable oxygen isotopes ($\delta^{18}O$) allow to determine fractions of sea-ice melt and meteoric water (comprising precipitation, river runoff, and glacial meltwater) (Dodd et al., 2009). Atlantic- and Pacific-derived waters have classically been distinguished by nutrient-based methods using nitrate-phosphate (N:P method) or phosphate-oxygen relationships (PO*; e.g., Ekwurzel et al., 2001; Yamamoto-Kawai et al., 2008; Jones et al., 2008a; Jones et al., 2008b; Bauch et al., 2011; Dodd et al., 2012; Newton et al., 2013; Alkire et al., 2015; Alkire et al., 2019; Forryan et al., 2019). However, there is an ongoing debate regarding the reliability of nutrient-based approaches for Arctic Ocean water masses, due to shelf-interaction processes taking place on the broad Arctic shelves such as denitrification in the Chukchi Sea, or seasonal variability (Ekwurzel et al. (2001); Bauch et al. (2011); Alkire et al. (2015); Alkire et al. (2019); Forryan et al. (2019)). New tracers have been investigated to differentiate between Pacific and Atlantic contributions, such as dissolved gallium (Whitmore et al., 2020) or neodymium isotopes (Laukert et al., 2017). Recently, also the use of anthropogenic radionuclides as tracers to distinguish between Atlantic- and Pacific-derived waters in the Arctic Ocean has been suggested (Alkire et al., 2019; Forryan et al., 2019). The long-lived radionuclides ^{129}I and ^{236}U behave conservatively in seawater and are transported by Atlantic-origin waters in the Arctic Ocean (Casacuberta et al., 2018). Recent studies used the ^{129}I and ^{236}U signal to track pathways of Atlantic-origin waters through the Arctic Ocean (Casacuberta et al., 2016), and the transient signal of both radionuclides has been successfully applied to estimate water mass ages and mixing regimes of Atlantic Water in the Arctic Ocean and Fram Strait (Christl et al., 2015b; Wefing et al., 2019; Wefing et al., 2021). So far, however, ^{129}I and ^{236}U have not been explored as tracers to differentiate between Pacific and Atlantic Water and to determine water mass fractions.

This study addresses the transient nature as well as the potential of ^{129}I and ^{236}U as tracers to distinguish between Atlantic- and Pacific-derived waters in Fram Strait. Firstly, temporal changes in the ^{236}U distribution across Fram Strait in the years 2016, 2018, and 2019 are presented and investigated in light of the time-dependent input of both radionuclides to the Arctic Ocean. Secondly, both radionuclides are combined with salinity in a steady-state mixing model to derive water mass fractions and their temporal variation in the EGC. Finally, strengths and weaknesses of both radionuclides as tracers of Atlantic and Pacific Water in Fram Strait are discussed and their

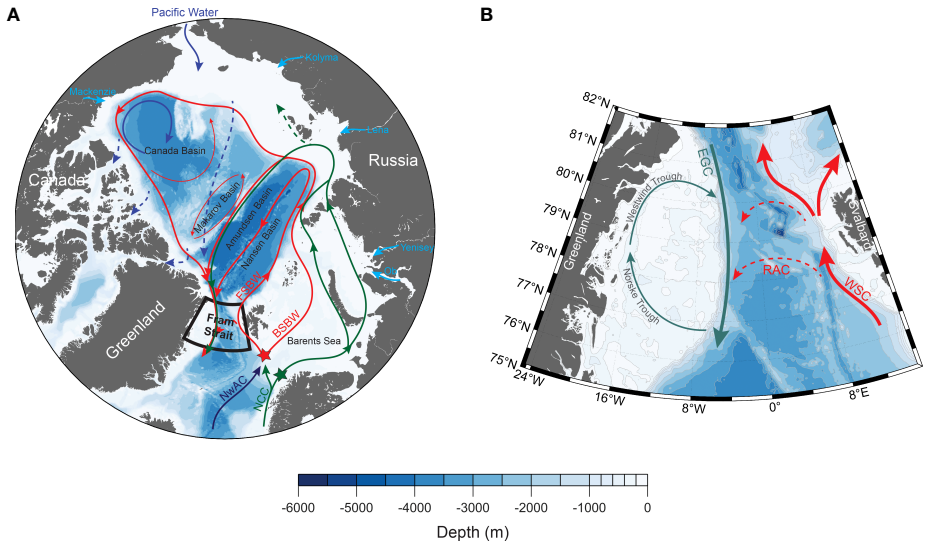

FIGURE 1
(A) Circulation of Atlantic (red and green) and Pacific (blue) waters in the Arctic Ocean. Green arrows depict the circulation of Atlantic Water originating from the Norwegian Coastal Current (NCC) in the surface layer. Red arrows depict the circulation of Fram Strait Branch Water (FSBW) and Barents Sea Branch Water (BSBW) in the mid-depth Atlantic layer. Star symbols show the locations where the surface (green star) and mid-depth Atlantic layer (red star) input functions of ^{129}I and ^{236}U to the Arctic Ocean, depicted in Figure 2, were defined. Light blue arrows depict inflow of major rivers draining into the Arctic Ocean. The black outline highlights the Fram Strait study area shown in **(B)**. The map was modified after Figure 1 in Wefing et al. (2021). NwAC: Norwegian Atlantic Current. **(B)** Map of Fram Strait with main circulation features in the upper water column including the West Spitsbergen Current (WSC), East Greenland Current (EGC), and Return Atlantic Current (RAC), as well as main topographic features on the Greenland shelf.

future potential as new water mass composition tracers is assessed.

2 Material and methods

2.1 Study area

Main circulation features in the upper water column of Fram Strait comprise the northward-flowing WSC and the southward-flowing EGC (Figure 1B). The WSC carries warm and saline Atlantic Water into the Arctic Ocean, which evolves into the so-called Fram Strait Branch Water (FSBW). Together with Barents Sea Branch Water (BSBW), FSBW constitutes the mid-depth Atlantic Layer of the Arctic Ocean. About half of the WSC, however, is known to recirculate already within Fram Strait and is then referred to as Return Atlantic Current (RAC; Marnela et al., 2013; de Steur et al., 2014). The extent, spatial and temporal variability, as well as mechanisms of this recirculation are subject to ongoing research (e.g., Hattermann et al., 2016; Kawasaki and Hasumi, 2016; Wekerle et al., 2017; Richter et al., 2018). The RAC joins the EGC, which carries Polar Waters of Atlantic- and Pacific-origin southward. Rudels et al. (2005) and Rudels et al. (2012) classified waters with a potential density (σ_Θ) below or equal 27.7 and a potential temperature below or equal 0°C and above 0°C as Polar Surface Water (PSW) and Warm Surface Water (PSWw), respectively. In this study, we do not distinguish between PSW and PSWw but refer to both water masses as PSW.

The western Fram Strait is dominated by the broad north-east Greenland continental shelf with depths between about 50 and 300 m. Its main topographic feature is a C-shaped trough system comprising Norske Trough and Westwind Trough (Figure 1B), with depths ranging mostly between about 300 and 500 m (Arndt et al., 2015). The troughs have been found to play an important role in the transport of warm Atlantic origin waters to glaciers terminating in Fram Strait, especially the so-called 79° N glacier (Nioghalvfjerdsbrae; Schaffer et al. (2017); Münchow et al. (2020)), suggesting an anti-cyclonic flow through Norske Trough and potentially further north through Westwind Trough. Schaffer et al. (2017) estimated a transit time of less than 1.5 years for waters transported by the WSC to reach the 79° N glacier.

In mid-depth layers (~400–1000 m) of Fram Strait, waters of Atlantic origin (i.e., FSBW or BSBW), which have circulated through the Arctic Ocean, are transported southwards, referred to as Arctic Atlantic Water (AAW) and Arctic Intermediate Water (AIW) (Rudels et al., 2005; Rudels et al., 2012). Below, a mixture of deep waters from the Eurasian and Canada Basin of the Arctic Ocean and the Nordic Seas is found.

2.2 Sources of ^{129}I and ^{236}U in the Arctic Ocean and Fram Strait

The main signal of the two long-lived anthropogenic radionuclides ^{129}I and ^{236}U in the Arctic Ocean can be attributed to liquid releases of two European nuclear fuel reprocessing plants located in La Hague (France) and Sellafield (United Kingdom), (Christl et al., 2015b; Casacuberta et al., 2016, Casacuberta et al., 2018). The amounts of released ^{129}I and ^{236}U have been changing over time. Overall, more ^{129}I has been released compared to ^{236}U (Casacuberta et al., 2016). The reprocessing plant signal is transported northward from the North Sea in the Norwegian Coastal Current (NCC; Edmonds et al. (2001); Gascard et al. (2004); Smith et al. (2011); Casacuberta et al. (2018)).

Another source of ^{236}U (and a minor amount of ^{129}I) is the global fallout from atmospheric nuclear weapon tests conducted in the 1950s and 60s. This signal can be found in all recently (i.e., less than about 70 years ago) ventilated water masses (e.g., Christl et al., 2015b). The global fallout signal in the North Atlantic Ocean is primarily carried northwards in the Norwegian Atlantic Current (NwAC). The admixture of NCC waters carrying the reprocessing plant radionuclides signal to the NwAC results in a time-dependent ^{129}I and ^{236}U signature labeling all Atlantic Water that enters the Arctic Ocean.

As a consequence of the (not spatially uniform) mixing of NCC and NwAC, different Atlantic branches entering the Arctic Ocean carry different ^{129}I and ^{236}U concentrations (Figure 2). The strongest reprocessing plant signal is found in the NCC (green datapoints in Figure 2) and the high ^{129}I concentrations observed in the surface layer of the Amundsen Basin in 2015 could clearly be attributed to waters originating from this branch (Casacuberta et al., 2018). Further downstream, the upper layer of the EGC in Fram Strait also showed high ^{129}I concentrations in 2016, suggesting the presence of a significant fraction of NCC-derived waters (Wefing et al., 2019). Waters entering the Arctic Ocean through Fram Strait and the Barents Sea Opening, offshore from the Norwegian coast, carry a smaller fraction of the NCC and therefore lower ^{129}I and ^{236}U concentrations. Casacuberta et al. (2018) defined different input functions for these two branches, suggesting that BSBW carries slightly higher ^{129}I and ^{236}U concentrations than FSBW (Figure 2).

Pacific Water entering the Arctic Ocean through Bering Strait has not been labeled by reprocessing plant releases but carries only the global fallout signal of ^{129}I and ^{236}U. Both radionuclides were introduced to the surface ocean *via* wet and dry deposition and not *via* air-sea gas exchange. One can therefore assume that most ^{129}I and ^{236}U from the nuclear weapon tests, conducted more than 50 years ago, has been distributed within the upper ocean and the global fallout signal in Pacific Water is considered constant in time [at 10^7 at·L^{-1} for ^{129}I and ^{236}U, Wefing et al., (2021)].

2.3 Sampling, chemical analysis, and measurement

Seawater samples for ^{129}I and ^{236}U analyses presented in this study were collected during three oceanographic expeditions to Fram Strait in 2016, 2018 and 2019. All samples were taken from 12-L Niskin bottles mounted on a conductivity-temperature-depth (CTD) rosette. For the analysis of ^{129}I, 200–500 ml of seawater were filled into plastic bottles without further treatment. For the analysis of ^{236}U, 3–5 L of seawater were collected in plastic cubitainers without further treatment. Whenever possible, seawater samples for ^{129}I and ^{236}U analysis were taken from the same Niskin bottle. All samples were shipped to the Laboratory of Ion Beam Physics at ETH Zurich for ^{129}I and ^{236}U analysis.

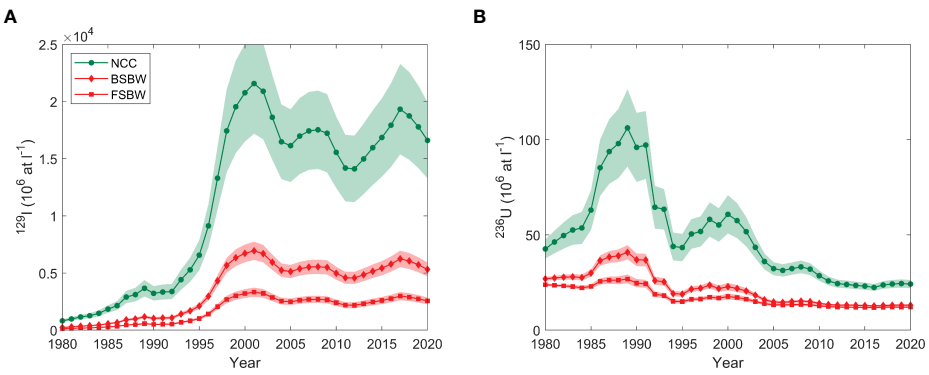

FIGURE 2
Input functions of ^{129}I **(A)** and ^{236}U **(B)** in the Norwegian Coastal Current (NCC), Barents Sea Branch Water (BSBW), and Fram Strait Branch Water (FSBW) after Casacuberta et al. (2018) and Wefing et al. (2021).

^{129}I and ^{236}U data from the 2016 expedition aboard R/V Polarstern (PS100, July-September 2016; Kanzow (2017)) have already been published in Wefing et al. (2019). Hydrographic data for this expedition were obtained from the PANGAEA database (Kanzow et al., 2017). Full-depth profiles for ^{129}I and ^{236}U analysis were collected along the 79° N transect and in several stations on the north-east Greenland shelf.

The 2018 and 2019 expeditions (FS2018, FS2019) were carried out by the Norwegian Polar Institute (NPI, Tromsø) aboard R/V Kronprins Haakon in August/September 2018 and September 2019, respectively. Hydrographic data from FS2018 and FS2019 were kindly provided by NPI (pers. communication P.A. Dodd, 2020). In both years, full-depth profiles of ^{236}U samples were collected along the 79° N transect with the main focus on the upper 400 m of the outflowing waters in the EGC. One ^{236}U profile was also taken in Norske Trough. In 2018 and 2019, only two and one full-depth profile, respectively, were collected for ^{129}I analysis.

For all samples, the chemical preparation and determination of ^{129}I and ^{236}U concentrations with Accelerator Mass Spectrometry (AMS) was performed at the Laboratory of Ion Beam Physics at ETH Zurich following the method described in Wefing et al. (2019). Note that samples for ^{236}U analysis collected during FS2018 and FS2019 were spiked with a new ^{233}U spike (PTB2014-1126, about 1 pg ^{233}U per sample). Technical details on the AMS measurement can be found in Vockenhuber et al. (2015) and Christl et al. (2015a).

Generally, ^{238}U concentrations are determined from measured ^{233}U/^{238}U atom ratios using the known amount of ^{233}U added as a spike, as also described in Wefing et al. (2019). Together with the measured ^{236}U/^{238}U atom ratios, this allows to infer ^{236}U concentrations. However, comparing the three sampling years, we noticed inconsistencies in the ^{238}U-salinity relationship from the measured ^{238}U compared to the theoretical relationship by Owens et al. (2011). Measured ^{238}U were all above the ^{238}U concentrations expected from salinity, especially for FS2019. A possible explanation could be the handling and storage of the ^{233}U spike, which was pre-weighed in small (1.5 ml) vials and stored for several months (longest for FS2019). A potential adsorption of ^{233}U onto the vial or an incomplete transfer from the vial into the seawater sample would lead to an overestimation of ^{233}U transferred into the sample and hence also ^{238}U in the sample. To ensure comparability among the different sampling years, we therefore decided to use the ^{238}U-salinity relationship and corresponding uncertainty from Owens et al. (2011) to calculate ^{238}U from salinity for all three expeditions. ^{236}U concentrations were then calculated from the measured ^{236}U/^{238}U atom ratio, propagating corresponding uncertainties. Atom ratios and concentrations are reported in Table S1 in the supplement.

3 Results

3.1 Hydrographic parameters and ^{236}U distribution across Fram Strait

In all sampling years, radionuclide samples were collected along a transect across Fram Strait, at about 79° N. Potential temperature, salinity, and ^{236}U concentrations are therefore depicted as sections through Fram Strait, showing the upper 1000 m of the water column between 12° W and 8° E (Figure 3). All available hydrographic and ^{236}U data along this transect was depicted here (Figures 3A–C).

The sections of potential temperature (Figures 3D–F) and salinity (Figures 3G–I) clearly showed cold and fresh PSW of Arctic origin residing in the upper water column of the western Fram Strait, including the north-east Greenland shelf. In the eastern Fram Strait, warm and saline Atlantic Water (AW) occupied the water column down to about 400-600 m. In the surface layer, the interface between PSW and AW was delineated by a sharp front in both potential temperature and salinity, located at about 2° W in 2016 and 2018. In 2019, PSW extended further to the east and the front was located east of the prime meridian (Figures 3F–I). Below PSW, increased potential temperature and salinity pointed to the presence of transformed Atlantic Water, i.e, water of Atlantic origin which has already circulated through the Arctic Ocean (AAW), in the western Fram Strait in all years.

In the ^{236}U sections across Fram Strait, the above-mentioned water masses are indicated based on the water mass classification in Rudels et al. (2005); Rudels et al. (2012) (Figures 3J–L). Note the difference in sampling resolution compared to hydrographic data, but also between 2016 and 2018/19, especially in PSW. The ^{236}U distribution across Fram Strait in 2016 has already been presented in Wefing et al. (2019), however, main features are summarized here again. ^{236}U concentrations were generally higher in outflowing Arctic water (PSW and AAW) compared to the inflowing AW. The front between PSW and AW in the surface, delineated in the 2° C isotherm (light gray), was well aligned with the strong eastward decrease in ^{236}U concentrations. For better visualization, the isoline for a ^{236}U concentration of 15×10^6 at·L^{-1} was also depicted in the sections (thick white line). In the upper 200–300 m, it closely followed the 2°C isotherm (Figures 3J–L). In all three years, the highest ^{236}U signal was found in PSW (upper 200 m of the EGC) and in (dense) AAW at around 400 to 750 m depth. The underlying waters with $\Theta < 0$°C (AIW) carried a lower tracer signal which decreased further with depth. Below 1000 m depth, ^{236}U concentrations were at the level of global fallout (around 10^6 at·L^{-1}) or below (not shown).

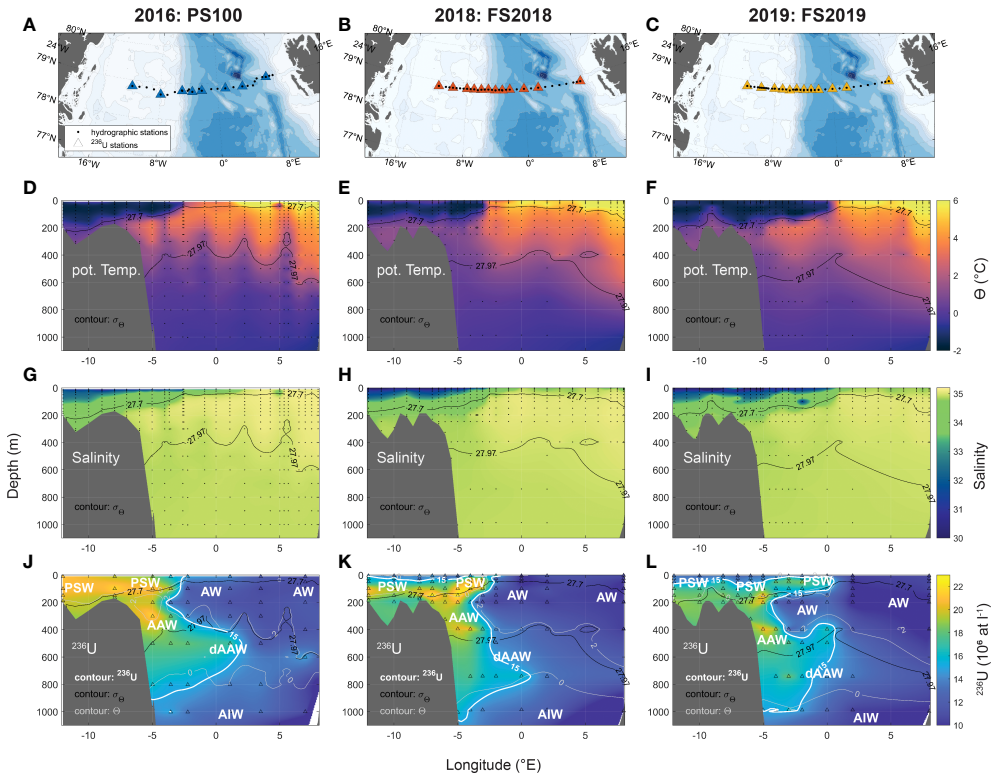

FIGURE 3
(A–C) CTD stations for hydrographic sampling (black dots) and ^{236}U sampling (colored triangles) during expedition PS100 in 2016 **(A)**, FS2018 **(B)**, and FS2019 **(C)**. **(D–F)** Transects of potential temperature (Θ) for 2016 **(D)**, 2018 **(E)**, and 2019 **(F)**. **(G–I)** Transects of salinity for 2016 **(G)**, 2018 **(H)**, and 2019 **(I)**. **(J–L)** Transects of ^{236}U/^{238}U for 2016 **(J)**, 2018 **(K)**, and 2019 **(L)**. In all transects, only the upper 1000 m are shown and bathymetry corresponds to bottom depths of all CTD stations along the transect. Isopycnals of 27.7 and 27.97 are shown in black. In ^{236}U transects, additionally ^{236}U isolines of 15 × 10^6 at · L $^{-1}$ are shown in white (bold), Θ isolines of 0 °C and 2 °C are shown in light gray, and water masses are indicated. PSW: Polar Surface Water, AW: Atlantic Water, (d)AAW: (dense) Arctic Atlantic Water, AIW: Arctic Intermediate Water.

From 2016 to 2018, ^{236}U concentrations in the upper 50 to 100 m of the EGC decreased (Figures 3J, K). Highest ^{236}U signals in 2018 (around 23×10^6 at·L^{-1}) were found between 100 and 200 m depth approximately at the shelfbreak (around 4–5 °W, Figure 3K), associated with the core of the EGC (velocity maximum from moorings at around 4° W; de Steur et al. (2018)). ^{236}U concentrations at similar depths decreased slightly from 2018 to 2019 (to around 20–21×10^6 at·L^{-1} ; Figure 3L). At the same time, the interface between in- and outflowing waters in the upper 100 m shifted significantly to the east in 2019 compared to 2018 and 2016. This shift was observed in Θ and salinity, but also in the ^{236}U distribution. The isoline of 15×10^6 at·L^{-1} ^{236}U shifted from about 2.5°E in 2016 and 2018 to about 0.4°W in 2019 (average of eastward extent over 0–100 m depth). In contrast, no significant temporal changes were observed in mid-depth waters (AAW and dAAW). Note that below about 200 m depth, however, the sampling resolution for ^{236}U was lower and differed between 2016 and 2018/2019 (Figures 3J–L).

3.2 ^{236}U and ^{129}I profiles of matching stations

To account for differences in the sampling locations over time, a direct comparison of data from all three years was performed for eight stations which were identified as “matching stations” among the expeditions (Figure 4A). Station 1 is located in Norske Trough, stations 2 and 3 cover the north-east Greenland shelf, stations 4–7 cover the central Fram Strait, and station 8 is located in the WSC close to Svalbard. Profiles of ^{236}U and ^{129}I data for the different sampling years show the temporal evolution of both radionuclides at these eight stations (Figures 4B–I).

At the shelf stations (stations 1-3), ^{236}U concentrations decreased from 2016 to 2018/19 from about 20–22×10^6 at·L^{-1} to 14–20×10^6 at·L^{-1} in the upper 100 m (Figures 4B–D). For greater depths, the decrease was less pronounced or not observed. For stations 2 and 3, ^{236}U in the deepest samples (150–200 m depth) agreed within uncertainties for all years.

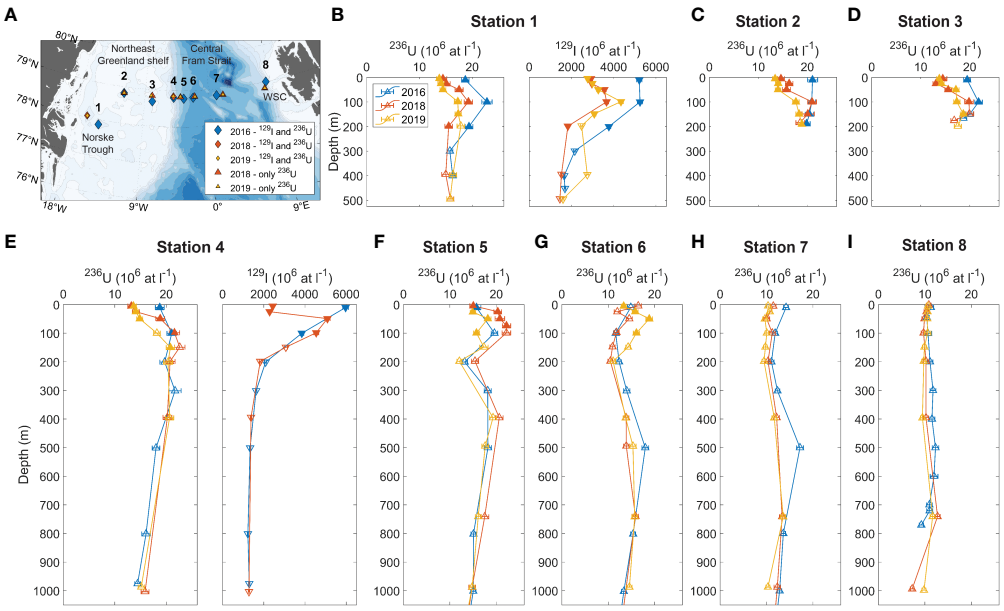

FIGURE 4
(A) Map showing locations of eight matching stations among the different expeditions. Colored diamonds show stations of available ^{129}I and ^{236}U data for 2016 (blue), 2018 (red) and 2019 (yellow). Colored triangles show stations where only ^{236}U data are available. **(B–I)** Profiles of ^{236}U (and ^{129}I for station 1 and 4) at matching stations 1-8 for 2016 (blue), 2018 (red), 2019 (yellow). Filled symbols indicate samples classified as PSW or PSWw.

Similar trends were observed for ^{129}I at station 1, with a decrease from about 5000–6000×10^6 at·L^{-1} measured in the surface samples in 2016 to about 2000–4000×10^6 at·L^{-1} in 2018/2019. At about 400 m depth, however, ^{129}I was similar in 2016 and 2018, and increased in 2019. This trend was not observed in ^{236}U at the same station. Slight temporal changes were also observed for potential temperature and salinity at the shelf stations (Figures S1, S2). In the upper 100 m, salinity generally decreased from 2016 to 2018/19 (Figures S1A-C), whereas potential temperature decreased at station 1 but increased slightly at stations 2 and 3 (Figures S2A-C). At station 1, a significant increase in potential temperature was observed at around 150–200 m depth, accompanied by a slight increase of salinity.

Among the deep stations in central Fram Strait (stations 4-7), no differences in ^{129}I and ^{236}U were observed below 1000 m depth, hence only the upper 1000 m are shown. At station 4, located at the shelf break, similar trends were observed as for the shelf stations, with a decrease of both ^{129}I and ^{236}U in the surface from 2016 to 2018/19 (Figure 4E). In the upper 100 m depth at station 5, slightly higher ^{236}U concentrations were observed for 2018 compared to 2016 and 2019 (Figure 4F).

In contrast to all other stations, station 6 showed significant differences between 2016/18 and 2019, related to the previously mentioned shift of the interface between in- and outflowing waters in the surface layer (observed in Θ , salinity, and ^{236}U, see Figure 3). In 2019, the upper 200 m were characterized by significantly higher ^{236}U concentrations compared to 2016 and 2018 (Figure 4). No ^{129}I concentrations are available for 2018 and 2019, but both potential temperature and salinity decreased significantly from 2018 to 2019 at the same depths (Figures S1F and S2F). Overall, the profiles of ^{236}U, Θ , and salinity at station 6 in 2019 rather resembled those of station 5 (Figures S1E and S2E), whereas in 2016 and 2018, station 6 appeared similar to station 7 (Figures S1G, S2G). The zig-zag structure observed in ^{236}U and also in Θ in the upper 50 m of station 6 in 2018 might also hint at a mixture of in- and outflowing waters in the upper water column. At around 500 m depth, a slightly higher ^{236}U concentration was found in 2016.

Further to the east, at station 7, only a slight decrease of ^{236}U concentrations from 2016 to 2018/19 was observed in the upper water column, accompanied by a significant increase in potential temperature and salinity (Figures S1G, S2G). At station 8, comprising inflowing Atlantic Water, no significant changes were observed in ^{236}U throughout the water column, whereas potential temperature and salinity decreased at the surface (Figures S1H, S2H).

Overall, the comparison of profiles from matching stations between 2016, 2018 and 2019 confirmed that the greatest temporal changes in ^{236}U concentrations were observed in the upper water column in samples classified as PSW, especially in stations on the north-east Greenland shelf. Changes in ^{236}U were accompanied by changes in available ^{129}I and partly also by changes in potential temperature and salinity.

4 Discussion

Generally, the observed temporal changes in ^{236}U and ^{129}I across Fram Strait could have been caused by two processes that shall be discussed in the following:

(i) The transient nature of ^{129}I and ^{236}U, i.e., temporally changing inputs of both radionuclides into the Arctic Ocean (Figure 2). This naturally leads to changes in their distribution across the Arctic Ocean and Fram Strait over time as shown in earlier time-series studies on ^{129}I (e.g., Smith et al., 2011).

(ii) Changes in the water mass composition of the EGC as a consequence of upstream circulation changes. This leads to changes in ^{129}I and ^{236}U across Fram Strait due to mixing of water masses carrying different tracer signals, such as changing fractions of Pacific- and Atlantic-origin waters.

4.1 Temporal changes of ^{236}U and ^{129}I as a consequence of their time-dependent input functions

To account for the transient nature of ^{129}I and ^{236}U (process (i)), the temporal variability in their input to the Arctic Ocean (Figure 2) needs be projected to the sampling location and time, i.e., Fram Strait in 2018 and 2019. This projection requires knowledge of the travel time of water from the initialization point of the input function (Barents Sea opening; Casacuberta et al. (2018); Wefing et al. (2021)) to the sampling location.

One approach to estimate travel times are "tracer ages" derived from the combination of ^{129}I and ^{236}U in a simple binary mixing model as described in recent studies (Christl et al., 2015b; Wefing et al., 2019; Wefing et al., 2021). Briefly, this binary mixing model is based on the assumption that the flow of Atlantic-derived water in the surface Arctic Ocean is purely advective in the sense that tracer signals from different years of the input function do not mix. Mixing only occurs between Atlantic Water carrying the input function signal from a certain year, and water carrying a constant global fallout signal (in the surface Arctic Ocean, this corresponds to Pacific Water). Both endmembers are plotted in ^{236}U-^{129}I tracer space. Mixing lines constructed between each year of the input function (i.e., the annual input function tracer concentrations, Figure 2) and the global fallout signal permit to define both a tracer age and a dilution factor of the input function tracer signal (further details are given in Wefing et al., 2021).

Since a complete dataset of both tracers was only available for 2016, we applied the binary mixing model to all PSW and PSWw samples from the matching stations from expedition PS100 (a plot of the binary mixing model is shown in Figure S3A). Note that we used the NCC input function for these calculations, hence tracer ages and dilution factors (reported in Table S1) are given relative to tracer concentrations at the Barents Sea Opening. The NCC input function was used to ensure comparability to tracer ages and dilution factors based on PS100 that were already reported in Wefing et al. (2021). Differences between results from this study and from Wefing et al. (2021) are due to the slightly adjusted ^{236}U concentrations (based on the ^{238}U-Salinity relationship, see 4.3).

The calculation of projected ^{129}I and ^{236}U concentrations for 2018 and 2019 is illustrated with the example of a PSW sample in 2016 that has a tracer age of 15 years and a dilution factor of 4. This sample hence carried a mixture of about 25% of the input function signal from 2001 with about 75% of the GF signal. Assuming that the circulation pattern did not change over time, one would hence always expect to find the input function signal of 15 years previous to the sampling year at the sampling location and depth of this sample, diluted with the same fraction of GF water. For the sampling years of 2018 and 2019, one would therefore expect the tracer signal from the input function years of 2003 and 2004, respectively.

The obtained projected ^{129}I and ^{236}U concentrations are depicted in Figure 5, together with the measured profiles from 2018 and 2019. Uncertainties for projected concentrations correspond to the propagated uncertainty of the NCC input function (Figure 2). For depths shallower than 50 m, the projected concentrations largely exceeded the measured ones, both for ^{129}I and ^{236}U. Below, the measured concentrations fell in the projected range, except for station 1 (Figure 5A). At this station, measured ^{129}I and ^{236}U concentrations in 2018 and 2019 reached a maximum at 100 m depth, where they agreed with projected concentrations, and decreased towards greater depths, where ^{129}I fell below the projected ^{129}I concentration.

Overall, the transient nature of ^{129}I and ^{236}U (process (i) above) can hence explain the concentrations measured in 2018 and 2019 for most samples below 50 m depth. In shallower depths and for the deepest PSW samples of station 1, however, the ^{129}I and ^{236}U concentrations were lower than what was expected from the propagation of the input function signal, based on the tracer ages determined for 2016. We therefore conclude that this was due to a change in water mass composition, i.e., process (ii) introduced above.

4.2 Combination of ^{129}I and ^{236}U to investigate changes in the upper EGC water mass composition

For the use of ^{129}I and ^{236}U to investigate changes in the water mass composition, we expanded the previously introduced binary mixing model to include all water masses (i.e., endmembers) expected in the upper EGC. Classically, these were Pacific- and Atlantic-derived water, meteoric water and sea-ice melt (e.g., Dodd et al., 2012; Rabe et al., 2013). For the ^{129}I-^{236}U mixing model, two new aspects need to be addressed:

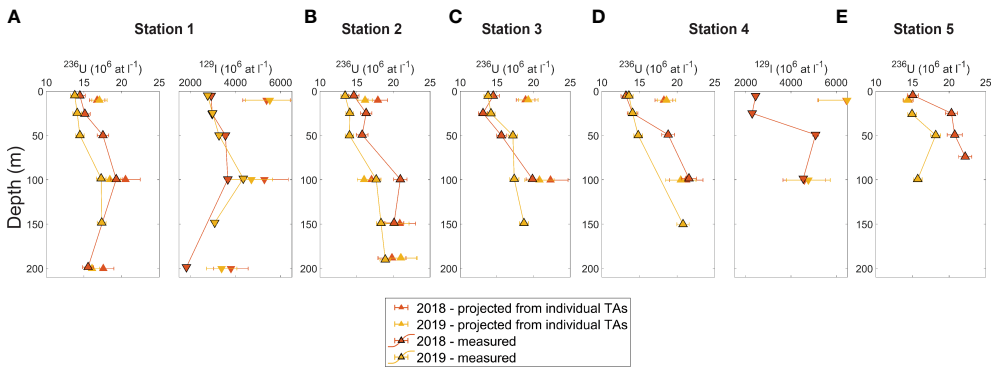

FIGURE 5
(A–E) Profiles of measured (data points with black outline) and projected (data points with no outline) ^{236}U (and ^{129}I for station 1 and 4) at matching stations for 2018 (red) and 2019 (yellow).

(i) There are two different "Atlantic Water" endmembers in the ^{236}U-^{129}I tracer space. Water of Atlantic origin found in the upper EGC has either been advected from the Eurasian Basin surface layer or corresponds to the RAC carrying the recirculated WSC tracer signal. This is of special importance on the north-east Greenland shelf (Figure 4A, station 1), where the presence of RAC has been identified based on potential temperature and salinity characteristics in earlier studies (e.g., Schaffer et al., 2017). ^{129}I and ^{236}U concentrations in Eurasian Basin surface water are related to the NCC input function, whereas the RAC is expected to carry the tracer signal defined for the FSBW input function (Casacuberta et al., 2018). Consequently, the upper water column of the EGC has to be considered as a mixture of five endmembers here: Atlantic-derived water that has circulated through the Eurasian Basin in the Arctic Ocean surface layer (ATL), Pacific-derived water (PAC), meteoric water (MW), sea-ice meltwater (SIM) and recirculating Atlantic Water (RAC) (Table 1). While this generally complicates the quantification of endmember fractions, it also provides a unique advantage of ^{129}I and ^{236}U, namely the possibility to distinguish between the two "Atlantic Water" endmembers. Note that in the following, the term "Atlantic-derived water" (ATL) will be used when referring to the Atlantic-origin waters advected from the Eurasian Basin only. Atlantic Water recirculating in Fram Strait will be referred to as RAC.

To obtain the transient tracer signal for ATL, the NCC input function was diluted 50:50 with the global fallout background signal (Figure S4). This was necessary since Wefing et al. (2021) found that a dilution of about 50% of the NCC input function with global fallout background occurs between the initialization point of the NCC input function (Barents Sea opening) and the surface of the Amundsen Basin. A fraction of about 50% Pacific Water is not very likely to be found in that part of the Arctic Ocean, hence a dilution with Pacific Waters cannot explain the lower concentrations found in the Amundsen Basin compared to the NCC input function. Instead, we suggest that a mixture of the NCC input function with the BSBW or FSBW input function (which carry a higher proportion of global fallout compared to the NCC, Casacuberta et al. (2018)) takes place in the Barents Sea, effectively reducing the ^{129}I and ^{236}U signal transported to the Eurasian Basin surface layer.

(ii) The ATL and RAC endmembers are not constant in time. The transient nature of ^{129}I and ^{236}U in Atlantic Water was used above to determine tracer ages. To asses temporal changes in the contribution of different endmembers in Fram Strait, however, we defined steady-state ATL and RAC endmembers for each sampling year (details are outlined in Supplement S4). A steady-state ATL water endmember was estimated using the mean tracer age of the subset of PSW samples from 2016 (15±4 years). Tracer ages determined from the few available combined ^{129}I and ^{236}U samples from 2018 and 2019 were in a similar range as those for 2016 (Figures S3B, C), hence we decided to use the same mean tracer age for all three years. A mean ATL concentration was then calculated taking the range of mean tracer age ± standard deviation and averaging over the corresponding years of the time-dependent ATL endmember defined above. Note that the result is different for each sampling year, since the mean tracer age is subtracted from the respective sampling year. Details are outlined in Supplement S4. To estimate an uncertainty range of the steady-state ATL endmember, we used the minimum and maximum tracer age from 2016 to obtain minimum and maximum estimates of the ATL concentration (see Table 1 and Supplement S4). For the RAC endmember, ^{129}I and ^{236}U concentrations from the FSBW input function defined in Casacuberta et al. (2018) of the corresponding sampling year were used (see Table 1 and Supplement S5).

For each sampling year, the endmembers outlined above were plotted in ^{236}U vs. ^{129}I tracer space with PSW data on top,

TABLE 1 Endmembers and corresponding salinity, ^{129}I, and ^{236}U concentration used in steady-state mixing models for PSW samples.

Endmember	Acronym	Salinity	^{129}I (10^6 at $\cdot L^{-1}$)	^{236}U (10^6 at $\cdot L^{-1}$)
Atlantic-derived water (Eurasian Basin)	ATL	32.8[a]	2016: (9200^{+1600}_{-2500})[b]	2016: $(29.8^{+5.6}_{-10.5})$[b]
			2018: (9400^{+1400}_{-2300})[b]	2018: $(27.3^{+8.1}_{-10.1})$[b]
			2019: (9300^{+1500}_{-2200})[b]	2019: $(26.0^{+9.4}_{-9.0})$[b]
Return Atlantic Current	RAC	34.9[g]	2016: (2600 ± 200)[c]	2016: (2600 ± 200)[c]
			2018: (2900 ± 100)[c]	2018: (12.0 ± 0.1)[c]
			2019: (2900 ± 100)[c]	2019: (12.1 ± 0.1)[c]
Pacific Water	PAC	32[g]	10[d]	10[d]
Meteoric water	MW	0[g]	83[e]	11.7[e]
Sea-ice meltwater	SIM	4[g]	427[f]	1.1[f]

[a]average salinity from Amundsen Basin PSW samples collected in 2015 (Casacuberta et al., 2018).
[b]see Supplement S4.
[c]see Supplement S5.
[d]global fallout (Casacuberta et al., 2016; Wefing et al., 2021).
[e]average of samples from Lena river collected in 2014 (Casacuberta et al., 2016).
[f]average of Arctic Ocean sea-ice samples collected in 2015 (Casacuberta et al., 2018).
[g]taken from Dodd et al. (2012).

color-coded by potential density (Figure 6). The ATL endmember was characterized by highest concentrations of both radionuclides. The RAC endmember carried significantly higher ^{129}I concentrations compared to the PAC endmember but similar ^{236}U concentrations as PAC. For the SIM endmember, we used an average of all sea-ice data presented in Casacuberta et al. (2018), which was characterized by low ^{129}I and ^{236}U concentrations. The MW endmember in principle includes both river water and glacial melt, but ^{129}I and ^{236}U data was only available for the Lena river draining into the Kara Sea (Casacuberta et al., 2016). Note that the temporal variability of this data is not known. As a best guess, we therefore used an average of all river data from Casacuberta et al., 2016, which plotted close to the PAC endmember.

Samples with low potential densities (σ_Θ<26.5) largely fell on or close to the PAC-ATL mixing line for 2018 and 2019 and partly below in 2016 (Figure 6). The sample with lowest ^{236}U concentration in 2016 (Figure 6A, st. 5), plotting significantly below the PAC-ATL mixing line, had a lower tracer age compared to the other samples and was hence in line with more recent years of the input function (indicated by the gray arrow in Figure 6A; more recent years were characterized by lower ^{236}U concentrations). Samples with higher densities generally plotted above the ATL-PAC mixing line, implying higher ^{236}U concentrations (and relatively lower ^{129}I) than expected. They rather fell on mixing lines of PAC with earlier years of the ATL input function (earlier years were characterized by higher ^{236}U concentrations). This was in agreement with an

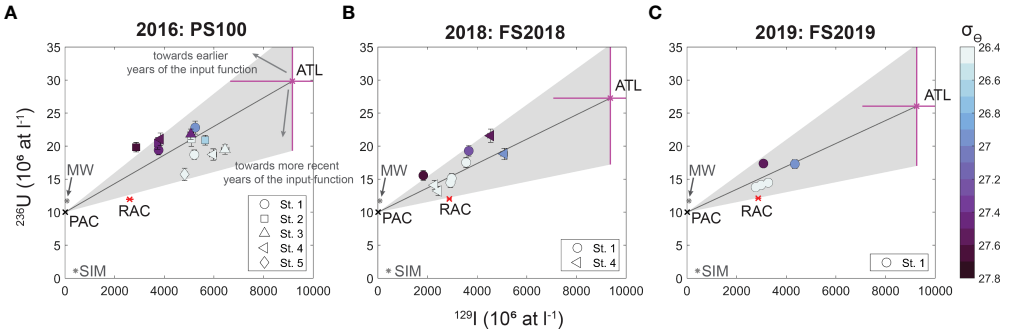

FIGURE 6
^{236}U-^{129}I steady state mixing models for 2016 **(A)**, 2018 **(B)**, 2019 **(C)**. For the ATL endmember, the magenta symbol shows the mean, error bars correspond to a minimum and maximum estimate to account for the transient nature of the ATL input function (see Table 1 and Supplement S4). The gray area illustrates the range of PAC-ATL mixing lines including this uncertainty. PSW samples from matching stations between the three sampling years (Figure 4A) are plotted on top, color coded by potential density (σ_Θ). Different symbols refer to different stations. Acronyms are explained in Table 1.

increase of tracer ages with depth, i.e., the presence of older components of the ATL input function (see Supplement Table S1). Overall, almost all samples fell in the range spanned by the uncertainties of the ATL endmember defined above. From 2016 to 2019, an overall decrease of ^{129}I and ^{236}U concentrations was observed in the mixing plots. This translates to a shift of all samples towards the PAC and RAC endmember, implying a decrease in the ATL fraction over time (Figure 6).

The combination of ^{129}I and ^{236}U is a powerful tracer pair to distinguish PAC and ATL, i.e., Pacific-and Atlantic origin waters advected from the Arctic Ocean, as already shown in earlier studies (Casacuberta et al., 2016; Wefing et al., 2021). With the presence of RAC in Fram Strait, however, this tracer pair alone cannot distinguish if the decrease in the ATL fraction was counterbalanced by an increased proportion of the PAC, or the RAC endmember. The latter plots close to the PAC-ATL mixing line in ^{236}U-^{129}I tracer space. The fact that ^{236}U and ^{129}I showed similar trends for the three endmembers (PAC, ATL, RAC) implies that the combination of both does not significantly improve the endmember differentiation compared to using either ^{129}I or ^{236}U alone. Instead, the combined use of one radionuclide with another tracer having different endmember values for PAC and RAC, such as salinity, could provide more insights. In earlier studies on the Arctic Ocean, salinity was mainly used together with δ^{18}O to distinguish saline (i.e., PAC or ATL) waters from MW and SIM (e.g., Yamamoto-Kawai et al., 2008). Here we use it together with ^{236}U and ^{129}I, respectively, to differentiate PAC from RAC.

4.3 Combination of salinity with ^{236}U and ^{129}I to quantify water mass fractions

The endmembers discussed above were hence plotted in ^{236}U vs. salinity (Figures 7A-C) and ^{129}I vs. salinity (Figures 7D-F) tracer space, overlaid by the PSW data. Note the higher number of ^{236}U data points compared to ^{129}I. Mixing lines connect PAC, ATL, and RAC. For ATL, the mean salinity determined from the Amundsen Basin surface samples collected in 2015 was used as the endmember value, salinities of the other endmembers were taken from Dodd et al. (2012) (see Table 1). In the mixing plot, PAC and RAC were well distinguished by salinity, whereas ^{236}U or ^{129}I served to distinguish ATL from both. Dilution with the MW and SIM endmembers, both characterized by very low salinities, was indicated with mixing lines from PAC and ATL.

Samples with lowest potential densities (σ_Θ<26.5) had low salinities and largely plotted left of the ATL-PAC mixing line for all sampling years and for both tracer combinations (Figure 7). This was probably caused by a dilution with SIM and/or MW. SIM and MW fractions calculated from available salinity and δ^{18}O data for 2016 ranged up to −10% and 15%, respectively (the negative fractions imply upstream formation of sea-ice; see

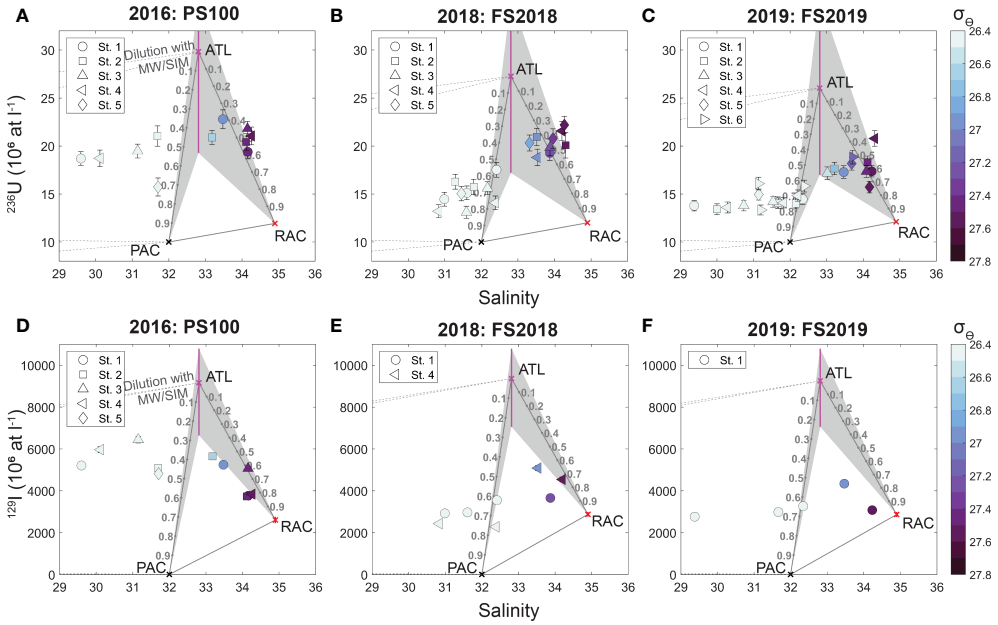

FIGURE 7
^{236}U-Salinity **(A–C)** and ^{129}I-Salinity **(D–F)** steady state mixing models for 2016, 2018, 2019. PSW samples from matching stations between the three sampling years (Figure 4A) are plotted on top, color coded by potential density (σ_Θ). Numbers along the PAC-ATL and RAC-ATL mixing lines denote fractions of PAC and RAC waters, respectively. Note the better data coverage for ^{236}U compared to ^{129}I. Different symbols refer to different stations. Acronyms are explained in Table 1.

Supplement S6). Although the low-density samples did not plot directly on the PAC-ATL mixing line, rough estimates for their PAC (or ATL) fractions could still be obtained. ^{236}U-salinity and ^{129}I-salinity mixing plots for each year largely showed a similar range for these samples. In 2016, Pacific Water fractions ranged between 30-70% (Figures 7A–D) and increased to about 60-90% in 2018 and 2019 (Figures 7B–F). The combination of ^{236}U or ^{129}I with salinity hence pointed to an increase in the PAC fraction in the uppermost layer of the EGC from 2016 to 2018/19 of about 20%.

For samples with higher densities (σ_Θ>26.5), the ^{236}U-salinity and ^{129}I-salinity mixing plots showed different fractions. In the former, samples plotted closer to the ATL endmember for all sampling years (Figures 7A–C). In the ^{129}I-salinity mixing plot, the same samples plotted close to the RAC endmember instead, implying only very low fractions of ATL (Figures 7D–F). In ^{236}U-salinity space, highest-density PSW samples (σ_Θ>27) plotted right of the ATL-RAC mixing line and partly also outside the uncertainty band. This points to an inaccurate definition of the ATL or RAC endmember, suggesting that both or one of the two are in fact characterized by higher ^{236}U concentrations. In contrast, in the ^{129}I-salinity mixing plot, almost all samples with σ_Θ>26.5 plotted inside the domain (Figures 7D–F), pointing to a reasonable definition of the endmembers. RAC fractions estimated from the ^{129}I-salinity combination reached up to 90% for some samples, suggesting almost no ATL. If these fractions are valid is difficult to assess, since we are not aware of any other tracer to estimate RAC fractions in the western Fram Strait.

The significant differences observed between the tracer combinations for dense samples in PSW suggest that the definition of the RAC and/or ATL endmembers have to be improved. Especially the ATL endmember is difficult to assess due to the transient tracer signal and the long travel times of waters from the Barents Sea Opening, where the NCC tracer input function was defined, through the Arctic Ocean to Fram Strait. Generally, the fact that samples largely plot inside the domain for the ^{129}I-salinity combination indicates that the ^{129}I endmember values are more reliable compared to ^{236}U. This might be due to the GF background signal for ^{236}U, which is not of concern for ^{129}I. In addition, the dynamic range between RAC and ATL is larger for ^{129}I compared to ^{236}U.

Despite the inaccuracy in the RAC and ATL endmembers and the inconsistency between absolute fractions derived from ^{236}U or ^{129}I, the observed temporal trends in ATL vs. RAC fractions of dense PSW samples were similar for both. From 2016 to 2018/19, a slight increase in the RAC fraction of about 10-20% was evident. For denser PSW (σ_Θ>26.5), the combination of ^{236}U or ^{129}I with salinity hence pointed to an increase in the RAC fraction from 2016 to 2018/19, counterbalancing a decrease in ATL.

4.4 Comparison to earlier studies

The combination of ^{129}I, ^{236}U, and hydrographic data revealed changes in the water mass composition of the EGC between 2016 and 2019, which could likely be attributed to an increase in the Pacific Water fraction in shallow (low-density) samples as well as an increase in recirculating Atlantic Water below. Significant year-to-year variations in Pacific Water fractions exported through Fram Strait were also observed in earlier studies based on the combination of salinity, δ^{18}O, and nutrient measurements (Falck et al., 2005; Dodd et al., 2012). Although the reliability of quantifying absolute Atlantic and Pacific Water fractions based on nitrate-to-phosphate ratios is under debate (e.g., Alkire et al., 2019), time series of tracer measurements still provide insights into the temporal variability of different water mass fractions. For the years of available ^{129}I and ^{236}U data, δ^{18}O, nitrate, and phosphate measurements are only available for 2016, hence we cannot compare the temporal trends observed in ^{129}I and ^{236}U to nutrient-based estimates.

Changes in freshwater transport through Fram Strait were also derived from a mooring array in the EGC at about 79° N, which allows for a continuous monitoring of salinity and velocity. Between 1977 and 2015, significant variations in freshwater transport were observed (de Steur et al., 2018). Since 2015, freshwater transport in the EGC has been decreasing, which was related to a salinification of lower halocline waters counterbalancing a freshening of the top layer (Karpouzoglou et al., 2022). Based on the mooring data alone, it could not be determined if this "Atlantification" of the western Fram Strait was caused by an increase in Atlantic Water recirculation or in advection of Atlantic-origin waters from the Eurasian Basin. The temporal changes observed in ^{129}I and ^{236}U concentration presented here, combined salinity, clearly point to an increase in recirculation (i.e., the RAC endmember), instead of more Eurasian Basin waters (i.e., ATL), especially for station 1 in Norske Trough. Since increased recirculation was not directly observed in the mooring data (Karpouzoglou et al., 2022), it most likely occurred north of the section considered here.

The water mass composition in the EGC is closely linked to the upstream ocean dynamics (e.g., Dodd et al., 2012; Rabe et al., 2013), hence changes observed in outflowing waters in Fram Strait relate to changes in the Arctic Ocean circulation pattern. This includes the variability of Pacific Water advection pathways, freshwater build-up within, and release from, the Beaufort Gyre, as well as variability in the advection of river water. Karpouzoglou et al. (2022) reported on a direct correlation between Beaufort Gyre freshwater content and southward freshwater transport through Fram Strait between 2003 and 2019. It has also been suggested that these changes are at least partly related to the state of atmospheric circulation,

classically characterized by the Arctic Oscillation (AO) index (e.g., Morison et al., 2012). This finding was supported by the eastward shift of the PSW-AW interface (i.e., in- and outflowing waters) between 2018 and 2019, that was observed in the data presented here. Taking the eastward extension of the 15×10^6 at·L^{-1} ^{236}U isoline as a measure of the PSW extent, the interface shifted by about 3° in longitude in the surface layer (about 0–100 m depth), whereas deeper layers did not change significantly (Figures 3J–L). A possible explanation is the faster response of the surface layer to changes in atmospheric circulation patterns while deeper layers were less affected. The shift in the surface layer was also observed in hydrographic data, however, for deeper layers the ^{236}U concentration provided a more reliable measure of the eastward extent of Arctic-derived waters.

4.5 Strengths and limitations of the ^{129}I-^{236}U tracer pair to determine water mass composition in Fram Strait

The ^{129}I-^{236}U tracer pair is a novel approach for the quantification of water mass fractions exiting Fram Strait in the EGC, which provided promising results in the pilot study presented here. However, some limitations of this approach should be taken into account. A weakness of both radionuclides regarding their use as water mass composition tracers lies in their time-dependent Atlantic Water input function. For the steady-state mixing models presented here, the ATL endmember was estimated taking the upstream circulation processes into account. This can be achieved by using both tracers for an estimation of circulation times and dilution processes that alter the tracer signal of the input function. In this regard, a better understanding of the evolution of Atlantic Waters during their passage through the Arctic Ocean would be beneficial, which could be achieved through an intensified sampling program including ^{129}I and ^{236}U, as well as the incorporation of both tracers into circulation models as in Karcher et al. (2012) and Smith et al. (2021).

Since the ^{129}I and ^{236}U endmembers of MW and SIM are not well constrained, the effect of dilution with those waters was not investigated in detail here. Especially for samples close to Greenland, dilution with glacial meltwater probably plays a more important role. When considering the temporal changes in the water mass composition between 2016 and 2019, however, the influence of MW and SIM is negligible since it affects samples from all years and is not expected to have changed significantly during this timeframe.

In contrast to other tracers used to distinguish Atlantic- and Pacific-origin components in Arctic Ocean surface waters (e.g., N:P ratios, NO*, Gallium), ^{129}I and ^{236}U tracer signals are different for recirculating Atlantic Waters in Fram Strait and those advected from the Eurasian Basin. On one hand, this complicates the quantification of water mass fractions in the EGC, since it introduces another endmember compared to classical approaches. However, it also provides the opportunity to differentiate both Atlantic-derived waters. Differentiating the origin of waters in the EGC is important to understand the dynamics behind the "Atlantification" of the western Fram Strait (Karpouzoglou et al., 2022). An increase in recirculating waters can lead to increased heat transport towards the Greenland shelf, where it impacts glacial melt processes (Schaffer et al., 2017), or increased southward heat transport towards the sub-polar North Atlantic. Changes in the origin of Atlantic Waters will likely also impact nutrient dynamics and primary production in the EGC (Tuerena et al., 2021).

5 Conclusions

We presented a time-series of ^{129}I and ^{236}U measurements from Fram Strait, covering the years 2016, 2018, and 2019. The combination of both radionuclides was used together with hydrographic data to identify and investigate changes in the water mass composition of the upper EGC. The overall distribution of both radionuclides was similar among all three years, clearly highlighting differences in ^{129}I and ^{236}U concentrations between inflowing Atlantic Water and outflowing Arctic Water, as well as differences between the surface layer and the mid-depth Atlantic layer. In the upper water column of the EGC, composed of PSW, temporal variations were observed. Especially between 2016 and 2018, ^{129}I and ^{236}U concentrations in the upper 100 m depth decreased substantially.

^{129}I-^{236}U-based tracer ages from the entrance to the Arctic Ocean to Fram Strait were estimated to account for the transient nature of the input functions of both tracers. We concluded that the observed changes in the upper 50 m of PSW between 2016 and 2019 could not be attributed to changes in the input function alone, but were caused by a change in the water mass composition of the EGC. ^{129}I and ^{236}U were therefore combined in a steady-state mixing model in order to investigate the proportions of Pacific and Atlantic-derived waters in both sampling years. It was found that both radionuclides alone do not serve to estimate Pacific Water fractions in Fram Strait due to the presence of recirculating Atlantic Water, which carries a similar tracer signal. Using the combination of ^{129}I and ^{236}U with salinity instead, we found an increase in Pacific Water in shallow PSW samples between 2016 and 2019. At the same time, an increase in recirculating Atlantic Water was observed for samples below. The fraction of Atlantic Waters advected from the Eurasian Basin decreased over time in all PSW samples.

The Arctic region is already undergoing major changes as a consequence of anthropogenic climate change, which are only expected to become even more severe in the future. Changes in the freshwater budget and freshwater export to the North

Atlantic *via* the EGC might have a substantial impact on the Atlantic Meridional Overturning Circulation. ^{129}I and ^{236}U proved to be useful tracers for the origin of waters exported through Fram Strait. In the future, combining anthropogenic radionuclides with other water mass tracers that are emerging as an alternative to nutrient relationships, such as dissolved Gallium or Nd isotopes (Whitmore et al., 2020; Paffrath et al., 2021), could help to further disentangle water masses. This requires a coordinated sampling effort during upcoming expeditions, as well as specifically targeting the endmembers of ^{129}I and ^{236}U. Generally, the use of ^{129}I and ^{236}U to quantify water masses is expected to become less complicated further upstream, in the central Arctic Ocean, closer to the source region of both tracers.

Data availability statement

The original datasets presented in this study can be found in the Supplementary Material (Table S1).

Author contributions

A-MW and NC contributed to conception and design of the study. A-MW performed investigation, formal analysis, and wrote the original draft of the manuscript. MC and NC performed AMS measurements and supported investigation and formal analysis. NC supervised the study and acquired funding. PD supported sample collection during expeditions FS2018 and FS2019 and provided hydrographic data. All authors contributed to manuscript revision and approved the submitted version.

Funding

Anne-Marie Wefing received funding from the ETH Doctoral Grant ETH-06 16-1 "Combining U-236 with other multi-sourced anthropogenic tracers as a new tool to study ocean circulation". Núria Casacuberta's research was supported by the Swiss National Science Foundation (AMBIZIONE PZ00P2_154805 and PRIMA PR00P2_193091), the European Research Council (ERC) under the European Union's Horizon 2020 research and innovation programme (Grant agreement No. GAP-101001451), and the Laboratory of Ion Beam Physics at ETH Zurich, which is partially funded by its consortium partners EAWAG, EMPA and PSI. Statement: Open access funding provided by ETH Zurich

Acknowledgments

The authors acknowledge captain and crew of the RV Kronprins Haakon as well as all people involved in the sampling activities across Fram Strait. Special thanks go to Christof Vockenhuber for support with ^{129}I measurements. This publication was adapted from Chapter 5 of the doctoral thesis by A-MW (Wefing, 2021).

Conflict of interest

The authors declare that the research was conducted in the absence of any commercial or financial relationships that could be construed as a potential conflict of interest.

Publisher's note

Supplementary material

The Supplementary Material for this article can be found online at: https://www.frontiersin.org/articles/10.3389/fmars.2022.973507/full#supplementary-material

References

Alkire, M. B., Morison, J., and Andersen, R. (2015). Variability in the meteoric water, sea-ice melt, and pacific water contributions to the central Arctic ocean 2000-2014. *J. Geophysical Research: Oceans* 120, 1573–1598. doi: 10.1002/2014JC010023

Alkire, M. B., Rember, R., and Polyakov, I. (2019). Discrepancy in the identification of the Atlantic/Pacific front in the central Arctic ocean: NO versus nutrient relationships. *Geophys. Res. Lett.* 46, 3843–3852. doi: 10.1029/2018GL081837

Arndt, J. E., Jokat, W., Dorschel, B., Myklebust, R., Dowdeswell, J. A., and Evans, J. (2015). A new bathymetry of the northeast Greenland continental shelf: Constraints on glacial and other processes. *Geochem. Geophys. Geosyst.* 16, 3733–3753. doi: 10.1002/2015GC005931

Årthun, M., Eldevik, T., and Smedsrud, L. H. (2019). The role of Atlantic heat transport in future Arctic winter Sea ice loss. *J. Climate* 32, 3327–3341. doi: 10.1175/JCLI-D-18-0750.1

Bauch, D., van der Loeff, M. R., Andersen, N., Torres-Valdes, S., Bakker, K., and Abrahamsen, E. P. (2011). Origin of freshwater and polynya water in the Arctic ocean halocline in summer 2007. *Prog. Oceanography* 91, 482–495. doi: 10.1016/j.pocean.2011.07.017

Beszczynska-Möller, A., Woodgate, R., Lee, C., Melling, H., and Karcher, M. (2011). A synthesis of exchanges through the main oceanic gateways to the Arctic ocean. *Oceanography* 24, 82–99. doi: 10.5670/oceanog.2011.59

Casacuberta, N., Christl, M., Vockenhuber, C., Wefing, A.-M., Wacker, L., Masqué, P., et al. (2018). Tracing the three Atlantic branches entering the Arctic ocean with 129I and 236U. *J. Geophysical Research: Oceans* 123, 6909–6921. doi: 10.1016/j.epsl.2016.02.020

Casacuberta, N., Masqué, P. G., Henderson, M., Rutgers van-der-Loeff, D., Bauch, C., Vockenhuber, A., et al (2016). First 236U Data from the Arctic Ocean and Use of 236U/238U and 129I/236U as a New Dual Tracer. *Earth and Planetary Science Letters* 440, 127–34. doi: 10.1016/j.epsl.2016.02.020

Christl, M., Casacuberta, N., Lachner, J., Maxeiner, S., Vockenhuber, C., Synal, H.-A., et al. (2015a). Status of 236U analyses at ETH Zurich and the distribution of 236U and 129I in the north Sea in 2009. *Nucl. Instruments Methods Phys. Res. Section B: Beam Interact. Materials Atoms* 361, 510–516. doi: 10.1016/j.nimb.2015.01.005

Christl, M., Casacuberta, N., Vockenhuber, C., Elsässer, C., Bailly du Bois, P., Herrmann, J., et al. (2015b). Reconstruction of the 236U input function for the northeast Atlantic ocean: Implications for 129I/236U and 236U/238U-based tracer ages. *J. Geophysical Research: Oceans* 120, 7282–7299. doi: 10.1002/2015JC011116

de Steur, L., Hansen, E., Mauritzen, C., Beszczynska-Möller, A., and Fahrbach, E. (2014). Impact of recirculation on the East Greenland current in fram strait: Results from moored current meter measurements between 1997 and 2009. *Deep Sea Res. Part I: Oceanographic Res. Papers* 92, 26–40. doi: 10.1016/j.dsr.2014.05.018

de Steur, L., Peralta-Ferriz, C., and Pavlova, O. (2018). Freshwater export in the East Greenland current freshens the north Atlantic. *Geophys. Res. Lett.* 45, 13,359–13,366. doi: 10.1029/2018GL080207

de Steur, L., Pickart, R. S., Macrander, A., Våge, K., Harden, B., Jónsson, S., et al. (2017). Liquid freshwater transport estimates from the East Greenland current based on continuous measurements north of Denmark strait. *J. Geophys. Res. Oceans* 122, 93–109. doi: 10.1002/2016JC012106

de Steur, L., Pickart, R. S., Torres, D. J., and Valdimarsson, H. (2015). Recent changes in the freshwater composition east of Greenland. *Geophys. Res. Lett.* 42, 2326–2332. doi: 10.1002/2014GL062759

Dodd, P. A., Heywood, K. J., Meredith, M. P., Naveira-Garabato, A. C., Marca, A. D., and Falkner, K. K. (2009). Sources and fate of freshwater exported in the East Greenland current. *Geophysical Res. Lett.* 36, L19608. doi: 10.1029/2009GL039663

Dodd, P. A., Rabe, B., Hansen, E., Falck, E., Mackensen, A., Rohling, E., et al. (2012). The freshwater composition of the fram strait outflow derived from a decade of tracer measurements. *J. Geophysical Research: Oceans* 117, C11005. doi: 10.1029/2012JC008011

Edmonds, H. N., Zhou, Z. Q., Raisbeck, G. M., Yiou, F., Kilius, L., and Edmond, J. M. (2001). Distribution and behavior of anthropogenic 129I in water masses ventilating the north Atlantic ocean. *J. Geophysical Research: Oceans* 106, 6881–6894. doi: 10.1029/1999JC000282

Ekwurzel, B., Schlosser, P., Mortlock, R. A., Fairbanks, R. G., and Swift, J. H. (2001). River runoff, sea ice meltwater, and pacific water distribution and mean residence times in the Arctic ocean. *J. Geophysical Research: Oceans* 106, 9075–9092. doi: 10.1029/1999JC000024

Falck, E., Kattner, G., and Budéus, G. (2005). Disappearance of pacific water in the northwestern fram strait. *Geophysical Res. Lett.* 32, L14619. doi: 10.1029/2005GL023400

Forryan, A., Bacon, S., Tsubouchi, T., Torres-Valdés, S., and Naveira Garabato, A. C. (2019). Arctic Freshwater fluxes: Sources, tracer budgets and inconsistencies. *Cryosphere* 13, 2111–2131. doi: 10.5194/tc-13-2111-2019

Gascard, J.-C., Raisbeck, G., Sequeira, S., Yiou, F., and Mork, K. A. (2004). The Norwegian Atlantic current in the lofoten basin inferred from hydrological and tracer data (129I) and its interaction with the Norwegian coastal current. *Geophysical Res. Lett.* 31, L01308. doi: 10.1029/2003GL018303

Haine, T. W., Curry, B., Gerdes, R., Hansen, E., Karcher, M., Lee, C., et al. (2015). Arctic Freshwater export: Status, mechanisms, and prospects. *Global Planetary Change* 125, 13–35. doi: 10.1016/j.gloplacha.2014.11.013

Hattermann, T., Isachsen, P. E., von Appen, W.-J., Albretsen, J., and Sundfjord, A. (2016). Eddy-driven recirculation of Atlantic water in fram strait. *Geophysical Res. Lett.* 43, 3406–3414. doi: 10.1002/2016GL068323

Håvik, L., Pickart, R. S., Våge, K., Torres, D., Thurnherr, A. M., Beszczynska-Möller, A., et al. (2017). Evolution of the East Greenland current from fram strait to Denmark strait: Synoptic measurements from summer 2012. *J. Geophysical Research: Oceans* 122, 1974–1994. doi: 10.1002/2016JC012228

Holliday, N. P., Bersch, M., Berx, B., Chafik, L., Cunningham, S., Florindo-López, C., et al. (2020). Ocean circulation causes the largest freshening event for 120 years in eastern subpolar north Atlantic. *Nat. Commun.* 11, 585. doi: 10.1038/s41467-020-14474-y

Jones, E. P., Anderson, L. G., Jutterström, S., Mintrop, L., and Swift, J. H. (2008b). Pacific freshwater, river water and sea ice meltwater across Arctic ocean basins: Results from the 2005 beringia expedition. *J. Geophys. Res.* 113, C08012. doi: 10.1029/2007JC004124

Jones, E., Anderson, L., Jutterström, S., and Swift, J. (2008a). Sources and distribution of fresh water in the East Greenland current. *Prog. Oceanography* 78, 37–44. doi: 10.1016/j.pocean.2007.06.003

Kanzow, T. (2017). "The expedition PS100 of the research vessel POLARSTERN to the fram strait in 2016," in *Reports on polar and marine research* (Bremerhaven: Alfred-Wegener-Institut).

Kanzow, T., von Appen, W.-J., Schaffer, J., Köhn, E., Tsubouchi, T., Wilson, N., et al. (2017). *Physical oceanography measured on water bottle samples from CTD/Large volume Watersampler-system during POLARSTERN cruise PS100 (ARK-XXX/2)*. Bremerhaven, PANGAEA: Alfred Wegener Institute, Helmholtz Centre for Polar and Marine Research. doi: 10.1594/PANGAEA.871028

Karcher, M., Smith, J. N., Kauker, F., Gerdes, R., and Smethie, W. M. (2012). Recent changes in Arctic ocean circulation revealed by iodine-129 observations and modeling. *J. Geophysical Research: Oceans* 117, C08007. doi: 10.1029/2011JC007513

Karpouzoglou, T., de Steur, L., Smedsrud, L. H., and Sumata, H. (2022). Observed changes in the Arctic freshwater outflow in fram strait. *J. Geophysical Research: Oceans* 127, e2021JC018122. doi: 10.1029/2021JC018122

Kawasaki, T., and Hasumi, H. (2016). The inflow of Atlantic water at the fram strait and its interannual variability. *J. Geophysical Research: Oceans* 121, 502–519. doi: 10.1002/2015JC011375

Laukert, G., Frank, M., Bauch, D., Hathorne, E. C., Rabe, B., von Appen, W.-J., et al. (2017). Ocean circulation and freshwater pathways in the Arctic Mediterranean based on a combined Nd isotope, REE and oxygen isotope section across fram strait. *Geochimica Cosmochimica Acta* 202, 285–309. doi: 10.1016/j.gca.2016.12.028

Marnela, M., Rudels, B., Houssais, M.-N., Beszczynska-Möller, A., and Eriksson, P. B. (2013). Recirculation in the fram strait and transports of water in and north of the fram strait derived from CTD data. *Ocean Sci.* 9, 499–519. doi: 10.5194/os-9-499-2013

Morison, J., Kwok, R., Peralta-Ferriz, C., Alkire, M., Rigor, I., Andersen, R., et al. (2012). Changing Arctic ocean freshwater pathways. *Nature* 481, 66–70. doi: 10.1038/nature10705

Muilwijk, M., Smedsrud, L. H., Ilicak, M., and Drange, H. (2018). Atlantic Water heat transport variability in the 20th century Arctic ocean from a global ocean model and observations. *J. Geophys. Res. Oceans* 123, 8159–8179. doi: 10.1029/2018JC014327

Münchow, A., Schaffer, J., and Kanzow, T. (2020). Ocean circulation connecting fram strait to glaciers off northeast Greenland: Mean flows, topographic rossby waves, and their forcing. *J. Phys. Oceanogr.* 50, 509–530. doi: 10.1175/JPO-D-19-0085.1

Newton, R., Schlosser, P., Mortlock, R., Swift, J., and MacDonald, R. (2013). Canadian Basin freshwater sources and changes: Results from the 2005 Arctic ocean section. *J. Geophys. Res. Oceans* 118, 2133–2154. doi: 10.1002/jgrc.20101

Owens, S., Buesseler, K., and Sims, K. (2011). Re-evaluating the 238U-salinity relationship in seawater: Implications for the 238U-234Th disequilibrium method. *Mar. Chem.* 127, 31–39. doi: 10.1016/j.marchem.2011.07.005

Paffrath, R., Laukert, G., Bauch, D., Rutgers van der Loeff, M., and Pahnke, K. (2021). Separating individual contributions of major Siberian rivers in the transpolar drift of the Arctic ocean. *Sci. Rep.* 11, 8216. doi: 10.1038/s41598-021-86948-y

Rabe, B., Dodd, P. A., Hansen, E., Falck, E., Schauer, U., Mackensen, A., et al. (2013). Liquid export of Arctic freshwater components through the fram strait 1998–2011. *Ocean Sci.* 9, 91–109. doi: 10.5194/os-9-91-2013

Rahmstorf, S., Box, J. E., Feulner, G., Mann, M. E., Robinson, A., Rutherford, S., et al. (2015). Exceptional twentieth-century slowdown in Atlantic ocean overturning circulation. *Nat. Clim Change* 5, 475–480. doi: 10.1038/nclimate2554

Richter, M. E., von Appen, W.-J., and Wekerle, C. (2018). Does the East Greenland current exist in the northern fram strait? *Ocean Sci.* 14, 1147–1165. doi: 10.5194/os-14-1147-2018

Rudels, B., Anderson, L., Eriksson, P., Fahrbach, E., Jakobsson, M., Jones, E. P., et al. (2012). "Observations in the ocean," in *Arctic Climate change*, vol. vol. 43 . Eds. P. Lemke and H.-W. Jacobi (Dordrecht: Springer Netherlands), 117–198.

Rudels, B., Björk, G., Nilsson, J., Winsor, P., Lake, I., and Nohr, C. (2005). The interaction between waters from the Arctic ocean and the Nordic seas north of fram strait and along the East Greenland current: Results from the Arctic ocean-02 oden expedition. *J. Mar. Syst.* 55, 1–30. doi: 10.1016/j.jmarsys.2004.06.008

Schaffer, J., von Appen, W.-J., Dodd, P. A., Hofstede, C., Mayer, C., de Steur, L., et al. (2017). Warm water pathways toward nioghalvfjerdsfjorden glacier, northeast Greenland. *J. Geophys. Res. Oceans* 122, 4004–4020. doi: 10.1002/2016JC012462

Serreze, M. C., Barrett, A. P., Slater, A. G., Woodgate, R. A., Aagaard, K., Lammers, R. B., et al. (2006). The large-scale freshwater cycle of the Arctic. *J. Geophysical Research: Oceans* 111, C11010. doi: 10.1029/2005JC003424

Smith, J. N., Karcher, M., Casacuberta, N., Williams, W. J., Kenna, T., and Smethie, W. M. (2021). A changing Arctic ocean: How measured and modeled 129I distributions indicate fundamental shifts in circulation between 1994 and 2015. *J. Geophysical Research: Oceans* 126, e2020JC016740. doi: 10.1029/2020JC016740

Smith, J. N., McLaughlin, F. A., Smethie, W. M., Moran, S. B., and Lepore, K. (2011). Iodine-129, 137Cs, and CFC-11 tracer transit time distributions in the Arctic ocean. *J. Geophysical Res.* 116, C04024. doi: 10.1029/2010JC006471

Terhaar, J., Kwiatkowski, L., and Bopp, L. (2020). Emergent constraint on Arctic ocean acidification in the twenty-first century. *Nature* 582, 379–383. doi: 10.1038/s41586-020-2360-3

Timmermans, M.-L., and Marshall, J. (2020). Understanding Arctic ocean circulation: A review of ocean dynamics in a changing climate. *J. Geophys. Res. Oceans* 125, e2018JC014378. doi: 10.1029/2018JC014378

Tuerena, R. E., Hopkins, J., Buchanan, P. J., Ganeshram, R. S., Norman, L., Appen, W.-J., et al. (2021). An Arctic strait of two halves: The changing dynamics of nutrient uptake and limitation across the fram strait. *Global Biogeochemical Cycles* 35, e2021GB006961. doi: 10.1029/2021GB006961

Vockenhuber, C., Casacuberta, N., Christl, M., and Synal, H.-A. (2015). Accelerator mass spectrometry of 129I towards its lower limits. *Nucl. Instruments Methods Phys. Res. Section B: Beam Interact. Materials Atoms* 361, 445–449. doi: 10.1016/j.nimb.2015.01.061

Wang, Q., Wekerle, C., Wang, X., Danilov, S., Koldunov, N., Sein, D., et al. (2020). Intensification of the Atlantic water supply to the Arctic ocean through fram strait induced by Arctic Sea ice decline. *Geophys. Res. Lett.* 47, e2019GL086682. doi: 10.1029/2019GL086682

Wefing, A.-M. (2021). 129I and 236U as a new tracer pair to study water mass circulation in the arctic ocean and fram strait. Ph.D. thesis, ETH Zurich, Zurich. doi: 10.3929/ethz-b-000491713

Wefing, A.-M., Casacuberta, N., Christl, M., Gruber, N., and Smith, J. N. (2021). Circulation timescales of Atlantic water in the Arctic ocean determined from anthropogenic radionuclides. *Ocean Sci.* 17, 111–129. doi: 10.5194/os-17-111-2021

Wefing, A.-M., Christl, M., Vockenhuber, C., Rutgers van der Loeff, M., and Casacuberta, N. (2019). Tracing Atlantic waters using 129I and 236U in the fram strait in 2016. *J. Geophysical Research: Oceans* 124, 882–896. doi: 10.1029/2018JC014399

Wekerle, C., Wang, Q., Danilov, S., Schourup-Kristensen, V., von Appen, W.-J., and Jung, T. (2017). Atlantic Water in the Nordic Sea: Locally eddy-permitting ocean simulation in a global setup. *J. Geophysical Research: Oceans* 122, 914–940. doi: 10.1002/2016JC012121

Whitmore, L. M., Pasqualini, A., Newton, R., and Shiller, A. M. (2020). Gallium: A new tracer of pacific water in the Arctic ocean. *J. Geophys. Res. Oceans* 125, e2019JC015842. doi: 10.1029/2019JC015842

Yamamoto-Kawai, M., McLaughlin, F. A., Carmack, E. C., Nishino, S., and Shimada, K. (2008). Freshwater budget of the Canada basin, Arctic ocean, from salinity, d18O, and nutrients. *J. Geophys. Res.* 113, C01007. doi: 10.1029/2006JC003858

frontiers | Frontiers in Marine Science

TYPE Original Research
PUBLISHED 06 October 2022
DOI 10.3389/fmars.2022.987315

OPEN ACCESS

EDITED BY
Núria Casacuberta,
ETH Zürich, Switzerland

REVIEWED BY
Wei-Koon Lee,
MARA University of Technology, Malaysia
TaeKeun Rho,
Korea Institute of Ocean Science and Technology (KIOST), South Korea

*CORRESPONDENCE
Guebuem Kim
gkim@snu.ac.kr

SPECIALTY SECTION
This article was submitted to Marine Biogeochemistry, a section of the journal Frontiers in Marine Science

RECEIVED 06 July 2022
ACCEPTED 20 September 2022
PUBLISHED 06 October 2022

CITATION
Cho H-M, Han Y, Kim Y-I, Baek C and Kim G (2022) Tracing the depth-dependent changes in organic carbon and nutrient fluxes using high-resolution ^{228}Ra profiles in the upper East Sea (Japan Sea). *Front. Mar. Sci.* 9:987315. doi: 10.3389/fmars.2022.987315

Tracing the depth-dependent changes in organic carbon and nutrient fluxes using high-resolution ^{228}Ra profiles in the upper East Sea (Japan Sea)

Hyung-Mi Cho[1,2], Yongjin Han[1], Young-Il Kim[3], Cheolmin Baek[1] and Guebuem Kim[1]*

[1]School of Earth and Environmental Sciences/RIO, Seoul National University, Seoul, South Korea, [2]Department of Ocean Sciences, Inha University, Incheon, South Korea, [3]East Sea Research Institute, Korea Institute of Ocean Science & Technology, Uljin, South Korea

Vertical profiles of ^{228}Ra (half-life: 5.75 years) in the ocean provide valuable information on water mixing and ages of the upper ocean. However, its application is hampered by extremely low levels of ^{228}Ra in the deep ocean. In this study, we measured high-resolution ^{228}Ra/^{226}Ra ratio profiles (>21 depths) in the East Sea (Japan Sea) by mooring Mn-fiber. Using the measured ^{228}Ra profile from ^{228}Ra/^{226}Ra ratios and ^{226}Ra activities, together with other previously published data, we estimated the vertical eddy diffusivity (8.7–9.6 cm^2 s^{-1}) in the permanent thermocline and water ages (10–15 years) in the upper 500–1000 m range. The estimated decomposition rate of organic carbon based on oxygen utilization rates using Ra-ages between 100 and 1000 m was 4.4 ± 0.8 mol C m^{-2} yr^{-1}. Our results show that ~50% of the upward nutrients through 100 m support export production, and that dissolved organic carbon accounts for ~20% of carbon export. This ^{228}Ra approach provides a holistic understanding of carbon and nutrient cycles in the ocean.

KEYWORDS

Ra-228, Ra-226, nutrients, export production, eddy diffusivity, water age, East Sea

Introduction

The vertical water ventilation rate of the ocean thermocline determines the fluxes of nutrients, organic carbon, and other chemical constituents in the ocean. However, it is challenging to determine vertical water mixing rates owing to their dynamic nature, including wind-driven agitation, eddies, fronts, and thermohaline circulation. Thus, geochemists often use tracers to gauge the time-integrated vertical mixing rates in the ocean. The transient tracers for water ages include chlorofluorocarbons (CFCs),

δ^3He-^{3}H, and ^{137}Cs (Jenkins, 1988; Min and Warner, 2005; Hahm and Kim, 2008; Tsabaris et al., 2020), and the steady-state tracers include cosmogenic ^{14}C, ^{228}Ra, and ^{226}Ra over a basin scale (Moore, 1972; Sarmiento et al., 1976; Moore, 2000; Nozaki and Yamamoto, 2001; Charette et al., 2007).

Transient tracers can be used to determine pathways over a certain period after their arrival in the ocean. Atmospheric concentrations of CFCs began to increase in the 1930s and have decreased since the mid-1990s (Dutay et al., 2002; Bullister, 2015). CFC-11 and CFC-12 enter the surface ocean *via* gas exchange and have been successfully used as time-dependent ocean tracers for the last three decades (Bullister and Weiss, 1983; Warner et al., 1996; Min and Warner, 2005). ^{3}H (half-life: 12.3 years) was introduced into the atmosphere from nuclear bomb tests in the 1950s and the 1960s. The ^{3}H-^{3}He parent-daughter pair has been applied to estimate water circulation, mixing rates, and water ages (Jenkins, 1977; Jenkins, 1988; Hahm and Kim, 2008). Bomb-produced ^{137}Cs (half-life: 30.2 years), which peaked during the 1960s, has also been used to trace water mixing (Ito et al., 2003; Tsumune et al., 2003), although it undergoes unknown scavenging, land-based redistribution, and source-input variations. Overall, the use of transient tracers for water-mass mixing rates includes large uncertainties because the time and amount of their inputs to the ocean are not well defined.

Steady-state tracers are not significantly affected by time-dependent variations in source terms; however, their natural source inputs vary significantly over space and time. Their main advantage is the continuous integration of natural processes over a certain period (depending on the half-life of the radionuclides). A cosmogenic nuclide, ^{14}C (half-life: 5730 years), has been useful in estimating global deep-water ages (Matsumoto, 2007), but its application often includes large uncertainties owing to bomb-produced source inputs. The tracers ^{228}Ra (half-life: 5.75 years) and ^{226}Ra (half-life: 1622 years) have been found to be useful for tracing water mixing rates and submarine groundwater discharge over a basin scale (Moore, 2000; Moore, 2003). The main sources of ^{228}Ra and ^{226}Ra in the ocean are marine sediments and groundwater (Moore, 1972; Trier et al., 1972; Kaufman et al., 1973; Sarmiento et al., 1976; Sarmiento et al., 1982; Ku and Luo, 1994; Van Beek et al., 2008; Xu et al., 2022). However, the main disadvantage of ^{228}Ra application in the ocean is that a sample volume of >1000 L for deep water is required to obtain reliable vertical profiles.

Many traditional transient tracers will be phased out in the future; therefore, the use of steady-state tracers will become important for studying oceanic processes. In this study, we attempted to (1) obtain water ages and vertical eddy diffusivities integrated over a period of a decade based on high-resolution ^{228}Ra profiles obtained using a mooring system and (2) apply such physical information to evaluate oxygen utilization rate (OUR) and decomposition rate of organic carbon, as well as to measure the fluxes of nutrients and dissolved organic carbon (DOC) at depths of 100 m and 200 m. This was performed in the East/Japan Sea (hereafter referred to as the East Sea), which is a semi-closed marginal sea in the northwestern Pacific. It is often regarded as a miniature global ocean because it has its own thermohaline ventilation system with a turnover time of approximately 100 years (Kim et al., 2001).

Materials and methods

Study site

The East Sea is a semi-closed marginal sea located in the northwestern Pacific region between the Eurasian continent and Japan. The East Sea consists of three major basins: the Ulleung Basin (UB) in the southwest (>2000 m deep), the Yamato Basin in the south (>2000 m deep), and the Japan Basin in the north (~4000 m deep; Isobe and Isoda, 1997). Water exchange between the East Sea and North Pacific Ocean is limited to the upper layer (~150 m) through four channels: the Korea, Tsugaru, Soya, and Tatar straits (Talley et al., 2003). The temperature of the water masses below approximately 300 m is uniform at 1°C across the entire ocean (Chang et al., 2016). The surface ocean includes various oceanic features, such as subpolar fronts in the central region of the East Sea, warm water in the south, cold water in the north, and numerous eddies (Kim and Legeckis, 1986; Kubota, 1990; Park et al., 2007).

Sampling and analytical methods

Since the activity of ^{228}Ra is extremely low in deep-sea water, we determined the ratios of ^{228}Ra and ^{226}Ra by mooring MnO_2-impregnated fibers (Mn-fibers) at fixed stations where the sediment traps were deployed. Approximately 20 Mn-fibers packed in mesh bags were attached to a wire at each sampling depth (>21 depths). Mn-fiber samples were collected after mooring for 12 days (May 18–29, 2017) at station EC1, 166 days (October 16, 2017 to March 30, 2018) at station EC-trap1, and 164 days (October 17, 2017 to March 29, 2018) at station EC-trap2 in the UB (Figure 1). We neglected any Ra adsorbed onto the Mn-fiber during deployment and retrieval. In addition, samples of approximately 60 L were taken at five depths from mooring station EC1 using a rosette sampler to quantitatively measure ^{226}Ra activity. The collected seawater sample was gravity-fed through a column of acrylic fiber impregnated with MnO_2 at<1 L min^{-1} onboard (Moore, 1976). The activities of ^{228}Ra were then calculated by multiplying the measured ^{226}Ra activities by the measured ^{228}Ra/^{226}Ra ratios in the Mn-fiber samples.

The ^{228}Ra/^{226}Ra activity ratios and ^{226}Ra activities of the samples were measured using a gamma counter. Mn-fiber samples were rinsed gently with distilled water to remove any

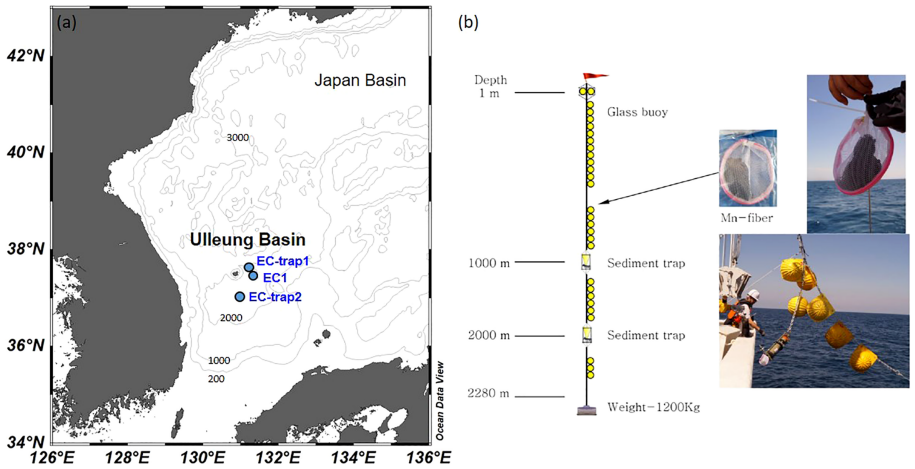

FIGURE 1
(A) Geographic locations of Ra mooring stations (blue circle) in the Ulleung Basin (UB) of the East Sea (Japan Sea) in 2017. **(B)** A simplified schematic of the mooring system (left) and photographs of Mn-fiber mesh bags attached to the mooring line (right).

salts, and then the Mn-fibers were ashed at 820°C for 16 h in a muffle furnace and transferred to a sealed vial. The ^{228}Ra/^{226}Ra activity ratios were measured using a high-purity Germanium well-type detector (CANBERRA Industries Inc., Meriden, CT, USA) by counting its daughter nuclide ^{228}Ac at 911 keV and ^{214}Pb at 351.9 keV, respectively.

Calculation of vertical eddy diffusivity based on a ^{228}Ra profile

If the offshore vertical distribution of ^{228}Ra is governed by eddy diffusion, a simple one-dimensional diffusion model (Moore, 2000; Charette et al., 2007) can be expressed as

$$\frac{dA}{dt} = K_Z \frac{\partial^2 A}{\partial z^2} - \lambda A \quad (1)$$

where A is the activity of ^{228}Ra (dpm/100 L), K_z is the vertical eddy diffusion coefficient, z is the depth (m), and λ is the decay constant of ^{228}Ra. In this model, we assume that the only source of Ra is the surface and that the advection or biological effect for Ra is negligible. Assuming a steady-state, Eq. (1) can be written as

$$A_Z = A_0 \cdot exp\left[-z\sqrt{\frac{\lambda}{K_Z}}\right] \quad (2)$$

where A_Z is the Ra activity at a water depth z (m) below the surface. Here, A_0 is the Ra activity at a depth of 100 m (bottom of the mixed layer).

If the ^{228}Ra sources are from both the surface and bottom, although the other assumptions remain the same, the K_Z value can be obtained by applying a two-source diffusion model (Cai et al., 2002). Taking the boundary conditions $A = A_0$ at $z = 0$ and $A = A_L$ at $z = z_L$, the equation can be expressed as

$$Az = \left(A_L \sinh\left[(\lambda/K_V)^{1/2} z\right]\right) + A_0 \sinh\left[(\lambda/K_V)^{1/2}(z_L - z)\right]\left(\sinh\left[(\lambda/K_V)^{1/2} z_L\right]\right)^{-1} \quad (3)$$

where λ is the decay constant of ^{228}Ra and the boundary value A_L is fixed at depth z_L (2280 m). By fitting the above equation to the vertical profile of ^{228}Ra with an observed value (A_L = 5.93 dpm/100 L) at 2280 m, we obtain the following equation:

$$A = (59.3 \sinh(0.002z) + 100.8 \sinh[0.002(2280 - z)])/47.8 \quad (n = 22,\ R = 0.96) \quad (4)$$

Calculation of water ages based on a ^{228}Ra profile

The decay of ^{228}Ra can be also used to determine the water mass age at each depth in the upper 1000 m, by assuming the constant initial ^{228}Ra activity in the surface and downward supply using the equation

$$\left[^{228}Ra\right]_{obs} = \left[^{228}Ra\right]_i e^{-\lambda_{228} t} \quad (Eq.5)$$

where $[228Ra]_{obs}$ is observed activity of ^{228}Ra at the sampling depth, $[228Ra]_i$ is the initial activity of ^{228}Ra in the surface water, λ_{228} is the decay constant for the ^{228}Ra, and t is the water age. Here, we obtained water ages only for the upper 1000 m where the contribution of bottom sources is relatively small based on the ^{228}Ra vertical profiles.

Results

Vertical profiles of Ra isotopes

Relatively higher $^{228}Ra/^{226}Ra$ activity ratios (~1.0) were observed at the surface and decreased sharply at mid-depths across the thermocline (~0.2 at 500 m), similar to previously published data in the East Sea (Figure 2A). Although the duration and seasons of mooring were different, the $^{228}Ra/^{226}Ra$ profiles at stations EC1, EC-trap1, and EC-trap2 were consistent, indicating the reliability of this approach. In contrast, the $^{228}Ra/^{226}Ra$ activity ratios increased toward the bottom at station EC1, where the sampling approached ~33 m above the bottom (Figure 2A). This trend was not observed at stations EC-trap1 and EC-trap2, where the deepest sampling depths were 260 m and 100 m above the bottom, respectively. The activities of ^{226}Ra were lowest (9.7 ± 0.2 dpm/100 L) at the surface and increased by a factor of ~2 with depth (Figure 2B). Such a gradual vertical increase in ^{226}Ra is commonly observed in the major oceans (Inoue et al., 2020; Hsieh et al., 2021). The calculated ^{228}Ra activities were higher (11 ± 4 dpm/100 L) at the surface and decreased exponentially with depth across the thermocline (Figure 2C and Supplementary Table 1).

Vertical eddy diffusivity

The observed ^{228}Ra data in the East Sea indicate that water mixing in the thermocline is dominated by eddy diffusion, because the plot (K_Z) of $ln(A_0/A_z)$ versus depth z (m) is linear (Supplementary Figure 1), as explained by Moore (2000). If only the surface supply of ^{228}Ra was assumed, based on Equation (2), the vertical eddy diffusion coefficient (K_Z) across 100–400 m in the East Sea was estimated to be approximately 8.7 $cm^2\ s^{-1}$. If the supply of ^{228}Ra from the surface and bottom layers is considered, based on Equation (3), the vertical eddy diffusion coefficient (K_Z) was estimated to be 8.7–9.6 $cm^2\ s^{-1}$.

The results of the K_Z fitting to the ^{228}Ra profiles are shown in Figure 3A. The best-fit curve to the profile ranged between 2 and 14 $cm^2\ s^{-1}$, which agrees with the values obtained using Equations (2) and (3).

Discussion

Vertical distribution characteristics of Ra isotopes in the UB

In general, ^{228}Ra activity is higher in the surface layer of the global ocean because it is mainly supplied by the continental shelf bottom sediment and the subsequent rapid horizontal mixing (Moore, 1969; Nozaki et al., 1998). In the East Sea, the higher ^{228}Ra activity water was mainly from the continental shelf of the Yellow Sea and East China Sea (Cho et al., 2019). Owing to the long water residence times (~5 years) and large shelf dimensions (~1 × 10^6 km^2), these activities are known to be the highest in the world's oceans (40 ± 20 dpm/100 L, Nozaki et al., 1991; Su et al., 2013). An increase in ^{228}Ra activity in the bottom layer of the deep ocean has also been observed (~6 dpm/100 L at 2280 m to ~1.6 dpm/100 L at 1500 m) associated with its bottom sediment supply. Moore (1969) showed that the increase in ^{228}Ra in the bottom layer is generally observed within 100 m

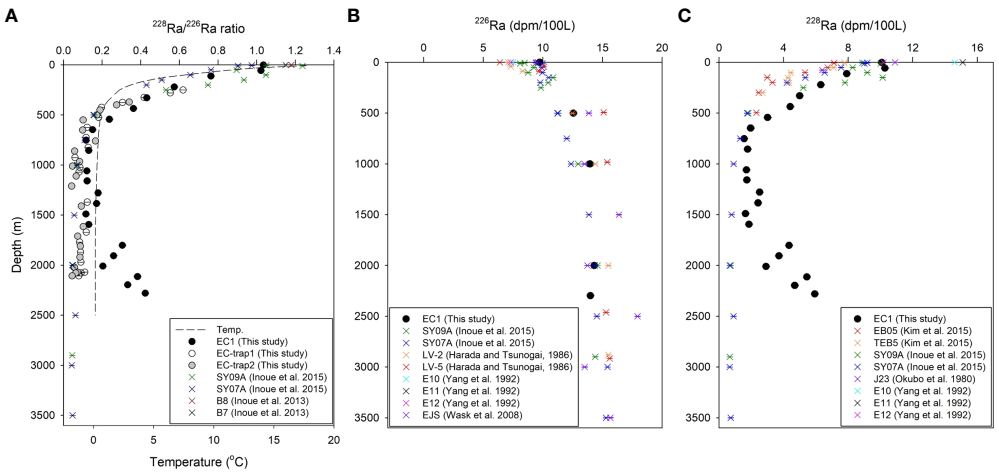

FIGURE 2
Depth profiles of **(A)** 228Ra/226Ra ratios **(B)** ^{226}Ra, and **(C)** ^{228}Ra at stations EC1, EC-trap1, EC-trap2, and other stations from previous studies. The bottom depth at station EC1 is 2313 m.

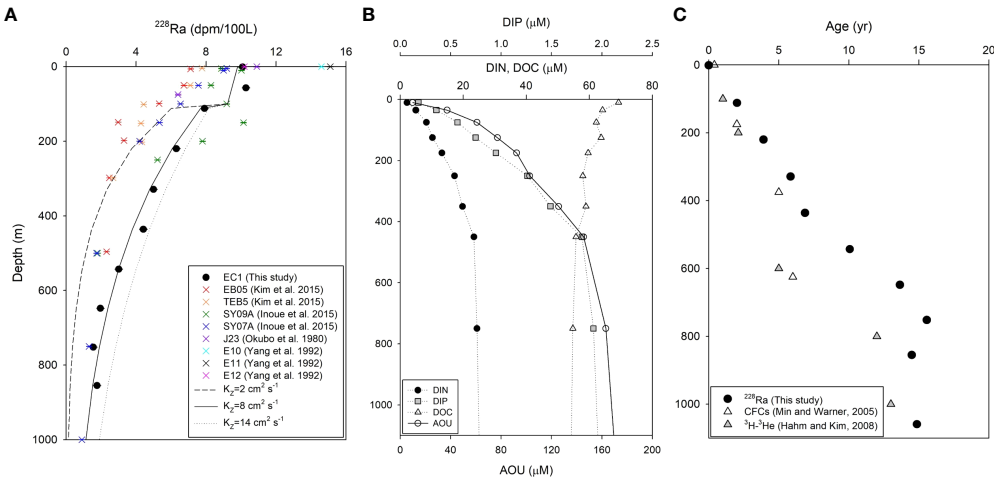

FIGURE 3
(A) Model estimates of K_z fitted to the ^{228}Ra profiles in the Ulleung Basin (UB). **(B)** Vertical profiles of apparent oxygen utilization (AOU), dissolved inorganic nitrogen (DIN) and phosphorus (DIP), and dissolved organic carbon (DOC) from 2006 to 2017 in the UB, East Sea. The dataset is available at the JOISS portal system (http://joiss.kr) which collects and provides marine research data in Korea. **(C)** Comparison of ^{228}Ra-ages (circles; this study), CFC-11/CFC-12 ratio ages (white triangle; Min and Warner, 2005) in the UB, and ^{3}H-^{3}He ages in the Japan Basin (Hahm and Kim, 2008).

from the bottom, which is the benthic boundary layer of the major ocean. This increase is commonly observed in the major oceans (Huh and Ku, 1998; Cai et al., 2002; Charette et al., 2007).

Owing to its relatively long half-life (1622 years), the effect of radioactive decay is negligible in this sea. A constant vertical value from 1000 m to the bottom for ^{226}Ra was observed (Figure 2B) owing to the well-mixed nature of the deep East Sea (Matsuno et al., 2015). Although there is a significant supply of ^{226}Ra, together with ^{228}Ra from the shelf water, it seems to be much smaller than the supply from the bottom of the East Sea.

Vertical eddy diffusivity in the UB

The vertical eddy diffusion coefficient (K_Z) estimated using the ^{228}Ra tracer, in this study, ranged from 8.7 to 9.6 cm^2 s^{-1} in the UB. In the Yamato and Japan basins the vertical eddy diffusivities obtained from ^{236}U data for six stations varied between 3.4 and 5.6 cm^2 s^{-1} (Sakaguchi et al., 2016) in the 150 m bottom depth (>3000 m) layer. As such, the vertical eddy diffusivity determined from the vertical ^{90}Sr and ^{137}Cs distributions from the surface to ~2000 m was 4.8 ± 0.7 cm^2 s^{-1} (Hirose and Povinec, 2020). The eddy diffusivity from the gradient of the ^{228}Ra activity around the Yamato Ridge was calculated as ~6 cm^2 s^{-1} from the surface to ~1000 m (Tanaka et al., 2006).

The eddy diffusivity in the 100–400 m depth observed in this study was higher than those observed off the coast of Southern California in the equatorial Pacific (1.6 cm^2 s^{-1} for the upper 150 m, Knauss et al., 1978), the equatorial Atlantic (0.1 cm^2 s^{-1} at 150 m and 0.5 cm^2 s^{-1} at 150–225 m, Moore, 1972), and the South China Sea (0.2 cm^2 s^{-1} for the upper 300 m, Cai et al., 2002). However, the eddy diffusivity in this sea is one to two orders of magnitude lower than that obtained in the Crozet Plateau region, Southern Ocean (11–100 cm^2 s^{-1} in the upper 300 m, Charette et al., 2007) using a 1-D eddy-diffusion-mixing model applied to a ^{228}Ra profile.

Vertical exchange of nutrients and DOC

The vertical upward/downward fluxes of nutrients and DOC were calculated by multiplying the calculated eddy diffusivity by nutrient gradients and DOC. In this study, we used datasets for nutrients and DOC in the East Sea from 2006 to 2017. The dataset is available from the JOISS portal system (http://joiss.kr), which collects and provides marine research data in Korea. The concentrations of dissolved inorganic nitrogen (DIN) and phosphorus (DIP) exhibited nutrient depletion at the surface and increased with depth, whereas the vertical trend of DOC was higher in the surface layer than in the deep ocean (Figure 3B). The concentrations of nutrients (DIN and DIP) and DOC showed good negative and positive correlations with ^{228}Ra activity, respectively, in the 100–400 m layer (Supplementary Figure 2).

The DIN, DIP, and DOC gradients through 100 m (the annual average euphotic zone) were calculated to be approximately 0.06, 0.005, and -0.04 μM m^{-1}, respectively. From these gradient values and the calculated vertical eddy diffusivity, we calculated the vertical nutrient and DOC fluxes. The upward fluxes of DIN and DIP at a depth of 100 m were

estimated to be ~1.8 mol N m^{-2} yr^{-1} and ~0.1 mol P m^{-2} yr^{-1}, respectively, and the downward flux of DOC was estimated to be ~1.3 mol C m^{-2} yr^{-1}. Similarly, the upward fluxes of DIN and DIP at a depth of 200 m were estimated to be ~1.2 mol N m^{-2} yr^{-1} and ~0.1 mol P m^{-2} yr^{-1}, respectively, and the downward flux of DOC was estimated to be ~0.6 mol C m^{-2} yr^{-1}. The ventilation of water, export production, and the exchange of chemical species in the upper ocean of the East Sea were estimated for a water depth of 200 m in previous studies (Jenkins, 2008; Hahm and Kim, 2008; Kim and Kim, 2013), as the mixed layer in winter often extends to 200 m in the northern part of the sea (Lim et al., 2012). Thus, in this study, for easy comparison with previous studies, we calculated the vertical exchange of nutrients and carbon through 200 m.

Water ages and oxygen utilization rate

We obtained water ages in the UB of the East Sea using Equation (5) finding that it increased with depth and was approximately 15 years at 800 m (Figure 3C). The age of the oldest water in this study agrees with that estimated using ^{3}H-^{3}He tracers. However, the ages of the intermediate water mass between 500 and 800 m calculated in this study were much older than those estimated using CFC-11/CFC-12 ratios or ^{3}H-^{3}He (Figure 3C). This difference could be due to large uncertainties (< 50%) in the CFC ratio age (Min and Warner, 2005) or a more active supply of surface water during the winter of 2000–2001, as suggested by previous studies (Kim et al., 2002; Talley et al., 2003). Yoon et al. (2018) suggested a reduced formation of intermediate water based on the decline in oxygen content.

The OUR in subsurface water between 100 and 1000 m can be determined by the good correlation between the apparent oxygen utilization (AOU) and water age (Figure 4). The AOU is defined as the difference between the oxygen equilibrium value with the atmosphere at the temperature and salinity of the water and the observed oxygen concentration in the same seawater sample. Assuming that the oxygen saturation is almost 100% in the surface water, the integration of OUR in the water column yields a net oxygen consumption of 4.6 ± 1.0 mol m^{-2} yr^{-1} in the layer between 100 and 500 m, and approximately 1.7 ± 0.4 mol m^{-2} yr^{-1} in the layer between 500 and 1000 m based on the slope of AOU versus water ages (Figure 4). The AOU values were calculated based on oxygen, temperature, and salinity data (2006–2017) available on the JOISS portal system (http://joiss.kr).

OUR and carbon export

The OUR values can be converted to the decomposition rate of organic carbon in the water mass using C:O stoichiometry

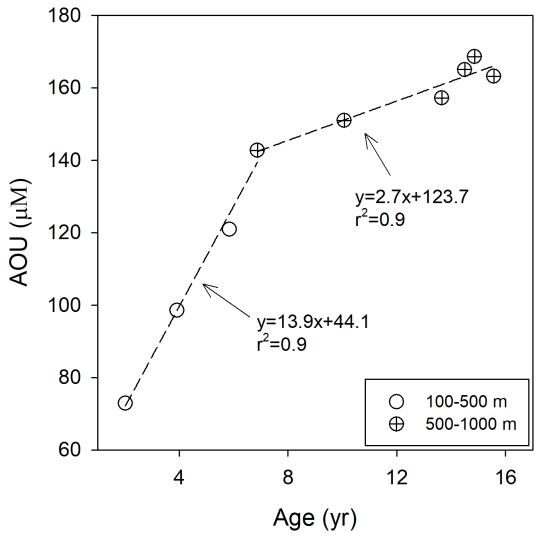

FIGURE 4
Water mass ages versus apparent oxygen utilization (AOU) from 100 to 1000 m in the Ulleung Basin.

(Anderson and Sarmiento, 1994). The estimated decomposition rate of sinking organic carbon in the upper 100–500 m is 3.2 ± 0.7 mol m^{-2} yr^{-1}, and 1.2 ± 0.3 mol m^{-2} yr^{-1} at a water depth of 500–1000 m (Figure 5). This result is similar to the estimated export production (~5.3 mol C m^{-2} yr^{-1}) in the UB of 200–1600 m by using ^{3}H and ^{3}He tracers (Kim and Hahm, 2001). Our method showed that ~65% and ~90% of the sinking organic carbon decomposed at depths of 100–500 and 100–1000 m, respectively (Figure 5). Owing to the limitation of age calculation based on ^{228}Ra, we could not estimate the OUR below 1000 m. Particulate organic carbon (POC) sinking fluxes in the UB at 1000 m were 0–2.6 (0.8 ± 0.5) mol C m^{-2} yr^{-1} based on the sediment trap (Kwak et al., 2017; Kim et al., 2020). Kim et al. (2020) showed that approximately 96% of sinking organic matter is re-mineralized in the upper 1000 m, based on sediment trap studies in this sea. The difference in the DIN fluxes (~0.6 N) between the 100 m (~1.8 N) and 200 m (~1.2 N) depths should be due to the decomposition of DOC and POC fluxes at depth.

According to Kim et al. (2011), POC sinking fluxes in the upper 100 m of the UB were estimated to be 4.9 ± 2.3 mol C m^{-2} yr^{-1} based on measured seasonal variations in $^{234}Th/^{238}U$ disequilibria. As observed in this study, the estimated upward flux of DIN through 100 m supplies approximately 200% of the carbon (DOC + POC) export (Figure 5) based on the Redfield stoichiometry of C:N=106:16. This difference is reasonable because the nutrients that reached the euphotic zone can only be utilized from spring to fall. The estimated downward flux of DOC through 200 m is 50% of that at 100 m. This result shows the effective remineralization of DOC in the subsurface layer as

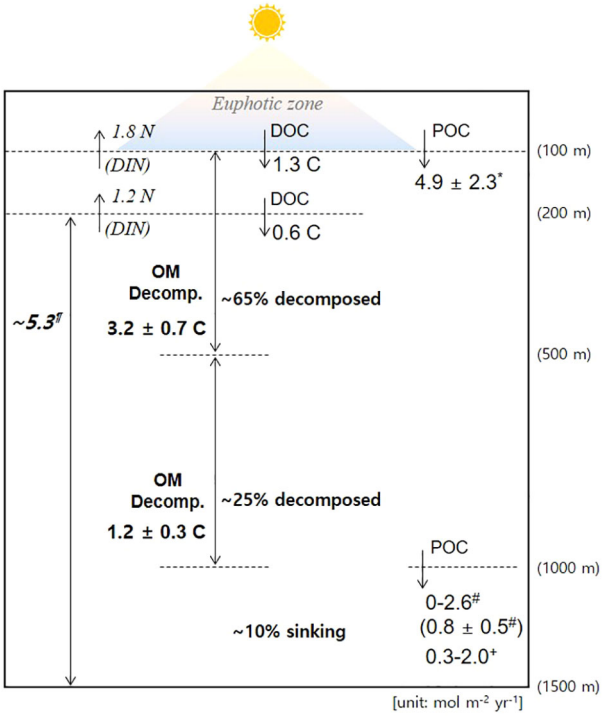

FIGURE 5
A schematic of the vertical fluxes of dissolved inorganic nitrogen (DIN) and organic carbon in the upper East Sea. The vertical fluxes of DIN and dissolved organic carbon (DOC) are based on the DIN and DOC gradients and the estimated eddy diffusivity. OM Decomp. denotes the decomposition rate of organic matter/carbon, which is estimated based on the Ra-age-based oxygen utilization rates (OUR). The downward fluxes of particulate organic carbon (POC) are from previous studies: #Sediment trap (at 1000 m, Kim et al., 2020), +Sediment trap (at 1000 m, Kwak et al., 2017), *234Th method (Kim et al., 2011), and ¶carbon export production using ^{3}H and ^{3}He tracers (Kim and Hahm, 2001).

opposed to the unusually slow degradation in the deep layer (Kim et al., 2015). Our results show that DOC accounts for approximately 20% of the total organic carbon export at 100 m (Figure 5), which is lower than that in other regions, including the northern slope of the South China Sea (Zhang et al., 2020), northwestern Sargasso Sea (Carlson et al., 1994), and subtropics (Doval and Hansell, 2000). Kim et al. (2015) showed that DOC in the deep ocean of the East Sea is highly conservative and uniform owing to the lower temperature. Thus, it is likely that POC plays a major role in carbon sequestration in this sea.

Conclusion

^{228}Ra profiles were used to estimate the vertical nutrient and organic carbon fluxes in the UB of the East Sea. The vertical eddy diffusivity (K_z) was estimated to be approximately 8.7–9.6 cm^2 s^{-1} using one-dimensional diffusion-mixing models of the ^{228}Ra profiles. By combining the vertical eddy diffusivity with the dissolved nutrients and DOC profiles, we estimated the upward fluxes of DIN and DIP and the downward DOC flux at depths of 100 m and 200 m. In addition, the OUR was estimated by dividing the AOU by the ^{228}Ra age. Then, the decomposition rates of organic carbon at different water depths (i.e., upper 500 and 1000 m) were obtained using the OUR. These results suggest that high-resolution measurements of vertical ^{228}Ra profiles are useful for understanding the cycling of carbon and nutrients at different water depths. Our approach can be s similarly applied to other marginal seas and global oceans.

Data availability statement

The datasets presented in this study can be found in online repositories. The names of the repository/repositories and accession number(s) can be found in the article/Supplementary Material.

Author contributions

H-MC and GK wrote the manuscript and analyzed the data. GK contributed to the conception of the study. YH and Y-IK

contributed to sample collection. YH and CB performed the chemical measurements of radium isotopes. All authors contributed to the article and approved the submitted version.

Funding

This work was supported by the project titled "Deep Water Circulation and Material Cycling in the East Sea (20160400)", funded by the Ministry of Oceans and Fisheries, Korea, and the National Research Foundation (NRF) funded by the Korean government (NRF-2018R1A2B3001147). This research was also supported by the Research Program for the carbon cycle between oceans, land, and atmosphere of the National Research Foundation (NRF) funded by the Ministry of Science and ICT (2022M3I6A1085698). This study was also partially supported by Korea Institute of Marine Science & Technology Promotion(KIMST) funded by the Ministry of Oceans and Fisheries(20220533).

Conflict of interest

The reviewer TR declared a shared parent affiliation with the author Y-IK to the handling editor at the time of review.

The remaining authors declare that the research was conducted in the absence of any commercial or financial relationships that could be constructed as a potential conflict of interest.

Publisher's note

Supplementary material

The Supplementary Material for this article can be found online at: https://www.frontiersin.org/articles/10.3389/fmars.2022.987315/full#supplementary-material

SUPPLEMENTARY FIGURE 1
ln(A0/AZ) values against water depth (m) at the EC1 station, where A0 is the ^{228}Ra activity at the boundary (100 m depths, bottom of the mixed layer), and AZ is the 228Ra activity water depth z (m).

SUPPLEMENTARY FIGURE 2
Correlations between ^{228}Ra activities and the concentrations of (a) dissolved inorganic nitrogen (DIN) and phosphorus (DIP) and (b) dissolved organic carbon (DOC) from 100 m to 400 m (the permanent thermocline of the East Sea).

References

Anderson, L. A., and Sarmiento, J. L. (1994). Redfield ratios of remineralization determined by nutrient data analysis. *Glob. Biogeochem. Cycles* 8 (1), 65–80. doi: 10.1029/93GB03318

Bullister, J. (2015). *Atmospheric histories, (1765–2015) for CFC-11, CFC-12, CFC-113, CCl4, SF6 and N2O, NDP-095* (Oak Ridge, Tennessee: Carbon Dioxide Information Analysis Center, Oak Ridge National Laboratory, US Department of Energy). doi: 10.3334/CDIAC/otg.CFC_ATM_Hist_2015

Bullister, J. L., and Weiss, R. F. (1983). Anthropogenic chlorofluoromethanes in the Greenland and Norwegian seas. *Science* 221, 265–268. doi: 10.1126/science.221.4607.265

Cai, P., Huang, Y., Chen, M., Guo, L., Liu, G., and Qiu, Y. (2002). New production based on ^{228}Ra-derived nutrient budgets and thorium-estimated POC export at the intercalibration station in the south China Sea. *Deep-Sea Res. I: Oceanogr. Res. Pap.* 49 (1), 53–66. doi: 10.1016/S0967-0637(01)00040-1

Carlson, C. A., Ducklow, H. W., and Michaels, A. F. (1994). Annual flux of dissolved organic carbon from the euphotic zone in the northwestern Sargasso Sea. *Nature* 371 (6496), 405–408. doi: 10.1038/371405a0

Chang, K.-I., Zhang, C.-I., Park, C., Kang, D.-J., Ju, S.-J., Lee, S.-H., et al. (2016). *Oceanography of the East Sea (Japan Sea)* (Switzerland: Springer International Publishing).

Charette, M. A., Gonneea, M. E., Morris, P. J., Statham, P., Fones, G., Planquette, H., et al. (2007). Radium isotopes as tracers of iron sources fueling a southern ocean phytoplankton bloom. *Deep-Sea Res. II: Top. Stud. Oceanogr.* 54, 1989–1998. doi: 10.1016/j.dsr2.2007.06.003

Cho, H.-M., Kim, G., Kwon, E. Y., and Han, Y. (2019). Radium tracing cross-shelf fluxes of nutrients in the northwest pacific ocean. *Geophys. Res. Lett.* 46, 11321–11328. doi: 10.1029/2019GL084594

Doval, M. D., and Hansell, D. A. (2000). Organic carbon and apparent oxygen utilization in the western south pacific and the central Indian oceans. *Mar. Chem.* 68 (3), 249–264. doi: 10.1016/S0304-4203(99)00081-X

Dutay, J. C., Bullister, J. L., Doney, S. C., Orr, J. C., Najjar, R., Caldeira, K., et al. (2002). Evaluation of ocean model ventilation with CFC-11: Comparison of 13 global ocean models. *Ocean Model.* 4 (2), 89–120. doi: 10.1016/S1463-5003(01)00013-0

Hahm, D., and Kim, K. R. (2008). Observation of bottom water renewal and export production in the Japan basin, East Sea using tritium and helium isotopes. *Ocean Sci. J.* 43, 39–48. doi: 10.1007/BF03022430

Hirose, K., and Povinec, P. P. (2020). ^{90}Sr and ^{137}Cs as tracers of oceanic eddies in the sea of Japan/East sea. *J. Environ. Radioact* 216, 106179. doi: 10.1016/j.jenvrad.2020.106179

Hsieh, Y. T., Geibert, W., Woodward, E. M. S., Wyatt, N. J., Lohan, M. C., Achterberg, E. P., et al. (2021). Radium-228-derived ocean mixing and trace element inputs in the south Atlantic. *Biogeosciences* 18 (5), 1645–1671. doi: 10.5194/bg-18-1645-2021

Huh, C. A., and Ku, T. L. (1998). A 2–d section of ^{228}Ra and ^{226}Ra in the northeast pacific. *Oceanol. Acta* 21 (4), 533–542. doi: 10.1016/S0399-1784(98)80036-4

Inoue, M., Takehara, R., Hanaki, S., Kameyama, H., Nishioka, J., and Nagao, S. (2020). Distributions of radiocesium and radium isotopes in the western Bering Sea in 2018. *Mar. Chem.* 225, 103843. doi: 10.1016/j.marchem.2020.103843

Isobe, A., and Isoda, Y. (1997). Circulation in the Japan basin, the northern part of the Japan Sea. *J. Oceanogr.* 53, 373–382.

Ito, T., Aramaki, T., Kitamura, T., Otosaka, S., Suzuki, T., Togawa, O., et al. (2003). Anthropogenic radionuclides in the Japan Sea: their distributions and transport processes. *J. Environ. Radioact* 68 (3), 249–267. doi: 10.1016/S0265-931X(03)00064-X

Jenkins, W. J. (1977). Tritium-helium dating in the Sargasso Sea: A measurement of oxygen utilization rates. *Science* 196 (4287), 291–292. doi: 10.1126/science.196.4287.291

Jenkins, W. J. (1988). The use of anthropogenic tritium and helium-3 to study subtropical gyre ventilation and circulation. *Philos. Trans. A. Math. Phys. Eng. Sci.* 325 (1583), 43–61. doi: 10.1098/rsta.1988.0041

Jenkins, W. J. (2008). The biogeochemical consequences of changing ventilation in the Japan/East Sea. *Mar. Chem.* 108 (3-4), 137–147. doi: 10.1016/S0265-931X(03)00064-X

Kaufman, A., Trier, R. M., Broecker, W. S., and Feely, H. W. (1973). Distribution of ^{228}Ra in the world ocean. *J. Geophys. Res.* 78, 8827–8848. doi: 10.1029/JC078i036p08827

Kim, D., Choi, M. S., Oh, H. Y., Song, Y. H., Noh, J. H., and Kim, K. H. (2011). Seasonal export fluxes of particulate organic carbon from ^{234}Th/^{238}U disequilibrium measurements in the ulleung Basin[1] (Tsushima basin) of the East Sea[1] (Sea of Japan). *J. Oceanogr.* 67 (5), 577–588. doi: 10.1007/s10872-011-0058-8

Kim, K. R., and Hahm, D. S. (2001). An estimation of the new production in the southern East Sea using helium isotopes. *J. Korean Soc. Oceanogr.* 36 (1), 19–26.

Kim, T.-H., and Kim, G. (2013). Factors controlling the C:N:P stoichiometry of dissolved organic matter in the n-limited, cyanobacteria-dominated East/Japan Sea. *J. Mar. Syst.* 115-116, 1–9. doi: 10.1016/j.jmarsys.2013.01.002

Kim, M., Kim, Y.-I., Hwang, J., Choi, K. Y., Kim, C. J., Ryu, Y. J., et al. (2020). Influence of sediment resuspension on the biological pump of the southwestern East Sea (Japan Sea). *Front. Earth Sci.* 8. doi: 10.3389/feart.2020.00144

Kim, K. R., Kim, G., Kim, K., Lobanov, V., Ponomarev, V., and Salyuk, A. (2002). A sudden bottom-water formation during the severe winter 2000–2001: The case of the East/Japan Sea. *Geophys. Res. Lett.* 29 (8), 75–71. doi: 10.1029/2001GL014498

Kim, T.-H., Kim, G., Lee, S. A., and Dittmar, T. (2015). Extraordinary slow degradation of dissolved organic carbon (DOC) in a cold marginal sea. *Sci. Rep.* 5 (1), 1–6. doi: 10.1038/srep13808

Kim, K., Kim, K. R., Min, D. H., Volkov, Y., Yoon, J. H., and Takematsu, M. (2001). Warming and structural changes in the East (Japan) Sea: A clue to future changes in global oceans? *Geophys. Res. Lett.* 28 (17), 3293–3296. doi: 10.1029/2001GL013078

Kim, K., and Legeckis, R. (1986). Branching of the tsushima current in 1981–83. *Prog. Oceanogr.* 17 (3-4), 265–276. doi: 10.1016/0079-6611(86)90049-2

Knauss, K. G., Ku, T. L., and Moore, W. S. (1978). Radium and thorium isotopes in the surface waters of the East pacific and coastal southern California. *Earth Planet. Sci. Lett.* 39 (2), 235–249. doi: 10.1016/0012-821X(78)90199-1

Kubota, M. (1990). Variability of the polar front in the Japan Sea. *Sora to Umi* 12, 35–44.

Ku, T. L., and Luo, S. (1994). New appraisal of radium 226 as a large-scale oceanic mixing tracer. *J. Geophys. Res. Oceans* 99 (C5), 10255–10273. doi: 10.1029/94JC00089

Kwak, J. H., Han, E., Hwang, J., Kim, Y. I., Lee, C. I., and Kang, C. K. (2017). Flux and stable c and n isotope composition of sinking particles in the ulleung basin of the East/Japan Sea. *Deep-Sea Res. II: Top. Stud. Oceanogr.* 143, 62–72. doi: 10.1016/j.dsr2.2017.03.014

Lim, S., Jang, C. J., and Park, J. (2012). Climatology of the mixed layer depth in the East/Japan Sea. *J. Mar. Sys* 96, 1–14. doi: 10.1016/j.jmarsys.2012.01.003

Matsumoto, K. (2007). Radiocarbon-based circulation age of the world oceans. *J. Geophys. Res. Oceans* 112, C9004. doi: 10.1029/2007JC004095

Matsuno, T., Endoh, T., Hibiya, T., Senjyu, T., and Watanabe, M. (2015). Formation of the well-mixed homogeneous layer in the bottom water of the Japan Sea. *J. Oceanogr.* 71, 441–447. doi: 10.1007/s10872-015-0303-7

Min, D. H., and Warner, M. J. (2005). Basin-wide circulation and ventilation study in the East Sea (Sea of Japan) using chlorofluorocarbon tracers. *Deep-Sea Res. II: Top. Stud. Oceanogr.* 52, 1580–1616. doi: 10.1016/j.dsr2.2003.11.003

Moore, W. S. (1969). Oceanic concentrations of ^{228}radium. *Earth Planet. Sci. Lett.* 6, 437–446. doi: 10.1016/0012-821X(69)90113-7

Moore, W. S. (1972). Radium-228: Application to thermocline mixing studies. *Earth Planet. Sci. Lett.* 16, 421–422. doi: 10.1016/0012-821X(72)90161-6

Moore, W. S. (1976). Sampling ^{228}Ra in the deep ocean. *Deep Sea Res. Oceanogr. Abstr.* 23, 647–651. doi: 10.1016/0011-7471(76)90007-3

Moore, W. S. (2000). Determining coastal mixing rates using radium isotopes. *Cont. Shelf Res.* 20, 1993–2007. doi: 10.1016/S0278-4343(00)00054-6

Moore, W. S. (2003). Sources and fluxes of submarine groundwater discharge delineated by radium isotopes. *Biogeochemistry* 66, 75–93. doi: 10.1023/B:BIOG.0000006065.77764.a0

Nozaki, Y., Dobashi, F., Kato, Y., and Yamamoto, Y. (1998). Distribution of Ra isotopes and the ^{210}Pb and ^{210}Po balance in surface seawaters of the mid northern hemisphere. *Deep-Sea Res. I: Oceanogr. Res. Pap.* 45, 1263–1284. doi: 10.1016/S0967-0637(98)00016-8

Nozaki, Y., Tsubota, H., Kasemsupaya, V., Yashima, M., and Naoko, I. (1991). Residence times of surface water and particle-reactive ^{210}Pb and ^{210}Po in the East China and yellow seas. *Geochim. Cosmochim. Acta* 55, 1265–1272. doi: 10.1016/0016-7037(91)90305-O

Nozaki, Y., and Yamamoto, Y. (2001). Radium 228 based nitrate fluxes in the eastern Indian ocean and the south China Sea and a silicon-induced "alkalinity pump" hypothesis. *Glob. Biogeochem. Cycles* 15, 555–567. doi: 10.1029/2000GB001309

Park, K. A., Ullman, D. S., Kim, K., Chung, J. Y., and Kim, K. R. (2007). Spatial and temporal variability of satellite-observed subpolar front in the East/Japan Sea. *Deep-Sea Res. I: Oceanogr. Res. Pap.* 54, 453–470. doi: 10.1016/j.dsr.2006.12.010

Sakaguchi, A., Nomura, T., Steier, P., Golser, R., Sasaki, K., Watanabe, T., et al. (2016). Temporal and vertical distributions of anthropogenic ^{236}U in the Japan Sea using a coral core and seawater samples. *J. Geophys. Research: Oceans* 121, 4–13. doi: 10.1002/2015JC011109

Sarmiento, J. L., Feely, H. W., Moore, W. S., Bainbridge, A. E., and Broecker, W. S. (1976). The relationship between vertical eddy diffusion and buoyancy gradient in the deep sea. *Earth Planet. Sci. Lett.* 32, 357–370. doi: 10.1016/0012-821X(76)90076-5

Sarmiento, J. L., Rooth, C. G. H., and Broecker, W. S. (1982). Radium 228 as a tracer of basin wide processes in the abyssal ocean. *J. Geophys. Res. Oceans* 87, 9694–9698. doi: 10.1029/JC087iC12p09694

Su, N., Du, J., Li, Y., and Zhang, J. (2013). Evaluation of surface water mixing and associated nutrient fluxes in the East China Sea using ^{226}Ra and ^{228}Ra. *Mar. Chem.* 156, 108–119. doi: 10.1016/j.marchem.2013.04.009

Talley, L. D., Lobanov, V., Ponomarev, V., Salyuk, A., Tishchenko, P., Zhabin, I., et al. (2003). Deep convection and brine rejection in the Japan Sea. *Geophys. Res. Lett.* 30 (4), 1159. doi: 10.1029/2002GL016451

Tanaka, K., Inoue, M., Komura, K., and Misonoo, J. (2006). Vertical profiles of ^{226}Ra, ^{228}Ra and ^{137}Cs activities in seawater around the yamato ridge and coastal areas of the Sea of Japan. *Chikyu Kagaku* 40, 167–176.

Trier, R. M., Broecker, W. S., and Feely, H. W. (1972). Radium-228 profile at the second GEOSECS intercalibration station 1970, in the north Atlantic. *Earth Planet. Sci. Lett.* 16, 141–145. doi: 10.1016/0012-821X(72)90249-X

Tsabaris, C., Kaberi, H., Pappa, F. K., Leivadaros, P., Delfanti, R., Krasakopoulou, E., et al. (2020). Vertical distribution and temporal trends of ^{137}Cs at lemnos and Cretan deep basins of the Aegean Sea, Greece. *Deep-Sea Res. II: Top. Stud. Oceanogr.* 171, 104603. doi: 10.1016/j.dsr2.2019.06.011

Tsumune, D., Aoyama, M., and Hirose, K. (2003). Behavior of ^{137}Cs concentrations in the north pacific in an ocean general circulation model. *J. Geophys. Res. Oceans* 108 (C8), 3262. doi: 10.1029/2002JC001434

Van Beek, P., Bourquin, M., Reyss, J. L., Souhaut, M., Charette, M. A., and Jeandel, C. (2008). Radium isotopes to investigate the water mass pathways on the kerguelen plateau (Southern ocean). *Deep-Sea Res. II: Top. Stud. Oceanogr.* 55, 622–637. doi: 10.1016/j.dsr2.2007.12.025

Warner, M. J., Bullister, J. L., Wisegarver, D. P., Gammon, R. H., and Weiss, R. F. (1996). Basin-wide distributions of chlorofluorocarbons CFC-11 and CFC-12 in the north pacific: 1985–1989. *J. Geophys. Res. Oceans* 101, 20525–20542. doi: 10.1029/96JC01849

Xu, B., Cardenas, M. B., Santos, I. R., Burnett, W. C., Charette, M. A., Rodellas, V., et al. (2022). Closing the global marine ^{226}Ra budget reveals the biological pump as a dominant removal flux in the upper ocean. *Geophys. Res. Lett.* 49 (12), e2022GL098087. doi: 10.1029/2022GL098087

Yoon, S.-T., Chang, K.-I., Nam, S., Rho, T., Kang, D.-J., Lee, T., et al. (2018). Re-initiation of bottom water formation in the East Sea (Japan Sea) in a warming world. *Sci. Rep.* 8, 1–10. doi: 10.1038/s41598-018-19952-4

Zhang, M., Wu, Y., Wang, F., Xu, D., Liu, S., and Zhou, M. (2020). Hotspot of organic carbon export driven by mesoscale eddies in the slope region of the northern south China sea. *Front. Mar. Sci.* 7. doi: 10.3389/fmars.2020.00444

Frontiers in Marine Science

Explores ocean-based solutions for emerging global challenges

The third most-cited marine and freshwater biology journal, advancing our understanding of marine systems and addressing global challenges including overfishing, pollution, and climate change.

Discover the latest Research Topics

See more →

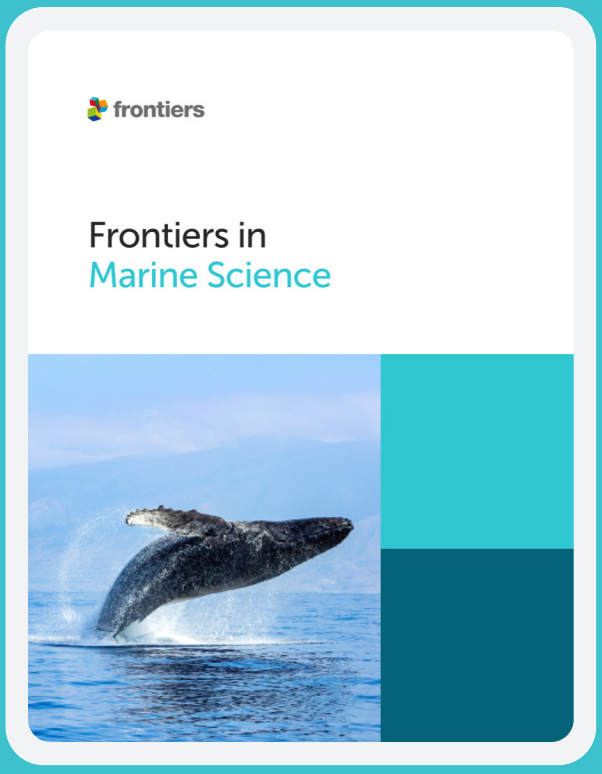

Frontiers

Avenue du Tribunal-Fédéral 34
1005 Lausanne, Switzerland
frontiersin.org

Contact us

+41 (0)21 510 17 00
frontiersin.org/about/contact